Nuno Miguel Pinto Neves

Mestre em Engenharia de Materiais

Al-doped ZnO ceramic sputtering targets based on nanocrystalline powders produced by emulsion detonation synthesis – deposition and application as a transparent conductive oxide material

Dissertação para obtenção do Grau de Doutor
em Ciência e Engenharia de Materiais

Orientador: Doutora Isabel Maria das Mercês Ferreira, Professora Associada, Faculdade de Ciências e Tecnologia – Universidade Nova de Lisboa

Co-orientador: Doutora Ana Lúcia Lagoa, Investigação e Desenvolvimento de Nanomateriais, INNOVNANO – Materiais Avançados, SA

Júri:
Presidente: Professora Doutora Maria Luísa Dias de Carvalho de Sousa Leonardo
Arguentes: Professora Doutora Paula Maria Lousada Silveirinha Vilarinho
Professor Doutor Carlos José de Macedo Tavares
Vogais: Professor Doutor Albano Augusto Cavaleiro Rodrigues de Carvalho
Professora Doutora Elvira Maria Correia Fortunato
Professora Doutora Regina da Conceição Corredeira Monteiro
Professora Doutora Olinda Maria Quelhas Fernandes Conde

FACULDADE DE CIÊNCIAS E TECNOLOGIA
UNIVERSIDADE NOVA DE LISBOA

Junho de 2015

Nuno Miguel Pinto Neves

Mestre em Engenharia de Materiais

Al-doped ZnO ceramic sputtering targets based on nanocrystalline powders produced by emulsion detonation synthesis – deposition and application as a transparent conductive oxide material

Dissertação para obtenção do Grau de Doutor
em Ciência e Engenharia de Materiais

Orientador: Doutora Isabel Maria das Mercês Ferreira, Professora Associada, Faculdade de Ciências e Tecnologia – Universidade Nova de Lisboa

Co-orientador: Doutora Ana Lúcia Lagoa, Investigação e Desenvolvimento de Nanomateriais, INNOVNANO – Materiais Avançados, SA

Júri:
Presidente: Professora Doutora Maria Luísa Dias de Carvalho de Sousa Leonardo
Arguentes: Professora Doutora Paula Maria Lousada Silveirinha Vilarinho
Professor Doutor Carlos José de Macedo Tavares
Vogais: Professor Doutor Albano Augusto Cavaleiro Rodrigues de Carvalho
Professora Doutora Elvira Maria Correia Fortunato
Professora Doutora Regina da Conceição Corredeira Monteiro
Professora Doutora Olinda Maria Quelhas Fernandes Conde

FACULDADE DE CIÊNCIAS E TECNOLOGIA
UNIVERSIDADE NOVA DE LISBOA

Junho de 2015

Al-doped ZnO ceramic sputtering targets based on nanocrystalline powders produced by emulsion detonation synthesis – deposition and application as a transparent conductive oxide material

Copyright: Nuno Miguel Pinto Neves

FCT/UNL e UNL

A Faculdade de Ciências e Tecnologia e a Universidade Nova de Lisboa têm o direito, perpétuo e sem limites geográficos, de arquivar e publicar esta dissertação através de exemplares impressos reproduzidos em papel ou de forma digital, ou por qualquer outro meio conhecido ou que venha a ser inventado, e de a divulgar através de repositórios científicos e de admitir a sua cópia e distribuição com objectivos educacionais ou de investigação, não comerciais, desde que seja dado crédito ao autor e editor.

Acknowledgments

This thesis is a result of about five years of hard work, during which for sure I learnt a lot, from both professional and personal point of view. Besides the personal effort made during countless days and nights of work, when I think back and look around there are a number of people without whom this thesis might have not be written, and to whom I am greatly indebted.

First and foremost, I would like to express my sincere gratitude to my supervisor Professor Isabel Ferreira, for providing me the privilege to work with her in this project, for the form she guided my work with their knowledge and singular enthusiasm, for their support and encouragement, for all the suggestions and “crazy ideas”, for their friendship and patience, and of course for the countless long talks held in the late afternoon. Thank you for everything.

To my friend and supervisor in Innovnano Dr. Ana Lagoa, for all the support in the company throughout this years, for many scientific discussions and for being always available to help professionally and personally. Without her knowledge, ideas and advices, this work would not have taken the same direction.

To Professor Rodrigo Martins and Professor Elvira Fortunato, for allowing me to work in this prestigious research group during these years, for their support, incentive and fellowship. Even having developed large part of the work out of the research center, they always made me feel like “part of the group”. Thank you for the confidence in me and my work.

To CUF group where Innovnano is incorporated, for investing in my professional and personal development. To Dr. André de Albuquerque and Eng. João Calado I express my sincere thanks for the opportunity to take this project to the end. It is gratifying and I am proud to be part of CUF group.

To Dr. Raquel Barros, a special and grateful thank. Without her friendly help in the clean chamber and on the characterization of the thin films this work would not have been possible. Thanks for the good times we spent together, for never having said no to the “crazy schedules” that I proposed to work, for your endless patience, and for our Sushi sessions! You are a good friend!

To Eng. Ana Casaca for the support in terms of the company intellectual property management and for making easy what is commonly complicated.

To Professor Pedro Mantas, for the few but always motivating and interesting conversations. Their personal advices were essential.

To Eng. Sílvio Pratas, which more than a co-worker at Innovnano is a great friend. Thanks for all the good moments over these years and for teaching me to enjoy a good Alentejo wine.

To my colleagues and co-workers in Innovnano, MSc. Sofia Soares, MSc. Marisa Rodrigues and MSc. Cristina Mesquita, for the friendship, professional and personal support. Thank you very much!

To Eng. Elsa Antunes for their support and guidance during part of this journey. Even being on the other side of the world, I could not forget to thank you.

To Dr. Andrei Galatanu from the National Institute of Materials Physics in Romania for the thermal measurements, availability and knowledge sharing.

To the Centre for Renewable Energy Systems Technology (CREST), namely to Professor John Walls, DR. Jake Bowers and MSc. Patrick Isherwood for the scientific talks and the work developed together in AZO thin films.

To MSc. Rosa Calinas for the SEM and TEM analyses performed in the University of Texas at Austin.

To Eng. Ana Bicho from Solarplus, for providing their manufacturing facilities for the tests with the industrial ceramic targets.

To professor Ana Rego, for the XPS measurements and characterization done at IST.

To Professor Jorge Frade, for providing his lab over these years for the preparation of CIP samples.

To Professor Jorge Saraiva and MSc. Rui Queirós from DQUA, for the uncountable CIP tests performed in their facilities.

To past and present co-workers in CENIMAT and DCM that, direct or indirectly, contributed to this work: Professor Pedro Barquinha, Professor Luis Pereira, Professor Teresa Cidade, MSc. Sónia Pereira, MSc. Alexandra Gonçalves, MSc Mafalda Costa, Dr. Joana Loureiro, MSc. Paulo Duarte, Dr. Ana Baptista, Dr. Rita Braquinho, MSc. Lídia Santos, Dr. Joana Vaz Pinto, Msc. Diana Gaspar, Msc. Andreia Araújo, MSc. António Vicente, Dr. Iwona Wojcik, Dr. Pawel Wojcik, Dr. Ana Pimentel, Dr. Daniela Nunes, Dr. Sergey Filonovich, MSc. Jonas Duermeier, Dr. Tito Busani, Msc. Tiago Mateus, Dr. Elangovan Elamurugu, Eng. Nuno Correia, Dr. Vitor Figueiredo, and others that probably I did not mention. Your help was essential Thank you all!

To all co-workers of Innovnano not mentioned above, which direct or indirectly helped me in this journey.

For all the true moments of friendship and fun, I must thank to my longtime friends César Esteves, Eduardo Arvins, José Pedro, Bruno Tiago, Vitor Oliveira, Luís Pereira and Pedro Moreira. Everything is turned much easier having friends like them in our side.

To all my family, especially to my brother Hugo for being my best friend and an example for me, my nieces Beatriz and Inês for their special hugs and for being my princesses, my grandparents Virgílio and Fátima, two people with a huge heart, my uncle Virgílio for being a “second father”, and to the most important persons in my life: my parents Fernando and Virginia for their love and comprehension, for devoting their life to give me the best anyone could have. I own them all that I am today and no words ever be enough to thank them!

Finally, to Ana, a special person in my life, who supported me and stood by me during the tough last years. Words will never be enough to express how grateful I am for their endless love and care. Without her all this process would have been much harder, probably impossible.

Abstract

Transparent conducting oxides (TCOs) have been largely used in the optoelectronic industry due to their singular combination of low electrical resistivity and high optical transmittance. They are usually deposited by magnetron sputtering systems being applied in several devices, specifically thin film solar cells (TFSCs). Sputtering targets are crucial components of the sputtering process, with many of the sputtered films properties dependent on the targets characteristics.

The present thesis focuses on the development of high quality conductive Al-doped ZnO (AZO) ceramic sputtering targets based on nanostructured powders produced by emulsion detonation synthesis method (EDSM), and their application as a TCO. In this sense, the influence of several processing parameters was investigated from the targets raw-materials synthesis to the application of sputtered films in optoelectronic devices.

The optimized manufactured AZO targets present a final density above 99 % with controlled grain size, an homogeneous microstructure with a well dispersed $ZnAl_2O_4$ spinel phase, and electrical resistivities of $\sim 4 \times 10^{-4}$ Ωcm independently on the Al-doping level among 0.5 and 2.0 wt. % Al_2O_3. Sintering conditions proved to have a great influence on the properties of the targets and their performance as a sputtering target. It was demonstrated that both deposition process and final properties of the films are related with the targets characteristics, which in turn depends on the initial powder properties.

In parallel, the influence of several deposition parameters in the film´s properties sputtered from these targets was investigated. The sputtered AZO TCOs showed electrical properties at room temperature that are superior to simple oxides and comparable to a reference TCO – indium tin oxide (ITO), namely low electrical resistivity of 5.45×10^{-4} Ωcm, high carrier mobility (29.4 $cm^2V^{-1}s^{-1}$), and high charge carrier concentration (3.97×10^{20} cm^{-3}), and also average transmittance in the visible region > 80 %. These superior properties allowed their successful application in different optoelectronic devices.

Keywords: *Nanostructured powders synthesis; Al-doped zinc oxide; sintering; ceramic sputtering targets; transparent conducting oxides, thin films, magnetron sputtering.*

Resumo

Os óxidos condutores transparentes (TCOs) têm sido amplamente utilizados na indústria optoelectrónica devido à combinação única de baixa resistividade eléctrica e elevada transmitância óptica. São geralmente depositados por pulverização catódica assistida por magnetrão em inúmeros dispositivos, especificamente células solares de filme fino (TFSCs). Os alvos para deposição catódica são componentes cruciais no processo de pulverização, com muitas das propriedades dos filmes pulverizados a dependerem das características dos alvos.

Esta tese de doutoramento foca o desenvolvimento de alvos cerâmicos condutores de óxido de zinco dopado com alumínio (AZO) de elevada qualidade para deposição catódica, a partir de pós nanoestruturados produzidos pelo método de síntese por detonação de emulsão (EDSM). Para tal, foi investigada a influência dos diversos parâmetros de processamento desde a síntese dos pós usados no fabrico dos alvos até à aplicação dos filmes pulverizados em dispositivos optoelectrónicos.

Os alvos de AZO optimizados apresentam uma densidade final superior a 99 % com um tamanho de grão controlado, uma microestrutura homogénea com uma fase espinela $ZnAl_2O_4$ bem distribuída, e resistividades eléctricas de $\sim 4 \times 10^{-4}$ Ωcm independentemente da quantidade de Al como dopante no intervalo 0.5 – 2.0 % em peso de Al_2O_3. As condições de sinterização demonstram ter um efeito preponderante nas propriedades finais dos alvos e na sua performance como alvo de deposição catódica. Foi demonstrado que tanto o processo de deposição como as propriedades dos filmes estão correlacionados com as características dos alvos, que por sua vez dependem das propriedades do pó inicial.

Em paralelo, foi estudada a influência de diversos parâmetros de deposição nas propriedades dos filmes depositados com esses alvos. Os TCOs de AZO pulverizados apresentam propriedades eléctricas à temperatura ambiente superiores às dos óxidos binários e comparáveis com um TCO de referência – óxido de índio dopado com estanho (ITO), nomeadamente baixa resistividade eléctrica, (5.45×10^{-4} Ωcm), elevada mobilidade (29.4 $cm^2V^{-1}s^{-1}$), elevada concentração de portadores de carga (3.97×10^{20} cm^{-3}), e ainda uma transmitância média no visível superior a 80 %. Estas propriedades permitiram a aplicação com sucesso destes filmes em diferentes dispositivos optoelectrónicos.

Termos chave: *Síntese de pós nanoestruturados; óxido de zinco dopado com alumínio; sinterização; alvos cerâmicos de pulverização catódica; óxidos condutores transparente; filmes finos; pulverização catódica.*

Table of contents

List of figures

List of tables

Abbreviations

AES	Auger electron spectroscopy
AFM	atomic force microscopy
ALD	atomic layer deposition
AVT	average transmittance in the visible range
AZO	aluminum doped zinc oxide
AZO_A	aluminum doped zinc oxide (0.5 wt. % Al_2O_3)
AZO_B	aluminum doped zinc oxide (1.0 wt. % Al_2O_3)
AZO_BD	aluminum doped zinc oxide powder before deagglomeration/disaggregation
AZO_C	aluminum doped zinc oxide (1.5 wt. % Al_2O_3)
AZO_D	aluminum doped zinc oxide (2.0 wt. % Al_2O_3)
AZO_NST	non-sintered aluminum doped zinc oxide ceramic target
AZO_PM	aluminum doped zinc oxide powder synthesized via metals
AZO_PN	aluminum doped zinc oxide powder synthesized via nitrates
AZO_ST	sintered aluminum doped zinc oxide ceramic target
BET	method for measuring surface area, designed by Brunauer, Emmett, and Teller
CAGR	compound annual growth rate
CCR	constant cooling rate
CEMOP	Centre of Excellence in Microelectronics Optoelectronics and Processes
CENIMAT	Centro de Investigação de Materiais
CHR	constant heating rate
CIGS	copper indium gallium (di)selenide
CIP	cold isostatic pressing
CREST	Centre for Renewable Energy Systems Technology
CS	conventional sintering
CTE	coefficient of thermal expansion
CUF	Companhia União Fabril
DC	direct current
DR	deposition rate
DSC	differential scanning calorimetry
D50	mean particle size
EDS	energy dispersive X-ray spectroscopy
EDSM	emulsion detonation synthesis method
EQE	external quantum efficiency

FTO	fluorine doped tin oxide
FWHM	full width at half maximum
GD	green density
GIZO	gallium indium zinc oxide
GPS	gas pressure sintering
GPSM	gaseous phase synthesis method
GSD	granule size distribution
GZO	gallium doped zinc oxide
HD	high density targets
HEBM	high energy ball milling
HIP	hot isostatic pressing
HP	hot pressing
HRTEM	high-resolution transmission electron microscopy
HT	holding time
HV	Vickers hardness
ITO	indium doped tin oxide
INCO	international nickel company
I3N	Instituto de Nanoestruturas, Nanomodelação e Nanofabricação
LCD	liquid crystal display
LD	low density targets
LED	light emitting diode
LPSM	liquid-phase synthesis method
m_ZnO	micrometric commercial zinc oxide
MBE	molecular beam epitaxy
MFP	mean free path
MOCVD	metal-organic chemical vapour deposition
MSR	maximum value of shrinkage rate
n_ZnO	nanometric commercial zinc oxide
NIR	near infrared
NST	non-sintered
PF	power factor
PLD	Pulsed laser deposition
PSD	particle size distribution
PV	photovoltaic
PVD	physical vapour deposition

QREN	Quadro de Referência Estratégico Nacional
RF	radio-frequency
RMS	root mean square roughness
RT	room temperature
sm_ZnO	submicrometric commercial zinc oxide
SEM	scanning electron microscopy
SPS	spark plasma sintering
SPSM	solid-phase synthesis method
SSA	specific surface area
ST	sintered
STEM	scanning-transmission electron microscopy
TCO	transparent conducting oxide
TD	theoretical density
TE	thermoelectric
TEM	transmission electron microscopy
TE-TF	thermoelectric thin film
TFSC	thin film solar cell
TFT	thin film transistor
TGA	thermo-gravimetric analysis
TSO	transparent semiconductor oxide
TSS	two-step sintering
TT	thermal treatment
UP	uniaxial cold pressing
UV	ultraviolet
VIS	visible
XPS	X-ray photoelectron spectroscopy
XRD	X-ray diffraction
XRF	X-ray fluorescence
ZnO_N	undoped zinc oxide synthesized in INNOVNANO
ZT	figure of merit

Symbols

a	particle radius
$at.\%$	atomic percentage
a_{hr}	heating rate
a_{ind}	indent half diagonal
A	total surface (interface) area of the compact
A_b	Absorption
A_{ind}	surface area of the resulting indentation
A_s	absolute surface area of a solid
b	grain size exponent in equation 4.4
$\vec{B}$	magnetic field
c	speed of light
C_p	specific heat
C_v	vacancy concentration under a plan
d_c	critical size of a stable germ
d_{film}	film thickness
d_{hkl}	interplanar spacing
d_l	average length of the diagonal left by the indenter
d_p	pore size
d_s	diameter of the sample
d_{spt}	sputtered particles diameter
D	thermal diffusivity
D_c	crystallite size
D_{Gas}	gas diffusivity coefficient (from the particle surfaces to the neck)
D_{GB}	grain boundary diffusion coefficient (from the grain boundary to the neck)
$D_{L(GB)}$	lattice diffusion coefficient (from the grain boundary to the neck)
$D_{L(S)}$	lattice diffusion coefficient (from the particle surfaces to the neck)
D_S	surface diffusion coefficient (from the particle surfaces to the neck)
E	Young´s modulus
$\vec{E}$	electric field
E_B	electron binding energy
E_F	Fermi level
E_g	bandgap energy

E_{kin}	kinetic energy of the emitted photoelectron
E_{opt}	optical bandgap
E_p	plasma energy
E_{ph}	incident photons energy
f_V	volume fraction of the secondary phase particles
F	axial force
$\vec{F}$	Lorentz force
FF	filling factor
F_{GB}	free energy gradient generated by grain boundaries curvature differences
F_P	pinning force per unit of volume of the sample
G	Particle size
G_s	grain size
G_{s0}	initial grain size
h	Planck´s constant
h_s	height of the sample
I	Current
I_{DS}	drain-to-source current
J_{SC}	short-circuit current
k	thermal conductivity
k_B	Boltzmann constant
k_{EC}	extinction coefficient
k_{EL}	heat transfer in the material by electrons – electric thermal conductivity
k_F	Fermi wave factor
k_{PH}	heat transfer in the material by phonons – phonon thermal conductivity
K_0	pre-exponential coefficient
K_{IC}	fracture toughness
l	length at time t
$\bar{l}$	arithmetic mean linear intercept
l_0	Initial size of the sample
l_{ind}	Palmqvist crack length
L	length of the line across the image
m	grain growth exponent
m^*	effective mass of the electron
m_c^*	effective mass of carriers in conduction band

m_{cv}^*	combined effective mass
m_v^*	effective mass of carriers in valence band
m_1	exponent in equation 4.1 dependent on the sintering mechanism
m_d	mass of the dry sample
m_s	mass of the soaked sample
m_{sample}	mass of the sample
M	molar mass of the compound
M_{GB}	intrinsic mobility of the grain boundary
M_p	pore mobility
n_1	exponent in equation 4.1 dependent on the sintering mechanism
n_{RI}	refraction index
N	number of grains traversed
N_A	Advogadro´s number
N_e	carrier concentration
N_S	sheet carrier density
pO_2	oxygen partial pressure
P	pressure
P_1^*	effective compressive pressure at the contact area during the initial stage
P_2^*	effective compressive pressure at the contact area during the final stage
$P_{appl.}$	applied pressure during sintering
P_{dep}	deposition pressure
P_{out}	output power
P_{RF}	radio frequency power density
P_v	porosity
P_0	saturated vapour pressure
q	electron charge
Q_G	apparent activation energy for grain growth
Q_{GB}	activation energy for grain boundaries motion
Q_i	activation energy for sintering in the initial stage
Q_{int}	activation energy for sintering in the intermediate stage
r	radius of neck curvature
r_s	secondary phase particle radius
R	gas constant
R_b	semiconductor channel resistance
R_c	contact resistance between the channel layer and the source/drain contact

	materials
R_f	reflectance
R_H	Hall coefficient
R_{HS}	sheet Hall coefficient
R_{int}	internal resistance of the thermoelectric element
R_s	series resistance
R_S	sheet resistance
R_{sheet}	sheet resistance
R_{sp}	geometrical spreading resistance
S	Seebeck coefficient
S_g	effective cross-sectional area of one adsorbate gas molecule
S_n	area of the aggregate
s_{th}	sample thickness
S_y	sputter yield
t	time
t_d	deposition time
T	absolute temperature
T_{MSR}	maximum shrinkage rate temperature
T_r	transmittance
T_{subs}	Substrate temperature
$T_{Y-onset}$	onset shrinkage temperature
$\vec{v}$	particle velocity
V_0	molar volume of the gas
V_a	adsorbed gas volume
V_{DS}	drain voltage
V_{GB}	motion speed of grain boundary
V_{GS}	gate voltage
V_H	Hall voltage
V_m	molar volume of the solid
V_M	monolayer adsorbed gas quantity
V_O	oxygen vacancy
V_{OC}	open circuit voltage
V_{out}	output voltage at the load resistance terminals
w	transport mechanism exponent in sintering
$wt.\%$	weight percentage

W	distance between the two electrodes
x	neck radius
Y	linear shrinkage
Zn_i	zinc interstitial
α	absorption coefficient
α_e	scale exponent
β	Full width at half maximum in radians
γ_a	energy per unit area
γ_s	specific surface energy of the solid
γ_{GB}	energy of grain boundary per unit area
δ	effective stress
ΔE_{BM}	Burstein-Moss shift
ΔG_n	free enthalpy of formation of an aggregate
Δp	vapour pressure difference – transport from the particle surfaces to the neck
η	viscosity
η_s	solar cell efficiency
θ	Bragg angle
λ	Wavelength
μ_e	carrier mobility
μ_{gb}	carrier mobility by grain boundaries scattering mechanism
μ_{ii}	carrier mobility by ionized impurity scattering mechanism
μ_{ni}	carrier mobility by neutral impurities scattering mechanism
μ_{ph}	carrier mobility by lattice vibration scattering mechanism
μ_{sat}	saturation mobility
ν	frequency of the incident photon
Ω	volume occupied by a vacancy
ρ	material density
ρ_e	electrical resistivity
ρ_f	final density
ρ_{liq}	density of the immersion liquid
ρ_r	relative density
ρ_{theo}	theoretical density
σ	electrical conductivity
$\sum$	sintering stress

τ	lifetime between collisions
ϕ	work function
φ_{GB}	diffusion thickness of grain boundary diffusion

Chapter 1. Motivation, objectives, and structure of the dissertation

The fast growing and further development of the worldwide market of energy (photovoltaics, architectural and window glasses) and information (displays) technologies will be only sustainable if either, low-cost materials, environmental friendly and low temperature processing technologies will be used. Transparent electronics based on thin films deposition is globally considered as one of the most promising technologies in the development of new electronic devices (Fig 1.1) instead of the traditional silicon technology. Sputtering is and will remain in the next years the key physical vapor deposition (PVD) method for the fabrication of such thin film devices having the sputtering targets a direct impact on its final costs that can go beyond 20 %. In all these applications, transparent conducting oxides (TCOs) layers are an essential part of the devices, contributing in average to 4 – 8 % and 10 – 15 % of the total production cost, respectively for solar cells and displays. Advances in sputtering targets production and research work on non-toxic and less expensive TCOs materials are essential for the sustainable development of new electronic devices based on sputtered thin films.

Fig. 1.1. *Examples of transparent electronics applications – From left to right: Semi-transparent a-Si:H thin film solar cell deposited on glass substrate and Samsung mobile phone with flexible and transparent 4.3'' AMOLED display [1]).*

1.1. Motivation

In recent years there has been great interest in the room-temperature (RT) devices processing, with special focus on the flexible optoelectronics using polymeric substrates or even paper [2], which limits the handling temperatures to values below 200 °C. The TCOs industry has been dominated by indium tin oxide (ITO) due to its excellent optical and electrical properties. However the drawbacks of ITO related with the impossibility of working in flexible substrates, due to its high processing temperatures (250 - 350 °C) [3], added to indium extremely high price, has stimulated the research world to explore alternative materials with reduced or no indium amount. Sputtered TCOs thin films are commonly produced using ceramic sputtering targets. Quality of sputtered thin films not only depends on process and equipment parameters but also

on the configuration and characteristics of the targets and the raw materials used for sputtering. Focused on the constant search for markets with high added value, INNOVNANO expects to enter the ceramic sputtering targets market with a low-cost/high performance material for TCOs thin films deposition that corresponds to the customers' requirements. For this purpose, the research work presented here is of great interest to INNOVNANO in particular, and for the sputtering targets market in general, since it is based on the development, characterization and optimization of high quality conductive ceramic targets prepared with home-synthesized nanostructured powders, and its potential application as a TCO in transparent electronic devices, like thin film solar cells (TFSCs), thin film transistors (TFTs), or thermoelectric materials (TEs).

1.2. Objectives

The main objective of this dissertation is the development of high quality and low-cost lab scale and industrial scaled-up aluminum doped zinc oxide (AZO) ceramic sputtering targets for use in sputtering systems. For such purpose, a novel powder synthesis method was initially adjusted and implemented for the production of AZO nanostructured powders with high sinterability, without neglecting the industrialization and subsequently the economic viability for INNOVNANO as a powder producer and sputtering targets manufacturer. The effect of different processing parameters in structural, morphological, compositional, electrical, thermal and mechanical properties of AZO ceramic sputtering targets is studied and simultaneously correlated with the sputtered TCOs thin films properties. TCOs thin films properties are also characterized and improved varying several deposition conditions. The work proceeded using the produced sputtering targets in thin films deposition as a transparent electrode in TFSCs primarily in lab scale and then on an industrial scale. Also the application of the deposited thin films as source/drain contacts to GaInZnO (GIZO) TFTs and as a TE thin film material is considered. This research work was developed throughout a co-promotion QREN-Adi project (QREN/3435 - Nanoxides) between INNOVNANO - Materiais Avançados, S.A. and the materials research center CENIMAT/I3N.

1.3. Structure of the dissertation

The dissertation is structured according to the following scheme. The current chapter provides a brief introduction into the research topic, the motivation and the main objectives of this research work. In chapter 2 is provided some fundamental background of the research area through a survey of the literature on the main subjects covered in the research work. The chapter comprises a section devoted to the presentation of the main synthesis methods for the production of nanoparticles emphasizing INNOVNANO process. Current developments on TCOs are also shown, highlighting the zinc oxide (ZnO) based materials and their application as transparent electrodes. An overview about sputtering targets production and a global market prospect for sputtered thin films and sputtering targets, as well as some general aspects about solid state sintering of ceramics are also described, with particular focus on undoped and Al-doped ZnO systems. The details of the experimental procedures and characterization techniques used in this work can be found in chapter 3. The presentation and discussion of the main results are divided in two chapters, which are mainly based on data already published or submitted. Chapter 4 is devoted to the synthesis, post-processing and characterization of the powder. Chapter 5 constitutes one of the key points of this dissertation, presenting the results regarding the use of INNOVNANO synthesized powders to produce AZO ceramic targets for sputtering deposition. The influence of

powder composition and of several processing parameters on structural, morphological, compositional, electrical, thermal and mechanical properties is analyzed. The presentation of the main results obtained in TCOs thin films, the correlation with sputtering targets properties and the integration of the TCOs thin films in lab-scale TFSCs, TFTs and TE devices is also discussed in chapter 5. This chapter ends with the results concerning the industrial production of a-Si:H TFSCs using large-size manufactured AZO sputtering targets and the market position of the targets developed throughout this work. The dissertation ends with chapter 6, which contains the main conclusions of this dissertation as well as some prospects for further work.

1.4. References

[1] http://getandroidstuff.com/samsung-flexible-transparent-amoled-display-showed-fpd-2010/ consulted on 15/04/2013.

[2] Barquinha, P., Martins, R., Pereira, L. and Fortunato, E., Transparent Oxide Electronics: From Materials to Devices. First Edition. Published 2012 by John Wiley & Sons, Ltd.

[3] Fortunato, E., Ginley, D., Hosono, H. and Paine, D. C., Transparent conducting oxides for photovoltaics. *MRS Bull*, 2007, **32**(3) 242-7.

Chapter 2. Introduction

In this chapter is provided a brief overview of the different topics covered by the research work within this dissertation, starting with a general overview of the nanotechnology market trends and the most commonly methods used for synthesis of metal-oxide nanoparticles with a special emphasis given to INNOVNANO's novel process. A review concerning the state of the art of transparent conductive oxides (TCOs) focusing zinc oxide based materials is also shown, followed by a brief description about the production of sputtering targets and its global market for thin films production by sputtering techniques. Since the core of this work is the production of ceramic sputtering targets, the essential theoretical aspects related with solid state sintering of ceramics are also described here, emphasizing the sintering and densification of undoped and aluminum doped zinc oxide (AZO) systems.

2.1. Nanotechnology and nanomaterials

Nanomaterials are facing a fast development in recent years due to their potential applications for a wide range of technological areas such as electronics, ceramics, catalysis, cosmetics, etc. Materials at nanometer scale are known to possess unusual and interesting properties or combination of properties distinct from those obtained with conventional micro and sub micrometric materials, e.g. increased mechanical strength, enhanced diffusivity, higher specific heat and electrical resistivity [1, 2]. These improvements in the materials properties has led to greater interaction between researchers from different fields like physics, chemistry, mechanics and materials science or even biology and medicine.

Several suggestions concerning the definition of nanoscale have been proposed among nanotechnology experts during the last years without complete consensus. With the intention of solving this issue, the European commission published in 2011 a recommendation document on the definition of nanomaterial. According with the definition, nanomaterial means a natural, incidental or manufactured material containing particles, in an unbound state or as an aggregate or as an agglomerate and where, for 50 % or more of the particles (in number), one or more external dimensions is below 100 nm [3].

2.1.1. Global market trends

Despite the relatively fragile condition of the global economy in the last years, the market for nanotechnology products has been growing, and almost doubled between 2009 and 2012 from 11.7 to 20.8 US billion dollars (Fig. 2.1). At the beginning of the year, International Monetary Fund expressed in its *World Economic Outlook Update* (January 23, 2013) an optimistic prevision that the world economy will continue to grow avoiding a global recession. Taking into account the global economic trends, recent research works estimate that the global market for nanotechnology products growth sharply over the coming years reaching 26.7 US billion dollars in 2015 and 50.9 US billion dollars in 2017 with a compound annual growth rate (CAGR) of 18.7 % from 2012 through 2017 [4, 5]. These market values consider nanomaterials (nanoparticles, nanotubes, nanostructured materials, nanoscale thin films and nanocomposites), nanotools (nanolithography tools and scanning probes microscopes) and nanodevices (nanosensors and nanoelectronics). Specifically the nanomaterials market is responsible for more than 76 % of the

nanotechnology products market, being predicted a similar market trend with an increase from 15.9 to 37.3 US billion dollars with a similar CAGR (18.6 %).

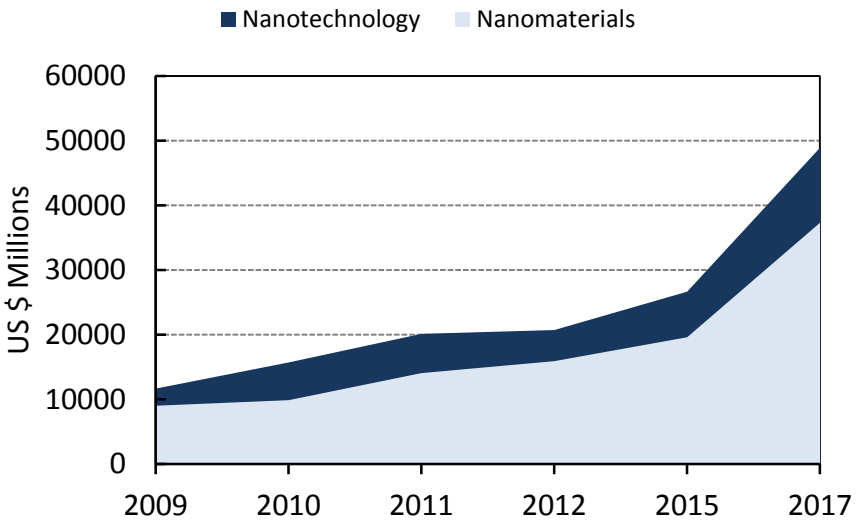

Fig. 2.1. *Global nanotechnology market, 2009 – 2017 (US $ millions) (Adapted from [4] and [5]).*

Nanomaterials can be classified into nanocrystalline materials and nanoparticles. The former are polycrystalline bulk materials with grain sizes in the nanometer range while the latter refers to ultrafine dispersive particles having diameters with at least one dimension below 100 nm. Nanoparticles are generally considered as the building blocks of bulk nanocrystalline materials.
As the market for nanoparticles expands, numerous efforts have been made in order to industrialize the nanoparticles production. Existing production technologies are continually being refined and new synthesis processes developed. In the next subchapter are reviewed the most important methods for the synthesis of metal-oxide nanoparticles highlighting the industrialized and near industrialization ones.

2.2. Overview of nanoparticles synthesis technologies

The large potential of nanoparticles and nanostructures in high-performance applications has been recognized and is responsible for an increased interest of both scientific and commercial sectors. The nanoparticles technology is already considered one of the key technologies to materialize nanotechnology in commercial applications. Typically composed of several tens or hundreds of atoms or molecules, nanoparticles can have a wide range of sizes and morphologies and can be used to manufacture components, devices or coatings with specific properties. Two physical phenomena distinguish the properties of nanoparticles from those of conventional bulk materials, namely the larger ratio of surface to volume and the confinement phenomena. In comparison to bulk materials, nanoparticles have a higher specific surface area with a higher amount of surface atoms/molecules that have different properties than those of bulk material [2]. As a consequence the properties of nanostructures are more closely related to the states of individual molecules, molecules on surface or interfaces than on the properties of bulk material. At the nanoscale, the electron motion in atoms is extremely confined (quantum confinement) due to the limited space for movement available for electrons. A transition between the discrete energy levels of the atoms and the continuous energy bands of the solid state bulk materials is

performed widening up the bandgap and also the bandgap energy. As a result the use of nanoparticles emerges as a reality to obtain novel properties for already well known materials [6].
A wide range of synthesis methods has emerged, developed and optimized for the production of nanoparticulate materials. Depending on the synthesis method is possible to achieve nanoparticles with different particle sizes, morphologies, composition and/or degree of homogeneity. There is no single technique considered as the most suitable for the production of different types of nanomaterials. Each one of the several developed techniques has advantages and disadvantages being more or less suitable.
The different synthesis methods for producing metal-oxide nanoparticles can be divided into three major categories as depicted in Fig. 2.2, according to their working principle: solid-phase; liquid-phase; and gaseous-phase; being grouped in top-down and bottom-up classes. In the next subsections are presented and described the most commonly used techniques for each category with special attention to the already industrialized or near industrialization ones.

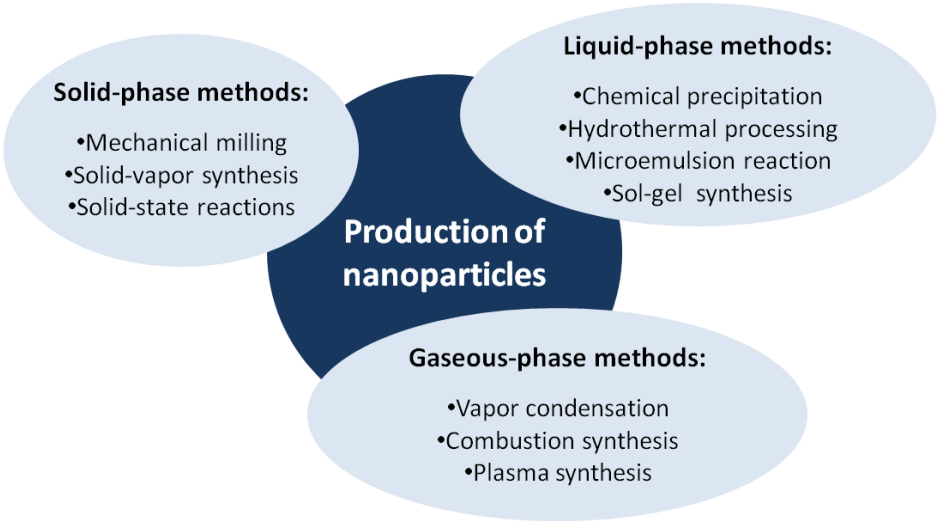

Fig. 2.2. *Overview of the main manufacturing methods for metal-oxide nanoparticles (Adapted from [2]).*

2.2.1. Solid-phase synthesis methods

Included in the top-down nanomanufacturing techniques, the solid-phase synthesis methods (SPSM) consist in the division of a massive solid into smaller portions. This approach may involve milling or attrition (mechanical milling), volatilization of a solid followed by condensation of the volatilized components (solid-vapor synthesis), and chemical methods (solid-state reactions).

2.2.1.1. Mechanical milling

Mechanical milling/alloying powder processing technique was originally developed by John Benjamin at the International Nickel Company (INCO) in the sixties, and comes out from a long search to produce oxide dispersion strengthened superalloys for gas turbine applications [7]. Firstly correlated with the dry mechanical preparation of alloys, the term *Mechanical Alloying* was generalized to comprise all processes that may result from high-energy ball milling (e.g. mechanical milling with and without chemical reactions).

During mechanical milling process, raw materials with a size of several microns are submitted to severe plastic deformations, undergo a repetitive cold welding and fracturing mechanism, and then a significant reduction of the particle size is obtained [8]. Recognized as one of the most versatile process for the fabrication of a broad range of nanocrystalline powders (simple and low cost process), mechanical milling can be carried out by either a ball mill or an attritor mill and can occur without or with solid-state chemical reactions [2, 9-11]. If in the first case no chemical variations are observed (size reduction/mechanical amorphization), the same cannot be said about the second approach, being the milling stage entitled as mechanochemical synthesis process (size reduction/mechanochemical amorphization).

Mechanical milling can be accomplished by wet or dry and the powder properties are affected by several factors like the type of mill (e.g. ball or attritor), ball to powder mass ratio, balls characteristics, solids content of the suspension (when wet milled), rotation velocity of the mill, milling time or milling media (e.g. water or ethanol).
The high energy ball milling (HEBM) process can be distinguished from other milling processes by the high rate of transfer energy involved, balls to mixture ratio, the strong interaction between balls and mixture, high frequency impact with compressive forces (milling balls/container/mixture) and long processing times [2, 10]. Besides the simple blending and homogenization of powders, HEBM enables the production of nanocrystalline compounds and mixtures as well as the synthesis of new phases [12-15].

Despite being widely used in industry, one of the main issues of this method for the production of nanocrystalline powders is the contamination of the powders during milling stage. The small size of the powder particles achieved, availability of large surface area, and formation of new surfaces during milling contributes to the powder contamination which limits its use in the most demanding applications in terms of purity. However, several efforts have been made in order to avoid/minimize this issue with very promising results [10].

2.2.1.2. Solid-vapor synthesis

Solid-vapor synthesis is characterized by the chemical reactions between the solid and the vapor phases occurring in specific chambers, leading to the formation of highly saturated vapor and subsequently production of nanoparticles. The vapor phase can be created either by external gas flow or by the decomposition of chemicals during the powder synthesis. The reaction mechanisms are similar to those in gaseous-phase synthesis methods (to be discussed in section 2.2.3) being the nanoparticles growth controlled by temperature, flow rate, and pressure of vapor phase [2]. The main difference is that in solid-vapor technique, synthesis takes place at the solid surface.

2.2.1.3. Solid-state reactions

Another way to synthesize nanoparticles is by solid-state reaction. This method uses solid starting materials to produce nanomaterials. Thermophysical synthesis of coarse solids promotes particle size reduction without chemical change induced by thermal and/or mechanical energy. The main factors that can affect the feasibility and the rate of a solid state reaction include the structural properties of the reactants, reaction conditions, specific surface area of the powders, and the thermodynamic free energy changes associated with the reaction [16]. Due to its limited chemical

homogeneity, and in order to increase the powders reactivity, starting materials are usually subjected to a milling stage before solid-state reaction synthesis.

In contrast to mechanical milling, the solid-state reaction and solid-vapor synthesis processes are usually carried out in joule heat furnaces, as in chemical vapor synthesis, at a rather high temperature (thermally activated processes). The two processes can be accomplished in a short period, unlike mechanical milling, which usually takes from at least a few hours to several days at temperatures close to room temperature. Furthermore, due to the strong mechanical forces in milling, it is not realistic to form 1-d nanostructures by mechanical milling, but it is possible to synthesize complex nanostructures by the two other processes [2]. Although still remaining as one of the most used techniques, the limitations of SPSM are well known [2, 9, 10]. Its large particle size, broad size distribution, contamination and limited chemical homogeneity, opened a door to the development and optimization of several others synthesis methods.

2.2.2. Liquid-phase synthesis methods

Liquid-phase synthesis methods (LPSM) have already a remarkable role in the production of nanoparticles. The atomic scale homogenization of the starting materials, the precise control of stoichiometry even with complex chemical compositions and the commonly lower reaction temperatures and pressures make liquid-phase route very attractive for the production of nanoparticles.

A wide range of LPSM have been developed [17-20]: The well known hydrothermal synthesis method in which nanoparticles are usually produced by means of hydrolysis reactions of precursor salts in aqueous solutions under controlled pressure and temperature in an autoclave [19, 21-24]; or the microemulsion (micelle/reverse micelle) reaction methods which in a simple way include a group of synthesis processes in a thermodynamically stable colloidal system composed of two immiscible fluids, typically a hydrophilic liquid (e.g. water or aqueous solution) and lipophilic liquid (oil) stabilized by a surfactant [2, 18, 25]. All LPSM have its own advantages and disadvantages. However environmental issues related with the large amount of residues resulting from synthesis, processing costs, the synthesis mechanisms control, the requirement of subsequent steps (e.g. calcination for conversion to the oxide, and milling) or the low production rate, has hindered the transition to large-scale production of most of them. In this field, chemical precipitation and sol-gel synthesis appear as the most promising LPSM for the production of metal-oxide nanoparticles with important worldwide producers opting for them for several years.

2.2.2.1. Chemical precipitation synthesis

Considered one of the most suitable LPSM for the production of metal-oxide nanoparticles, chemical precipitation allows the synthesis of nanoparticles with controlled composition and particle size. A typical scheme of the main stages of chemical precipitation is shown in Fig. 2.3. The process begins by the preparation of the main solutions, dissolving the starting materials (metal oxides, metal salts and organometallic compounds or their hydrates) in solvents (e.g. deionized water, ethanol, methanol and acidic solutions) [26-28]. The solutions are then stirred for several hours at low temperatures until the complete reaction of the starting materials occurs.

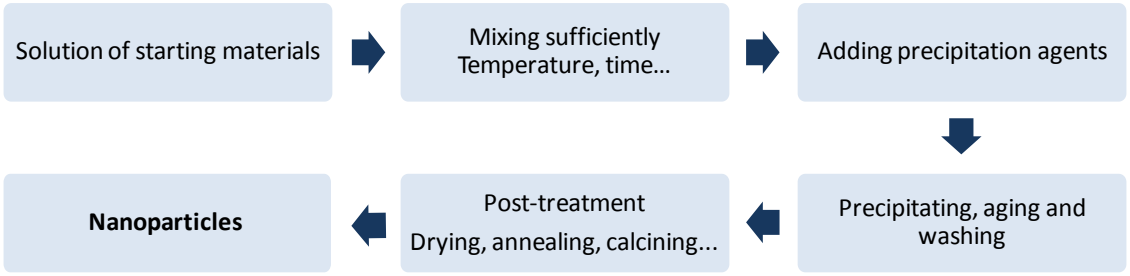

Fig. 2.3. *Main steps of chemical precipitation synthesis method for the production of nanoparticles (Adapted from [2]).*

Two precipitation processes exist in chemical precipitation synthesis. Firstly, the low solubility of reaction products in the main solvent promotes their precipitation after the reactions are over. Secondly, the reaction products can dissolve in the main solvent as the starting materials. Thus, a precipitation agent (antisolvent) is added to the solution to precipitate the reaction products [29]. The precipitation agent is miscible with the main solvent but cannot dissolve the reaction products, leading to the precipitation of reaction products in the main solvent-precipitation agent mixture. This second process is a form of co-precipitation, in which the precipitation is a pH-value-sensitive process, as solubility is pH-value-dependent [28]. A controlled pH value forces the reaction products to precipitate. Basic materials like NH_4OH, NaOH or $NaCO_3$ are common precipitation agents of metal salts since they require a basic or weak acidic environment for precipitation.

After the complete precipitation, whose duration could take several days depending on the amount of material, the precipitates are collected by filtration or centrifugation being washed several times with a solvent (e.g., distilled water) in order to improve the purity. Then precipitates are dried at temperatures higher than 100 °C for sufficient time or freeze-dried. The resulting precursor powders are generally poorly ordered, with low crystallinity and uncontrolled size and size distribution. The last stage of precipitation method involves a thermal treatment of the precursor powder at high temperatures for several hours [17, 28-30]. During thermal treatment most chemical reactions involve dehydration and the temperature contributes to the adjustment of the crystal structures and morphology. Depending on the thermal cycle it is possible to control the precursor powders crystallinity, crystal size, size distribution or phase transformation.

2.2.2.2. Sol-gel synthesis method

The sol–gel processing method has been used for producing metal-oxide nanopowders with high purity and high homogeneity for many years [8]. Since the first silica and alumina gels produced by Ebelman [31] in 1846 and Cossa [32] in 1870 respectively, several materials have been synthesized using the sol-gel technique [20, 33-38]. Sol-gel synthesis is similar to chemical precipitation. Typically the reactions take place in inexpensive reactors and use metal chlorides, metal nitrates and alkoxides as starting materials. The main difference of the sol-gel method is the formation of a sol-gel containing the nanomaterials as the precursor material for further drying and calcination at specific temperatures for a few hours.

Sol-gel synthesis involves the generation of a colloidal suspension (“sol”), which is subsequently converted to a viscous gel and solid material. In this process, reactive metal precursors were firstly hydrolyzed, followed by condensation and polymerization reactions (nucleation) [39, 40].

Several factors are known to affect the hydrolysis reaction which plays a critical role in the formation and morphology of the resulting particles [39, 41, 42]. These include the nature of starting species and solvent, the concentration of each species in the solvent, the temperature, the water to precursor molar ratio or the presence of acid or base catalysts.
Subsequent condensation of the "sol" particles (gelation) eliminates either water or alcohol to produce metal oxide or hydroxide linkages [42]. Depending on how the drying is carried out, the sol-gel will have different properties. If a supercritical drying is used, the original 3D structure is preserved and a low-density gel (aerogel) obtained. On the other hand, if the gel is dried slowly in a thermal-evaporation process, the 3D structure collapses creating a high-density gel (xerogel) [43].
Nowadays, sol-gel appears as one of the most versatile methods for the production of metal-oxide nanoparticles with a wide range of possible applications as a bulk material [20, 41, 44] or directly as a thin film [43, 45, 46]. The high purity and compositional homogeneity resulting from the molecular level mixing of the raw materials, the precise stoichiometry of the final products, the small particle size and narrow size distribution are the main advantages of this process, which cannot be easily reproducible with other synthesis methods. The major technical issues to overcome are the very low production rate of nanopowders, the extremely high cost of some of the precursors, and the reproducibility due to the difficulties in simultaneously control of all the process parameters. There are also some environmental issues related to the large volumes of contaminating solvent (usually water). Closed-loop processes are starting to be tested to solve this problem [2, 46, 47].

2.2.3. Gaseous-phase synthesis methods

Gaseous-phase synthesis method (GPSM) is the most successful nanomaterials manufacturing method for the production of metal-oxide nanoparticles. Contrary to the already presented LPSM, GPSM is usually a continuous process which contributes to its predominance in industry. Other advantages of the gaseous-phase processes are the production of particles with high purity composed of nonporous primary particles with small sizes, and relatively narrow size distribution. The disadvantages include difficulties in producing unagglomerated particles and multicomponent materials [48].
Depending on the state of the precursors (liquid, solid, and vapor) and energy sources to evaporate the materials, there is a wide range of GPSM available, including vapor condensation [49], combustion synthesis [50, 51], laser-ablation [52, 53], and thermal plasma synthesis [54-57]. Among these techniques, vapor condensation is the most basic and all others derive from it. In general vapor condensation synthesis consists in the generation of a supersaturated vapor followed by its condensation. Depending on the nucleation process, the synthesis may include physical or chemical vapor condensation. In the first case the nucleation depends on the degree of supersaturation of a pressure vapor, while in chemical vapor condensation the nucleation is determined by the chemical reaction of vapor-phase molecules [2]. Oppositely to LPSM, in GPSM the agglomeration of particles frequently occurs as a result of absence of appropriate stabilization. Smaller particle size is commonly associated with lower evaporation temperature, low gas pressure and high cooling rate [2]. Industrially, the most widely used techniques are combustion synthesis and thermal plasma synthesis with a very significant weight in terms of volume production of metal-oxide nanoparticles at a global level.

2.2.3.1. Combustion synthesis

Due to its great potential for large-scale production and its low cost, combustion synthesis is considered one of the most successful industrial techniques in the production of metal-oxide nanoparticles [58]. Depending on the chemical environment in the flame, the heat of combustion can activate oxidation, hydrolysis and reduction reactions which make this method available for the production of various nanoceramics, semiconductors and even pure metals [2]. Typically hydrocarbons (methane and ethylene) and their mixtures with inert gas, or sometimes hydrogen gas, are the fuel gas, while oxygen and air are the most economic and convenient oxidizer sources. Contrary to gaseous fuel and oxidizer, the precursor can be vapor, liquid or solid states. Several factors (sometimes correlated between them) contribute to the final physical and chemical characteristics of nanoparticles produced by combustion synthesis. Some examples are the flame configuration [59] (also affected by the gas flow rates of fuel, oxidizer, and carrier gas), feeding state of the precursors, flame temperature, and particle time residence [2, 48]. Fig. 2.4 illustrates a typical combustion synthesis process for the production of metal-oxide nanoparticles. In this process the precursor mixture is dispersed by oxygen and fed into the premixed methane/oxygen stream. After evaporation and burning of the precursor, particles are formed by condensation, coalescence and coagulation. The weakest points of the method, in addition to the operational discontinuity, are the strong agglomeration of the particles, difficulty in controlling the stoichiometry and the high internal porosity of the particles, which is often observed and is highly disadvantageous when conducting a subsequent sintering stage.

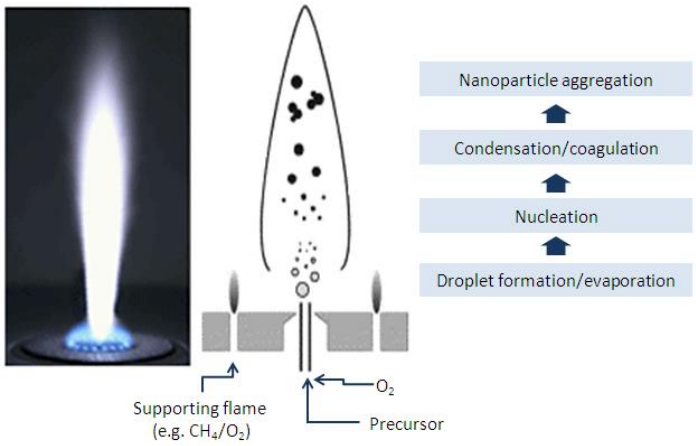

Fig. 2.4. *Schematic illustration of a combustion synthesis process (adapted from [60]).*

2.2.3.2. Thermal plasma synthesis

Thermal plasma synthesis (Fig. 2.5) has been an efficient method for generating nanoparticles. This process allows extremely high temperatures in a thermal plasma reactor, which make possible the complete dissociation of injected reactants and the formation of high-temperature materials from the vapor-phase. The high energy densities in thermal plasma can lead to very high production rates in small reactors. In addition, the high quenching rates attainable with a plasma process make high levels of supercooling or supersaturation possible, and this in turns leads to the production of nanosized particles [55]. The most widely used electrical methods for producing plasma are high-intensity arcs and inductively coupled high-frequency discharge [56].

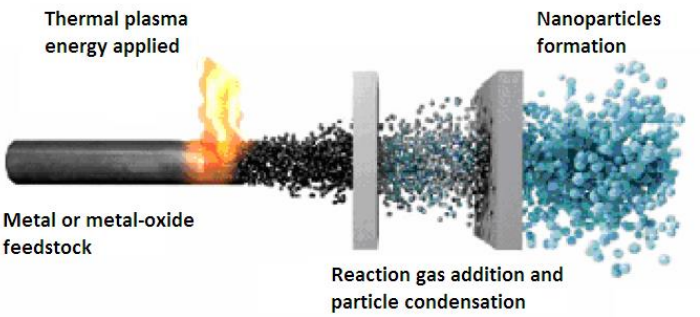

Fig. 2.5. *Schematic view of a plasma evaporation process (adapted from [61]).*

Nanoparticles in plasma can be accomplished through two different routes: evaporation – condensation or evaporation – reaction – condensation. As shown in Fig. 2.5 thermal plasma synthesis uses plasma to produce the vapor, which is cooled by injecting an inert (e.g. Ar or N_2) or reactive gas (e.g.CH_4 or NH_3), thereby forming the first nucleation centers. The subsequent addition of oxygen, for example, allows the production of metal-oxide nanoparticles. The condensation and the nanoparticles formation occur under a forced flow that disperses the germs limiting Brownian motion and coalescent coagulation [61]. The main advantage of the plasma synthesis method is the flexibility and versatility of the range of materials that can be synthesized being possible to use solid, liquid, and gas phase precursors for the nanoparticles production. The high production rate of nanoparticles by this method is also a primordial advantage in terms of industrialization. However, the high energy density of this process leads to strong gradients and inherent non-uniformities. In addition, the extremely high energy consumption of plasma synthesis equipments results in low yields. Nowadays plasma synthesis is at the stage between applied research and pilot line being expected to reach industrialization after solving the main issues concerning the perfect understanding and control of the particles formation in plasma atmosphere and its economic limitations [62].

2.3. INNOVNANO – Novel emulsion detonation synthesis method

According to research undertaken by *Abercade Consulting Company* [63], the largest share in the structure of nanopowders market output belongs to metal-oxide nanoparticles which constitute about 80 % of the nanopowder market volume, while the share of fine metal powder is of the order of 15 %. Complex metal-oxides and mixtures are available in the market in limited amounts (approximately 5 %).

Geographically, the world nanopowder production is distributed unevenly throughout countries. Only industrially developed countries are now producing nanomaterials in commercially reasonable amounts. Most producing countries depend heavily on the import of raw materials. Many countries such as Brazil, South Africa, Russia and Australia are major producers of raw materials but they do not produce nanoparticles in substantial quantities. In contrast, United States produces most of them in sufficient amounts to meet its own demands being responsible for more than 50 % of nanopowders production. European producers of nanopowders have a production deficit for domestic level of consumption, and the production of some special powders that become increasingly important is either non-existent or minimal. As a result, European consumers have to import large amounts of various nanopowders from North America and Asia [63].

The high demand for metal-oxide nanoparticles and the insufficiency of its production (especially in Europe) has been seen as a real possibility of investment with high added value for the future investors. As mentioned in chapter 1, the nanoparticles studied during this research work were obtained through a new synthesis process developed by INNOVNANO – Materiais Avançados, S.A., a Portuguese company dedicated to the large-scale nanoparticles synthesis.

2.3.1. Overview of the company – research areas and future prospects

Headquartered in Lisbon, INNOVNANO Materiais Avançados, S. A. is part of CUF, the largest chemical company in Portugal (one of the largest in Europe) and an organization with decades of invaluable expertise in the development and commercialization of novel and efficient industrial processes. Having as core values the Innovation, Competence and Personal Development as central to the success of their business, CUF through INNOVNANO aims to become in the next years one of the majors producers of metal-oxide nanoparticles at a global scale, thus entering a market in constant development with great potential for exponential economic growth in the coming years as already presented in the market forecast shown in Fig. 2.1. Some years have passed since CUF´s incursion in nanomaterials in 2003 with the discovery of a new, disruptive technology called Emulsion Detonation Synthesis Method (EDSM) (Fig. 2.6). Between 2004 and 2009, INNOVNANO devoted mainly to the research and development of its new synthesis process. The aim throughout these six years was to evaluate the potential of the EDSM that was developing, in particular, the kind of materials that are possible to synthesize, type of precursors and its validation, and optimization of the pilot plant, in order to take full advantage of the benefits inherent to the process and minimize its disadvantages when compared with the existing nanoparticles synthesis methods. This investigation procedure yielded six worldwide patents, four of which have already been granted.

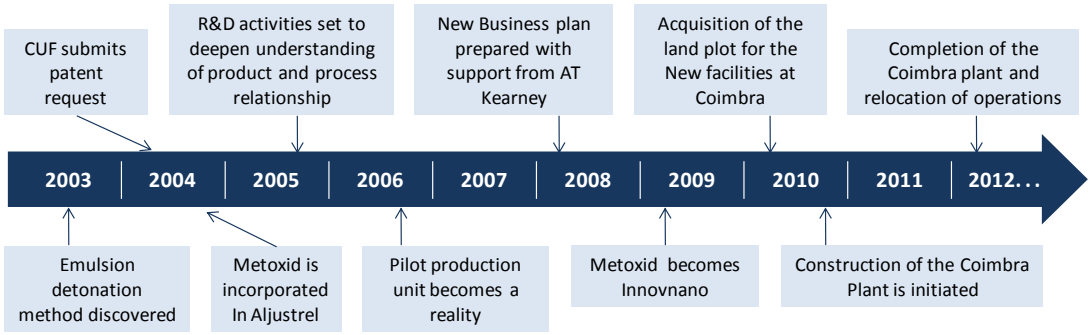

Fig. 2.6. *Some important dates since the discovery of EDSM in 2003 until the beginning of industrial production in INNOVNANO plant (2012).*

The construction of the new modular design production center in Coimbra in 2012 (Fig. 2.7) allows INNOVNANO to scale-up production up to 1000 tons per year. As the only company in Portugal that is currently dedicated to the large-scale production of nanopowders, INNOVNANO manufactures a diverse range of metal-oxide nanostructured powders including a range of yttria stabilized ZrO_2 (2YSZ, 3YSZ, 4YSZ and 8YSZ), $MgAl_2O_4$, $LiMn_2O_4$, MgO, SiO_2 and ZnO.

Besides producer and supplier of nanopowders, INNOVNANO desire to migrate progressively for an integrative model taking advantage of their unique synthesis method, thus preserving for the company the highest added value in the product chain. One great example of this integrative

model is the AZO ceramic sputtering targets production using homemade nanopowders which is currently underway based on the research work developed and presented throughout this dissertation.

Fig. 2.7. *INNOVNANO production plant built in Coimbra (Portugal) in 2012.*

2.3.2. Emulsion detonation synthesis method

Emulsion detonation synthesis method (EDSM) developed and patented by INNOVNANO [64, 65] can be included in a new category (high pressure) of the gaseous phase reaction.
It is well known that dynamic shock induce chemical reactions. EDSM is based on the detonation of two water-in-oil (W/O) emulsions (initiator and secondary emulsions) which occurs at extremely high pressures (>10.000 bar) and temperatures (range of 500 °C to 3000 °C) in one single reaction step (Fig. 2.8), which allows producing high purity (> 99.9 %) nanostructured powders at an industrial level with high reproducibility.

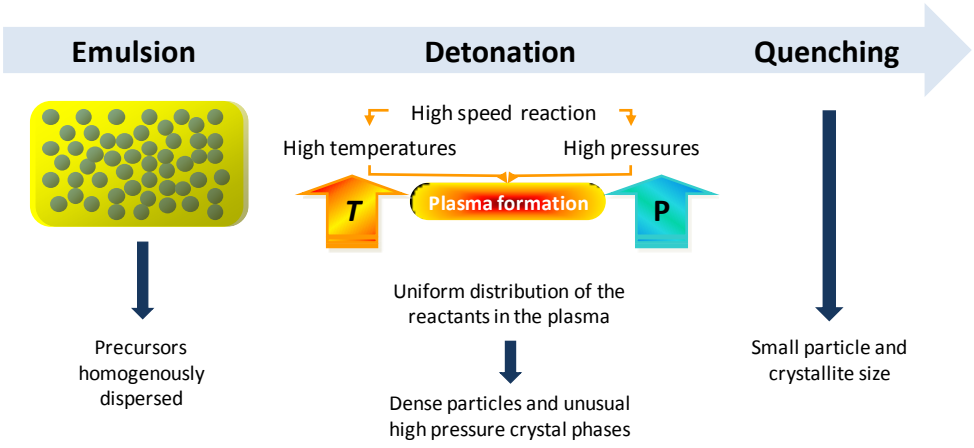

Fig. 2.8. *Schematic presentation of INNOVNANO emulsion detonation synthesis process.*

Supported by these temperature conditions and, in particular, the extreme pressure at which the process occurs, EDSM tries to take advantage of the relation between the diameters of the first stable liquid particles to be formed during gaseous phase reaction and the saturation degree of the metal-oxide.

Generically, gaseous phase comprises three stages in the synthesis of nanoparticles, namely the production of the compound in the vapour phase, condensation in the form of nanoparticles and

control and preservation of the dispersed nanocrystalline state. The control of condensation and the post-condensation stage are of extremely importance during the synthesis of nanoparticles in gaseous phase. It is difficult to model the formation of the first stable liquid particles formed (aerosol) by condensation, owing to the large number of experimental parameters and the difficulty in controlling them.

Condensation occurs when a vapour phase is taken to a supersaturated state, either by rapid isobaric cooling, i.e., at constant pressure *P*, or by isothermal compression, i.e., at constant temperature *T* (Fig. 2.9).

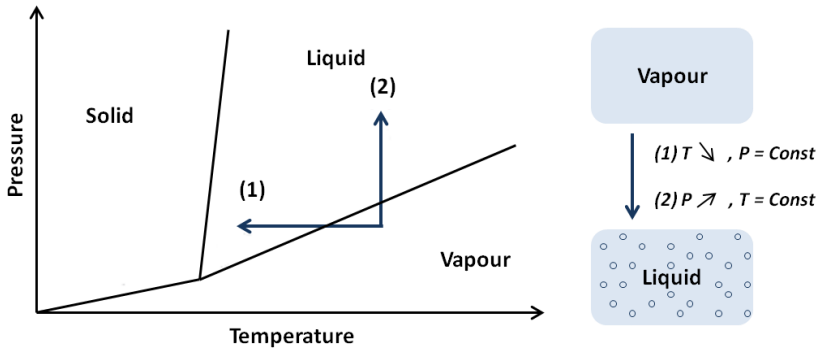

Fig. 2.9. *(P,T) phase diagram of a pure substance showing the two routes leading to a supersaturated vapour state: (1) isobaric cooling, (2) isothermal compression (adapted from [61]).*

The saturated vapour pressure P_0 is the pressure of the vapour of the compound in thermodynamic equilibrium conditions. The vapour pressure is related to the absolute temperature *T* by the Clapeyron relation [61]:

$$\ln P_0 = A - \frac{B}{T_0} \qquad \text{(eq. 2.1)}$$

where *A* and *B* are constants depending on the kind of vapour. If a vapour is under a pressure *P* when the equilibrium conditions gives P_0 such that $P > P_0$, the vapour is said to be in a non-equilibrium supersaturated state. This state will be broken to reach equilibrium under the effect of statistical fluctuations, and this will lead to the appearance of the liquid phase. The quantity $S = P/P_0$ is called the degree of supersaturation.

For the formation of an aggregate of n atoms, there are n – 1 combination stages, each one involving an energy reduction of $dG/dn = -k_B T \ln(P/P_0)$. The free enthalpy of formation of an aggregate (ΔG_n) is the sum of the enthalpy of the reversible reaction in which *n* atoms condense into an aggregate and the surface energy of the aggregate thereby formed:

$$\Delta G_n = \gamma_a S_n - (n-1) k_B T \ln \frac{P}{P_0} \qquad \text{(eq. 2.2)}$$

where γ_a is the energy per unit area, S_n is the area of the aggregate and k_B is the Boltzmann constant. This equation illustrates the existing competition between the negative condensation energy and the positive surface energy, which means that, if the aggregate is too small, the surface energy will be greater than the condensation energy. As a consequence the free enthalpy will be positive and the germ will evaporate. The free enthalpy varies as $\ln(P/P_0)$. If $P < P_0$ there

will be no stable germ. So, in order to form a stable germ, *P* must be sufficiently greater than P_0 to compensate the surface energy that is created, i.e., the formation of stable germs is thus more favourable for higher degrees of supersaturation ($P >> P_0$).

From eq. 2.2 it is observed that there are a critical number of atoms in the germ for which the condensation energy is greater than the surface energy. Considering a spherical aggregate, the critical size of a stable germ d_c can be attained based on Kelvin-Gibbs equation defined as [61]:

$$d_c = \frac{4\gamma M}{\rho N_A k_B T ln(P/P_0)} \qquad \text{(eq. 2.3)}$$

where *M* is the molar mass of the compound, ρ is the density, and N_A is Advogadro´s number. So, the critical size d_c will be smaller if the degree of supersaturation (P/P_0) is made higher.

The formation of a vapor with pressure in a high degree of supersaturation reached during EDSM promotes the formation of stable critical aggregates with very small size. The ultra-fast quenching controls the nanometric state avoiding the excess of coalescent coagulation which usually occurs in the hottest regions.

The high pressure gas phase reaction has several advantages comparatively to the low pressure methods, namely the fact that it allows combining and obtaining a large set of materials with different crystalline structures and nanometric composites in a single stage, in large amounts, and with high phase homogeneity, from the high pressure reaction of the various elements in the gas phase. On the other hand, the wide range of precursors that can be used allows a larger variety of materials that can be processed when compared with others synthesis methods. The production of nanoparticles by EDSM comprises four different stages [64]:

a) Preparation of the initiator and secondary (W/O) emulsions including the corresponding precursors in the desired ratio: the flexibility in formulation of the emulsion allows including in its composition a large set of precursors, from metals, metal alloys, to different metal salts;
b) Detonation reaction of the (W/O) emulsions with the formation of a gaseous plasma that contains the required materials in the gaseous phase: the extremely fast detonation reaction rates (in the order of microseconds) generate high pressures which ensure a complete transformation degree of the precursors into a gas plasma that already contains the required materials/composites;
c) Condensation and formation of the nanocrystalline particles at high pressures in a high supersaturation state: in order that the condensation phenomenon of the materials occurs and results in the production of a large amount of nanometric-sized particles, the gaseous plasma has to achieve high pressures in a high supersaturation state. The size of the first condensates will decrease with increasing supersaturation degree, as measured from the relation between the reaction pressure and atmospheric pressure (P/P_0). The pressure levels generated by the detonation of the emulsion ensure maximization of the (P/P_0) relation and consequent production of nanometric-sized particles;
d) Ultrafast cooling rate (quenching) (up to 10^8 Ks^{-1} to 10^9 Ks^{-1}) of the particles to control and preserve their nanometric size: after the formation of the first particles, the

nanometric state will be rapidly destroyed by the beginning of the coalescence phenomenon among particles, being therefore indispensable a ultra fast cooling rate as soon as they are formed, or their dispersion in a high speed gas flow, for controlling process.

The water-in-oil (W/O) emulsion is particularly suited for the powder synthesis by detonation for several reasons [65]: Firstly, the high homogeneity grade of all the components assures complete chemical reactions during detonation; Secondly the flexibility in terms of possible precursors and components that allows a strict control of purity and final properties of the synthesized powders; Finally the stability and safety of the emulsion due to the higher water content of its composition.

As pointed out before, the reaction synthesis takes place by the combination of high temperatures, high dynamic pressures, and quenching, which potentiates the production of already known materials with improved properties and also the synthesis of compounds difficult to obtain by common synthesis techniques, both at large scale and without costs increase.

Due to the shock wave induced reaction in EDSM, high pressure reactions, that by other process take hours or days, take place in micro-seconds enabling the synthesis of large quantities of high pressure synthesis products. Orthorhombic ZrO_2 that is formed at pressures above 3.5 GPa (being investigated as a possible material for thermal barrier coatings due to its high stability to thermal cycling (much smaller volume change) than the ambient pressure monoclinic phase) [66, 67], or some perovskite structures (e.g. $SrGeO_3$ or $SrSiO_3$) [68, 69], may therefore be produced in a short time with high reproducibility, contrary to the currently observed. In addition, the extremely high pressures induce amorphous phase, changing crystalline forms into less crystalline or amorphous substances leading to products with better performances for specific applications (e.g. improved catalytic properties, materials with superior magnetic properties or even enhanced bioactivity) [70].

On the other hand, the high temperatures reached during emulsion detonation synthesis (without high energy output) also allow synthesizing several compounds that are not possible at room temperature. Furthermore, the combination of high pressures and high temperatures make possible and reproducible difficult reactions, such as solid-state ones.

Immiscible phases that were mixed at high temperatures and pressures remain mixed not being possible a phase separation due to quenching. Composites of two or more materials (e.g. ZrO_2 – Al_2O_3 composite) in a single particle maintaining the individual crystalline structures of both alumina and zirconia, were already successfully synthesized at INNOVNANO.

Thereafter, EDSM emerge as an extremely effective method for the production of small primary particle size and high specific surface area (SSA) nanoparticles with multiple crystalline structures, such as metal-oxides (binary, ternary, or other crystalline structures), non-oxides with crystalline structure of the nitride type (e.g. AlON, AlN, SiAlON) or carbide type (e.g. SiC), composites (e.g. Al_2O_3 – ZrO_2) and solid solutions.

2.3.2.1. Emulsion detonation synthesis versus competitors´ synthesis methods

As presented before, the evaluation of the most important synthesis methods for the production of nanoparticles shows that sol-gel (section 2.2.2.2) and plasma synthesis (section 2.2.3.2) are

those with the greater potential. A comparison between EDSM, sol-gel and plasma synthesis is presented in Table 2.1, emphasizing the benefits and disadvantages of each one concerning the readiness for market, economic aspects, quality of the product, and manufacturing process.

Table 2.1. *Comparison between the sol-gel, plasma synthesis and emulsion detonation synthesis methods (adapted from [62]).*

	Sol-gel	Plasma synthesis	Emulsion detonation synthesis
Readiness for marketing			
Year 2007	Between applied research and pilot line	Between applied research and pilot line	Between applied research and pilot line
Year 2010	Pilot line	Between pilot line and production level	Between pilot line and production level
Year 2013	Between pilot line and production level	Production level	Production level
Economic aspects (general)			
Cost of the equipment	+	-	0
Production rate	--	++	++
Energy consumption	+	--	+
Yield	-	0	+
Economic aspects (specific)			
Need for solvents	--	0	++
Cost of precursors	-	+	+
Cost of all raw materials and supplies	--	0	+
Energy needed for the reaction itself	+	--	+
Overall energy consumption	0	--	+
Maintenance	0	-	-
Manual labor	-	0	0
Quality of the products			
Purity	++	++	+
Homogeneousness	++	+	++
Uniformity	+	0	+
Reproducibility	++	+	+
Equiaxed	++	-	0
Manufacturing process			
Controllability of the process	+	+	+
Environmental friendliness	-	0	+
Range of processable materials	0	++	++
Processing temperature	++	-	+
Composites/multimetal compounds	+	++	++

Legend: ++ very good; + good; 0 average; - bad; -- very bad

Besides the quality of the product, it is known that the probability of success of a particular synthesis method is directly related to its economic viability, especially when thinking about production at industrial level.

The need for high quantity of solvents has a negative impact on production costs, not only because of their acquisition value, but also because costs associated with either recycling back into the process or for residual disposal. In this aspect sol-gel method is clearly in disadvantage to the other two processes since it requires a big amount of solvent to be used per kg of powder produced. Generally, plasma synthesis also required solvents (organic or water) to dissolve the precursors or to suspend them. However, there is no need for disposal since they are burned during synthesis. In some cases, plasma synthesis powder precursors can be added without the need of a solvent. EDSM does not require any specific solvent during synthesis.

In terms of costs of the precursors sol-gel has a need for soluble precursors (alkoxides or metal salts) which are expensive and does not allow substitution by cheaper precursors. On the other hand, plasma synthesis and EDSM have a wide variety of choices of precursors which allow the selection of the most cost effective precursors. For raw materials in general, each process has its own specificities:

- Sol-gel needs solvents, catalysts, etc;
- Plasma synthesis requires solvents, gas feed for the plasma quenching gas, electrodes, etc;
- EDSM uses oils, emulsifiers, ammonium nitrate, plastic, initiation plate, etc.

These, added to the cost of precursors, leads to the balance presented in Table 2.1.

The energy consumption costs was divided in Table 2.1 into the energy needed for the reaction itself that considers only the process of turning precursors into the desired compound, and the overall energy consumption including post-production processes such as collection, deagglomeration or post-treatment.
In terms of energy needed for the reaction itself, only the energy to reach the gel was considered since it is a room temperature process. Plasma synthesis requires a continuous high input of energy in order to sustain the reaction, which takes place at high temperatures (for plasma formation). EDSM needs a high discontinuous input of initiation energy. The high temperatures and pressures of the reaction are, however, self-sustained (the reaction itself produces these conditions).
The overall energy consumption, include post-production aspects considering packaging a common stage to all processes. In sol-gel, after the production of the gel, several steps are necessary, such as evaporation of the solvent (high energy demanding) and sometimes thermal treatment of the products. Other steps (deagglomeration, functionalization, etc) may or may not be needed according to the application. General operation of the equipment (valves, pumps, stirrers, etc.) also requires energy. Plasma synthesis requires, among other aspects, collection of the synthesized materials. Pre-preparation of the solution or suspension of precursors, their injection in the reactor, injection of the quenching gas, operation of valves, pumps, etc., all consumes energy. Similarly to sol-gel, deagglomeration or functionalization stages may or may not be needed. In EDSM should be considered the collection of the materials and general

operation of the equipment (reactor, valves, robotics, emulsion preparation, etc). One more time, other steps like deagglomeration or functionalization, may or may not be needed depending on the application and/or synthesis conditions. The synthesized powder always requires a heat treatment to remove the carbon inherent to the detonation synthesis.

In relation to the manual labor, all processes can be automatized, but the lower production yield of sol-gel process leads to a more negative weight in this issue.
The maintenance costs of a sol-gel installation are considered very acceptable since the process occurs at room temperature and does not necessary use corrosive solvents or precursors. On the other hand, plasma synthesis and EDSM presents higher maintenance costs. Plasma synthesis is a high temperature continuous process that requires highly resistant materials that are subjected to continuous thermal and abrasive strain. In turn, EDSM falls into a similar situation as in plasma synthesis, with highly resistant materials subjected to pressure peaks, high temperature and abrasion.

The very good quality of the nanoparticles produced by the sol-gel method is the major advantage of this process with special emphasis on the very narrow particle size distribution when compared with plasma synthesis and EDSM. However it is inappropriate for the synthesis of large amounts of nanoparticles. The excellent homogeneity and uniformity (due to the extreme synthesis conditions reached during detonation) are the principal advantages of the EDMS process. In addition, the large range of processable materials, the possibility of producing composites/multimetal compounds, the economical viability, and the high production rates and environmental friendliness, makes EDSM an extremely solid process to be one of the world leaders in the production of nanoparticles.

2.4. Synthesis of aluminum-doped zinc oxide nanoparticles

In sections 2.2 and 2.3 were presented the most important synthesis methods for nanoparticles production, emphasizing the ones with highest potential for industrialization. Concerning the materials, the synthesis of aluminum-doped zinc oxide (AZO) nanoparticles is of great interest since its industrial application is growing fast, especially due to the possibility of direct deposition of nanoparticles as a thin film layer for optoelectronic applications [70-73], and also due to the advantages in terms of processing and final characteristics of the ceramic pieces in high-performance applications [74, 75]. For instance, the homogeneous dispersion of additives is one of the most important characteristics during the powder processing and is usually promoted by using nanoparticles rather than large particles as raw materials [74]. Although most commercially available AZO powders are still being produced by solid reaction where a ball milling technique is normally used to mix the powders and/or precursors [74, 76], almost all production routes previously presented and some alternative ones are used for the synthesis of nanosized AZO particles. As described in the preceding sections (2.2 and 2.3) for nonspecific metal-oxide nanoparticles, depending on the synthesis method, it is possible to achieve AZO nanoparticles with different particle sizes, degree of agglomeration, morphologies, composition and/or degree of homogeneity.

Synthesis methods such as sol-gel [20], precipitation [17, 18, 28, 29], microemulsion reaction method [18] or hydrothermal synthesis [19, 21, 22] are widely used for the production of nanosized AZO particles.

In addition, AZO nanoparticles are also largely produced by gaseous-phase synthesis such as laser-ablation [77], vapor condensation [78] or flame spray pyrolysis [51, 79-81]. Following the same way from general production of metal-oxide nanoparticles, nanosized AZO particles production faces serious problems in terms of industrialization. On the one hand, the high costs associated to some of the processes invalidate their scale-up to an industrial level despite the quality of the nanoparticles formed. On the other hand, there are also limitations in controlling the particle size, the degree of homogeneity of Al in ZnO particles, the degree of agglomeration and the ZnO:Al stoichiometry.

In general AZO particles synthesized by co-precipitation [82-84] and solvothermal decomposition [85] are typically characterized by wide particle size distributions and heterogeneous Al doping concentrations on the final microstructures. Kim [79] observed that the synthesis and processing of AZO nanoparticles by liquid-feed flame spray pyrolysis using liquid Al and Zn precursors led to uncontrolled ZnO:Al stoichiometries segregations of the spinel ($ZnAl_2O_4$) and wurtzite phase (ZnO) combined with evaporation of the metallic Zn phase. Hidayat, *et al.* [80] and Hsiao, *et al.* [81] also produced AZO powders by spray pyrolysis and obtained highly agglomerated particles with poor redispersing characteristics. Similar behaviour was also observed by Strachowski *et al.* [78], Piticescu, *et al.* [21] and Chen, *et al.* [20] using respectively vapour condensation, hydrothermal and sol-gel techniques. The processing of suitable AZO nanoparticles in large scale is therefore still challenging.

2.5. Transparent conductive oxides (TCOs)

Transparent Conducting Oxides (TCOs) are considered key materials for transparent electronics as they simultaneously display two distinct properties: optical transparency in the visible range of electromagnetic spectrum and high electrical conductivity (Fig. 2.10). Since this dissertation is based on the optimization of ceramic sputtering targets for TCOs thin films deposition, in this section is provided an overview of the most relevant properties and applications of these materials, with special emphasis on the TCOs based in two binary compounds, Al_2O_3 and ZnO (AZO).

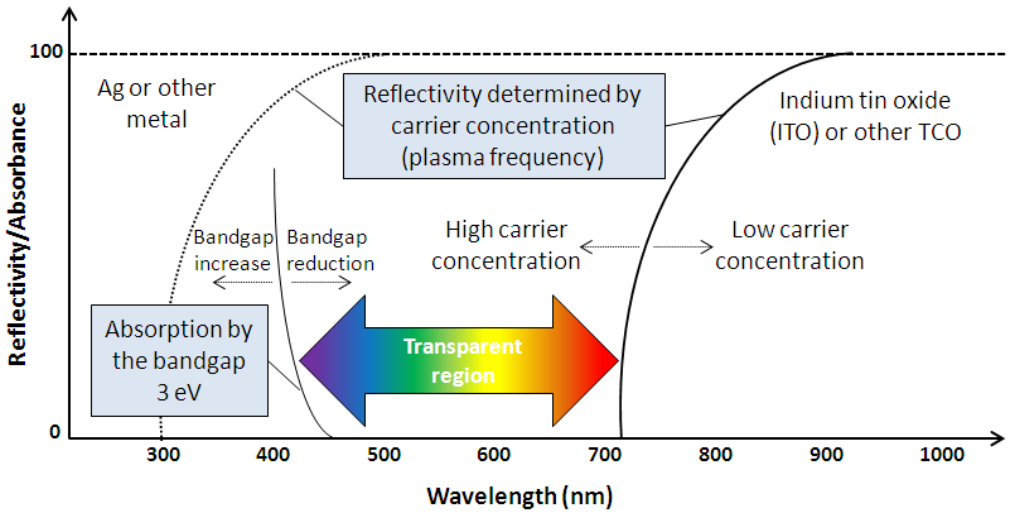

Fig. 2.10. *General conditions for transparent conducting materials: i) bandgap higher than 3 eV; ii) carrier concentration below 10^{21} cm^{-3} (adapted from [86]).*

2.5.1. History - Past, present and future of TCOs

Over the centuries, each material was associated with its own specific properties. When characterized as thin films, for instance, metals are normally described by having a high electrical and thermal conductivity and opacity. In turn, ceramics are generally seen as electrical insulating materials, which can be optically transparent due to their usually large bandgap ($E_g \geq 3$ eV). Thus, the discovery of simultaneously conductive and transparent materials has become a challenge. The first material where this combination of properties was observed dates from 1907, when Badeker produced the first TCO, the cadmium oxide (CdO) [87]. However, it took about 40 years until the development of new TCOs with superior properties, especially the ones based on SnO_2, In_2O_3 and ZnO due to the improvements in production and characterization techniques. It was during the Second World War that brought the first applications of these materials. By that time, SnO_2 was used as defroster at high altitudes in the warplanes, thereby enabling the aircraft pilots to maintain visibility [88, 89]. Since then, SnO_2, which was obtained by spray pyrolysis, began to be used in several applications such as window defroster or transparent electrical contacts replacing metals commonly used in these applications such as gold or silver [89]. However, despite its low electrical resistivity (~10^{-5} Ωcm), these films had an optical transmittance below 80 %, which was a limitation, especially when used as transparent electrical contacts. Nevertheless, this limitation was suppressed in 1956 with the appearance of the SnO_2-Sb_2O_3 TCO with a transmittance above 85 % in the visible region and an acceptable electrical resistivity of about 10^{-2} Ωcm, turning this kind of materials as an alternative to metal thin films [89]. Moreover, SnO_2-Sb_2O_3 thin films also presented high chemical stability, mechanical strength and good compatibility with different substrates [89, 90].

During the following decades, the severe increase in oil prices led to the search for alternative energy sources, in particular photovoltaics, which indirectly resulted in a strong and ongoing progress in TCOs development [91]. Besides polycrystalline TCOs, the 90s was marked by the development of a new class of amorphous oxides with properties comparable to those of polycrystalline materials. In 1990, Belligham *et al.* in an early work [92] presented amorphous In_2O_3 with electrical and optical properties comparable to those of widely studied polycrystalline In_2O_3. Some years later, in 1996, Hosono *et al.* boosted singularly the development of this class of oxides with the presentation of a new theory for the formation of amorphous oxides [93]. Also the first p-type TCOs were presented in this decade using NiO or $CuAlO_2$ [94, 95].

Nowadays, TCOs are used in a wide range of applications, where flat panel displays and thin film solar cells are the larger market for TCOs. Both have costs constrains as the global prices are decreasing fast. Thus, the searches for low cost and abundant material become challenging and several alternatives appeared, including conductive polymers [96], carbon nanotubes [97], or graphene [98]. Recently, TCOs have generated a new area of electronics known as transparent electronics [86, 99]. In this new field of applications the transparent metal oxides besides a passive role (TCOs) can perform also as an active component [99]. Used as semiconductor material (called by TSO – Transparent Semiconductor Oxide) in thin film transistors (TFTs), these materials are in direct competition with traditional silicon-based technology [100, 101]. The distinction between TSOs and TCOs is essentially based on the electrical resistivity (ρ_e) and carrier concentration (N_e). While for TCOs high N_e and low ρ_e are needed, in TSOs higher ρ_e and lower N_e are useful for the active layer in a TFT if it enables fully depletion of the semiconductor to switch-off the TFT [102]. To

achieve such characteristics in TSOs the incorporation of n-type dopants must be controlled in low levels which means the addition of intentionally compensating dopants, and/or acting at the oxidation level (since oxygen vacancies are well-known donors in most TCOs) [99].

2.5.2. General properties of TCOs

The generality of TCOs are based on simple oxides: CdO, In_2O_3, SnO_2, Ga_2O_3 and ZnO. However, in order to present electrical properties similar to metals without compromising transparency, simple metal oxides are usually degenerately doped. Similarly to classical semiconductors, such as single crystalline silicon, electrical conductivity in TCOs is predominantly carried out by electrons, being TCOs extrinsically or/and intrinsically doped. In the first case the doping is usually attained by the introduction of extrinsic substitutional elements in the crystal structure lattice, such as metal ions with different valences that are introduced in the cationic sites leading to the formation of free carriers [102-105]. In intrinsic TCOs, the conduction electrons come from intrinsic defects such as oxygen vacancies or interstitial metal cations that are responsible for shallow donor or impurity states sited near the conduction band. The excess or donor electrons are thermally ionized at room temperature, and move into the conduction band [105]. In both, extrinsic or intrinsic doping, the structural imperfection, or in other words the deviation from stoichiometry, is the main reason behind electrical conductivity in TCOs. In order to keep charge neutrality, the defects give rise to electrons that, depending on their energy level, can be ready for electrical conduction, increasing carrier concentration (N_e) and consequently the electrical conductivity (σ) [103].

TCOs are constituted by heavy metal cations with a $(n-1)d^{10}s^0$ ($n > 4$) outside shell electronic configuration and oxygen anions [93]. These materials have a wide bandgap (E_g) in which the *ns* orbitals of the heavy metal cations primarily constitute the bottom part of the conduction band and the oxygen *2p* orbitals form the top of valence band. The spatial scattering of the outside *ns* orbitals with spherical symmetry in the heavy metal cations is much larger than in light metal cations such as Al or Mg, leading to a broad conduction band. The large radii and spherical s-orbitals allow a good pathway for electron transport, due to the easy overlap of orbitals in the neighbouring cations [106]. Since the carrier mobility (μ_e) is proportional to the width of the conduction band, TCOs presents low ρ_e contrary to light metal oxides such as Al_2O_3 and MgO which are typical insulators, with the donor and acceptor levels too far from the conduction and valence bands. The metal ion radius, metal-oxygen bond length and metal-oxygen-metal angle are among the critical parameters that determine the μ_e of these TCOs [107].

Regardless of their structure (polycrystalline or amorphous) or how the carriers are created, most of the studied TCOs are of n-type and presents E_g greater than 3 eV, carrier concentrations in the range 10^{18} – 10^{21} cm^{-3} and carrier mobilities higher than 10 $cm^2V^{-1}s^{-1}$, which allow obtaining thin films with transmittance above 80 % in the visible range and low electrical resistivity (10^{-3} – 10^{-4} Ωcm). In Table 2.2 are summarized the basic electrical properties found for the three most common TCOs, considering In_2O_3:Sn, ZnO:Al, and SnO_2:F TCO:n-type dopant combinations.

Table 2.2. *Electrical properties of In_2O_3, ZnO and SnO_2 thin films. Electrical resistivities reported are for best-case polycrystalline films (adapted from [99]).*

Material	Bandgap (eV)	Electrical resistivity (Ωcm)	Electron concentration (cm^{-3})	Mobility ($cm^2V^{-1}s^{-1}$)
In_2O_3	3.75	1×10^{-4}	$>10^{21}$	35
ZnO	3.35	1.25×10^{-4}	$>10^{21}$	20
SnO_2	3.6	2×10^{-4}	$>10^{20}$	15

All presented TCOs are composed by metallic cations and oxide anions with ns^0 and $2s^22p^6$ valence electron configurations, respectively, with n = 4 for ZnO and n = 5 for In_2O_3 and SnO_2.
All these three metal-oxides present μ_e of the same order of magnitude in single crystals (160 – 240 $cm^2.V^{-1}.s^{-1}$), which is much higher than the μ_e obtained in thin films [99, 107]. This is due to the fact that thin films have usually polycrystalline structure, independently on the deposition method and processing conditions. Therefore, grain boundary scattering limits the carriers transport, reducing μ_e [108, 109]. Furthermore, the thin films generally have N_e values much higher than undoped single crystals, which is due to intrinsic defects created during deposition that behave as shallow donor levels.

Oppositely, when intentionally doped, single crystals of ZnO reach higher N_e values ($N_e > 10^{20}$ cm^{-3}) and a similar μ_e is obtained in both doped single crystals and polycrystalline thin films for the same N_e. This happens because for this N_e values, μ_e is mainly controlled by ionized impurity scattering independently of the material structure [108]. Thus, by manipulating the deposition conditions, it might be possible to reach thin films with controllable N_e and μ_e, to be used either as TCOs or TSOs. However, in polycrystalline TSOs with very low N_e the energy associated with the grain boundaries is too high, so electrons cannot surpass it , i.e., carrier transport starts to be dominated by the energy barriers at the grain boundaries, which can only be overcome using higher N_e [99, 110]. Thus, even with different structural properties, ZnO, In_2O_3 and SnO_2 electrical properties at the N_e ranges of interest for TCOs and TSOs are mainly controlled by the same mechanisms, ionized impurity scattering and grain barrier inhibited transport, respectively. This way, the typical electrical properties of these polycrystalline thin films are similar.

As mentioned before, ZnO, In_2O_3 and SnO_2 have been predominantly used as TCOs. However, stimulated by the need to rapidly answer to the strong demands of world market, not only in terms of technological but also sociological requirements [90], the field of TCOs has recently be expanded to a broader ranges of oxides. Nowadays, world research in TCOs, apart from simple oxides, is focused on the production of binary, ternary or multicomponent oxides TCOs, as detailed in Table 2.3 [88, 111, 112].

Table 2.3. *Typical elements/compounds used as TCO materials (adapted from [90]).*

TCO material	Dopant or compound
ZnO	Al, Ga, In, B, F, Ge, Y, Sc, V, S, Ti, Zr, Hf
In_2O_3	Sn, Ge, Mo, F, Ti, Zr, Hf, Nb, Ta, W, Te
SnO_2	Sb, F, As, Nb, Ta
CdO	In, Sn
$ZnO\text{-}In_2O_3$	$Zn_2In_2O_5$, $Zn_3In_2O_6$
$ZnO\text{-}SnO_2$	Zn_2SnO_4, Zn_3SnO_3
$In_2O_3\text{-}SnO_2$	$In_4Sn_3O_{12}$
$CdO\text{-}SnO_2$	Cd_2SnO_4, $CdSnO_3$
$CdO\text{-}In_2O_3$	$CdIn_2O_4$
$GaInO_3$, $(Ga,In)_2O_3$	Sn, Ge
$ZnO\text{-}In_2O_3\text{-}SnO_2$	$Zn_2In_2O_5\text{-}In_4Sn_3O_{12}$
$CdO\text{-}In2O_3\text{-}SnO_2$	$CdIn_2O_4\text{-}Cd_2SnO_4$

Taking advantage of its unique characteristics such as high electrical conductivity, high transparency in the visible range, high reflectivity in the infrared region, high mechanical hardness or high sensitivity to gas pressure, optimized TCOs have been used in a wide range of applications. Among several others, these materials have been applied as transparent heat reflectors in energy-efficient windows, heating stages for optical microscopes, abrasion- and corrosion-resistant coatings, antistatic surface layers on temperature control coatings in orbiting satellites and gas sensors. When used as transparent electrodes TCOs are extensively used in solar cells, light-emitting diodes (LEDs), flat panel displays, electrochromic windows and as a thermoelectric material [99, 102].

2.5.2.1. Theoretical approaches and limitations over TCOs electrical and optical properties

The improvement of electrical properties of TCOs is physically limited. Carrier concentration (N_e) and carrier mobility (μ_e) cannot be separately increased as carrier transport is limited primarily by ionized impurity scattering.

In very high doping concentrations the μ_e of the TCOs and their optical transmittance in the near infrared (NIR) region are lowered. Bellingham *et al.* [92] reported that μ_e and therefore ρ_e of TCOs (ITO, SnO_2, ZnO) are limited by ionized impurity scattering for N_e values above 10^{20} cm^{-3}. Ellmer [108, 113] also showed that ρ_e and μ_e were nearly independent of the deposition method and limited to about 2×10^{-4} Ωcm and 50 $cm^2V^{-1}s^{-1}$, respectively. ITO thin films also have a N_e limit of about 1.5×10^{21} cm^{-3} with the same σ and μ_e limits previously stated [114]. All the recently developed TCO materials, including doped and undoped binary, ternary or multicomponent oxides face the same limitations. Furthermore, the high doping concentration is not a good practical solution since it also contributes to the clustering of the dopant ions [115] which amplify considerably the scattering rate, and it could also generate a nonparabolic dispersion relation of the conduction band, and so

these electrons responds to forces much like they would be in vacuum, though with a different effective mass (m^*). This has to be taken into account for degenerately doped semiconductors with filled conduction bands [116].

Electrical resistivity (ρ_e) of n-type TCO thin films is correlated with carrier concentration (N_e) and carrier mobility (μ_e) of TCOs by the following equation:

$$\rho_e = \frac{1}{N_e q \mu_e} \qquad \text{(eq. 2.4)}$$

where q is the electron charge. In turn, the mobility can be defined by the ratio between the product of electron charge (q) and its lifetime between collisions (τ) and the effective mass of the electron (m^*) as shown in eq. 2.5:

$$\mu_e = \frac{q\tau}{m^*} \qquad \text{(eq. 2.5)}$$

Since N_e and τ are inversely correlated, the magnitude of μ_e is limited.

Usually, τ is a function of several different dispersion mechanisms in films, such as phonon-assisted scattering (also called by lattice vibration scattering) (μ_{ph}), ionized impurity scattering (μ_{ii}), scattering by neutral impurities (μ_{ni}) and grain boundary scattering (μ_{gb}). Thus, carrier mobility (μ_e) can be seen as the sum of μ_e associated to each dispersion mechanism (eq. 2.6), presenting each scattering mechanism a dependence on temperature (T) (μ_{ph}: $T^{-3/2}$; μ_{ii}: T^X(0 < X < 3/2; μ_{ni}: T^X(0 < X < 1)) [117]:

$$\frac{1}{\mu_e} = \frac{1}{\mu_{ph}} + \frac{1}{\mu_{ii}} + \frac{1}{\mu_{ni}} + \frac{1}{\mu_{gb}} \qquad \text{(eq. 2.6)}$$

From all the scattering mechanisms, ionized impurity scattering dominates in several highly degenerate TCOs (i.e. with a high carrier concentration) such as Sn-doped In_2O_3 (ITO – Indium Tin Oxide), Ga-doped ZnO (GZO – Gallium Zinc Oxide) or Al-doped ZnO (AZO – Aluminum Zinc Oxide) [90]. The high N_e of the thin films also affects the Fermi level (E_F) as presented in eq. 2.7:

$$E_F = \frac{h^2 k_F^2}{8\pi^2 m^*} \qquad \text{(eq. 2.7)}$$

where, h is the Planck constant and k_F the Fermi wave vector defined as:

$$k_F = (3\pi^2 N_e)^{\frac{1}{3}} \qquad \text{(eq. 2.8)}$$

The E_F variation in thin films due to N_e also affects other properties, particularly the bandgap (also called energy gap) (E_g). As N_e increases, E_F has a dislocation towards the conduction band since lower energy states are filled. Thus, it is necessary to provide more energy to the electrons from the valence band so they take the free states within the conduction band. This magnification effect of the bandgap, known as Burstein-Moss shift (ΔE_{BM}) is frequently observed in TCOs (Fig. 2.11) and can be described as [118-121]:

$$\Delta E_{BM} = \frac{h^2 k_F^2}{2m_{cv}^*} \qquad \text{(eq. 2.9)}$$

where m_{cv}^* represents the combined effective mass defined as:

$$\frac{1}{m_{cv}^*} = \frac{1}{m_c^*} + \frac{1}{m_v^*} \quad \text{(eq. 2.10)}$$

where m_c^* and m_v^* correspond respectively to the effective mass of carriers in conduction and valence bands. Subsequently optical bandgap (E_{opt}) can be displayed as:

$$E_{opt} = E_g + \Delta E_{BM} \quad \text{(eq. 2.11)}$$

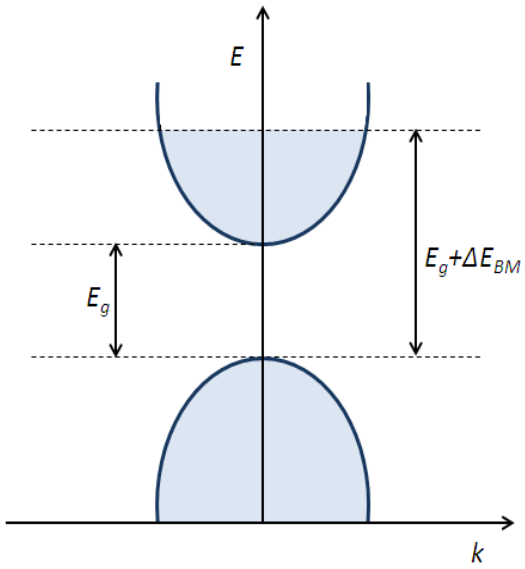

Fig. 2.11. *Bands diagram representation of the Burstein-Moss effect (adapted from [122]).*

As previously mentioned, besides low ρ_e, high performance TCOs should present a very low absorption coefficient (α) in the UV-VIS-NIR region. Transmission (T_r) in the near UV is limited by E_g as photons with energy larger than E_g are absorbed. A second transmission edge exists at the NIR region, mainly due to reflection (R_f) at the plasma frequency. Ideally, a TCO with a wide E_g should not absorb photons in the UV-VIS-NIR region. However, even if such TCOs films could be deposited, reflection and interference would also affect transmittance and consequently fully transparency over a wide region cannot be obtained.

The optical properties of thin films TCOs (T_r, R_f, and optical absorption (A_b)) depends on its refraction index (n_{RI}), extinction coefficient (k_{EC}), E_g, and geometry. The n_{RI} and k_{EC} depend on the type of material and on its chemical composition and structure, while the geometry depends on the film thickness, thickness uniformity, and film surface roughness. There is a negative relation between N_e and the position of the NIR absorption edge, but positive between N_e and the UV absorption edge, since E_g increases with N_e due to the Burstein-Moss effect.

2.5.3. Most commonly used TCOs – trends, limitations and future perspectives

The unique properties of TCOs allow its use in a broad range of applications. Industrially, the most extensively used TCO is the extrinsically doped indium tin oxide (In_2O_3:Sn, ITO), being the compounds fluorine doped tin oxide (SnO_2:F, FTO), and cadmium stannate (Cd_2SnO_4) also widely used. However, the extremely high prices of indium associated with its rarity, and the high toxicity of fluorine and cadmium are important limitations that must be considered, leading researchers to look for alternative materials. Zinc is more abundant than indium and tin (132 ppm compared

with 0.1 and 2 ppm, respectively) and less toxic than cadmium and fluorine, which makes ZnO a very suitable alternative TCO [108]. In the following subsections it will be presented the main characteristics, applications and limitations of undoped and Sn-doped In_2O_3 (ITO) and a review regarding undoped and doped ZnO focusing on Al-doped ZnO (AZO) as a substitute TCO material over ITO.

2.5.3.1. Undoped and Sn-doped In_2O_3 (ITO) thin films

Indium oxide (In_2O_3) has a cubic bixbyite crystalline structure (Fig. 2.12), with a lattice parameter of 10.117 Å and a density of 7.17 $g.cm^{-3}$, containing each unit cell 32 atoms of indium and 48 atoms of oxygen [102, 123, 124].

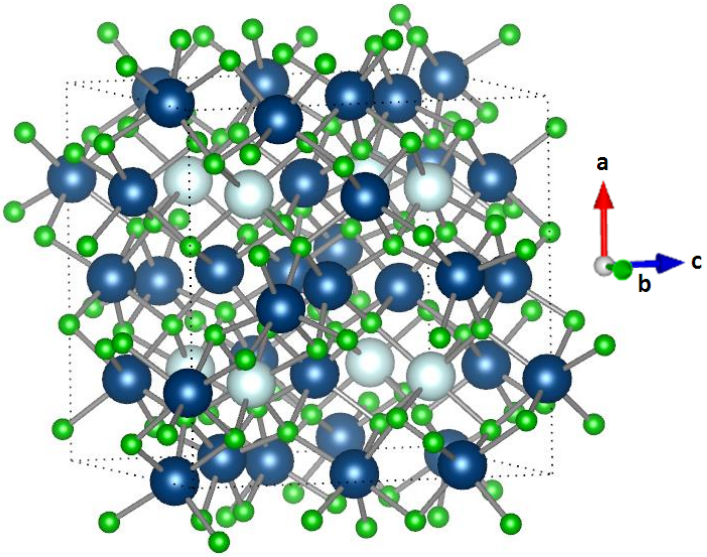

Fig. 2.12. *Cubic crystalline structure (bixbyite) of In_2O_3. The large spheres represent the In metallic cations (dark and light blue spheres illustrate the two distinct positions of In in the unit cell), while the small green spheres represent oxygen anions.*

The bixbyite structure can be derived from the face-centered cubic structure of fluorite (CaF_2) removing a quarter of the anions. The main difference between these structures is the coordination of the metal atoms. Fluorite is eight-fold coordinated to neighboring oxygen atoms (MO_8), i.e., each Ca atom is coordinate by 8 F atoms. In the case of In_2O_3 bixbyite structure, the coordination is MO_6 where indium has two distinct positions in the unit cell [123]. In this case each indium atom is coordinated with only 6 oxygen atoms resulting in a distorted structure with distinct In-O bond lengths. In fact, considering the electron configuration of both atoms indium (In: $1s^2|2s^22p^6|3s^23p^63d^{10}|4s^24p^64d^{10}|5s^25p$) and oxygen (O: $1s^2|2s^2\ 2p^4$) [125], is evident that oxygen atoms need two more p-electrons to reach a stable 8-electron configuration. On the other hand, indium atoms have three electrons over a stable electron configuration. Consequently, the stoichiometry of the oxide is In_2O_3 giving rise to the transition of electrons from indium to oxygen and a crystal structure with In^{3+} and O^{2-} ions in the lattice [126]. The MO_6 coordination forces the displacement of the indium from the center of the cube. Thus, the unit cell has two unequal In positions, with one-quarter of the indium atoms located at the center of a less distorted trigonally oxygen octahedron, and the remaining three-quarters positioned at the center of a more distorted and less symmetric octahedron that results from the removal of two oxygen atoms from

the same face of the octahedron. So, the characteristics of the defect structure are determined by this particular arrangement in atoms [127].

As presented in Table 2.2, In_2O_3 is an n-type semiconductor with a high carrier concentration and a wide bandgap (E_g). The Burstein-Moss shift for degenerately doped In_2O_3 with the increase of N_e is larger than 0.6 eV when the Fermi level (E_F) is above the minimum of the conduction band [92, 121]. The carriers in intrinsic oxides result from the formation of oxygen vacancies that provide free electrons according to the following equilibrium equations (Kröger-Vink notation) [128]:

$$2In_{In}^{x} + 3O_O^x \Leftrightarrow 2In_{In}^{x} + 3V_O^{\bullet\bullet} + 6e' + \frac{3}{2}O_2(g) \qquad \text{(eq. 2.12)}$$

$$O_O^x \Leftrightarrow \frac{1}{2}O_2 + V_O^{\bullet\bullet} + 2e' \qquad \text{(eq. 2.13)}$$

where, In_{In}^{x} represents a In atom which has remained in the same position (x means that there was no change in the oxidation state), $V_O^{\bullet\bullet}$ represents an oxygen vacancy positively charged (+2), and e' represents the free electron generated to keep charge neutrality (apostrophe means that the electron is negatively charged).

Considering these equations, becomes visible that oxygen vacancies are assumed to be the main sources of the shallow donor levels that yield the characteristic n-type conduction to In_2O_3. These donor levels are usually very close to the minimum of conduction band, in the range of 0.008 – 0.03 eV, depending on the donor concentration, with degeneracy starting at a donor density of 1.48×10^{18} cm^{-3} [102]. Taking into account that N_e and ρ_e of In_2O_3 thin films is directly influenced by oxygen, becomes essential its control during deposition.

When extrinsically doped with high valence impurities, which is the case of Sn, the electrical properties of In_2O_3 are considerably improved [121]. Indium tin oxide (ITO) is the most widely used TCO in optoelectronic industry especially due to its exceptional electrical ($\rho_e \approx 10^{-4}$ Ωcm) and optical (transmittance > 85 %) properties [121, 129-131]. It is transparent and colorless as a thin film and yellowish to grey as bulk material. ITO is a solid solution of indium (III) oxide (In_2O_3) and tin (IV) oxide (SnO_2), with typically 90 wt. % In_2O_3, 10 wt. % SnO_2 [132].

Fig. 2.13 shows the band diagram of ITO with low and high doping level, respectively. The lower limit of the conduction band is formed by In *5s* orbitals, while the upper limit of the valence band, which is about 3.5 eV below the lower limit of the conduction band, is formed by O *2p* orbitals. As already mentioned, In_2O_3 thin films are generally found in a reduced state with absence of oxygen ions in the In_2O_3 structure. Each oxygen vacancy is surrounded by *5s* orbitals from In^{3+} which stabilized from In:*5s* band due to the lack of covalent bond with O^{2-}. So, In:*5s* orbitals corresponding to each oxygen vacancy form donor states just below the conduction band trapping two electrons per oxygen vacancy, being formed a donor level approximately 0.03 eV below the conduction band. When Sn is added to In_2O_3 as a dopant, Sn^{4+} cations replace In^{3+} cations in the lattice providing one additional free electron. Thus, in the case of ITO coexists two different mechanisms of generation of free carriers: the first, resulting in the formation of oxygen vacancies in In_2O_3, and the second from the substitution of In^{3+} by Sn^{4+}, allowing to obtain carrier concentrations as higher as 10^{21} cm^{-3} [121, 133, 134]. The increase in the concentration of free carriers as a result of the high level of doping, promotes a shift of Fermi level (E_F) into the conduction

band. Thus, the bandgap (E_g) is increased from 3.5 to 3.7 eV due to carriers generated by oxygen vacancies and Sn ions [102, 135].

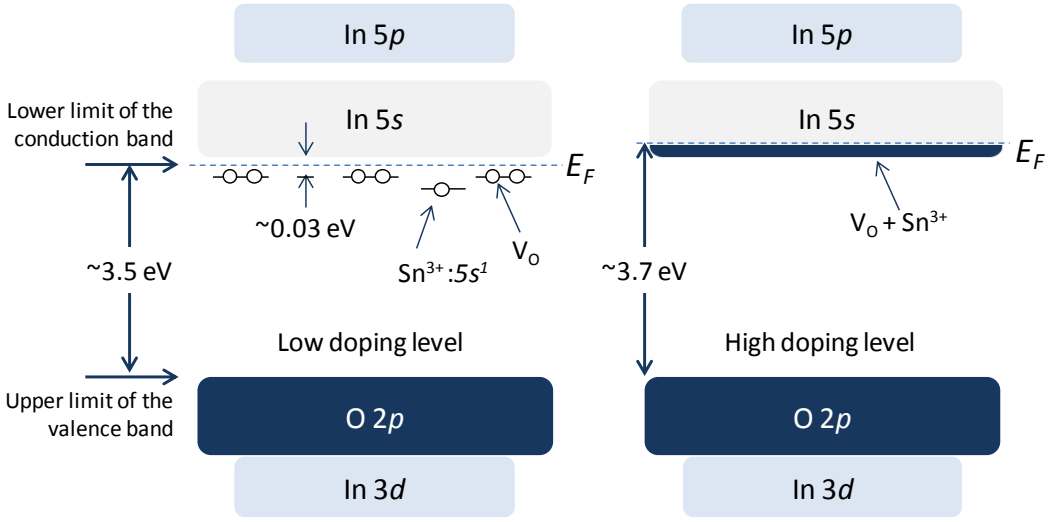

Fig. 2.13. *Bands diagram of ITO with different doping levels (Adapted from [122]).*

2.5.3.2. Undoped and Al-doped ZnO (AZO) thin films

The predicted growth of global market of energy (photovoltaics, architectural and window glasses) and information (displays) technologies will be only sustainable if low cost materials, environmental friendly, non-toxic, and low temperature processing technologies will be employed. In all these applications TCOs layers are an integrating part of the devices, with an average weight in total production costs of 4 – 8 % and 10 – 15 %, respectively for solar cells and displays [136].

The high price of indium has been driven by the increased consumption in optoelectronics devices and by its scarcity in nature leading to a predictable supply break within the next decades [137]. These aspects open priorities to the development of alternative materials, where ZnO based materials, in particular Al-doped zinc oxide (AZO), have consistently committed the highest importance [138].

Intrinsic ZnO is a wide bandgap n-type semiconductor (~3.2 – 3.4 eV) with the hexagonal crystal structure of wurtzite (Fig. 2.14), lattice parameters of 3.2498 and 5.2067 Å, respectively for a_0 and c_0 and a density of 5.61 g.cm^{-3}. Each hexagonal cell contains two molecules of ZnO where Zn atoms are tetrahedrally surrounded by O atoms. Perpendicularly to the c-axis, the unit cell consists of alternating Zn and O planes, resulting in a classical polar structure. The bands structure is analogous to In_2O_3, being the lower limit of the conduction band constituted by Zn *3s* orbitals and the upper limit of the valence band by O *2p* orbitals [90].

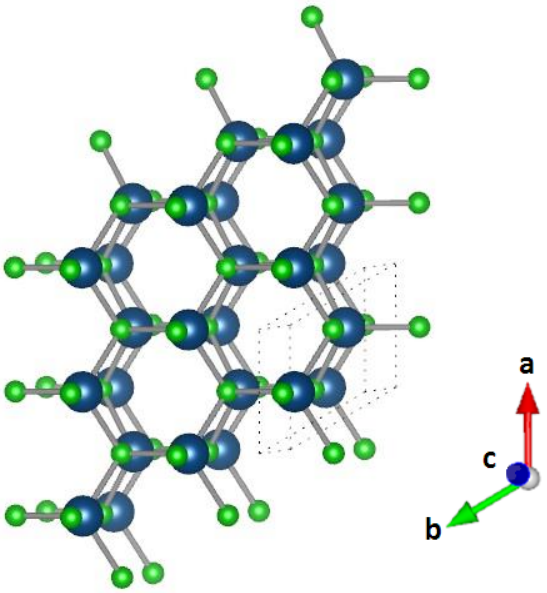

Fig. 2.14. *Hexagonal crystalline structure (wurtzite) of ZnO. The large dark blue spheres represent the Zn metallic cations, while the small green spheres represent the oxygen anions.*

The remarkable properties of ZnO contributed to an intensive research in the last decades being used in many areas, from rubber and concrete industries to medicine and cosmetics. Recently, ZnO has been widely used in TCOs applications, both as passive and active layer. The worldwide use of ZnO is exceeding 1.2 million tonnes annually [139]. ZnO offers numerous advantages like low cost (resource availability), capability to be processed at room temperatures, high electron mobility (200 $cm^2V^{-1}s^{-1}$, in crystal form) and a strong resistance to high energy radiation, which makes it suitable for space applications. In addition, ZnO is thermally and chemically stable and compatible with lithography processes in microelectronics [108, 140].

Free carriers in undoped ZnO have been attributed to the presence of native defects, such as Zn interstitials (Zn_i) and oxygen vacancies (V_O) [140], being the electrical conductivity of ZnO affected by additional electrons resulting from oxygen vacancies (eq. 2.13 presented for In_2O_3 system) or by the ionization of interstitial zinc atoms as shown in equations 2.14 and 2.15:

$$ZnO\ (s) + xZn(g) \leftrightarrow ZnO(s) + Zn_i^x \qquad \text{(eq. 2.14)}$$

$$Zn_i^x \rightarrow Zn_i^{\bullet} + e' \qquad \text{(eq. 2.15)}$$

where, Zn_i^x represents a Zn atom in an interstitial position (x means that there was no change in the oxidation state), $Zn_i^{\bullet}$ correspond to an interstitial Zn atom positively charged (+1).

A schematic representation of the typical defects responsible for the improvement of electrical properties in intrinsically doped ZnO is shown in Fig. 2.15.

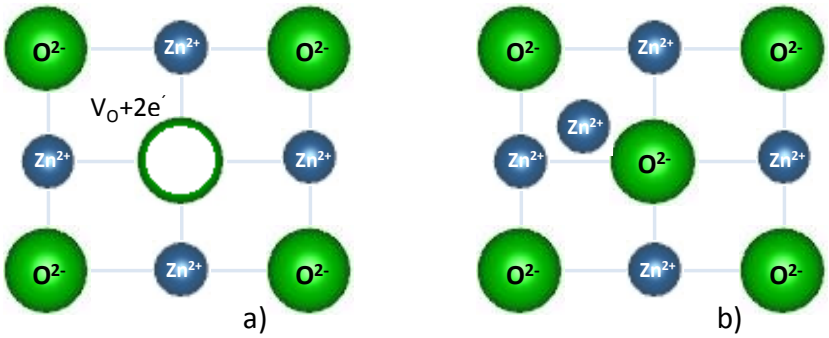

Fig. 2.15. *Typical point defects observed in intrinsically doped ZnO – a) Oxygen vacancy (V_O), and b) Zn^{2+} in an interstitial position (Zn_i).*

These point defects are always present in the material and can act as shallow n-type donors, with energy levels of about 30 meV below conduction band [141]. An annealing step in a reducing atmosphere after deposition has been widely reported [142-145] as a way to increase the oxygen deficiency, and therefore the carrier concentration in the thin film due to the release of trapped carriers at the grain boundaries via oxygen annihilation in the ZnO crystals [146]. In addition to the native defects, also hydrogen doping has been reported as way to enhance n-type conductivity in undoped ZnO thin films [147-149].

Generically, intrinsic doped ZnO thin films have carrier concentrations in the range of $10^{17} – 10^{19}$ cm^{-3} [150] and electrical resistivity of $10^{-1} – 10^{-3}$ Ωcm, which are unsatisfactory for their application as a transparent electrode in optoelectronic applications where high conductivity is required [90, 102].

As described for In_2O_3, the improvement of ZnO electrical properties can be reached by doping it with foreign elements. The donors can come either from group III atoms (B, In, Sn, Ga, or Al), or group VII atoms (Cl, Br or F), being incorporated substitutionally at the Zn and O sites, respectively, acting as a shallow donors. So, as illustrated in table 2.4, it is possible to obtain ZnO thin films with carrier concentrations of $10^{19} – 10^{21}$ cm^{-3} and ρ_e of $10^{-3} – 10^{-4}$ Ωcm [151-157]. In fact, ZnO extrinsically doped with some of these elements leads to some of the most conductive TCOs available today.

Table 2.4. Electrical resistivity and carrier concentration obtained for various impurity-doped ZnO thin films prepared with optimal doping content (adapted from [131]).

Dopant	**Dopant concentration (wt %)**	**Electrical resistivity × 10^{-4} (Ωcm)**	**Electron Concentration × 10^{20} (cm^{-3})**
Al_2O_3	0.5 – 2	0.85	15.0
Ga_2O_3	2 – 7	1.2	14.5
B_2O_3	2	2.0	5.4
F	0.5 (at %)	4.0	5.0
None	0	4.5	2.0

As stated before, among the impurity-doped ZnO TCOs, Al-doped zinc oxide (AZO) appears as the most promising and investigated material for ITO replacement. Optical transmittance above 80 % in the visible range and an improved electrical behavior, together with all the advantages already mentioned for undoped ZnO, makes AZO a desirable TCO material for optoelectronic devices development [130, 158-160], mainly in the production of transparent electrode for light-emitting diodes [161, 162], thermoelectrics [163, 164], thin film transistors [110, 165], or thin film solar cells [166-170]. Table 2.5 shows a comparison between the properties of AZO and ITO thin film transparent electrodes. AZO are known to be more easily etched (less stable) by both acid and alkaline solutions than ITO, which can be either an advantage or a disadvantage depending on the application. On the one hand, the lower stability of AZO requires extra care when lithography processes are used (e.g. in the preparation of transparent electrodes for flat panel displays), but it is also an advantage when etched surfaces are used to improve the TCO layer performance as in the case of several thin film solar cells [131].

Table 2.5. *Some AZO and ITO thin film transparent electrode properties (adapted from [131]).*

Property	AZO	ITO
Low resistivity (Ωcm)	10^{-5}	10^{-5}
Practical resistivity (Ωcm)	$2 – 3 \times 10^{-4}$	1×10^{-4}
Transmittance (%)	> 80	> 80
E_g (eV)	3.4	3.7
Refraction index (n_{RI})	2	2
Work function	4.6	4.8 – 5.0
Cost	Inexpensive	Very expensive

The effect of dopant ions and its location in the ZnO structure have been reported [171, 172]. When introduced as a doping element Al needs to be incorporated either in lattice sites and/or interstitially into zincite crystal structure to increase concentration of the charge carriers in the material. The substitution of Zn^{2+} ion by Al^{3+} in the lattice site provides a free electron (charge carrier) (Fig. 2.16 a)) promoting the enhancement of the conductivity [173] accordingly to the following equation:

$$Al_{Zn}^{x} \rightarrow Al_{Zn}^{\bullet} + e' \qquad \text{(eq. 2.16)}$$

where, Al_{Zn}^{x} represents a Al atom which is in a Zn position (x means that there was no change in the oxidation state), $Al_{Zn}^{\bullet}$correspond to a Al atom which is in a Zn position positively charged (+1) and e' represents the free electron generated to keep charge neutrality (apostrophe means that the electron is negatively charged).

Al incorporation is facilitated by both the small difference in electronegativity values of Zn (1.65) and Al (1.61) and the smaller ionic radii of Al (0.054 nm) when compared with Zn (0.074 nm). In general, doping ions can be located totally within the ZnO lattice as a substitute in the Zn sites. However, especially for higher doping concentrations, the dopant can also be sited between

crystallites as a non-conductive inter-grain layer causing an electrical isolation of the individual crystallites, which is undesirable for TCOs.

A controlled adjustment on the doping level to a small range of values is crucial in order to enhance the thin films properties. The material would be expected to incorporate a uniform and homogeneous distribution of dopant ions in the correct locations, up to a limit concentration. Concentrations above that limit could lead to dopants occupying adjacent or proximal lattice sites as schematically represented in Fig. 2.16 b), causing ion vacancies, resulting in a neutral defect, which would not contribute to the improvement of the electrical conductivity of thin films [174]. Compositions above the solubility limit of Al in ZnO lattice, promotes the formation of Al-O clusters or the amorphous gahnite spinel phase ($ZnAl_2O_4$) [175, 176].

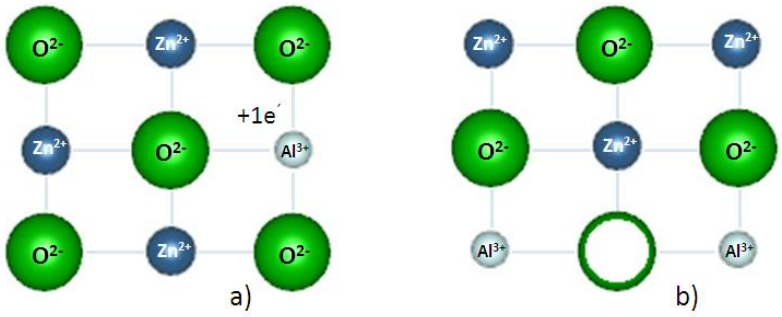

Fig. 2.16. *Schematics of the conduction mechanisms in extrinsically doped ZnO – a) Al^{3+} occupying a Zn^{2+} site in the ZnO lattice, and b) Al^{3+} occupying adjacent sites.*

The TCOs and in particular AZO thin films can be deposited by several physical and chemical deposition techniques, including sputtering [151, 153, 157, 164], metal organic chemical vapor deposition (MOCVD) [177], sol-gel processes [173, 178, 179], atomic layer deposition (ALD) [180], thermal evaporation [181], spray pyrolysis (SP) [71, 145, 182], molecular beam epitaxy (MBE) [183], pulsed laser deposition (PLD) [162, 184], spin coating [185] or more recently the ink jet printing [186].

The properties of TCOs thin films depend not only on the deposition technique, but also on the process parameters used in each technique [113]. Industrially, sputtering is the most used technique to prepare thin films owing to the simplicity of the method, safety, capability to be scaled-up to large glass substrates, high deposition rate at room temperature without toxic gas emissions, and low production cost [88]. In this method, that will be described in more detail in chapter 3, the properties of the deposited thin films are strongly dependent on several parameters, such as the power density, power source (RF, DC or both), substrate temperature, type of gas added to the process, sputtering atmosphere, equipment design, distance from target to substrate and working gas pressure.

The influence of sputtering atmosphere on AZO thin films deposition, for example, can be easily understood following the schematic Brouwer diagram plotted in Fig. 2.17, which shows the AZO log-log plot of defects concentration *versus* oxygen partial pressure (pO_2) [187]. As shown, the formation of killer defects, in this case Zn vacancies, results in ionic compensation of the donor species ($Al_{Zn}^{\bullet}$) rather than the desired carrier generation. In the high-pO_2 regime the electroneutrality condition is $2[V_{Zn}^{''}] = [Al_{Zn}^{\bullet}]$. As pO_2 is reduced, however, the electron population steadily rises until becomes the prevalent species compensating the donors. In low-

pO_2 regime, the electroneutrality condition becomes $n = [Al_{Zn}^{\bullet}]$. This means that the electron population in AZO can be changed by orders of magnitude through control of pO_2 during thin film deposition, with high oxygen contents yielding films with very small carrier contents (and Fermi levels in the bandgap) and low oxygen contents yielding degenerate films (and Fermi levels above the conduction band minimum).

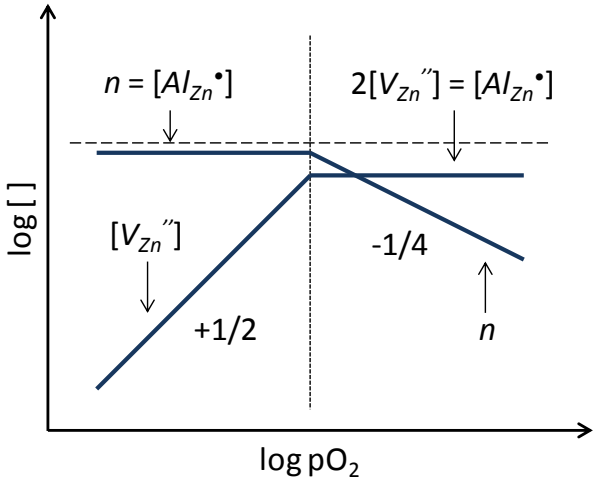

Fig. 2.17. *Schematic Brouwer diagram (log concentration versus log pO_2) for ZnO:Al (AZO). Vertical dotted line separates different electroneutrality regimes. Fractions indicate line slopes, n represents the concentration of electrons, $[Al_{Zn}^{\bullet}]$ the Al donors, and $[V_{Zn}^{"}]$ the doubly charged Zn vacancies (adapted from [187]).*

In addition, regardless of the deposition method, both growth structure and optoelectronic properties of the thin films can be also influenced by the type of underlying substrate (crystalline, amorphous or organic) [161, 162].

2.6. Global market of sputtered TCO thin films and sputtering targets

As mentioned already several times, TCOs are an integrating part of many optoelectronic devices. Thus, the market of this class of materials is closely linked with the devices were they are applied. In terms of surface area covered, and their total value, the three largest applications of TCOs thin films are: coatings on architectural glass (low thermal emission glass), flat panel displays, and photovoltaics [90].

The strong development of areas such as renewable energy and energy efficiency, driven by the need to reduce dependence on fossil fuels after the oil crisis experienced in United States during the 70s in the last century served as driving force to the first developments in the photovoltaics, and low thermal emission (low-e) glass industries. Thus, and indirectly, were created conditions for the growth of the TCOs market. In low-e glass is estimated that the demand for the coming years in Europe exceeds 100 million square meters per year [90].

Flat panel displays market which is dominated by liquid crystal display (LCD) technology (> 90 %), have had a remarkable growth during last decade (Fig. 2.18). The revenues increased from approximately 40 US billion dollars in 2003 to a value of about 140 US billion dollars in 2013, being expected a growth rate stabilization of about 2 – 3 % annually for the next years due to the maturation phase of LCDs in the market [188].

Fig. 2.18. *Flat panel display market revenues and growth between 2003 and 2015 (Adapted from [188]).*

Photovoltaics industry has by far the largest share of the global market of thin films in energy applications (>90 %) being estimated that the thin film solar cells market growth at a compound annual growth rate (CAGR) of around 25 – 30 % until 2020 [90]. Thin films production market in the global solar PV market grew from around 4 % in 2003 to ~30 % in 2013 (Fig. 2.19). Global thin film PV market is expected to generate 9.85 US billion dollars by 2017 with an estimated CAGR of 8 % over the next five years [189]. It is estimated that in 2020 thin film solar PV increase its market share to ~38 % with expectations that in the long-term thin film solar PV technology would surpass conventional crystalline silicon technology [190].

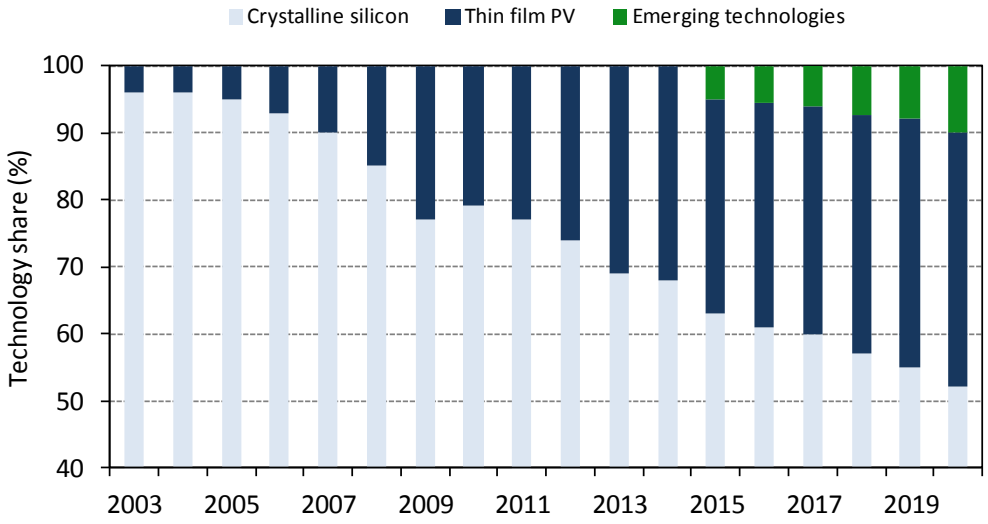

Fig. 2.19. *Thin film market share in terms of module production between 2003 and 2020 (Adapted from [190]).*

In Fig. 2.20 is illustrated the market share evolution until 2020. Due to its higher efficiency and reduced manufacturing costs it is expected that CIGS (cooper indium gallium (di)selenide) technology is accounted for 40 % of the market share in 2020 surpassing both a-Si and CdTe technologies. Investments over 2 billion dollars have already been made for the CIGS market development by various companies. The CIGS technology´s value proposition is that it offers,

combined advantages of both c-Si, which gives reasonably good efficiency and thin-film PV technologies, which claim potential advantages on cost, weight, flexibility, and manufacturability [190].

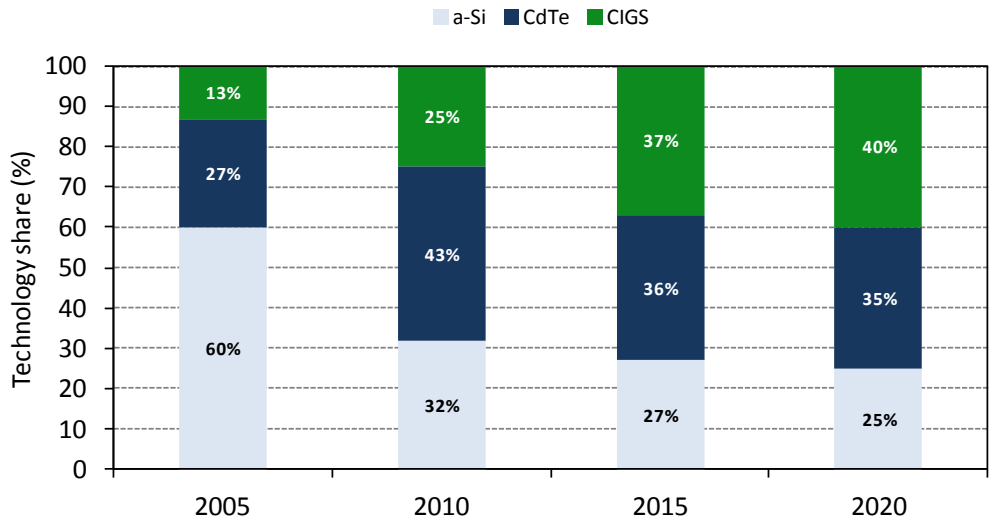

Fig. 2.20. *Thin film solar cells market share by technology type between 2005 and 2020 (adapted from [190]).*

As mentioned above, sputtering is the key technology for the fabrication of thin-film-based low-e glass, flat panel display devices and thin film solar cells. Since the source of the deposited material is a sputtering target, also the sputtering targets market has grown and predicts that it will continue to rise over the coming years. Sputtering targets market was dominated by the microelectronics sector for several years but it is being eclipsed by advanced displays and solar cells, which already appear as the main consumers of sputtering targets.

The dramatic global economy stagnation over the last years affected many sectors were sputtering targets are used, leading to a steep drop in sales. Based on recent studies showing that a recovery is taking place in the global economy, it is expected that sputtering targets and sputtered films market should restart growth during next years. Accordingly with the BCC Research market forecasting released in 2011 (Fig. 2.21) [191], the global market for sputtering targets was estimated to reach 5.9 US billion dollars by 2016 with a CAGR of 12.3 % in this period. In terms of unit volume, the projections indicate that worldwide production of sputtered films will increase at a CAGR of 8.6 % until 2016 resulting in the production of approximately 1.8 billion square meters of thin films in 2016 consuming more than 9 million kg of sputtering target material. The global market for sputtering targets is estimated to reach nearly 1.7 million units in 2016 corresponding to a CAGR of 8.4 % [191].

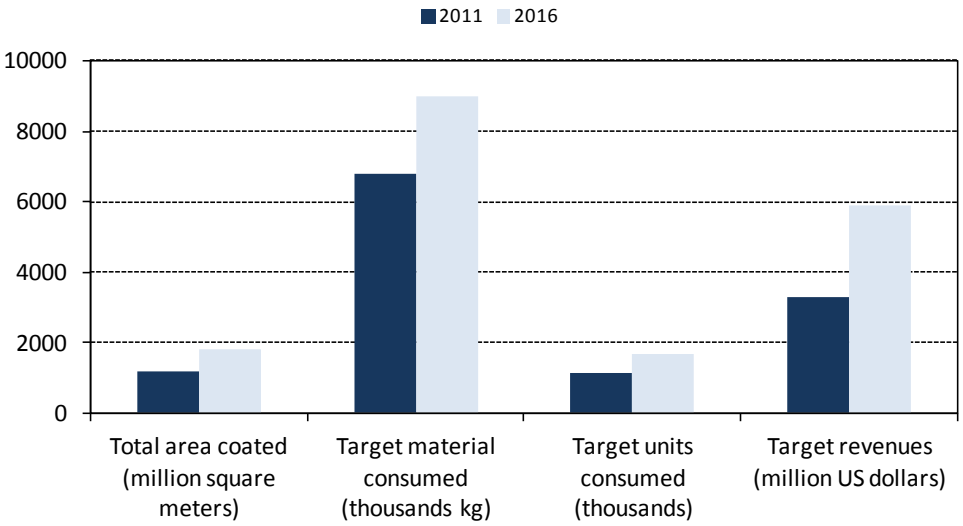

Fig. 2.21. *Global market for sputtered films and sputtering targets in 2011 and forecast for 2016 (adapted from [191]).*

The market studies show that both, sputtered films and sputtering target markets will continue to grow in the near future becoming a market opportunity for INNOVNANO. The predicted growth of flat panel displays and thin film solar cells is encouraging the development of new and/or improved materials. In this area AZO appears as a strategic material for the company´s entry in the ceramic sputtering targets market since it is one of the strongest alternatives over ITO and FTO with a real and stabilized market and considerably lower production costs.

2.7. Sputtering targets production

Sputtering targets are critical components of the sputtering deposition technique, with many of the properties of sputtered films dependent on the targets characteristics [192-195]. Target properties such as chemical purity, chemical homogeneity, target density, shape, structure (grain size, precipitates, crystallinity, porosity), or manufacturing process directly affect the microstructure at the atomic level of the sputtered film [191]. A poor quality sputtering target is usually responsible for instability and reproducibility problems during deposition with consequent reduction of sputtered thin films quality. Microstructural and chemical characteristics of sputtering targets are controlled at different degrees depending on the intended application. The most stringent requirements come from the semiconductor industry, which demands high purity, high-density, homogeneity and fine-grained targets to minimize defects in the deposited films.

Sputtering targets are fabricated in a variety of shapes, sizes, and materials. The production route used depends on the target material. In general sputtering targets can be divided in two groups: metallic and ceramic targets. For the production of metallic targets, induction melting and casting followed by thermomechanical processing are usually used. In turn, the manufacture of ceramic targets is in general based on powder consolidation techniques like conventional sintering (CS), hot-pressing (HP) or hot isostatic pressing (HIP). Most recently other techniques have been used. For example, plasma-spray techniques have been applied for the production of a full range of planar and cylindrical rotatable targets, including metal, alloy and ceramic targets. High-purity

carbon and graphite targets can be formed by chemical vapor deposition from hydrocarbon gases, while multicomponent oxide targets have been produced by slurry processing methods [191].

Ceramic targets are less used due to two main disadvantages. One is that most of the ceramic materials are nonconductive and cannot be operated using Direct Current (DC) power. The systems with Radio Frequency (RF) power are expensive and induce a low sputter rate. The second disadvantage is the high production cost of ceramic target materials. However, when a high quality thin film with precise stoichiometry and reproducibility of the layer is required, ceramic targets are preferred. The best example is the production of ITO and AZO TCO layers with their respective ceramic sputtering targets (Fig. 2.22) where homogeneous electrical and optical properties on large-area substrates are required.

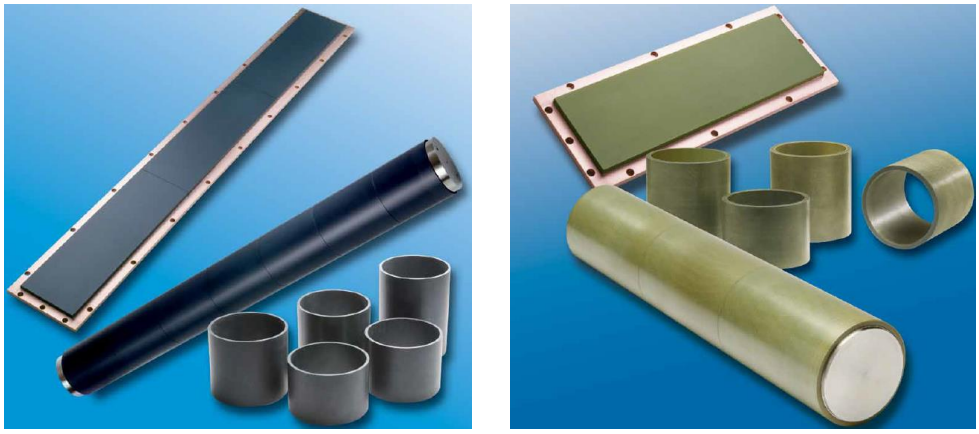

Fig. 2.22. *Examples of ITO (left) and AZO (right) industrial planar and rotary ceramic targets produced by Umicore [196].*

2.7.1. AZO ceramic sputtering targets

In general the characteristics of the transparent electrodes are influenced by those of the sputtering targets [192-194]. In turn, the quality of the targets is influenced by the started powder used and its sintering conditions [192]. For AZO the final density of the targets and their microstructural and chemical characteristics play an important role in the production of high quality ceramic sputtering targets, responsible for the formation of electrically conductive transparent thin films with the required specifications and without structural defects [74].

During sputtering of AZO ceramic targets some of the major problems are related with the formation of nodules and abnormal discharges, which are related with gradients of electrical resistivity in the targets ((impurities, second phase precipitates and/or porosity) affecting target lifetime and subsequent thin film characteristics [194, 197]. Furthermore a higher target density also enhances deposition rate [198]. Thus, attempts to reach high density AZO ceramic targets with well controlled microstructure become a crucial issue for both researchers and target manufactures.

Several studies have been published about the manufacturing of AZO ceramic targets, by changing the doping concentration [199], consolidation method [200-204], initial particle size of the powders [74, 75], or sintering atmosphere [192-195].

2.7.1.1. Consolidation techniques

Many studies have demonstrated that Al suppresses the densification of ZnO reducing the sinterability of the compacts. Therefore, high sintering temperatures are required to improve final densities of the targets, which affect negatively their microstructure [197, 205-207]. This effect is magnified for targets produced by conventional sintering and for high doping concentrations were full densification remains a challenge.

Several authors have tried to improve the final density of AZO targets using different consolidation methods. Hwang *et al.* [200] studied the densification of Al-doped ZnO compacts with different amounts of Al applying external pressure during a preliminary heat treatment at 900 °C prior to the final main sintering at 1250 – 1350 °C. The authors achieved significant improvements in final density especially for higher Al doping quantities (3 wt. % Al) for which conventional sintering was not effective. Other authors [201, 202] used HP technique in order to reduce the sintering temperature and improve the final density of the AZO sputtering targets and respective electrical properties. Zhang *et al.* [203] obtained high density AZO ceramic targets (99 %) with controlled grain size, good distribution of aluminum in the microstructure and less spinel phase ($ZnAl_2O_4$) formation by two-step sintering (TSS) using a first and second step sintering temperatures of 1050 °C and 1000 °C respectively, and 20 h of holding time at second step sintering temperature. Sun *et al.* [204] prepared an ultra-high density AZO target by slip-casting without abnormal grain growth, free of defects and with homogeneous distribution of Al species after pressureless sintering at 1400 °C for 2 h.

Of all the consolidation techniques, HP and HIP remain the most used for AZO ceramic targets production but other techniques are emerging in the research world like TSS and SPS that enhance the attainment of high density targets at low temperature, with homogeneous microstructure, and without grain overgrowth (the major limitations of CS).

2.7.1.2. Raw materials

The final properties of a ceramic are strongly dependent on the properties of the starting materials and the way they are manufactured [74, 75, 192, 194, 208, 209]. The progress in ceramic powder processing techniques, including the homogeneity of raw materials, formation of uniform green bodies, and analytical control of shrinkage behavior during sintering, is very important to make better ceramics targets. Beyond the Al content or consolidation method, the initial powder characteristics such as primary particle size and homogeneity of the doping element in the ZnO matrix are of extremely importance for the sintering behavior of the AZO ceramic pieces.

As described in the previous section, high density AZO targets (> 98 % of theoretical density (TD)) with controlled and homogeneous microstructure can be obtained using pressure assisted sintering methods (HP and HIP). However, the acquisition and maintenance of the equipment for these sintering processes are very expensive and are responsible for a significant increase in the manufacturing costs of the targets and of optoelectronic devices made with them. Furthermore, when compared with conventional sintering, these equipments are complex and industrially limited since high capacity furnaces are required for larger targets mass production [208]. Alternatively, pressureless sintering has been applied. AZO targets are generally produced using micro or submicrometric composite powders obtained by mixing ZnO and Al_2O_3 powders via

mechanical grinding, followed by CS. The major constraint remains the required high sintering temperatures to reach acceptable final density [194, 205, 210]. Huang *et al.* [194], for example, sintered several AZO targets with different Al_2O_3 contents (1.0 – 5.0 wt. %) at 1400 °C for 6 h using ZnO and Al_2O_3 powders with a mean particle size (D50) of respectively 1 and 0.2 µm. Wu and co-workers [205] used submicrometric powders with a D50 of 0.4 µm and 0.2 µm, respectively for ZnO and Al_2O_3, and reached acceptable densities at temperatures above 1400 °C with a holding time of 1 h, consistent with the lowest targets electrical resistivities achieved. Liu and Jeng [210] prepared a 3 inches AZO target by mixing ZnO and Al_2O_3 powders with respectively 2.58 and 0.55 µm of D50. The authors needed temperatures above 1450 °C to reach final densities 97 % of TD. These excessive sintering temperatures promote the grain overgrowth and are responsible for the formation of pores and large amounts of heterogeneous zones rich in $ZnAl_2O_4$ spinel phase. Furthermore, high sintering temperatures are not desired also due to the volatilization of ZnO [206].

Alternatively the sinterability of AZO targets and their microstructural homogeneity can be improved by using starting powder with smaller particle size, improving its reactivity during sintering [74, 211]. Thus, the use of nanoparticles appears as a solution to obtain higher densification rates and therefore produce high density ceramic targets at lower sintering temperatures with enhanced homogeneity via CS method [212].

In section 2.2 were presented the main methods to synthesize nanopowders, some of them designed for the production of powders with high chemical homogeneity. Yang and co-workers [211], for example, synthesized Y-doped AZO (AZO:Y) nanoparticles by a co-precipitation process. The authors fabricated full density (99.98 % of TD) AZO:Y ceramic target with a grain size of 2.2 µm by pressureless sintering in air at 1300 °C for 8 h. Cai *et al.* [28] synthesized ultra-fine Al-doped ZnO nanopowders by chemical precipitation in which Al_2O_3 was more easily and uniformly introduced as dopant in ZnO than in traditional mechanical grinding method. The ceramic target was prepared by sintering at 1200 °C for 4 h. Finally, Zhang *et al.* [203] used nanopowders of AZO with a mean particle size of 30 nm prepared by the sol-gel method followed by TSS. The authors reached a final density greater than 99 % of TD with a grain size of 1.2 µm. Despite these promising results, the high production costs of raw materials continue to be a strong limitation to the use of nanopowders in the manufacturing of advanced ceramics. In fact, as stated in section 2.2.1.1, even with inferior homogeneity, the easier and less expensive way to reduce the powder particle size remains the mechanical milling process. However, by using the wet milling process with liquid dispersion media such as water or ethanol, often leads to the formation of strong agglomerates during drying, masking the sintering advantages related with the use of smaller particle sizes [74].

2.7.1.3. Oxygen content – Influence of sintering atmosphere

One of the key properties of AZO ceramic targets is their electrical conductivity, which is a requirement for DC-magnetron sputtering. Besides their structural and morphological characteristics, the electrical conductivity of both AZO targets and films is extremely sensitive to the oxygen content [130].

Highly conductive AZO ceramic targets with reduced oxygen content have been proposed [192, 194]. Minami and co-workers [192] used several commercial targets provided by different suppliers and

found a correlation between the oxygen content in the ceramic targets and its electrical resistivity, as illustrated in Fig. 2.23. The authors found that electrical resistivity of the ceramic targets is reduced when lowering their oxygen content.

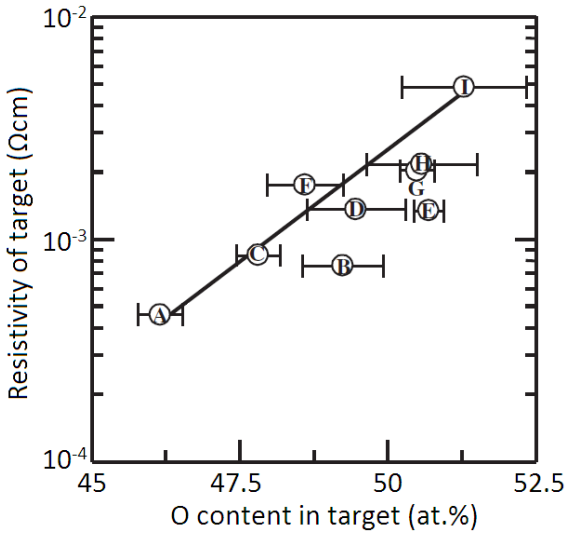

Fig. 2.23. *Electrical resistivity as a function of oxygen content in AZO ceramic targets (adapted from [192]).*

Huang *et al.* [194] sintered several AZO ceramic targets in air and under controlled atmosphere. They found that a gas mixture of Ar and CO during sintering is appropriate to produce targets with substantially higher electrical conductivity. A reduction in ρ_e from 8.85 x 10^{-4} to 1.93 x 10^{-4} Ωcm was observed for AZO (2 wt. % Al_2O_3) targets sintered in air and in Ar + CO respectively. According to that study, the formation of oxygen vacancies during sintering in Ar + CO atmosphere is responsible for the increase in N_e and σ.

2.7.1.4. Thermal and mechanical properties

The mechanical and thermal properties are extremely important for targets lifetime since they are submitted to thermal tensile stress during sputtering process. So, the thermal diffusivity and thermal conductivity of AZO ceramic targets have to be as high as possible to avoid the formation of cracks. Generally, higher final densities give rise to greater thermal diffusivity, heat capacity, and thermal conductivity of the targets. Target lifetime is also affected by their mechanical properties. Targets with high flexural strength and fracture toughness are desired. High final densities and small grain size leads to superior mechanical properties of the targets. However, small grain size reduces the thermal conductivity [208]. Studies that correlate thermal and mechanical properties of AZO targets are still missing.

2.8. Correlation between AZO ceramic sputtering targets and sputtered thin films

In the previous section were presented some of the main factors that should be considered to prepare AZO ceramic sputtering targets with enhanced quality. The search for high density targets, the reduction of sintering temperature to avoid morphological inhomogeneity or the control of the oxidation state to reach highly conductive targets are known to be determinant for

good quality targets fabrication. However, research works that correlate the properties of AZO targets and corresponding thin films are scarce in literature [192-195, 197, 205, 210].

In this section are revised the main results concerning the correlation between sputtering targets and sputtered thin films. Minami and co-workers are the leading players in this field [130, 131, 192, 193]. The authors used several commercial targets provided by different suppliers with electrical resistivity ranging between 4.8 x 10^{-3} and 4.6 x 10^{-4} Ωcm to investigate the effect of target properties on the AZO thin films deposited by DC magnetron sputtering. Their studies reveal that the use of targets with lower resistivity can enhance deposition rate, crystal perfection and resistivity homogeneity over the substrate surface while the electrical arc discharge at the target and the films resistivity are lowered [192, 193]. Huang *et al.* [194] also observed a better spatial distribution and reduction in electrical resistivity of sputtered films when AZO targets with higher conductivity are used. It must be noted that the carrier concentration and Hall mobility of AZO targets are different from those of AZO films, though their electrical resistivities are comparable. This observation led Huang [194] and Minami [192, 193] to assume that the dominant factor controlling the conductivity of targets and films is different. According to the authors, AZO targets generally present higher Hall mobility and lower carrier concentration than the corresponding thin films. Based on the much larger grain size and better crystallinity of AZO targets compared to AZO films it is reasonable to assume that the higher electron mobility of AZO targets is ascribed to the decrease of electron scattering from crystal and boundary defects. Furthermore, the atomic rearrangement among Zn, Al and O atoms during the deposition helps to obtain AZO films with more Al available as an active dopant and better doping uniformity leading to high carrier concentrations in the AZO films than that in the AZO targets [194, 213].

When preparing transparent and highly conductive impurity-doped ZnO films, controlling the oxidation of Zn is more difficult than with other binary compounds such as SnO_2 and In_2O_3, because Zn is more chemically active in an oxidizing atmosphere than either Sn or In. Due to this binding energy of Zn and O, the activity and amount of oxygen must be precisely controlled during the deposition. Thus, pure and doped ZnO films with low resistivity are possible only in depositions under less oxidizing atmospheres than in In_2O_3 and SnO_2 films.

High density ITO ceramic targets with a high oxygen deficiency were developed over the last decade by sufficiently reducing the source material. In DC magnetron sputtering depositions using these reduced ITO targets, the electrical resistivity and its spatial distribution on the substrate surface can be improved by introducing oxygen gas into the chamber during depositions, even on low temperature substrates [102, 130]. In the same way as ITO, the oxygen content of AZO targets is also critical in the preparation of thin films by magnetron sputtering. Highly conductive AZO thin films with enhanced spatial resistivity homogeneity can be achieved by reducing the amount of oxygen during deposition. Under controlled conditions without O_2 introduction in the chamber, the oxidation occurring on the surface of the substrate is dominated by the activity and quantity of the oxygen generated from the AZO ceramic target reaching the substrate surface as demonstrated in Fig. 2.24 [130, 131].

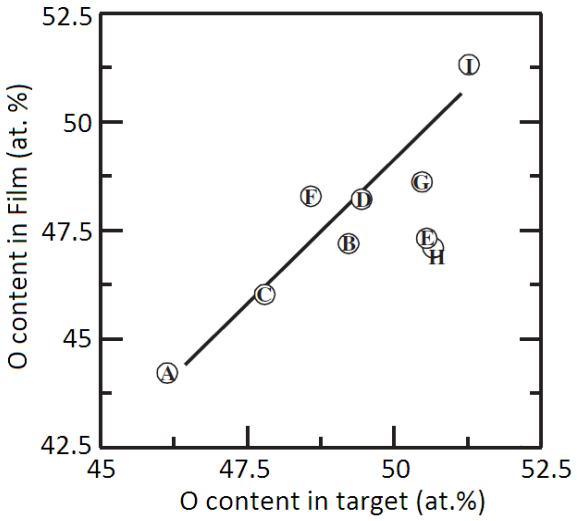

Fig. 2.24. *Oxygen content of AZO thin films as a function of oxygen content in targets (adapted from [192]).*

The preparation of AZO ceramic targets with a high oxygen deficiency has proved to be difficult because of the higher vapor pressure of Zn, relative to that of In, at high temperature. Thus, the introduction of O_2 gas into the chamber in the preparation of AZO thin films in sputtering apparatuses is generally unnecessary and unreasonable because of the excessive oxygen supplied by the sputtering target [130].

Since high quality AZO thin films are correlated with sputtering targets characteristics, the characteristics of the powders, its processability, and its correlation with the mechanisms involved in the sintering and densification of undoped and Al-doped ZnO becomes crucial for the production of AZO ceramic sputtering targets with the desired structural, mechanical, thermal and electrical properties.

2.9. Processing of nanosized ceramic powders

Nanosized powders normally have a very small crystallite size, a high degree of amorphization and a high specific surface area. These factors are essential to improve the reactivity and sinterability of the powders, but are also responsible for a greater tendency of particles agglomeration. The susceptibility for the formation of strong agglomerates in nanosized powders resulting from the high surface area and the excessive free energy of these systems is detrimental for processing and achievement of the desired microstructures [214]. Besides the agglomeration, the strong attraction between the particles and its high surface areas increases the friction between particles limiting the compaction [215]. The presence of strong agglomerates in the green body after the conformation process creates packaging heterogeneities as well as interagglomerate porosity, which are responsible for the main microstructural defects in the sintered body. Moreover, this inhomogeneity in the green bodies can strongly influence the sintering kinetics and microstructural development [215, 216]. The shrinkage rate and final density of the sintered body decrease dramatically as the amount of aggregates in the initial compact increases. Generally are reached heterogeneous microstructures with large pores formed between agglomerates that, once formed, are virtually impossible to be removed during pressureless sintering [217]. Basically, two types of agglomerates may be formed during ceramic powder processing: strong and weak agglomerates. The weak agglomerates are formed due to Van der Waals, electrostatic, magnetic

and/or by capillary forces, being easily broken using deflocculants [214, 218]. In strong agglomerates, also called aggregates, the bonds between the particles are generally primary chemical bonds formed by chemical reaction or sintering (coalesced particles). In Fig. 2.25 is shown schematically the difference between powder agglomerates and aggregates.

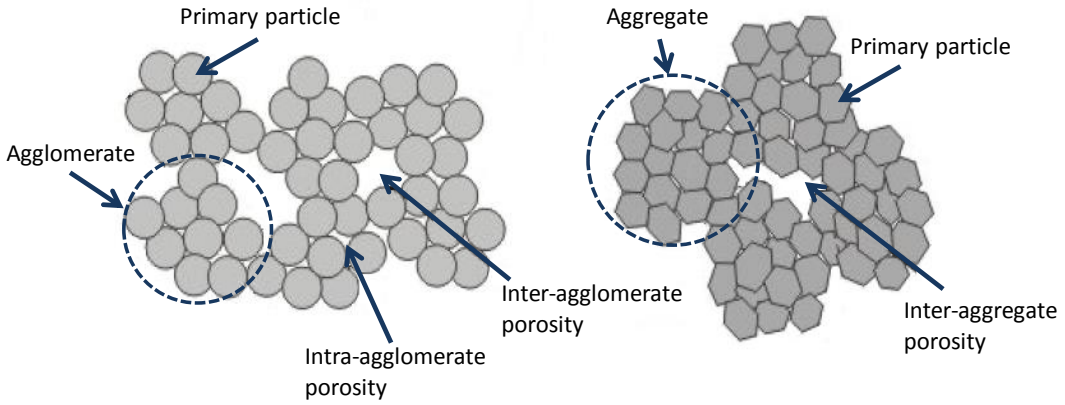

Fig. 2.25. *Schematic presentation of agglomerated and aggregated powders (adapted from [219]).*

2.10. Sintering – Basic concepts

The use of sintering process dates back to the beginnings of civilization. It is believed that the first material to be sintered were bricks that were put on bonfires to increase its mechanical strength [220]. However, despite its high usage, a detailed study of the sintering process just began in the ´20s of last century. The first sintering theories emerged in the mid-40s, and the first quantitative models from Frenkel and Kuczynski [221, 222] were published in the late ´40s. Then came works developed by other researchers as Lenel Coble, Kingery and Berg [223-225]. Currently, sintering theories remain matters of extreme relevance and subject of intense investigation in ceramicist´s research world basically because of two factors: the first is related to the difficulty in obtaining a quantitative theoretical description that expresses exactly the complex interactions between the geometric and thermodynamic factors that occur during the sintering process; the second factor is related with the emergence of new nanostructured ceramic materials, which are obtained from nanometric powders [226].

The sintering process plays a predominant role in the production of ceramics. Ceramic sintering means that ceramic bodies, i.e., systems of consolidated powders, are burned at elevated temperatures to generate a microstructure with the desired properties [227]. Generally, the properties of ceramics are strongly dependent on the microstructure. Important microstructural features are: the size and shape of the grains; the size, amount, and distribution of pores in the structure; and the nature and distribution of any secondary phases. These microstructural features must be controlled in the sintering process in order to achieve the desired properties. For the most of applications, microstructural control usually means the attainment of high density, a desired grain size, and a homogeneous microstructure. Thus, the detailed understanding of the sintering process is of considerable importance where the main subjects of sintering studies are the densification and the grain growth during sintering.

2.11. Solid state sintering

2.11.1. Driving force for sintering

The driving force for sintering results from the reduction of the total interfacial energy of a powder compact, which is expressed as $\gamma_s A$, where γ_s represents the specific surface (interface) energy and A the total surface (interface) area of the compact. The reduction of the total energy of the system can be expressed as:

$$\Delta(\gamma_s A) = \Delta\gamma_s A + \gamma_s \Delta A \qquad \text{(eq. 2.17)}$$

Here, the change in interfacial energy ($\Delta\gamma_s$) is due to densification and the change in interfacial area is due to grain coarsening. For solid state sintering, $\Delta\gamma_s$ is related to the replacement of solid/vapour interfaces (surface) by solid/solid interfaces [228]. As schematically shown in Fig. 2.26, the reduction in total interfacial energy occurs via densification and grain growth, the basic phenomena of sintering.

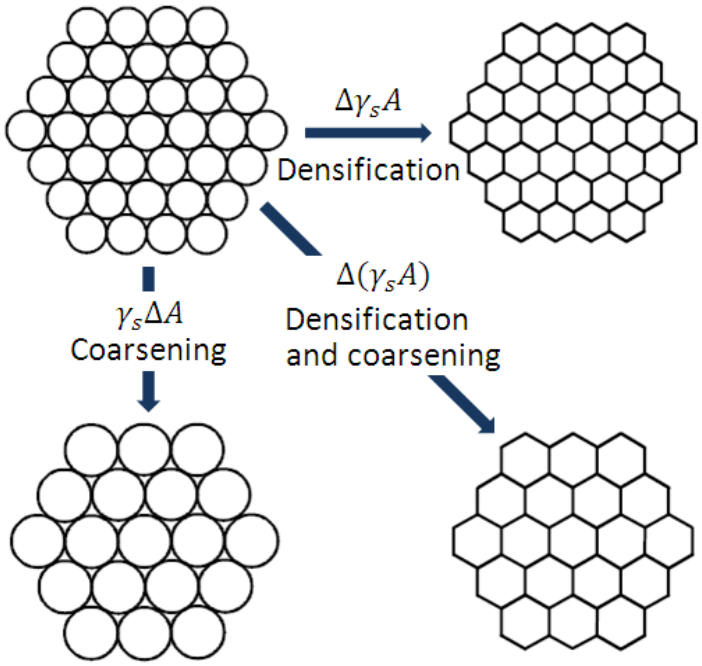

Fig. 2.26. *Basic phenomena occurring during sintering under the driving force for sintering, $\Delta(\gamma A)$(adapted from [228]).*

The sintering of powder compacts with complex-shaped particles of different sizes cannot be easily explained. However, the mechanisms involved in the sintering of powder compacts can be investigated considering spherical particles of the same size. The driving force for sintering is largely dependent on the geometry and size of neck formed between particles. Following Frenkel [221] and Kuczynski's [222] pioneering work, numerous models for initial stage of sintering have been developed. These models predict the rate of neck growth and densification for simple geometries like a pair of spheres. In Fig. 2.27 are presented two alternative two-sphere models for neck growth [225]: one without shrinkage a) and other with shrinkage b). In Fig. 2.27 a) the distance between the particles remains constant but the neck size increases as the sintering time

increases. In the model with shrinkage (Fig. 2.27 b)), the neck size increases with sintering time by material transport between the particles and thus resulting in shrinkage.

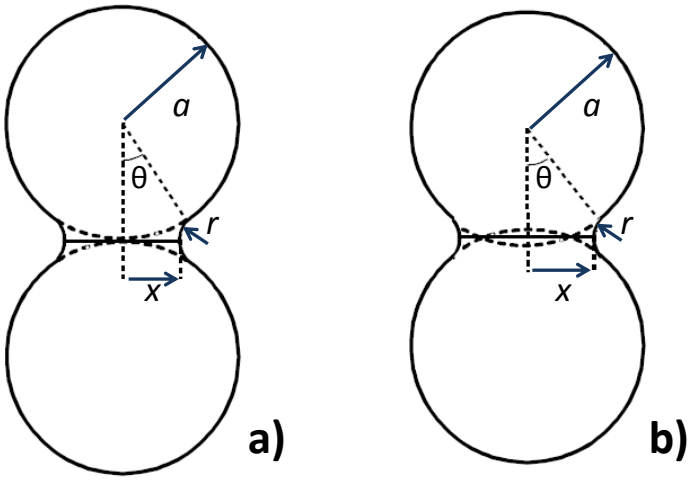

Fig. 2.27. *Two-particle models for initial sintering stage: a) without shrinkage, b) with shrinkage (adapted from [225]).*

Here, a is the particle radius, x is the neck radius and r is the radius of neck curvature. To have densification, it is necessary the transport of material from particles to the porous neck between them. The driving force for sintering that enables this material transport is translated into a driving force acting at the atomic level (and thus bringing about atomic diffusion) by means of curvature difference that occurs in different parts of the compacted particles [227]. Based on Young and Laplace equation, the effective stress (δ) derived from the differences in curvatures between the neck and the grain boundary plan is given by [228, 229]:

$$\delta = \gamma_s \left(\frac{1}{r} - \frac{1}{x}\right) \qquad \text{(eq. 2.18)}$$

where γ_s is the specific surface energy of the solid (solid surface energy). Considering $x/a < 1$ and $r < x$, the effective stress can be given as [228]:

$$\delta = \frac{\gamma_s}{r} \qquad \text{(eq. 2.19)}$$

Thus, the neck curvature causes a tensile stress in its surface and a compressive stress in the grain boundary. These stress variations causes also a deviation in the chemical potential and in concentration of vacancies between these regions that determine the material flow from the lower vacancies concentration region to the region of higher concentration of vacancies (Fig. 2.28). The relationship which links surface energy, curvature and concentration difference is the Gibbs-Thomson equation:

$$C_v(\delta) = C_v(\delta = 0) exp\left(\frac{2\gamma_s \Omega}{r k_B T}\right) \qquad \text{(eq. 2.20)}$$

where C_v is the vacancy concentration under a surface which has a radius of curvature r exposed to a stress δ, $C_v(\delta = 0)$ is the vacancy concentration under a plan, and Ω is the volume occupied by a vacancy.

The surface of the neck submitted to the tensile stress has a high vacancies concentration, whereas the grain boundary region, subjected to compressive stress, has a lower vacancies concentration. Thus, the vacancies diffusion occurs from the neck to the grain boundary region, which requires an equivalent diffusion of atoms in the opposite direction, i.e., from the grain boundary to the neck [229].

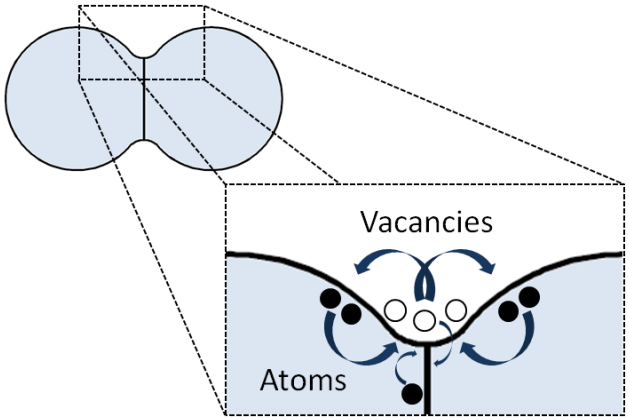

***Fig. 2.28**. Migration of atoms and vacancies due to the difference in chemical potential (adapted from [227]).*

In addition to the differences in curvature between the neck and the grain boundary, the stress is also caused by the difference in curvature between the particle and the neck surfaces with consequent dissimilarity in vacancies concentration. This difference in vacancies concentration enables the matter transport to the neck region. Although it contributes to the neck growth and change of the pores shape, this matter flow does not promote densification since it does not cause the reduction of the distance between the centers of the particles. The stresses caused by differences of curvature of the surfaces can also interfere with the vapour pressure on these surfaces, which may cause a matter transport in the gaseous phase (vapour transport) contributing to the neck growth without densification [230].
Neck growth and subsequent stages promotes the diminution in curvatures differences. The material transport tends to decrease during the sintering process with the consequent reduction of the thermodynamic gradient [230].

2.11.2. Mechanisms of transport in the initial stage of sintering

The material transport due to the difference in interface curvature occurs under the parallel actions of various mechanisms. The mass transport mechanisms determine how the material flows in response to the driving force for sintering [220]. The dominant mechanism can vary depending on, for example, particle size, neck radius, temperature and time for a given system. These mechanisms can be divided roughly into two main classes: surface transport mechanisms and lattice transport mechanisms, which can be identified by the sources, sinks, and the material transport paths operating in the process [227]. The vacancies and atoms can move along the surface of the particles (surface diffusion), throughout the lattice (volume diffusion and viscous flow), along the grain boundaries (grain boundary diffusion), or through the pores (gas phase transport) [220]. Two mechanisms could act in the gas phase transport: the evaporation-condensation mechanism is dominant when the distance between the evaporation region and the

condensation region is shorter than the mean free path of gas atoms; while if it is much longer than the mean free path of gas atoms, the gas diffusion mechanism is prevalent, unless the reaction of gas atoms at the interface is slower than gas diffusion.
The major mechanisms of material transport and their related parameters are listed in Table 2.6. Figure 2.29 shows a schematic representation of the matter transport paths for the transport mechanisms listed in Table 2.6.

Table 2.6. *Material transport mechanisms during sintering (adapted from [228, 231]).*

Material transport mechanism	Material source	Material sink	Related parameter
1. Surface diffusion	Grain surface	Neck	Surface diffusivity (D_S)
2. Lattice diffusion	Grain surface	Neck	Lattice diffusivity ($D_{L(S)}$)
3. Gas phase transport			
3.1. Evaporation/condensation	Grain surface	Neck	Vapor pressure difference (Δp)
3.2. Gas diffusion	Grain surface	Neck	Gas diffusivity (D_{Gas})
4. Grain boundary diffusion	Grain boundary	Neck	Grain boundary diffusivity (D_{GB})
5. Lattice diffusion	Grain boundary	Neck	Lattice diffusivity ($D_{L(GB)}$)
6. Viscous flow	Bulk grain	Neck	Viscosity (η)

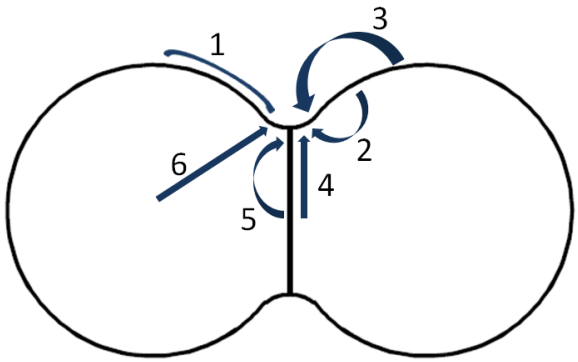

Non-densifying mechanisms:

1. Surface diffusion;
2. Lattice diffusion (from the surface);
3. Gas phase transport :
   - 3.1. Evaporation-condensation;
   - 3.2. Gas diffusion.

Densifying mechanisms:

4. Grain boundary diffusion;
5. Lattice diffusion (from the grain boundary);
6. Viscous flow (by dislocation motion).

Fig. 2.29. *Schematic representation of the material transport paths during sintering and corresponding sintering mechanisms (adapted from [228]).*

A distinction is commonly made between densifying and non-densifying mechanisms. Both surface and lattice transport mechanisms promotes the neck growth but only the lattice transport mechanisms cause densification during sintering. In this case, the material transport must be from

inside of the particle to the neck. Surface diffusion (D_S), gas phase transport (Δp and/or D_{Gas}) and lattice diffusion from the particle surfaces to the neck ($D_{L(S)}$) lead to the neck growth and coarsening of the particles without shrinkage (illustrative model in Fig. 2.27 a)). Grain boundary diffusion (D_{GB}) and lattice diffusion from the grain boundary to the neck ($D_{L(GB)}$) are the most important densifying mechanisms during sintering of ceramics. Diffusion from the grain boundaries to the pores permits neck growth as well as shrinkage (illustrative model in Fig. 2.27 b)) [232]. Therefore, the grain boundary is the source of material transport for densification and shrinkage in crystalline powder compacts. Less frequently, viscous flow by dislocation motion can also cause neck growth and densification through deformation (creep) of the particles in response to the sintering stress. Although this mechanism is frequently identified as one of the major mechanisms in pressure-assisted sintering, it is less important under atmospheric sintering, occurring only when the particles are in point contact at the very beginning of sintering [228].
In general, the densification rate increases with the decrease of particle size and by increasing sintering temperature and time. A quantitative explanation of this general tendency can be drawn from the kinetic equations for densifying mechanisms of initial sintering stage, as summarized in Table 2.7 [228]:

Table 2.7. *Summary of kinetic equations for densifying mechanisms of initial sintering stage.*

Material transport mechanism	Neck growth	Shrinkage	Scale exponent α_e
Grain boundary diffusion from grain boundary to neck	$x^6 = \frac{48 D_{GB} \varphi_{GB} \gamma_s V_m a^2}{RT} t$ (eq. 2.21)	$\frac{\Delta l}{l_0} = \left(\frac{3 D_{GB} \varphi_{GB} \gamma_s V_m}{4RTa^4}\right)^{1/3} t^{1/3}$ (eq. 2.24)	4
Lattice diffusion from grain boundary to neck	$x^4 = \frac{16 D_{L(GB)} \gamma_s V_m a}{RT} t$ (eq. 2.22)	$\frac{\Delta l}{l_0} = \left(\frac{D_{L(GB)} \gamma_s V_m}{RTa^3}\right)^{1/2} t^{1/2}$ (eq. 2.25)	3
Viscous flow	$x^2 = \frac{4\gamma_s a}{\eta} t$ (eq. 2.23)	$\frac{\Delta l}{l_0} = \frac{3\gamma_s}{8\eta a} t$ (eq. 2.26)	1

Here, D_{GB} is the grain boundary diffusion coefficient, $D_{L(GB)}$ the lattice diffusion coefficient from grain boundary, φ_{GB} is the diffusion thickness of grain boundary diffusion, V_m the molar volume of the solid, R is the gas constant, t the sintering time, $\Delta l/l_0$ the linear shrinkage (l_0 is the initial size of the sample), and α is a scale exponent.

2.11.3. Mechanisms of transport in the intermediate and final stages of sintering

When necks form between particles in the powder compacts, pores form interconnected channels along 3-grain edges. As the sintering proceeds, pore channels disconnect while isolate

pores form at the same time that grains grow. Coble [233, 234] proposed two geometrical models for the changes in shape of pores during intermediate and final sintering stages: the channel pore model and the isolated pore model.

Coble´s microstructure model of intermediate stage of sintering considers grains with cylinder-shaped pores along all the grain edges being assumed equal shrinkage of pores in a radial direction. Considering an atom flux through the cylindrical pores, two mechanisms are available for matter transport in the intermediate stage: lattice diffusion and grain boundary diffusion. The densification rates for lattice diffusion and grain boundary diffusion mechanisms are expressed by eqs. 2.26 and 2.27 respectively:

$$\frac{d\rho_r}{dt} = \frac{336 D_{L(GB)} \gamma_s V_m}{RT {G_s}^3} \qquad \text{(eq. 2.27)}$$

$$\frac{d\rho_r}{dt} = \frac{854 D_{GB} \varphi_{GB} \gamma_s V_m}{RT {G_s}^4} \left(\frac{1}{P_v}\right)^{1/2} \qquad \text{(eq. 2.28)}$$

where, $d\rho_r/dt$ is the densification rate (ρ_r is the relative density), G_s is the grain diameter, and P_v the porosity.

In the final stage of sintering, Coble considers grains with spherical pores at their corners and suggests concentric sphere diffusion of atoms to the pore surface. The author found that the densification rate is inversely proportional to the grain size cubed (eq. 2.29), the same relation found for the dependence of neck growth and shrinkage on particle size in the initial stage model (eq. 2.24).

$$\frac{d\rho_r}{dt} = \frac{288 D_{L(GB)} \gamma_s V_m}{RT {G_s}^3} \qquad \text{(eq. 2.29)}$$

However, a fundamental aspect is not taken into account in the Coble's model, namely, the grain boundary as the atom source for densification. Taking into account the Herring´s scaling law concept, sintering kinetics at the final stage can be predicted [235, 236], entering with the effect of pore surface area on the material flux from the grain boundary to the pore. Adopting this concept, Kang and Jung [236] derived the densification rate not only for lattice diffusion but also for grain boundary diffusion as shown in equations 2.30 and 2.31 in that order:

$$\frac{d\rho_r}{dt} = \frac{441 D_{L(GB)} \gamma_s V_m}{RT {G_s}^3} (1 - \rho_r)^{1/3} \qquad \text{(eq. 2.30)}$$

$$\frac{d\rho_r}{dt} = \frac{735 D_{GB} \varphi_{GB} \gamma_s V_m}{RT {G_s}^4} \qquad \text{(eq. 2.31)}$$

The authors found that in the case of grain boundary diffusion, the dependence of densification rate on grain size is the same as in the initial stage model (inversely proportional to the fourth of grain size). For lattice diffusion, the size dependence is similar to the one found using Coble's model (densification rate inversely proportional to the cube of grain size) with the difference that contains a relative density term (ρ_r).

2.11.4. Stages of sintering

Solid state sintering can be divided into three different stages: initial, intermediate and final. These sintering stages represent the geometric evolution involved in the transformation of a green compacted powder in a dense and resistant solid. As mentioned above, simplified models can represent each of these three stages: the two-particle model for the initial stage; the channel pore model for the intermediate stage; and the isolated pore model for the final stage. Figure 2.30 schematically depicts the typical densification curve of a compact through these stages over sintering time.

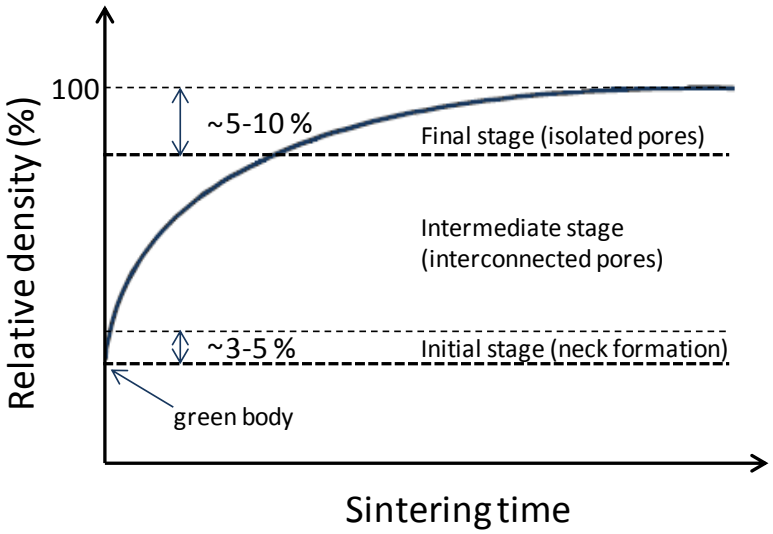

Fig. 2.30. *Schematic showing the densification curve of a powder compact and the three sintering stages (adapted from [228]).*

The initial stage starts as soon as some degree of atomic mobility is achieved and, during this stage, concave necks between the individual particles are formed reducing the total energy of the system. The amount of densification is small, typically 3 – 5 % of linear shrinkage, and it can be considerably lower if the coarsening mechanisms are very active [227]. In this stage, the necks growth is reduced and independent of each other. This stage ends when the necks start to interact as a consequence of its growth or the shrinkage reaches 5 % (if it takes place). At this stage, the particles remain identifiable and the pores keep a three-dimensional interconnected structure (open porosity), being usually observed a decrease in particles surface roughness.

The intermediate stage is characterized by the simultaneous densification, pore rounding and grain growth. The neck growth emphasized in the initial stage loses its identity and the structure of the pores around the necks becomes important [220]. The high curvatures observed in the initial stage are reduced and the microstructure consists of a complex three-dimensional interpenetrating network of solid particles and continuous, channel-like pores. This stage is considered valid to 5 – 10 % porosity and therefore covers most of the densification. Grain growth (coarsening) starts to become significant [227, 228]. To calculate the sintering rates, the geometric models consider the pores geometry as being cylindrical pores located at the three point junctions (channel pore model).

The final stage of sintering begins when the pores become isolated (preferably positioned in four grains junctions) as a result of densification [227]. Compared with the initial and intermediate stages, this stage is a slower process [220]. The grain growth is usually more extensive in the final stage and difficulties are commonly encountered in the removal of the last few percent of porosity [228].

2.11.5. Grain growth

Besides the densification also grain growth causes a decrease in free energy of the system during sintering, by reducing the amount of high-energy solid-solid interfacial area through grain growth. The grain growth occurs when grain boundaries move, being driven by the change in free energy associated with the elimination of particle-particle interfaces and consequent decrease in the total number of grains. Thus, when a polycrystalline aggregate is heated, the grain boundaries move, some grains disappear and the average grain size increases. If all the grains have the same energy, grains with six sides are formed with angles of 120°. Grains with less than six sides have concave boundaries, when viewed from the center of the grain and tend to shrink and disappear when the grain boundaries migrate towards the center of curvature. Grains with more than six sides are convex contours that tend to growth. For a pure material with a single phase, grain growth rate is directly proportional to the motion speed of grain boundary, V_{GB}, which can be expressed by:

$$V_{GB} = M_{GB} F_{GB} \qquad \text{(eq. 2.32)}$$

where, M_{GB} is the intrinsic mobility of the boundary, dependent on the temperature (eq. 2.33), and F_{GB} is the free energy gradient generated by grain boundaries curvature differences (eq. 2.34) which can be given respectively by:

$$M_{GB} = M_0 exp\left(\frac{-Q_{GB}}{RT}\right) \qquad \text{(eq. 2.33)}$$

$$F_{GB} = \gamma_{GB}\left(\frac{1}{r_1} + \frac{1}{r_2}\right) \qquad \text{(eq. 2.34)}$$

Here, Q_{GB} is the activation energy for grain boundaries motion, γ_{GB} is the energy of grain boundary per unit area, and r_1 and r_2 are the curvature radius of the grain boundaries. Assuming that boundary curvature $1/r_1 + 1/r_2 \cong 1/G_s$, the grain growth rate is given by:

$$V_{GB} = \frac{dG}{dt} = \frac{M_{GB}\gamma_{GB}}{G_s} \qquad \text{(eq. 2.35)}$$

Integrating eq. 2.34:

$$G_s{}^2 - G_{s0}^2 = M_{GB}\gamma_{GB} t \qquad \text{(eq. 2.36)}$$

where G_{s0} is the initial grain size $(t = 0)$ [229].

It is often observed that the experimental grain growth rate is less than that one given by the previous equation. This is attributed to factors that inhibit the grain boundaries motion, like secondary phases or pores [237]. Thus, one can express eq. 2.37 as:

$$G_s{}^m - G_{s0}^m = K_0 t\ exp(-\frac{Q_G}{RT}) \quad \text{(eq. 2.37)}$$

where K_0 is the pre-exponential coefficient, Q_G the apparent activation energy for grain growth, and m the grain growth exponent (larger grain growth exponents indicate small grain growth rate).

The attainment of dense ceramics, free of porosity, is commonly affected by grain growth rate and pore mobility. If the grain growth is fast compared with pore mobility, the pores are separated from the grain boundaries resulting in a lower densification rate. On the other side, if the pore mobility is high, via surface diffusion or evaporation-condensation, the pores may remain with the motion of the grain boundaries continuing to shrink. Therefore, the grain boundary mobility depends on its curvature, usually measured by the pore size and transport mechanism. Thus:

$$M_p = \frac{A}{d_p^w} \quad \text{(eq. 2.38)}$$

where, M_p is the pore mobility, d_p is the pore size, A is a constant containing the material parameters, and w determines the transport mechanism ($w = 4$ for surface diffusion, $w = 3$ for lattice diffusion, and $w = 2$ for evaporation-condensation mechanism) [220].

The diffusion pathways depend on pore location: pores in grain boundaries can be eliminated by grain boundary diffusion or by lattice diffusion; while pores inside the grains can only be removed by lattice diffusion. Thus, the location of the pores and its mobility becomes a critical factor for densification since lattice diffusion is a slow and ineffective process in the elimination of the pores that eventually become lodged inside the grains [229].

2.11.6. Particle size effect

The matter transport rates for the solid-state sintering mechanisms depend strongly on the particle size of the powder. Nanocrystalline materials contain a large fraction of atoms at the grain boundaries. These numerous interfaces can provide a high density of short diffusion paths during sintering. Consequently, it is expected that these materials exhibit an increase in diffusivity compared to polycrystalline materials of the same composition with the conventional particle size (in the order of microns) [238]. Among the consequences that this higher diffusivity may bring, the increased sinterability of nanosized powders is the more relevant, with impact in the sintering temperatures of the powders.

The effect of particle size on sintering is well explained by Herring´s scaling law [239]. Herring assumed a single transport mechanism during the sintering with a degree of sintering measured by the neck growth ratio *x*/*a*. The author also considered that the microstructure evolved with a similar shape during sintering. According to him, if two powders are available for sintering, the required time to achieve an equivalent degree of sintering is given by:

$$t_2 = t_1 \left(\frac{D_2}{D_1}\right)^m \quad \text{(eq. 2.39)}$$

where t_1 is the time to sinter particles with size D_1 with a neck growth rate of x_1/D_1, t_2 is the time to sinter particles with size D_2 with a neck growth rate of $x_2/D_2 = x_1/D_1$ and m depends on the sintering mechanism.

Accordingly with eq. 2.39, for an equivalent sintering level, the sintering time depends only on particle size ratio. Assuming sintering conditions where the densifying mechanisms dominate, then the rate of densification is predicted to vary as $1/G_s^m$, where G_s is the particle size, and the exponent m = 4 for grain boundary diffusion and m = 3 for lattice diffusion as demonstrated in sections 2.11.2 and 2.11.3. As an example, for a process governed by lattice diffusion, an increase in particle size of twice will increase the sintering time (for an equivalent neck growth) 16 times. Thus, reduction of the particle size provides an important method for speeding up sintering [220, 227].

Based on eq. 2.19 of section 2.11.1, which provides the driving force for sintering is easy to confirm that the intrinsic driving force of nanocrystalline ceramics, which have usually pores in the range of 5 nm, is very high, in the order of 400 MPa (assuming $\gamma_s \cong 1$ Jm^{-2}). On the other side, conventional ceramics with pores around 1 μm have a sintering stress of only 2 MPa. Thus, theoretically, a nanocrystalline ceramic should have a large thermodynamic driving force for the pores shrinkage, which should densify well, even if the kinetic conditions are unfavorable, such as, for example, the use of lower sintering temperatures.

2.11.7. Pressure-assisted sintering

Besides the decrease in particle size, one of the most common methods to increase the driving force of densification and densification kinetics is the application of an external pressure to the powder compact during sintering. Once the grain growth is not related to the applied external pressure, the effect of an external pressure is more effective in systems where grain growth rate is higher relatively to densification rate. As the densification rate is enhanced by external pressure, the sintering temperature as well as the sintering time can be reduced and grain growth further suppressed [228]. Furthermore, shape forming and densification can often be accomplished in a single step.

Two different types of pressure are available: unidirectional and isostatic. The former is typified by hot pressing (HP) and the latter by hot isostatic pressing (HIP). During HP a uniaxial pressure is applied to the powder compact in a graphite die using pressures of 20 – 50 MPa. HIP is usually done after encapsulation of the powder compacts within a container, using an inert gas of a higher pressure than that of HP (up to 300 MPa). As a variation of HIP, gas pressure sintering (GPS) uses pressure below 10 MPa so, it makes possible the sintering of materials with a high vapour pressure. Two-stage sintering is usually performed: low pressure sintering before the isolation of pores and high pressure sintering after the pore isolation [240].

Recently, a new HP technique where a pulsed electric field is applied has been developed, so-called spark plasma sintering (SPS) [241]. The experimental set-up is similar to that of HP with a graphite die and graphite punches. The heating of the sample, however, is achieved by Joule effect heating a resistance with a pulsed current (typically a few thousand amperes) under a pulsed DC voltage (typically a few volts). A high heating rate of more than a few hundred K.min^{-1} can be achieved. In SPS, the densification is very fast, taking a few minutes, while grain growth is

very limited at process temperatures lower than HP temperatures. The main limitations of this technique are related with the scale-up of the process to an industrial level. Furthermore, the mechanism of the SPS process still unclear.

2.11.7.1. Driving force of pressure-assisted sintering and inherent sintering mechanisms

The driving force for densification under an external pressure ($P_{appl.}$) is determined by the pressure itself and also the contact area relative to the cross-sectional area of the particles. Considering the HP of a powder compact with a simple cubic packing of spherical particles, the effective compressive pressure (P_1^*) at the contact area during the initial stage (eq. 2.40) and the effective pressure (P_2^*) during the final stage of sintering (eq. 2.41) can be expressed as [228]:

$$P_1^* \approx \frac{4a^2}{\pi x^2} P_{appl.} + \frac{\gamma_s}{r} \qquad \text{(eq. 2.40)}$$

$$P_2^* \approx \frac{P_{appl.}}{\rho_r} + \frac{2\gamma_s}{r} \qquad \text{(eq. 2.41)}$$

As in the case of pressureless sintering, several densification mechanisms can be active in HP or HIP. In addition to lattice and grain boundary diffusion, plastic deformation and creep, which are unimportant in pressureless sintering, can be major mechanisms during sintering under external pressure. The major densification mechanism for a given system can vary with experimental and compact conditions, such as temperature, pressure, particle size and neck size [228].

The densification rate by plastic deformation or power-law creep is, in general, independent of particle (grain) size. On the other hand, the densification rate of both lattice and grain boundary diffusion depends on both effective pressure and grain size. The reduction of pore size often results in the increase of capillary pressure above the external pressure. So, the final densification is expected always to be governed by pressureless sintering kinetics. The densification rate in pressure-assisted sintering is the sum of those due to the capillary pressure and to the external pressure. The contribution of capillary pressure increases as the external pressure and pore size decreases with densification enhancement.

2.12. Undoped ZnO - Sintering and densification

Over the last years many studies related with sintering and grain growth of microcrystalline ZnO powder compacts have been published [242-245]. High final densities (95 – 98 %) with grain sizes around 9 µm were reported for the sintering of high purity ZnO micrometric powders (~99.9%) at temperatures between 1100 and 1200 °C [243-245]. Gupta and Coble [244, 245] studied the densification and grain growth at the intermediate and final stages of ZnO powder compacts sintered in air and oxygen atmosphere by isothermal sintering techniques. They found an increase in density and a reduction in grain size when ZnO is sintered in oxygen instead of air atmosphere. The authors have also observed a good agreement between diffusion coefficients from the sintering data and the ones related to the lattice diffusion coefficients directly measured for zinc. Their results were also consistent with the expected effect of oxygen pressure on zinc diffusivity when the transport of zinc in the lattice occurs by an interstitial mechanism. Hence, they conclude that lattice diffusion of interstitial zinc is the main transport mechanism for the densification and grain growth of ZnO. Senda and Bradt [243] studied the grain growth of ZnO for sintering temperatures

ranging from 900 to 1400 °C in air, using the phenomenological kinetic grain growth equation (eq. 2.37) shown above. They obtained a grain growth exponent of 3 while the apparent activation energy was 224 ± 16 kJ.mol^{-1}, which agrees with the conclusion of Gupta and Coble [244, 245], concerning a grain growth process controlled by zinc interstitial lattice diffusion mechanism. Senos [76] investigated the sintering kinetics of ZnO in the initial and intermediate stages using a constant heating rate sintering technique (CHR). The author also stated that after a short initial period of particle rearrangement, the densification of ZnO was controlled by lattice diffusion of interstitial Zn. In another study, Han *et al.* [246] report activation energy of ~320 kJ.mol^{-1} in the earlier sintering stage for the sintering of ZnO and conclude that the densification in the earlier stage of sintering is controlled by a combination of both grain boundary sliding and volume diffusion mechanisms.

The influence of atmosphere during the sintering of ZnO has been extensively studied. According to Coble [247], the sintering atmosphere influences the densification rate, grain growth and/or limitations in final densities of sintered ceramic oxides. As mentioned by Gupta and Coble [244, 245] the sintering of ZnO in oxygen stimulates an increase in final density and simultaneously a decrease in final grain size of the ceramic parts. Other authors have reported similar effect [248, 249]. Moriyoshi and co-workers [250] investigated the effect of oxygen, nitrogen, and helium atmospheres on the densification of ZnO powder compacts, and observed that the densification rate was inversely proportional to the oxygen partial pressure, i.e., the higher is the oxygen partial pressure, the lower the densification rate became. This behavior is a consequence of the change in the number of vacancies when oxygen partial pressure varies. For a sintering process controlled by diffusion, an increase in the vacancies concentration in the lattice causes an increase of the diffusion coefficient of the lattice, and thus, an increase in the densification rate [247]. Quadir and Readdey [251], observed an enhancement of vapour transport during sintering in hydrogen atmosphere, which led to a decrease in the densification rate and in the final density, mainly through a rapid particle coarsening which is accentuated with hydrogen pressure and temperature.

During the last decade, due to the strong development of nanotechnology, the interest in the sintering and grain growth of metal-oxide nanopowders has been renewed. Several studies of nanometric ZnO with an average particle size from 5 to 100 nm were reported [252-258]. The results showed to be possible the preparation of high density ceramics with 95 – 98 % of TD at 950°C [252] and 1050°C [253] with final grain sizes of 3 µm and 5 – 10 µm respectively. Hynes *et al.* [254] have obtained ZnO samples with high density using pressureless isothermal sintering at 650 – 700 °C. According to the researchers, the rapid densification of ZnO nanopowder was promoted by the small particle size, which increases the driving force for sintering, and, possibly, by the higher surface energy, which also increases the sintering rate. The authors have also shown that during sintering the most probable mechanisms are rearrangement of the nanoparticle grains, with simultaneous surface and boundary diffusion, and vapour transport above 900 °C. Roy *et al.* [255] sintered isothermally ZnO nanometric powder in a wide range of temperatures (450 – 1400 °C) and holding times, using a commercial powder with particle size of ≈100 nm and the same powder after grinding (≈30 nm). They reached full density at 800 °C with a final grain size of ~1.5 µm and found that densification and grain growth tends to be more sensitive to sintering temperature than to holding time. Qin *et al.* [256] have done a similar study using powder with a

mean particle size of 20 nm, in air, and obtained a grain growth kinetic exponent of about 6 and an apparent activation energy for grain growth of ~64 kJ.mol^{-1}, less than the reported in previous works for microcrystalline ZnO (200 – 300 kJ.mol^{-1}). Ewsuk and Ellerby [257] studied the sintering behavior of micro (average grain size of 0.79 μm and specific surface area of 3.2 m^2.g^{-1}) and nanocrystalline (average grain size of 48 nm and specific surface area of 30 m^2.g^{-1}) ZnO compacts, and compared the influence of different heating rates in the final density of the compacts using dilatometric linear shrinkage measurements. They conclude that the most significant difference between the two powders is the enhancement of densification at lower temperatures in nanocrystalline ZnO powder, which is derived from the effect of particle size. Apparent activation energy for densification was about 268 kJ.mol^{-1} and 296 kJ.mol^{-1} for the nano and microcrystalline powders, respectively.

2.13. Al-doped ZnO - Sintering and densification

A large number of experiments have been performed to investigate the role of different dopants during sintering of ZnO [251, 259-263]. Silicon, for example, is known to inhibit grain growth of ZnO, while titanium enhances it by forming a liquid phase [259]. Antimony forms a second phase at the grain boundaries of ZnO, retarding the grain growth of ZnO by second-phase pinning of the grain boundaries [260].

Some trivalent dopants like Al, Ga, and In, are found to decrease the electrical resistivity of ZnO [261]. This decrease together with the modification of the crystallographic parameters indicates that when those cations enter in the ZnO lattice, they occupy substitutional positions. In general, the sintering is retarded when doping with trivalent cations. Due to its properties as a dopant in ZnO, as well as its low cost and abundance, the sintering of Al-doped ZnO has been subject of several investigations [76, 206, 251, 262, 263].

Komatsu *et al.* [262] studied the shrinkage of ZnO doped with 1.2 mol % Al under isothermal conditions at temperatures in the range 800–1000 ◦C in air. The authors reported a slight decrease in the activation energy for densification, from 193 kJ.mol^{-1}, for undoped ZnO, to 176 kJ.mol^{-1} for Al-doped ZnO. Quadir and Readey [251] investigated the effect of Al doping (1–10 mol % Al) on grain growth of ZnO sintered in hydrogen. They detected the presence of $ZnAl_2O_4$ spinel phase for higher doping concentrations and a retardation of ZnO grain growth with the Al addition. Nunes and Bradt [263] also studied the effect of Al_2O_3 doping concentration during liquid phase sintering of ZnO doped with Bi_2O_3 in air. They have detected the formation of the spinel phase, $ZnAl_2O_4$, and the inhibition of ZnO grain growth with Al addition, even in the presence of the Bi_2O_3-rich liquid phase. The authors proposed that the retarded grain growth is a result of the spinel particle pinning the ZnO grain boundaries and consequently reducing their mobility. They published a grain growth exponent and activation energy for ZnO grain growth of ≈4 and ≈400 kJ.mol^{-1}, respectively, independently of the Al-doping concentration. Senos [76] studied the densification of undoped and Al-doped ZnO in air, using a constant heating rate sintering method. The addition of Al was found to contribute to the reduction in densification rate and grain growth. Senos found an activation energy of ≈420 kJ/mol for the densification independent of the Al content (from 0.032 to 0.32 mol %). The mechanism of densification was proposed to be the lattice diffusion affected by the presence of $ZnAl_2O_4$ particles on the pore surfaces. Han *et al.* [206] studied the densification and grain growth of ZnO doped with 0.08 to 1.2 mol % Al under

isothermal sintering from 1100 to 1400 ◦C in air. The authors reported the formation of a stable $ZnAl_2O_4$ at ~800 ℃ and a solubility limit of Al in ZnO lattice of ≈600 atomic ppm at 1200 ℃. The reduction of grain growth with Al doping and an increase in grain growth exponent from 3 to undoped ZnO to 4 – 6 for Al-doped ZnO was also observed. Spinel phase was identified as having an effective drag (pinning) on the migration of ZnO grain boundaries. On the other side, Han *et al.* also observed a reduction in the driving force for densification with the increase of Al content. These two effects of Al on densification rate are competitive since the grain growth leads to an increase of the densification rate, while the decrease of the sintering stress retards the densification. However, according to Han, the grain growth becomes the more important factor on densification in the final stage of sintering.

As mentioned in section 2.7.1.2., many efforts have been made to reduce the delaying observed on ZnO sintering when doped with Al. The possibility of using raw materials with smaller particle size than conventional micrometric powders appears as a good possibility for obtaining high density AZO ceramic pieces at lower temperatures by pressureless sintering, instead of pressure assisted sintering processes. Studies about the sintering behavior of small particle size Al-doped ZnO are still lacking.

2.14. References

[1] Bhushan, B., Handbook of Nanotechnology. First Edition, ISBN: 978-3540012184 Published 2004 by Springer.

[2] Zhong, W.-H., Li, B., Maguire, R. G., Dang, V. T., Shatkin, J. A., Gross, G. M. and Richey, M. C., Nanoscience and nanomaterials – Synthesis, manufacturing and industry impacts. First edition, ISBN: 978-1605950136 Published 2012 by DEStech Publications, Inc.

[3] European commission recommendation on the definition of nanomaterial, Official Journal of the European Union (2011/696/EU), 18 October 2011, L275/38 – L275/40.

[4] McWilliams, A., Nanotechnology: A realistic market assessment (Market research report – NAN031D). ISBN: 1-59623-627-2. Published 2010 by BCC Research.

[5] Various analysts, 2012 Nanotechnology research review (Market research report – NAN047D). ISBN: 0-89336-554-8. Published 2012 by BCC Research.

[6] Manzoor, U., Islam, M., Tabassam, L., and Rahman, S. U., Quantum confinement effect in ZnO nanoparticles synthesized by co-precipitate method. *Physica E*, 2009, **41**(9) 1669-72.

[7] Benjamin, J. S., Dispersion strengthened superalloys by mechanical alloying. *Metall. Trans.*, 1970, **1**(10) 2943-51.

[8] Tjong, S. C. and Chen, H., Nanocrystalline materials and coatings. *Mater. Sci. Eng., R*, 2004, **45**(1-2) 1-88.

[9] Koch, C. C. and Cho, Y. S., Nanocrystals by high energy ball milling. *Nanostruct. Mater.*, 1992, **1**(3) 207-12.

[10] Suryanarayana, C., Mechanical alloying and milling. *Prog. Mat. Sci.* 2001, **46**(1-2) 1-184.

[11] Glushenkov, A. M., Zhang, H. Z. and Chen, Y., Reactive ball milling to produce nanocrystalline ZnO. *Mater. Lett.*, 2008, **62**(24) 4047-49.

[12] Matteazzi, Basset, D., Miani, F. and Le Caer, G. R., Mechanosynthesis of nanophased materials. *Nanostruct. Mat.*, 1993, **2**(3) 217-229.

[13] Salah, N., Habib, S. S., Khan, Z. H., Memic, A., Azam, A., Alarfaj, E., Zahed, N. and Al-Hamedi, S., High-energy ball milling technique for ZnO nanoparticles as antibacterial material. *Int. J. Nanomed.*, 2011, **6** 863-9.

[14] Lee, J. S., Park, K., Kang, M.-I, *et al.*, ZnO nanomaterials synthesized from thermal evaporation of ball-milled ZnO powders. *J. Cryst Growth*, 2003, **254**(3–4) 423–31.

[15] Damonte, L. C., Mendonza, Z. L. A., Soucase, M. B. and Hernandez, F. M. A., Nanoparticles of ZnO obtained by mechanical milling. *Powder Technol.*, 2004, **148**(1) 15–19.

[16] Anthony R. W., Solid State Chemistry and its Applications. First edition, ISBN: 0-471-903779 Published 1984 by Wiley & Sons.

[17] Suwanboon, S., Amornpitoskuk, P., Haidoux, A. and Tedenac, J.C., Structural and optical properties of undoped and aluminium doped zinc oxide nanoparticles via precipitation method at low temperature. *J. Alloys Compd.*, 2008, **462**(1-2) 335-9.

[18] Ciupina, V., Carazeanu, I. and Prodan, G., Characterization of $ZnAl_2O_4$ nanocrystals prepared by coprecipitation and microemulsion techniques. *J. Optoelectron. Adv. Mater.*, 2004, **6**(4) 1317-22.

[19] Huang, S., Xiao, Q., Zhou, H., Wang, D. and Jiang, W., Hydrothermal synthesis and conductive properties of Al-doped ZnO rod-like whiskers. *J. Alloys Compd.*, 2009, **486**(1-2) L24-L26.

[20] Chen, K. J., Fang, T. H., Hung, F. Y., Ji, L. W., Chang, S. J., Young, S. J. and Hsiao, Y. J., The crystallization and physical properties of Al-doped ZnO nanoparticles. *Appl. Surf. Sci.*, 2008, **254**(18) 5791-5.

[21] Piticescu, R.R., Piticescu, R.M. and Monty, C.J., Synthesis of Al-doped ZnO nanomaterials with controlled luminescence. *J. Eur. Ceram. Soc.*, 2006, **26**(14) 2979-83.

[22] Burunkaya, E., Kiraz, N., Kesmez, O., Çamurlu, H.E., Asilturk, M. and Arpaç, E., Preparation of aluminum-doped zinc oxide (AZO) nano particles by hydrothermal synthesis. *J. Sol-Gel Sci. Technol.*, 2010, **55**(2) 171-6.

[23] Baruah S. and Dutta J., Hydrothermal growth of ZnO nanostructures. *Sci. Technol. Adv. Mater.*, 2009, **10**(1) 013001 (18pp).

[24] Samanta, C., Stefania, A., Laura, F., Francesca, P. and Dario, L., Solvothermal synthesis and properties control of doped ZnO nanoparticles. *J. Colloid Interface Sci.,* 2009, **329**(1) 73-80.

[25] Ganguli, A. K., Ahmad, T., Vaidya, S. and Ahmed J., Microemulsion route to the synthesis of nanoparticles. *Pure Appl. Chem.*, 2008, **80**(11) 2451-77.

[26] Gao, L., Li, Q., Luan, W., Kawaoka, H., Sekino, T. and Niihara, K., Preparation and electric properties of dense nanocrystalline zinc oxide ceramics. *J. Am. Ceram. Soc.*, 2002, **85**(4) 1016-8.

[27] Fujita, K., Matsuda, K. and Mitsuzawa, S., Formation of Zinc Oxide by homogeneous precipitation method. *Bull. Chem. Soc. Jpn.*, 1992, **65**(8) 2270-1.

[28] Cai, L., Jiang, G., Zhu, C. and Wang, D., High quality Al-doped ZnO thin films deposited using targets prepared by chemical coprecipitation. *Phys. Status Solidi A*, 2009, **206**(7) 1461-4.

[29] Fangli, Y., Peng, H., Chunlei, Y., Shulan, H. and Jinlin, L., Preparation and properties of zinc oxide nanoparticles coated with zinc aluminate. *J. Mater. Chem.*, 2003, **13**(3) 634-7.

[30] Rodríguez-Paéz, J.E., Caballero, A.C., Villegas, M., Moure, C., Durán, P. and Fernández, J.F., Controlled precipitation methods: formation mechanism of ZnO nanoparticles. *J. Eur. Ceram. Soc.*, 2001, **21**(7) 925-30.

[31] Ebelmen, M., Recherches sur les combinaisons des acides borique et silicique avec les e´thers. *Ann. Chim. Phys.*, 1846, **16** 129-66.

[32] Cossa, A. *Il Nuevo Cimento* **1870,** *3*, 228.
[33] Sarkar, D., Mohapatra, D., Ray, S., Bhattacharyya, S., Adak, S. and Mitra, N., Synthesis and characterization of sol-gel derived ZrO2 doped Al2O3 nanopowder. Ceram. Int., 2007, 33(7) 1275-82.
[34] Han, C,-H., Han, S.-Do, Gwak, J. and Khatkar, S. P., Synthesis of indium tin oxide (ITO) and fluorine-doped tin oxide (FTO) nanopowder by sol-gel combustion hybrid method. *Mater. Lett.*, 2007, **61**(8-9) 1701-3.
[35] Zhong, X., Yang, B., Zhang, X., Jia, J. and Yi, G., Effect of calcining temperature and time on the characteristics of Sb-doped SnO2 nanoparticles synthesized by the sol-gel method. *Particuology*, 2012, **10**(3), 365-70.
[36] Ahn, J. Y., Cheon, H. K., Kim, W. D. *et al.*, Aero-sol-gel synthesis and photovoltaic properties of mesoporous TiO2 nanoparticles. *Chem. Eng. J.*, 2012, **188** 216-21.
[37] Xu, Z.Q., Deng, H., Li, Y., Guo, Q.H. and Li, Y.R., Characteristics of al-doped c-axis orientation ZnO thin films prepared by the sol-gel method. *Mater. Res. Bull.*, 2006, **41**(2) 354-8.
[38] Wu, K.-Y., Wang, C.-C. and Chen, D.-H., Preparation and conductivity enhancement of Al-doped zinc oxide thin films containing trace Ag nanoparticles by sol-gel process. *Nanotechnol.*, 2007, **18**(30) 305604 (6pp).
[39] Pierre, A. C., Introduction to sol-gel processing. First edition, Published 1998 by Kluwer Academic Publishers.
[40] M.Z.-C. Hu, M. Z.-C., Payzant, E. A. and Byers, C. H., Sol-gel and ultrafine particle formation via dielectric tuning of inorganic salt-alcohol-waters solutions. J. Colloid Interface Sci., 2000, **222**(1) 20–36.
[41] Spanhel, L. and Anderson, M. A., Semiconductor clusters in the sol-gel process: quantized aggregation, gelation, and crystal growth in concentrated zinc oxide colloids. *J. Am. Chem. Soc.*, 1991, **113**(8) 2826-33.
[42] Brinker, C. J. and Scherer, J. W., Sol-gel science: the physics and chemistry of sol–gel processing, Published 1990, Academic Press.
[43] Znaidi, L., Sol–gel-deposited ZnO thin films: A review. *Mater. Sci. Eng. B*, 2010, **174**(1-3) 18-30.
[44] Chu, S. Y., Yan, T. M. and Chen, S. L., Analysis of ZnO varistors prepared by the sol-gel method," *Ceram. Int.,* 2000, **26**(7) 733-7.
[45] Chakravarty, R. and Periasamy, C., Effect of aluminium doping on structural and optoelectronic properties of sol-gel derived nanocrystalline ZnO thin film. *Sci. Adv. Mater.*, 2011, **3**(2) 276-83.
[46] Xu, Z.Q., Deng, H., Li, Y., Guo, Q.H. and Li, Y.R., Characteristics of al-doped c-axis orientation ZnO thin films prepared by the sol-gel method. *Mater. Res. Bull.*, 2006, **41**(2) 354-8.
[47] Jones, R.W., Fundamental principles of sol-gel technology, the institute of metal. Published 1989 by The Institute of Metals, London.
[48] Kammler, H. K., Madler, L. and Pratsinis, S. E., Flame synthesis of nanoparticles. *Chem. Eng. Technol.*, 2001, **73**(6) 583-96.
[49] Vaghayenegar, M., Kermanpur, A. and Abbasi, M.H., Bulk synthesis nanoparticles by the one-step electromagnetic levitational gas condensation method. *Ceram. Int.*, 2012, **38**(7) 5871-8.
[50] Hembram, K., Sivaprahasam, D. and Rao, T.N., Combustion synthesis of doped nanocrystalline ZnO powders for varistor applications. *J. Eur. Ceram. Soc.*, 2011, **31**(10) 1905-13.
[51] Ahmad, M., Ahmed, E., Zhang, Y., Khalid, N.R., Xu, J., Ullah, M. and Hong, Z., Preparation of highly efficient Al-doped ZnO photocatalyst by combustion synthesis. Curr. Appl Phys., 2012.
[52] Gafiychuk, V.V., Ostafiychuk, B.K., Popovych, I.D. and Serednytski, A.S., ZnO nanoparticles produced by reactive laser ablation. *Appl. Surf. Sci.*, 2011, **257**(20) 8396-401.
[53] Ismail, R.A., Ali, A.K., Ismail, M.M. and Hassoon, K.I., Preparation and characterization of colloidal ZnO nanoparticles using nanosecond laser ablation in water. *Appl. Nanosci.*, 2011, **1**(1) 45-9.
[54] Ashkarran, A.A., Iraji zad, A., Mahdavi, S.M. and Ahadian, M.M., ZnO nanoparticles prepared by electrical arc discharge method in water. *Mater. Chem. Phys.*, 2009, **118**(1) 6-8
[55] Rao, N., Girshick, S., Heberlein, J., McMurry, P., Jones, S., Hansen, D. and Micheel, B., Nanoparticle formation using a plasma expansion process. *Plasma Chem. Plasma Process.*, 1995, **15**(4) 581-606.
[56] Gutsch, A., Kramer, M., Michael, G., Muhlenweg, M., Pridohl, M. and Zimmermann, G., Gas-phase production of nanoparticles. Degussa AG - Project House Nanomaterials, KONA, 2002. **20**, 24-35.
[57] Ko, T.S., Yang, S., Hsu, H.C. *et al.*, ZnO nanopowders fabricated by DC thermal plasma synthesis. *Mater. Sci. Eng. B*, 2006, **134**(1) 54-8.
[58] Swihart, M. T., Vapor-phase synthesis of nanoparticles. *Curr. Opin. Colloid Interface Sci.*, 2003, **8** 127-33.
[59] Panda, S. S., Mishra, D. P. and Upadhyaya, A., Effect of varying gas-flow conditions on the characteristics of the diffusion flame and silica powders prepared using flame combustion synthesis. *Powder technol.*, 2009, **191**(1-2) 164-9.
[60] Strobel, R., Stark, W. J., Madler, L., Pratsinis, S. E. and Baiker, A., Flame-made platinum/alumina: structural properties and catalytic behaviour in enantioselective hydrogenation. *J. Catal.*, 2003, **213**(2) 296-304.
[61] Champion, Y., Nanomaterials and nanochemistry – Gas phase synthesis of nanopowders. pp. 395-427. First edition, ISBN: 978-3-540-72993-8 Published 2007 by Springer Berlin Heidelberg.
[62] Ratchev, S. and Turitto, M., Minam – Micro and nanomanufacturing strategic research agenda. Published 2008.
[63] http://abercade.ru/en/materials/industrynews/443.html consulted on 15/04/2013.
[64] Calado, J.M. and Antunes, E.M., Nanometric-sized ceramic materials, process for their synthesis and uses thereof, patent WO 2009144665 (2009).

[65] Calado, J.M. and Antunes, E.M., Nanocrystaline spherical ceramic oxides, process for their synthesis and use thereof, patent WO 2009040770 (2009).

[66] Lefller, M.P. and Helble, J.J., Development of nanoscale ceramics for advanced power applications. University of Connecticut: Department of Chemical Engineering. Final project report (2000).

[67] Kawasaki, S. and Yamanaka, T., Elastic properties of monoclinic and orthorhombic ZrO2. J. *Mater. Sci. Lett.*, 1994, **13**(7) 514-5.

[68] Singh, P. and Goodenough, J. B., $Sr_{1-x}K_xSi_{1-y}Ge_yO_{3-0.5x}$: a new family of superior oxide-ion conductors. *Energy Environ. Sci.*, 2012, **5**(11) 9626-31.

[69] Mizoguchi, H., Kamiya, T., Matsuishi, S. and Hosono, H., A germinate transparent conductive oxide. *Nat. Commun.*, EISSN 2041-1723, 2011, **2**, 470.

[70] Hoang, V.V. and Ganguli, D., Amorphous nanoparticles – experiments and computer simulations. *Phys. Rep.*, 2012, **518**(3) 81-140.

[71] Muiva, C., Sathiaraj, T. and Maabong, K., Effect of doping concentration on the properties of aluminum doped zinc oxide thin films prepared by spray pyrolysis for transparent electrode applications, *Ceram. Int.*, 2011, **37**(2) 555-60.

[72] Marotti, R. E., Bojorge, C. D., Broitman, E., Cánepa, H. R., Badán, J. A., Dalchiele, E. A. and Gellman, A. J., Characterization of ZnO and ZnO:Al thin films deposited by the sol-gel dip-coating technique. *Thin solid films*, 2008, **517**(3) 1077-80.

[73] Zhong, W.-W., Liu, F.-M., Cai, L.-G., Peng-ding, Zhou, C.-C., Zeng, L.-G., Liu, X.-Q. and Li, Y., Elaboration and characterization of Al doped ZnO nanorod thin films annealed in hydrogen. *J. Alloys Compd.*, 2011, **509**(9) 3847-51.

[74] Tanami, J., Nakano, H., Wakihara, T., and Komeya, K., Development of advanced ceramics by powder composite process, *Kona Powder and Part. J.*, 2010, **28** 227-40.

[75] Falk, G., Sintering of transparent conductive oxides: From oxide ceramic powders to advanced optoelectronic materials; pp 587-609 in *Sintering of ceramics – New emerging techniques*, Chapter 26, Germany, 587-610, 2012.

[76] Senos, A. M. R., Sintering kinetics in open porosity stages of zinc oxide. Ph.D. thesis, University of Aveiro, Aveiro, Portugal, 1993 (in potuguese).

[77] Dorcioman, G., Ebrasu, D., Enculescu, I., Serban, N., Axente, E., Sima, F., Ristoscu, C. and Mihailescu, I. N., Metal oxide nanoparticles synthesized by pulsed laser ablation for proton exchange membrane fuel cells. *J. Power Sources*, 2010, **195**(23) 7776-80.

[78] Strachowski, T., Grzanka, E., Lojkowski, W. *et al.*, Morphology and luminescence properties of zinc oxide nanopowders doped with aluminum ions obtained by hydrothermal and vapor condensation methods. *J. Appl. Phys.*, 2007, **102**(7) 073513 - 073513-9.

[79] Kim, M., Mixed-metal oxide nanopowders by liquid-feed flame spray pyrolysis (LF-FSP): Synthesis and processing of core-shell nanoparticles. Ph.D. thesis, The University of Michigan, Michigan, 2008.

[80] Hidayat, D., Ogi, T., Iskandar, F. and Okuyama, K., Single crystal ZnO:Al nanoparticles directly synthesized using low-pressure spray pyrolysis. *Mater. Sci. Eng. B*, 2008, **151**(3) 231-7.

[81] Hsiao, K.-C., Liao, S.-C. and Chen, Y.-J., Synthesis, characterization and photocatalytic property of nanostructured Al-doped ZnO powders prepared by spray pyrolysis. *Mater. Sci. Eng. A*, 2007, **447**(1-2) 71-6.

[82] Shui, A., Wang, S., Wang, H. and Cheng, X., Preparation and properties of aluminum-doped zinc oxide powders with the coprecipitation method. *J. Ceram. Soc. Japan*, 2009, **117**(5) 703-5.

[83] Nayak, J., Kimura, S., Nozaki, S., Ono, H. and Uchida, K., Yellowish-white photoluminescence from ZnO nanoparticles doped with Al and Li. *Superlattices Microstruct.*, 2007, **42**(1-6) 438-43.

[84] Aimable, A., Strachowski, T., Wolska, E., Lojkowski, W. and Bowen, P., Comparison of two innovative precipitation systems for ZnO and Al-doped ZnO nanoparticle synthesis. *Process. Appl. Ceram.*, 2010, **4**(3) 107-14.

[85] Thu, T. V. and Maenosono, S., Synthesis of high-quality Al-doped ZnO nanoink. *J. Appl. Phys.*, 2010, **107**(1) 014308 – 014308-6.

[86] Facchetti, A. and Marks, T. J., Transparent electronics: From synthesis to applications. First Edition, ISBN: 978-0470990773, Published 2010 by Wiley & Sons.

[87] Badeker, K., Über die elektrische Leitfähigkeit und die thermoelektrische Kraft einiger Schwermetallverbindungen, *Annalen der Physik* **327**, 749–66

[88] Gordon, R., G., Criteria for choosing transparent conductors. *MRS Bull.*, 2000, **25**, 52-7.

[89] Holland, L., Vacuum deposition of thin films. First Edition, Published 1956 by Wiley & Sons.

[90] Ginley, D., S., Handbook of transparent conductors, First Edition, ISBN: 978-1441916372, Published 2010 by Springer.

[91] Rosenfeld, A., H., Kaarsberg, T., M. and Romm, J., Technologies to reduce carbon dioxide emissions in next decade. *Phys. Today*, 2000, **53**(11) 29-34.

[92] Bellingham, J., R., Phillips, W., A. and Adkins, C., J., Electrical and optical properties of amorphous indium oxide. *J. Phys.: Condens. Matter.*, 1990, **2**(28) 6207

[93] Hosono, H., Yasukawa, M. and Kawazoe, H., Novel oxide amorphous semiconductors: transparent conducting amorphous oxides. *J. Non-Cryst. Solids*, 1996, **203** 334-44.

[94] Sato, H., Minami, T., Takata, S. and Yamada, T., Transparent conducting p-type NiO thin films prepared by magnetron sputtering. *Thin Solid Films*, 1993, **236**(1-2) 27-31.

[95] Kawazoe, H., Yasukawa, M., Hyodo, H., Kurita, M., Yanagi, H. and Hosono, H., P-type electrical conduction in transparent thin films of $CuAlO_2$, *Nature,* 1997, **389** 939-42.

[96] Kim, Y., H., Sachse, C., Machala, M., L., May, C., Müller-Meskamp, L. and Leo, K., Highly conductive PEDOT:PSS Electrode with optimized solvent and thermal post-treatment for ITO-free organic solar cells. *Adv. Funct. Mater.*, 2011, **21**(6) 1076-81.

[97] Chien, Y.-M., Lefevre, F., Shih, I. and Izquierdo, R., A solution processed top emission OLED with transparent carbon nanotube electrodes. *Nanotechnol.*, 2010, **21**(13) 134020.

[98] Kim, K. S., Zhao, Y., Jang, H., Lee, S. Y., Kim, J. M., Kim, K. S., Ahn, J.-H., Kim, P., Choi, J.-Y. and Hong, B. H., Large-scale pattern growth of graphene films for stretchable transparent electrodes. *Nature*, 2009, **457**(7230) 706-10.

[99] Wager, J. F., Keszler, D. A. and Presley, R. E., Transparent Electronics, First edition, ISBN: 978-0387723419, Published 2008 by Springer.

[100] Fortunato, E., Barquinha, P., Pereira, L., Goncalves, G. and Martins, R., Advanced materials for the next generation of thin film transistors, in Idmc'07: Proceedings of the International Display Manufacturing Conference 2007, C.H. Chen and Y.S. Tsai, eds, Taipei: Society Information Display, Taipei Chapter, 371–3.

[101] Fortunato, E., Barquinha, P., Pereira, L., Goncalves, G. and Martins, R., Imid/Idmc 2006: The 6th International Meeting on Information Display/the 5th International Display Manufacturing Conference, Digest of Technical Papers 2006 605-8.

[102] Hartnagel, H., Dawar, A., Jain, A. and Jagadish, C., Semiconducting transparent thin films. Bristol: IOP Publishing, 1995.

[103] Norton, D. P., Heo, Y. W., Ivill, M. P., Ip, K., Pearton, S. J., Chisholm, M. F. and Steiner, T., ZnO: growth, doping & processing. *Mater. Today*, 2004, **7**(6) 34-40.

[104] Chiang, H. Q., Development of oxide semiconductors: materials, devices, and integration, in *Electrical And Computer Engineering*. Ph.D. thesis Oregon: Oregon State University, 2007.

[105] Lany, S. and Zunger, A., Dopability, intrinsic conductivity, and nonstoichiometry of transparent conducting oxides. *Phys. Rev. Lett.*, 2007, **98**(4) 045501-4.

[106] Hosono, H., Ionic amorphous oxide semiconductors: Material design, carrier transport, and device application. *J. Non-Cryst. Solids,* 2006, **352**(9-20) 851-8.

[107] Shimakawa, K., Narishima, S., Hosono, H. and Kawazoe, H., Electronic transport in degenerate amorphous oxide semiconductors. *Philos. Mag. Lett.*, 1999, **79**(9) 755-61.

[108] Ellmer, K., Resistivity of polycrystalline zinc oxide films: current status and physical limit. *J. Phys. D: Appl. Phys.*, 2001, **34**(21) 3097.

[109] Okude, M., Ueno, K., Itoh, S., Kikuchi, M., Ohtomo, A. and Kawasaki, M., Effect of in situ annealed SnO_2 buffer layer on structural and electrical properties of (001) SnO_2/TiO_2 heterostructures. *J. Phys. D: Appl. Phys.*, 2008, **41**(12) 125309.

[110] Barquinha, P., Martins, R., Pereira, L. and Fortunato, E., Transparent oxide electronics: from materials to devices. First edition, ISBN: 978-0470683736, Published 2012 by Wiley & Sons.

[111] Coutts, T. J., Young, D. L., Li, X., Mulligan, W. P. and Wu, X., Search for improved transparent conducting oxides: A fundamental investigation of CdO, Cd_2SnO_4, and Zn_2SnO_4. *J. Vac. Sci. Technol., A*, 2000, **18**(6) 2646-60.

[112] Minami, T., Takata, S. and Kakumu, T., New multicomponent transparent conducting oxide films for transparent electrodes of flat panel displays. *J. Vac. Sci. Technol., A*, 1996, **14**(3) 1689-93.

[113] Ellmer, K., Magnetron sputtering of transparent conductive zinc oxide: relation between the sputtering parameters and the electronic properties. *J. Phys. D: Appl. Phys.*, **33**(4) R17-R32 (2000).

[114] Frank, G. and Köstlin, H., Electrical properties and defect model of tin-doped indium oxide layers. *Appl. Phys., A*, 1982, **27**(4) 197-206.

[115] Ebert, P., Zhang, Z., Kluge, F., Simon, M., Zhang, Z. and Urban, K., Importance of Many-Body Effects in the Clustering of Charged Zn Dopant Atoms in GaAs. *Phys. Rev.Lett.*, 1999, **83**(4) 757-60.

[116] Pisarkiewicz, T., Zakrzewska, K. and Leja, E., Scattering of charge carriers in transparent and conducting thin oxide films with a non-parabolic conduction band. *Thin Solid Films*, 1989, **174**(1) 217-23.

[117] Zhang, D. H. and Ma, H. L., Scattering mechanisms of charge carriers in transparent conducting oxide films. *Appl. Phys. A,* 1996, **62**(5) 487-92.

[118] Moss, T. S., The Interpretation of the Properties of Indium Antimonide. *Proc. Phys.l Soc. Sect.B,* 1954, **67**(10) 775.

[119] Burstein, E., Anomalous Optical Absorption Limit in InSb. *Phys. Rev.*, 1954, **93**(3) 632-33.

[120] Coutts, T. J., Young, D. L. and Li, X., Characterization of transparent conducting oxides. *MRS Bull.,* 2000, **25**(8) 58-65.

[121] Hamberg, I., Granqvist, C. G., Berggren, K.-F.. Sernelius, B. E. and Engström, L., Band-gap widening in heavily Sn-doped In_2O_3. *Phys. Rev. B*, 1984, **30**(6) 3240-9.

[122] Gonçalo, P. G., Filmes finos de óxido de índio e zinco e sua aplicação em díodos orgânicos emissores de luz. Ph.D. thesis. New University of Lisbon, Portugal, 2011.

[123] Marezio, M., Refinement of the crystal structure of In_2O_3 at two wavelengths. *Acta Crystallogr.*, 1966, **20**(6) 723-8.

[124] Bates, J. L., Griffin, C. W., Marchant, D. D. and Garnier, J. E., Electrical conductivity, Seebeck coefficient and structure of In_2O_3-SnO_2. *Am. Ceram. Soc. Bull.*, 1986, **65**(4) 673-8.

[125] Chopra, K. L., Major, S. and Pandya, D. K., Transparent conductors – a status review. *Thin solid films*, 1983, **102**(1) 1-46.

[126] Mayr, M., High vacuum sputter rol coating: a new large-scale manufacturing technology for transparent conductive ITO layers, Proc. Soc. Vac. Coaters, 1986, **29** 77-94.

[127] Hwang, J.-H., Edwards, D. D., Kammler, D. R. and Mason, T. O., Point defects and electrical properties of Sn-doped In-based transparent conducting oxides. *Solid State Ionics*, **129**(1-4) 135-44.

[128] De Wit, J. H. W., Structural aspects and defect chemistry in In_2O_3, *J. Solid State Chem.*, 1977, **20**(2) 143-8.

[129] Ellmer, K. and Mientus, R., Carrier transport in polycrystalline ITO and ZnO:Al II: The influence of grain barriers and boundaries. *Thin Solid Films*, 2008, **516**(17) 5829-35.

[130] Minami, T., Present status of transparent conducting oxide thin-film development for Indium-Tin-Oxide (ITO) substitutes. *Thin Solid Films*, 2008, **516**(17) 5822-28.

[131] Minami, T., Transparent conducting oxide semiconductors for transparent electrodes. *Semicond. Sci. Technol.*, 2005, **20**(4) S35-S44.

[132] Stadler, A., Transparent Conducting Oxides-An Up-To-Date Overview. *Materials***,** 2012, *5*(4), 661-83.

[133] Granqvist C. G. and Hultaker, A., Transparent and conducting ITO films: new developments and applications. *Thin Solid Films*, 2002, **411** 1-5.

[134] Shigesato, Y. and Paine, D. C., Study of the effect of Sn doping on the electronic transport properties of thin film indium oxide. *Appl. Phys. Lett.*, 1993, **62**(11) 1268-70.

[135] Fan, J. C. C. and Goodenough, J. B., X-ray photoemission spectroscopy studies of Sn-doped indium-oxide films, *J. Appl. Phys.*, 1977, **48**(8) 3524-31.

[136] Jau, H.-C., Cheng, K.-T., Lin, T.-H., Lo, Y.-S., Chen, J.-Y., Hsu, C.-W. and Fuh, A. Y.-G., Photo-rewritable flexible LCD using indium zinc oxide/polycarbonate substrates. *Appl. Opt.*, 2011, **50**(2) 213-7.

[137] Tolcin, A. C., Indium, In: Minerals Yearbook: Metals and Minerals, U. S. Department of the interior, U. S. Geological Survey, 2011, 35.1-35.5.

[138] Ellmer, K., Klein, A. and Rech, B., Transparent conductive zinc oxide – Basics and applications in thin films solar cells. First edition, ISBN: 978-3540736127, Published 2008 by Springer.

[139] Müllera, J., Jiri Springerb, B.R. and Vanecekb, M., TCO and light trapping in silicon thin film solar cells. *Sol. Energy*, 2004, **77**(6) 917-30.

[140] Fortunato, E., Gonçalves, A., Pimentel, A., Barquinha, P., Gonçalves, G., Pereira, L., Ferreira, I. and Martins, R., Zinc oxide, a multifuctional material: from material to device applications. *Appl. Phys. A*, 2009, **96**(1) 197-205.

[141] Look, D. C., Farlow, C., Reunchan, P., Limpijumnong, S., Zhang, S. B. and Nordlund, K., Evidence for native-defect donors in *n*-type ZnO. *Phys. Rev. Lett.*, 2005, **95**(22) 225502.

[142] Kim, K.-K., Niki, S., Oh, J.-Y., Song, J.-O., Seong, T.-Y., Park, S.-J., Fujita, S. and Kim, S.-W., High electron concentration and mobility in Al-doped ZnO epilayer achieved via dopant activation using rapid-thermal annealing. *J. Appl. Phys.*, 2005, **97**(6) 1–3.

[143] Musat, V., Teixeira, B., Fortunato, E., Monteiro, R. C. C., Effect of post-heat treatment on the electrical and optical properties of ZnO:Al thin films. *Thin solid films*, 2006, **502**(1-2) 219-22.

[144] Lee, J.-H., Yeo, B.-W. and Park, B.-O., Effects of the annealing treatment on electrical and optical properties of ZnO transparent conduction films by ultrasonic spraying pyrolysis. *Thin solid films*, 2004, **457**(2) 333-7.

[145] Nunes, P., Fernandes, B., Fortunato, E., Vilarinho, P. and Martins, R., Performances presented by zinc oxide thin films deposited by spray pyrolysis. *Thin Solid Films*, 1999, **337**(1-2) 176-9.

[146] Major, S., Banerjee, A. and Chopra, K. L., Optical and electronic properties of zinc oxide films prepared by spray pyrolysis. *Thin Solid Films*, 1985, **125**(1-2) 179–85.

[147] Van de Walle, C. G., Hydrogen as a cause of doping in zinc oxide. *Phys. Rev. Lett.*, 2000, **85**(5) 1012-5.

[148] Hofmann, D. M., Hofstaetter, A., Leiter, F., Zhou, H. J., Henecker, F., Meyer, B. K., Orlinskii, S. B., Schmidt, J. and Baranov, P. G., Hydrogen: A relevant shallow donor in zinc oxide. *Phys. Rev. Lett.*, 2002, **88**(4), 045504-7.

[149] Cox, S. F. J., Davis, E. A., Cottrell, S. P., *et al.*, Experimental confirmation of the predicted shallow donor hydrogen state in zinc oxide. *Phys. Rev. Lett.*, 2001, **86**(12) 2601-4.

[150] Zhang, S. B., Wei, S. H. and Zunger, A., Intrinsic *n*-type versus *p*-type doping asymmetry and the defect physics of ZnO. *Phys. Rev. B*, 2001, **63**(7) 075025-31.

[151] Jeong, S. H. and Boo, J. H., Influence of target-to-substrate distance on the properties of AZO films grown by RF magnetron sputtering. *Thin Solid Films*, 2004, **447-8** 105-110.

[152] Alaya, A., Nouiri, M., Ayadi, Z. Ben, Djessas, K., Khirouni, K. and Mir, L. El, Elaboration and characterization of Si(n)/PS/ZnO(n) structure obtained by rf-magnetron sputtering from aerogel nanopowder target material. *Mater. Sci. Eng., B*, 2009, **159-60** 2-5.

[153] Kim, Y. H., Lee, K. S., Lee, T.S., Cheong, B.-ki, Seong, T.-Y. and Kim, W. M., Electrical, structural and etching characteristics of ZnO-Al films prepared by rf magnetron. *Curr. Appl. Phys.*, 2010, **10**(2) S278-81.

[154] Fortunato, E., Assunção, V., Goncalves, A., Marques, A., Águas, H., Pereira, L., Ferreira, I., Vilarinho, P. and Martins, R., High quality conductive gallium-doped zinc oxide films deposited at room Temperature. *Thin Solid Films*, 2004, **451-452** 443-7.

[155] Kim, Y., Lee, W., Jung, D.-R., Kim, J., Nam, S., Kim, H., *et al.*, Optical end electronic properties of post-annealed ZnO-Al thin films. *Appl. Phys. Lett.*, 2010, **96**(17) 171902 – 171902-3.

[156] Ruske, F., Roczen, M., Lee, K., Wimmer, M., Gall, S., Hupkes, J., *et al.*, Improved electrical transport in Al-doped zinc oxide by thermal treatment. *J. Appl. Phys.*, 2010, **107** 013708 – 013708-8.

[157] Guillen, C. and Herrero, J., Optical, electrical and structural characteristics of Al:ZnO thin films with various thicknesses deposited by DC sputtering at room temperature and annealed in air or vacuum. *Vacuum*, 2010, **84** [7] 924-9.

[158] Fortunato, E., Nunes, P., Marques, A., Costa, D., Águas, H., Ferreira, I., Costa, M. E. V. *et al.*, Transparent, conductive ZnO:Al thin film deposited on polymer substrates by RF magnetron sputtering. *Surf. Coat. Technol.*, 2002, **151–152** 247–51.

[159] Badadhe S. and Mulla, I., Effect of aluminium doping on structural and gas sensing properties of zinc oxide thin films deposited by spray pyrolysis. *Sens. Actuators, B*, 2011, **156**(2) 943-8.

[160] Wang, T., Diao, X. and Ding, P., Orthogonal optimization for room temperature magnetron sputtering of ZnO:Al films for all-solid electrochromic devices, *Appl. Surf. Sci.*, 2011, **257**(8), 3748-52.

[161] Zhao, J., Xie, S., Han, S., Yang, Z., Ye, L. and Yang, T., Organic light emitting diodes with AZO films as electrodes. *Synth. Met.*, 2000, **114**(3) 251-4.

[162] Kim, H., Piqué, A., Horwitz, J. S., Murata, H., Kafafi, Z. H., Gilmore, C. M. and Chrisey, D. B., Effect of aluminum doping on zinc oxide thin films grown by pulsed laser deposition for organic light-emitting devices. *Thin Solid Films*, 2000, **377-378** 798–802.

[163] Li, L., Fang, L., Chen, X. M., Liu, J., Yang, F. F., Li, Q. J., Liu, G. B. and Feng, S. J., Influence of oxygen argon ration on the structural, electrical, optical and thermoelectrical properties of Al-doped ZnO thin films. *Physica E: Low-dimensional Systems and Nanostructures*, 2008, **41**(1) 169-74.

[164] Li, L., Fang, L., Zhou, J., Liu, Z. Y., Zhao, L. and Jiang, S., X-ray photoelectron spectroscopy study and thermoelectrics Properties of Al-doped ZnO thin films. *J. Electron. Spectrosc. Relat. Phenom.*, 2009, **173**(1) 7-11.

[165] Yun, D.-J. and Rhee, S.-W., Deposition of Al-doped ZnO thin-films with radio frequency magnetron sputtering for a source/drain electrode for pentacene thin-film transistor. *Thin Solid Films*, 2009, **517**(16) 4644-9.

[166] Nomoto, J.-ichi, Hirano, T., Miyata, T. and Minami, T., Preparation of Al-doped ZnO transparent electrodes suitable for thin-film solar cell applications by various types of magnetron sputtering. *Thin Solid Films*, 2011, **520**(5) 1400-6.

[167] Fortunato, E., Ginley, D., Hosono, H. and Paine, D.C., Transparent conducting oxides for photovoltaics. MRS Bulletin 32 (2007) 242-7.

[168] Calnan, S. and Tiwari, A., High mobility transparent conducting oxides for thin film solar cells. *Thin Solid Films*, 2010, **518**(7) 1839-49.

[169] Rath, J., Liu, Y., Jong, M., Wild, J., Schuttauf, J., Brinza, M. and Schropp, R., Transparent conducting oxide layers for thin film silicon solar cells. *Thin Solid Films*, 2010, **518**(24) e129-e135.

[170] Chang, P.-K., Tsai, F.-J., Lu, C.-H., Yeh, C.-H., Wang, N.-F. and Houng, M.-P., Improvement of AZO/p-a-SiC:H contact by the p-μc-Si-H insertion layer and its application to a-Si:H solar cells. *Solid-state Electron.*, 2012, **72** 48-51.

[171] Liu, T., Xu, H., Chin, W. S., Yong, Z. and Wee, A. T. S., Local structural evolution of Co-doped ZnO nanoparticles upon calcination studied by in situ quick-scan XAFS. *J. Phys. Chem. C*, 2008, **112**(10) 3489-95.

[172] Zou, C. W., Yan, X. D., Han, J., Chen, R. Q., Gao, W. and Metson, J., Study of a nitrogen-doped ZnO film with synchrotron radiation. *Appl. Phys. Lett.*, 2009, **94**(17) 171093-5.

[173] Jimenez-Gonzalez, A. E., Urueta, J. A. S. and Suarez-Parra, R., Optical and electrical characteristics of aluminum-doped ZnO thin films prepared by sol gel technique. *J. Cryst. Growth*, 1998, **192**(3-4) 430-8.

[174] Serier, H., Gaudon, M. and Ménétrier, M., Al-doped ZnO powdered materials: Al solubility limit and IR absorption properties. *Solid State Sci.*, 2009, **11**(7) 1192-7.

[175] Cheng, H., Xu, X. J., Hng, H. H. and Ma, J., Characterization of Al-doped ZnO thermoelectric materials prepared by RF plasma powder processing and hot press sintering. *Ceram. Int.*, 2009, **35**(8) 3067-72.

[176] Kao, M., Chen, H. and Young, S., Effects of preannealing temperature of ZnO thin films on the performance of dye-sensitized solar cells. *Appl. Phys. A: Materials Science & Processing*, 2010, **98**(3) 595-9.

[177] Doyoung, K., Ilgu, Y. and Hyungjun, K., Fabrication of rough Al doped ZnO films deposited by low pressure chemical vapor deposition for high efficiency thin film solar cells, *Curr Appl Phys*, 2010, **10**(3) S459-S462.

[178] Khan, F., Singh, S., Husain, M. and Singh, P., Sol-gel derived hydrogen annealed ZnO:Al films for silicon solar cell application, *Sol. Energy Mater. Sol. Cells,* 2012, **100** 57-60.

[179] Musat, V., Teixeira, B., Fortunato, E., Monteiro, R. C. C. and Vilarinho, P., Al-doped ZnO thin films by sol–gel method. *Surf. Coat. Tech*., 2004, **180-181** 659-62.

[180] Dhakal, T., Nandur, A., Christian, R., Vasekar, P., Desu, S., Westgate, C., *et al.*, Transmittance from visible to mid infra-red in AZO films grown by atomic layer deposition system, *Sol. Energy*, 2012, **86**(5) 1306-12.

[181] Periasamy, C. and Chakrabarti, P., Tailoring the structural and optoelectronic properties of Al-doped nanocrystalline ZnO thin films. *J. Electron. Mater.*, 2011, **40**(3) 259-66.
[182] Nunes, P., Malik, A., Fernandes, B., Fortunato, E., Vilarinho, P. and Martins, R., Influence of the doping and annealing atmosphere on zinc oxide thin films deposited by spray pyrolysis, *VACUUM,* 1999, **52**(1-2) 45-9.
[183] Look, D., Reynolds, D., Litoon, C., Jones, R., Eason, D. and Cantwell, G., Characterization of homoepitaxial p-type ZnO grown by molecular beam epitaxy, *Appl. Phys. Lett.*, **81**(10) 1830-32.
[184] Gondini, P., Ghidelli, M., Fonzo, F., Bruno, P., Martí-Rujas, J., Bottani, C. *et al.*, Structural and functional properties of Al:ZnO thin films grown by Pulsed Laser Deposition at room temperature, *Thin Solid Films*, 2012, **520**(14) 4707-11.
[185] Ng, Z.-N., Chan, K.-Y. and Tohsophon, T., Effects of annealing temperature on ZnO and AZO films prepared by sol–gel technique, *Appl. Surf. Sci.*, 2012, **258**(24) 9604-9.
[186] Hoffman, R. C., Dilfer, S., Issanin, A. and Schneider, J., Solution processed ZnO – Challenges in processing and performance on flexible substrates. *Phys. Status Solidi (a)*, 2010, **207**(7) 1590-5.
[187] Klein, A., Korber, C., Wachau, A., Sauberlich, F., Gassenbauer, Y., Harvey, S. P., Proffit, D. E. and Mason, T. O., Transparent conducting oxides for photovoltaics: Manipulation of Fermi level, work function and energy band alignment. *Mater.*, 2010, **3**(11) 4892-914.
[188] http://www.displayforum.de/market.htm consulted on 21/09/2013.
[189] Various analysts, Growth opportunities in global thin film solar PV module market 2012 – 2017: Trend, forecast and opportunity analysis. Published 2012 by Research and Markets.
[190] Various analysts, Thin - Film Photovoltaic (PV) Cells Market Analysis to 2020 - CIGS (Copper Indium Gallium Diselenide) to Emerge as the Major Technology by 2020. Reference code: GBIAE0010MR. Published 2010 by GBI Research.
[191] Various analysts, 2011 Sputtering targets and sputtered films: technology and markets (Market research report – SMC037E). ISBN: 1-56965-745-9. Published 2011 by BCC Research.
[192] Minami, T., Oda, J.-ichi, Nomoto, J.-ichi and Miyata, T., Effect of target properties on transparent conducting impurity-doped ZnO thin films deposited by DC magnetron sputtering. *Thin Solid Films,* 2010, **519**(1) 385-90.
[193] Oda, J.-ichi, Nomoto, J.-ichi, Miyata, T. and Minami, T., Improvements of spatial resistivity distribution in transparent conducting Al-doped ZnO thin films deposited b DC magnetron sputtering. *Thin Solid Films,* 2010, **518**(11) 2984-7.
[194] Huang, H. S., Tung, H. C., Chiu, C. H., Hong, I. T., Chen, R. Z., Chang, J. T., *et al.*, Highly conductive alumina-added ZnO ceramic target prepared by reduction sintering and its effects on the properties of deposited thin films by direct current magnetron sputtering. *Thin Solid Films*, 2010, **518**(21) 6071-5.
[195] Fang, G., Li, D., and Yao, B.-L., Fabrication and characterization of transparent conductive ZnO:Al thin films prepared by direct current magnetron sputtering with highly conductive ZnO($ZnAl_2O_4$) ceramic target, *J. Cryst. Growth*, 2003, **247**(3-4) 393-400.
[196] http://www.pvmaterials.umicore.com/productsServices/PVDmaterial/ consulted on 05/10/2013.
[197] Fukushima, H., Zinc oxide ceramics and a manufacturing method for the same, a sputtering target. Patent application publication US 2009/0197757 A1 (2009).
[198] Wu, M.-W., Two-step sintering of aluminum-doped zinc oxide sputtering target by using a submicrometer zinc oxide powder. *Ceram. Int.*, 2012, **38**(8) 6229-34.
[199] Zhang, J., Zhang, W., Zhao, E. and Jacques, H. J., Study of high density AZO ceramic target. *Mater. Sci. Semicond. Process.*, 2011, **14**(3-4) 189-92.
[200] Hwang, B., Paek, Y.-K., Yang, S.-H., Lim, S., Seo, W.-S. and Oh, K.-S., Densification of Al-doped ZnO via preliminary heat treatment under external pressure. *J. Alloys Compd.*, 2011, **509**(27) 7478-83.
[201] Sato, Y., Oba, F., Yodogawa, M., Yamamoto, T. and Ikuhara, Y., Al-doped ZnO ceramics fabricated by mechanical alloying and high-pressure sintering technique. *J. Mater. Sci. Lett.*, 2003, **22**(17) 1201-4.
[202] X-ming, W., Xue, B., H-ying, D., Z-xia, S., Jing, S., S-gang, L. and S-tao, H., Preparation of Al-doped ZnO sputter target by hot pressing. *Trans. Nonferrous Met. Soc. China,* 2011, **21**(7) 1550-6.
[203] Zhang, Y., Yang, Y., Zhang, X., Wang, W., Cui, P., Song, W. and Tan, R., Two-step sintering of pristine and aluminum-doped zinc oxide ceramics, *Int. J. Appl. Ceram. Technol.*, 2011, **9**(5) 960-7.
[204] Yi-hua, S., Wei-hao, X., Chen-hui, L. and Lu, Y., Effect of dispersant concentration on preparation of an ultrahigh density ZnO–Al_2O_3 target by slip casting, J. Am. Ceram. Soc., 2009, **92**(9) 2168-71.
[205] Wu, M.-W., Liu, D.-S. and Su, Y.-H., The densification, microstructure, and electrical properties of aluminum-doped zinc oxide sputtering target for transparent conductive oxide film. *J. Eur. Ceram. Soc.*, 2012, **32**(12) 3265-75.
[206] Han, J., Mantas, P. Q. and Senos, A. M. R., Densification and grain growth of Al-doped ZnO. *J. Mater. Res.*, 2001, **16**(2) 459-68.
[207] Chou, Y.-H., Chau, J., Wang, W., Chen, C., Wang, S. and Yang, C., Preparation and characterization of solid-state sintered aluminum-doped zinc oxide with different alumina contents, *Bull. Mater. Sci.*, 2011, **34**(3) 477-82.
[208] Medvedovski, E., Alvarez, N., Yankov, O. and Olsson, M.K., Advanced indium-tin oxide ceramics for sputtering targets. Ceram Int., 2008, **34**(5) 1173-82.

[209] Zhu, G., Zhi, Li., Yang, H., Xu, H. and Yu, A., Effect of target density on microstructural, electrical, and optical properties of indium tin oxide thin films. *J. Electron. Mater.*, 2012, **41**(9) 2376-9.
[210] Liu, C. P. and Jeng, G. R., Properties of aluminum doped zinc oxide materials and sputtering thin films. *J Alloys Compd*, 2009, **468**(1–2) 343–9.
[211] Yang, Y., Lan, P., Wang, M., Wei, T., Tan, R. and Song, W., Nearly full-dense and fine-grained AZO:Y ceramics sintered from corresponding nanoparticles. *Nanoscale Res. Lett.*, 2012, **7**(1) 481-7.
[212] Zhu, G., Yang, Z., Zhi, L., Yang, H., Xu, H. and Yu, A., Preparation and sintering behavior of the tin-doped indium oxide nanopowders. *J. Am. Ceram. Soc*, 2010, **93**(9) 2511-4.
[213] Coutts, T. J., Perkins, J. D., Ginley, D. S. and Mason, T. O., Transparent conducting oxides: Status and opportunities in basic research. *Electrochem. Soc. Proc.*, 1999, **99**(11) 274.
[214] Halloran, J. W., Role of powder agglomerates in ceramic processing. In Advances in Ceramics, Forming of Ceramics 9, ed. J. A. Mangels and G. L. Messing. Am. Ceram. Soc., Columbus,OH, 1984, 67–75.
[215] Ferkel, H. and Hellmig, R. J., Effect of nanopowder deagglomeration on the densities of nanocrystalline ceramics green bodies and their sintering behavior. *Nano. Mat.*, 1999, **11**(5) 617-22.
[216] Lange, F. F., Sinterability of agglomerated powders. *J. Am. Ceram. Soc.*, 1984, **67**(2) 83-9.
[217] Wu, J. M. and Wu, C. H., Sintering behavior of highly agglomerated ultrafine zirconia powders. *J. Mat. Sci.*, 1988, **23**(9) 3290-9.
[218] Reed, J. S., Principles of ceramics processing. Second edition, Published 1995 in New York by Wiley & Sons.
[219] Mayo, M. J., Processing of nanocrystalline ceramics from ultrafine particles. *Int. Mat. Rev.*, 1996, **41**(3) 85-115.
[220] German, R. M., Sintering: Theory and practice. First edition, ISBN: 978-0471057864 Published 1996 by Wiley & Sons.
[221] Frenkel, J., Viscous flow of crystalline bodies under the action of surface tension. *J. Phys.* USSR, 1945, **9** 385-91.
[222] Kuczynski, G. C., Self-diffusion in sintering of metallic particles. *Trans. Met. Soc. Am. Inst. Min. Metall. Engrs. ,* 1949, **185** 169-78.
[223] Coble, R. L., Initial Sintering of alumina and hematite. *J. Am. Ceram. Soc.*, 1958, **41**(2) 55-62.
[224] Coble, R. L., Effects of particle size distribution in initial stage sintering. *J. Am. Ceram. Soc.*, 1973, **56**(9) 461-6.
[225] Kingery, W. D. and Berg, M., Study of the initial stages of sintering solids by viscous flow, evaporation-condensation, and self-diffusion. *J. Appl. Phys.*, 1955, **26**(19) 1205-12.
[226] Groza, J. R., Nanosintering. Nano. Mat., 1999, **12**(5) 987-92.
[227] Shaw, N. J., Densification and coarsening during solid state sintering of ceramics: A review of the models – I – Densification. *Pow. Met. Int.*, 1989, **21**(3) 16-21.
[228] Kang, S.-J. L., Sintering – Densification, grain growth & microstructure. First edition, ISBN: 07506 63855 Published 2005 by Elsevier.
[229] Chiang, Y.-M., Birnie, D. P. and Kingery, W. D., Physical ceramics – principles for ceramic science and engineering. First edition, ISBN: 978-0471598732 Published 1997 by Wiley & Sons.
[230] Kingery, W. D., Bowen, H. K. and Uhlmann, D. R., Introduction to ceramics. Second edition, ISBN: 978-0471478607 Published 1976 by Wiley & Sons.
[231] Ashby, M. F., A first report on sintering diagrams. *Acta Met.*, 1973, **22**(3) 275-89.
[232] Jonghe, L. C. and Rahaman, M. N., Sintering of ceramics. *Handbook of Advanced ceramics*, Chapter 4, p. 187-264 Published 2003 by Elsevier.
[233] Coble, R. L., Sintering of crystalline solids. I. Intermediate and final state diffusion models, *J. Appl. Phys.*, 1961, **32** 787–92.
[234] Coble, R. L. and Gupta, T. K., Intermediate stage sintering*, in Sintering and Related Phenomena*, G. C. Kuczynski, N. A. Hooton and C. F. Gibbon (eds), p. 423 – 44, Published 1967 by Gordon and Breach.
[235] Zhao, J. and Harmer, M. P., Sintering kinetics for a model final-stage microstructure: A study of Al_2O_3, *Phil. Mag. Lett.*, 1991, **63**(1) 7–14.
[236] Kang, S.-J. L. and Jung, Y.-I., Sintering kinetics at final stage sintering: model calculation and map construction. *Acta Mater.*, 2004, **52**(15) 4373–8.
[237] Shaw, N. J., Densification and coarsening during solid state sintering of ceramics: A review of the models – II – Grain growth. *Adv. Ceram.*, 1989, **21**(5) 31-33.
[238] Suryanarayana, C., Nanocrystalline Materials. *Int. Mat. Reviews*, 1995, **40**(2) 41-64.
[239] Herring, C., Effect of change of scale on sintering phenomena. *J. Appl. Phys.*, 1950, **21**() 301-3.
[240] Kang, S.-J. L., Greil, P., Mitomo, M. and Moon, J.-H., Elimination of large pores during gas-pressure sintering of β´ sialon. *J. Am. Ceram. Soc.*, 1989, **72**(7), 1166–9.
[241] Dobedoe, R. S., West, G. D. and Lewis, M. H., Spark plasma sintering of ceramics. *Bull. Eur. Ceram. Soc.*, 2003, **1** 19-24.
[242] Han, J., Mantas, P. Q. and Senos, A. M. R., Grain growth in Mn-doped ZnO. *J. Eur. Ceram. Soc.*, 2000, **20**(16) 2753-8.
[243] Senda, T. and Bradt, R. C., Grain growth in sintering ZnO and ZnO-Bi_2O_3 ceramics. *J. Am. Ceram. Soc.*, 1990, **73**(1) 106-14.
[244] Gupta, T. K. and Coble, R. L., Sintering of ZnO: I, densification and grain growth. *J. Am. Ceram. Soc.*, 1968, **51**(9) 521-5.

[245] Gupta, T. K. and Coble, R. L., Sintering of ZnO: II, Density decrease and pore growth during the final stage of the process. *J. Am. Ceram. Soc.*, 1968, **51**(9) 525-8.
[246] Han, J., Senos, A. M. R. and Mantas, P. Q., Nonisothermal sintering of Mn doped ZnO," *J. Eur. Ceram. Soc.*, 1999, **19**(6-7) 1003-6.
[247] Coble, R. L., Sintering alumina: Effect of atmosphere. *J. Am. Ceram. Soc.*, 1962, **45**(3) 123-7.
[248] Nicholson, G.C., Grain growth in zinc oxide. *J. Am. Ceram. Soc.*, 1965, **48**(4) 214-5.
[249] Dutta, S. K. and Spriggs, R. M., Grain growth in full dense ZnO. *J. Am. Ceram. Soc.*, 1970, **53**(1) 61-62.
[250] Moriyoshi, Y., Ikuma, Y., Maruyama, O. and Komatsu, W., The retardation of sintering shrinkage of ZnO in nitrogen atmosphere. *Z. Phys. Chem.*, 1980, **261** 825-8.
[251] Quadir, T. and Readey, D. W., Microstructure development of zinc oxide in hydrogen. *J. Am. Ceram. Soc.*, 1989, **72**(2) 297-302.
[252] Cai, F., He, X. R. and Zhang, L. C., Fabrication, properties and sintering of ZnO nanopowder. *Mater.Lett.*, 2008, **62**(8-9) 1223-5.
[253] Chu, M. T., Rahaman, M. N., De Jonghe, L. C. and Brooke, R. J., Effect of heating rate on sintering and coarsening. *J. Am. Ceram. Soc.*, 1991, **74**(6) 1217-25.
[254] Hynes, A. P., Doremus, R. H. and Siegel, R. W., Sintering and characterization of nanophase zinc oxide. *J. Am. Ceram. Soc.*, 2002, **85**(8) 1979-87.
[255] Roy, T. K., Bhowmick, D., Sanyal, D. and Chakrabarti, A., Sintering studies of nano-crystalline zinc oxide. *Ceram. Int.*, **34**(1) 81-7.
[256] Qin, X. J., Shao, G. J., Liu and Wang, W. K., Sintering characteristics of nanocrystalline ZnO. *J. Mater.Sci.,* 2005, **40**(18) 4943-6.
[257] Ewsuk, K. G. and Ellerby, D. T., Analysis of nanocrystalline and microcrystalline ZnO sintering using master sintering curves. *J. Am. Ceram.Soc.*, 2006, **89**(6) 2003-9.
[258] Wang, J. and Gao, L., Photoluminescence properties of nanocrystalline ZnO ceramics prepared by pressurelless sintering and spark plasma sintering. *J. Am. Ceram. Soc.*, 2005, **88**(6) 1637-9.
[259] Trotelj, M. and Kolar, D., Sintering of ZnO in the presence of liquid phase. In *Science of Ceramics*, vol. 9, ed. K. J. de Vires, Nederlandse Keramische Vereniging, Stoke-on-trent, UK, 127-35.
[260] Bradt, R. C., Nunes, S. I., Senda, T., Suzuki, H. and Burkett, s. L., Grain growth control via in-situ particle formation and Zener drag (pinning) during the sintering of ZnO. In *Sintering Technology*, ed. R. M. German and R. G. Cornwall, Marcel Dekker, Inc., 1996, 389-97
[261] Miyoshi, T., Maeda, K., Takahashi, K. and Yamazaki, T., Effects of dopants on the characteristics of ZnO varistors. In *Advances in Ceramics*, Vol 1, ed. L. M. Levinson and D .C. Hill, *Am. Ceram. Soc*. 1981, 309-15.
[262] Komatsu, W., Miyamoto, M., Hujita, S. and Moriyoshi, Y., Effect of dopants on sintering of zinc oxide and nickel oxide. *Yogyo Kyokaishi*, 1968, **76** 407-12.
[263] Nunes, S. I., and Bradt, R. C., Grain growth of ZnO in ZnO-Bi_2O_3 ceramics with Al_2O_3 additions. *J. Am. Ceram. Soc.*, 1995, **78**(9) 2469-75.

Chapter 3. Experimental details

The experimental research work performed can be divided into three main parts: the synthesis and characterization of the powders; the production and characterization of the ceramic targets; and the deposition and characterization of thin films and devices. This chapter summarizes and describes the relevant techniques used for that end. Regarding the production of the powders, the main focus is given to the synthesis process, since it is preponderant to obtain the raw materials used in the production of the ceramic targets studied throughout this dissertation. Ceramic targets production routes and characterization techniques aiming the analysis of targets properties are also covered in this chapter, giving special relevance to the structural, morphological, compositional, thermal, mechanical, and electrical characterization techniques. The last part of this chapter has the description of the deposition technique used to prepare the thin films: sputtering. Structural, morphological, compositional, surface, optical and electrical characterization techniques for deposited thin films are also described. It should be noted that the production and characterization of the powders and ceramic targets was mainly performed in INNOVNANO – Materiais Avançados, SA, while the production and characterization of thin films and devices was held at CENIMAT/I3N. Specific techniques that have been used punctually in the course of this research will be detailed when used.

3.1. Powder: Synthesis and characterization techniques

3.1.1. Synthesis

Emulsion detonation synthesis method (EDSM) (already described in section 2.3 of chapter 2) was used to produce high purity (> 99.9 %) undoped and Al-doped ZnO nanostructured powders with Al doping concentrations between 0.5 and 2.0 wt. % Al_2O_3. Several precursors were tested being the resulting powders characterized in terms of particle size distribution (PSD), crystalline structure, and morphology. The economic feasibility of using each one of these precursors (cost vs. yield) was also evaluated. Metallic precursors allow us to obtain a high conversion rate onto the final product by unit of the initial composition with high purity levels. On that basis, the metallic precursors were chosen for the synthesis of the powders used throughout this work. The production of ZnO and AZO powders by EDSM involved the following steps:

a) Preparation of the initiator and secondary water/oil (W/O) emulsions including the corresponding metal precursors in the desired ratio (Zn and Al metals with controlled PSD);
b) Detonation reaction of the (W/O) emulsions with the formation of a gaseous plasma that contains the required materials in the gaseous phase (fast detonation reaction rates at high pressures);
c) Condensation and formation of the nanocrystalline ZnO or AZO particles at high pressures in a high supersaturation state;
d) Quenching (up to 10^8 Ks^{-1} to 10^9 Ks^{-1}) of the particles to control and preserve the nanometric size of the particles.

The mechanism for the formation of undoped and Al-doped ZnO nanostructured powders by EDSM occurs by means of an exothermal reaction usually according to the following kinetics equations [1]:

$$M\ (s) \rightarrow M\ (l) \qquad \text{(eq. 3.1)}$$

$$M\ (l) \rightarrow M\ (g) \qquad \text{(eq. 3.2)}$$

$$M\ (g) + O\ (g) \rightarrow MO\ (g) \qquad \text{(eq. 3.3)}$$

$$MO\ (g) \rightarrow MO\ (l) \qquad \text{(eq. 3.4)}$$

$$MO\ (l) \rightarrow MO\ (s) \qquad \text{(eq. 3.5)}$$

where M, O, s, l and g represents, respectively, the metallic element, oxygen, solid state, liquid state and gaseous state. The first two stages (eq. 3.1 and eq. 3.2) occurs in the phase designated as Von Neumann spike that corresponds to the maximum compression originated by the shock wave, causing the heating of the metal and its consequent transformation from solid to liquid phase and subsequently to gaseous phase. The vapour phase metal-oxide formation (eq. 3.3) occurs in the phase nominated as reaction zone, which corresponds to the zone preceding and sustaining the passage of the shock wave ending in the point C, J (Chapman, Jouguet) in the case of ideal detonations. Finally, the fourth and fifth stages (eq. 3.4 and eq. 3.5) occur in the phase designated as Taylor zone, which corresponds to the adiabatic expansion of the gases resulting from the reaction in a radial direction, wherein, the faster the quenching of the particles, the smaller they will become [1-3].

In order to obtain primary particles in the nanometric scale it is crucial to have a detonation temperature at the point C, J (Chapman, Jouguet) lower than the melting point of the desired material. Considering the experimental difficulties of measurement, the detonation temperature at point (C, J) was predicted from the composition and initial density of the emulsion making use of a thermochemical program named THOR [4,5] which uses state equations and numerical methods for the calculation of the equilibrium products composition and properties of reactive systems under combustion/detonation.

The desired final compositions were achieved varying the ratio between the metal precursors Zn and Al in the secondary emulsion matrix before the detonation. The amount of precursors added was chosen ensuring that both the emulsion stability and the desired production rate were achieved. The initiation of the reaction was assured by the base or initiator emulsion, solely based on ammonium nitrate (NH_4NO_3), water, mineral oil and an emulsifying agent in controlled and optimized proportions [6].

Besides the final products, only a small amount of gas reaction products such as CO, CO_2, H_2O, NO, NH_3 and N_2 were produced without the appearance of high amounts of solid contaminants. The final density and the sensitivity of the emulsion was controlled by the amount of an organic sensitizer (0.2 – 2.0 %) added to the emulsion which was adjusted in order to guarantee an emulsion density value lower than 1.25 $g.cm^{-3}$ and subsequently enough sensitivity to attain a detonation rate higher than 4000 $m.s^{-1}$. Fig. 3.1 summarizes the overall EDSM process and a SEM image of the nanoparticles obtained.

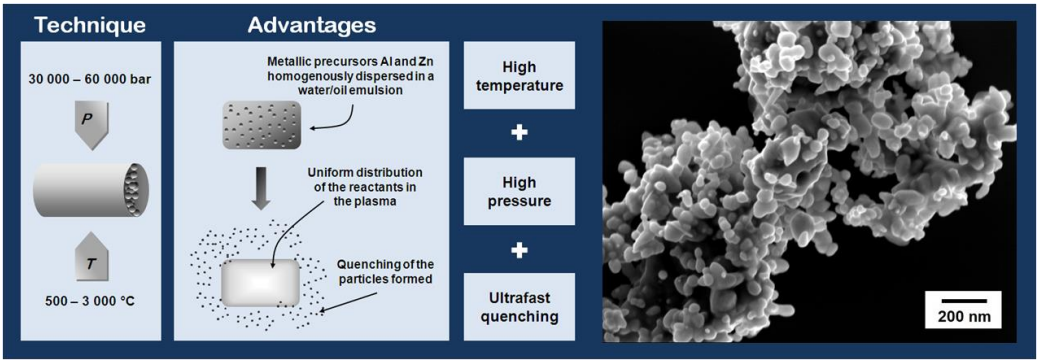

Fig. 3.1. *Schematic presentation of INNOVNANO synthesis process – Nanocrystalline ceramic AZO powder formation.*

3.1.2. Subsequent processing stages – thermal treatment, deagglomeration and drying

After synthesis the powders were thermally treated, wet deagglomerated/disaggregated and dried. The thermal treatments were performed in appropriate furnaces between 300 and 900 °C for 1 – 8 h of holding time (HT) and constant heating/cooling rate (CHR/CCR) of 10 °C.min^{-1}.

Lab scale deagglomeration/disaggregation of the particles was carried out in water using a nano bead mill (Dispermat - SL12-nano) (Fig. 3.2) that worked at 5500 rpm ensuring that the final particle size distributions of the different powders are similar. During this stage, the solids content of the suspensions, the speed of the recirculation pump, the rotational speed of the mill, and the composition, amount and size of the grinding balls were adjusted in order to obtain a compromise between the time consumption, amount of powder processed and contamination inherent to this stage. After optimization, the milling conditions were kept constant for all the synthesized powders. Thereafter, the powders were dried under controlled conditions and sieved at 150 µm.

Fig. 3.2. *Nano bead mill DISPERMAT® SL-nano from VMA available at INNOVNANO.*

Large scale processing was performed in a similar manner to the lab scale, with a stage of thermal treatment after synthesis, followed by deagglomeration/disaggregation in water using an industrial ball mill (under optimized conditions). The deagglomerated powders (in suspension) were industrially spray-dried without and with binders, and used to produce the industrial sputtering targets. The amount/type of binders, the solids content of the suspension and the

spray drier parameters (inlet and outlet temperatures, atomization pressure, suction fan speed and nozzle type) were adjusted to ensure the desired granule size distribution and the typical atomized powders characteristics (flowability, bulk density, tap density and moisture percentage). Details about the optimization of spray-drying conditions and atomized powders characteristics are shown in section 5.7.1 of chapter 5.

3.1.3. Characterization techniques

The synthesized powders were analyzed as-produced, thermally treated and after deagglomeration step. The most relevant techniques used to characterize the powders are described below.

3.1.3.1. Particle and granule size distribution – CPS and Malvern

Particle size distribution (PSD) of the powders was calculated by sedimentation using a CPS Disc centrifuge – Model DC 20000 form CPD Instrument, Inc (Fig. 3.3). The CPS Disc Centrifuge separates particles by size using centrifugal sedimentation in a liquid medium. The sedimentation is stabilized by a slight density gradient within the liquid. The sedimentation of the particles occurs within an optically clear and rotating disc. When particles approach the outside edge of the rotating disc, they block/scatter a portion of a light beam that passes through the disc [7]. The change in light intensity is continuously recorded, and converted by the operating software (CPSV95) into a PSD (D10, D50 and D90 values presented throughout this dissertation means respectively that, 10 %, 50 % and 90 % of the measured particles have a size below those values). The equipment allows PSD analysis in a range of 5 nm to 10 µm. The powder (~60 mg) was dispersed in distilled water (150 ml) and followed by ultrasonic bath for 2 min. The particles shape factor was optimized for the measurement taking into account the typical morphology of the particles. The disc speed used was 15000 rpm. Average particle size was calculated using the results obtained on three different measurements for each powder.

A Malvern Mastersizer 2000 (Fig. 3.3) was used for granule size distribution (GSD) of atomized powder. This equipment uses the technique of laser diffraction to measure the size of the particles. The sample (in aqueous medium) passes through the measurement area of the optical bench, where a laser beam illuminates the particles [8]. A series of detectors then accurately measure the intensity of light scattered by the particles within the sample over a wide range of angles, which are converted in the size of the analyzed particle by the algorithm of the adequate refraction model [9]. GSD in volumetric percentage is then obtained. The GSD were obtained in water without ultrasonic to ensure that the granules are not broken during measurement.

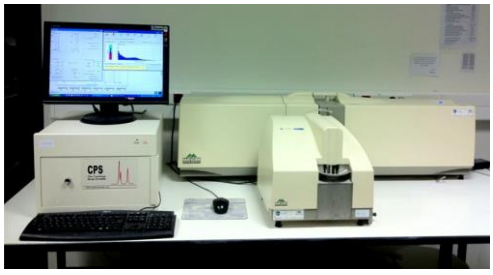

Fig. 3.3. *CPS Disc centrifuge – Model DC 20000 and Malvern Mastersizer 2000 equipments existing at INNOVNANO.*

3.1.3.2. Dilatometry tests

Dilatometry is a technique used for highly precise measurement of dimensions changes in a sample at a programmed temperature cycle. This technique is a powerful tool in the development and evaluation of sintering processes of ceramic materials. The equipment gives information about linear thermal expansion/shrinkage ($Y = \Delta L/L_0$) and respective shrinkage rate (dY/dt). The linear shrinkage, Y, as a function of temperature, T, or time, t, is determined by the ratio between the variation in the initial length of the sample (L_0) and the length at time t (L) ($\Delta L = L_0 - L$) and its initial length (L_0). The relative density (ρ_r), at any given time can also be determined from the shrinkage data using the following equation:

$$\rho_r(t) = \frac{\rho_0}{(1-Y)^3} \qquad \text{(eq. 3.6)}$$

where ρ_0 is the green density of the sample. Considering an isotropic shrinkage and a constant sample weight during the dilatometric analysis and differentiating equation 3.6, the densification rate $d\rho_r/dt$, was obtained using the following equation:

$$\frac{d\rho_r}{dt} = \frac{3\rho_0}{(1-Y)^4}\frac{dY}{dt} \qquad \text{(eq. 3.7)}$$

In this work, the sintering behavior of the powders was studied using a vertical dilatometer Linseis L-75 Platinum Series in air (Fig.3.4). The shrinkage of an alumina sample was also measured under identical sintering conditions as the compacted powders in order to correct the differences of shrinkage between the dilatometer rod and the sample holder. Several undoped and Al-doped ZnO cylindrical green bodies with a relative density of 35 – 62% ± 1 % (geometric density) of theoretical density (TD) (5.61 g.cm^{-3}) (more information about powder compacts preparation can be found in section 3.2.1.1) were nonisothermal sintered up to 1500 °C with constant heating rate (CHR) from 1 to 15 °C.min^{-1}. The cooling rate was kept constant at 10 °C.min^{-1}.

Fig. 3.4. *Linseis L-75 Platinum Series vertical dilatometer available at INNOVNANO.*

3.1.3.3. Structural and morphological characterization

3.1.3.3.1. X-ray diffraction (XRD)

X-ray diffraction is a non-destructive powerful technique widely used in Materials Science to identify crystalline phases and to quantify some structural properties, namely, the degree of crystallinity, lattice parameters, crystallite size and if any preferential crystallographic orientation occurs [10,11]. In this technique, a monochromatic X-Ray beam is directed to a material leading all electrons in its path to oscillate at the same frequency as the incident beam. This will cause constructive (in phase) and destructive (out phase) interference of the waves emitted by the atoms. A diffracted beam results from the constructive interferences, requiring that both the waves emitted by all the atoms lying in a single plane and the scattering of waves by successive planes are in phase. For a given X-ray radiation of wavelength (λ), with a value close to the inter-planar spacing (d_{hkl}), that reached the material with a certain incident angle (θ), constructive interferences occur when the phase difference between the waves dispersed by the distinct atomic planes are multiple (n) of the wavelength (λ). The condition of the constructive interference is given by the Bragg´s law (Fig. 3.5 (left)):

$$n\lambda = 2d_{hkl}sin\theta \qquad \text{(eq. 3.8)}$$

By varying 2θ (the diffraction angle) and measuring the diffracted beam intensity, which depends on the number of atomic planes equally spaced, a diffractogram is obtained and it can be compared with a database to identify the sample´s structure [12]. During this dissertation, the PDF-4+ database from the International Center for Diffraction Data (ICDD) are used as reference to determine the material structural properties.

The width of an XRD diffraction peak in a θ-2θ scan is related to the average crystallite size in the samples. The equation relating the full width at half maximum (FWHM) of a diffraction peak to the average dimension D_c of crystallites in the direction perpendicular to the substrate surface is known as Scherrer formula [13], and it is given by:

$$D_c = \frac{k\lambda}{\beta cos\theta} \qquad \text{(eq. 3.9)}$$

where β is the FWHM in radians, θ is the peak position in degrees and *k* is a constant close to 1. In this thesis was used the value of *k* = 0.94 in accordance with what is presented for ZnO and Al-doped ZnO [14]. The identification of crystalline phases and crystallite size determination of the powders were carried out on a Bruker D8 Advance X-ray diffractometer (XRD) with Cu Kα radiation (λ = 1.5406 Å) (Fig. 3.5 (right)). The diffraction intensities were measured using a scan speed of 0.5 s every 0.019° in the 2θ range from 20° to 80° at RT. Rietveld refinement was applied in the determination of crystallite sizes using Diffrac^{Plus} TOPAS software from Bruker AXS. Widely used in the characterization of crystalline materials, Rietveld refinement uses a least squares approach to refine a theoretical line profile until it matches the measured profile. Additionally, the software also provides information about preferred orientation and strain [15].

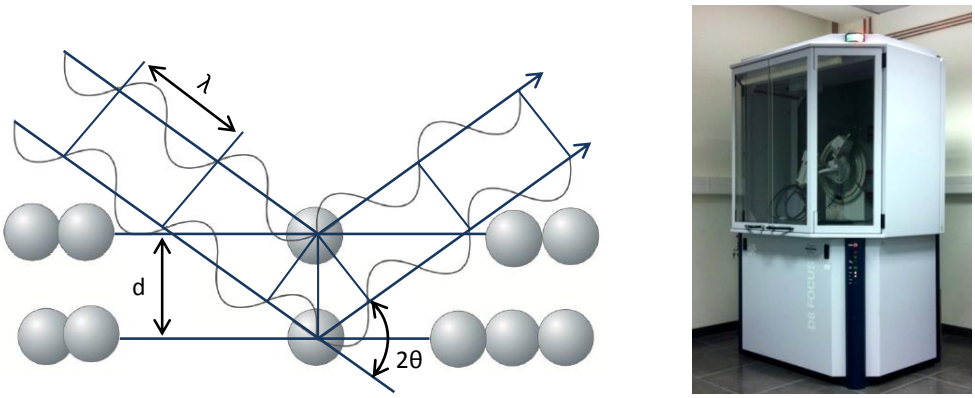

Fig. 3.5. *Schematic representation of Bragg´s Law (left) and Bruker D8 Advance X-ray diffractometer available at INNOVNANO (right).*

3.1.3.3.2. *<u>True density - Gas pycnometry</u>*

Gas pycnometers are commonly used to determine the true density (or more accurately, the volume) of powders and bulk materials. The true volume of a solid is calculated from the measured drop in pressure when a known amount of gas is allowed to expand into a chamber containing the sample. Thus, the true volume of a sample obtained by pycnometry excludes any pore volume accessible to the gas. Closed porosity, i.e., the one that does not communicate with the surface of the sample is included in the measured volume. Helium is the most used gas, because, due to its small size, it can penetrate the finest pores. Furthermore it is also inert and the most ideal gas, assuring maximum accuracy. The true density is obtained by dividing the weight of the sample by the true volume. In this method a sample of a known mass is placed into a cell of known volume. Then, the gas is introduced into the cell which is in vacuum, so the gas occupies the entire volume of the cell that is not occupied by the sample. The actual volume of the sample is determined and then the true density of the sample material can be accurately determined [16].

The true densities of the powders used throughout this research work were determined in vacuum using an AccuPyc II 1340 pycnometer from Micrometrics (Fig 3.6) and helium as measurement gas. For each sample the true density results of the mean values obtained in 10 different cycles.

Fig. 3.6. *Accupyc II 1340 picnometer from Micrometrics available at INNOVNANO.*

3.1.3.3.3. Specific surface area (SSA)

Specific surface area (SSA) is defined as the ratio A_s/m_s (m^2/g) between the absolute surface area A_s of a solid and its mass m_s (sample weight). The surface area includes all parts of accessible inner surfaces (mainly pore wall surfaces). One of the most common methods in the analysis of SSA is the Brunauer-Emmett-Teller (BET) method [17], which was used in this work. The BET method involves the determination of the amount of the adsorptive gas required to cover the external and the accessible internal pore surfaces of a solid with a complete monomolecular layer. This monolayer capacity can be calculated from the adsorption isotherm by means of the BET equation which is given by [18]:

$$\frac{P}{V_a(P_0-P)} = \frac{c-1}{V_M c} \times \left(\frac{P}{P_0}\right) + \frac{1}{V_M c} \qquad \text{(eq. 3.10)}$$

where P and P_0 are the equilibrium and the saturation pressure of the gas at the temperature of adsorption, V_a is the adsorbed gas volume, V_M is the monolayer adsorbed gas quantity and c is the dimensionless constant that is related to the enthalpy of adsorption of the adsorbate gas on the powder sample.

The gases used as adsorptives have to be only physically adsorbed by weak bonds at the surface of the solid (van der Waals forces) and can be desorbed by a decrease of pressure at the same temperature. The determination is usually carried out at the temperature of liquid nitrogen (≈ -196 °C). The plot of $P/V_a(P_0 - P)$ as a function of P/P_0 in the range of 0.05 < P/P_0 < 0.50 gives a straight line and is known as BET plot. The value of the slope s and the y-intercept i of the line are used to determine the monolayer adsorbed gas quantity V_M and the BET constant c based on the equations 3.11 and 3.12 respectively:

$$V_M = \frac{1}{s+i} \qquad \text{(eq. 3.11)}$$

$$c = \frac{s}{i} + 1 \qquad \text{(eq. 3.12)}$$

The SSA can be calculated from the volume of adsorbed gas, V_m using the equation:

$$SSA = \frac{V_M N_A S_g}{m_{sample} V_0} \qquad \text{(eq. 3.13)}$$

where N is the Avogadro´s number, S_g is the effective cross-sectional area of one adsorbate gas molecule, V_0 the molar volume of the gas and m_{sample} the mass of the sample.

In this work, a Quantachrome Nova 1000*e* Series system (Fig. 3.7) equipped with NovaWin software was used in the SSA measurement of the powders. The samples were firstly degassed in vacuum at 300 °C for 1h30m to remove gases and vapours that may have become adsorbed onto the surface after manufacture and during treatment or handling. The analyses were performed in liquid nitrogen using gaseous nitrogen as adsorbate gas. For each sample the value of V_a was measured at 10 values of P/P_0 in the relative pressure range 0.05 to 0.50.

Fig. 3.7. *Quantachrome Nova 1000E Series equipment existing at INNOVNANO.*

3.1.3.3.4. Scanning electron microscopy (SEM)

Scanning electron microscopy (SEM) developed by Max Knoll [19] at the beginning of the 30´s, can supply high resolution images of the surface of a sample at the nanometer scale. To obtain an image by SEM a highly energetic electron beam (generally between 0.1 and 30 keV) is directed at the sample and several interactions can occur, such as absorption of electrons by the sample, reflection of primary (backscattered) electrons, emission of secondary electrons, emission of Auger electrons and characteristic X-rays [20]. Secondary electron detectors are standard equipment in all SEM systems. In this type of detectors, SEM images are formed by the detection of secondary electrons emitted by the sample. In this case, surface morphology can be analyzed, since the number of secondary electrons emitted depends on the angle between the incident beam and the sample surface where it collides. Therefore a contrast is obtained between steep and flat regions of the sample and translated in the final image. On other type of detectors, for example, the image is obtained due to backscattered electrons, where the contrast is achieved as a result of the different atomic numbers of elements. Heavy elements backscatter electrons more strongly than light elements appearing brighter in the image, providing this imaging mode information about the chemical composition of the sample.

In this work, morphological characterization of the powders was carried out by scanning electron microscopy (SEM) using a Hitachi S-5500 available in the Center for Nano and Molecular Science – University of Texas, Austin. The S-5500 is an in-lens field-emission gun SEM with a 0.4 nm lateral resolution at 30 keV. The system is also equipped with a dark-field (DF) detector and a bright-field (BF) detector for scanning-transmission electron microscopy (STEM) imaging. The BF/DF duo-STEM detector allows simultaneous observation of BF and DF STEM images. The acceptance angle of the DF STEM signal is variable and can be selected from the menu. An energy dispersive spectroscopy detector (Bruker EDS Quantax 4010) is also installed for elemental stoichiometric ratios, multiple elemental line scanning, and 2-dimensional mapping. Additionally, Zeiss Auriga CrossBeam scanning electron microscope/focused ion beam (SEM-FIB) system (Fig. 3.8) with a maximum acceleration potential of 30 keV and a resolution of 1.0 nm at 15 keV existent in CENIMAT was also used to investigate the powders morphology. The system is equipped with an Oxford INCA 350 Energy-dispersive X-ray spectroscope (EDS) for compositional analysis.

Prior to analysis, the powder samples were dispersed in ethanol and ultrasonic bath. The powder was placed in a graphite conductive adhesive, dried and covered also with a thin layer of graphite to prevent charge accumulation during image acquisition.

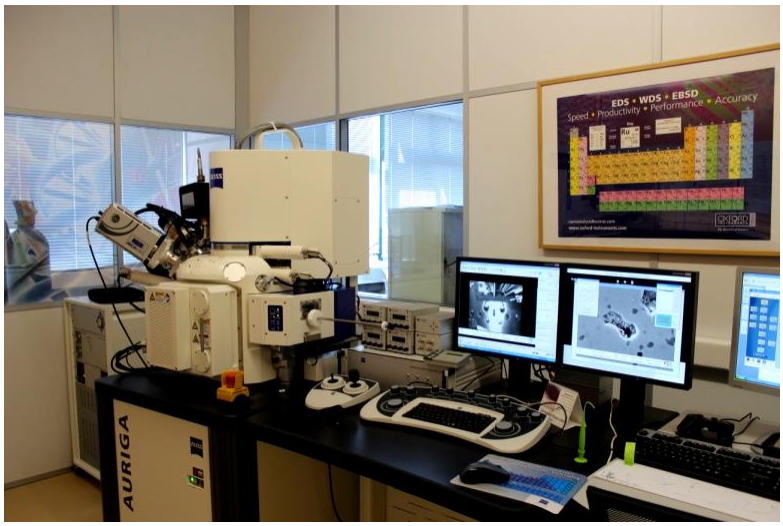

Fig. 3.8. *Zeiss Auriga CrossBeam SEM-FIB system available at CENIMAT/I3N.*

3.1.3.3.5. Transmission electron microscopy (TEM)

Firstly developed by Max Knoll and Ernst Ruska in 1931 [21], the transmission electron microscopy (TEM) system is based on the interaction of a highly energetic electron beam with a sample. The range of acceleration voltages, typically between 100 and 400 kV, is much higher than in SEM, and the analyzed samples have to be very thin in order to be transparent to electrons [20]. The transmitted and forward scattered electrons form a magnified image with very high resolution, allowing the analysis of features at the atomic scale. Moreover, the scattered electrons can also form a diffraction pattern providing information about the structure of the material. Contrast formation is highly dependent on the imaging mode (for instance, bright-field and dark-field modes), but generically is related with mass, thickness, diffraction and phase contrast [20]. BF is the most commonly used imaging mode. In this case the contrast is basically formed due to the increased electron scattering as the beam passes by atoms with higher atomic numbers or by thicker regions of the sample that appear as dark regions in the image (a less intensive beam arrives at the transmitted electron detector) providing information, for example, about the morphology of the sample [22, 23]. By regulating the magnetic lenses, image can be acquired by the back focal plane of the lens, resulting in a diffraction pattern defined by Bragg´s law. This allows to clearly distinguishing between amorphous and crystalline samples/phases and for the latter, information concerning the space group symmetries, atomic arrangement, crystalline phases and the crystal's orientation to the beam path can be obtained [24].

For transmission electron microscopy (TEM) the powder samples were first poured into ethanol (purity > 99.8 %) and dispersed by ultrasonics. The dispersed powders were put onto lacy copper grids (specially designed for TEM observation) and dried. Upon sample preparation high-resolution TEM (HRTEM), and STEM were performed in a JEOL 2010 F transmission electron microscope (Fig. 3.9) available in the Center for Nano and Molecular Science – University of Texas, Austin. This instrument is a 200 keV field-emission gun HRTEM microscope with a 0.19 nm point-

to-point resolution. The system is equipped with a high-angle annular dark-field detector (HAADF), and with low angle bright field and dark field detectors for scanning-transmission electron microscopy (STEM) imaging. The equipment is also equipped with an energy dispersive spectroscopy (EDS) detector (EDS–Detector: Thermonoram) for chemical analysis.

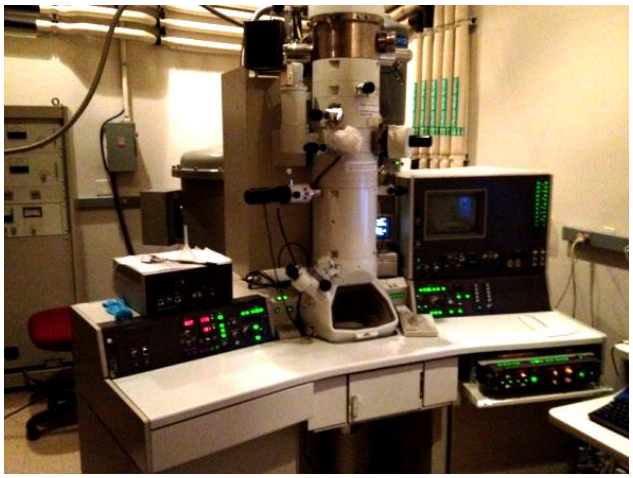

Fig. 3.9. *JEOL 2010 F transmission electron microscope (TEM) existing at the Center for Nano and Molecular Science – University of Texas.*

3.1.3.4. Thermal characterization

3.1.3.4.1. Differential scanning calorimetry/ Thermo-gravimetric analysis (DSC/TGA)

Differential scanning calorimetry (DSC) is a thermo-analytical technique developed by E.S. Watson and M. J. O´Neill in 1962 [25]. This technique is based on the measurement (as a function of temperature) of the difference in the amount of heat required to increase the temperature of a sample and corresponding reference. Both the sample and reference are maintained at very nearly the same temperature throughout the experiment.

The basic principle underlying this technique is that, when the sample undergoes a physical transformation such as phase transitions, more (or less) heat will need to flow through the sample than through the reference to maintain both at the same temperature. Whether more or less heat must flow to the sample in relation to the reference depends on whether the process is exothermic or endothermic. The result of a DSC experiment is a curve of heat flux versus temperature or versus time. Thermogravimetric analysis (TGA) is one of the members of the family of thermal analysis techniques used to characterize a wide variety of materials, providing supplementary characterization information to the DSC technique. TGA measures the amount and rate (velocity) of change in the mass of a sample as a function of temperature or time in a controlled atmosphere. This technique can analyze materials that exhibit either mass loss or gain due to decomposition, oxidation or loss of volatiles (such as moisture).

Thermal gravimetric analyses (TGA) as well as differential scanning calorimetry (DSC) were conducted simultaneously in the powders between 20 – 1500 °C with a CHR of 5 °C.min^{-1} in Ar using a STA 449 F3 *Jupiter*® from NETZSCH (Fig. 3.10) available in CENIMAT/I3N. An empty Al_2O_3 crucible was also heated under identical conditions and used as correction file during the trials.

Fig. 3.10. *NETZSCH STA 449 F3 Jupiter® DSC-TGA equipment available at CENIMAT/I3N.*

3.1.3.5. Compositional characterization

Synthesized undoped and Al-doped ZnO powders were chemically analyzed. The chemical composition of the powders was carried out by energy-dispersive X-rays spectroscopy (EDS), X-ray fluorescence (XRF) and X-ray photoelectron spectroscopy (XPS). A brief description of these techniques is presented in the next subsections.

3.1.3.5.1. Energy-dispersive X-ray spectroscopy (EDS)

Energy-dispersive X-ray spectroscopy (EDS) is commonly used in elemental and compositional analysis of a sample. This technique is based on the detection of secondary X-rays emitted as a result of the ionization of atoms due to the interaction of a high energetic electron beam with the sample. The incident beam ejects electrons from one of the inner shells (lower-energy levels) of the material under analysis, giving rise to holes. To facilitate the return of the atom to the ground state, electrons of the outer shells (higher-energy levels) tend to occupy the holes left by the ejected electrons. The difference in energy between these levels, which is a signature of a chemical element, can be released in the form of X-rays that are collected by a suitable detector (energy dispersive spectrometer) allowing the identification and quantification of the constituent elements of the sample to be measured (Fig. 3.11) [26].

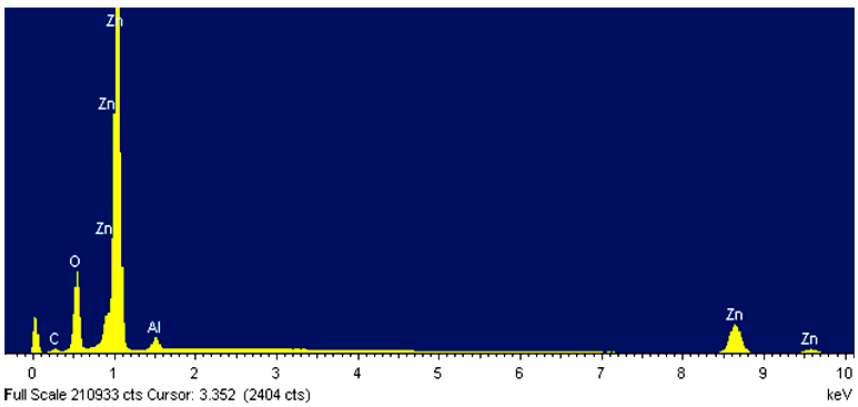

Fig. 3.11. *Typical example of an EDS spectrum.*

The same apparatus used in a typical SEM can be used to generate the electron beam and emit the secondary X-rays from the sample (see section 3.1.3.3.4). For that reason, the EDS analysis capability is usually integrated in SEM systems by equipping them with an X-ray detector. EDS provides a quick analysis of the individual chemical elements in a sample, by comparing the experimental spectra to known X-rays energies. Depending on the type of detector, elements as light as Be can be detected [26]. In this work was used an Oxford INCA Energy 350 system EDS coupled to the SEM-FIB referred in section 3.1.3.3.4.

3.1.3.5.2. X-ray fluorescence (XRF)

X-ray fluorescence (XRF) technique is commonly used in qualitative and quantitative elemental analysis of any kind of samples, both in research and industrial level. XRF is based on the same principle as EDS, but now the samples are illuminated by an intense X-ray beam typically produced from a rhodium target (tungsten, molybdenum and chromium can also be used). The same kind of detectors as in the case of EDS can be employed in XRF systems, which are able to analyze elements until Be, although most conventional XRF equipments are limited to the detection of elements with higher atomic number than Na [20, 26]. Compared with other techniques, the main advantages of XRF are the easy and fast acquisition of data (only a few minutes), which can be done in air (i.e., not requiring vacuum), and the fact that the samples to be analyzed do not require any special preparation. Furthermore it has the advantage of being non-destructive and not too expensive. However, due to the difficulty of focusing the incident X-ray beam in a small spot, the resolution is affected. Additionally, matrix effects affect the XRF measurements, due to the absorption of secondary X-rays by the sample itself [20].

A properly calibrated Bruker-AXS S4 Pioneer X-ray Fluorescence Spectrometer with a rhodium X-ray source (Fig. 3.12) existent in INNOVNANO was used to evaluate the chemical composition of the undoped and Al-doped ZnO powders. SpectraPlus software controls the spectrometer.

Fig. 3.12. *Bruker-AXS S4 Pioneer X-ray Fluorescence Spectrometer available at INNOVNANO.*

3.1.3.5.3. X-ray photoelectron spectroscopy (XPS)

X-ray photoelectron spectroscopy (XPS) is a powerful tool for obtaining chemical compound information on sample surface [27]. XPS can provide information about the surface of the sample, with most of the signal arising from the top 0.5 – 5 nm, while the EDS and XRF techniques provide compositional analysis in the bulk of the sample [20, 26].

XPS analysis involves the irradiation of a sample with soft monochromatic X-rays at E ~ 200 – 2000 eV emitted by an X-ray source, and then the measurement of the energy states of electrons ejected from the sample surface, by means of an energy analyzer (spectrometer). Fig. 3.13 shows schematic diagram of XPS setup and photoelectron emission process. The energy analyzer acts as a band pass filter, allowing only electrons with a particular kinetic energy passing through the electron detector. The emitted electron is usually called the 'photoelectron'. The energy of the ejected electron is related with the binding energy of the atom from which the electron is ejected, i.e., the difference in energy between the ionized and neutral atoms [26]. The binding energy (E_B) of electrons in the sample can be determined by the following equation [28]:

$$E_{kin} = hv - E_B - \phi \qquad \text{(eq. 3.14)}$$

where E_B is the electron binding energy, E_{kin} is the kinetic energy of the emitted photoelectron, hv is the photon energy, and ϕ is the work function of the material under study. The binding energy of an electron depends on the sub-shell from which is originated. For example, E_B of electrons originating from the oxygen 1s orbital is about 531 eV, and Zn $2p_{3/2}$ is E_B ~1022 eV. The characteristic energies at which electrons are emitted from the various sub-shells allow the atom to be identified. Equation 3.14 shows that E_{kin} varies with hv, but the E_B is independent of hv. XPS are therefore usually plotted in terms of binding energy. Apart from identifying the chemical species, XPS can be used to identify chemical state. This is because chemical bonding of an atom has an influence on the binding energy of all electrons. Detection of elements with atomic number above Li is possible by XPS [28].

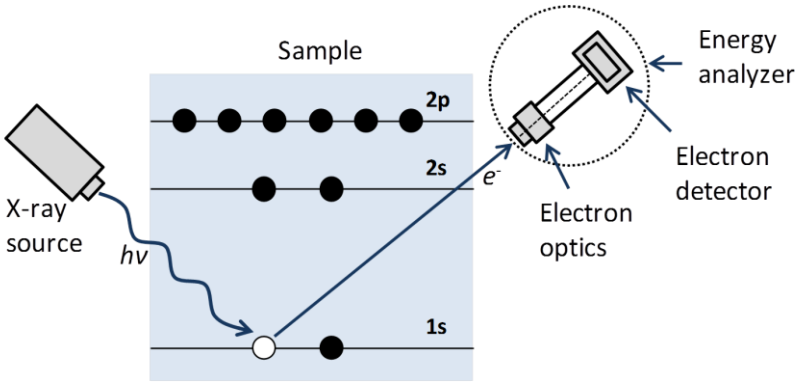

Fig. 3.13. *Schematic presentation of photoelectron emission process for X-ray photoelectron spectroscopy (XPS) (Adapted from [27]).*

The powders surface chemical compositions were examined by X-ray photoelectron spectroscopy (XPS) using a XSAM800 (KRATOS) spectrometer available at Instituto Superior Técnico operated in the fixed analyzer transmission (FAT) mode, with a pass energy of 20 eV, the non-

monochromatized AlKα X-radiation ($h\nu$=1486.6 eV) and a power of 120 W (10 mA×12 kV). XPS acquisition and data treatment details were published elsewhere [29].

3.2. Ceramic targets: Production and characterization techniques

3.2.1. Ceramic targets production

The manufacturing of the undoped and Al-doped ZnO ceramic targets was performed adopting a variety of conformation methods and sintering techniques. This section describes the path followed by the powders from compaction to the final polishing stage.

3.2.1.1. Preparation of powder compacts

Undoped and Al-doped ZnO cylindrical powder compacts were uniaxially cold pressed (UP) in a hydraulic press. Several dies were used to prepare samples with different dimensions (lab scale targets). For dilatometric analysis, compacts of ~6.4 mm diameter and variable height were UP in a hydraulic press. The influence of heating rate, temperature, holding time and green density (GD) on the final properties of the sintered targets was evaluated in a lab furnace by conventional sintering (CS) in air. To this end, compacted green bodies of ~20 mm diameter and 2 – 2.4 mm height were UP in a hydraulic press. Some targets were cold isostatic pressed (CIP) at 300 MPa for 30 min using a U33 high pressure system from Unipress Equipment, in order to enhance the GD of the compacts. The scale-up effect on densification was also studied using different diameter dies (12.7, 25, and 65 mm) to prepare the green compacts. Table 3.1 summarizes the different dies used to prepare the ZnO and AZO powder compacts and corresponding GD range used in CS studies (in air and argon). All these lab scale targets were pressed without binders or additives.

Table 3.1. *Different dies used in the preparation of ZnO and AZO powder compacts which were conventionally sintered in air and argon – Conformation methods and GD range studied for each die.*

Die size (mm)	Conventional sintering (air)	Conventional sintering (Ar atm.)
6.4	UP/UP+CIP 35% ≤ GD ≤ 62%	--
12.7	UP/UP+CIP 52% ≤ GD ≤ 62%	--
20	UP/UP+CIP 46% ≤ GD ≤ 62%	UP+CIP GD ≈ 62%
25	UP/UP+CIP 52% ≤ GD ≤ 62%	--
40	UP/UP+CIP 52% ≤ GD ≤ 62%	--
65	UP/UP+CIP 46% ≤ GD ≤ 62%	UP+CIP GD ≈ 62%

Large dimensions rectangular ceramic compacts (192 mm × 144 mm × 13 mm) were also prepared by UP using Laeis industrial hydraulic press equipment placed at Alpha Ceramics – Germany. The pressing force was varied between 100 and 160 MPa. The green compacts were pressed using

atomized powder with and without binders. More details about atomized powder and green compacts characteristics are shown in sections 5.7.1 and 5.7.2 of Chapter 5.

3.2.1.2. Consolidation techniques

Different consolidation techniques/sintering atmospheres were used in the production of undoped and Al-doped ZnO sintered targets. Apart from the CS method in air and under controlled atmosphere, hot-pressing (HP) and spark plasma sintering (SPS) conformation/sintering techniques were also employed to produce the ceramic targets. In the following are indicated and described the conformation/sintering conditions used throughout this research.

3.2.1.2.1. Conventional sintering

The sintering of the uniaxially and cold isostatic pressed powder compacts without binders or additives (preparation description and samples dimensions in section 3.2.1.1) was mainly performed in air under nonisothermal conditions using a laboratory furnace. The samples were sintered at temperatures between 300 and 1500 °C for 1 – 16 h of HT at a constant heating/cooling rate of 5 °C.min^{-1}. The dimensions and weight of samples was controlled before and after sintering. The effect of sintering atmosphere was assessed using a controlled atmosphere furnace. Samples with 20 and 65 mm diameter (Table 3.1) and different compositions (0.5 – 2.0 wt% Al_2O_3) were sintered in argon at 1200 – 1400 °C for 2 – 16 h of HT. The heating/cooling rate was similar to the one used for CS in air (5 °C.min^{-1}). The argon flux was kept at 50 ml.min^{-1} during sintering.

AZO green bodies with binders (used for large targets production) were sintered in air at 1300 °C for 2 h using an industrial furnace. From RT until 500 °C a CHR of 1°C.min^{-1} was used followed by a dwell of 4h at 500°C. The sintering cycle proceeded with a CHR of 5 °C.min^{-1} until 1300 °C. The sintered targets were cooled at a rate of 5 °C.min^{-1} until 600 °C and then furnace cooled to RT.

3.2.1.2.2. Hot-pressing sintering (HP)

As described in section 2.11.7, hot-pressing (HP) is a consolidation process based on the simultaneous application of enough heat and pressure to a powder that induces sintering and creep processes (Fig. 3.14) [30], where shape forming and densification can be accomplished in a single step. The loose powder is generally put in a graphite die that allows induction or resistance heating up to temperatures above 2000 °C. In this work, the powders were hot-pressed in argon without gas flow using HPW 315/400-2200-1000 equipment from Roedenthal. The heating rate was 10 °C.min^{-1}, and the pressure applied during sintering was 50 MPa. The sintering temperature and HT varied between 950 – 1200 °C and 1 – 2 h, respectively.

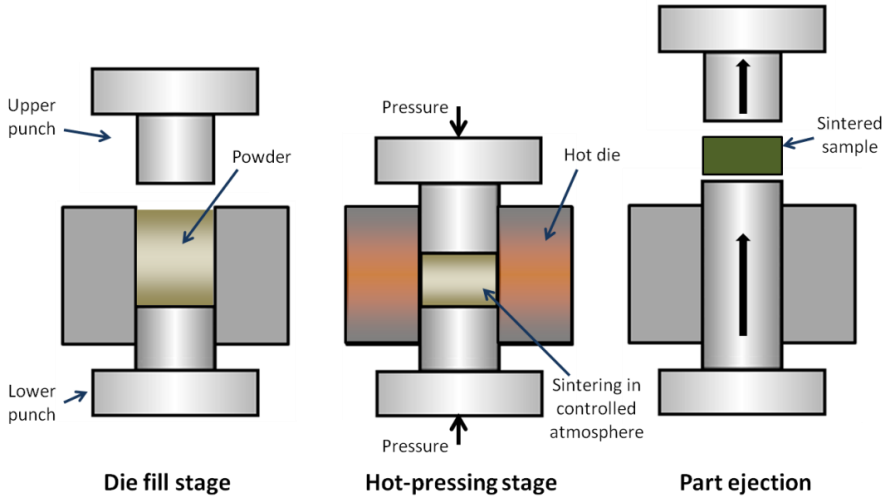

Fig. 3.14. *Hot-pressing sintering diagram (adapted from [31]).*

3.2.1.2.3. Spark plasma sintering (SPS)

SPS is a technique that allows sintering at low temperatures during short periods. The process relies on charging the gaps between the powder particles and applying, locally and momentarily, spark plasma. The SPS instrument comprehends the following components: vertical single-axis pressurization system, water-cooled chamber, atmosphere controls, vacuum exhaust unit, DC pulse generator and controller (Fig. 3.15). The powder materials are stacked between the die and punch on the sintering stage and held between the electrodes. The repeated application of an ON-OFF DC pulse, result in spark discharges between the powder particles and in Joule effect heating, producing efficient sintering with low power consumption. Through pulse application the local temperature instantly rises to 1200~2700 °C and under pressure the process finishes within a few minutes [32, 33]. The high temperatures at the gaps causes melting and vapourization at the surfaces, and constricted shapes or “necks” form between the particles. The necks progress during sintering and can result in 99 % dense sintered material. Since the temperature increase is concentrated at the particles surface, the internal structure and grain growth can be preserved/controlled [32].

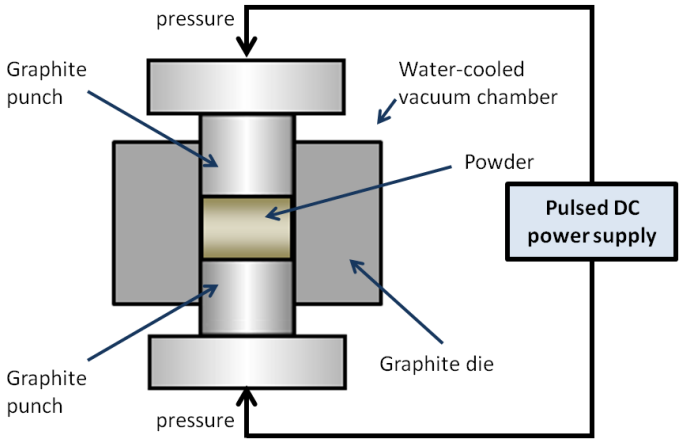

Fig. 3.15. *Spark plasma sintering diagram (adapted from [34]).*

SPS offer many advantages over HP sintering or CS, that include concentration of the sintering energy at the intergranular regions and easy control of the sintering energy, as well as high sintering speed, reproducibility, safety and reliability [32, 33]. The main drawback of this technique is usually related to the inability of getting sintered samples with homogeneous microstructure owing to the very different thermal cycles experience by the powder compacts surface and its interior (mainly for larger samples). SPS was applied to manufacture 2 inches (~51 mm diameter) AZO ceramic targets. The sintering was performed in a graphite mould under an axial compressive force of 50 MPa in vacuum using a SPS system existing in Fraunhofer Institute for Ceramic Technologies and Systems (Germany). Sintering temperatures and dwell times in the range of 900 – 1150 °C and 15 – 30 min respectively were used. The heating rate was fixed in 100 °C.min^{-1}.

3.2.1.3. Density measurement

The green density (GD) of the compacts was measured geometrically and is given by the ratio between the weight and the geometric volume of the samples (geometric density):

$$GD = \frac{m}{\pi\left(\frac{d_s}{2}\right)^2 h_s} \qquad \text{(eq. 3.15)}$$

where m, d_s and h_s are respectively the mass, the diameter and the height of the sample. The GD of the samples was determined considering the average value reached for three different samples pressed under the same conditions. The maximum deviation in geometric GD, determined in the different samples was below 1 % for the investigated GD range (35 % to 62 % of theoretical density (5.61 g.cm^{-3})). Final densities (ρ_f) of the sintered samples were measured by the Archimedes liquid immersion technique [35] considering the following equation:

$$\rho_f = \frac{m_d}{m_s - m_i} \times \rho_{liq} \qquad \text{(eq. 3.16)}$$

where m_d is the mass of the dry test sample, m_s is the mass of the soaked test sample, m_i is the mass of the immersed sample and ρ_{liq} is the density of the immersion liquid (in this case, distilled water). The final densities were obtained by the average of three different samples sintered under the same conditions. The relative density (ρ_r) and its derivative as a function of time ($d\rho_r/dt$) were also measured from the dilatometric measurements of linear shrinkage using equations 3.6 and 3.7 shown in section 3.1.3.2 assuming an isotropic linear shrinkage.

3.2.1.4. Polishing

Independently on the sintering technique, the sintered ceramic targets surfaces always presents surface irregularities, requiring a fine polishing after sintering. Moreover, the accuracy of the results reached with some characterization techniques depends on the quality of the surface to be analyzed.

Polishing was done in a Struers TegraPol-25 polishing machine equipped with a TegraForce-5 automatic samples mover existing at INNOVNANO. The samples were firstly ground with abrasives in order to remove scratches until the desired surface finishing was obtained. After that, the fine polishing was performed using 9, 3 and 1 µm diamond paste. Polishing step was employed in the preparation of samples for several characterization techniques used during this research work.

3.2.2. Characterization techniques

Structural, morphological, compositional, electrical, thermal and mechanical characterization of the sintered ceramic targets was performed using a variety of techniques. Relevant details about these techniques are presented below.

3.2.2.1. Structural and morphological characterization

3.2.2.1.1. X-ray diffraction (XRD)

The phase analyses of sintered undoped and Al-doped ZnO samples were carried out on a Bruker D8 Advance X-ray diffractometer (XRD) with Cu Kα radiation (λ=1.5406 Å) under the same scanning speed and in the same diffraction angle (2θ) range as described in section 3.1.3.3.1. Rietveld refinement was applied in the determination of lattice parameters using Diffrac^{Plus} TOPAS software from Bruker AXS. For XRD analysis, the sintered samples were polished in the same way as described in section 3.2.1.4.

3.2.2.1.2. Scanning electron microscopy (SEM) – grain size measurement

SEM analysis of the ZnO and AZO sputtering targets were carried out using the same Zeiss Auriga CrossBeam SEM-FIB equipment described in section 3.1.3.3.4. For microstructural observation and grain size measurement, several produced and commercially available sputtering targets (final density ≥ 90 % of theoretical density (TD) of the material) were fine polished according to the procedure outlined in section 3.2.1.4. Subsequently, the polished sections were thermally etched at temperatures of 100 °C lower than the sintering temperatures for 15 minutes, with a constant heating/cooling rate of 10 °C.min.$^{-1}$. In addition, the fracture sections of some samples were also observed by SEM. EDS (section 3.1.3.5.1) was used for the compositional analysis of certain selected SEM samples.

The grain size of the main phase (ZnO) in 2D polished and thermally etched sections of the samples was measured from SEM micrographs using the linear intercept method, or Hein´s method, established in 1903 [36]. By measuring the length of random intercepts, the average grain size can be calculated using the following equation:

$$\bar{l} = L/N \qquad \text{(eq.3.17)}$$

where $\bar{l}$ is the arithmetic mean linear intercept, or Heyn grain size, L is the length of the line across the image and N is the number of grains traversed. Over 300 grains were measured for each sample to calculate the average grain size. The grain shape was assumed to be spherical in order to transform the results of 2D to 3D, using the correction factor given by Fullman [37]:

$$G_s = 1.5\bar{l} \qquad \text{(eq. 3.18)}$$

where G_s is the calculated 3D grain size and 1.5 the transformation factor. Image analysis software (ImageJ) was used for comparison. For the Al-doped ZnO samples, containing a secondary spinel phase ($ZnAl_2O_4$), the particle size of the secondary phase was also measured using ImageJ, given that the minority secondary phase particles can be easily distinguished from the main phase in the SEM micrographs. More than 300 particles of the secondary phase were examined for each sample. The volume fraction of the minority secondary phase in 3D was

calculated as the ratio of the total secondary phase area in polished section and the total solid section area [38].

3.2.2.2. Compositional characterization

Sintered ceramic targets were chemically analyzed in order to assess its final composition and correlate it with the corresponding raw materials (synthesized powders). For this purpose, the sintered targets were fine polished and characterized by Energy-dispersive X-ray spectroscopy (EDS) technique (described in section 3.1.3.5.1), X-ray photoelectron spectroscopy (XPS) (described in section 3.1.3.5.3) and Auger electron spectroscopy (AES) presented below.

3.2.2.2.1. Auger electron spectroscopy (AES)

Auger electron spectroscopy (AES) is a widely used technique to determine elemental composition, being often used in the analysis of a wide range of bulk material surfaces, thin films and interfaces. When a high energy beam (2 – 50 keV) is focused on the sample surface, besides the X-ray emission by electrons coming from outer levels to inner levels, can also happen that the energy associated with these electrons decay, originate the emission of a third electron – Auger electron. The Auger electron has a characteristic energy, which is specific to each element and its detection allows the determination of the chemical composition of the analyzed surface [26, 39]. Since the characteristic emission of Auger electrons is more probable for light elements than for heavy elements (where electrons are more strongly bounded to the nucleus), this technique enables the detection of elements with atomic number above 3 [39]. A great advantage of the AES is that it can be used to provide compositional information as a function of depth (in-deep analysis by ion sputtering). In this method, the sample is bombarded with highly energetic ions (mostly Ar^+ ions with energy of 1 to 5 keV), the surface atoms are sputtered away and the residual surface is analyzed.

AES analyses were carried out in Karlsruhe Institute of Technology (KIT), using a PHI 680 Scanning Auger Nanoprobe from Physical Electronics. The Auger depth profiles were measured with 3 kV electron beam acceleration and the argon ions energy was 2 keV for sputtering. The average sputter rate of the films was determined by profilometry. Quantification analyses were performed with accurate standards allowing achieving associated errors < 3 %.

3.2.2.3. Electrical characterization

Hall effect was discovered in 1879 by Edwin Hall, who submitted an electrically conductive material to a magnetic field perpendicular to the direction of the applied electrical current. Hall observed a potential difference on the side faces of this conductor in the presence of the magnetic field. Since then, this technique has been widely used. Besides allowing the measurement of the electrical resistivity (ρ_e), this technique also provides, in a simple and rapid way, the majority carrier type (electrons or holes), carrier concentration (N_e) and their Hall mobility (μ_e) [40, 41]. Hall effect is based on the Lorentz force ($\vec{F}$), which reflects how a charged particle is affected when subjected to magnetic and electric fields:

$$\vec{F} = q\left(\vec{E} + \vec{v} \times \vec{B}\right) \qquad \text{(eq. 3.19)}$$

where q is the electron charge (1.61 x 10^{-19} C), $\vec{E}$ is the electric field, $\vec{v}$ is the particle velocity and $\vec{B}$ is the magnetic field. Considering the van der Pauw configuration in Fig. 3.16 (left), the current I is injected at two non-adjacent electrodes (1 and 3) (I_{13}) while having a magnetic field perpendicular to the sample surface. The Lorentz force deflects carriers to one side of the sample, perpendicularly to $\vec{B}$ and $\vec{I}$, creating an electric field ($\vec{E}$) in the sample and a Hall voltage between the remaining two non-adjacent electrodes ($V_H = V_{24}$) for a constant magnetic field $\vec{B}$. When the system is in equilibrium the magnetic and electrostatic forces are balanced:

$$q(\vec{v} \times \vec{B}) = q\vec{E} \qquad \text{(eq. 3.20)}$$

Since $\vec{B}$, $\vec{I}$ and $\vec{E}$ are perpendicular, the vectors can be replaced by scalars. In this situation I is given by:

$$I = qN_e s_{th} W v \qquad \text{(eq. 3.21)}$$

where N_e is the carrier concentration, s_{th} is the sample thickness and W is the distance between the two electrodes. By substituting eq. 3.21 into eq. 3.20, the Hall coefficient (R_H) can be defined as:

$$\frac{1}{qN_e} = \frac{V_H s_{th}}{IB} = R_H \qquad \text{(eq. 3.22)}$$

where V_H is the Hall voltage measured by the system ($V_H = EW$). The sign of R_H indicates the type of majority carriers. The sign can be negative for electrons (n-type semiconductors) and positive for holes (p-type semiconductors). N-type conduction is observed for all the deposited thin films studied in this research work. If s_{th} is not known, one can still define a sheet Hall coefficient (R_{HS}):

$$R_{HS} = \frac{R_H}{S_{th}} = \frac{V_H}{IB} \qquad \text{(eq.3.23)}$$

which can be used to determine the sheet carrier density (N_S):

$$N_S = \frac{1}{qR_{HS}} \qquad \text{(eq. 3.24)}$$

If s_{th} is known N_e can be determined by:

$$N_e = \frac{1}{qR_H} \qquad \text{(eq. 3.25)}$$

Finally, R_{HS} can be employed to calculate the Hall mobility (μ_e) without requiring s_{th} by:

$$\mu_e = \frac{R_{HS}}{R_S} \qquad \text{(eq. 3.26)}$$

where R_S is the sheet resistance.

Throughout this research work, electrical properties of undoped and Al-doped ZnO sintered targets were examined by Hall effect using a Biorad HL 5500PC at room temperature (Fig. 3.16 (right)) on fine polished both sides samples (10 mm × 10 mm × 0.5 mm) using the van der Pauw configuration. The system is equipped with a high resistivity buffer amplifier that allows the measurement of highly resistive samples with more accuracy. In order to improve the electrical contact between the sample and the electrical probes, four Au electrodes were coated on the four corners of the square samples surface. For each sample, V_H was determined as the average of five hall measurement cycles at a constant magnetic field of 0.5 T.

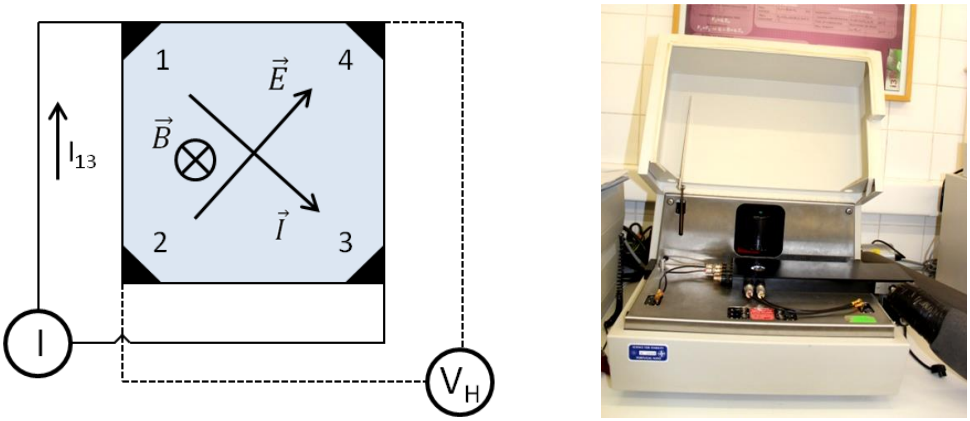

Fig. 3.16. *Schematic presentation of the van der Pauw configuration used for Hall effect measurements (left) and Biorad HL 5500PC Hall effect system available at CENIMAT/I3N (right).*

3.2.2.4. Thermal characterization

Thermal conductivity (k) describes the energy transport through a body (heat conduction) as a result of a temperature gradient and is usually presented in $Wm^{-1}K^{-1}$. Thermal conductivity of materials is given by the following equation:

$$k(T) = \rho(T) \times C_p(T) \times D(T) \qquad \text{(eq. 3.27)}$$

where T is the temperature at which measurement occurs, ρ is the material density, C_p is the specific heat in $Jg^{-1}K^{-1}$ and D is the thermal diffusivity in mm^2s^{-1}. All quantities on equation 3.27 can be functions of temperature. The thermal diffusivity (D) is a measure of how quickly a body can change its temperature. It increases with the ability of a body to conduct heat (k) and it decreases with the amount of heat needed to change the temperature of a body (C_p).

In this research work, transversal thermal diffusivity (*D*), thermal conductivity (*k*) and specific heat (C_p) were measured in several sintered AZO samples (10 mm × 10 mm × 0.5 mm) using laser flash equipment LFA 457 from Netzsch available in National Institute of Materials Physics, Romania. The values were recorded at 25 °C, 30 °C (to allow for auto adjustment parameters), 50 °C and then every 50 °C until 700 °C. Developed by Parker *et al.* in 1961 [42] the laser flash method is used to measure the thermal diffusivity (*D*) of materials. In a laser flash experiment for measuring k the front side of a plane-parallel sample is heated by a short laser pulse. The absorbed heat induced propagates through the sample and causes a temperature increase on the rear surface. This temperature rise is monitored as a function of time with an infrared detector. The thermal

diffusivity (D) and the specific heat (C_p) can be ascertained using the measured signal [43]. If the density (ρ) is known, the thermal conductivity (k) can be determined using equation 3.27.

3.2.2.5. Mechanical characterization

3.2.2.5.1. Vickers hardness and fracture toughness

Most hardness tests yield results based on a material's ability to resist indentation while under test. A material's ability to resist scratching is also considered a hardness test, as it is the measurement of the amount of energy absorbed by a material when struck by a falling object. Indentation hardness measures the resistance of a sample to material deformation due to a constant compression load from a sharp object (indenter). The test consists on the measuring of the critical dimensions of an indentation left by a specifically dimensioned and loaded indenter. Frequent indentation hardness scales are Brinell, Rochwell and Vickers.

The Vickers hardness test uses a square-based pyramid diamond indenter with an angle of 136° between the opposite faces at the vertex, which is pressed into the surface of the test sample using a prescribed force (F). The time for the initial application of the force is usually between 2 and 8 s, and the test force is maintained for 10 s to 15 s. After the force has been removed, the diagonal lengths of the indentation are measured and the arithmetic mean (d_l) is calculated. The Vickers hardness number (HV), is given by:

$$HV = \frac{F}{A_{ind}} \qquad \text{(eq. 3.28)}$$

where F is the applied load to the diamond indenter in kgf and A_{ind} is the surface area of the resulting indentation in mm^2 given by:

$$A_{ind} = \frac{{d_l}^2}{2sin(136°/2)} \approx \frac{{d_l}^2}{1.8544} \qquad \text{(eq. 3.29)}$$

where d_l is the average length of the diagonal left by the indenter in mm. Substitution in eq. 3.28, HV can be defined as:

$$HV = \frac{F}{A_{ind}} \approx \frac{1.8544F}{{d_l}^2} \qquad \text{(eq. 3.30)}$$

where F is in kgf and d_l is in mm. In SI units (N.m^{-2}) the HV value is obtained by multiplying F by 9.807 (standard gravity) and converting mm to m.

Fracture toughness (K_{IC}) is traditionally measured using the three-point bending test [44]. However, the samples preparation requires long time, because it is necessary to square off and pre-notched with a "V" or "U". New methods have been developed to measure K_{IC}, namely the crack indentation method. Different models may be used for the calculation depending on the shape of the cracks that are initiated and developed as a result of the indentation. Compared with conventional evaluation methods [44, 45], the indentation technique presents many advantages, among them the fact that is a much simpler experimental technique. The K_{IC} calculation, which is based on the values of load (F) and crack length (l_{ind}) depends on the shape of the crack. When the crack is developed only at the corners of the indent, called a Palmqvist type of crack (type Pq), the eq. 3.31 can be applied [46]:

$$K_{IC} = 0.0089\left(\frac{E}{HV}\right)^{2/5}\frac{F}{a_{ind}\sqrt{l_{ind}}} \qquad \text{(eq. 3.31)}$$

where E is the Young´s modulus, F is the applied load, a_{ind} is the indent half diagonal and l_{ind} the Palmqvist crack length.

Hardness and fracture toughness of AZO targets were characterized in INNOVNANO using WIKI 100B system from Affri equipped with Affri Fully Automatic System software (Fig. 3.17 a)). All the analyzed surfaces were fine polished accordingly to the procedure described in section 3.2.1.4.

In order to obtain representative average values for the evaluated hardness and fracture toughness properties, 10 Vickers indentations (F = 9.806 N) were preformed in different surface points of each sample. The HV value was measured based on standard BS EN 843-4 2005 considering the average value of 10 different measurements made in each sample. The test force was maintained for 15 s in each indentation. HV values are obtained automatically after indentation by the software. The measurements of fracture toughness were performed in the same indentations used for HV calculation. The crack length was measured by optical microscopy. The use of 1 kgf (9.806 N) of load was sufficient to obtain measurable crack lengths. The fracture toughness values were calculated based on Niihara equation [46].

3.2.2.5.2. Biaxial Flexural strength

Biaxial flexural strength (piston-on-three-ball test) was determined using a Universal Materials Testing Machine Zwick/Roell Z020 (Fig. 5.17 b)). For each sintering condition, 10 samples were fine polished in both surfaces with a controlled thickness between 1.20 – 1.25 mm and a known diameter. The presented flexural strength values (in MPa) for each tested condition were obtained from the average of 10 different samples. The test was performed considering the standard ISO 6872:2008 (E) (point 7.3.3).

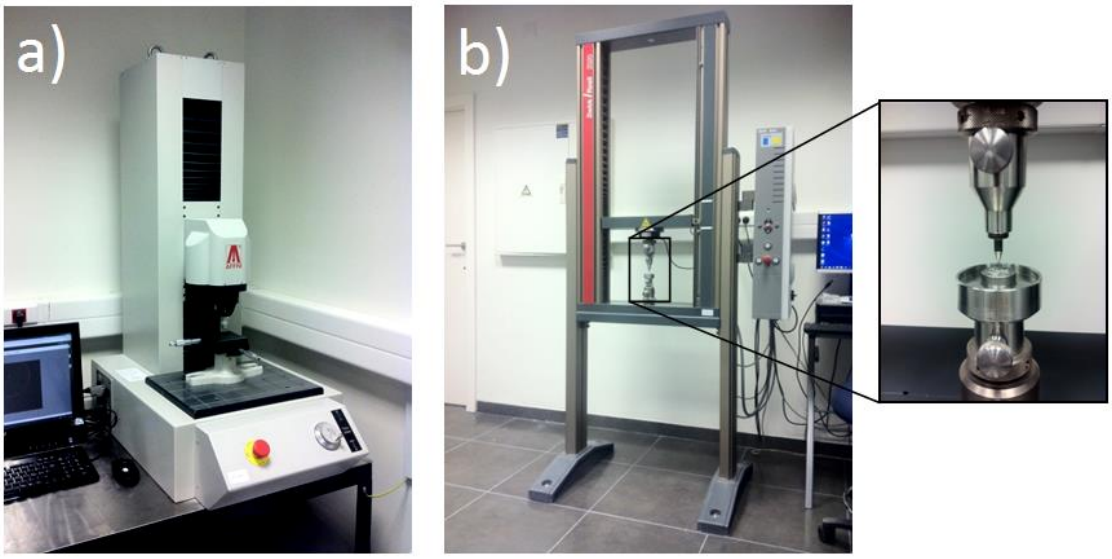

Fig. 3.17. *a) WIKI 100 Micro Vickers Hardness Tester and b) Zwick/Roell Z020 testing machines existing at INNOVNANO.*

3.3. Thin films: deposition and characterization techniques

3.3.1. Thin films deposition

A wide range of deposition techniques can be used to fabricate thin films. Since this research work is based on the production and optimization of ceramic targets to be used in sputtering systems, a description of the sputtering technique used throughout this research work is presented herein.

3.3.1.1. Sputtering

Sputtering is one of the most used physical vapour deposition (PVD) techniques, being very versatile for a wide range of applications. Mostly used by the microelectronics industry in the production of integrated circuits and in the optoelectronics industry for the depositions of TCOs, sputtering is also used in other industries such as the production of reflective glass for intelligent buildings, in the manufacture of ophthalmic lenses or in the fabrication of mirrors [47].

Comparatively to other thin film deposition techniques, sputtering provides several advantages, such as low substrate temperatures, good film thickness and composition control, good adhesive strength, highly dense films, possibility to deposit a broad range of materials (either by using different target compositions, a reactive gas or simultaneous sputtering from two or more target sources (co-sputtering)) and good scalability to large areas [48-50]. Similarly to other PVD techniques (such as thermal evaporation or pulsed laser deposition (PLD)), atoms or molecules are physically removed from a source material, in vacuum, and transported to a substrate, forming a thin film. Sputtering consists on the ejecting of atoms from the surface of a source material (sputtering target) as a result of collisions and momentum transfer from incoming highly energetic ions that are created due to ionization of gaseous species. [51].

The sputtering process is initiated in a vacuum chamber containing two electrodes, cathode and anode, being the source material (sputtering target) placed on the cathode and the substrate on the anode, which is generally grounded (Fig. 3.18). An inert gas is introduced into the chamber, typically argon, due to its low cost and high impact section (high atomic mass (39.9 $g.mol^{-1}$)), and an electric field is applied between the two electrodes [51, 52].

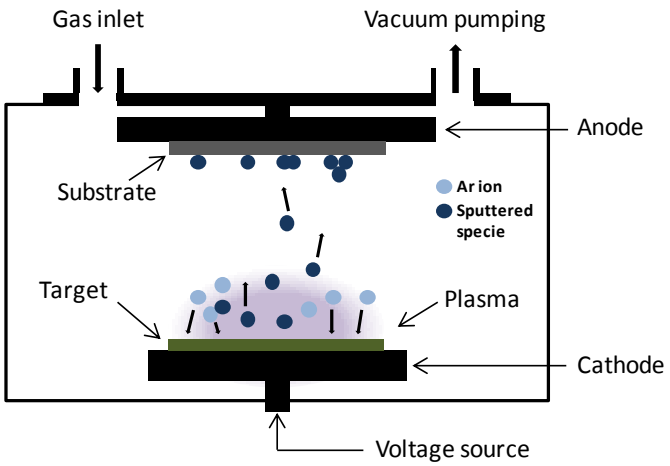

Fig. 3.18. *Schematic representation of a sputtering deposition system (Adapted from [53]).*

Under these conditions, electrons (which are in the proximity of the cathode) are accelerated towards the anode, colliding with the gas atoms, resulting on different reactions depending on the transferred energy in the collision process [52, 54]:

- Excitation of the Ar electrons to metastable levels in the form:

$$e^- + Ar \rightarrow Ar^* + e^- \quad \text{(eq. 3.32)}$$

- The Ar atoms loose an electron (ionization) in the form:

$$e^- + Ar \rightarrow Ar^+ + 2e^- \quad \text{(eq. 3.33)}$$

In the first case, after electronic excitation, when electrons fall to their initial shells, the energy can be released by a photon, creating the so-called glow discharge or plasma (in the case of Ar, for example, is observed a violet colour). The region where the plasma occurs consists of a positive space charge since the mass of the electrons is much smaller than that of the positive ions. Thus, electrons are quickly accelerated away from the cathode, giving rise to a strong electric field in front of the target that provides the ion acceleration required for sputtering deposition.

In the second case, ionization creates additional electrons, which can participate in further excitation and ionization reactions, and positive gas ions, Ar^+, that are accelerated in the cathode direction (target) by the electric field, ejecting different particles, including secondary electrons, atoms and molecular aggregates [51, 53]. Different phenomena occur at the target by the action of the incident ions on its surface (Fig. 3.19). The main interactions for the sputtering deposition technique are [51, 54]:

- The release of secondary electrons from the target that are accelerated towards the substrate/anode colliding with Ar atoms, promoting further ionization and excitation reactions and subsequent sustainment of the plasma. Note that these emitted electrons can also reach the substrate causing undesired re-sputtering from the deposited film;

- The atoms or molecular aggregates release from the sputtering target are deposited into the substrate. The sputter yield (S_y) is one of the main parameters in the characterization of the sputtering process, defined by the ratio between the number of ejected atoms from the target by each incident ion. Typically, the kinetic energy of the incident ions varies between 25 eV and 10 keV. For values below 25 eV the energy yield is very low (< 10^{-4} atoms/ion). In turn, at very high energies (> 10 keV), incident ions penetrate deeper into the target, resulting in a dissipation of energy within it and a consequent decrease in the ejection of surface atoms and S_y [52]. Besides the energy of the ions, sputter yield also depends on the ions incident angle, binding energy of the atoms in the target, the masses of the ions and target atoms, and on the crystalline structure of the target material [52, 55]. In their way to the substrate, dissociation of the sputtered species can also occur.

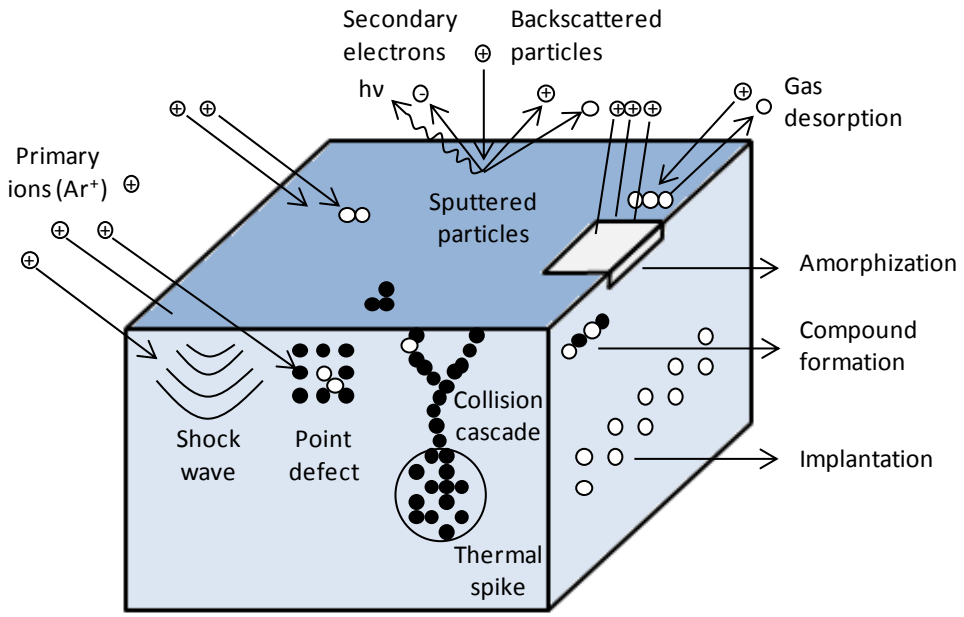

Fig. 3.19. *Main effects resulting from the interaction between the incident ions and the sputtering target surface during sputtering (adapted from [51]).*

Thin films can also be deposited by using a reactive gas inside the system (e.g. O_2 or H_2), in addition or in substitution of the inert gas. This process is known as reactive sputtering and is widely used to produce different materials, such as oxides or nitrides by using oxygen or nitrogen, respectively [52]. For example, indium, tin or zinc oxides based thin films TCOs are frequently produced by sputtering metallic targets in an oxidizing atmosphere [48, 49]. Even if the deposition is performed from ceramic targets that already possess the desired thin film composition, reactive sputtering is useful to control film´s stoichiometry, mainly on the compensation of more volatile elements (e.g. O_2) lost in the transport process between the target and the substrate [56]. However, high concentrations of reactive gases can induce re-sputtering effects on the substrate due to the incidence of negative ions, which is particularly relevant in the case of oxygen, given its high electronegativity [51, 57].

Although the use of metallic targets results in a much higher film growth rate than the use of ceramic targets (e.g. the energy required to sputter a metal atom of Zn is lower than the corresponding compound ZnO) the processing conditions are dependent of the reactive gas (e.g. O_2 for obtaining ZnO),) [58]. If the amount of O_2 is too low the sputtered films will have a metallic appearance, while if it is too high the growth rate will decrease substantially. So, there is a need of a precise control of oxygen to obtain the necessary stoichiometry and optimized films. In the case of ceramic targets, the processing conditions available extend considerably, being the control of the sputtering process easier [58].

Depending on how the electronic excitation in sputtering systems is created, two different categories can be used: direct current (DC), where a DC voltage between the cathode and anode is applied, and radio-frequency (RF) where a high frequency (typically 13.56 MHz) voltage is supplied to the target creating the potential difference between the electrodes [51]. Two distinct ionization mechanisms can be identified for DC and RF discharges, originating significantly

different potential distributions for these two excitation modes. The discharge voltage, i.e. the negative DC voltage, which is measured at the target, is much lower for RF compared to DC excitation. This difference (up to a factor of seven for lower power) is due to the different processes at the target and also plasma [49].

The DC discharge is based upon the generation of ion-induced secondary electrons at the cathode (target). Therefore, large target voltages are necessary to sustain the plasma because the electron emission increases almost linearly with the ion velocity [49]. For that reason, DC sputtering systems are restricted to the usage of conductive targets, because insulating materials are not capable to ensure a high concentration of negative charges on the target surface (cathode) to ensure the ejection of sufficient secondary electrons to keep the plasma active [48, 52]. Alternatively, on RF sputtering systems, both conductive and insulating sputtering targets can be used. In this case, the RF plasma is mainly driven by ionization due to electrons, which perform an oscillating motion of the plasma body. Due to the high frequency voltage applied, even if the target does not supply enough secondary electrons during the negative portion of the RF signal (when the positive ions are attracted to it), electrons from the plasma are attracted towards the target during the positive portion of the RF signal. Since the target area is much smaller than the grounded anode (constituted both by the substrate area as well as the chamber walls) and given the lower mass of electrons relatively to ions, a self-biased DC voltage emerges in the target, creating the conditions for sputtering to occur [52]. This kind of excitation observed in RF systems is much more effective compared to the ionization by non-oscillating secondary electrons and leads to lower target voltages in an RF discharge.

The choice between DC or RF systems depends largely on the properties of the target. Nonetheless, it may be assumed that the RF systems are more versatile because they allow the deposition of conductive or insulating materials.

Despite obtaining films with good properties for a wide range of applications using both DC and RF systems, there are two main problems: the low deposition rates and the overheating and also degradation of the substrate surface due to the secondary electron bombardment of the target [48]. A way to overcome these drawbacks is to use magnetron sputtering (Fig. 3.20). In magnetron sputtering the plasma is confined to a region close the target surface by a magnetic field, which is created due to strong magnets placed behind the target. This way, secondary electron movement is confined to the region right above the target surface, reducing the substrate heating. This simultaneously reduces the substrate bombardment by electrons and increases the probability of ionization of neutral gaseous molecules, which results in higher sputtering and growth rates [52]. Since in magnetron sputtering systems the availability of ions for a given pressure is higher than in diode systems, lower deposition pressures can also be used. The disadvantage of magnetron sputtering systems is the poor target utilization, since material from the path defined by the magnetic field is preferentially sputtered.

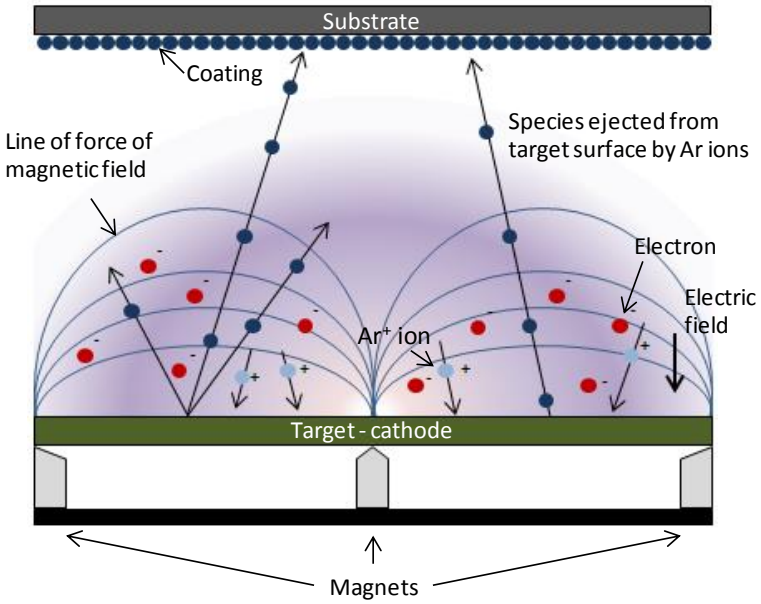

Fig. 3.20. *Schematic representation of the magnetron sputtering deposition process (Adapted from [51]).*

In this work, two RF magnetron sputtering systems were used to produce undoped and Al-doped ZnO thin films. The systems are similar (AJA, Model ATC ORION 8 (Fig. 3.21 (a)) with the difference being the sputtering targets dimensions that can be deposited on each system. Most of the work was performed in the AJA system existent in CEMOP that is prepared for two inches sputtering targets. The second system used is located at CREST – Loughborough University, and was used to evaluate the performance of several targets manufactured with three inches diameter. The systems are equipped with a load-lock chamber for sample introduction/removal, so very low pressures are achieved in the main chamber (≤ 0.05 mPa). Both systems have more than one magnetron (Fig. 3.21 (b)) allowing for co-sputtering and subsequent production of multicomponent materials, although this was not explored in this research work being all the thin films compositions obtained directly from pre-defined ceramic target compositions. The systems can be almost totally computer-controlled and provide the possibility of heating the substrate up to 850 °C. Sputtering of two inches targets was carried out without intentional heating, while three inches targets were sputtered in a range of temperatures between room temperature and 450 ◦C. In both cases was used a base pressure of 3.4×10^{-4} Pa. Target to substrate (soda-lime glass) distance was fixed at 15 cm and, during the deposition the substrate was kept rotating to allow for enhanced uniformity on the resulting thin films.

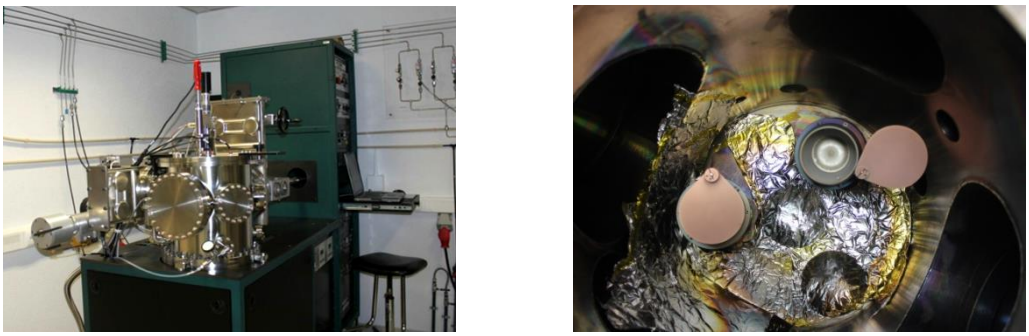

Fig. 3.21. *a) AJA ATC Orion 8 RF magnetron sputtering system used for the deposition of TCOs and b) detail of the main chamber, showing the magnetrons' configuration.*

The thin films were produced either on silicon wafers or on soda lime glass substrates, depending on the characterization technique they are aimed for. Prior to deposition, pre-sputtering (sputtering with the shutter closed to prevent deposition) of 15 or more minutes was performed to assure thin films reproducibility. Some RF sputtering deposition parameters were varied to study their influence on the final properties of the deposited TCOs layers: working pressure (P_{dep}) between 0.13 and 0.53 Pa, and RF power density (P_{RF}) between 100 and 250 W. The percentage of oxygen content in the Ar+O_2 mixture (% O_2) was varied between 0 and 10 % during the optimization of the deposition parameters being consistently obtained worse results with O_2 addition, leading us to perform the optimization of the deposition parameters with no O_2 input. The effect of sputtering targets characteristics was widely explored by using different ceramic targets prepared during the experimental work. The influence of target density, aluminum content and sintering conditions on sputtered thin films was investigated and compared with literature results. Table 3.2 summarizes the different ceramic lab targets produced and sputtered in this PhD work. Several commercial targets were also sputtered for comparison (composition 98:2 wt. % ZnO:Al_2O_3).

Table 3.2. *Undoped and Al-doped ZnO (aluminum concentration varying between 0.5 and 2.0 Al_2O_3 wt. %) ceramic targets manufactured and used for thin films deposition during the experimental work.*

Non sintered	Conventional sintering (air)		Conventional sintering (Ar atm.)	Hot-pressing (HP)	Spark plasma sintering (SPS)
98:2	98:2	LD target HD (several targets)	98:2	98:2	98:2
98.5:1.5	98.5:1.5	--	--	--	--
99:1	99:1	--	--	--	--
99.5:0.5	99.5:0.5	--	--	99.5:0.5 (2 and 3" targets)	--
--	Undoped ZnO	LD target HD target	--	--	--

3.3.2. Characterization techniques

The oxide thin films were characterized using a broad range of techniques to study their structural, morphological, compositional, optical and electrical properties. Relevant details about the techniques used to characterize the sputtered thin films are given below.

3.3.2.1. Structural and morphological characterization

3.3.2.1.1. X-ray diffraction (XRD)

X-ray diffraction technique (described in section 3.1.3.3.1) was used to analyze the crystalline phases of thin-films deposited on soda-lime glass substrate and determining the structural properties of these phases such as the degree of crystallinity, preferred orientation and average

crystallite size (D_c). The analyses were performed at room temperature using a Panalytical X'Pert PRO diffractometer existent in CENIMAT (Fig. 3.22), in Bragg-Brentano (θ/2θ coupled) geometry with Cu Kα line radiation (λ = 1.5406 Å) and varying 2θ between 10º and 80º.

Fig. 3.22. *Panalytical X'Pert PRO diffractometer existent at CENIMAT/I3N.*

3.3.2.1.2. *Scanning electron microscopy (SEM)*

Besides the SEM analysis of the synthesized powders and sintered ceramic targets (described in sections 3.1.3.3.4 and 3.2.2.1.2, respectively), also the undoped and Al-doped ZnO thin films surface morphology and cross sections were examined using the already mentioned Zeiss Auriga System, existent in CENIMAT/I3N.

3.3.2.1.3. *Profilometry*

Thin films thicknesses were determined in a profilometer Ambios XP-Plus 200 Stylus (soda-lime glass substrate) (Fig. 3.23 (left)) existent in CENIMAT/I3N. Here it is necessary to create a zone without film and generate a well-defined step to allow accurate film thickness measurement (Fig. 3.23 (right)). Based on the thickness and deposition time, the deposition rate (DR) was determined using the following equation:

$$DR = \frac{d_{film}}{t_d} \qquad \text{(eq. 3.34)}$$

where d_{film} is the film thickness and t_d the deposition time.

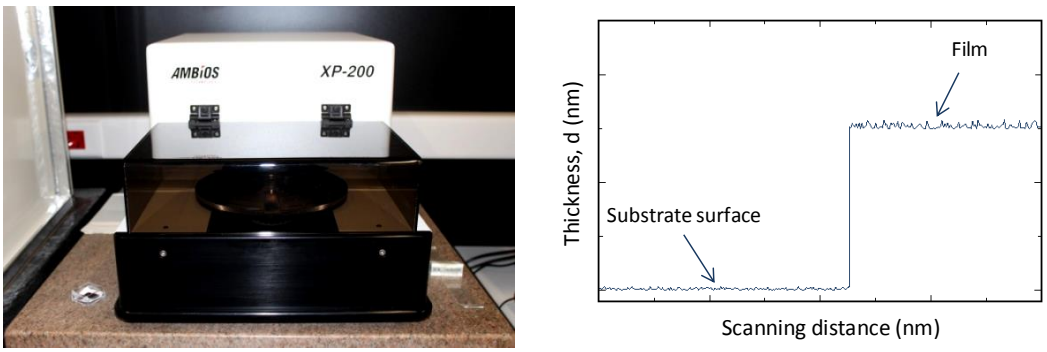

Fig. 3.23. *Ambios XP-Plus 200 Stylus profilometer existent at CENIMAT/I3N (left) and typical step corresponding to a thin film deposited on a substrate (right).*

3.3.2.1.4. Atomic force microscopy (AFM)

Created in 1986 by Binning, Quate and Gerber [59], atomic force microscopy (AFM) is a relatively recent technique that combines the principles of the scanning tunneling microscopy (STM) and the stylus profilometry. AFM provides very high resolution three dimensional surface profiles, where atomic scale features can be detected. Contrarily to SEM or TEM techniques, the samples measurement can be performed in air ambient and does not require any special preparation. Given the low sample requirements and large imaging possibilities, AFM is presently used in several research fields, such as materials science, chemistry, biology and physics. Contact mode AFM is one of the most widely used scanning probe modes, and operate by scanning a sharp tip, which is attached to a cantilever, across the sample at extremely low force (around 10^{-9} N, similar to interatomic force range) (Fig. 3.24 (left)). Either the repulsive force between the tip and sample or the actual tip deflection is recorded relatively to spatial variation and then converted into an analogue image of the sample´s surface. The small cantilever deflection can be measured by using a laser beam reflected from the top surface of the cantilever into a photodiode. Other imaging modes are available, such as the tapping mode, which is particularly useful to analyze soft samples (even liquids) that can be damaged when using contact mode [60].

AFM analysis of surface morphology and calculation of root-mean-square roughness (R_{rms}) was performed on AZO thin films deposited on silicon substrates, using an MFP-3D AFM system from *Asylum Research* existent in CENIMAT/I3N (Fig. 3.24 (right)). The images are acquired in tapping mode (also called intermittent contact and AC mode) with a Si_3N_4 tip and a scan rate of 1 Hz.

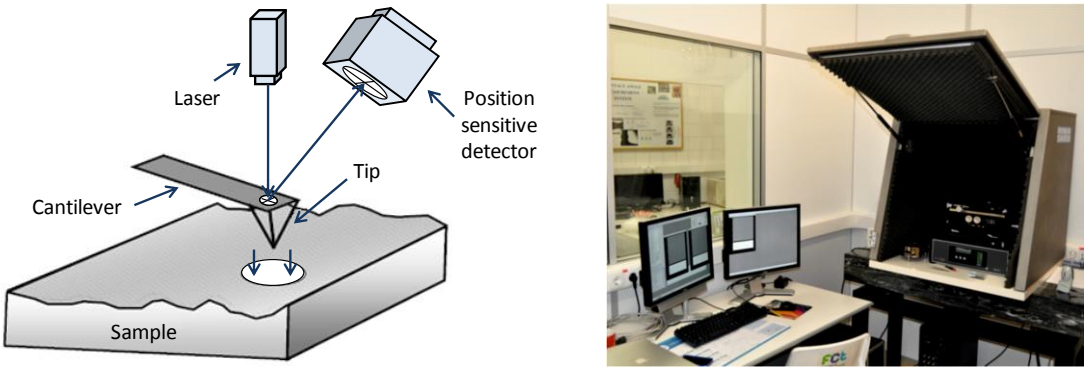

Fig. 3.24. *Schematic diagram of AFM principle (left) and Asylum MFP-3D atomic force microscope system available at CENIMAT/I3N (right).*

3.3.2.2. Compositional characterization

Similarly to the powders and sintered ceramic targets, compositional characterization was also determined in thin films. Thin films surface and bulk composition was examined and correlated with the corresponding ceramic sputtering target by Energy-dispersive X-ray spectroscopy (EDS), X-ray photoelectron spectroscopy (XPS), and Auger electron spectroscopy (AES) which are already described in sections 3.1.3.5.1, 3.1.3.5.3 and 3.2.2.2.1, respectively.

3.3.2.3. Optical characterization

The interaction of photons with a material can generate a multitude of effects. The incident photons can be, emitted, reflected, absorbed or transmitted and each one of these phenomena can be explored by different techniques [20]. The energy (E_{ph}) of the incident photons and the material itself will determine which of the photon-material interactions occur (eq. 3.35):

$$E_{ph} = hv = \frac{hc}{\lambda} \qquad \text{(eq. 3.35)}$$

where h is the Planck´s constant, v is the photon frequency, c is the speed of light and λ is the photon wavelength. Photons with a higher energy than E_g(~ 3 eV) are absorbed, while photons with lower energy than plasma energy (E_p) can be absorbed or reflected. Between these two energy limits (bandgap and plasma) photons are mostly transmitted and/or reflected. In this work the optical characterization of deposited thin film TCOs was done using the UV-Vis-Near-infrared (NIR) transmittance spectroscopy characterization technique.

3.3.2.3.1. UV-Vis NIR transmittance spectroscopy

The absorption coefficient (α), the refractive index (n_{RI}), the optical band gap energy (E_{opt}) and transition type, the thin film´s thickness (d_{film}) and the degree of transparency for a given wavelength [20, 61] can be determined from transmittance (T_r) spectra obtained in a spectrophotometer. α can be determined by:

$$\alpha = \frac{1}{d_{film}} ln\left(\frac{1}{1-A_b}\right) \qquad \text{(eq. 3.36)}$$

where A_b is the optical absorption of the thin film ($A_b = 1 - T_r - R_f$). Neglecting R_f leads to $A_b \approx 1 - T_r$ and, although slightly inaccurate α values are obtained, the evolution of α with E_{ph} is not severely affected, thus no significant errors in optical bandgap (E_{opt}) determination are introduced. E_{opt} corresponds to the fundamental absorption process, i.e., to the excitation of a valence electron to a higher energy state. Assuming parabolic valence and conduction bands, the optical band gap can be calculated in a standard manner by plotting $(\alpha hv)^x$ versus (hv) (Tauc´s plot). The E_{opt} value is obtained by the intersection of the straight line of the linear zone (linear fit) with the abscissa. The value of x depends on the transition type, assuming values of 2, 2/3, 1/2 or 1/3 depending if the transition is allowed direct, forbidden direct, allowed indirect or forbidden indirect, respectively [62]. TCOs have majorly direct transition ($x = 2$) (value considered in the course of this investigation).

The transmittance spectra of the ZnO and Al-doped ZnO TCO thin films deposited on glass substrates were acquired in double beam Shimadzu UV-3101 PC spectrophotometer system existent at CEMOP (Fig. 3.25), by varying λ between 250 and 2500 nm. This technique was mainly used to assess the transparency of the sputtered ZnO and AZO thin films by averaging transmittance data between 400 and 700 nm (average visible transmittance, AVT). The absorption coefficient and the optical band gap energy were also measured according to the methodology described above.

Fig. 3.25. *UV-Vis-NIR Shimadzu UV-3101PC spectrophotometer system existent in CEMOP/I3N.*

3.3.2.4. Electrical characterization

In the same way as that presented for the sintered targets (section 3.2.2.3), electrical characterization of ZnO and AZO TCOs thin films deposited on soda-lime glass substrate was performed using the Hall effect. In each sample four silver contacts were created in van der Pauw configuration and each sample was subjected to five cycles of measurement with a constant field of 0.5 T at RT. The thicknesses considered during the tests were obtained by profilometry technique described in section 3.3.2.1.3.

3.4. References

[1] Calado, J.M. and Antunes, E.M., Nanocrystaline spherical ceramic oxides, process for their synthesis and use thereof, patent WO 2009040770 (2009).

[2] Medvedev, A.E., Fomin, V.M. and Reshtnyak, A.Yu., Mechanisms of detonation of emulsion explosives with microballoons. *Shock Waves*, 2008, 18(2) 107-15.

[3] Cooper, P.W., Explosives Engineering, New York: Wiley-VCH, 1996. ISBN 0-471-18636-8.

[4] Campos J, Durães L, Mendes R, Andrade-Campos A, Matias T, Portugal A, *et al.* Mechanisms of ceramic particle formation from detonation of metal/nitrates compositions. In: Fraunhofer-Institut für Chemische Technologie, editor. *Proc. of the 40th international annual conference of ICT*. Karlsruhe: DWS Werbeagentur und Verlag GMbH; 2009 [CD-ROM] (18pp.).

[5] Durães L. Simulation and analysis of gaseous systems formed by the decomposition of energetic materials. *MSc Thesis*. Coimbra: University of Coimbra; 1999.

[6] Calado, J.M. and Antunes, E.M., Nanometric-sized ceramic materials, process for their synthesis and uses thereof, patent WO 2009144665 (2009).

[7] CPS disc centrifuge operating manual, CPS Instruments, Inc., 2005.

[8] Malvern mastersizer 2000 user manual, man 0101, Issue 1.3, Malvern Instruments Ltd., 1997.

[9] Sample dispersion and refractive index guide (reference manual), man 0396, Issue 1.0, Malvern Instruments Ltd., 2007.

[10] Cullity, B. D. and Stock, S. R., Ellements of X-Ray Diffraction. Third edition, ISBN: 0201610914 Published 1956 by Addison-Wesley.

[11] Pereira, L., Produção e caracterização de silício policristalino e sua aplicação a TFTs, in *Materials Ing.* vol. PhD thesis: Faculdade de Ciências e Tecnologia, Universidade Nova de Lisboa, 2008.

[12] Atkins, P. W., Physical chemistry. Sixth edition, Published 1998 by Oxford University Press.

[13] Patterson, A. L., The Scherrer formula for X-ray particle size determination. *Phys. Rev.*, 1939, **56**(10) 978-82.

[14] Li, B. S., Liu, Y. C., Chu, Z. S., Shen, D. Z., Lu, Y. M., Zhang, J. Y. and Fan, X. W., High quality ZnO thin films grown by plasma enhanced chemical vapour deposition. *J. Appl. Phys.*, 2002, **91**(1) 501-5.

[15] Rodriguez-Carvajar, J., Recent advances in magnetic structure determination by neutron power diffraction. *Physica B: Condensed Matter.*, 1993, **192**(1-2) 55-69.

[16] Keng, E. Y. H., Air and helium pycnometer. *Powder Technol.*, 1969, **3**(3) 179-80.

[17] Brunauer, S., Emmett, P. H. and Teller, E., Adsorption of gases in multimolecular layers. *J. Am. Chem. Soc.*, 1938, **60**(2), 309-19.

[18] Webb, P. A., Analytical methods in fine particle technology. First edition, ISBN: 978-0965678308 Published 1997 by Micromeritics Instrument Corporation.

[19] Knoll, M. and Lubszynski, G., Microscopic electron illustration through secondary electrons. *Physikalische Zeitschrift*, 1933, **34**() 671-4.

[20] Schroder, D. K., Semiconductor Material and Device Characterization. Third edition, ISBN: 978-0471739067 Published 2006 by Wiley & Sons.

[21] http://en.wikipedia.org/wiki/Transmission_electron_microscopy consulted on 30/01/2014.

[22] Sohn, W., Choi, J., Kim, K., Oh, J., Kim, S. and Jang, J., Crystalline orientation of polycrystalline silicon with disklike grains produced by silicide-mediated crystallization of amorphous silicon. *J. Appl. Phys.*, 2003, **94** 4326-31.

[23] Quli, F. and Singh, J., Transmission electron microscopy studies of metal-induced crystallization of amorphous silicon. *Mater. Sci. Eng. B*, 1999, **67**(3) 139-44.

[24] Williams, D. B. and Carter, C. B., Transmission electron microscopy – Part 1: Basics. Second edition, ISBN: 978-0387765020 Published 2009 by Springer.

[25] Watson, E. S. and O´Neill, M. J., Differential microcalorimeter, patent US 3263484 A (1962).

[26] Brundle, C. R., Evans Jr, C. A. and Wilson, A., Encyclopedia of Materials Characterization – Surfaces, Interfaces and thin films. First edition, ISBN: 0750691689 Published 1992 by Butterworth-Heinemann.

[27] Nix, R., An Introduction to Surface Chemistry – Part 5: Surface Analytical Techniques. http://www.chem.qmw.ac.uk/surfaces/scc/ (2005) consulted on 30/01/2014.

[28] Hufner, S., Photoelectron spectroscopy, principles and application. Third edition, ISBN: 978-3662092804 Published 2003 by Springer-Verlag.

[29] Garbout, A., Bouattour, S., Botelho do Rego, A.M., Ferraria A. and Kolsi, W., Synthesis, Raman and X-ray diffraction investigations of rubidium-doped $Gd_{1.8}Ti_2O_{6.7}$ pyrochlore oxide via a sol gel process. *J. Cryst. Growth*, 2007, **304**(2) 374-82.

[30] German, R.M., A-Z of Powder Metallurgy. First edition, 978-1856174299 Published 2005 by Elsevier.

[31] http://www.substech.com/dokuwiki/doku.php?id=solid_state_fabrication_of_metal_matrix_composites consulted on 26/01/2014.

[32] Tokita, M., Mechanism of Spark Plasma Sintering and its application to ceramics. Nyn Seramikkasu, 1997, **10** 43-53.

[33] Dobedoe, R. S., West, G. D. and Lewis, M. H., Spark plasma sintering of ceramics. *Bull. Eur. Ceram. Soc.*, 2003, **1** 19-24.
[34] http://www.substech.com/dokuwiki/doku.php?id=spark_plasma_sintering consulted on 25/01/2014.
[35] Standard ISO 18754:2013, Fine ceramics (advanced ceramics, advanced technical ceramics) determination of density and apparent density.
[36] Engqvist, H. and Uhrenius, B., Determination of the average grain size of cemented carbides. *International Journal of Refractory Metals & Hard Materials*, 2003, **21**(1-2) 31-5.
[37] Fullman, R. L., Measurement of Particle Sizes in Opaque Bodies. *Trans. AIME*, 1953, **197** 447.
[38] Underwood, E. E., Microstructural analysis – Quantitative Stereology for Microstructural Analysis. First edition, ISBN: 978-1461586951 Published 1973 by Elsevier.
[39] Childs, K. D., Carlson, B. A., L Vanier, L. A., Moulder, J. F., Paul, D. F., Stickle, W. F. and Watson, D. G., Handbook of Auger Electron Spectroscopy. Third edition, Published 1995 by Physical Electronics Inc.
[40] HL5500 PC Hall effect measurement system - User Manual, Issue 5.0: Accent 2003.
[41] Yang, E. S., Microelectronic Devices. First edition, ISBN: 978-0071003742 Published 1988 by McGraw-Hill.
[42] Parker, W. J., Jenkins, R. J., Butler, C. P. and Abbott, G. L., Flash method of determining thermal diffusivity, heat capacity and thermal conductivity. *J. Appl. Phys.*, 1961, **32**(9) 1679.
[43] Laser Flash Apparatus LFA 457 *MicroFlash* user manual, Netzsch-Gerätebau GmbH, 2011.
[44] Chermant, J. L. and Osterstock, F., Fracture toughness and fracture of WC-Co composites. *J. Mater. Sci.*, 1976, **11**(10) 1939-51.
[45] Chicot, D., Pertuz, A., Roudet, F., Staia, M. H. and Lesage, J., New developments for fracture toughness determination by Vickers indentation. *Mater. Sci. Technol.*, 2004, **20**(7) 877-84.
[46] Niihara, K., Morena, R. and Hasselman, D. P. H., A fracture mechanics analysis of indentation induced – Palmqvist crack in ceramics. *J. Mater. Sci. Lett.*, 1983, **2**(5) 221-3.
[47] http://en.wikipedia.org/wiki/Sputter_deposition consulted on 31/01/2014.
[48] Hartnagel, H., Dawar, A., Jain, A. and Jagadish, C., Semiconducting transparent thin films. Bristol: IOP Publishing, 1995.
[49] Ellmer, K., Magnetron sputtering of transparent conductive zinc oxide: relation between the sputtering parameters and the electronic properties. *J. Phys. D: Appl. Phys.*, **33**(4) R17-R32 (2000).
[50] Jaeger, R. C., Introduction to Microelectronic Fabrication. Second edition, ISBN: 978-0201444940 Published 2001 by Addison-Wesley.
[51] Barquinha, P., Transparent oxide thin-film transistors: production, characterization and integration. PhD thesis, Faculdade de Ciência e Tecnologia, Universidade Nova de Lisboa, 2010.
[52] Wasa, K., Kitabatake, M., Adachi, H., Thin film materials technology: sputtering of compound materials. First edition, ISBN: 978-0815514831 Published 2005 by William Andrew.
[53] Gonçalves, G. P., Filmes finos de óxido de índio e zinco e sua aplicação em díodos orgânicos emissores de luz. PhD thesis: Faculdade de Ciências e Tecnologia, Universidade Nova de Lisboa, 2011.
[54] Vossen J. L. and Kern, W., Thin Film Processes. Second edition, ISBN: 978-0127282503 Published 1979 by New York: Academic Press, Inc.
[55] Andersen, H., Bay, H., Behrisch, R., Robinson, M., Roosendaal, H. and Sigmund, P., Sputtering by Particle Bombardment I: Physical Sputtering of Single-Element Solids. First edition, ISBN: 978-3540105213 Published 1981 by Springer.
[56] Ellmer, K. and Wendt, R., D.c. and r.f. (reactive) magnetron sputtering of ZnO:Al films from metallic and ceramic targets: a comparative study. *Surf. Coat. Technol.*, 1997, **93**(1) 21-6.
[57] Song, Q. M., Wu, B. J., Xie, B., Huang, F., Li, M., Wang, H. Q., Jiang, Y. S. and Song, Y. Z., Resputtering of zinc oxide films prepared by radical assisted sputtering. *J. Appl. Phys*, 2009, **105**(4) 044509.
[58] Ginley, D. S., Handbook of transparent conductors, First Edition, ISBN: 978-1441916372, Published 2010 by Springer.
[59] Binnig, G., Quate, C. F. and Gerber, C., Atomic force microscope. *Phys. Rev. Let.,* 1986, **56**(9) 930-3.
[60] Meyer, E., Atomic force microscopy. *Prog. Surf. Sci.*, 1992, **41**(1), 3-49.
[61] Chiang, H. Q., Development of oxide semiconductors: materials, devices, and integration. In *Electrical And Computer Engineering*. Vol. PhD thesis Oregon: Oregon State University, 2007.
[62] Buchholz, D.B., Liu, J., Marks, T.J., Zhang, M., Chang, R.P.H., Control and characterization of the structural, electrical, and optical properties of amorphous zinc-indium-tin oxide thin films. *ACS Appl. Mater. Interfaces*, 2009, **1**(10) 2147-53.

Chapter 4. Powder: Synthesis and characterization

In this chapter is shown and discussed the synthesis and characterization of undoped and Al-doped ZnO powders used to produce the ceramic sputtering targets. The chapter is divided into two sections. The first one (4.1) shows the effect of particle size on the pressing and sintering processes for undoped ZnO powder compacts made with three commercial ZnO powders with different particle sizes. This study allows the comparison between the performances of nanoparticles synthesized by EDSM and the commercial ones. The second section (4.2) shows the impact of different precursors on the properties of powders synthesized by EDSM. The properties of undoped and Al doped ZnO powders with different concentrations produced at INNOVNANO are also evaluated as well as the feasibility of EDSM to produce doped metal oxide nanopowders in alternative to conventional powder mixtures.

The main results presented throughout this chapter led to the publication of two papers in peer reviewed journals:

- Neves, N., Barros, R., Antunes, E., Ferreira, I., Calado, J., Fortunato, E. and Martins, R., Sintering behavior of Nano- and Micro- sized ZnO powder targets for rf magnetron sputtering applications. *J. Am. Ceram. Soc*., 2012, **95**(1) 204-10.
- Neves, N., Lagoa, A., Calado, J., Rego, A. M. B., Fortunato, E., Martins, R. and Ferreira, I., Al-doped ZnO nanostructured powders by emulsion detonation synthesis – Improving materials for high quality sputtering targets manufacturing. *J. Eur. Ceram. Soc.*, 2014, **34**(10) 2325-38.

4.1. Particle size effect on sintering behavior of undoped ZnO

The understanding of densification kinetics during the earlier stage of sintering and its variation with the initial particle size becomes essential for the production of ceramic pieces with the desired structural and morphological properties. For that propose, the nonisothermal sintering behavior of three different types of as-received commercial Aldrich ZnO powders (purity > 99.9 %) (micrometric – Ref. 96479 (m_ZnO), submicrometric – Ref. 205532 (sm_ZnO) and nanometric powder – Ref. 544096 (n_ZnO)) was studied by dilatometry technique.

The sintering kinetics for the early stages can be predicted using various sintering kinetic models [1-4]. The activation energy for densification during the early stage of sintering can be described by the classical model developed by Johnson [2] at constant heating rate (CHR) sintering. Several models were proposed to understand the sintering behavior during the initial stage. A general equation for shrinkage rate ($dY\ /\ dt$) is [2]:

$$\frac{dY}{dt} = A_0 \frac{1}{G^{m_1} Y^{n_1}} \frac{exp\left(-\frac{Q_i}{RT}\right)}{T} \qquad \text{(eq. 4.1)}$$

where $Y = \Delta l / l_0$ is the linear shrinkage, A_0 is a constant, only dependent of material and of sintering mechanism, G is the particle size, Q_i is the activation energy for sintering in the initial stage, R is the gas constant, T is the absolute temperature, t is the time and the exponents m_1

and n_1 can take vales of $m_1 = 1$ and $n_1 = 0$ for viscous flow, $m_1 = 3$ and $n_1 = 1$ for volume diffusion, and $m_1 = 4$ and $n_1 = 2$ for grain boundary diffusion mechanism. Applying logarithms in both terms, we can determine the activation energy value in the initial stage from the Arrhenius plot of $\ln(T \cdot dY\ /\ dt)$ versus $1/T$. Assuming that grain growth does not occur in the initial stage of sintering, the general equation for sintering proposed by Woolfrey and Bannister [3] is given by:

$$T^2 \frac{dY}{dt} = \left[\frac{a_{hr} Q_i}{(n_1+1)R}\right] \cdot (Y) \qquad \text{(eq. 4.2)}$$

where T, Y, Q_i, R and n_1 have the same meaning referred in eq. 4.1 and a_{hr} is the heating rate. Based on this equation, under conditions of CHR, a plot of $T^2\ dY/dt$ versus Y provides a straight variation with a slope of $a_{hr} \cdot Q_i/(n_1+1)R$, where Q_i and n can be determined from $Q_i/(n_1+1)$.

The influence of green density (GD) under nonisothermal conditions was investigated in the three types of powders. In order to verify the influence of particle size, sintering temperature and holding time on densification and grain growth, the samples were submitted to a CHR of 5 °C.min^{-1} at temperatures between 400 and 1200°C and HT between 1 and 8 h. The scale-up effect on densification was also evaluated.

4.1.1. Commercial ZnO powder characterization

The PSD obtained for the powders as well as its SSA and crystallite size are displayed in Table 4.1.

Table 4.1. *Physical characteristics of commercial ZnO powders.*

Powder	PSD (µm)			Specific surface area ($m^2 \cdot g^{-1}$)	Crystallite size (TEM) (nm)
	D10	D50	D90		
m_ZnO	0.611	1.129	1.698	6.869	198
sm_ZnO	0.123	0.283	0.836	7.354	137
n_ZnO	0.031	0.086	0.236	13.280	80

The data show SSA for n_ZnO superior to the one obtained for sm_ZnO and n_ZnO. The crystallite size obtained by XRD for n_ZnO is similar to the D50 for the same powder, which allows concluding that n_ZnO is composed of deagglomerated single crystals. X-ray diffraction measurements show Zincite (ZnO) as the single phase present in all three powders (Fig. 4.1). For n_ZnO (Ref. 544906), the average particle size (G) was calculated based on eq. 4.3, assuming that the particles have a spherical shape:

$$G = \frac{6}{SSA_{BET} \cdot \rho_{theo}} \qquad \text{(eq. 4.3)}$$

where SSA_{BET} is the SSA and ρ_{theo} is the theoretical density (TD) of the powder (5.61 g.cm^{-3}).

The obtained value (81 nm) agrees with the D50 value and the crystallite size obtained by XRD. On the other side, comparing the D50 of m_ZnO (1.129 µm) with the corresponding crystallite size

(198 nm) is shown that the particles of m_ZnO powder are formed by several aggregated crystallites. The same is observed for sm_ZnO powders but with a smaller difference between crystallite size and mean particle size (137 and 283 nm for crystallite size and D50, respectively) leading to the conclusion that the degree of aggregation is substantially inferior to that of m_ZnO powder.

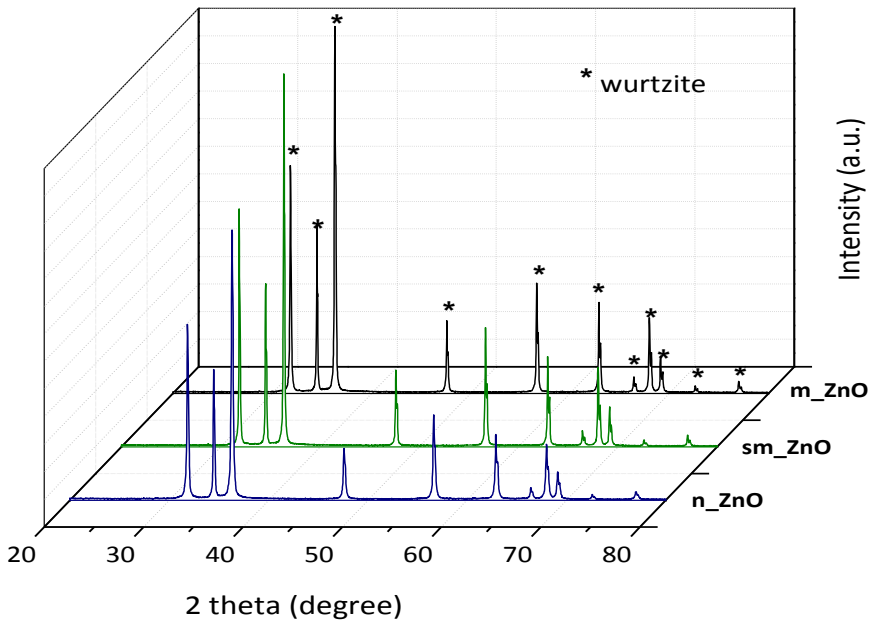

Fig. 4.1. *X-ray diffraction of m_ZnO, sm_ZnO and n_ZnO commercial powders.*

4.1.1.1. Constant heating rate sintering analysis – densification behavior

4.1.1.1.1. Effect of green density

To verify the influence of GD on linear shrinkage and shrinkage rate of the ZnO powders, samples prepared with different GD (35, 44 and 62% of TD) were sintered at a CHR of 5 °C·min^{-1}. As expected, the linear shrinkage decreases for samples prepared with higher GD, independently of initial particle size of the powder (Fig. 4.2 a), c) and e)).

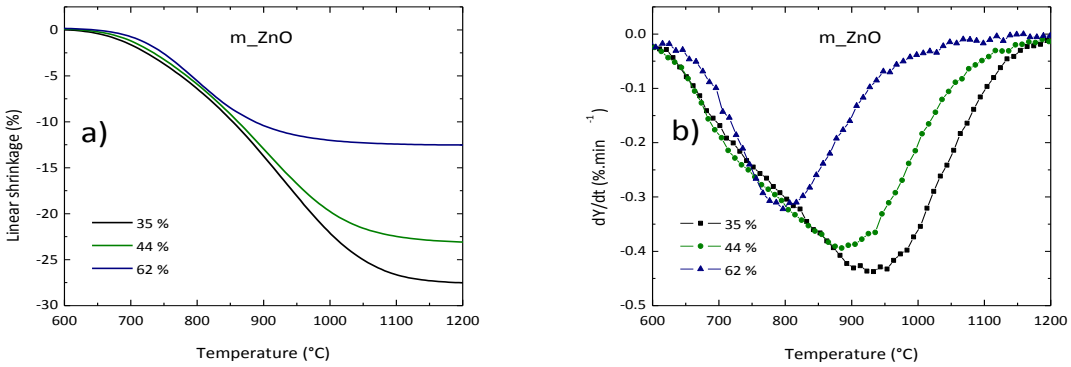

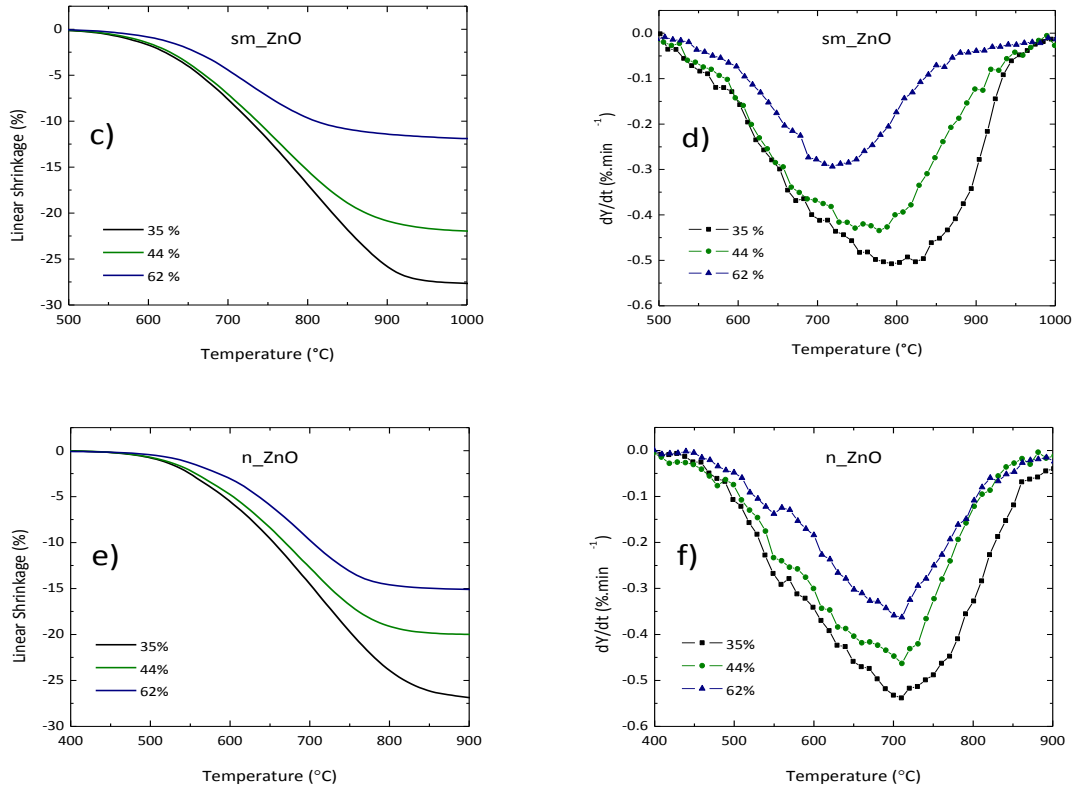

Fig. 4.2. *Linear Shrinkage (a), c) and e)) and shrinkage rate (b), d) and f)) with temperature of the powders as a function of GD for a CHR of 5 °C.min^{-1}.*

As shown in Fig. 4.2 f), the temperature of maximum shrinkage rate (MSR) of n_ZnO powder, is approximately 710°C for all samples. However, for m_ZnO and sm_ZnO powders (Fig. 4.2 b) and d)) the temperature of MSR (T_{MSR}) decreases as the green density increases, especially for the powder with larger particle size (m_ZnO). Generically, the MSR values tend to decrease for higher green densities and increase for small particle size powders (Table 4.2).

Table 4.2. *Influence of GD on MSR and corresponding T_{MSR} for each studied powder.*

Samples GD	m_ZnO		sm_ZnO		n_ZnO	
	MSR (%.min^{-1})	T_{MSR} (°C)	MSR (%.min^{-1})	T_{MSR} (°C)	MSR (%.min^{-1})	T_{MSR} (°C)
35%	-0.441	934	-0.505	803	-0.537	712
44%	-0.394	885	-0.443	770	-0.465	709
62%	-0.322	803	-0.294	719	-0.363	711

Several factors can contribute to these results. First, n_ZnO powders have higher surface energy related to smaller particle size and higher SSA than the ones in micro size range [5, 6]. Furthermore, there is an increased fraction of mass transport by grain-boundary diffusion, as a consequence of the large boundary area associated to nanoparticles [7, 8]. This is of high importance to the study of early sintering stages. As suggested by Lange [9], for temperatures below the value in which is

obtained the greater linear shrinkage rate, the sintering kinetic is dominated by densification mechanisms, and above this temperature, nondensification mechanisms such as grain growth will prevail.

4.1.1.1.2. Influence of heating rate

The influence of heating rate (a_{hr}) on the nonisothermal sintering behavior of n_ZnO is shown in Fig. 4.3. The obtained linear shrinkage curves shows a delay in the onset temperature for the densification (Fig. 4.3 a)). The shrinkage rate $dY\ /\ dt$ is lower for slower heating rates, and the higher values of shrinkage rate are close to 700°C for all heating rates (Fig. 4.3 b)). Oppositely, sm_ZnO and m_ZnO powders show respectively an increase in T_{MSR} from ~710 to ~760 °C and from ~765 °C to ~860 °C with the heating rate. The inflection corresponding to the MSR value can be attributable to the increase in the grain growth rate with consequent reduction in $dY\ /\ dt$ [10].

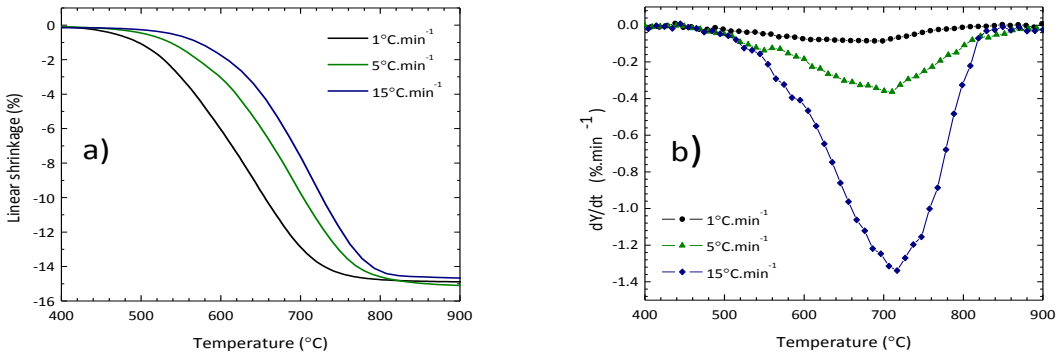

Fig. 4.3. *Linear shrinkage a) and shrinkage rate b) of n_ZnO powder (~ 62% TD) for heating rates of 1, 5 and 15 °C.min^{-1}.*

4.1.1.1.3. *Activation energy and sintering mechanisms in the initial stage*

Particle size measurements from SEM micrographs show no significant variations for linear shrinkage up to 3 %. Therefore, the activation energies for the initial stage of sintering were calculated considering the slopes in Fig. 4.4, according to eq. 4.1.

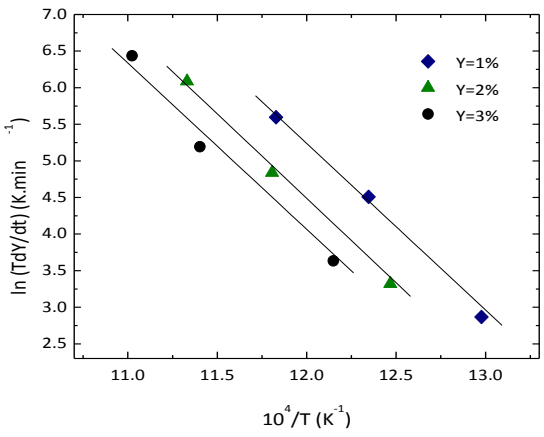

Fig. 4.4. *Arrhenius plot $ln(T \cdot dY/dt)$ versus $1/T$ for 1, 2 and 3% constant linear shrinkage values for n_ZnO sintered at different heating rates (1, 5 and 15 °C.min^{-1}).*

For n_ZnO powder the activation energy for densification (Q_i) is ~201 ± 3 kJ.mol^{-1}, which is in good agreement with the theoretical values of pure ZnO (200 – 300 kJ.mol^{-1}) obtained by other authors [7, 8, 11, 12] and the values obtained in this work for sm_ZnO (~332 ± 20 kJ.mol^{-1}) and m_ZnO (~273 ± 9 kJ.mol^{-1}).

On the basis of model proposed by Woolfrey and Bannister [3], we can determine the sintering mechanism for the initial sintering stage with a plot of $\ln(Y)$ as a function of $\ln(a_{hr})$ (Fig. 4.5) at a constant temperature and considering the slope equal to $-1/(n_1+1)$. The temperature range used in the calculation of the slope for n_ZnO powder (500 to 550 °C) is the one that ensures no significant grain growth during the initial stage of sintering. The obtained n_1 value was 0.75, which lies between the theoretical values for the viscous flow and volume diffusion. These values are consistent with those obtained by Han *et al.* [13] (0.6 for pure ZnO with a mean particle size of 0.260 µm similar to sm_ZnO), who found two different regions for ZnO and Mn-doped ZnO: in the first one a viscous flow mechanism prevails, whereas the second one is governed by the volume diffusion.

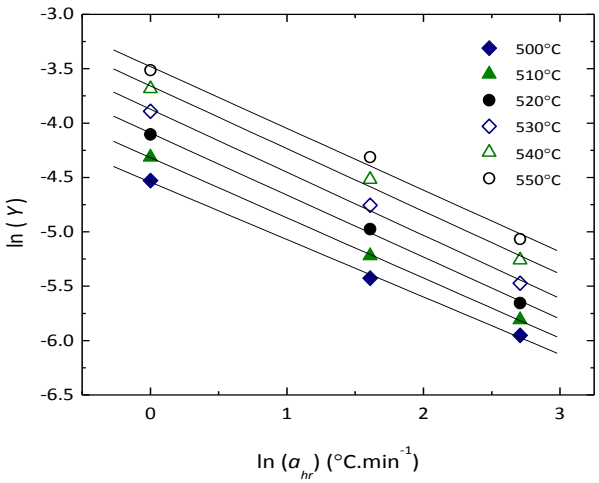

Fig. 4.5. *$ln(Y)$ versus $ln(a_{hr})$ plot for a temperature range between 500 °C and 550 °C.*

4.1.1.1.4. <u>Densification and grain growth</u>

The effect of sintering temperature on the densification of the samples prepared with different commercial ZnO powders was studied in compacts of identical green density (~62% TD) sintered in a dilatometer at different temperatures and constant HT of 2 h. As shown in Fig. 4.6, considerable higher densities at lower temperatures can be achieved for n_ZnO powder. For a sintering temperature of 700 °C, the relative density of samples prepared with n_ZnO powder is ~ 97%, which is higher than that obtained for the sm_ZnO powder (~88% TD). On the other hand, for the m_ZnO powder sintered at this temperature, the increase in density is quite low (~68% TD) when compared to the one obtained by uniaxial cold pressing, 62% TD. Above 800°C the targets made with n_ZnO and sm_ZnO powders reached final densities near TD, while for the ones made with m_ZnO it happens only at 1200°C. These results show that sintering becomes more favorable as the particle size of the powders decreases, which is related to the larger SSA and surface energy of the smaller particles.

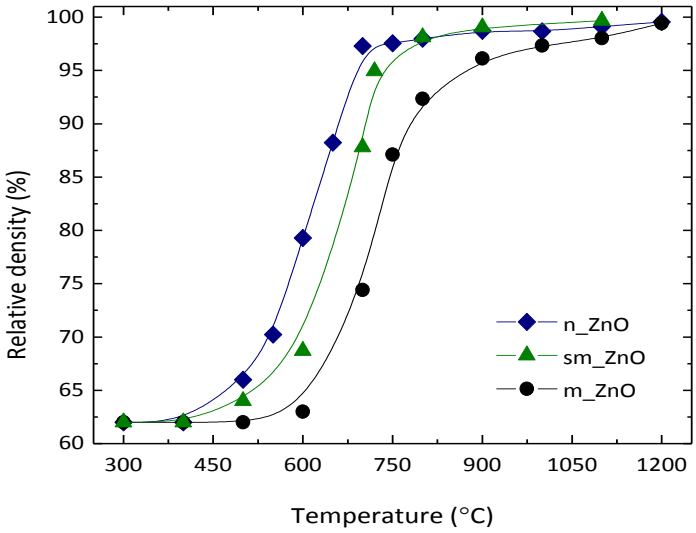

Fig. 4.6. *Influence of sintering temperature on relative density of n_ZnO, sm_ZnO and m_ZnO with CHR of 5°C.min^{-1}.*

The influence of HT in densification and grain growth during sintering of n_ZnO was studied at constant temperature chosen according to the T_{MSR} observed for n_ZnO (~710 °C). The selected temperature is below T_{MSR} to avoid a grain overgrowth. Thus, samples with ~62 % TD were sintered at 680 °C at a CHR of 5 °C.min^{-1} using different HT between 1 – 8 h. Results for the relative density and grain size are shown in Table 4.3.

Table 4.3. *Influence of HT on sintering and relative density of n_ZnO powder.*

Powder	Sintering cycle		Relative density (%)	Grain size (µm)
n_ZnO	680°C	1h	93.19	0.41
		2h	94.92	0.56
		4h	97.86	0.67
		8h	98.47	0.75

The results reveal a moderate increase in grain size as the HT raises, for a temperature below T_{MSR}. Samples with densities above 93% were obtained with grain size between 410 and 750 nm (Fig. 4.7 a) and b)). At this temperature, high densities were obtained without grain overgrowth. A microstructure with a wide dispersion of grain sizes is observed in SEM micrographs. Hynes *et al.* [7] also identified similar variation of grains size during sintering of nanocrystalline ZnO. A decrease in porosity when density rises from 93.19 % to 98.47 % TD was also observed.

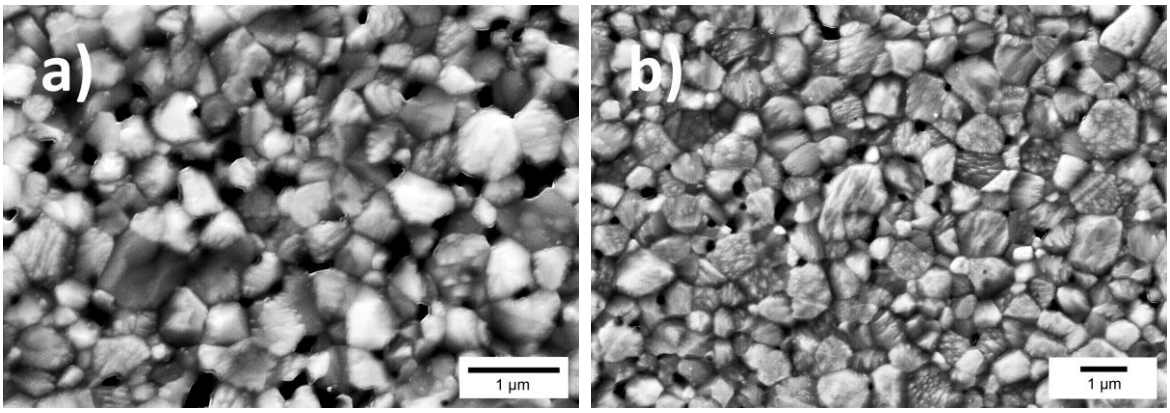

Fig. 4.7. *SEM micrographs of n_ZnO samples sintered at 680 °C: a) 1 h and b) 8 h.*

Fig. 4.8 shows the influence of temperature on the relative density and grain size for n_ZnO sintered at different temperatures. The samples sintered with the n_ZnO powder acquired a high density (> 97 %) at a relatively low temperature of 680 °C. The density is substantial enhanced from 79.29 % to 97.30 % when temperature changes from 600 to 700 °C. This behavior is accomplished by an increase of grain size from 0.240 µm to 0.775 µm. The same trend is observed as the temperature increases further, going from ~1 µm at 750 °C up to ~5 µm at 1100 °C. The densification and grain growth are both driven by diffusive mechanisms that are influenced by several parameters like pressure, particle size or temperature, resulting in the simultaneous activation of densification and grain growth, particularly in the final sintering stage [14].

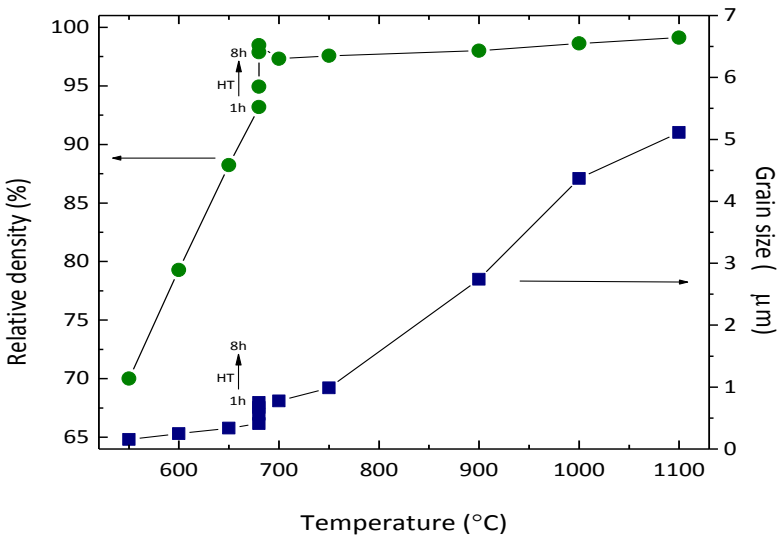

Fig. 4.8. *Relative density and grain size of nanocrystalline ZnO compacts sintered at different temperatures and a constant HT of 2h.*

Above 90% TD (final sintering stage), grains can grow when the continuous network of pores breaks down on grain boundaries and grains tend to grow rapidly [15], invalidating the advantages of using nano-sized particles (Fig. 4.9 a) and b)). However, it is remarkable that the dispersion on grains size tends to disappear as the temperature increases, producing compact samples with mean grain size above 5 µm at 1100°C.

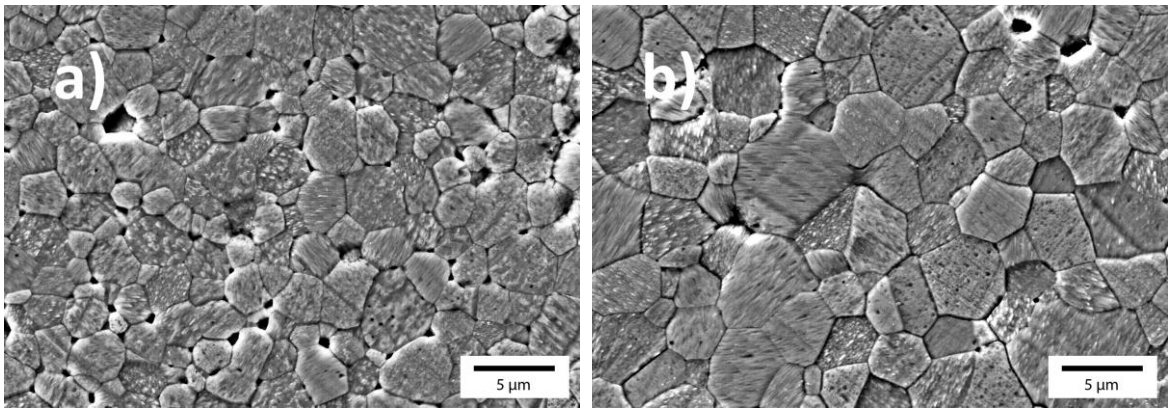

Fig. 4.9. *SEM micrographs of n_ZnO samples sintered at: a) 900 °C/2 h and b) 1100 °C/2 h.*

4.1.1.1.5. Scale-up effect

The scale-up effect was checked by studying the influence of sample sizes on the final relative density. For that, several dies with different diameters keeping constant the ratio between thickness and target diameter were used. Fig. 4.10 shows the relative density as a function of sintering temperature for samples with ~52 % TD sintered during 2 hours of HT and CHR of 5 °C.min^{-1}.

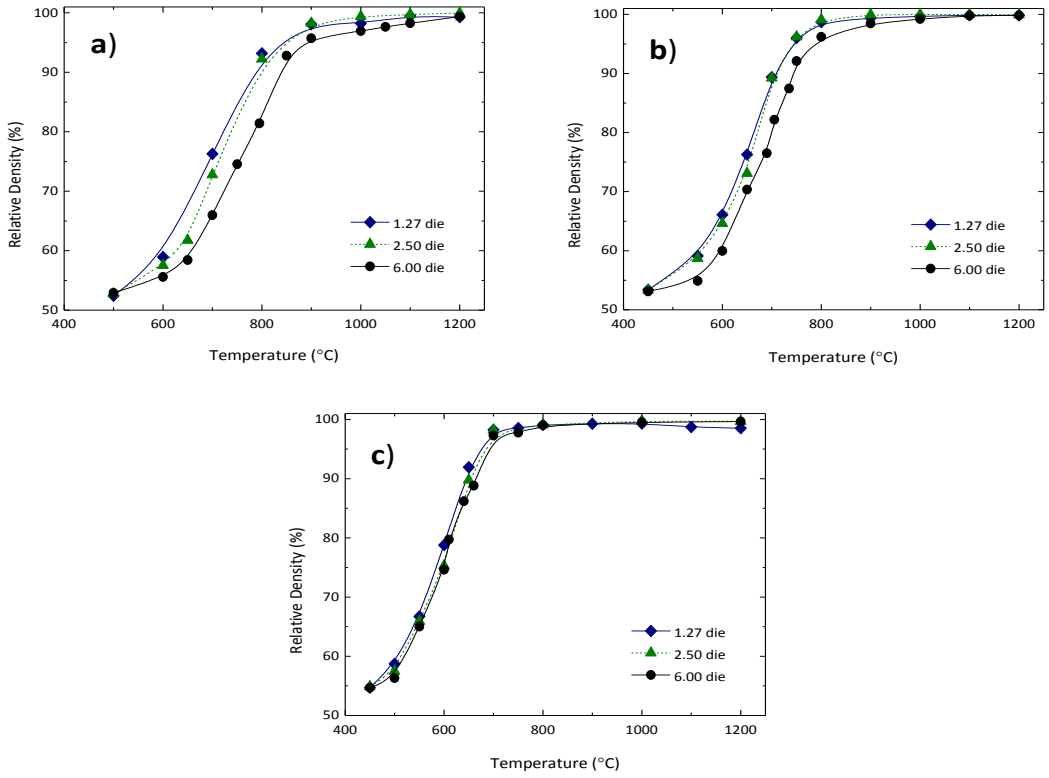

Fig. 4.10. *Relative density versus temperature for samples with a green density of ~52 % TD and different diameters – a) m_ZnO, b) sm_ZnO, c) n_ZnO.*

As observed, the samples produced with m_ZnO (Fig. 4.10 a)) and sm_ZnO (Fig. 4.10 b)) show a tendency for a delay in densification especially those of 6 cm die. Interestingly no significant variations in the sintering behavior is observed for samples made of n_ZnO (Fig. 4.10 c)) powders.

Thus, we can conclude that targets densification is improved by using nanoparticles. This behavior corroborates the previous discussion related to the high sinterability of n_ZnO powder. The lower sintering temperature of nanocrystalline powders is related to the existence of a large fraction of atoms at grain boundaries, which causes an increase in the diffusivity between particles compared with polycrystalline materials with larger particle sizes (micrometric powders). Moreover, the higher reactivity correlated with the higher SSA of n_ZnO powder acts as a driving force for sintering, as the surface diffusion between the particles increases, favoring the sintering mechanisms at low temperatures [16, 17]. The non-dependence of target size on densification for n_ZnO is an advantage for the production of ZnO sputtering targets as it is possible to achieve good target properties and reproducibility at substantially much lower temperatures, avoiding some problems associated with scale-up effect.

4.2. Undoped and Al-doped ZnO powders by emulsion detonation synthesis

This section reports the fabrication and characterization of undoped and Al-doped ZnO nanostructured powders with different compositions (0.5 – 2.0 wt. % Al_2O_3) produced by EDSM with a high production rate and economic feasibility. It was observed that Al has no noticeable impact on the detonation process. Therefore, highly homogeneous nanostructured powders with enhanced sinterability were obtained independently on the Al-doping level. Chemical, structural and morphological characterization of the final product confirms the method as highly efficient and high throughput for producing high quality nanostructured powders that allows the fabrication of high density AZO ceramic targets with different compositions at competitive costs.

4.2.1. Powder synthesis - precursors

As previously mentioned, one of the great advantages of EDSM is the wide range of precursors that can be used in the synthesis of the compounds. The type/amount of precursors has great influence in the final characteristics of the synthesized powders, since they directly influence the detonation parameters. Different precursors have been tested in order to assess its effect in the final properties of the powders. A previous optimization for each precursor has been performed to outline the best compromise in terms of emulsion stability, amount of precursors, conversion of reactants into the final products, production rate and final chemical composition of the synthesized powders. In Table 4.4 are summarized the main characteristics of two AZO powders (98:2 wt. % ZnO:Al_2O_3) synthesized with nitrates (AZO_PN) and metals (AZO_PM) as precursors.

Table 4.4. *Physical characterization of Al-doped ZnO powders (98:2 wt. % ZnO:Al_2O_3) synthesized with different precursors.*

Powder	Real density ($g.cm^{-3}$)	PSD (µm)			SSA (m^2g^{-1})	Crystallite size (XRD) (nm)
		D10	D50	D90		
AZO_PN	5.40	0.019	0.052	1.039	17.59	32.1
AZO_PM	5.42	0.022	0.251	1.305	7.78	71.4

The results show that AZO_PN powders have higher SSA (17.59 $m^2.g^{-1}$) and smaller crystallite size (24.1 nm) than AZO_PM powders. In Fig. 4.11 is shown the PSD of both powders. AZO_PM powder presents a tri-modal distribution with nanometric, submicrometric and some micrometric particles (agglomerates and aggregates inherent to the detonation process). In terms of weight fraction (%), approximately 44.4 % are between 3.90 and 0.43 µm, 26.6 % between 0.43 µm and 69 nm and 29 % between 69 and 15 nm. The mean particle size (D50) of AZO_PN reduces considerably from 251 nm to 52 nm, mainly due to the reduction of the number of aggregated particles with micrometric and submicrometric size. In terms of PSD (weight fraction (%)), approximately 21.8 % of the particles are between 3.9 and 0.43 µm, 19 % between 0.43 µm and 80 nm and 59.2 % between 80 and 15 nm.

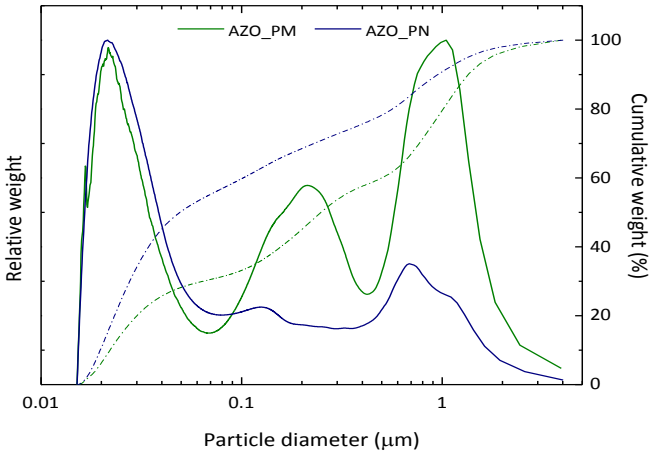

Fig. 4.11. *PSD (weight fraction) of Al-doped ZnO 98:2 wt. % powders synthesized with different precursors. The dashed lines represent the cumulative curves (in percentage of relative weight) of each synthesized powder.*

The differences in AZO_PN powder characteristics arose from the lower detonation temperatures (less energetic reaction) and faster quenching of the formed particles, and consequent reduction of the time at which the primary particles are subjected to high temperatures. These synthesis conditions contributed to obtain powders with smaller and more rounded crystallites (32.1 nm) than in AZO_PM powders. Likewise, the number of coalesced particles and consequently the number of agglomerated and aggregated particles decrease as observed in SEM images of Fig. 4.12 a) and b).

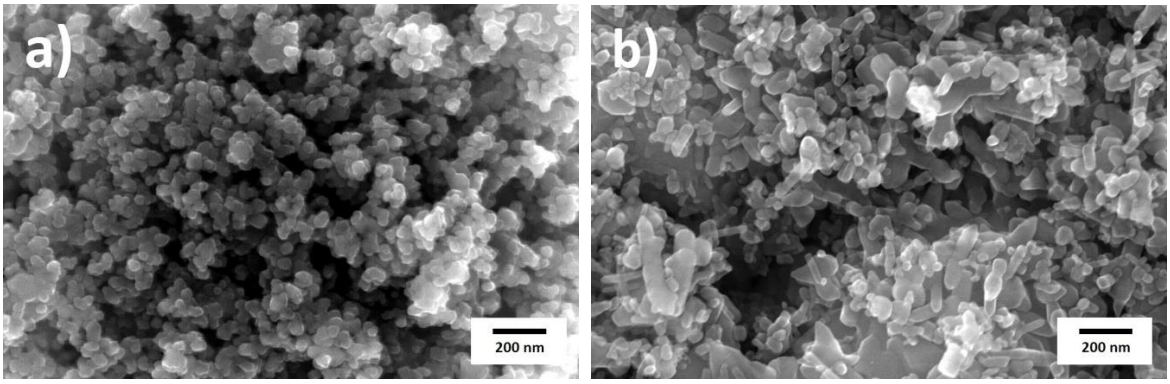

Fig. 4.12. *SEM images of Al-doped ZnO (98:2 wt. %) powders synthesized by EDS with different precursors: via nitrates (left) and via metals (right).*

Independently on the precursors, one of the great advantages of EDSM is the high chemical homogeneity of the synthesized powders. Small area element composition analysis using TEM-EDS (Fig. 4.13 a)) indicates that Al content in AZO_PM is about 2.91 mol. % which is in good agreement with the expected doping concentration (2 wt. % Al_2O_3). This is also a good indication that doping was successfully achieved and Al is well dispersed in the ZnO structure. Morphological characterization shown in TEM image (Fig. 4.13 b)) reveals that INNOVNANO AZO_PM powder is composed essentially by two different types of nanometric particles (round and rod shaped particles) composed by monocrystals.

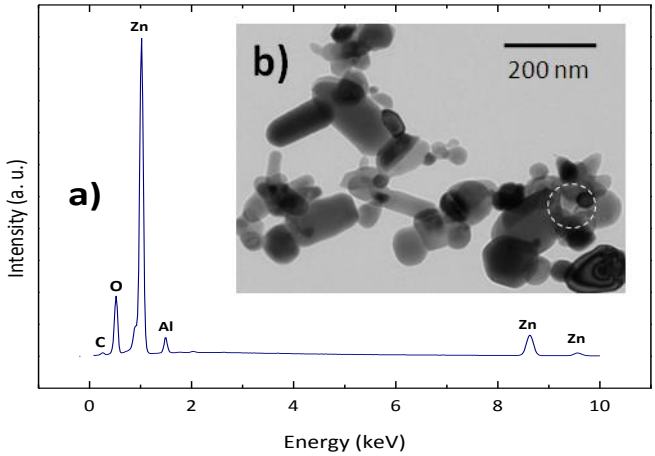

Fig. 4.13. *a) EDS recorded from the circular region presented in b); b) TEM image of as-produced Al-doped ZnO powder (AZO_PM).*

Besides metals and nitrates, preliminary tests using acetates as precursors were also performed. Fig 4.14 shows the influence of using acetates as precursors during the synthesis of AZO. While metals and nitrates gave rise to round or rod shape particles, the powders obtained with acetates precursors have a sheet-like nanostructure. These sheets or plackets are themselves porous, as can be observed in the higher magnification SEM image of Fig. 4.14. Although this is not a desired structure for producing compact ceramic targets, it is very interesting for applications where porosity and high surface to volume ratio, nanometer scale thickness, excellent permeation and distinct optical and photocatalytic behavior are necessary, such as sensors [18, 19]. Thus, EDSM is as a versatile method for the production of undoped and Al-doped ZnO powders with different reproducible structures at high throughput and competitive production costs.

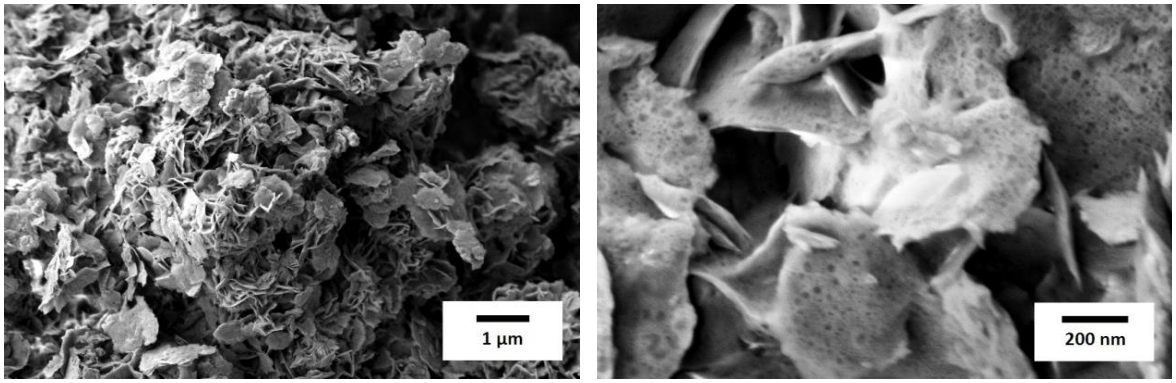

Fig. 4.14. *SEM images showing the sheet-like nanostructured AZO powder (98:2 wt. %) synthesized by EDS using acetates as precursors.*

As stated in section 3.1.1 during this research work that focused on the production of ceramic sputtering targets, the undoped and Al-doped ZnO powders characterized and presented hereinafter were synthesized via metallic precursors.

4.2.2. Powder characterization

In this section undoped ZnO (ZnO_N) and Al-doped ZnO nanostructured powders with respectively 0.5 (AZO_A), 1.0 (AZO_B), 1.5 (AZO_C) and 2.0 (AZO_D) wt % of Al_2O_3 (ZnO:Al_2O_3) were characterized as-produced, thermally treated and after deagglomeration step.

SEM micrograph (Fig. 4.15) shows the typical morphology of the as-produced AZO_D powder (2.0 wt% of Al_2O_3). The powder is formed by clusters of nanometric particles with loose appearance and some aggregates of round and rod shaped particles that are inherent to the EDSM process as mentioned before. The high temperatures reached during the synthesis promote the aggregation of nanoparticles (particles coalescence) which is correlated to their transition from the gaseous to solid state during the synthesis process. The observed morphology is consistent with the tri-modal PSD obtained for the same powder (Fig. 4.11). It should be noted that both morphology and PSD are similar in all the studied compositions before disaggregation/deagglomeration independently on the Al-doping level.

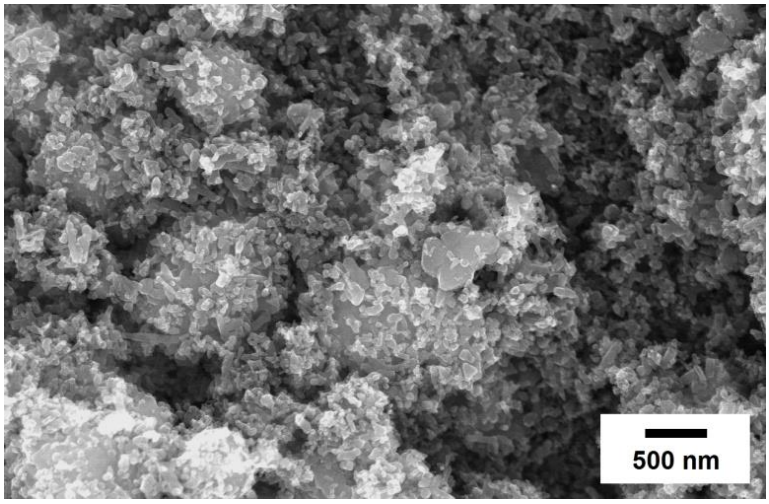

Fig. 4.15. *SEM photograph showing the general morphology of as-produced Al-doped ZnO powders.*

The influence of Al doping on the real density, PSD, SSA and crystallite size is shown in Table 4.5. Al-doping and undoped powders have comparable particle size and shape, SSA and agglomeration degree. SSA values are within the range 7.56 – 7.92 $m^2.g^{-1}$ and the crystallite size is between 71.4 nm and 75.2 nm. Therefore, we may assume that Al doping has no relevant influence in the physical characteristics of as-produced powders. Thus, the development of a standard disaggregation process was less demanding allowing us to easily achieve disaggregated nanostructured powders with similar properties, which allow the understanding of Al-doping level effect on the sintering kinetics after disaggregation.

These results confirm the feasibility, stability and reproducibility of the EDSM for the production of AZO nanostructured powders where small variations in Zn/Al precursor's ratio have no influence on the main parameters of EDMS process (pressure, temperature and quenching rate) and consequently, on the final properties of the powders. This independence of physical

characteristics with the doping level is not commonly observed in other synthesis methods used for the production of nanoparticles where significant changes occurs with the increase in Al-doping level, mainly in terms of final particle size [20-22].

Table 4.5. *Physical characterization and chemical composition of as-produced INNOVNANO undoped and Al-doped ZnO nanostructured powders.*

Powder	Real density ($g.cm^{-3}$)	PSD (µm)			SSA ($m^2.g^{-1}$)	Crystallite size (XRD) (nm)	Composition (at. %)		Ratio
		D10	D50	D90			Al	Zn	Al/Zn
ZnO_N	5.47	0.021	0.251	1.317	7.92	75.2	–	–	–
AZO_A	5.45	0.020	0.242	1.275	7.73	71.9	0.75	99.25	0.008
AZO_B	5.43	0.021	0.269	1.342	7.56	72.8	1.52	98.48	0.015
AZO_C	5.42	0.021	0.256	1.371	7.64	73.7	2.28	97.72	0.023
AZO_D	5.42	0.022	0.251	1.305	7.78	71.4	3.04	96.96	0.031

4.2.2.1. Chemical composition analysis

The chemical composition of the powders was investigated by ICP, XRF and XPS. Besides the main elements Zn and Al the ICP-MS and XRF analysis of the as-produced AZO powders reveal also some traces of Zr, Si and Fe, but as the concentration of these elements is very low, it may be ignored. Considering only Zn and Al elements, the chemical analysis shown in Table 4.5 indicates an atomic ratio of Al/Zn consistent with the stipulated stoichiometry of prepared mixtures before EDSM. This means that during the powders synthesis the precursors are successfully converted.

Surface chemical composition of the as-produced Al-doped ZnO (98:2 wt. %) nanostructured powder was analysed by X-ray photoelectron spectroscopy (XPS). Fig. 4.16 a) displays the overall XPS spectrum of the powder. The main features in the spectrum correspond to zinc, oxygen, aluminum and carbon photoelectrons and Auger electrons. The detailed regions for Zn 2p, Al 2p and O 1s photoelectrons are shown in Fig. 4.16 b), c) and d). C 1s was also acquired, mainly for binding energy calibration purposes. Zn $2p_{3/2}$ was fit with four components centered at 1017.6 ± 0.2, 1018.8 ± 0.2, 1021.4 ± 0.2, and 1022.2 ± 0.2 eV. They were assigned to two different metallic phases (inherent to the synthesis method): Zn bounded to O and Zn bounded to hydroxyl groups, respectively [23]. The two first components have a very low value when comparing to the reported for metallic zinc Zn $2p_{3/2}$ BE (NIST Database [23] presents a range of Zn 3 $p_{3/2}$ BE from 1020.8 eV to 1022.8 eV). This fact is ascribed to the existence of residual metallic zinc in a poor electrical contact with the ZnO phase. The ZnO phase being less conductive than the metallic one accumulates a large positive charge. Therefore, when the charge correction is performed, the metallic phase displays lower BE values.

Al 2p region was fit with two doublets with a split spin-orbit of 0.41 eV. The first one, with the component Al $2p_{3/2}$ centered at 73.9±0.3 eV, is assignable to Al-O bond, and the second one, with BE (Al $2p_{3/2}$) = 75.7 ± 0.2 eV to Al-OH bond [23]. Both correspond to the oxidation state III, consistent with the defect type Al_{Zn}. O 1s region was fit with 3 components centered at 530.3 ±

0.1 eV, 531.7 ± 0.2 eV and 532.9 ± 0.3 eV, assigned to O bonded to metal (Zn and/or Al), to OH and to organic O (mainly C-O), respectively [24].

Regarding the quantitative analysis, an Al/Zn ratio of 0.040 (estimated error is ± 10%) was obtained which is slightly above the expected value. The expected atomic ratio Al/Zn, given the weight ratio 2:98, was 0.033 at. %. XPS atomic ratios computed from photoelectrons with very different binding energies (very different kinetic energies) may be much distorted (relatively to real atomic ratios) if a contamination layer covers the surface. Zn 2p photoelectrons have a very low kinetic energy (KE ~ 465 eV) when compared to the one for Al 2p photoelectrons (KE ~ 1412 eV) and, therefore, when both have to cross an overlayer, Zn 2p photoelectrons are much more attenuated than the Al 2p photoelectrons and, therefore the XPS ratio Al/Zn should come higher than the real. To ensure that this effect is not present in this sample, both the Zn 2p photo electrons and the Zn 3p (KE ~ 1398 eV) ones were used to compute the Al/Zn ratio. Within the experimental error they are similar, attesting that the contamination does not distort the atomic ratios involving Zn 2p photoelectrons. This means that no or very small aluminium positive segregation at the surface exists. An atomic ratio O/Zn of 0.9 was obtained and confirms an oxygen deficiency (nonstoichiometry) on the AZO powder surface. As mentioned before, due to the synthesis process, it is not surprising the presence of carbon in the powder. The fact that the quantitative information extracted from two Zn photoelectrons having kinetic energies so distinct as Zn 2p and Zn 3p ones, shows that besides carbon under the form of an overlayer, also some carbon mixed with the oxide is present in the powder.

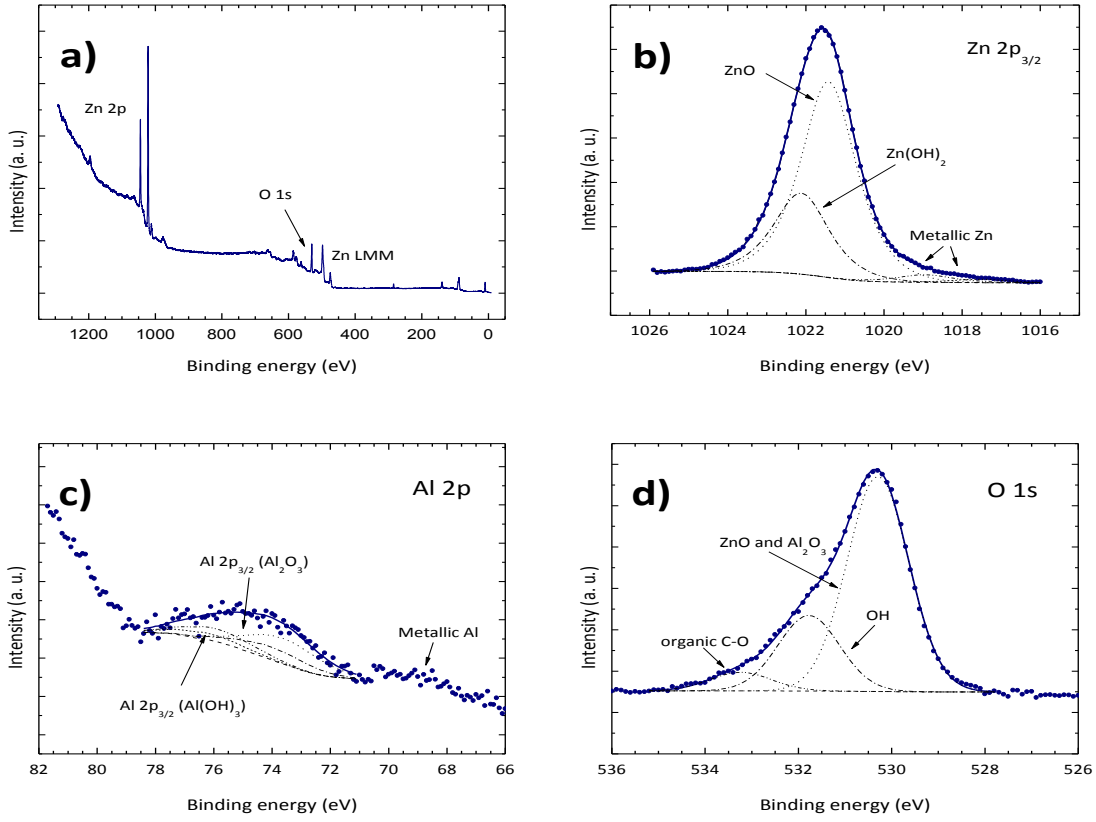

Fig. 4.16. *a) X-ray photoelectron spectroscopy (XPS) survey spectra of as-produced AZO_D powder sample; b) Zn $2p_{3/2}$, c) Al 2p and d) O 1s XPS regions.*

4.2.2.2. Structural analysis

The XRD patterns of as-produced undoped and Al-doped ZnO INNOVNANO nanostructured powders are plotted in Fig. 4.17. The diffraction intensities were measured using a scan speed of 0.5 s every 0.019° in the 2θ range from 20° to 80° at room temperature. Independent of Al content, all the samples present the corresponding ZnO peaks identified as wurtzite. In order to investigate the possibility of a secondary phase formation during the powders synthesis, a lower scan speed (0.019° step each 30 s) was performed within a specific range of 2θ angles (55° – 75°) where particular diffraction planes associated with gahnite ($ZnAl_2O_4$) phase formation could be detected. Except for undoped ZnO, the diffraction planes (422), (511), (440) and (620) corresponding to $ZnAl_2O_4$ were identified confirming its presence in the Al-doped powders after synthesis. Inset shows the magnified spectra in the 2θ range 58.5° - 60.5° revealing a (*hkl*) peak known as gahnite (511) diffraction plan that increases with the Al doping concentration.

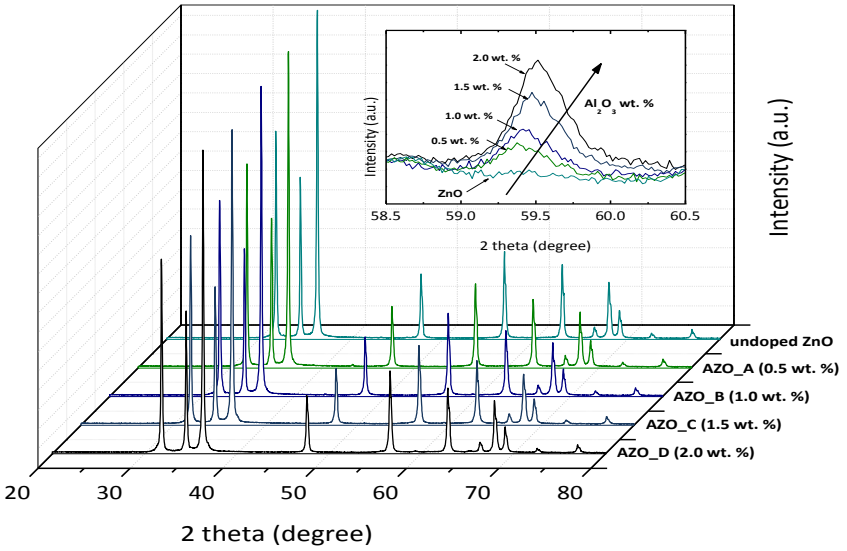

Fig. 4.17. *X-ray diffraction patterns of undoped and Al-doped ZnO powders synthesized by EDSM. Insets showing gahnite ($ZnAl_2O_4$) as a secondary phase present in the as-produced AZO powders.*

The $ZnAl_2O_4$ phase is formed at high temperatures [25] and its formation as a secondary phase normally occurs during a calcination step at elevated temperatures, or during a sintering stage [26, 27]. As explained before, EDSM is a non-equilibrium process, generating a high pressure for a short duration and high temperatures that, in the case of AZO synthesis, can easily reach temperatures above 2000 °C [28]. The compositions used in this work are above the solid solubility limit of Al in ZnO lattice. Subsequently, besides ZnO, also the $ZnAl_2O_4$ spinel phase formation is promoted during EDSM due to the excess of Al that cannot enter in ZnO structure as a solid solution. This fact could be an advantage during the sintering stage of AZO samples since $ZnAl_2O_4$ will be perfectly dispersed in the final microstructure avoiding large gradients in the electrical resistivity of the sintered samples that often lead to a decrease of its efficiency as a ceramic sputtering target [29, 30]. Moreover, the presence of $ZnAl_2O_4$ in the as-produced powder, the perfect distribution of Al in each individual ZnO particle (showed and discussed later) and the extreme synthesis conditions during the detonation, suggest that Al^{3+} ions occupied the position of Zn^{2+} ions in the ZnO lattice as a substitutional atom and reach the solubility limit during the powder synthesis reacting the remaining Al with ZnO to form $ZnAl_2O_4$.

The obtained Bragg reflection peaks of the synthesized nanostructured powders are broadened, which may result from small particle size and/or the presence of microstrain. The mean particle size of the powders was calculated based on the Scherrer equation [31] and refers to the mean size of crystallites of the aggregated/agglomerated particles. Typically, the powders have a mean crystallite size of 75 ± 5 nm.

4.2.2.3. Morphological analysis

SEM and TEM analyses of Al-doped ZnO (98:2 wt. % ZnO:Al_2O_3) shown in Fig. 4.18 a) and b) respectively, exhibit both rod and spherical particles with a characteristic size distribution (in number) centered at ~45 nm (Fig. 4.18 c)) which is consistent with the CPS measurement (40 nm). However, in terms of volume fraction, the mean particles diameter increases for values in the range of 70-80 nm (inset in Fig. 4.18 c)).

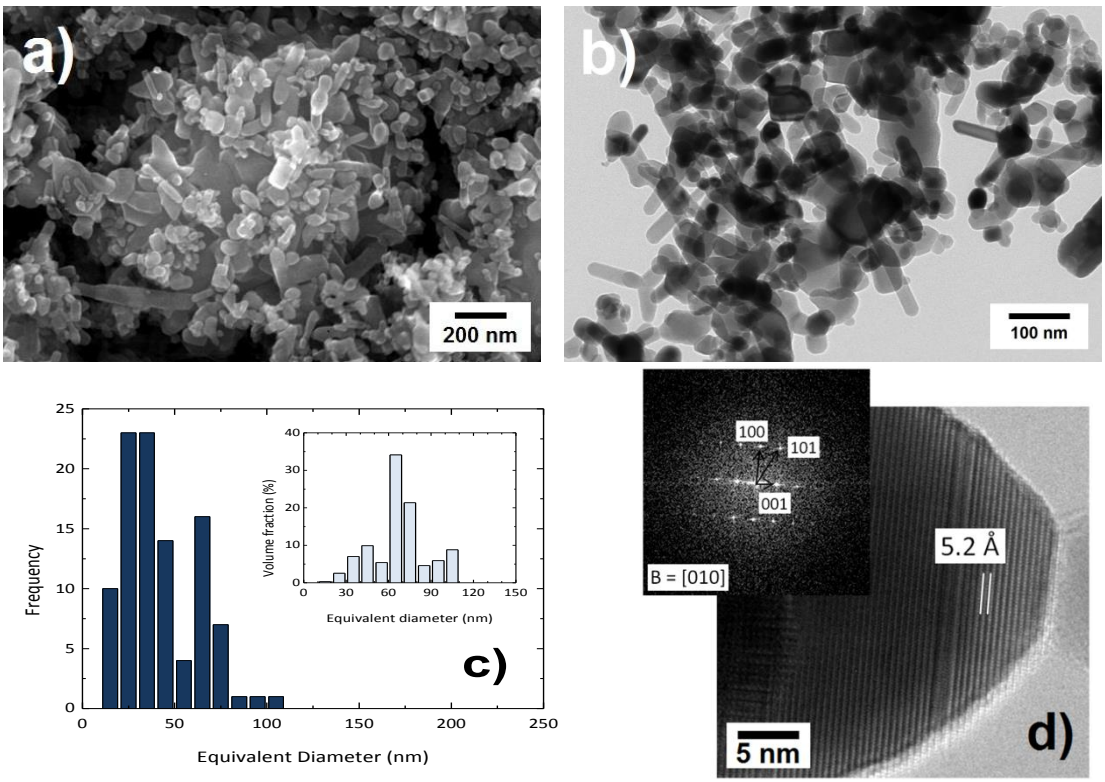

Fig. 4.18. *a) SEM and b) TEM images of Al-doped ZnO (2.0 wt. % Al_2O_3) nanostructured powder, c) typical size distribution (in number) of the particles accordingly to SEM and TEM analysis (Inset shows the equivalent diameter derived from the particles volume fraction), d) HRTEM image and the inset with the SAED pattern of the single-crystalline particle.*

These results are consistent with the crystallite size calculated for the as-produced powders by XRD (Table 4.5). This was expected since crystallite size measurements using X-ray diffraction are calculated from Scherrer equation that provides the mean volume-weighted size of the crystallite. On the other hand, the CPS weight fraction based PSD shows a D50 of about 250 nm which could be justified by the existence of some large particles (≥ 1 µm) and several aggregates composed by a high number of coalesced primary particles (Fig. 4.18 a) and b)). The crystallite size of nanoparticles formed during the EDSM is essentially defined in the Taylor zone (gas expansion), being smaller for higher cooling rates [32]. Thus, the small crystallite size obtained and its narrow

size distribution (in number) (Fig. 4.18 c)) confirm the high quenching rate during the powder synthesis and also demonstrates the feasibility of this method to produce AZO powders with controlled nanosized primary particles. High-resolution TEM (HRTEM) was used to characterize the as-synthesized Al-doped ZnO (98:2 wt. %). HRTEM of an individual nanoparticle is shown in Fig. 4.18 d) as well as the corresponding Fast Fourier Transform (FFT) image (Fig. 4.18 d) inset). The BF-HRTEM and the correspondent FFT show, in this region, AZO nanoparticle single crystal with wurtzite hexagonal structure (for beam direction B = [010]). The crystal lattice fringes can be seen in the image. Several nanoparticles were analyzed and no gahnite structure (cubic $ZnAl_2O_4$) was identified by HRTEM, which should be correlated with the lower crystallinity of the $ZnAl_2O_4$ spinel phase and also to the small amounts of this phase in the powder (Fig. 4.17).

An ensemble of some AZO_D ($ZnO:Al_2O_3$ 98:2 wt. %) nanostructured powder particles before deagglomeration/disaggregation are shown in Fig. 4.19 (STEM image). The EDS mapping in STEM gives the qualitative distribution of constituent elements Al, O and Zn. The mapping shows a homogeneous distribution of Al into the ZnO matrix. In fact, except for AZO_A where the lower Al doping concentration (0.5 wt. % Al_2O_3) did not allow an accurate small area element quantitative EDS analysis, all the other AZO powder particles have Al concentrations in concordance with the ones predicted for each composition.

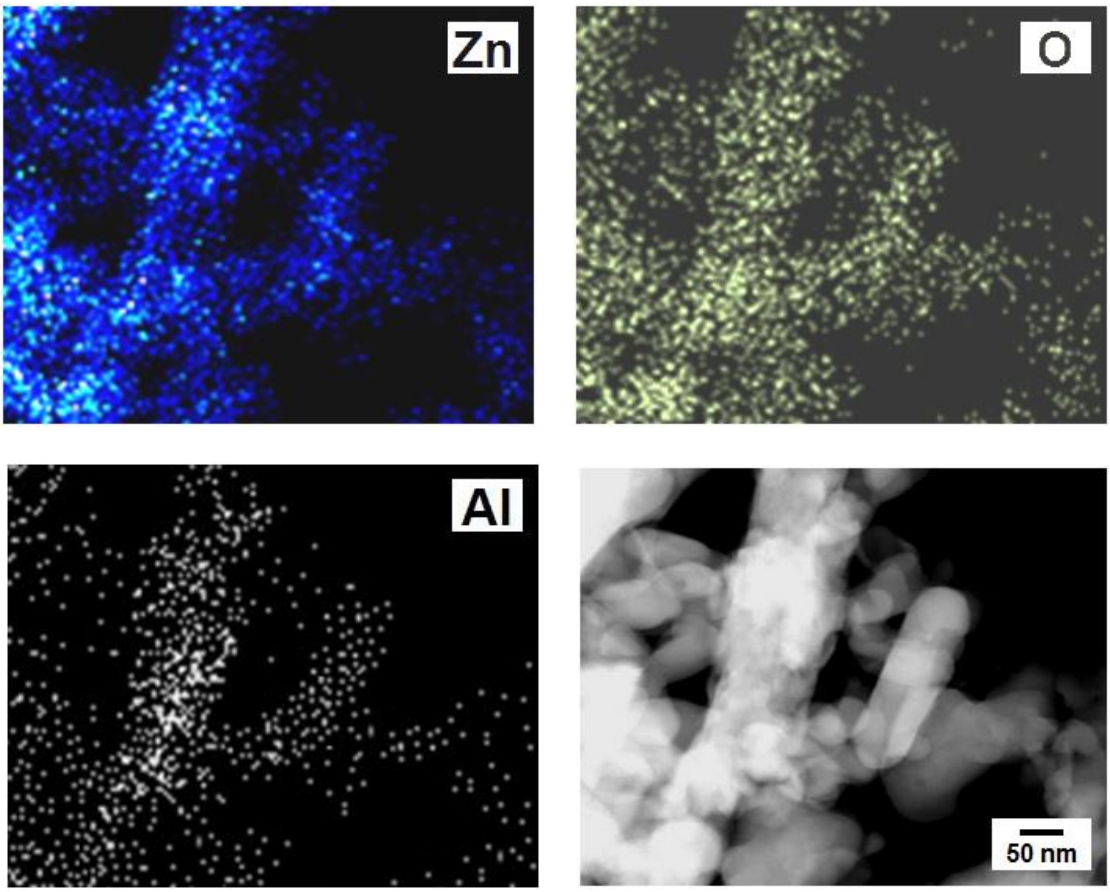

Fig. 4.19. *Morphology and composition of AZO_D nanostructured powder after thermal treatment at 600 °C for 2 h. TEM bright-field image of some agglomerated AZO particles and mapping acquired by EDS in STEM showing distributions of Zn, O and Al.*

4.2.2.4. Processing stages – Thermal treatment

As stated in chapter 3 (section 3.1.1), during the EDSM, besides some gas reaction products, also carbon traces are present in the as-produced powder (confirmed by XPS analysis), giving rise to a grey color synthesized powder. The carbon removal took place during a thermal treatment (TT) for a certain time after the AZO powders synthesis. The carbon is eliminated and a white powder without gas reaction products is obtained.

It is well known that a TT stage, especially in the case of high SSA powders, can change irreversibly their physical properties promoting particles coalescence and agglomeration, which reduces powder sinterability even when submitted to subsequent deagglomeration process [33]. So, the TT temperature should be high enough to remove the carbon from the powder (>500 °C), without affecting its physical properties.

In order to assure that the effect of TT on physical properties is minimized, the variation of SSA and crystallite size as a function of TT temperature (range of 300 °C to 900 °C) (Fig. 4.20) and HT (range of 1 h to 8 h) (Fig. 4.21 a) and b)) were studied using AZO_D as a reference (similar behavior was observed for the other studied compositions). Accordingly with Fig. 4.20 the powder SSA and crystallite size remains approximately constant with TT in the range of 300 - 500 °C at a constant HT of 2 h (reduction of SSA from 7.78 to 7.08 $m^2.g^{-1}$ and increase in crystallite size from 71 to 73 nm). At higher TT temperatures (500 °C - 650 °C) the SSA is reduced from 7.08 to 5.64 $m^2.g^{-1}$, while the crystallite size increases from 73 to 85 nm. Above 650 °C the SSA decreases considerably, while the crystallites grow drastically from 101 nm at 700 °C to 198 nm at 900 °C. Thus, the thermal treatment should be restricted to temperatures above 500 °C, to remove the carbon and some organic material, and below 650 °C to avoid the particles coalescence and excessive growth of crystallites (delimited by the dashed area in Fig 4.20). Likewise, Fig. 4.21 a) and b) indicate that an increase in HT promotes the reduction of SSA in the range 1 – 8 h. The crystallites grow considerably as HT increases being this variation more prominent in the range 1 – 4 h of HT. Thus, for an optimum combination of organics removal and preservation of initial powders' physical properties, a TT temperature between 550 °C - 650 °C and a HT of 1 - 2 h is advisable (limited by the dashed area in Fig. 4.21 a) and b)).

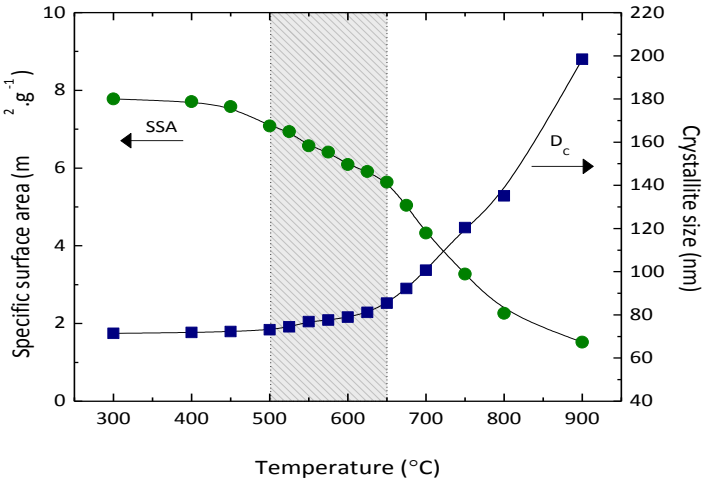

Fig. 4.20. *Specific surface area (SSA) and crystallite size of AZO_D (2.0 wt. % Al_2O_3) nanostructured powder versus thermal treatment temperature. The powders were thermally treated in the range of 300 °C – 900 °C for 2 h in air with a constant heating/cooling rate of 10 °C.min^{-1}.*

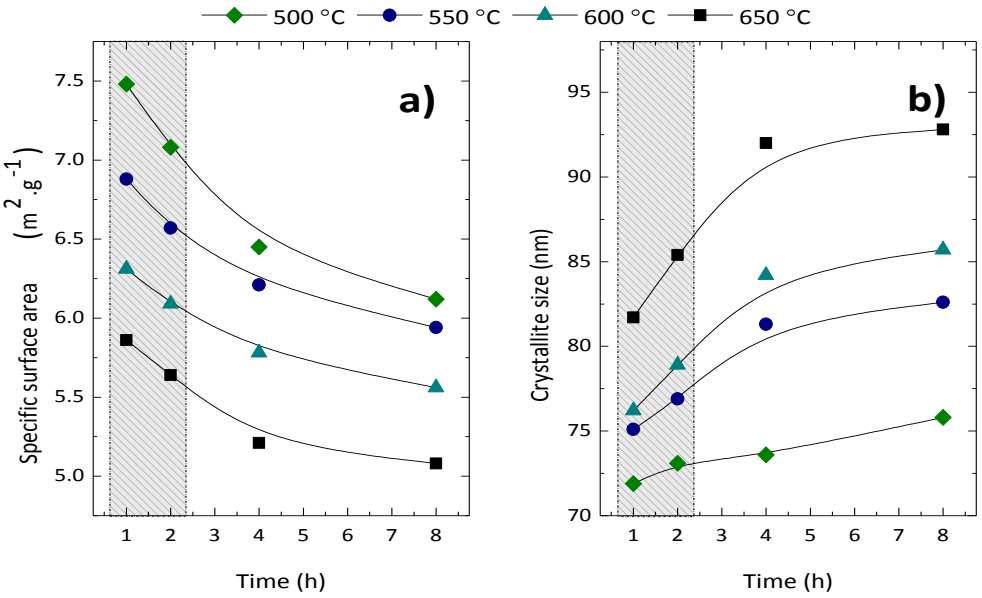

Fig. 4.21. *Variation of (a) specific surface area (SSA) and (b) crystallite size of AZO_D (2.0 wt. % Al_2O_3) nanostructured powder with holding time. The powders were thermally treated in the range of 500 – 650 °C for 1 – 8 h in air with a constant heating/cooling rate of 10 °C.min^{-1}.*

4.2.2.5. Processing stages – Disaggregation/deagglomeration

As mentioned above, due to the high detonation energy inherent to the production of undoped and Al-doped ZnO powders, the nanoparticles are normally agglomerated and/or aggregated containing also some large particles (Fig. 4.18 a) and b)). Typically, AZO agglomerates are formed by weak bonds between individual particles and/or aggregates, while the aggregates are composed by several primary nanoparticles that contact each other at surfaces or edges (coalesced particles) and cannot be easily broken.

It is well known that strong aggregates can reduce remarkably the sinterability of powders and consequently the advantage of nanopowders over conventional micropowders is lost.

In order to promote the densification of AZO compacts reducing their sintering temperature, a deagglomeration/disaggregation stage was performed after TT at 550 ºC for 1h. The disaggregation process reduces the formation of interparticle and interagglomerate pores leading to a more homogeneous microstructure. The disaggregation was executed using a ball mill, which was properly selected in order to guarantee that none or a very small amount of contaminants are introduced during this stage. Thus, it is guaranteed that disaggregation step has a smaller or negligible effect in terms of chemical composition of the powders and consequently of sintered targets. The disaggregation process was enhanced in order to reduce the time consumption and provide PSD and SSA values that are suitable for the production of ceramic targets with different sizes, even at an industrial level, and the possibility of fabricating large ceramic targets without affect significantly their sinterability.

Some physical characteristics of undoped and Al-doped ZnO nanostructured powders after disaggregation step are shown in Table 4.6.

Data reveals a narrow PSD (weight fraction values) compared to as-produced powders (Table 4.5) due to the breakdown of the aggregates and some micrometric particles, as revealed by the

change from tri-modal to a bi-modal PSD (Fig. 4.22) independently of Al-doping concentration. The D50 of the disaggregated powders is in the range 0.159 – 0.172 µm while D90 varies between 0.373 and 0.421 µm. No change in D10 particle size values was observed.

Table 4.6. *Physical characteristics of INNOVNANO undoped and Al-doped ZnO nanostructured powders after disaggregation stage.*

Powder	PSD (µm)			Real density ($g \cdot cm^{-3}$)	SSA ($m^2 g^{-1}$)	Crystallite size (XRD) (nm)
	D10	D50	D90			
Undoped ZnO	0.021	0.166	0.373	5.42	12.47	20
AZO_A	0.021	0.159	0.368	5.41	12.55	19
AZO_B	0.020	0.172	0.412	5.41	11.92	22
AZO_C	0.022	0.161	0.421	5.39	11.74	22
AZO_D	0.020	0.169	0.394	5.40	12.11	20

For AZO_D, for example, the D50 slightly reduces from 0.251 to 0.169 µm) with disaggregation. However, the D90 decreases considerably from 1.305 to 0.394 µm, changing from a tri-modal to a bi-modal particle distribution. About 69 % (weight fraction) of the particles are between 60 nm and 1 µm and the remaining 31 % are between 15 and 60 nm. The crystallite size of the AZO particles also reduces to values around 20 nm in good agreement with the broader peaks and crystallinity reduction (amorphization) observed in XRD (Fig 4.23).

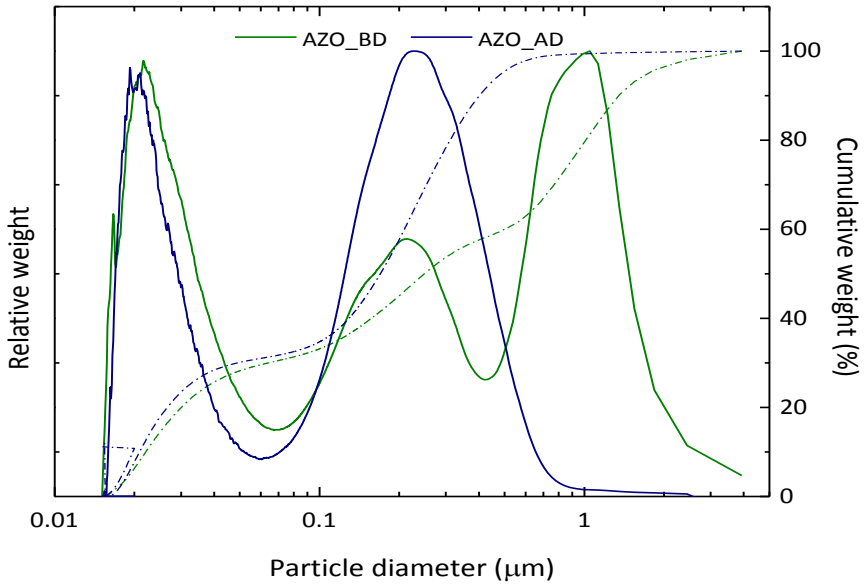

Fig. 4.22. *PSD (weight fraction) of Al-doped ZnO 98:2 wt% powders before (AZO_BD) and after disaggregation (AZO_AD) stage. The dashed lines represent the cumulative curves (in percentage of relative weight) of each powder.*

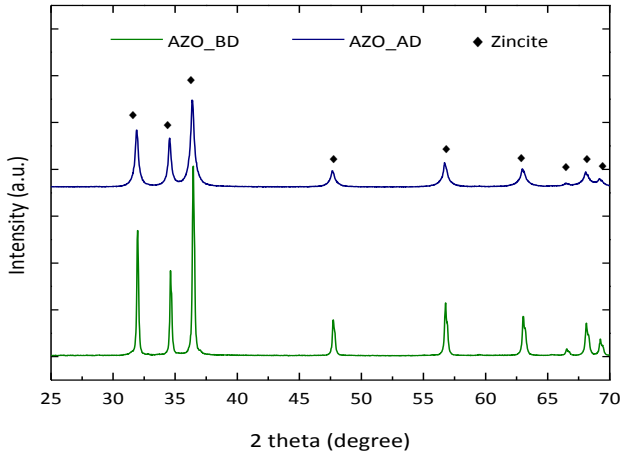

***Fig. 4.23**. XRD diffraction of Al-doped ZnO 98:2 wt% powders before (AZO_BD) and after disaggregation (AZO_AD).*

The linear shrinkage curves (Fig. 4.24 a)) for these two powders with respect to heating shows that the onset temperature for the densification of AZO_AD powder (considering the composition 98:2 wt. $ZnO:Al_2O_3$) is 740 °C, whereas for AZO_BD powder the densification starts only above 950 °C. This anticipation can be explained by the shrinkage rate curves (Fig. 4.24 b)). After milling, the maximum shrinkage rate temperature (T_{MSR}), was substantially reduced from 1470 to 1220 °C. The smallest width of the shrinkage rate curve (Fig. 4.24 b)) for AZO_AD powder represents a narrow distribution of particle sizes, agreeing well with the obtained results of PSD (see Fig.4.22). Earlier densification and higher sintering rate observed on AZO_AD compacts compared to AZO_BD can be explained by several factors like the higher surface energy related to smaller particle size and higher SSA [5, 6], together with an increased fraction of mass transport by grain-boundary diffusion, resulting from the large boundary area associated to nanoparticles [7, 8].

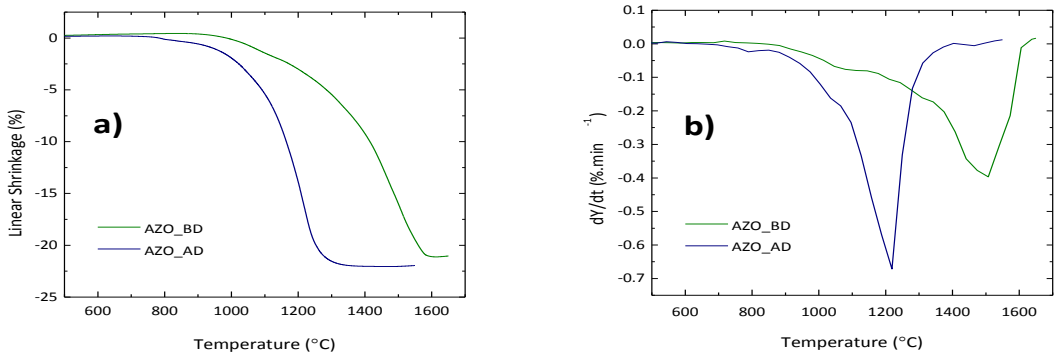

***Fig. 4.24**. Linear shrinkage a) and shrinkage rate b) with temperature of AZO powder (before and after disaggregation) for a constant heating rate of 5°C.min^{-1} (~ 44% TD).*

The real density values are comparable to those obtained in the as-produced powders (Table 4.5) and lower than TD (5.61 gcm^{-3}) while the SSA increases (values between 11.74 m^{2}g^{-1} to 12.55 m^{2}g^{-1}) after disaggregation step when compared with the as-produced (Table 4.5) and thermally treated powders (Fig. 4.20 and Fig. 4.21). Although most of the organic components are removed during TT, the lower real density values can be justified by several factors. Firstly by the formation of some hydroxyl groups ($Zn(OH)_2$) at the surface of the AZO nanopowders during the

disaggregation process (easily removed at 150 – 200 °C), and constitution waters that leaves at 300 – 400 °C (both well identified in TG/DSC analysis (Fig. 4.25)). Another factor could be the existence of some residual carbon which was identified by XPS analysis (not presented here) after disaggregation. Lastly, it may be derived from the amorphization of the powders inherent to the disaggregation stage (Fig. 4.23).

The TG curve of Fig. 4.25 shows a weight loss of about 0.6 % between room temperature and 220 °C for the disaggregated powder, revealing an endothermic peak at this temperature due to water removal. As the temperature increases up to 450°C, the total mass loss rises to ~1.2 %. In this range of temperatures, the DSC curve shows a broad peak with a small shoulder at ~310 °C, followed by a second endothermic peak of higher intensity at 410 °C. Above 450 °C no considerable weight loss or energy peaks were observed. These results are congruent with existence of waters residues (inherent to the disaggregation stage) and remaining carbon from the detonation. In fact even after TT a broad endothermic peak is identified in TG/DSC curves proving that the carbon is not completely removed during TT at 550 °C for 1 h. The carbon between the agglomerates/aggregates is hardly eliminated and the disaggregation favored the organic material removal, what justifies the largest peak observed.

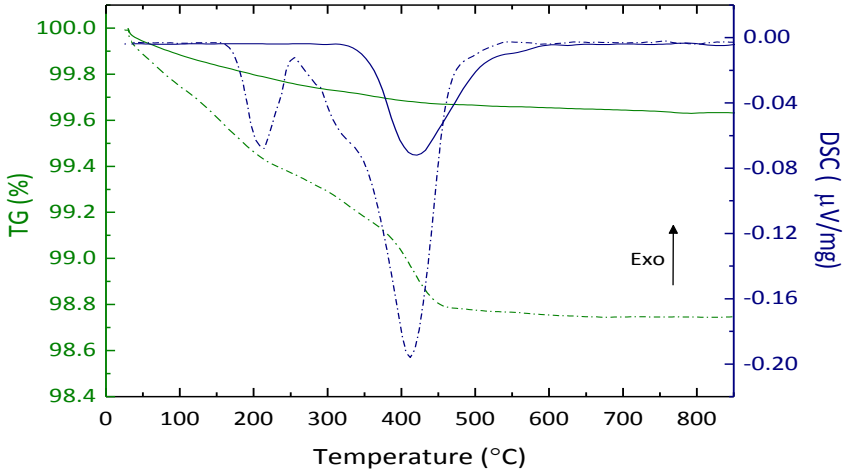

Fig. 4.25. *TG and DSC analysis of thermally treated (solid lines) and disaggregated (dashed lines) powders.*

The sintering study performed in this research work was restricted to undoped and Al-doped ZnO powders after disaggregation, since it allows achieving higher densities, at significantly lower temperatures, than that obtained in powders before disaggregation.

4.2.3. Constant heating rate sintering analysis

Since high quality AZO thin films are correlated with sputtering targets characteristics [29, 30, 34, 35], the understanding of the kinetics of densification in the initial and intermediate stages of sintering becomes essential for the production of AZO ceramic sputtering targets with desired structural, mechanical, thermal and electrical properties.

4.2.3.1. Densification behavior

The linear shrinkage (Y) and shrinkage rate (dY/dt) of ZnO as a function of Al doping, assuming isotropic shrinkage, is shown in Fig. 4.26 a) and b) respectively. Undoped ZnO (Fig. 4.26 a)) reveals

an onset shrinkage temperature ($T_{Y-onset}$) around 620 °C. The addition of Al strongly affects the densification, retarding $T_{Y-onset}$, which starts at ~ 740 °C for the lower Al concentration samples (0.5 wt. % Al_2O_3). As Al content increases, the $T_{Y-onset}$ still increases but moderately ($T_{Y-onset}$ of approximately 760 °C, 780 °C and 820 °C for AZO_B (1.0 wt. % Al_2O_3), AZO_C (1.5 wt. % Al_2O_3) and AZO_D (2.0 wt. % Al_2O_3), respectively), shifting the shrinkage curves to higher temperatures. With the advance of the sintering stage the effect of Al doping concentration in *Y* becomes more evident retarding the densification of the powders. The maximum shrinkage rate (MSR) was obtained for pure ZnO at ~850 °C (-0.550 %.min^{-1}) being observed a slightly reduction with Al addition (Fig. 4.26 b)). Oppositely, T_{MSR} has a substantial increase with the Al content from ~ 850 °C for pure ZnO to ~1200 °C for AZO_D (2.0 wt. % Al_2O_3). The systematic broadening of the shrinkage rate curves as Al is added, (more clear in AZO_C (1.5 wt. % Al_2O_3) and AZO_D (2.0 wt. % Al_2O_3)) confirms the retardant effect of Al on densification, due to the formation of higher amounts of $ZnAl_2O_4$ as a secondary phase during sintering of ZnO (Fig. 4.17). During sintering, the $ZnAl_2O_4$ particles are dragged and moved simultaneously with the pores surfaces hindering the movement of the surface and consequently reducing the driving force for densification [10, 27, 36].

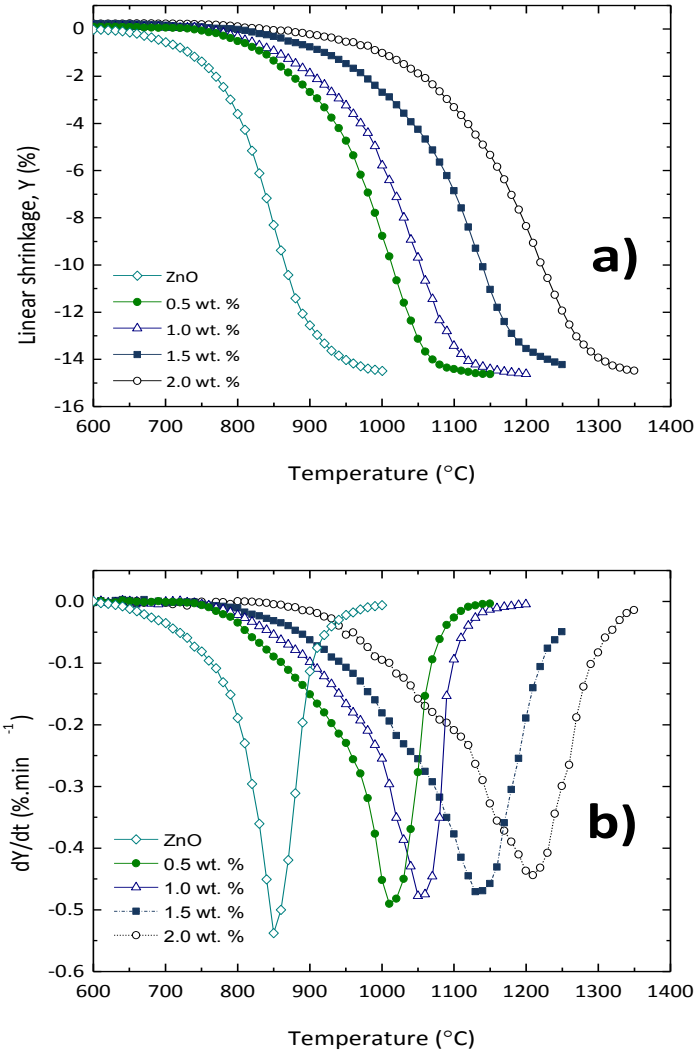

Fig. 4.26. *Temperature dependence of the linear shrinkage, Y a) and shrinkage rate, dY/dt b) of undoped and Al-doped ZnO compacts (~62% TD) in the range of 0 – 2.0 wt % Al_2O_3 (CHR of 5 °C min^{-1}).*

4.2.3.2. Activation energy and sintering mechanisms in the initial and intermediate stages

Plots of $ln(TdY/dt)$ versus $1/T$ at constant shrinkage (Y = 1 %) for undoped and Al-doped ZnO samples are shown in Fig. 4.27. The activation energies for densification in the initial stage (Q_i) obtained from the slopes of curves shown in Fig. 4.27 are displayed in Table 4.7. The obtained value for undoped ZnO (Q_i = 298 ± 48 kJ·mol^{-1}) is in agreement with the ones obtained in earlier studies [5, 10] and those of commercial ZnO powders presented in section 4.1. The Q_i increases considerably with Al addition but is less sensitive to the Al content variation (slightly changes from 466 to 532 kJ.mol^{-1} in the range 0.5 - 2.0 wt. % Al_2O_3). This increase in Q_i value when adding impurities is frequently reported by other authors [13, 37] and does not imply that the controlling sintering mechanism was altered. Senos [10] obtained a similar increase on Q_i, from 378 kJ.mol^{-1} (undoped ZnO) to 423 kJ.mol^{-1} (Al-doped ZnO samples with doping concentrations between 40 and 1600 ppm of Al_2O_3). The author achieved constant Q_i values (423 kJ·mol^{-1}), contrarily to our results, which can be explained by the much higher Al-doping concentrations used in this work. The Q_i values can be affected during the initial sintering stage by the presence of higher amounts of $ZnAl_2O_4$ spinel phase, responsible for the pinning of free surfaces and grain boundaries acting as retardant of densification.

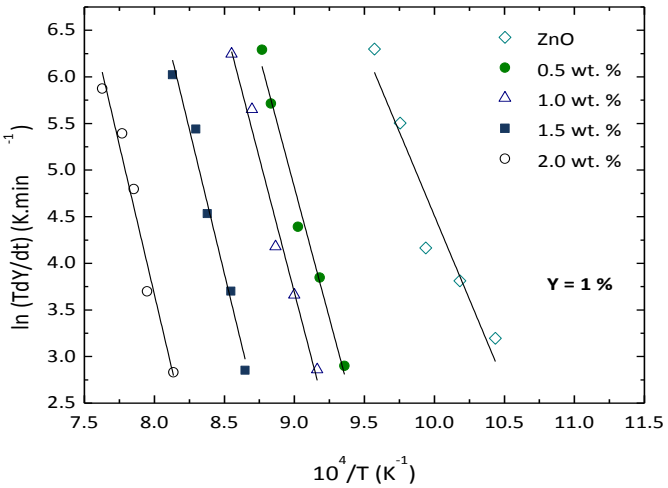

Fig. 4.27. *Arrhenius plots of $ln(TdY/dt)$ vs $1/T$ at constant linear shrinkage of 1 % for undoped and Al-doped ZnO samples sintered at different heating rates (1 °C, 3 °C, 5 °C, 10 °C and 15 °C.min^{-1}).*

The plot of ln (Y) as a function of $ln\,(a_{hr})$ (a_{hr} represents the heating rate) at constant temperatures for AZO_D (98:2 wt. % Al_2O_3) shown in Fig. 4.28 (for simplifying the graph, the plot of the other studied compositions are not shown, although they are similar), enables to determine the sintering mechanism for the initial stage [3]. The temperature range used in the calculation of each composition slope was chosen ensuring that the sintering of the compacts is limited to the initial stage ($Y \leq 2$ %). The calculated n_1 values (Table 4.7) vary between ~ 0.70 for pure ZnO and ~ 1.30 for AZO_D (98:2 wt. %). Similarly to the observed for commercial n_ZnO powder presented in section 4.1, a combination of viscous flow (also denominated as a grain boundary sliding mechanism since we have no liquid phase during sintering of undoped and Al-doped ZnO) and volume diffusion seems to control the shrinkage during the initial sintering stage of ZnO, which is also consistent with previous results [13]. The addition of Al in small quantities (0.5 and 1.0 wt. % Al_2O_3) increases the sintering exponent n_1 to ~ 1.10 indicating that the densification

process is controlled by volume diffusion. The slightly enhancement of n_1 exponents (n_1 ~ 1.30) for doped samples with 1.5 and 2.0 wt. % Al_2O_3, suggest that besides the volume diffusion, also grain boundary diffusion mechanism contributes to the shrinkage during the initial sintering stage for heavily Al doped samples.

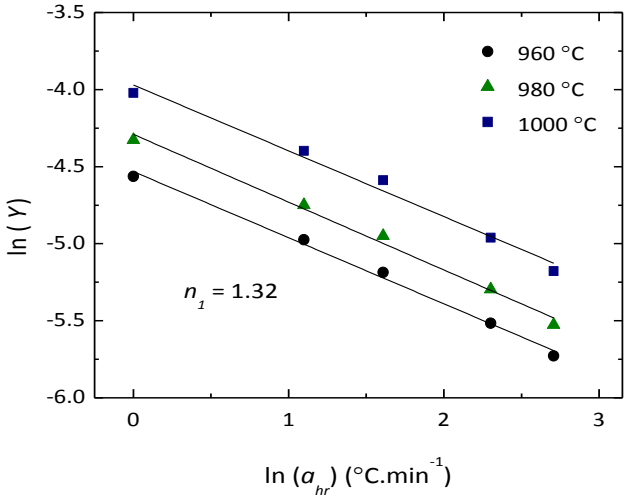

Fig. 4.28. *Linear shrinkage (Y) at constant temperatures as a function of the heating rate for AZO_D (98:2 wt. % Al_2O_3) sample.*

In the intermediate stage, the apparent activation energies for sintering were obtained considering the equation for the densification in the intermediate stage defined as [10, 37]:

$$\frac{d\rho_r}{dt} = \frac{C}{TG_s^b} exp\left(-\frac{Q_{int}}{RT}\right)\sum f(\rho) \qquad \text{(eq. 4.4)}$$

where $d\rho_r/dt$ and T are already defined, C is a constant depending on the material and on sintering mechanism, G_s is the average grain size, b the grain size exponent ($b = 2$ for volume diffusion and $b = 3$ for grain boundary diffusion mechanism), Q_{int} is the activation energy for sintering in the intermediate stage, R is the gas constant, $\sum$ the sintering stress and $f(\rho)$ a function of density depending on the model used.

The activation energies during the intermediate stage (Q_{int}) can be determined from eq. 4.4 assuming the average grain size (G_s) and the sintering stress ($\sum$) solely dependent of the density (ρ_r). Considering the densification curves obtained from eq. 3.6 and the densification rate curves from eq. 3.7, at different heating rates between 1 °C and 15 °C, Q_{int} was determined from the slopes of ln ($Td\rho_r/dt$) versus $1/T$ at constant $\rho_r$values between 70 and 85 % of TD. In Table 4.7, we show that Q_{int} are in line with the Q_i values obtained using the initial sintering stage model. The activation energy of undoped ZnO in the intermediate stage (Q_{int}) is higher for lower ρ_r (≤ 75 %) regardless of the studied composition. This behavior was already observed in previous studies [4, 10, 13] being attributed to the influence of the surface diffusion transport at low temperatures. This phenomenon is often accompanied by an initial pore growth and a fast reduction in the SSA that compete with the densification process. Since INNOVNANO undoped ZnO nanostructured powders have a high sinterability with fast reduction of SSA at lower temperatures this phenomenon can be amplified during the initial sintering stage promoting the increase in Q_{int} at

lower densities/sintering temperatures. On the other hand, for higher ρ_r values (> 75 %) the lower and approximately constant values of Q_{int} observed for undoped ZnO shows that the influence of surface diffusion mechanism tends to diminish, probably due to the decrease of the pores size as the densification enhances [10].

Among that, the Q_{int} values obtained for Al-doped ZnO remain unchanged with ρ_r and are similar (within the experimental errors) to Q_i value obtained in the earlier sintering stage. Despite the increase in Q_i and Q_{int} with Al content, the achieved narrow range of activation energies for densification in both, initial and intermediate stage (Table 4.7), and the near onset temperatures of linear shrinkage (Fig. 4.26 a)) observed for Al-doped ZnO samples, indicate that the densification of AZO is almost certainly controlled by the same mass transport mechanism (volume diffusion) in the range 62 % ≤ ρ_r ≤ 85 % without or with reduced interference of surface diffusion transport. The results are in good agreement with those obtained by Senos [10] at lower Al contents.

Table 4.7. *Initial stage activation energy for sintering (Q_i), kinetic exponents in the initial stage (n_1), and activation energies in the intermediate stage (Q_{int}) (70 ≤ ρ_r ≤ 85) for undoped and Al-doped ZnO samples.*

Powder	Q_i (kJ.mol^{-1})	n_1	Q_{int} (kJ.mol^{-1})			
			ρ_r = 0.70	ρ_r = 0.75	ρ_r = 0.80	ρ_r = 0.85
Undoped ZnO	298 ± 48	0.7	289	268	232	236
AZO_A	466 ± 35	1.1	458	461	443	435
AZO_B	479 ± 38	1.1	472	447	468	462
AZO_C	514 ± 45	1.3	528	531	512	524
AZO_D	532 ± 59	1.3	532	541	522	513

4.3. Conclusions

Initial stage sintering of three as-received commercial high purity ZnO micrometric (m_ZnO), submicrometric (sm_ZnO) and nanometric (n_ZnO)) powders were studied under nonisothermal conditions. The sintering behavior for sputtering target production where evaluated by changing the green density of samples from 62% of theoretical density (TD) to 35%. We observe that for n_ZnO powder the maximum shrinkage rate temperature (T_{MSR}) is not affected by GD and it is reached at lower temperatures (~710 °C) compared to m_ZnO and sm_ZnO powders. For these powders the temperature of maximum shrinkage rate increases from 803 °C to 934 °C and from 719 °C to 803 °C as TD changes from 62 % to 35 % TD, respectively. Small grain size (~0.560 µm) and highly dense targets were obtained for n_ZnO when sintered at temperatures below T_{MSR}. Heating rate from 1 °C.min^{-1} to 15 °C.min^{-1} led to lower activation energy for n_ZnO (~201 ± 3 kJ.mol^{-1}) than for the submicrometric (sm_ZnO) (~332 ± 20 kJ.mol^{-1}) and micrometric (m_ZnO) (~ 273 ± 9 kJ.mol^{-1}) powders. A combination of viscous flow and volume diffusion mechanism was found to probably control the initial stage of sintering for n_ZnO. It was observed that targets prepared with n_ZnO reach higher densities at significantly lower temperatures (~680 °C),

compared to sm_ZnO (~800 °C) and m_ZnO (> 900 °C). When sintered at temperatures below T_{MSR} for different holding times, submicrometric grains were obtained with controlled grain growth. No significant differences were observed for n_ZnO powder in terms of density when the size of targets was increased (scale-up effect), while for m_ZnO and sm_ZnO a delay in the densification was observed which is related with the higher sinterability of n_ZnO powder.

Undoped and Al-doped ZnO nanostructured powders with high chemical homogeneity was successfully synthesized by a novel non-equilibrium synthesis method which combines high pressures, high temperatures and ultrafast quenching providing an economical large-scale nanopowder synthesis method. During the synthesis, free atoms of the used precursors are firstly released and then rearranged with oxygen atoms coalescing and crystallizing into ZnO or Al-doped ZnO during the expansion of the detonation process. The synthesized powders present a controlled composition and morphology independent of the doping level. The nanopowders have a tri-modal particle size distribution after synthesis composed by individual round and rod shaped particles and some aggregates that were formed during the quenching of the particles. The mean particle size attained is between 40 – 45 nm with a SSA around 8.0 m^2g^{-1}. Due to the high temperatures reached during the synthesis, besides the main phase wurtzite (ZnO) a secondary phase ($ZnAl_2O_4$) is also identified in Al-doped ZnO synthesized powders suggesting that Al^{3+} ions occupy the position of Zn^{2+} ions in the ZnO lattice as a substitutional atom reaching the solubility limit during synthesis, reacting the remaining Al with ZnO to form $ZnAl_2O_4$. A thermal treatment at 500 – 650 °C for 1 – 2 h allows the removal of organic material inherent to the synthesis, keeping their properties almost unchanged. Also inherent to the synthesis process is the agglomeration of powders, being the sinterability improved by a deagglomeration step. These de-agglomerated powders can be sintered at 1100 – 1250 °C depending on the Al concentration with final densities above 98 % of theoretical density. Dilatometric studies performed in samples prepared with the synthesized powders after disaggregation demonstrate their high sinterability. The activation energy for densification in the earlier stage of sintering varies with the increase in Al from 295 $kJ.mol^{-1}$ to 435 – 531 $kJ.mol^{-1}$. In the intermediate stage, the activation energy of undoped ZnO reduces with densification at lower relative densities ($\rho_r \leq 75$ %), suggesting a surface diffusion mechanism that competes with densification. For Al-doped ZnO the Q_{int} values are unchanged with ρ_r indicating that the densification of AZO is controlled by volume diffusion in the range 62 % $\leq \rho_r \leq$ 85 %. A combination of grain boundary sliding mechanism and volume diffusion mechanism seems to control the shrinkage during the initial sintering stage of undoped ZnO. With the Al doping, the exponent n_1 increases to ~ 1.10 – 1.30 in the initial stage of sintering, indicating a densification process controlled by volume diffusion.

4.4. References

[1] Chu, M. T., Rahaman, M. N., De Jonghe, L. C. and Brooke, R. J., Effect of heating rate on sintering and coarsening. *J. Am. Ceram. Soc.*, 1991, **74**(6) 1217-25.

[2] Johnson, D. L., New method of obtaining volume, grain boundary, and surface diffusion coefficients from sintering data. *J. Appl. Phys.*, 1969, **40**(1) 192-200.

[3] Woolfrey, J. L., Bannister, M. J., Nonisothermal techniques for studying initial-stage sintering. *J. Am. Ceram. Soc.*, 1972, **55**(8) 390-4.

[4] Young, W. S. and Cutler, I. B., Initial sintering with constant rates of heating. *J. Am. Ceram. Soc.*, 1970, **53** 659-63.

[5] Ewsuk, K. G. and Ellerby, D. T., Analysis of nanocrystalline and microcrystalline ZnO sintering using master sintering curves. *J. Am. Ceram. Soc.*, 2006, **89**(6) 2003-9.

[6] Groza, J., R., Nanocrystalline powder consolidation methods. In: Koch CC, editor. *Nanostructured materials: processing and potential applications*. Norwich, NY: Noyes Publications/William Andrew Publishing; 2002. p. 78–115.

[7] Hynes, A. P., Doremus, R. H. and Siegel, R. W., Sintering and characterization of nanophase zinc oxide. *J. Am. Ceram. Soc.*, 2002, **85**(8) 1979-87.

[8] Qin, X. J., Shao, G. J., Liu and Wang, W. K., Sintering characteristics of nanocrystalline ZnO. *J. Mater.Sci.,* 2005, **40**(18) 4943-6.

[9] Lange, F., Powder processing science and technology for increased reliability. *J. Am. Ceram.Soc.*, 1989, **72**(1) 3-15.

[10] Senos, A. M. R., Sintering kinetics in open porosity stages of zinc oxide. Ph.D. thesis, University of Aveiro, Aveiro, Portugal, 1993 (in potuguese).

[11] Senda, T. and Bradt, R. C., Grain growth in sintering ZnO and ZnO-Bi_2O_3 ceramics. *J. Am. Ceram.Soc.*, 1990, **73**(1) 106-14.

[12] Gupta, T. K. and Coble, R. L., Sintering of ZnO: I, densification and grain growth. *J. Am. Ceram. Soc.*, 1968, **51**(9) 521-5.

[13] Han, J., Senos, A. M. R. and Mantas, P. Q., Nonisothermal sintering of Mn doped ZnO. *J. Eur. Ceram.Soc.*, 1999, **19**(6-7) 1003-6.

[14] Kumar, K, P., Keizer, K., Burggraaf, A. J., Okubo, T., Nagamoto, H. and Morooka, S., Densification of nanostructured titania assisted by a phase transformation. *Nature*, 1992, **358** 48–51.

[15] Mazaheri, M., Zahedi, A. M. and Sadrnezhaad, S. K., Two-step sintering of nanocrystalline ZnO compacts: effect of temperature on densification and grain growth. *J. Am. Ceram. Soc.,* 2008, **91**(1) 56-63.

[16] Liu, C., Wang, X., Jiang, Y., Wang, Y. and Hao, S., Progress on grain growth dynamics in sintering of nano-powders. *Rare Met.,* 2006, **25**(6) 471-5.

[17] Mazaheri, M., Zahedi, A. M., Haghighatzadeh, M. and Sadrnezhaad, S. K., Sintering of titania nanoceramic: Densification and grain growth. *Ceram. Int.*, 2009, **35**(2) 685–91.

[18] Kamalianfar, A., Halim, S. A., Naseri, M. G., Navasery, M., Din, F. U., Zahedi, J. A. M., Lim, K. P., Saion, E. B., Chen, C. K. and Monfared, A. L., Synthesis and characterization of ZnO flower-like multisheets grown on metal buffer layer. *Int. J. Electrochem. Sci.*, 2013, **8** 7724-33.

[19] Baruah, S. and Dutta, J., Hydrothermal growth of ZnO nanostructures. *Sci. Technol. Adv. Mater.*, 2009, **10**(1) 013001 (18pp).

[20] Huang, S., Xiao, Q., Zhou, H., Wang, D. and Jiang, W., Hydrothermal synthesis and conductive properties of Al-doped ZnO rod-like whiskers. *J. Alloys Compd.*, 2009, **486**(1-2) L24-L26.

[21] Ahmad, M., Ahmed, E., Zhang, Y., Khalid, N.R., Xu, J., Ullah, M. and Hong, Z., Preparation of highly efficient Al-doped ZnO photocatalyst by combustion synthesis. *Curr. Appl Phys.*, 2013, **13**(4) 697-704.

[22] Hartner, S., Ali, M., Schulz, C., Winterer, M. and Wiggers, H., Electrical properties of aluminum-doped zinc oxide (AZO) nanoparticles synthesized by chemical vapor synthesis. *Nanotechnol.*, 2009, **20**(44) 445701 (8pp).

[23] Naumkin, A. V., Kraut-Vass, A., Gaarenstroom, S. W. and Powell, C. J., NIST X-ray Photoelectron Spectroscopy Database, NIST Standard Reference Database 20, Version 4.1

[24] Musat, V., Fortunato, E., Purica, M., Mazilu, M., Botelho do Rego, A. M., Diaconu, B. and Busani, T., Multifunctional zinc oxide nanostructures for a new generation of devices. *Mater. Chem. Phys.*, 2012, **132**(2–3), 339-46.

[25] Hong, W. and De Jonghe, L. C., Reaction sintering of ZnO-Al_2O_3. *J. Am. Ceram. Soc.*, 1995, **78**(12) 3217-24.

[26] Zhang, Y., Wang, W., Tan, R., Yang, Y., Zhang, X., Cui, P. and Song, W. The solubility and temperature dependence of resistivity for aluminum-doped zinc oxide ceramic. *Int. J. Appl. Ceram. Technol.*, 2011, **9**(2) 374-81.

[27] Shirouzu, K., Kawamoto, T., Enomoto, N. and Hojo, J., Dissolution behavior of Al and formation process of $ZnAl_2O_4$ phases in Al_2O_3-doped ZnO sintered bodies. *Jpn. J. Appl. Phys.*, 2010, **49**(1) 010201-010201-3.

[28] Calado, J.M. and Antunes, E.M., Nanometric-sized ceramic materials, process for their synthesis and uses thereof, patent WO 2009144665 (2009).

[29] Minami, T., Oda, J.-ichi, Nomoto, J.-ichi and Miyata, T., Effect of target properties on transparent conducting impurity-doped ZnO thin films deposited by DC magnetron sputtering. *Thin Solid Films,* 2010, **519**(1) 385-90.

[30] Huang, H. S., Tung, H. C., Chiu, C. H., Hong, I. T., Chen, R. Z., Chang, J. T., *et al.*, Highly conductive alumina-added ZnO ceramic target prepared by reduction sintering and its effects on the properties of deposited thin films by direct current magnetron sputtering. *Thin Solid Films*, 2010, **518**(21) 6071-5.

[31] Patterson, A. L., The Scherrer formula for X-ray particle size determination. *Phys. Rev.*, 1939, **56**(10) 978-82.

[32] Calado, J.M. and Antunes, E.M., Nanocrystaline spherical ceramic oxides, process for their synthesis and use thereof, patent WO 2009040770 (2009).

[33] Du, S., Tian, Y., Liu, H., Liu, J. and Chen, Y., Calcination effects on the properties of gallium-doped zinc oxide powders. *J. Am. Ceram. Soc.*, 2006, **89**(8) 2440-3.

[34] Medvedovski, E., Alvarez, N., Yankov, O. and Olsson, M.K., Advanced indium-tin oxide ceramics for sputtering targets. Ceram Int., 2008, **34**(5) 1173-82.

[35] Zhu, G., Zhi, Li., Yang, H., Xu, H. and Yu, A., Effect of target density on microstructural, electrical, and optical properties of indium tin oxide thin films. *J.Electron. Mater.*, 2012, **41**(9) 2376-9.

[36] Han, J., Mantas, P. Q. and Senos, A. M. R., Densification and grain growth of Al-doped ZnO. *J. Mater. Res.*, 2001, **16**(2) 459-68.

[37] Han, J., Mantas, P. Q. and Senos, A. M. R., Sintering kinetics of undoped and Mn-doped zinc oxide in the intermediate stage. *J. Am. Ceram. Soc.*, 2005, **88**(7) 1773-8.

Chapter 5. AZO ceramic sputtering targets and sputtered thin films: production and characterization

In this chapter are presented the results regarding the use of INNOVNANO synthesized powders (described in the previous chapter) in the manufacturing of AZO ceramic targets for sputtering deposition. Here is presented and discussed in detail the fabrication of the targets considering the influence of several processing parameters on its final properties. These targets have been also compared with commercially available ones from different suppliers. The properties of sputtering targets and those of corresponding thin films deposited by magnetron sputtering are also compared and discussed. For each target composition, the deposition parameters were optimized and the sputtered thin films analyzed to evaluate the chemical, structural, optical and electrical characteristics. The optimized films were applied in the production of several optoelectronic devices and their performances are also shown.

The results presented in this chapter were partially published in the following peer reviewed journals:

- Neves, N., Barros, R., Antunes, E., Calado, J., Fortunato, E., Martins, R. and Ferreira, I., Aluminum doped zinc oxide sputtering targets obtained from nanostructured powders: Processing and application. *J. Eur. Ceram. Soc*., 2012, **32**(16) 4381-91.
- Neves, N., Barros, R., Lagoa, A., Calado, J., Fortunato, E., Martins, R. and Ferreira, I., Effect of the Al content in ZnO ceramic targets and in the corresponding thin films deposited at room temperature by rf magnetron sputtering. Submitted to the *Journal of European Ceramic Society.*
- Isherwood, P. J. M., Neves, N., Bowers, J. W., Newbatt, P. and Walls, J. M., High quality aluminium doped zinc oxide target synthesis from nanoparticulate powder and characterization of sputtered thin films. *Thin Solid Films*, 2014, **506** 108-14.
- Araújo, A., Barros, R., Mateus, T., Gaspar, D., Neves, N., *et al.*, Role of a disperse carbon interlayer on the performances of tandem a-Si solar cells. *Sci. Technol. Adv. Mater.*, 2013, **14**(4) 045009.
- Loureiro, J., Neves, N., Barros, R., Mateus, T., Santos, R., *et al.*, Transparent aluminium zinc oxide thin films with enhanced thermoelectric properties. *J. Mater. Chem. A*, 2014, **2**(18) 6649-55.
- Barros, R., Neves, N., Calado, J., Barquinha, P., G-Berasategui, E., Bayon, R., Martins, R., Ferreira, I. and Fortunato, E., Al-doped ZnO transparent conducting oxides using low cost powder compacted nanostructured ceramic targets. Submitted to the *Journal of Physics D: Applied Physics*.

5.1. Conventional sintering

The pressure-assisted sintering techniques (HP or HIP) are the most used in the production of high density AZO ceramic targets. For this specific application, conventional sintering (CS) presents

densification problems at low sintering temperatures being required extremely high temperatures to reach acceptable densification levels. Properties like final density, chemical, structural and morphological homogeneity or electrical characteristics of the targets are strongly affected by high sintering temperatures. However as shown in the previous chapter, INNOVNANO AZO powders can be sintered at lower temperatures with high final densities opening the possibility to the manufacturing of AZO targets by CS.
This subsection shows the results concerning the production, optimization and characterization of AZO ceramic targets by CS and its correlation with the corresponding thin films deposited by RF magnetron sputtering.

5.1.1. Green density effect on sintering

The processing stages of primary powders before sintering affect considerably the densification and physical properties of the sintered ceramics [1, 2]. In this context, the pressing stage plays a very important role, especially in the preparation of high quality ceramic parts of considerable dimensions. The effect of the green density (GD) on the sintering behavior of ceramics has been widely investigated [2, 3]. Krell *et al.* [2] compared the sintered density of submicron alumina prepared by uniaxial pressing (UP) and cold isostatic pressing (CIP) in addition to UP. The author observed a reduction in the sintering temperature and an increase in the final density of the sintered pieces for high GD compacts (CIPed samples), attributing the enhancement of densification to the higher homogeneity of particle coordination in the CIPed samples. Woolfrey [3] showed that the relative density (ρ_r) of UO_2 powder decrease considerably for compacts with GD below 40 %. The author correlated this behavior with a critical value of the ratio between pore size and particle size, above which pores stabilized and inhibited local shrinkage.

The limitations of UP are well known [4] and mainly related with unsymmetrical density gradients caused by non-uniform pressure inside the compact, and consequent warping and cracking of the compacts during sintering as well as inhomogeneous sintering behavior (more evident for larger parts).

UP was used to prepare the compacts for densification studies of undoped and Al-doped ZnO sintered by CS. However, due to the observed large friction forces between the particles and the die walls (wall friction effects) inherent to the powder characteristics (small particle size and high SSA of the powders), and the limitations of lab scale UP machines, some cracks in the powder compacts were detected above 55 % of TD during ejection. This limitation in terms of particles rearrangement during UP, led us to use CIP after UP at lower pressures in order to reach defects free compacts with improved GD. The main advantage of CIP is that it produces a much more uniform density distribution than does UP [5]. So, the isostatically pressed green compacts present a greater green strength and a more reproducible sintering shrinkage when compared to UP ones. It should be noted that after CIP, the pressure must be released at a sufficiently low rate, as either the pore pressure caused by entrapped air or relaxation of any sticking elastomeric mold can origin damage to the compacts [5].

Throughout this section the used powders were spray-dried without binders or additives. A detailed study regarding the optimization of the starting AZO powder characteristics for UP and/or UP + CIP (atomization stage) is presented in section 5.7.1, emphasizing the flowability and

handling characteristics of the powders (with additives) for industrial use (large sputtering targets production).

To study the effect of compaction pressure on sintering, the green bodies were obtained by UP for lower GDs and by UP followed by CIP for higher degrees of compaction (CIPed samples were primarily uniaxially pressed at 70 MPa). Due to the similarity between the pressing pattern of undoped ZnO and Al-doped ZnO (0.5 – 2.0 wt. % Al_2O_3) powders, only the variation of density versus compacting pressure for AZO_D (98:2 wt. % ZnO:Al_2O_3) is presented. It should be noted that after proper adjustments in the range of temperatures studied for each composition, all the powders exhibit similar behaviors, and the obtained conclusions concerning the effect of GD on densification can be generalized to the other investigated compositions.

Fig. 5.1 illustrates the ρ_r as a function of compaction pressure (different GDs) of AZO_D compacts sintered at 1150 °C for 2h. The major variation in terms of GD is observed for compaction pressures between 20 and 150 MPa with an increase of GD from 35 to 59 % of TD. The sintered samples show a similar trend, where for the same range of compaction pressure (20 – 150 MPa), ρ_r increases from 71.4 to 95.2 % of TD. Higher compaction pressures doesn´t change considerably both GD and ρ_r, with GD values between 61 and 66 % of TD, and ρ_r in the range of 95.8 – 97.7 % of TD.

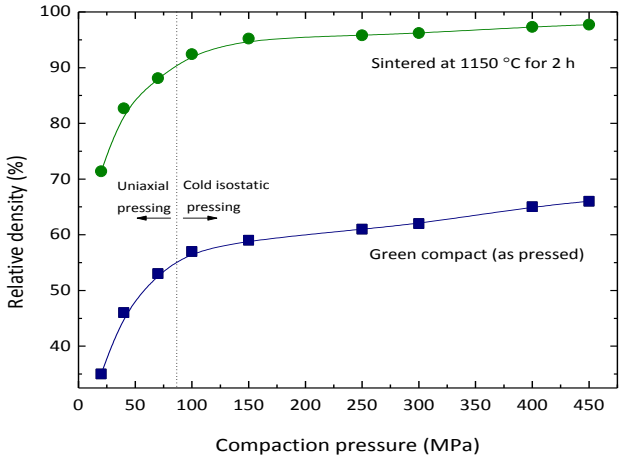

Fig. 5.1. *Variation of density versus compaction pressure for as-pressed AZO_D (GD) and AZO_D sintered at 1150°C for 2 h.*

Fig. 5.2 shows the influence of sintering temperature on the densification of AZO_D powder compacts prepared with three different green densities (GD = 46, 53 and 62 % of TD). The targets were sintered under nonisothermal conditions (in a laboratory furnace) at temperatures between 1000 and 1500 °C and a constant holding time (HT) of 2 h. For sintering temperatures up to 1200 °C the final density of the targets is strongly dependent on the GD and the enhancement in density is substantial. At 1100 °C, the 46 % and 53 % TD AZO samples reached a quite low final density (74.3 and 79.7 % TD) when compared to the one obtained by CIP (~90 % TD). High relative densities (>95 % TD) can be achieved at temperatures above 1150 °C using “CIPed” samples (GD = 62 % TD), comparing to the targets prepared with 53 and 46 % TD, that reached ρ_r of 88.1 and 82.7 %, respectively, at 1150 °C. For higher temperatures (> 1250 °C) all the samples have ρ_r above 95% resulting in the convergence of densification curves of both set of samples to the same

value (near the TD). At temperatures above 1400 °C, ρ_r decrease slightly independently of GD. This behavior has been identified by other authors [6, 7], being attributed to the volatilization of ZnO at higher temperatures.

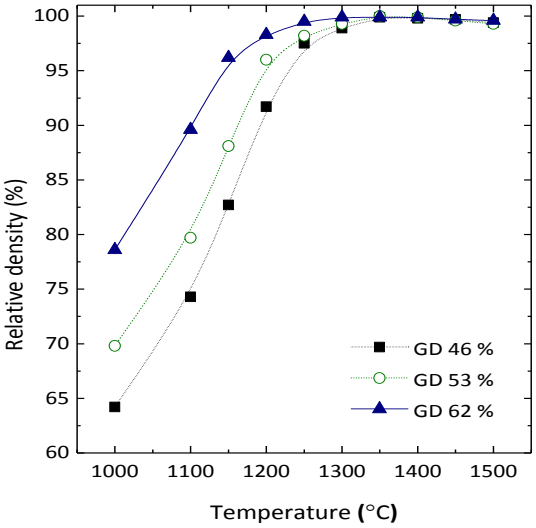

Fig. 5.2. *Influence of sintering temperature and GD on ρ_r of AZO_D powder (98:2 wt. % ZnO:Al_2O_3) at a CHR of 5 °C.min^{-1}.*

Fig. 5.3 shows the weight loss as a function of sintering temperature (Fig. 5.3 a)) and HT (Fig. 5.3 b)) for AZO_D samples. This composition was chosen taking into account the higher sintering temperatures needed to reach high densities with AZO_D. Between 1100 °C and 1300 °C the weight loss remains approximately constant at ~1.5 %, agreeing with the weight loss observed in TG analysis in the range 500 – 800 °C (Fig. 4.25). At 1350 °C, the weight loss increases slightly to ~1.7 %, while for sintering temperatures ≥ 1400 °C it raises to values of ~3 %. The influence of HT was investigated at 1200 °C, 1250 °C and 1300 °C for sintering times in the range 2 – 16 h. No influence of HT on weight loss was observed at temperatures < 1300 °C. However, at 1300 °C, the weight loss of the AZO_D samples increases substantially for sintering times of 8 h and mainly for 16 h. Thus, the INNOVNANO AZO targets must be sintered up to 1300 – 1350 °C and no longer than 4 h.

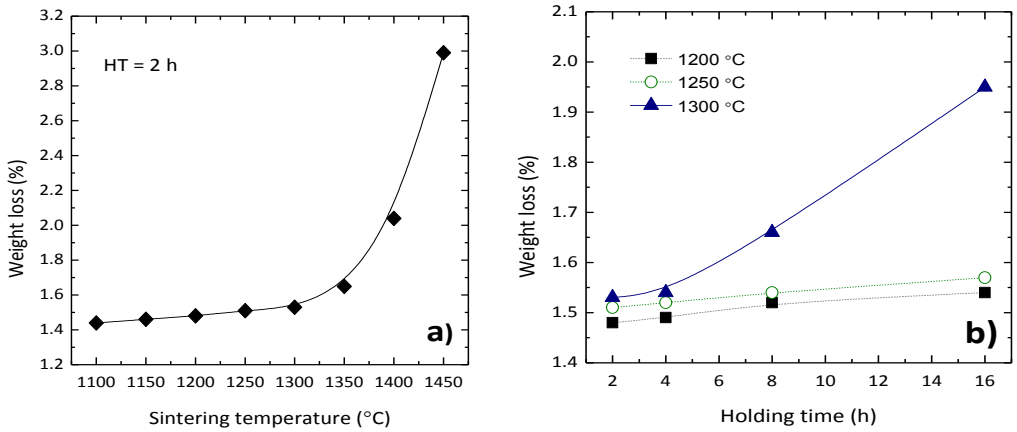

Fig. 5.3. *Weight loss of AZO_D samples as a function of a) sintering temperature (1100 – 1450 °C) and b) HT (2 – 16 h).*

The influence of HT and GD in densification during sintering was studied using different holding times (2, 4, 8 and 16 h) at 1100, 1150 and 1200 °C (Fig. 5.4 a), b) and c), respectively). The temperatures were chosen according to the T_{MSR} obtained from dilatometer analysis (~1220 °C) (Fig. 4.24 and Fig. 4.26), and the final densities presented in Fig. 5.2, where is observed a greater variation in ρ_r with temperature rise.

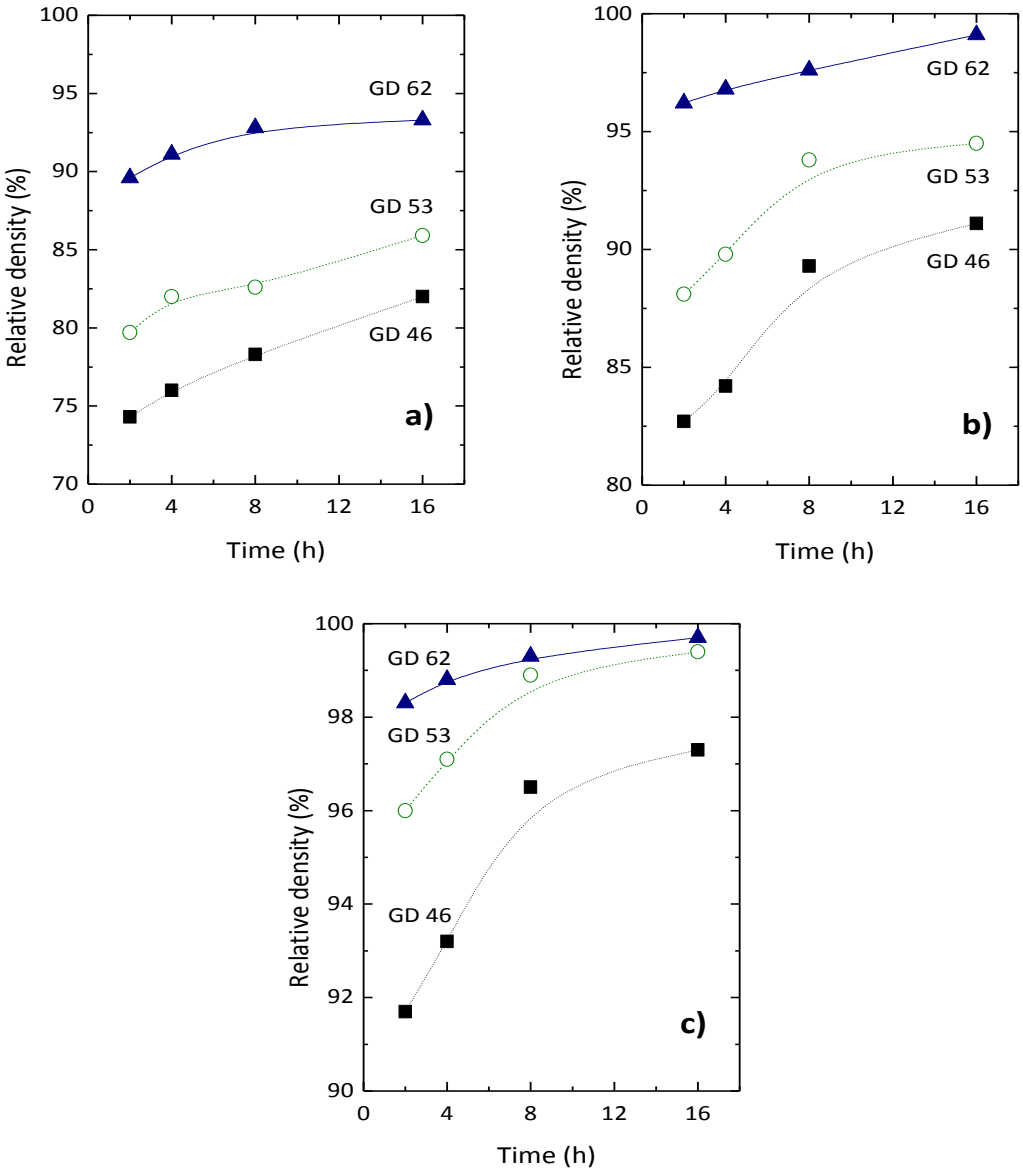

Fig. 5.4. *Influence of HT and GD at a) 1100 °C, b) 1150 °C and c) 1200 °C on ρ_r of INNOVNANO AZO_D powder (98:2 wt. % ZnO:Al_2O_3).*

HT has a substantial influence on ρ_r of targets made with smaller compaction degrees, mainly for HT up to 8 h. Samples with a GD of 46 % and 53 % sintered at 1100 °C show an increase in ρ_r from 74.3 to 82 % and from 79.7 to 85.9 % respectively, ranging HT between 2 h and 16 h. On the other side, ρ_r of "CIPed" targets (62 % TD) has a minor dependence on HT (from 89.6 (2 h) to 93.3 % TD (16 h)). The targets sintered at 1150 °C show a similar trend. In this case, ρ_r > 99 % can be achieved by sintering "CIPed" samples for 16 h (Fig. 5.4 b)). At 1200 °C (Fig. 5.4 c)), all the targets have final densities above 90% of TD independent on the HT.

Based on the above results, for CS, it was decided to consider ~62 % of TD (~3.47 g.cm^{-3}) (UP at 70 MPa followed by CIP at 300 MPa) the standard value for the GD of the AZO compacts presented henceforth in this research work.

5.1.2. Grain growth

In order to avoid possible defects in the targets microstructure that can cause mechanical failure or degradation of their electrical properties as well as the reduction of the sputtered films quality, is desired to have a controlled grain growth during sintering [8-11]. A small and homogeneous grain size, contributes to reduce the inter grain defects and induces a constant sputter rate over the entire target surface, producing films with uniform thickness and guarantying a longer lifetime of targets [9]. Fig. 5.5 shows the variation of grain size (G_S) and ρ_r of AZO_D samples as a function of sintering temperature.

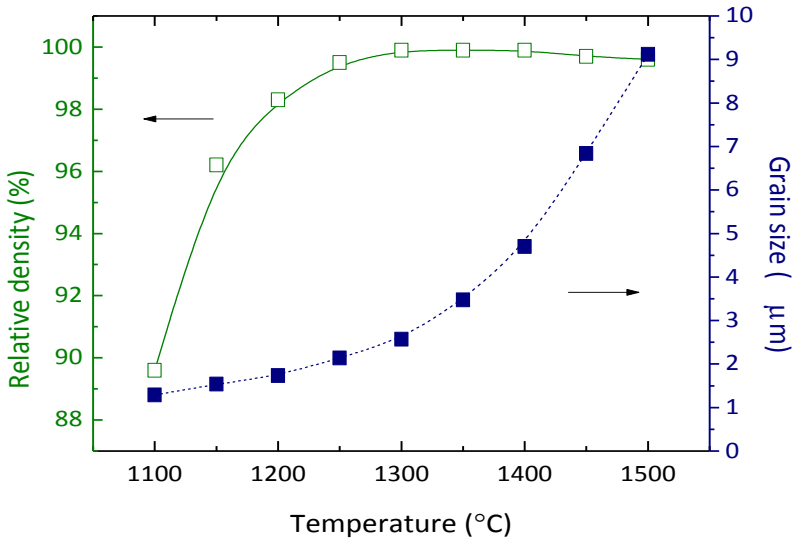

Fig. 5.5. *Relative density and grain size of Al-doped ZnO (98:2 wt. %) compacts sintered at different temperatures and a constant holding times.*

A nonlinear grain growth with temperature is observed, being identified two distinct regions: The first one, for sintering temperatures between 1100 and 1250 °C, in which G_S increases slightly (from 1.29 to 2.14 µm), and the second region, above 1250 °C, where the G_S increase from 2.87 to 9.12 µm. These results are consistent with the shrinkage rate curve of AZO_D presented previously (Fig. 4.26 b)) and the evolution of ρ_r with temperature of the sintered compacts (Fig. 5.3). The T_{MSR} (~1220 °C) delineates the region where the sintering kinetic is dominated by densification or non-densification mechanisms [12].

The effect of HT in the final G_S of the sintered targets was also evaluated considering the temperatures range from 1100 – 1300 °C and the same HT variation from Fig. 5.4. Despite the substantial increase in ρ_r with HT (Fig. 5.4), no significant grain growth was observed at 1100 °C and 1150 °C (not shown here) for AZO_D powder compacts. At temperatures between 1200 °C – 1300 °C the densities of the AZO_D samples are closer to the TD and the grain growth becomes more evident with the increase of HT (presented and discussed further (section 5.1.5.2) in parallel with the other studied compositions).

5.1.3. Structural characterization

The XRD patterns of "CIPed" Al-doped ZnO targets with GD ≈ 62 % sintered in air at different temperatures and holding times are shown in Fig. 5.6. Besides the three more pronounced peaks attributed to (100), (002) and (101) planes of ZnO (wurtzite), a secondary phase $ZnAl_2O_4$ (gahnite spinel) for sintered targets between 1150 and 1400 °C (Fig 5.6 (right)) is also present, revealing that AZO sintered targets do not consist of a single-phase structure, but a double-phase structure. This is in good agreement with Hong and Jonghe´s results [13] of a $ZnAl_2O_4$ spinel phase formation between 800 and 1000 °C at a CHR of 4 °Cmin^{-1}.

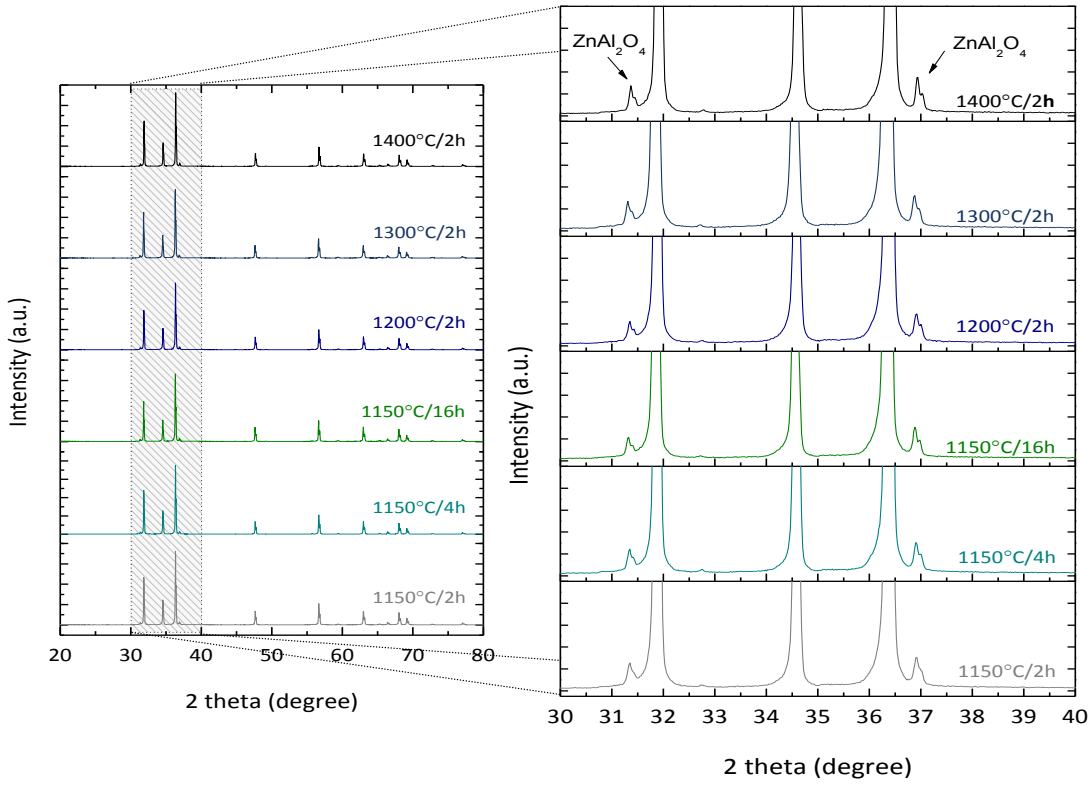

Fig. 5.6. *X-ray diffraction patterns of AZO 98:2 wt. % ceramic targets (62 % GD) at RT (left) showing wurtzite as the main phase of AZO targets; Detail illustrating the $ZnAl_2O_4$ spinel phase peak with HT and sintering temperature (right).*

When Al_2O_3 is added to ZnO particles a solid solution is formed due to the diffusion of Al_2O_3 into the ZnO lattice. The spinel phase ($ZnAl_2O_4$) is formed for a doping concentration above the solubility limit of Al in ZnO [14, 15] (more details about the solubility limit of Al in ZnO and its determination will be presented in section 5.1.5.3).

From XRD results, HT or temperature rise (between 1150 and 1400 °C) seems to have no, or very little, influence on the spinel phase concentration. The quantification analysis of spinel phase for all analyzed targets gives approximately 3.4 wt. % $ZnAl_2O_4$, which is consistent with theoretical values considering that we are working with a constant doping level above the solid solubility of Al in ZnO [7, 16].

5.1.4. Morphological characterization

The SEM images of AZO_D (98:2 wt. % $ZnO:Al_2O_3$) ceramic targets sintered at different temperatures (1100 – 1400 °C) for 2 h are displayed in Fig. 5.7 a) – d).

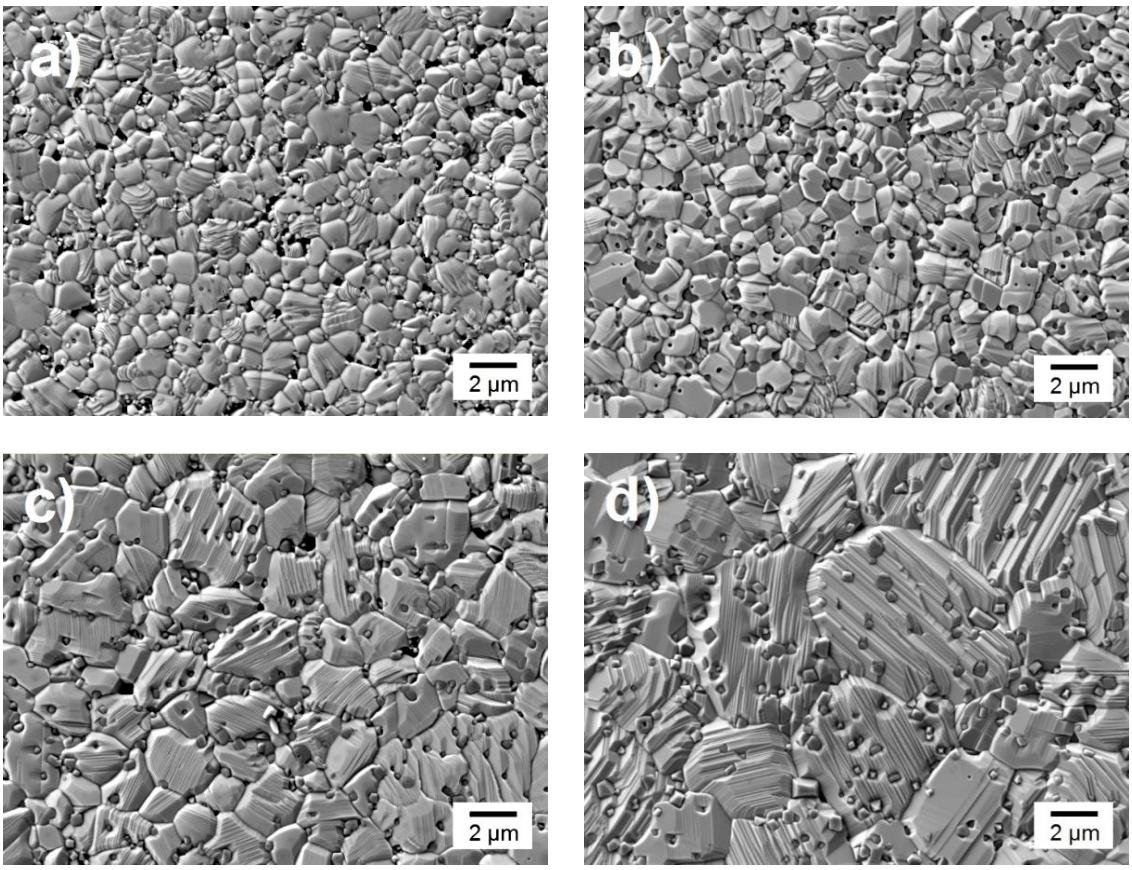

Fig. 5.7. *SEM micrographs of Al-doped ZnO 98:2 wt. % samples sintered for 2 h at: a) 1100 °C, b) 1200 °C, c) 1300 °C and d) 1400 °C.*

Besides the grain growth of the main phase, also an evolution of the $ZnAl_2O_4$ phase size and its position in the microstructure is observed with the increase of the sintering temperature. $ZnAl_2O_4$ spinel phase (darker spots confirmed by EDS analysis) appeared well dispersed inside the ZnO matrix for all sintered targets and become more visible for higher sintering temperatures (growing of $ZnAl_2O_4$ crystals with temperature). The secondary phase $ZnAl_2O_4$ forms preferentially in grain boundaries during sintering process, inhibiting the grain growth and reducing the driving force for sintering of Al-doped ZnO composites [16, 17]. However, for higher temperatures the number of grain boundaries decreases substantially with grain growth and a part of the spinel phase is embedded within the grains (Fig. 5.7 d)) (a more detailed description about the formation of the spinel phase and its effect on densification and grain growth is presented in section 5.1.5.2).

5.1.5. Effect of aluminum doping concentration

In section 4.2 from chapter 4, we have shown that INNOVNANO AZO powders have similar physical, structural and morphological characteristics after disaggregation independent on the aluminum content of the powders (0.5 – 2.0 wt. % Al_2O_3). Despite the real density which reduces

slightly with the amount of aluminum added, no significant differences were observed in terms of mean particle size, specific surface area (SSA) or crystallite size of the powders.

5.1.5.1. Densification

The influence of aluminum content on densification of several compacts sintered for 2 h at different temperatures is shown in Fig. 5.8.

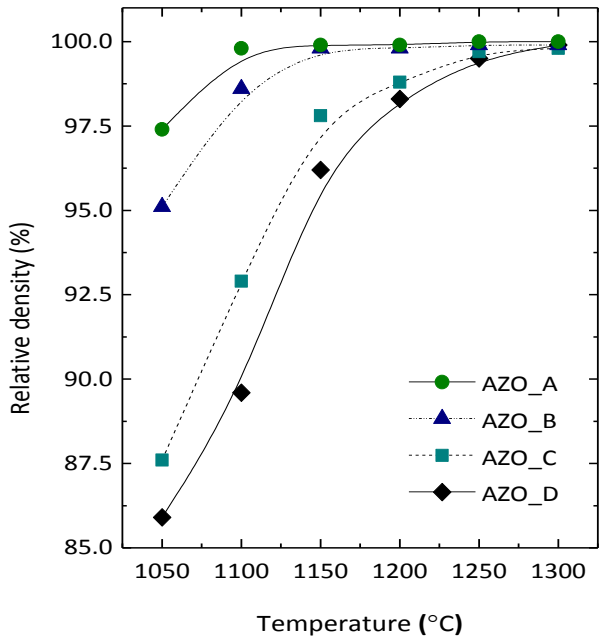

Fig. 5.8. *Effect of aluminum content (0.5 – 2.0 wt. % Al_2O_3) on ρ_r of Al-doped ZnO compacts sintered at different temperatures and a constant HT of 2 h.*

Comparing to the literature, final densities above 95 % of TD can be achieved, by CS, at lower sintering temperatures (< 1200 °C) independently of composition. This is attributed to the high sinterability of INNOVNANO nanostructured AZO powders. As it is well known, sintering is enhanced as particle size of the powders is reduced. According to Herring´s scaling law [18], the particle size is proportional to the reciprocal sintering rate, i.e. the smaller the particles the faster the sintering. These powders present a bi-modal PSD composed by small nanoparticles with a large fraction of atoms at grain boundaries which improves the diffusivity between particles. Moreover, its high SSA promotes sinterability at lower temperatures [19-22]. By increasing the aluminum content, the final densities of INNOVNANO AZO targets are reduced within the sintering temperatures range 1050 – 1200 °C. This delay in densification is in good agreement with the linear shrinkage and shrinkage rate curves obtained for each studied composition, as shown in Fig. 4.26 a) and b). On the other hand, for sintering temperatures above 1200 °C, ρ_r rises to 98 % independently of aluminum content.

The influence of HT and aluminum content on the densification at different sintering temperatures is shown in Fig. 5.9. The temperatures were selected according to the maximum shrinkage rate temperatures obtained from dilatometer tests, for each composition (Fig. 4.26 a) and b)), and the final densities presented in Fig. 5.8. There, we observe a great influence of both HT and composition on the final density.

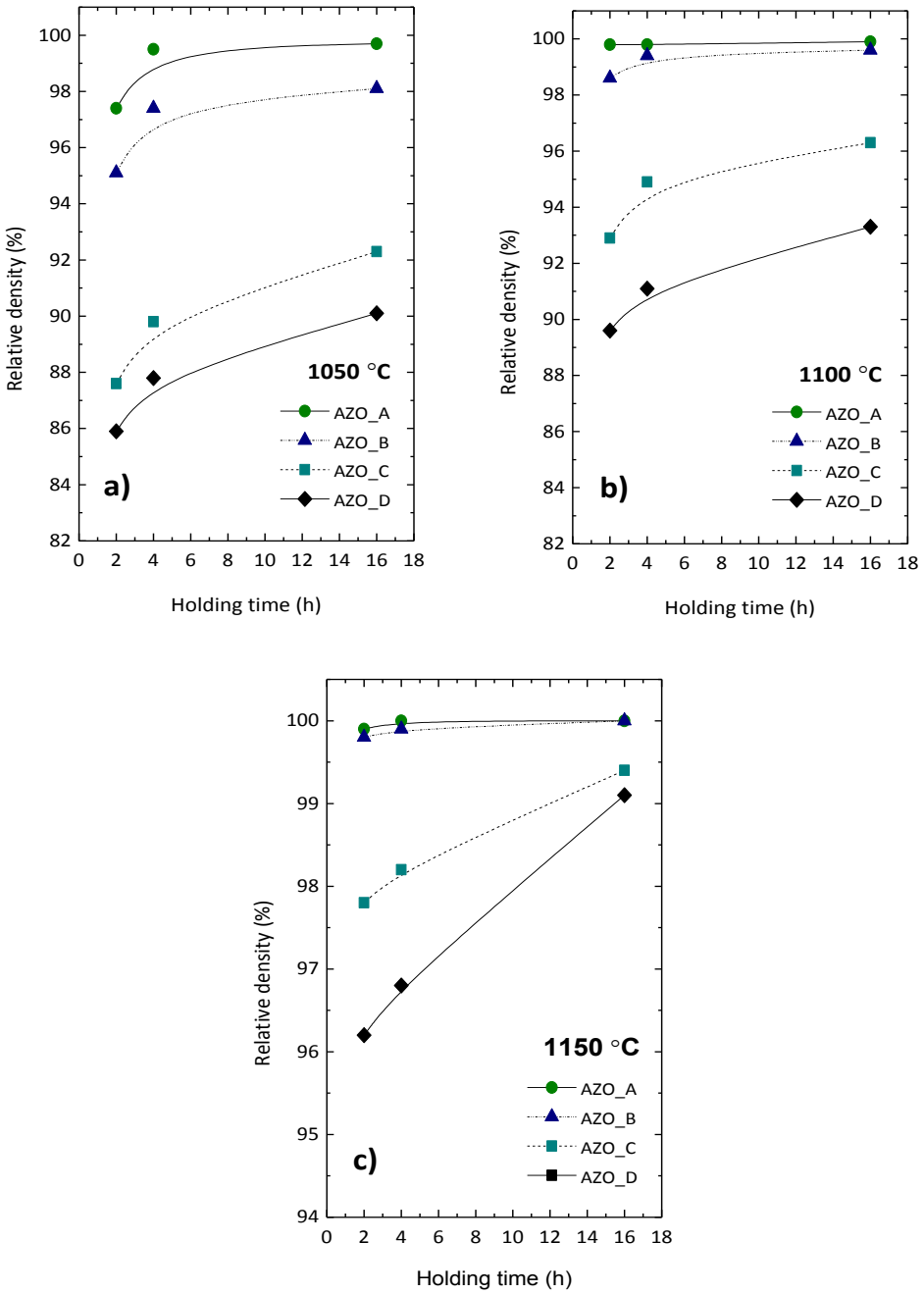

Fig. 5.9. *Influence of HT and aluminum content (0.5 – 2.0 wt. % Al_2O_3) on ρ_r of Al-doped ZnO compacts sintered at a) 1050 °C, b) 1100 °C and c) 1150 °C respectively.*

From the results shown in Fig. 5.9 we conclude that targets with 0.5 and 1.0 wt. % Al_2O_3 easily achieve densities above 95 % of TD, independently of sintering temperature (1050 – 1150 °C) and HT (2 – 16 h). However, for concentrations ≥ 1 % (AZO_C and AZO_D targets), the sintering temperatures must be above 1150 °C to reach such high densities. HT plays an important role on the final density of these compositions, which becomes higher for longer sintering times at temperatures between 1050 and 1150 °C. In this temperatures range (especially at 1100 and 1150 °C), AZO_A and AZO_B are already at an advanced phase of the final sintering stage where grain growth becomes predominant instead the densification [7]. Oppositely, AZO_C and AZO_D are

dependent on HT being necessary to increase the sintering temperature and/or HT to reach fully densified AZO targets.

5.1.5.2. Grain growth

Grain size (G_S) measurements as a function of sintering temperature and HT were performed for all the compositions. Fig. 5.10 shows the effect of Al doping concentration on the final G_S of samples sintered at different temperatures and a constant HT of 2 h.

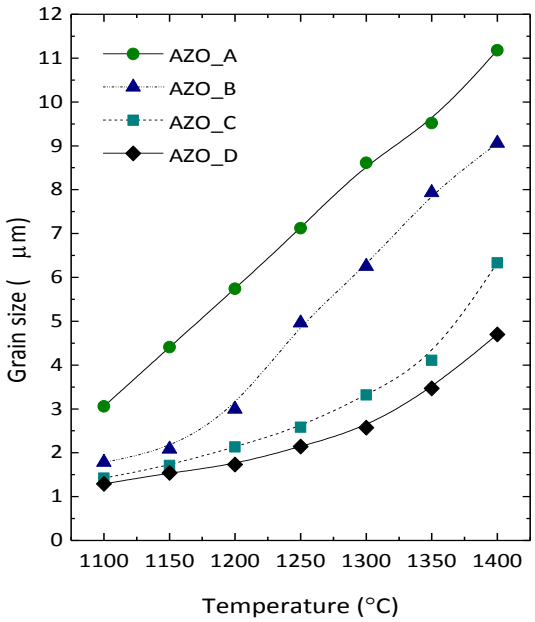

Fig. 5.10. *Effect of aluminum content (0.5 - 2.0 wt. % Al_2O_3) on grain size of AZO compacts sintered at different temperatures and a constant HT of 2 h.*

As expected the G_S raises with sintering temperature for all the compositions used. This variation in final G_S is more evident for lower doping levels (AZO_A and AZO_B) with grain overgrowth starting at substantially lower sintering temperatures. As shown in Fig. 5.10, between 1100 and 1400 °C the grain size of AZO_A enlarge linearly with temperature from 3.06 to 11.18 µm. This study was performed in a range of temperatures above the maximum shrinkage rate temperature (T_{MSR}) observed for AZO_A (~1000°C (Fig. 4.26)) and consequently at temperatures were the sintering kinetic is controlled by non-densification mechanisms where grain growth dominates explaining the observed grain overgrowth. AZO_B (1.0 wt. % Al_2O_3) targets present a small increase from 1.78 to 2.08 µm when temperatures changes from 1100 to 1150 °C and the same linear behavior as AZO_A with a substantial raise in final G_S from 2.99 to 9.06 µm in 1200 – 1400 °C temperature range. For AZO_C and AZO_D are observed two distinct regions (already discussed in section 5.1.2 for AZO_D). G_S of AZO_C is slightly higher than AZO_D throughout the studied temperatures with a significant grain growth above 1300 °C where the final density of the targets is near the TD (Fig. 5.8). These results agree with the linear shrinkage and shrinkage rate curves presented in Fig. 4.26.

The microstructures of AZO samples sintered at 1150 °C for 2 h are shown in Fig. 5.11. Full density targets (>99 % of TD) were reached at 1150°C for Al-doped ZnO with lower doping concentrations

(0.5 and 1.0 wt. % Al_2O_3). Final densities of 96.2 % and 97.8 % were achieved for 2.0 and 1.5 wt. % Al_2O_3, in that order. As mentioned above, G_S became smaller with the increase in Al concentration. Moreover, G_S distribution curves (not presented here) are narrower for high Al content samples allowing obtaining ceramic pieces with improved morphological homogeneity independently of the sintering temperature and HT. The same behavior was observed by Han [23] for specimens with low Al-doping concentrations (0.08 – 1.2 mol % Al) sintered under isothermal conditions at 1200 °C and HTs between 10 and 480 min.

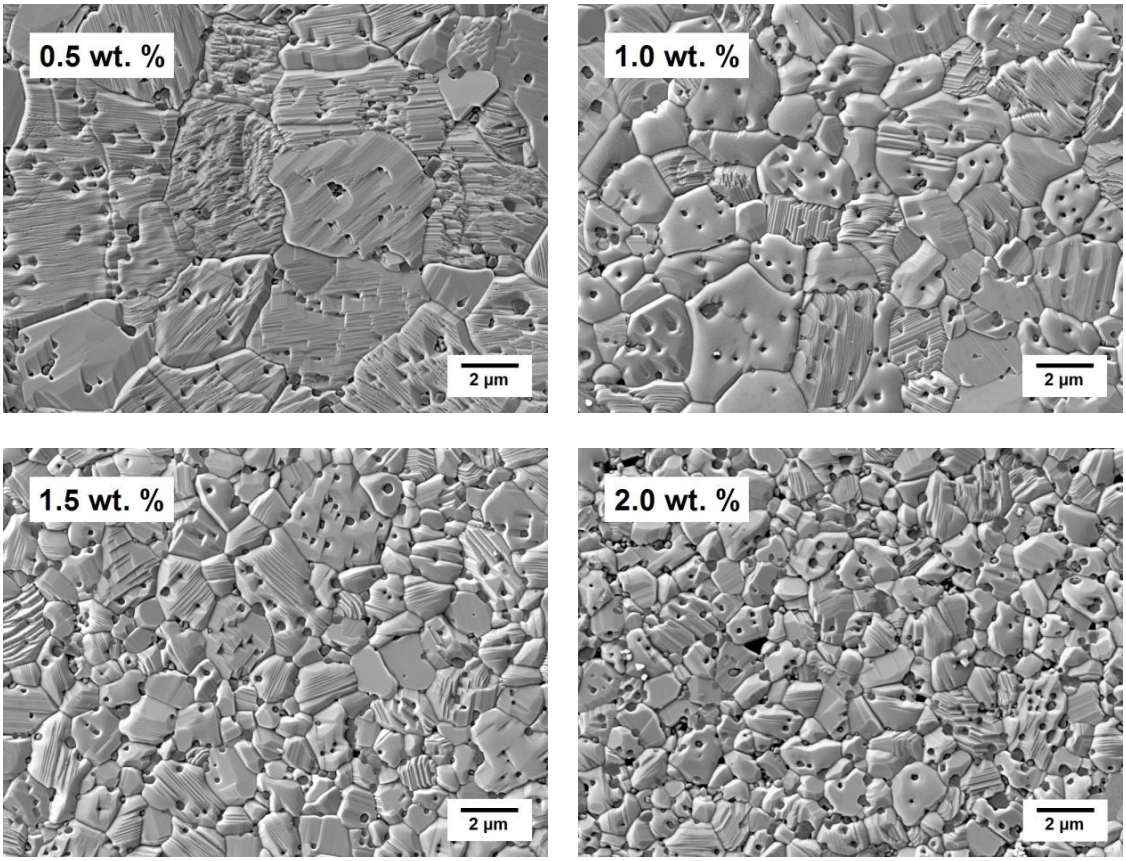

Fig. 5.11. *Microstructural analysis showing the typical morphology of INNOVNANO AZO ceramic targets with different aluminum contents sintered at 1150 °C with 2 h of HT.*

Fig. 5.12 shows the average G_S as a function of HT between 2 and 16 h and sintering temperatures of 1200, 1250 and 1300°C (Fig. 5.12 a), b) and c) respectively). These temperatures correspond to densities near the TD value (Fig. 5.8), and consequently where the non-densification mechanism prevails. Then, in this case, the influence of densification on the grain growth is neglected.

The average G_S increases with HT being more evident for targets prepared with low Al-doping concentrations. The larger amount of $ZnAl_2O_4$ spinel in AZO_C and AZO_D leads to a more evident particle drag effect reducing both the driving force of boundary mobility and the grain growth rate during sintering (details about $ZnAl_2O_4$ dragging effect are presented in the next subsection) [7, 24]. As a consequence G_S is smaller for higher aluminum contents. In general, the average G_S increases substantially when HT changes from 2 to 4 h with a tendency to stabilize if HT is extended to 16 h.

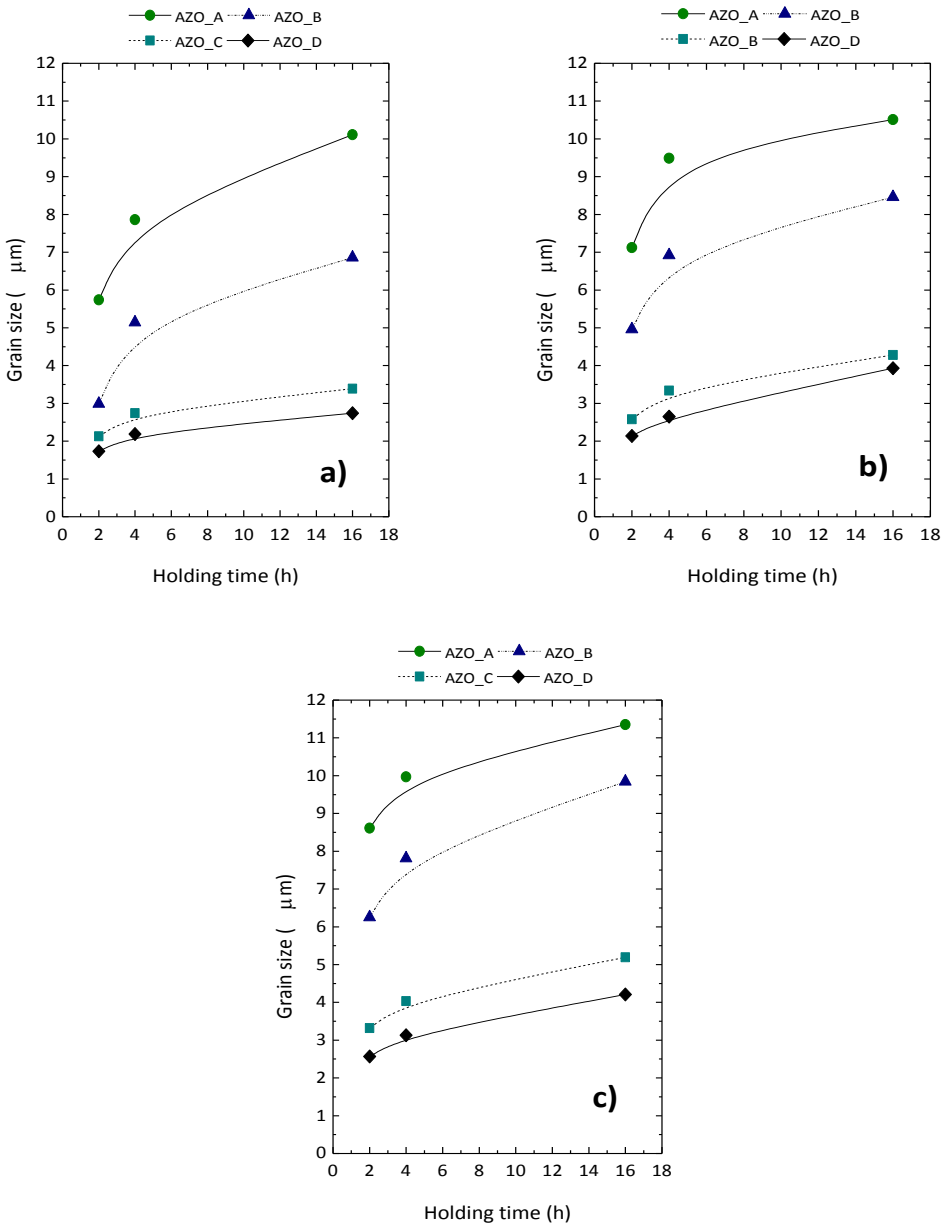

Fig. 5.12. *Influence of HT and doping concentration on grain size of Al-doped ZnO compacts sintered at a) 1200 °C, b) 1250 °C and c) 1300 °C respectively.*

The above results show that with pressure less sintering method is quite difficult the control of grain growth of targets prepared with low Al content. A substantial change is observed in the sintering behavior and intrinsic properties when the aluminum content increases from 1.0 to 1.5 wt. % Al_2O_3.

5.1.5.2.1. Dragging effect of $ZnAl_2O_4$ spinel phase on grain growth

The grain growth inhibition effect due to a secondary $ZnAl_2O_4$ spinel phase formation during the sintering of ZnO has been widely studied [7, 13, 15, 17, 24, 25]. Han *et al.* [7] found an increase in grain growth exponent (smaller grain growth rate) and in the activation energy for grain growth with the increase in the Al doping level attributing this effect to the secondary phase pinning effect. It is well known that second phase particles can inhibit grain growth by pinning or dragging the

migration of grain boundaries. The dragging/pinning effect resultant from the presence of $ZnAl_2O_4$ particles during the sintering of ZnO can be observed in Fig. 5.13. During sintering at low temperatures, the spinel particles are mainly located along the grain boundaries of ZnO, distorting and inhibiting them to migrate. According to the Zener pinning or drag effect theory, the pinning force per unit of volume of the sample, F_P, is given by [26-28]:

$$F_P = \frac{3 f_V \gamma_{GB} \sin\theta \cos\theta}{2 r_S^2} \qquad \text{(eq. 5.1)}$$

where f_V is the volume fraction of the secondary phase particles, γ_{GB} the grain boundary energy per unit area, θ the acute angle between the direction of the tangent of the grain boundary at the intersection point and that of the grain boundary movement, and r_S the secondary phase particle radius. As will be shown in Table 5.1 (section 5.1.5.3), the amount of $ZnAl_2O_4$ spinel phase increases as the Al doping concentration increases. Since r_S value just varies slightly with the increase of the Al content, for a similar sintering temperature and HT, accordingly with eq. 5.1, it becomes more effective the obstruction of grain growth as the Al content increases. On the other hand, the smaller are the $ZnAl_2O_4$ particles at the grain boundaries, the more are the drag forces created [7, 24, 26]. With the increase in the sintering temperature, the $ZnAl_2O_4$ spinel G_S enlarges and its effect on the grain boundary motion reduces. The grains of the main phase ZnO grow and the spinel phase particles are embedded within the ZnO grains (Fig. 5.7). This process is easier for lower Al doping level AZO_A and AZO_B samples due to the lower amount of spinel phase.

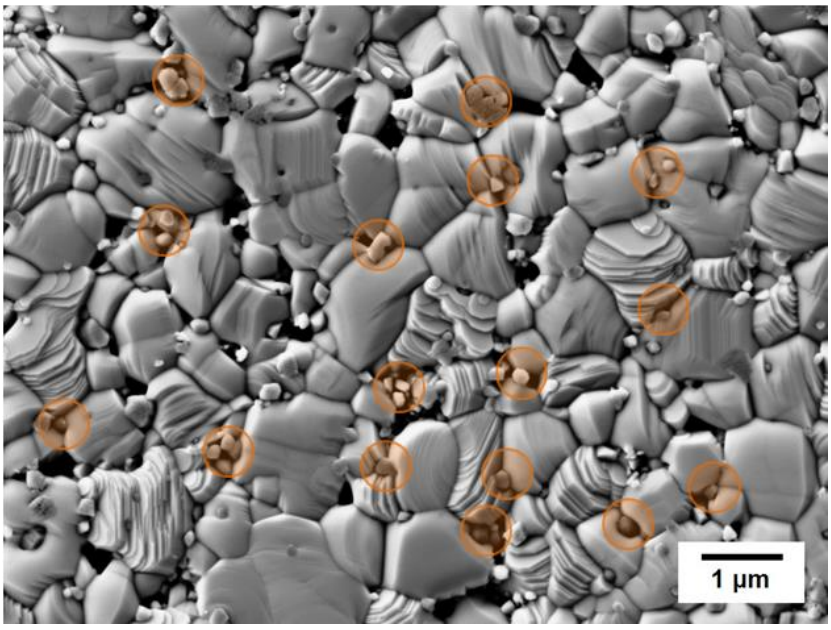

Fig. 5.13. *SEM micrograph of AZO_D (98:2 wt. % ($ZnO:Al_2O_3$)) sintered at 1100°C for 4 h – drag effect caused by $ZnAl_2O_4$ inclusions (some of them indicated by circles).*

As stated in section 2.11.1, during sintering the densification occurs by the movement of the pore surface towards the pore center (matter transport). Senos [25] suggested that during initial stage sintering of Al-doped ZnO (Al doping level above the solid solubility limit of Al in ZnO), small inclusions of $ZnAl_2O_4$ spinel phase can exert a force that prevents the motion of the surface analogously to the effect of inclusions on the grain boundary motion at an advanced sintering stage (grain growth inhibition discussed above) [29]. As a result, the sintering stress is reduced due

to the drag effect of $ZnAl_2O_4$ inclusions that may control the pores surface movement and therefore the densification process [25]. On the other side, Al doping inhibits the grain growth of ZnO. As stated in sections 2.11.3 and 4.2.3.2, the densification rate is proportional to $1/G_S^b$, meaning that the grain growth inhibition effect enhances the densification rate. Han *et al.* [7] observed the same two competing effects on the densification of Al-doped ZnO. According to the authors, during the initial stage of sintering the grain growth is negligible, and the retardant effect of $ZnAl_2O_4$ inclusions on densification dominates. At an advanced stage of sintering the densification becomes less significant and grain growth occurs. In the latter case, the inhibiting effect of Al doping on the grain growth of ZnO gives rise to the increase in densification rate. This competing effects are advantageous since enables the attainment of high density (near TD) ceramic targets as shown in Fig. 5.8.

5.1.5.3. Solubility limit of Al-doped ZnO and spinel phase formation

Quantitative analysis have shown that keeping constant the doping level (for AZO_D powder), the amount of spinel phase formed remains approximately constant at 3.4 wt. %, between 1150 and 1400 °C at HT in the range of 2 – 16 h. Fig. 5.14 show the XRD patterns of AZO targets sintered at 1300 °C at a constant HT of 2 h as a function of Al doping concentration. Since we are working above the solubility limit of Al in ZnO structure for all studied compositions (0.5 - 2.0 wt. % Al_2O_3), besides ZnO (wurtzite) main phase, also $ZnAl_2O_4$ spinel phase is identified in all the XRD patterns. Moreover, an increase in the intensity of spinel phase peaks is observed as the Al doping concentration raise from 0.5 to 2.0 wt. % Al_2O_3, revealing greater amount of secondary phase (view table 5.1 presented below).

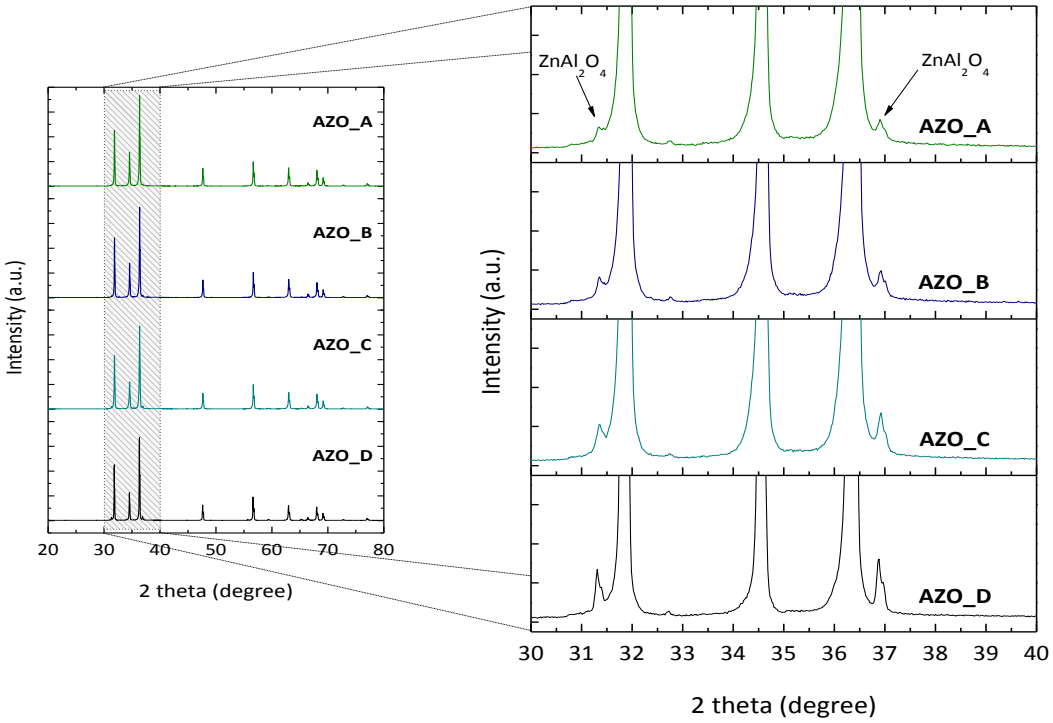

Fig. 5.14. *X-ray diffraction patterns of AZO ceramic targets (1300 °C and 2 h of HT) as a function of Al-doping concentration (0.5 – 2.0 wt. % Al_2O_3) (left); Detail illustrating the variance of the $ZnAl_2O_4$ spinel phase amount with Al doping level (right).*

Fig. 5.15 shows the microstructure and the EDS mapping of the elements present in AZO_D target sintered at 1450 °C for 2h. At this temperature the $ZnAl_2O_4$ phase is highly crystalline with crystal size above 2 µm which is not desirable for the production of AZO sputtering targets [30, 31]. However this allows performing EDS analysis in these grains without the contribution of elements from the ZnO matrix. The EDS mapping shows that the spinel phase locations present a higher amount of Al and O, while the Zn is less identified. The chemical analysis obtained by EDS in point 1 (Fig. 5.15) is displayed in Fig. 5.16 showing a typical composition of $ZnAl_2O_4$ phase.

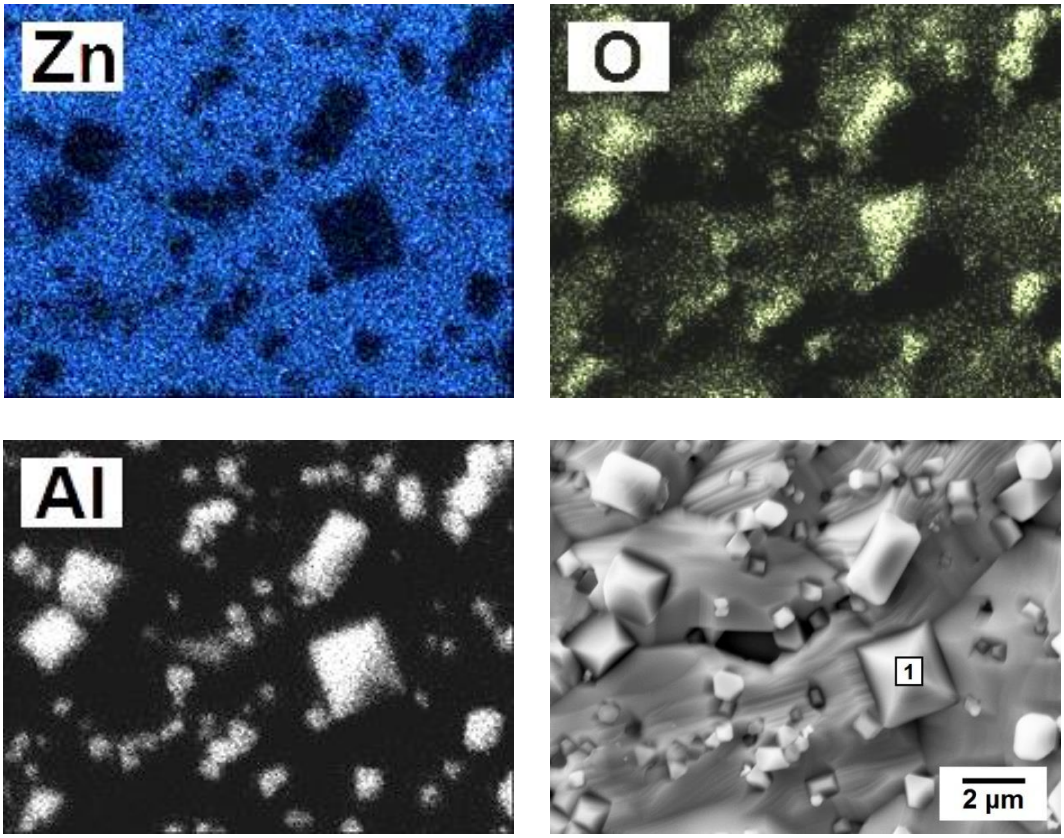

Fig. 5.15. *SEM image of AZO_D target sintered at 1450 °C for 2h – EDS mapping pictures of Zn, Al and O elements.*

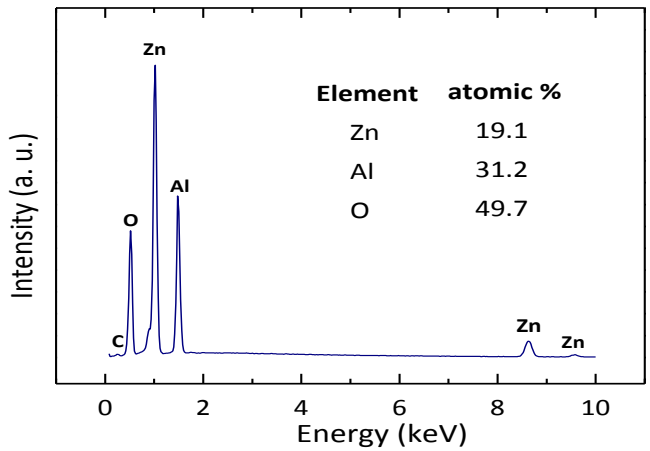

Fig. 5.16. *EDS recorded from spinel phase region (point 1 of Fig. 5.15).*

Table 5.1 shows the ratio between lattice parameters *a* and *c,* and the quantification of spinel phase formed during sintering. These values were determined for each composition by using a quantification program based on Rietveld refinement method on all the patterns [32] for samples sintered at different temperatures (1150 – 1300 °C) and holding times (2 – 16 h).

Table 5.1. *Lattice ratio and spinel phase quantification as a function of Al-doping concentration for samples sintered at 1300 °C and a constant HT of 2 h.*

Composition	[*c*/*a*] lattice ratio	$ZnAl_2O_4$ (wt. %)
AZO_A (0.5 wt. %)	1.6009	0.66
AZO_B (1.0 wt. %)	1.6007	1.57
AZO_C (1.5 wt. %)	1.6008	2.44
AZO_D (2.0 wt. %)	1.6008	3.35

Following the same path of AZO_D (section 5.1.3), no considerable influence of sintering temperature and/or HT was observed in terms of spinel phase quantification for all the compositions.

As reported by Hansson *et al.* [14], during sintering of Al-doped ZnO a spinel phase is formed at lower sintering temperatures when the solubility limit of Al in ZnO structure is exceeded. Several authors studied the solubility limit of $ZnO:Al_2O_3$ system without full agreement. Zhang *et al.* [15] investigated and presented a solubility limit value of Al in ZnO of 0.9 at. %. They also found a decrease in electrical resistivity of samples sintered at 1300 °C for 8 h for Al content of 0 – 0.8 at. % to a minimum of 1.45×10^{-3} Ωcm, while it increased for a range of 1.0 – 6.0 at. %. In contrast, Shirouzu *et al.* [17, 33] found a lower Al solubility limit of 0.3 at. % for targets sintered at 1400 °C for 10 h and suggested that $ZnAl_2O_4$ spinel phase formation occurs before the solubility limit of Al in ZnO structure, indicating a concurrent dissolution of Al and formation of $ZnAl_2O_4$ spinel during the sintering process. Finally, Han *et al.* [7], obtained an Al solubility limit of 0.06 at. % for samples sintered at 1200 °C for 8 h.

In this work, the solubility of Al in ZnO was determined in AZO_A (0.5 wt. % Al_2O_3) and AZO_B (1.0 wt. % Al_2O_3) based on SEM micrographs of samples sintered at 1200 ºC for 2 h [7, 34]. The molar concentrations of the spinel phase were calculated from their volume fractions considering 5.61 $g.cm^{-3}$ the TD of ZnO. The volume fraction (in three dimensions) of the $ZnAl_2O_4$ spinel phase considered in the determination of the solubility limit of Al in ZnO was calculated as the ratio of the total spinel phase area in the polished section and the total section area. The solubility limit of Al in ZnO lattice was calculated subtracting the amount of Al in the spinel phase from the total Al content in the samples. Using this procedure, the amount of Al dissolved in ZnO was determined to be around 0.09 at. % at 1200 °C (HT = 2h) for both AZO_A and AZO_B samples.

Several authors [17, 33, 35, 36] have found a reduction in [*c*/*a*] lattice ratio with Al addition associated to a distortion in the ZnO structure due to the substitution of Zn^{2+} sites by Al^{3+}. It was not observed relevant lattice distortions with the increase in Al content for targets sintered between 1150 and 1300 °C for 2 – 16 h. However, comparing to the undoped INNOVNANO ZnO ([*c*/*a*] = 1.6021) we notice a distortion of ZnO lattice when Al is inserted. Indeed, all the studied

compositions are above the solubility limit of Al in ZnO lattice, and the sintered targets have achieved the maximum compression (lower [*c*/*a*] lattice ratio). These results are different from those presented by Shirouzu *et al.* [33] since we obtained similar solubility of Al in ZnO on both AZO_A and AZO_B targets, pointing out a possible maximum solubility limit reached with only 0.5 wt. % Al_2O_3. This can be explained by the uniform distribution of Al in each individual ZnO particle that is inherent to INNOVNANO synthesis method. In fact, the same amount of spinel phase observed at different temperatures and holding times for AZO_D (2.0 wt. % Al_2O_3), and the presence of $ZnAl_2O_4$ in the as-synthesized powders, support the statement that besides the spinel phase formation, also the substitution of Zn^{2+} sites by Al^{3+} occurs during the powder synthesis which favors the attainment of maximum solubility limit before sintering, even for lower amounts of Al (0.5 wt. % Al_2O_3). This is an advantage of INNOVNANO synthesized powders since they are already conductive, opening up new opportunities for RF and/or DC sputtering deposition systems using non-sintered sputtering targets (section 5.2.3).

5.1.6. Electrical properties of AZO ceramic sputtering targets produced by CS

This section will address the correlation between the electrical properties of the targets and their dependence on sintering temperature, HT, G_S and Al-doping level. The effect of oxygen content on the electrical properties of the sintered targets will be discussed in section 5.2.

5.1.6.1. Structural and morphological effect

The relationship between sputtering targets and corresponding thin films has been analyzed by several authors [15, 37-43]. Minami *et al.* [37-39], have reported that high density AZO targets with lower ρ_e results in more stable dc-magnetron sputtering depositions with higher deposition rates, lower arcing and better uniformity in the resistivity of films. They also show that oxygen content in the deposited thin films decreases as the oxygen content in the target decreases, producing highly conductive thin films. Even not being easy to prepare targets with low oxygen content due to the higher vapor pressure of zinc at higher temperatures, the oxygen content can be improved using controlled atmospheres during sintering. Huang *et al.* [40] obtained an enhanced spatial distribution in electrical conductivity of thin films using a high conductive target prepared by reduction sintering. In this case, the mechanism of electrical conduction is simultaneously due to two different native point defects (aluminum substitution (Al_{Zn}) and oxygen vacancy (V_O)), increasing substantially the N_e and μ_e of the sintered targets. Wu *et al.* [41] studied the effect of sintering parameters on the densification, microstructure, and electrical properties of AZO sputtering targets. The authors found a correlation between ρ_r of the targets and their electrical properties. According to them, a higher ρ_r gives rise to highly conductive AZO ceramic targets with improved μ_e and N_e. Zhang *et al.* [15] studied the dependence of ρ_e on several parameters of AZO sintered targets concluding that it depends mainly on three factors: 1) free carriers, attributed to the substitution of Al^{3+} on Zn^{2+} as presented below:

$$Al_2O_3 + ZnO \rightarrow Zn_{Zn} + 2Al_{Zn}^{\bullet} + 3O_o^x + \frac{1}{2}O_2(g) + 2e^- \qquad \text{(eq. 5.2)}$$

2) the sintered target density, and 3) the $ZnAl_2O_4$ spinel phase formed beyond the solubility limit. Finally, Liu and Jeng [42] used CS to sinter 3 inches AZO targets (98:2 wt. % ZnO:Al_2O_3) observing a substantial improvement on the electrical properties for ceramic pieces with higher densities (near TD), the same trend observed by Han *et al.* [43] for lower Al-doping concentrations.

Fig. 5.17 shows the electrical behavior of AZO 98:2 wt. % targets sintered at different temperatures for 2 h.

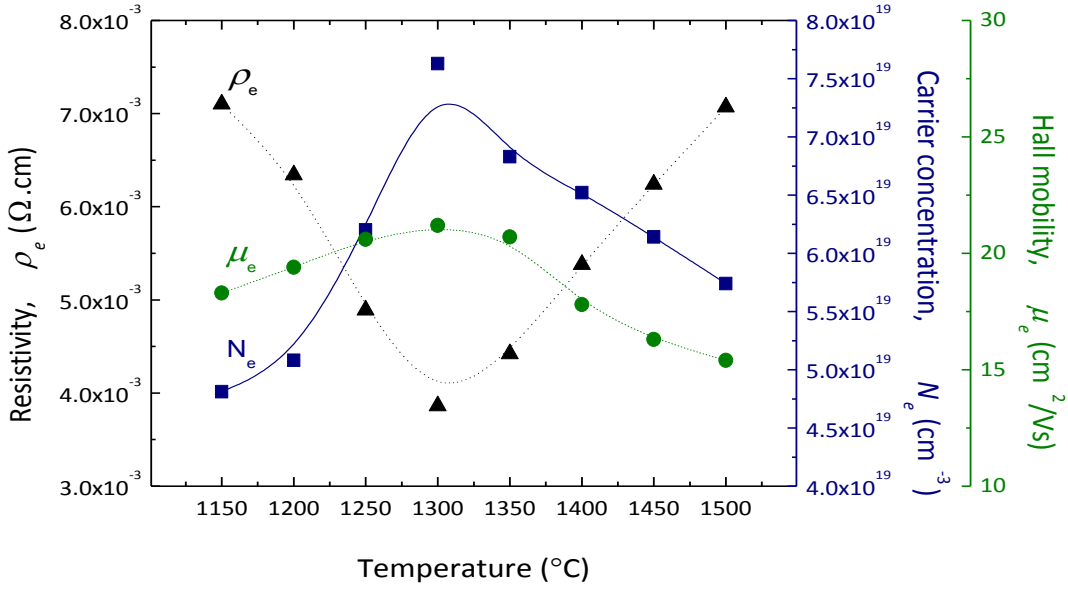

Fig. 5.17. *Room temperature electrical resistivity, carrier mobility, and carrier concentration as a function of the sintering temperature for the AZO_D (98:2 wt. % ZnO:Al_2O_3) targets (2 h of HT).*

The results show a decrease in ρ_e from 7.10 × 10^{-3} to 3.86 × 10^{-3} Ωcm when sintering temperature increases from 1150 °C to 1300 °C, respectively. This decrease is promoted by an increase in ρ_r from 96.2 to 99.9 % of TD (Fig. 5.5) and consequently, by the reduction of defects responsible for trapping carriers. This is in good agreement with previous works [41-44]. Usually, a decrease in ρ_e is related with an increase in μ_e and N_e. In this work, between 1150 and 1300 °C, μ_e increases slightly from 18.3 to 21.2 cm^{2}V^{-1}s^{-1} and N_e increases from 4.81 × 10^{19} to 7.63 × 10^{19} cm^{-3}. The lowest ρ_e values were attained for targets sintered between 1250 and 1350 °C to which is ascribed a μ_e around 20 cm^{2}V^{-1}s^{-1} and N_e of about 6.0 – 7.5 × 10^{19} cm^{-3}. Several authors [37, 40, 41] present significantly higher Hall mobility values (33.4 – 87.0 cm^{2}V^{-1}s^{-1}) for sintered targets which might be related with several factors like the initial powder characteristics, sintering method and/or sintering atmosphere, that play an important role on the final microstructure of the sintered targets and consequently on their electrical properties (discussed in section 5.2). Between 1250 – 1350 °C, the targets show ρ_r ≥ 99.5 % of TD and the grain size vary from 2.14 to 3.47 µm. However, for these targets, no significant increase was observed in terms of secondary phase distribution and their grain size. At higher sintering temperatures (1400 – 1500 °C), both μ_e and N_e decrease slightly and consequently ρ_e increases from 3.86 × 10^{-3} to 7.07 × 10^{-3} Ωcm.

Inherent to higher sintering temperatures, we observe a significant grain growth, not only for the main phase but also for the secondary phase ($ZnAl_2O_4$) (Fig. 5.18). Spinel phase acts as electron scattering centers, lowering the mobility of the electrons [45]. The larger $ZnAl_2O_4$ grains tend to be located in the ZnO grain boundaries and triple junction points, causing a decrease in homogeneity of the targets, which may affect not only the electrical resistivity of the ceramic targets but also the properties of the deposited thin films. Furthermore, the XPS analysis of sintered targets at high temperatures (> 1400 °C) shows a slightly increase of O content, which can be related with

the volatilization of ZnO, and consequently change in the composition, explaining so the observed increase in the electrical resistivity of these targets [6, 7, 42]. Several studies show that for Al-doped ZnO, the control of second phase precipitates is of extremely importance, since larger precipitates (> 2 μm) cause arcing and consequently particle generation during the sputtering process [9, 30, 31]. This microstructural inhomogeneity is also responsible for the appearance of undesired nodules in the AZO sputtering targets. Nodules formation and arcing during sputtering are correlated and has been subject of large number of studies to avoid or reduce its appearance/occurrence [9, 11, 30, 31, 46-49]. This question will be deepened in section 5.7.5, when presenting the results concerning the production of industrial AZO targets.

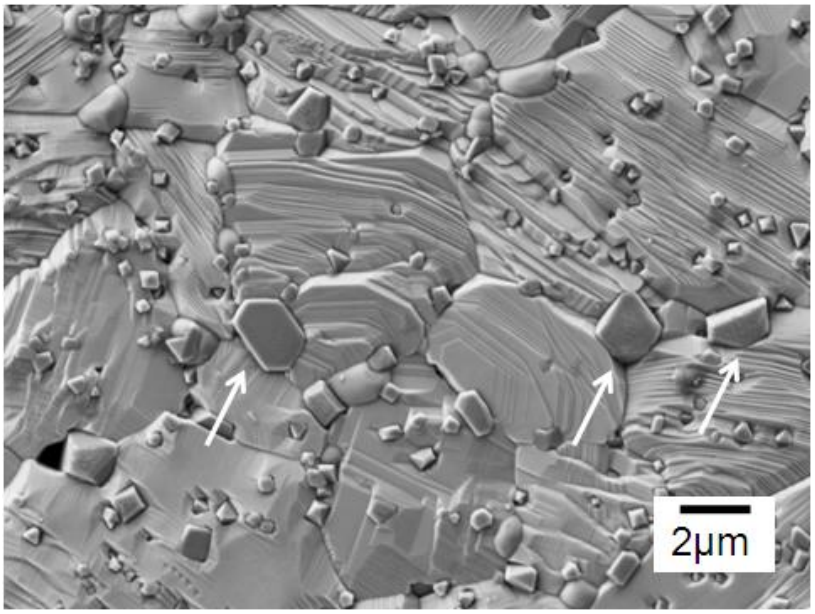

Fig. 5.18. *AZO 98:2 wt. % target sintered at 1450 °C for 2 h. Large $ZnAl_2O_4$ grains placed at the grain boundaries and triple junctions of ZnO (indicated by the arrows).*

The influence of HT on the properties of several AZO targets is shown in Table 5.2. For lower sintering temperatures (1150 °C), HT promotes the densification and a slight raise in the final grain size, but without significant influence in the electrical properties, with μ_e and N_e values among 17.2 – 19.1 $cm^2V^{-1}s^{-1}$ and 4.81 $\times$ 10^{19} – 5.25 $\times$ 10^{19} cm^{-3}, respectively. At 1300 °C, μ_e decreases from 21.2 to 16.4 $cm^2V^{-1}s^{-1}$, being this reduction more significant for samples sintered at 1400 °C (from 17.8 to 10.1 $cm^2V^{-1}s^{-1}$). However, N_e values stay approximately stable in the range 6.37 $\times$ 10^{19} – 7.63 $\times$ 10^{19} cm^{-3} in the temperature range of 1300 – 1400 °C. Consequently, for high density targets where grain growth is dominant, ρ_e tends to increase for targets sintered for long periods of time and this behavior is even more remarkable at higher sintering temperatures (1400 °C). This can be associated to grain overgrowth and changes in second phase size/distribution. Furthermore, as illustrated in Fig. 5.3, at temperatures above 1300 °C is observed a significant weight loss (zinc volatilization) that might also be responsible for the lower conductivity of the targets sintered at temperatures ≥ 1400 °C.

Table 5.2. *Properties of AZO targets as a function of the holding time at different sintering temperatures (1150, 1300 and 1400 °C).*

Sintering cycle		Relative density (%)	Grain size (µm)	Resistivity of target $\times 10^{-3}$(Ωcm)	Hall mobility (cm^2/Vs)	Carrier concentration $\times 10^{19}$ (cm^{-3})
1150 °C	2h	96.2	1.54	7.10	18.3	4.81
	4h	96.8	1.67	6.38	19.1	5.13
	16h	99.1	2.12	6.92	17.2	5.25
1300 °C	2h	99.9	2.57	3.86	21.2	7.63
	4h	100.0	3.13	4.55	18.9	7.26
	16h	99.9	4.21	5.62	16.4	6.77
1400 °C	2h	99.9	4.70	5.38	17.8	6.52
	4h	99.8	6.12	7.19	12.5	6.94
	16h	99.9	8.36	9.75	10.1	6.37

5.1.6.2. Effect of aluminum doping concentration

The final microstructure and the composition of a sputtering target influence their electrical properties having a direct impact in the characteristics of the films deposited by sputtering [37-42]. We have shown that large precipitates of $ZnAl_2O_4$ phase and large final grain sizes should be avoided as well as porosity in order to ensure that the target properties are ideal for thin films deposition. By reducing these defects, the formation of nodules and the abnormal discharges that can occur during the deposition of TCO thin films are avoided allowing the use of higher sputtering voltages during the deposition, enabling so higher deposition rates [30, 49].

Intending to find the sintering conditions that allow us to achieve the ideal electrical properties for each composition, several targets with different Al contents were produced and their electrical properties evaluated. The influence of sintering temperature on ρ_e, N_e and μ_e of INNOVNANO AZO targets is shown in Fig. 5.19. The range of temperatures shown in Fig. 5.19 varies depending on the composition since ρ_e of AZO_C and AZO_D at temperatures below 1150 °C is too high (porosity in the target), as well as the ρ_e of AZO_A and AZO_B above 1300 °C (grain size too high).

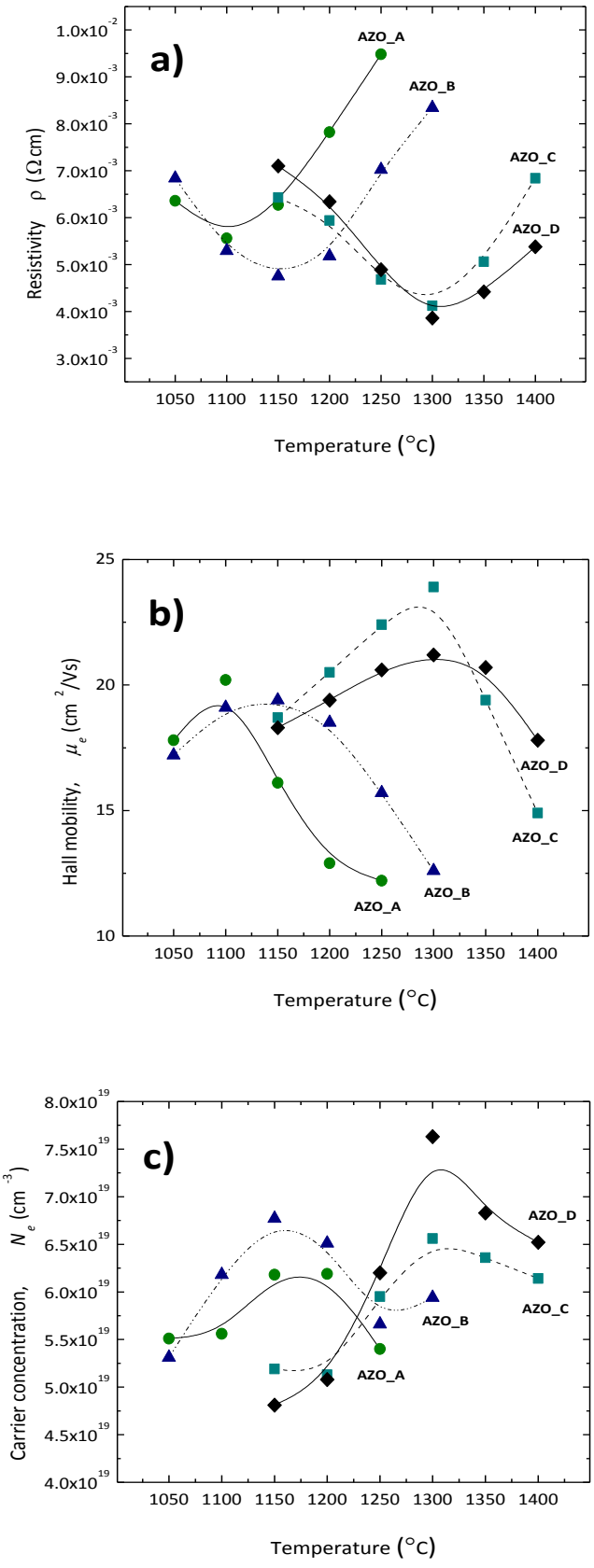

Fig. 5.19. *Room temperature a) ρ_e, b) μ_e, and c) N_e of differently doped AZO targets as a function of sintering temperature (2 h of HT).*

Minimum ρ_e values are identified in Fig. 5.19 a) for each composition being attained at different sintering temperatures. However, the lowest values reached for all compositions are very close, in the range of 3.86×10^{-3} – 5.56×10^{-3} Ωcm and corresponds to the highest μ_e achieved for each composition (Fig. 5.19 b)). Minami *et al.* [37] also measured the electrical properties of several AZO targets and found that ρ_e is mainly controlled by the O content in the target rather than de aluminum content. The lowest ρ_e values of 5.56×10^{-3} and 4.75×10^{-3} Ωcm obtained for AZO_A and AZO_B, respectively at 1100 and 1150 ºC, are explained by the high densities (near the TD) reached for this compositions at these temperatures (Fig. 5.8). Above 1150 °C the fast grain growth and a worse distribution of $ZnAl_2O_4$ phase in the ZnO structure seems to control ρ_e of AZO_A and AZO_B targets being that grain growth effect more evident for targets with lower Al concentrations. On the other hand, AZO C and AZO_D show the lowest ρ_e at 1300 °C (4.12×10^{-3} and 3.86×10^{-3} Ωcm respectively) in agreement with the results of section 5.1.5 where is shown a similar sintering behavior for both compositions. For these compositions ρ_e starts to increase substantially for temperatures above 1400 °C when the growth of $ZnAl_2O_4$ phase is considerable and the formed spinel grains behave as electron scattering centers lowering so the mobility of the carriers [45]. Furthermore, as discussed previously, at high sintering temperatures (> 1400 °C) a significant weight loss was observed, due to undesired volatilization of Zn affecting the Zn/Al ratio of the targets and consequently of the corresponding thin films. These results allows to conclude that INNOVNANO AZO sputtering targets prepared by CS should have a final density near the TD and a controlled grain size between 2 and 4 μm, dependent on the composition, in order to be obtained optimized electrical properties. Fig. 5.19 b) and c) shows in that order μ_e and N_e of the targets. The results have a similar behavior as ρ_e shown in Fig. 5.19 a), with μ_e and N_e increasing up to a maximum value that varies with the target composition and corresponds to the lowest ρ_e, decreasing again for higher sintering temperatures. In general, μ_e around 20 $cm^2V^{-1}s^{-1}$ were achieved for all the compositions, being its decrease mainly due to grain growth and non-uniform spinel phase distribution at an advanced phase of the final sintering stage. One would expect a decrease in μ_e with the increase in the amount of $ZnAl_2O_4$. However, for high density targets, μ_e seems to be independent on the amount of spinel phase and more dependent on its size/distribution. The same behavior was observed by Minami *et al.* [37] when comparing several AZO sputtering targets with different compositions. As the solubility of Al in ZnO structure is above the solubility limit, in all studied compositions, N_e of the targets is not correlated to the increase in the doping concentration (Fig. 5.19 c)), varying between 4.81×10^{19} and 6.77×10^{19} cm^{-3} in the range of temperatures studied.

The effect of HT (2 – 16 h) was evaluated keeping the temperature constant at 1150 and 1300 °C. Similarly to the observed for AZO_D (Table 5.2) all compositions present a substantial increase in ρ_e (due to a reduction in μ_e) with HT being this effect more pronounced at 1300 °C and for the lower doping concentrations (AZO_A and AZO_B). At 1150 °C ρ_e of AZO_A and AZO_B increases, respectively, from 6.27×10^{-3} to 8.82×10^{-3} Ωcm, and from 4.75×10^{-3} to 6.26×10^{-3} Ωcm with HT (2 → 16 h). At higher temperatures this variation is more pronounced. AZO_A, for example, presents an increase in ρ_e from 1.36×10^{-2} to 4.38×10^{-2} Ωcm for samples sintered at 1300 °C for 2 and 16 h of HT, respectively. AZO_C exhibits a similar behavior to AZO_D without considerable variation of ρ_e with HT (2 → 16 h) at 1150 °C (6.43×10^{-3} → 6.14×10^{-3} Ωcm) and a slight increase at 1300 °C from 4.12×10^{-3} to 6.12×10^{-3} Ωcm.

As previously mentioned, for lower Al contents the grains grows faster with sintering temperature than with HT and the $ZnAl_2O_4$ phase has the tendency to be deficiently distributed in the microstructure causing undesirable non-uniformities in AZO targets. This influences negatively the deposition stage and consequently the properties of the corresponding sputtered thin films. As a result, for lower doping levels (AZO_A and AZO_B), can be advantageous to prepare targets at lower sintering temperatures (1050 – 1100 °C) (were non-densification mechanisms prevails) for a longer period, since grain growth is easily controlled varying HT than sintering temperature (Fig. 5.10 and Fig. 5.12).

5.1.6.3. Scale-up effect

The minimum target size needed for sputtering systems is two inches (~5.1 cm). Thus, in order to test the studied AZO targets in the production of TCO thin films by magnetron sputtering technique, several targets with two inches (~5.1 cm) diameter and three millimeters thickness were produced. The targets were prepared in the same conditions as the previously studied 20 mm diameter targets. The GD of these targets was 62 % TD (after UP + CIP) and the sintering cycles were chosen taking into account the optimized electrical properties obtained for the small targets. The two inches INNOVNANO AZO targets were also characterized in terms of final microstructure and electrical behavior in order to understand if any scale-up effect is observed. The results are displayed in Table 5.3. For each composition, two different targets were sintered changing the sintering temperature. One target of each composition was sintered in the same conditions that lead to the lowest ρ_e achieved in preliminary studies (Fig. 5.19). The other target was processed above the optimum sintering temperature for each Al doping concentration.

Table 5.3. *Comparison between the properties obtained in small (20 mm diameter die) and two inches INNOVNANO AZO sputtering targets prepared with different compositions.*

Composition	Sintering cycle (HT = 2h)	Small targets			Two inches targets		
		ρ_r (%)	G_S (µm)	ρ_e (×10^{-3} Ωcm)	ρ_r (%)	G_S (µm)	ρ_e (×10^{-3} Ωcm)
AZO_A	1100 °C	99.8	3.06	5.56	99.6	2.98	5.83
	1300 °C	100	8.61	13.6	99.8	8.52	14.9
AZO_B	1150 °C	99.8	2.08	4.75	99.8	2.12	4.46
	1300 °C	99.9	6.25	8.34	99.6	6.04	8.72
AZO_C	1300 °C	99.8	3.32	4.12	99.7	3.14	4.01
	1400 °C	100	6.33	6.84	99.9	6.36	7.16
AZO_D	1300 °C	99.9	2.57	3.86	99.7	2.44	3.72
	1400 °C	99.9	4.70	5.38	99.8	4.63	5.47

Frequently, high temperatures or extension of the HT are required when the samples dimensions increases considerably, mainly due to thermal gradients that can occur between the inner and outer part of the ceramic pieces. However, the obtained results show no considerable scale-up

effect in terms of ρ_r, G_S and ρ_e of the two inches INNOVNANO AZO targets. This confirms our previous results that the use of more reactive powders is an advantage regarding the reproducibility of results obtained in smaller targets. Furthermore, we conclude that it is possible the production of two inches AZO targets with controlled final properties by CS method avoiding the use of more expensive sintering techniques such as hot pressing (HP) and hot isostatic pressing (HIP), commonly used to achieve full dense AZO ceramic targets.

5.1.7. AZO thin films sputtered from conventionally sintered sputtering targets - deposition and characterization

Some of the most important characteristics of a ceramic sputtering target are their chemical and structural homogeneity, final density and electrical conductivity. Taking these requirements into account and the characteristics presented in Table 5.3 we decided to perform the sputtering depositions using the two inches targets with lower ρ_e for each composition (Table 5.4). The depositions were performed by magnetron sputtering at RT and the sputtering parameters were optimized for each target varying the working pressure (P_{dep}), RF power (P_{RF}) and oxygen flow (% O_2) during deposition.

Table 5.4. *Morphological and structural properties of two inches AZO sputtering targets prepared by CS and used to produce TCO thin films by magnetron sputtering at RT.*

Composition	Sintering cycle	Relative density (%)	Grain size (μm)	Resistivity of target $\times 10^{-3}$ (Ωcm)	Hall mobility (cm^2/Vs)	Carrier concentration $\times 10^{19}$ (cm^{-3})
AZO_A	1100 °C/2h	99.6	2.98	5.83	18.7	5.73
AZO_B	1150 °C/2h	99.8	2.12	4.46	19.8	7.07
AZO_C	1300 °C/2h	99.7	3.14	4.01	22.4	6.95
AZO_D	1300 °C/2h	99.7	2.44	3.72	21.8	7.70

5.1.7.1. Deposition rate of Al-doped ZnO thin films

The deposition rate (DR) of sputtered AZO thin films as a function of P_{RF} and P_{dep} is shown in Fig. 5.20 a) and b), respectively. The thin films were deposited using AZO_D sputtering target and the thicknesses of the films were measured at the center of the substrates. As it can be observed, for a given working pressure (0.2 Pa), DR increases almost linearly with P_{RF} (100 → 250 W) from 2.15 to 6.05 $nm.min^{-1}$. This behavior is frequently observed during the sputtering deposition of AZO and other TCOs (e.g. IZO) [50, 51] and can be explained by the higher energy of the Ar ions colliding with the sputtering target which promotes the ejection of a larger number of species from it. On the other side, it is observed that DR decreases from 6.34 to 5.64 $nm.min^{-1}$ with increasing P_{dep} (0.13 → 0.4 Pa). A possible explanation for the decrease of DR with P_{dep} is that the mean free path (MFP) of sputtered species decreases with P_{dep} increase as can be observed in eq. 5.3 [52]:

$$MFP = \frac{kT}{\sqrt{2}\pi d_{spt}^2 P_{dep}} \qquad \text{(eq. 5.3)}$$

where, k is the Boltzmann constant, T is the temperature, d_{spt} is the sputtered particles diameter and P_{dep} the deposition pressure. In fact, for higher P_{dep}, the number of collisions between the atoms of environmental gas inside the vacuum chamber and the sputtered particles increases, resulting in the loss of energy of the sputtered particles through a thermalization process, and consequently in the reduction of DR. On the other side, for lower P_{dep}, the sputtered particles have high surface mobility because of the large MFP giving rise to higher DR.

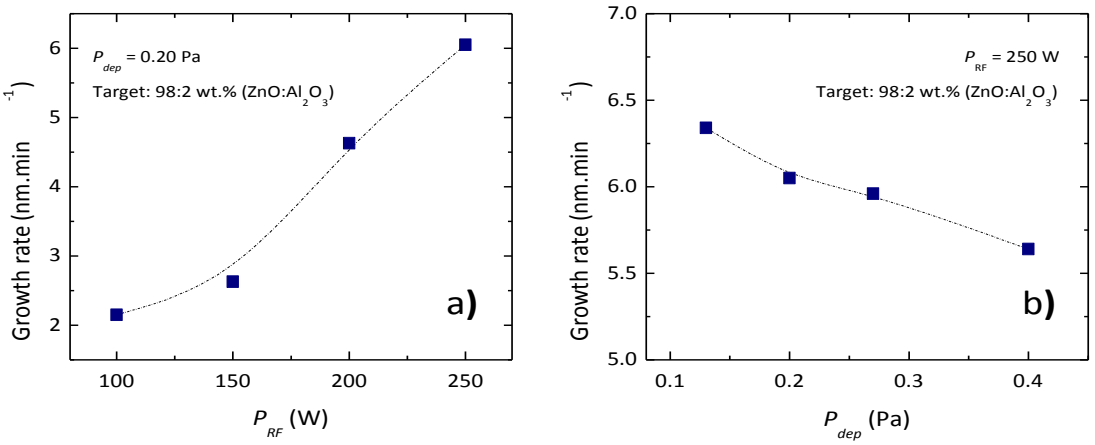

Fig. 5.20. *Deposition rate as a function of a) RF power and b) working pressure using AZO_D sputtering target (target composition: 98:2 wt.% ZnO:Al_2O_3).*

5.1.7.2. Effect of RF sputtering power on AZO thin films properties

As illustrated in Fig. 5.20, the growth rate increases with P_{RF} and deceases with P_{dep}. Pretests have shown that the use of P_{RF} above 250 W results in an earlier degradation of the target, which may lead to plasma instabilities during deposition and also breakage of the target in extreme conditions. Furthermore, in the previous section it was also found that the use of too high P_{dep} leads to a reduction of DR. Thus, in this section, the effect of P_{RF} on AZO thin films properties was studied keeping the P_{dep} value constant at 0.2 Pa. Noted that all films in this section were deposited without intentional heating of the substrate, being this condition designated as room temperature (RT).

Fig. 5.21 shows the variation of ρ_e, N_e and μ_e (measured at the central part of the soda-lime glass substrate) as a function of P_{RF} for films deposited using AZO_D target prepared by CS in air (Table 5.4). As P_{RF} increases from 100 to 250 W, ρ_e of the sputtered films decreases from 3.99 $\times$ 10^{-3} to 1.02 $\times$ 10^{-3} Ωcm, with a corresponding increase in both N_e (2.32$\times10^{20}$ to 4.79$\times10^{20}$ cm^{-3}) and μ_e (6.74 to 12.8 cm^{2}V^{-1}s^{-1}). The same behavior of the power on the resistivity of AZO films was also studied by Minami *et al.* [53] that achieved the lowest electrical resistivity for P_{RF} of 150 W in the power range of 50 – 150 W.

Comparing with the electrical properties of the corresponding AZO_D sputtering target (Fig. 5.17), AZO films presents lower μ_e and higher N_e, in agreement with the results obtained by Huang *et al.* and Wu *et al.* [40, 41]. These results demonstrate that the dominant factor of conductivity between the targets and films is completely different. Since AZO targets exhibit much better crystallinity and larger grain size than AZO films (Fig. 5.22 and Fig. 5.23), it's reasonable to believe that the

higher μ_e of AZO targets are ascribed to the reduction of electron scattering from crystal and boundary defects [40]. As mentioned before, during sintering process, part of Al, reacts to form spinel phase reducing the amount of Al responsible for generating carriers [41]. On the other hand, during the deposition of films occurs the atomic rearrangement among Zn, Al, and O [40] allowing the enhancement of the doping concentration and doping uniformity in AZO films and consequent attainment of higher N_e than that in the AZO targets.

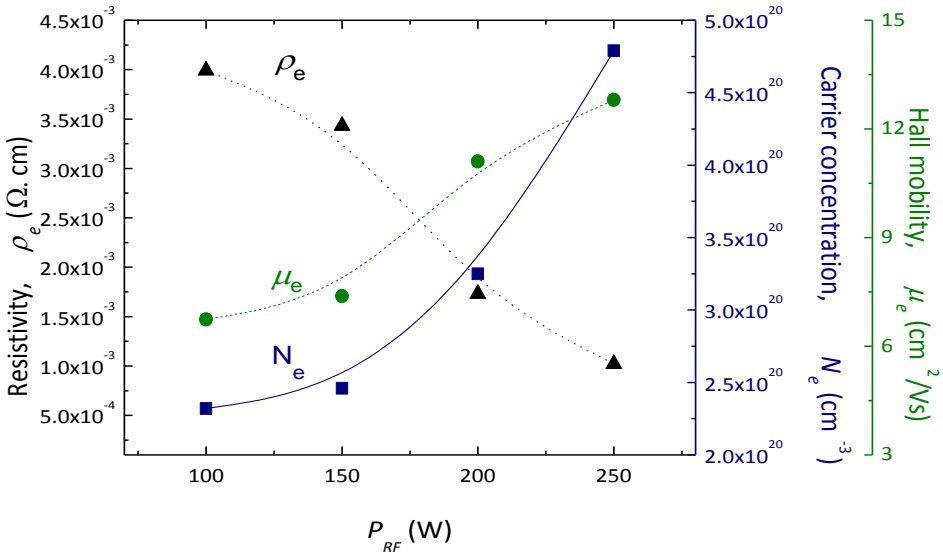

Fig. 5.21. *Electrical resistivity, carrier concentration and Hall mobility of AZO_D thin films as a function of P_{RF} deposited at an Ar pressure of 0.2 Pa.*

Fig. 5.22 shows the X-ray diffraction patterns (normalized to the film thickness) for AZO films as a function of P_{RF}. The sputtered films are polycrystalline with a hexagonal structure, preferentially oriented along c-axis (002), perpendicular to the substrate. The c-axis orientation in AZO films can be understood by the 'survival of the fastest' model proposed by Drift [54]. According to this model, the preferential (002) orientation is not affected by the crystallographic structure of the substrate, being the result of a self-ordering mechanism caused by the minimization of the crystal surface free energy as well as by the interaction between the deposited material and the substrate surface [55, 56]. Nucleation with different orientations can be formed at the initial stage of the deposition and each nucleus competes to grow. However, only nuclei having the fastest growth rate (lower surface energy) can survive. The grains become larger as film thickness increases, while the orientation distribution at the surface progress towards the direction corresponding to the lowest surface energy, i.e., c-axis crystallographic orientation is achieved [57-60]. In a previous work, Fujimura and co-workers [61] had already suggested that the surface energy density of the (002) planes is the lowest in the ZnO wurtzite crystal system.

The increase in P_{RF} value led to an increase in (002) peak intensity as well as an enhancement in the crystallite size from 24 to 29 nm, determined by the Scherrer formula (eq. 3.9) [62], being the crystallite size variation attributed to the higher substrate temperatures and growth rate during sputtering process induced by higher P_{RF} [63]. This explains the decrease of ρ_e shown in Fig. 5.21. As the crystallite size enlarges the grain boundary scattering weakens and therefore μ_e is increased with a subsequent improvement of the electrical conductivity [64].

Observing the inset of Fig. 5.20 it is possible identify a shift in the position of the (002) peak to a higher 2θ angle with the increase in P_{RF}. Peaks dislocation is usually related to residual stresses generated during the deposition and tends to be more evident for thinner films [64]. As shown in Fig. 5.20, DR increases with P_{RF} giving rise to thicker films, and consequently to the reduction of the stresses in crystal grains of the films. In fact, more than the effect of P_{RF}, the thickness and the crystallinity of the films seems to be the main factor responsible for the shift observed in the XRD patterns (considering the same composition), as will be demonstrated in section 5.2.3.2.

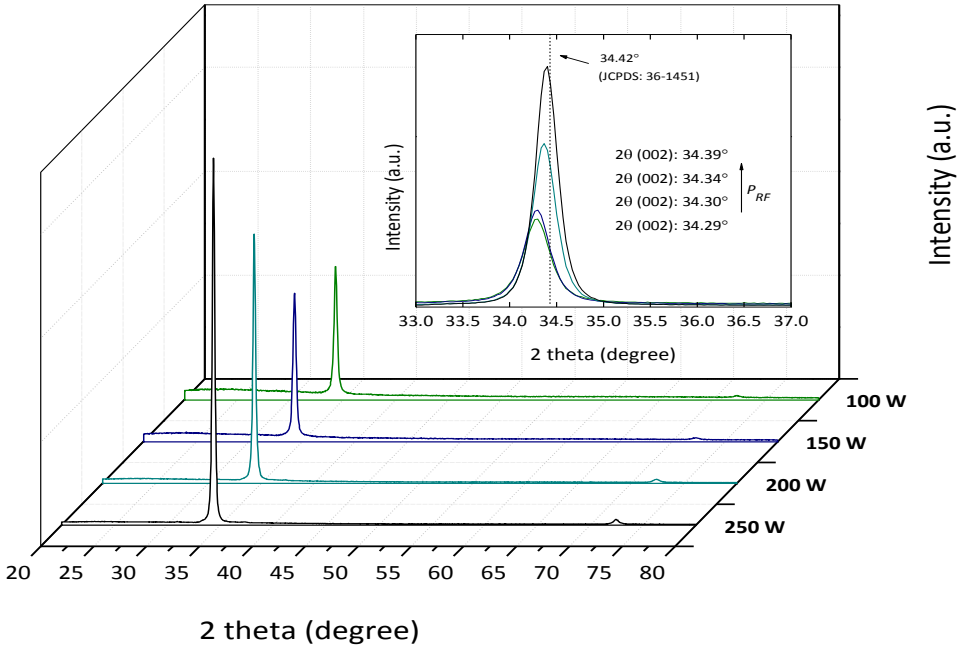

Fig. 5.22. *XRD patterns of AZO_D films deposited at RT as a function of P_{RF} (the diffractograms are normalized to the thickness of each film).*

SEM images of Fig. 5.23 show the morphology and cross-section of Al-doped ZnO thin films deposited at RT *(P_{RF} = 250 W; P_{dep} = 0.2 Pa)*. Uniform, small grain size, dense columnar structure and a very smooth surface is obtained in films with thickness of approximately 360 nm (similar to the value obtained by profilometry measurements).

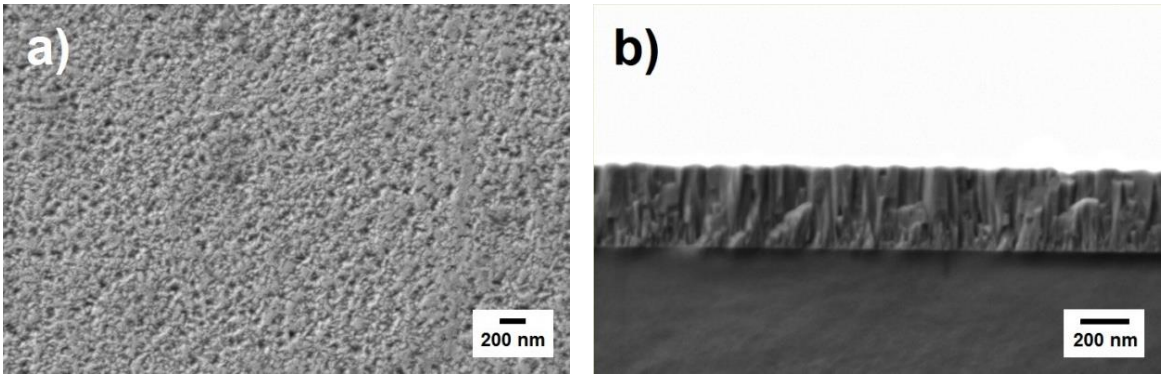

Fig. 5.23. *a) AZO films morphology and b) cross-section structure, deposited at RT (P_{RF} = 250 W; P_{dep} = 0.2 Pa).*

In Fig. 5.24 is shown the root-mean-square (RMS) obtained from AFM measurement. The RMS roughness increases slightly from 2.0 to 2.4 nm as the P_{RF} increases. The variation in films thickness with P_{RF} and the small variation in crystallite size reached from XRD measurements (Fig. 5.24) seem to be responsible for the increase of roughness.

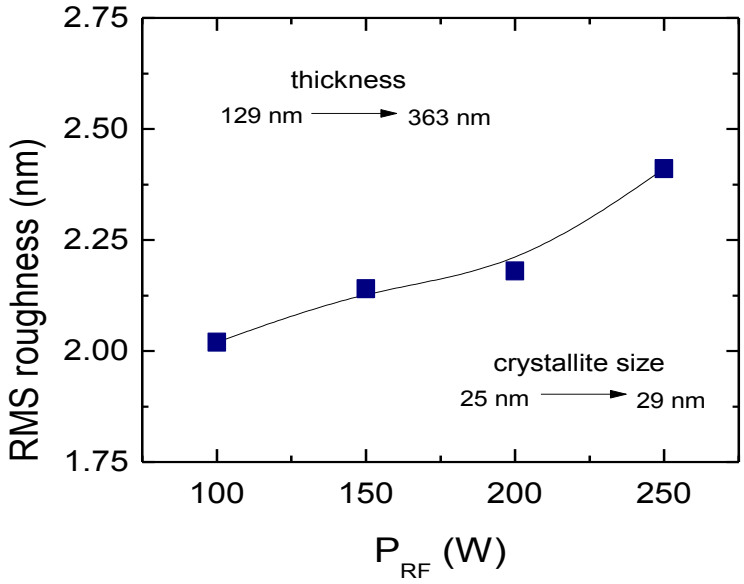

Fig. 5.24. *RMS roughness of the AZO thin films as a function of RF power.*

Fig. 5.25 shows the specular optical transmittance spectra of AZO thin films in the wavelength range 400 – 2500 nm, produced at different P_{RF}. All the thin films exhibit average transmittance above 90 % in the visible spectral range (400 – 750 nm) and show a sharp absorption edge at about 360 nm. Up to 1000 nm, the impact of the P_{RF} in the average optical transmission is minor. In the near-infrared (NIR) wavelength range is observed a decrease of transmittance as P_{RF} increases. While thin films deposited with AZO_D at lower P_{RF} (100 and 150 W) maintain a high transmittance up to wavelengths of 2500 nm (~60 %), at higher P_{RF} the transmittance diminishes to 30 and 12 % respectively for P_{RF} = 200 W and P_{RF} = 250 W. This behavior is a consequence of the film thickness increase (Fig. 5.20) and N_e (Fig. 5.21) due to the so called Moss-Burstein effect [44, 65]. This behavior is consistent with the changes in the electrical, morphological and structural properties discussed before.

As discussed in section 2.5.2.1, the optical bandgap (E_{opt}) can be defined as the minimum energy needed to excite an electron from the valence band to the conduction band. In pure undoped crystals the optical bandgap equals the energy separation between the band edges (E_g) (see Fig. 2.11) [10]. In general, changes in the bandgap energy of ZnO have been related to variations in the mean crystallite size, the internal stress and/or the free carrier concentration of films [66-70]. It is known that for heavy n-doped materials (the case of AZO compositions studied in this research work) the bandgap enlarges as N_e increases owing to the blocking of the lowest states of the conduction band by excess electrons [71]. This type of blocking of low energy transitions was already described in section 2.5.2.1, being known as Burstein-Moss effect [60]. These highly doped materials possess a wide energy bandgap (E_g > 3.4 eV) and are therefore transparent in the wavelength region from about 350 to > 800 nm, where the long wavelength cut-off depends on the charge carrier concentration [72]. The cut-off behavior at the blue end of the spectrum is

determined by direct electronic transitions from the valence band to the conduction band. Therefore, the direct optical bandgap (E_{opt}) of Al-doped ZnO can be determined from transmission and reflectance data measured at short wavelengths. Using the procedure described in section 3.3.2.3.1 is observed that E_{opt} increases from 3.44 to 3.65 eV with increasing P_{RF} (inset of Fig. 5.25), which in turn correspond to the increase of N_e from 2.32 × 10^{20} cm^{-3} to 4.79 × 10^{20} cm^{-3} and consequent reduction of ρ_e of the films shown in Fig. 5.21. This variation can be explained by the Burstein-Moss band filing effect [73, 74], which shifts positively the measured band-edge energy (blue shift) with increasing N_e (either by a more efficient Al doping or creation of extra oxygen vacancies). It is caused by filling of conduction band states by excess carriers provided by the impurities due to small density of states of ZnO near the conduction band minimum, being E_{opt} the sum of the bandgap of the lightly doped semiconductor (E_g) and bandgap widening due to the filling of the conduction band (ΔE_{BM}), as illustrated in eq. 2.11 and Fig. 2.11 from section 2.5.2.1.

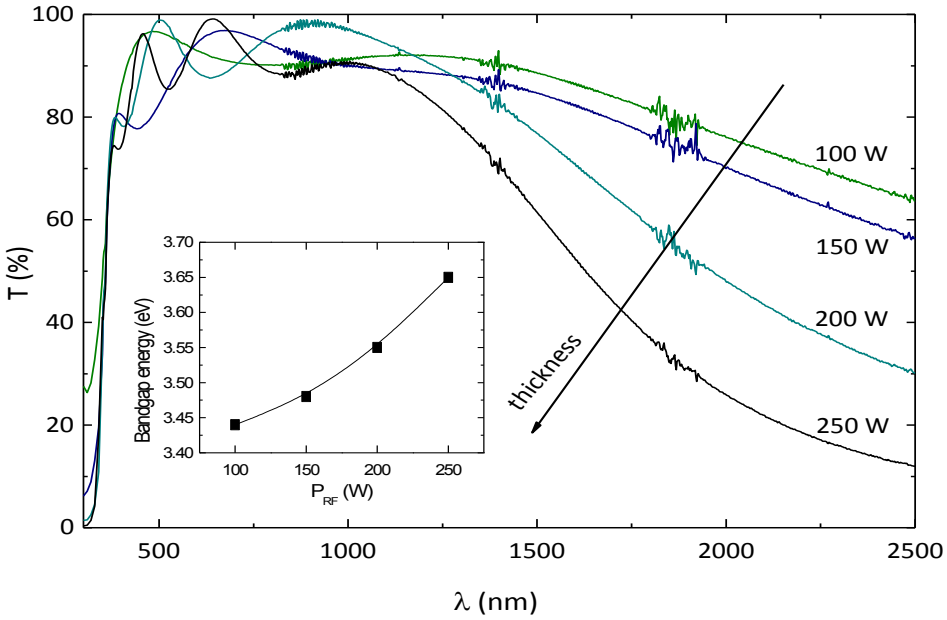

Fig. 5.25. *Optical transmittance spectra for AZO_D films sputtered with different RF powers (P_{dep}= 0.2 Pa). The inset shows the variation in optical band gap energy at different RF power.*

5.1.7.3. Effect of deposition pressure on AZO thin films properties

The effect of working gas pressure (P_{dep}) on the AZO films properties has already been introduced in section 5.1.7.1 when studying the deposition rate during sputtering. In this section, special attention is paid to the dependence of structural, electrical, morphological and optical properties of sputtered AZO thin films on P_{dep}. The RF power was fixed at 250 W. Similarly to the thin films deposited in section 5.1.7.2, all thin films in this section were deposited at RT.

Fig. 5.26. shows the variation of electrical resistivity (ρ_e), carriers mobility (μ_e) and carriers concentration (N_e) as a function of working pressure (P_{dep}) of the thin films deposited with the 2 wt. % Al_2O_3 target (AZO_D) at RT and P_{RF} = 250 W. As a general trend the electrical properties worsen with increasing P_{dep}. The lowest ρ_e values were achieved for P_{dep}= 0.13 and P_{dep}= 0.20

Pa (ρ_e = 9.92 x 10^{-4} and ρ_e = 1.02 x 10^{-3} Ωcm, respectively). At higher P_{dep} values, ρ_e increases followed by a decrease on N_e and μ_e. The same behavior was observed by Assunção *et al.* [75] for Ga-doped ZnO (GZO) system and also by other groups [57, 76] using the same material (AZO). That dependence probably arises from the higher energy of the sputtered particles at lower P_{dep} values, leading to an improved nucleation, crystallinity and degree of ionized donors and hence leading to a better conductivity of the films. As previously mentioned, high P_{dep} values will cause decrease in MFP of sputtered particles, leading to small diffusion energy which will eventually result in poor crystallinity with porous structure and poor electrical properties.

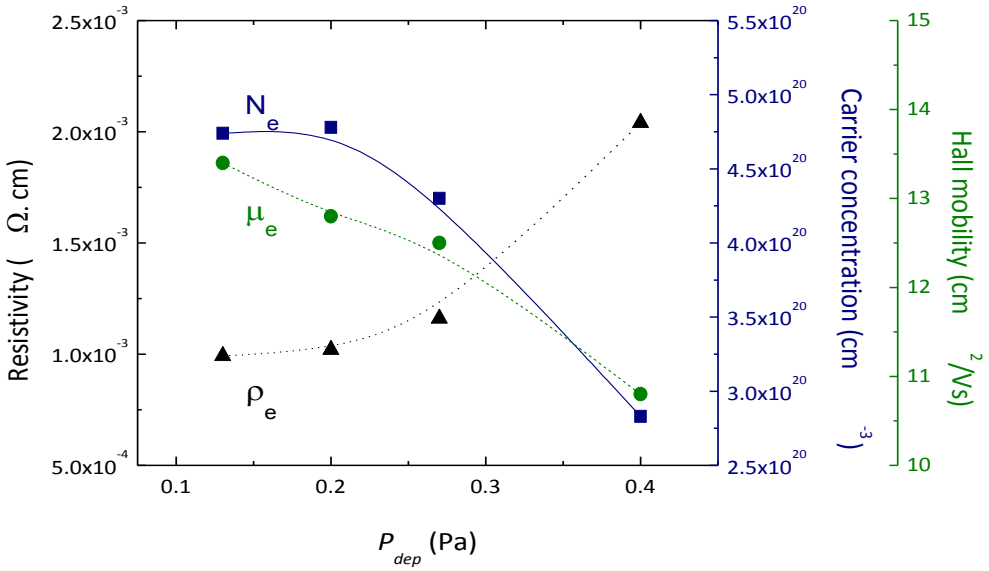

Fig. 5.26. *Electrical resistivity, carrier concentration and Hall mobility of AZO thin films as a function of P_{dep} deposited at an RF power of 250 W.*

Fig 5.27 shows the XRD diffraction patterns of as-deposited AZO thin films as a function of working pressure (P_{dep}) for a constant P_{RF} of 250 W. The thin films produced have also a hexagonal structure highly oriented along the c-axis (002) plane, growing perpendicular to the substrate. The peak intensity and crystallite size (see inset in Fig. 5.27) is higher for lower working pressures. Poor crystallinity and small grain size are largely responsible for the increase of the grain boundary barriers leading to the decrease of μ_e as it is observed in Fig. 5.26 [57]. The crystallite size is higher for lower P_{dep} (see inset of Fig 5.27). This fact can be explained by the species mobility. The working pressure can control the partial energy of the atoms during sputtering. As a consequence, there is a less chance of collisions between particles at low P_{dep} values, meaning that during the deposition, the sputtered species arrive to the substrate surface with high kinetic energy, their mobility is promoted, and then the atoms arrange themselves in a preferential way to form larger grains.

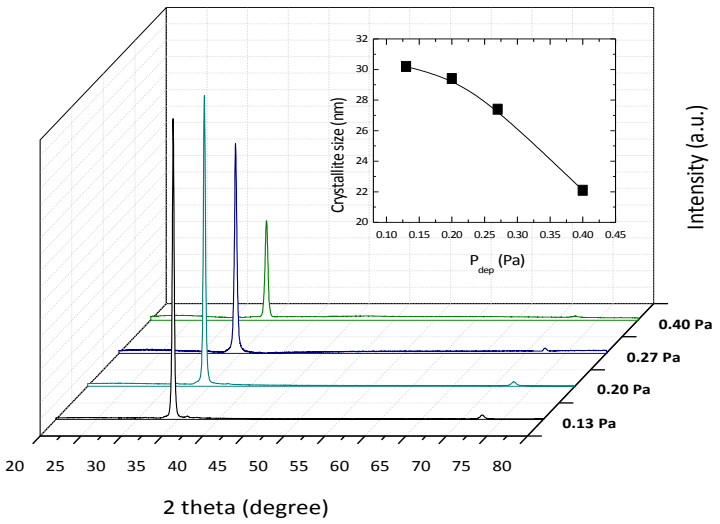

Fig. 5.27. *XRD patterns of AZO_D films deposited at RT as a function of P_{dep}(the diffractograms are normalized to the thickness of each film).*

The transmittance spectra of AZO films in the wavelength range of 300 to 2500 nm deposited at P_{RF} = 250 W and different working pressures are shown in Fig. 5.28. The mean transmittance in the visible range is above 90 **%** and the optical band gap energy (E_{opt}) of the films vary between 3.52 and 3.65 eV (see inset in Fig. 5.28), showing the already described blue shift relative to undoped ZnO (3.4 eV). The transmittance in the NIR region decreases for lower P_{dep}, which has been related to the absorption from the high free electrons concentrations, and is consistent with the electrical measurements presented in Fig. 5.26.

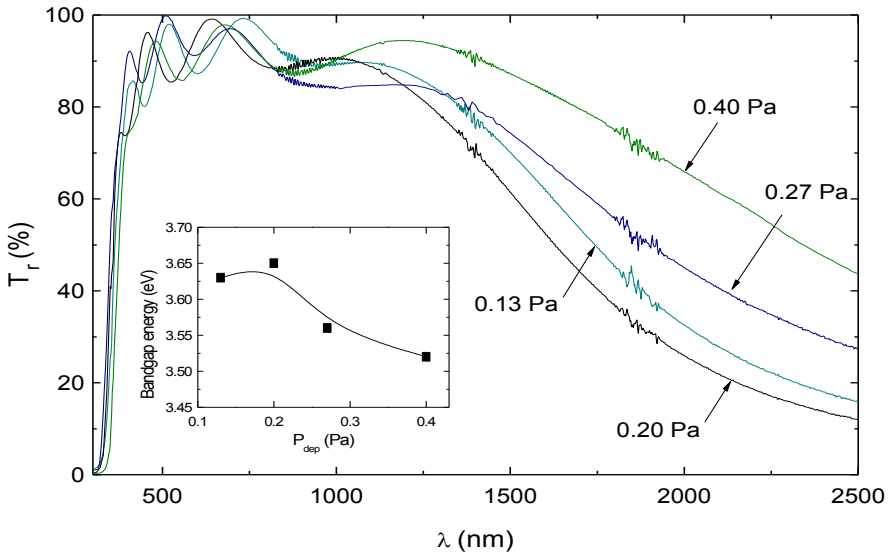

Fig. 5.28. *Optical transmittance as a function of wavelength for AZO_D films sputtered at different working pressures (P_{RF}= 250 W). The inset shows the variation in E_{opt} energy with the working pressure.*

Regarding the morphology of the films, is observed a decrease of the crystallite size (Fig. 5.27) and an increase of RMS roughness from 1.4 to 2.4 when P_{dep} increases from 0.13 Pa to 0.4 Pa. This is due to the fact that, as P_{dep} increases, the collision probability between the sputtered atoms and Ar ions increases so that the energy of the atoms arriving at the substrate surface is reduced and

surface migration is restricted. Furthermore, the Ar ions embedded in the film also limit surface migration. These factors lead to small grain size and rough morphology of the films [57].

5.1.7.4. Effect of Al-doping concentration on AZO thin films properties

The electrical properties of AZO films as a function of Al-doping concentration are presented in Fig. 5.29. The sputtered thin films prepared at RT, P_{RF} = 250 W and P_{dep} = 0.2 Pa show low ρ_e independently on the Al doping levels. As described to AZO ceramic targets, also during the deposition of films when the doping concentration is under the solubility limit, Al^{3+} ions easily replace the Zn^{2+} ions on substitutional sites providing electrons to the conduction band and lower ρ_e are achieved when compared with undoped ZnO thin films [77, 78]. As the aluminum content increases from 0.5 to 2.0 wt. % Al_2O_3 the electrical resistivity decreases from 2.83 × 10^{-3} Ωcm to 1.02 × 10^{-3} Ωcm. One the other hand, N_e, which is proportional to Al donors, rises for higher amounts of aluminum while μ_e decreases. The low ρ_e values of AZO_C and AZO_D are mainly due to high N_e while for small Al contents the low ρ_e values might be attributed to the higher μ_e of the films [79, 80]. The reduction in μ_e with the increase of Al content can be explained by the enhancement of scattering centers in the films. These scattering centers are formed by ionized Al or Al_2O_3 and its sub oxides which cause disturbance on the transport of carriers [79]. More details about the scattering mechanisms acting in sputtered AZO thin films will be discussed later in section 5.4.

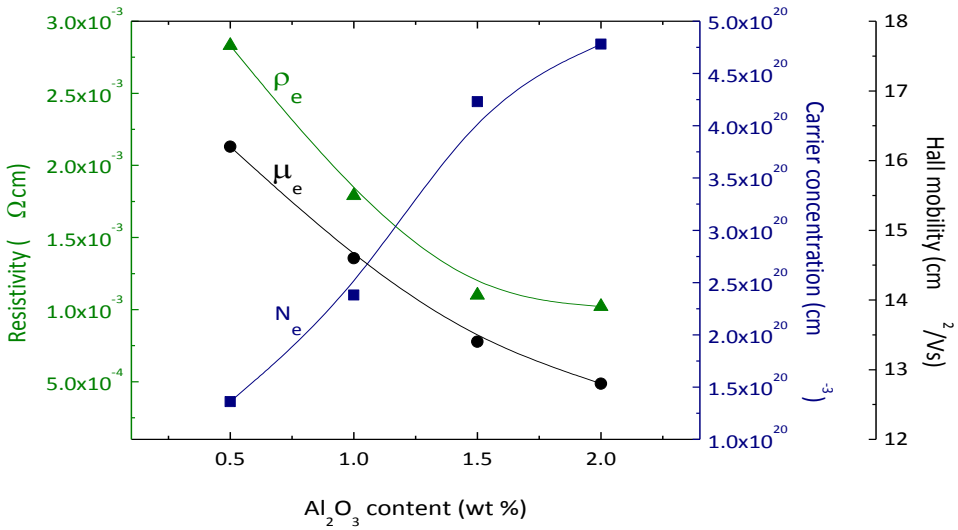

Fig. 5.29. *Effect of target doping concentration on electrical resistivity, Hall mobility and carrier concentration of AZO thin films deposited at RT (P_{RF} = 250 W; P_{dep} = 0.2 Pa).*

The same analyses were performed in thin films deposited from the two inches AZO_A target with higher electrical resistivity (see table 5.3). The films produced with this target (under the same sputtering conditions) have higher final ρ_e (7.28 × 10^{-3} Ωcm), and lower μ_e (11.5 $cm^2V^{-1}s^{-1}$), and N_e (7.46 × 10^{19} cm^{-3}) comparing with the results of films deposited with the lower resistivity AZO_A sputtering target (ρ_e = 2.83 × 10^{-3} Ωcm; μ_e = 16.2 $cm^2V^{-1}s^{-1}$; N_e = 1.36 × 10^{20} cm^{-3}). These results are consistent with the variation observed in the targets characteristics and show a correlation between targets and thin films electrical properties, not only due to the sintering atmosphere and consequent oxygen deficiency in the target as demonstrated by Minami *et al.* [37]

and Huang *et al.* [40], but also by the chemical and particularly the structural and morphological homogeneity of the targets.

The XRD patterns of the AZO thin films deposited on glass substrates by RF magnetron sputtering is shown in Fig. 5.30. The films are polycrystalline and also preferentially oriented along the c-axis ((002) diffraction peak). No Al, Al_2O_3 or $ZnAl_2O_4$ characteristic peaks were detected in the films, for all studied compositions, suggesting that Al replaces Zn substitutionally in the hexagonal lattice of ZnO wurtzite structure, or is segregated into the non-crystalline region of grain boundaries [78]. The XRD results show also a degradation of crystallinity with the increase of Al doping concentration.

One would expect a correspondence between the better crystal orientation and the improvement of the sputtered AZO thin films ρ_e, due to the reduction in the scattering of the carriers at the grain boundaries and crystal defects, which increases the apparent carrier mobility [81]. However, for the range of Al doping levels studied throughout this work (0.5 – 2.0 wt. % Al_2O_3) the increase of N_e with Al doping level appears to be the dominant factor concerning the reduction of ρ_e instead μ_e as illustrated in Fig. 5.29. The observed decrease in crystallinity can be due to two different factors: firstly, the segregation of Al in the grain boundaries (singly or combined) which usually occurs for higher doping concentrations [55, 56]; secondly, the one that seems to be the predominant factor in our case since we are working below or in the limit of the maximum solubility of Al in ZnO thin films (see section 5.1.7.4.1), the formation of stress induced by the substitution of Zn ions (0.74 nm) for smaller ions of Al (0.54 nm) [78, 80, 82-85]. This residual stress caused by the inclusion of Al in ZnO lattice is also responsible for the shift to higher 2θ values of the (002) peak [78, 86]. According to Bragg´s law (eq. 3.8), the peak shift of a specific plane to a higher angle means a decrease in the inter-planar distance of a specific plane [80]. The replacement of Zn atoms by smaller ionic radius atoms of Al is responsible for compressive stress induced by the reduction of the c-axis lattice parameter. The observed (002) peak shift to higher 2θ values with the increase of Al doping concentration is possibly explained by the greater number of Al atoms in substitutional positions in ZnO lattice, in line with the observed increase in N_e observed in Fig. 5.29.

The crystallite sizes of the films decreases from 52 to 29 nm as Al content increases, in good agreement with the SEM images of Fig. 5.31. Owing to the trivalent cation (Al) doping, the concentrations of the zinc interstitials are reduced for charge compensation, resulting in a reduced crystallite size and deteriorated crystallinity [87]. Also a decrease from 473 nm (AZO_A) to 363 nm (AZO_D) in film thickness and a reduction of the roughness of the films from 9.3 nm to 2.4 nm is observed as the Al content increases.

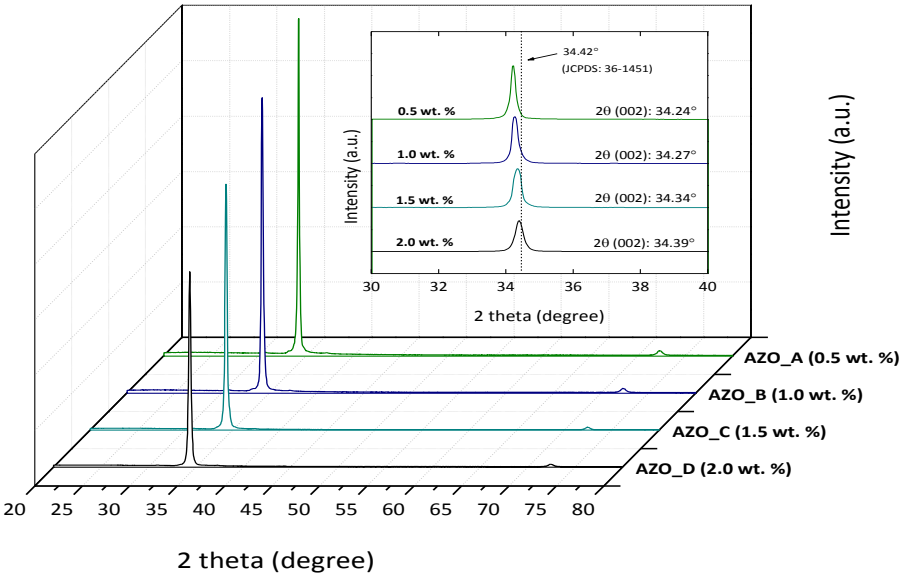

Fig. 5.30. *XRD patterns of Al-doped ZnO films deposited at RT as a function of aluminum concentration (the diffractograms are normalized to the thickness of each film).*

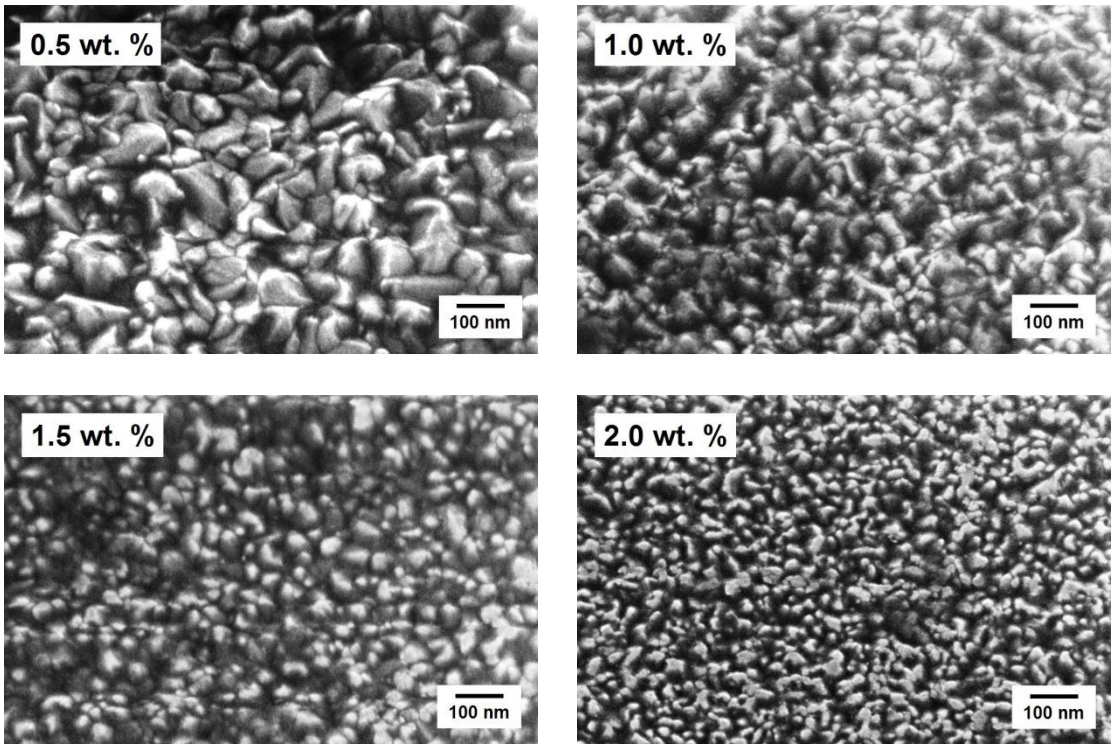

Fig. 5.31. *AZO films morphology as a function of aluminum concentration deposited at RT ((P_{RF} = 250 W; P_{dep} = 0.2 Pa).*

The optical transmission spectra of AZO thin films as a function of Al concentration is shown in Fig. 5.32. All films irrespective of the doping concentration exhibit a transmittance (T_r) above 80 % in the visible spectra range, which is close to that of the conventional ITO films, indicating that these materials are suitable for transparent electrode. In the NIR region the transmittance decreases, particularly for high aluminum doping concentrations reaching values of ≈ 17 % and ≈

12 % of transmittance for λ = 2500 nm for AZO_C and AZO_D in that order. For lower doping concentrations the NIR transmittance was ≈ 36 % and ≈ 55 % (λ = 2500 nm) for AZO_B and AZO_A, respectively. In section 2.5.3.2 was concluded that conduction characteristics of undoped ZnO films are primarily dominated by electrons generated from Zn interstitials (Zn_i) and oxygen vacancies (V_O). Typically, pure ZnO has a direct optical bandgap of 3.2 – 3.4 eV [69, 88]. On the other side, for AZO thin films, the contribution from Al^{3+} ions on substitutional sites of Zn^{2+} ions leads to the widening of E_{opt} caused by the increase of N_e. Using INNOVNANO AZO targets the films show an increase in E_{opt} from 3.45 to 3.65 eV as Al content rises, in good agreement with previous works [79, 89-91].

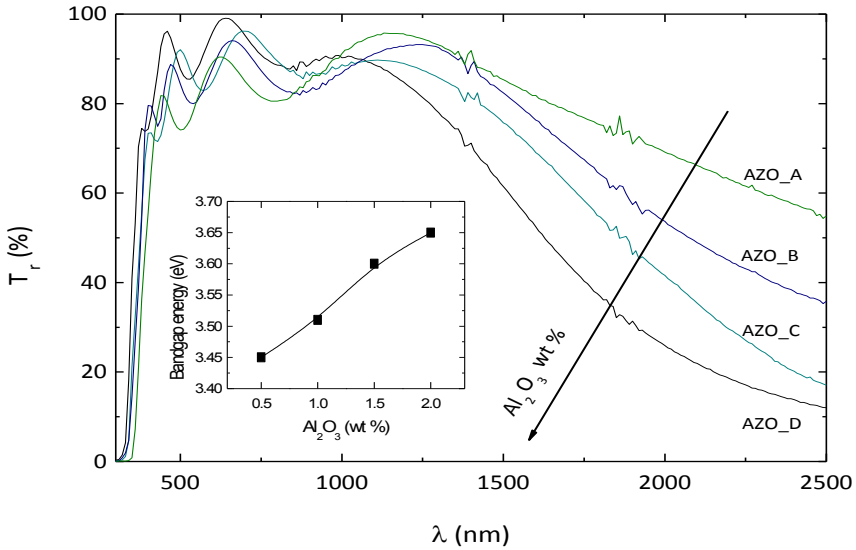

Fig. 5.32. *Optical transmittance of Al-doped ZnO films with the doping concentration. The inset shows the variation in optical bandgap.*

This broadening in E_{opt} with the increase of Al concentration agrees with the already presented Burstein-Moss effect [64, 65] which denotes a shift in Fermi level in the conduction band of semiconductors due to an increase of free electron concentration (see eq. 2.8 and eq. 2.9 from section 2.5.2.1). Hence, the valence electrons require extra energy to be excited by photons to higher energy states in the conduction band. The absorption coefficient (α) in the NIR region is directly dependent on N_e and μ_e as shown in eq. 5.4 [92]:

$$\alpha = \frac{C\lambda^2 N_e}{\mu_e} \qquad \text{(eq. 5.4)}$$

where *C* is a constant and λ is the wavelength of the incident radiation. The absorption coefficient increases with λ and N_e, decreasing with μ_e. Fig. 5.29 shows that for higher doping concentrations, the thin films exhibit an increase in N_e and a decrease in μ_e promoting the absorption for higher wavelengths.

5.1.7.4.1. Solubility limit of Al in ZnO sputtered thin films

The quality of AZO films is strongly dependent on the Al-doping level. When the Al content in ZnO is under the solubility limit, the supplied Al atoms easily replace the Zn ones as substitutional

atoms. However, when the solubility limit is exceeded, the Al atoms (individually or combined) locate to the interstitial sites and the wurtzite structure of ZnO starts to collapse. Moreover, as Al concentration is further increased, nano-sized metallic Al clusters and randomly oriented ZnO-based nanocrystals are formed, justifying the commonly observed deterioration of the crystallinity of heavily doped AZO thin films [1]. So, the understanding of the Al doping limit to produce high quality TCO materials is crucial.

As shown in section 5.1.5.3, the solubility limit value found for Al in ZnO bulk material is reduced (~0.09 at. % Al). In general the electrical properties of the films are superior to those of bulk materials since the solubility limit can be greatly enhanced in thin films [2]. Typically, AZO thin films exhibit higher N_e and lower μ_e than the sputtering targets with a slight reduction of the ρ_e [40, 41]. This is easily evidenced by the electrical properties of the targets and thin films presented respectively in Fig. 5.17 and 5.21. Several authors [78, 82, 89, 93, 94] have investigated about the Al doping limit which leads to improved electrical properties in AZO thin films. Deng *et al.* [78] studied the effect of Al doping concentration in AZO thin film properties varying the Al concentration between 1.80 and 8.06 at. % Al. The authors found an optimum Al doping level of 4.06 at. % Al and observed that above this value both N_e and μ_e deceases, suggesting that higher doping concentrations gives rise to excess of non-active Al atoms segregated onto the non-crystalline grain boundary, which act as scattering centers without contributing with carriers to the material. Muiva *et al.* [89] ranged the doping concentration between 1.0 – 10.0 at. % Al and found that above 2.5 at. % Al the properties of the films deteriorate. Bazzani *et al.* [93] investigated the critical dosage for an optimal AZO TCO and suggest 3 – 4 at. % Al as the doping level limits before optoelectronic degradation of the AZO films. Minami *et al.* [88] reported that when ZnO film is doped with Al or Si prepared by sputtering using ZnO:Al_2O_3 or ZnO:SiO_2 targets, N_e increases with increasing the amount of Al_2O_3 or SiO_2, and decreases when the amount of Al_2O_3 or SiO_2 in the target is over ~4 wt. %. Finally, Singh *et al.* [82] and Kim *et al.* [57] obtained a doping level of 2 wt. % Al_2O_3 (3.16 at. % Al) and 3 wt. % Al_2O_3 (4.71 at. % Al) respectively, from which the electrical conductivity of the films reaches its maximum value.

Based on the presented literature we can conclude that the Al doping concentration that gives rise to lower ρ_e values is in the range 2.5 – 4.5 at. % Al and may correspond to the solubility limit of Al in ZnO thin films and the border between active doping and non-active doping of Al in ZnO. The higher reported carrier concentrations for AZO are about 1.5×10^{21} cm^{-3}, which corresponds to a dopant concentration of 3.6 at. % relative to zinc atoms [72]. This fact explains why the standard composition of lab and industrial AZO sputtering targets is 98:2 wt. % ZnO:Al_2O_3 (3.16 at. % Al), the higher doping concentration investigated in this work (AZO_D).

5.1.8. Effect of sintering atmosphere during CS

As evidenced in the introduction of this dissertation (section 2.7.1.3) the oxygen content plays an important role in the performance of AZO targets affecting directly their electrical properties and consequently the properties of the sputtered TCO films. When preparing highly conductive and transparent AZO films, controlling the oxidation of Zn is much more complicated than with other binary compounds such as SnO_2 and In_2O_3, because Zn is more chemically active in an oxidizing atmosphere than either Sn or In [39]. Because of this binding energy of Zn and O, the activity and amount of oxygen must be precisely controlled during deposition. AZO films with low ρ_e are

achievable only by depositions in less oxidizing atmospheres than in depositions of SnO_2 and In_2O_3 films. For this reason, the preparation of ITO films by sputtering of ITO ceramic targets usually requires O_2 gas introduction during deposition in order to obtain a lower resistivity, while for AZO films, the introduction of O_2 is dispensable. So, in order to obtain highly conductive AZO sputtered films the oxygen content in the targets is very important, since the oxidization occurring on the surface of substrates is mainly dominated by the substrate temperature and the activity and quantity of the oxygen generated from the target reaching the substrate surface [95].

To evaluate the influence of sintering atmosphere on the properties of INNOVNANO AZO targets prepared by CS and corresponding sputtered thin films, several targets with different compositions (0.5 – 2.0 wt. % Al_2O_3) were prepared accordingly with the proceeding presented in section 3.2.1.2.1.

5.1.8.1. Influence of sintering atmosphere on target properties

The variation of ρ_r and G_S of the targets sintered in Ar with the sintering temperature and Al doping concentration is shown in Fig 5.33 a) and b) respectively. No significant differences in terms of densification behavior were observed regardless of the sintering atmosphere (see Fig. 5.8 for comparison). Final densities near the TD were achieved for all the compositions, being observed the same trend of AZO targets sintered by CS in air, with a retarding effect on densification with the increase of Al-doping level. Also the HT effect was evaluated for AZO_D samples sintered at 1200 °C for 2 h, 4 h, and 16 h (not shown here) showing a similar trend to the samples sintered in air (Fig. 5.4 c)).

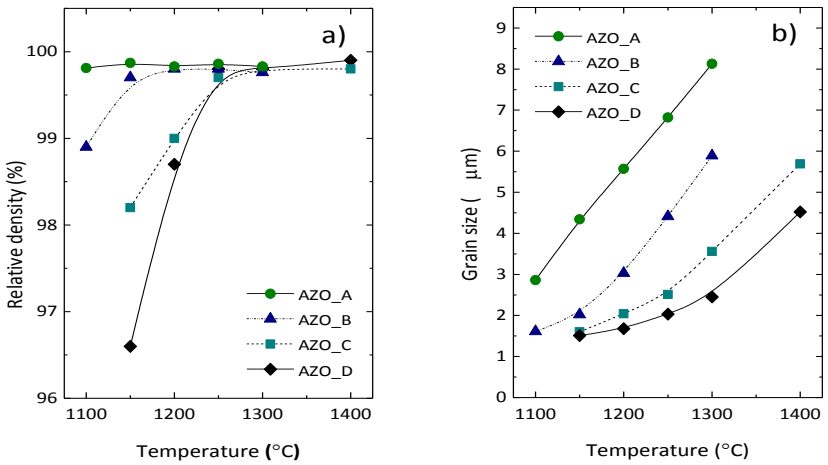

Fig. 5.33. *a) Relative density and b) grain size dependence on sintering temperature and composition for AZO samples sintered in Ar atmosphere ($P_{O_2} \sim 10^{-5}$ atm).*

In terms of G_S, each composition shows identical evolution with the sintering temperature as its corresponding sintered in air (see Fig. 5.10). However, a close look at the final G_S values, demonstrates a slightly tendency for a decrease considering the same sintering temperature, HT and composition. The SEM micrographs of AZO samples with different compositions sintered in Ar atmosphere at 1300 °C for 2 h are presented in Fig. 5.34. Similarly to the already observed for AZO targets sintered in air, despite the main phase (wurtzite), also the spinel phase gahnite ($ZnAl_2O_4$) can be easily identified.

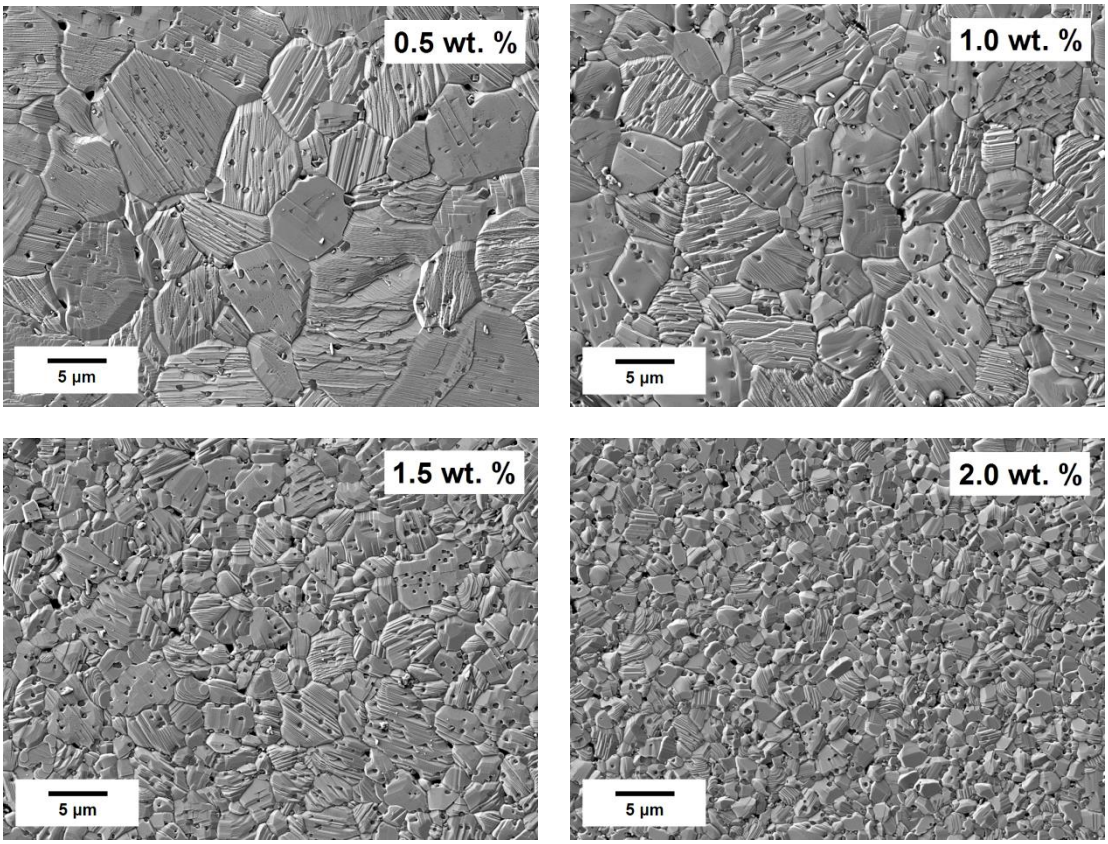

Fig. 5.34. *Microstructural analysis showing the typical morphology of INNOVNANO AZO ceramic targets with different aluminum contents sintered at 1300 °C with 2 h of HT under Ar atmosphere.*

The structural characterization of the samples sintered in Ar atmosphere was analyzed as a function of sintering temperature, HT and Al-doping level. Fig. 5.35 shows the XRD spectra from AZO_D sample sintered in argon at 1300 °C for 2 h. All the analyzed samples are composed by a primary phase (wurtzite) and a secondary phase (gahnite spinel) in agreement with SEM micrographs. The amount of $ZnAl_2O_4$ increases from 0.63 wt. % to 3.37 wt. % with the Al-doping level, corroborating the values presented in Table 5.1 (section 5.1.5.3) for targets prepared by CS in air.

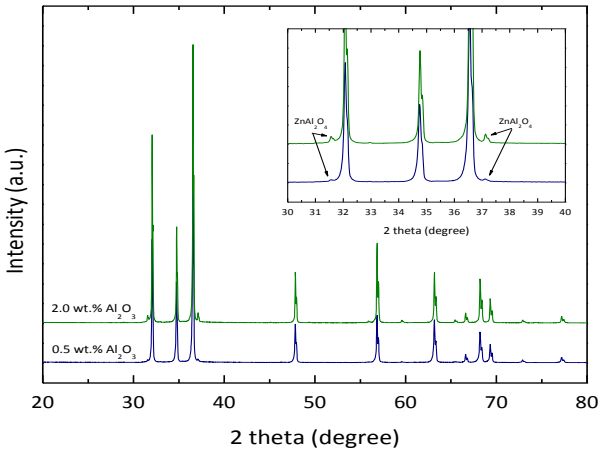

Fig. 5.35. *X-rays diffraction patterns of AZO ceramic targets (1300 °C and 2 h of HT) with 0.5 and 2.0 wt. % Al_2O_3 sintered in Ar atmosphere.*

Table 5.5 shows the electrical properties of several AZO targets with different compositions sintered under Ar atmosphere. The effect of sintering temperature was evaluated for AZO_D in the range 1200 – 1400 °C (HT = 2 h). Similarly to samples prepared by CS in air, the lowest ρ_e of AZO_D (1.11×10^{-3} Ωcm) was achieved at 1300 °C. Comparing with the values of Fig. 5.17, for the same range of sintering temperatures, the variation of ρ_e for the targets sintered in Ar is substantially lower than for the ones sintered in air. The impact of HT on the electrical properties of the targets was evaluated on AZO_D samples varying the HT between 2 h and 16 h at a constant temperature of 1300 °C. The ρ_r is similar for all samples (near the TD) and G_S increases from 2.45 μm to 3.84 μm with HT. It is observed the same trend (but much less pronounced) from targets prepared by CS in air, with a slight increase in ρ_e from 1.11×10^{-3} Ωcm to 1.44×10^{-3} Ωcm with HT. The effect of sintering atmosphere on AZO_C, AZO_B and AZO_A was evaluated using the same sintering cycles which gave rise to the best electrical properties of each composition during CS in air. Electrical resistivities of 1.19×10^{-3} Ωcm, 1.32×10^{-3} Ωcm and 1.58×10^{-3} Ωcm were attained respectively for AZO_C, AZO_B and AZO_A targets. In general, comparing with AZO targets produced by CS in air, it should be pointed out the substantial increase (in general ~2 times higher) in both μ_e (31.6 – 41.2 $cm^2V^{-1}s^{-1}$) and N_e (9.3×10^{19} – 1.39×10^{20} cm^{-3}), resulting in lower ρ_e of AZO targets sintered in Ar.

Table 5.5. *Electrical properties of AZO targets sintered in Ar atmosphere – Variation with sintering temperature (1200 – 1400 °C), HT (2 – 16 h) and Al-doping concentration (0.5 – 2.0 wt. % Al_2O_3).*

Composition	Sintering cycle		Electrical properties		
($ZnO:Al_2O_3$ wt. %)	(°C/h)		$\rho_e \times 10^{-3}$(Ωcm)	μ_e ($cm^2V^{-1}s^{-1}$)	$N_e \times 10^{20}$(cm^{-3})
98 : 2	1200	2 h	2.03	33.1	0.93
	1300	2 h	1.11	41.2	1.36
		4 h	1.27	37.8	1.30
		16 h	1.44	34.8	1.25
	1400	2 h	1.56	31.6	1.27
98.5 : 1.5	1300	2 h	1.19	38.9	1.35
99 : 1	1150	2 h	1.32	33.9	1.39
99.5 : 0.5	1100	2 h	1.58	35.2	1.12

The basic feature of ZnO defect chemistry is that ZnO is a non-stoichiometric oxide with metal in excess [23], which origins intrinsic donors in ZnO. As described in section 2.5.3.2, there are two kinds of intrinsic defects that may form and contribute appreciably to the formation of free electrons and conductivity of ZnO: oxygen vacancies (V_O) and zinc interstitials (Zn_i). These two types of defects have similar electrical properties, which makes it difficult to distinguish between them experimentally and which is more dominant to form and thus creates free carriers to lead to the conductivity of ZnO [23, 96-99]. Since the source of transport carriers on n-type ZnO is electrons form extrinsic doped impurities (Al-doping in our case) and native point defects, the enhanced conductivity of AZO targets within the same Al-doping concentration for sintering in Ar atmosphere should be associated with the increment of native point defects. During CS in Ar, the concentration increase of native point defects occurs due to the absence of oxygen during

sintering, resulting in a non-stoichiometric ZnO target with oxygen deficiency (see chemical quantitative analysis in section 5.5) as illustrated by eq. 5.5:

$$2ZnO\ (s) \leftrightarrow\ ZnO_{1-x} + xO_2 \qquad \text{(eq. 5.5)}$$

So, during CS in Ar atmosphere both extrinsic defects caused by the Al substitution into the lattice sites of Zn (Al_{Zn}) and intrinsic defects derived from the formation of non-stoichimetric ZnO_{1-x} with oxygen deficiency were produced, providing large amount of free electrons leading to enhanced conductivity.

Based on these results, we can state that the microstructural influence of the AZO targets is much smaller for samples sintered in Ar, than for samples sintered in air, and that the oxygen deficiency have a strong impact in the ρ_e of AZO bulk material.

5.1.8.2. Sputtering of Ar sintered AZO targets and their film properties

To evaluate the performance of AZO targets sintered in Ar atmosphere, a 2 inches AZO target with 2.0 wt. % Al_2O_3 was manufactured and used to deposit AZO films by RF magnetron sputtering technique. The target has a final density of 5.59 g.cm^{-3} (99.7 % of TD) and a grain size of 2.57 µm. The ρ_e, μ_e and N_e are respectively 1.04 × 10^{-3} Ωcm, 43.5 cm^{2}V^{-1}s^{-1} and 1.38 × 10^{-20} cm^{-3}. During deposition, P_{RF} and P_{dep} were kept constant at 250 W and 0.2 Pa in that order. The deposition was held for 1 h without O_2 flow. Sputtered film has a thickness of 432 nm (DR ≈ 7.2 nm.min^{-1}).

Fig. 5.36 a) and b) shows respectively the transmittance spectra in the optical wavelength range of 350 – 2500 nm and the XRD spectrum of the deposited film. The film exhibited an average transmittance above 80 % in the visible optical region and an E_{opt} of 3.72 eV. In the NIR T_r decreases due to the high free electrons concentrations (resulting from the Al doping and the creation of extra oxygen vacancies), in agreement with the electrical measurements presented above. Structural analysis showed that the sputtered film is highly oriented with the c-axis along the (002) plane perpendicular to the substrate. The estimated crystallite size of the film based on Scherrer equation (eq. 3.9) was 30 nm.

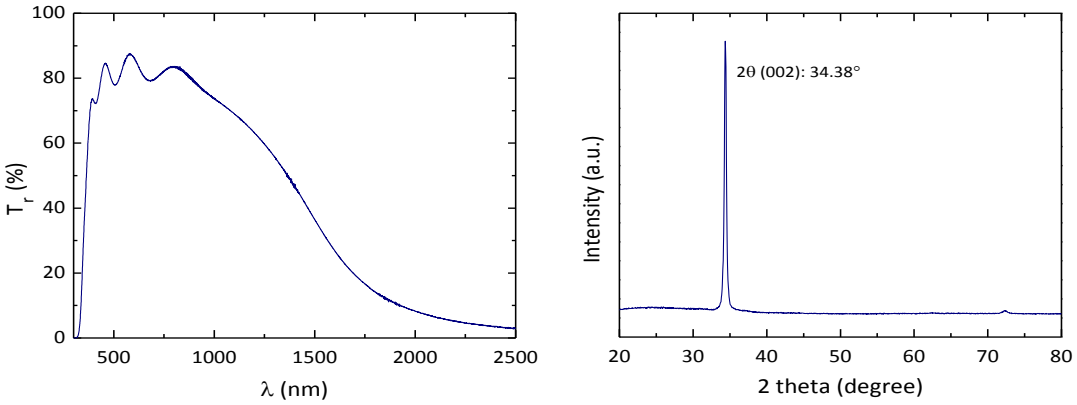

Fig. 5.36 *a) Transmittance spectra and b) XRD pattern of AZO thin film deposited at RT from the AZO target (98:2 wt. % ZnO:Al_2O_3) sintered in Ar atmosphere (P_{RF}= 250 W; P_{dep}= 0.2 Pa).*

The deposited AZO film has a ρ_e value of 8.86 x 10^{-4} Ωcm (μ_e of 11.7 cm^{2}V^{-1}s^{-1} and N_e of 6.02 x 10^{20} cm^{-3}), which correspond to a reduction of ~14 % comparing with thin films sputtered from

targets prepared by CS in air under the same deposition conditions. Although the AZO film deposited from the air sintered target exhibit slightly higher μ_e (12.8 $cm^2V^{-1}s^{-1}$) (section 5.1.7.2), the N_e value of the film deposited using Ar sintered target almost doubles, indicating that the decrease in ρ_e was mainly due to the increase of N_e in the sputtered films.

These results indicate that under the same deposition conditions the conductivity of deposited AZO films was enhanced using a less resistive AZO target.

5.2. AZO sputtering targets manufacture – Alternative methods and its effects on sputtered thin films

In this section, alternative methods were used in the production of AZO targets: hot pressing (HP) and spark plasma sintering (SPS). Both techniques were performed in controlled atmosphere by applying external pressure during sintering, enabling to reach high density AZO targets at lower temperatures and with improved electrical properties. The purpose of using these techniques was the optimization of sintering parameters taking into account the final microstructural and electrical properties of the targets as well as the optoelectronic properties of corresponding sputtered films. Additionally, non-sintered AZO targets were also prepared and used for thin films deposition and devices fabrication. Taking into account the properties of the synthesized powders and the absence of a sintering stage, these targets can be an alternative for the production of low-cost devices with improved performance.

5.2.1. AZO sputtering targets by hot-pressing (HP)

The use of reducing atmosphere during sintering may further enhance the conductivity of the targets and respective films. However excessive reducing environment can be catastrophic for the target due to undesirable reduction of the metal-oxide material to metal. Furthermore, even avoiding this, the oxygen content must be enough to ensure the high transparency of films.

Chopra *et al.* [100] stated that non-stoichiometric metal rich oxide should be used in the preparation of high quality TCO thin films. However, they also agree in a limit for the oxygen reduction. Ellmer [50] shown that films with an excessive oxygen deficiency are opaque. Accordingly to the author, the unmeasured reduction of the oxygen content during deposition is responsible for the reduction of ZnO phase and a corresponding increase of the un-oxidized, i.e. metallic Zn, leading to the darkening of the films. This can be explained by the stronger affinity of oxygen to Al and the much higher probability of re-evaporation of Zn compared to Al, due to the low melting point of Zn [101]. On the other side, the oxygen and N_e are inversely proportional, so when high quantities of oxygen are present the potential barrier between the gains increases leading to lower μ_e [102]. By increasing the amount of oxygen during (or after) deposition, the dopants become oxidized and hence lose its doping effect. A common complication is related with the appearance of secondary phases. Apart from ZnO, also $ZnAl_2O_4$, Al_2O_3 or ZnO_2 (a low temperature phase in the Zn-O system) can be formed [72].

In this section are shown the results concerning the deposition of films from 2" and 3" AZO targets produced in graphite dies by hot-pressing (HP) under reduced atmosphere using powders with 0.5 and 2.0 wt. % Al_2O_3. The production of metal oxide sputtering targets using graphite die

assemblies have been known to exhibit problems related with the interaction between the powdered target starting material and the graphite material of the die assembly [103]. Problems include both the degradation of the graphite dies and the full reduction of the metal oxide material to metal, at least in the form of a layer on the outer surface of the resulting target blank. To reduce this effect, the graphite dies were coated with high quality protection layer of hexagonal boron nitride. Additionally, to ensure the maximum uniformity of the sintered target, all the hot-pressed AZO targets were machined and polished after sintering to remove the surface layer of the targets.

5.2.1.1. Hot-pressed AZO targets – manufacturing and characterization

AZO targets were prepared by HP accordingly with the proceeding presented in section 3.2.1.2.2. Table 5.6 shows the relative density and final grain size of several 2" manufactured targets as a function of composition and sintering cycle.

Table 5.6. *Relative density and final grain size dependence on sintering cycle and composition of several 2" AZO targets sintered by HP (cooling/heating rate of 10 °Cmin^{-1}; external pressure of 50 MPa).*

Composition $ZnO:Al_2O_3$ (wt. %)	Sintering cycle (°C/h)	Relative density (%)	Grain size (μm)
98:2	1100/1h	98.2	1.10
	1150/1h	99.4	1.24
	1150/2h	99.6	1.36
	1200/1h	99.8	1.67
99.5:0.5	950/1h	96.3	0.63
	1025/1h	99.4	0.84
	1100/1h	99.7	2.12

Compared to CS technique (Fig. 5.8), HP allows obtaining high density sputtering targets at substantially lower sintering temperatures. Final densities near the TD were reached at 1150 °C and 1025 °C with 1 h of HT, respectively for AZO_D (2.0 wt. % Al_2O_3) and AZO_A (0.5 wt. % Al_2O_3) powders. A reduction of at least ~100 °C is accomplished by HP sintering with similar relative densities. Besides that, the heating/cooling rates are also faster (double) and the HT was halved leading to substantially shorter sintering cycles. A substantial decrease of final grain size is another important characteristic of samples prepared by HP whose values are between 0.6 and 2.0 μm depending on the sintering cycle and Al-doping concentration. As indicated in chapter 2 (section 2.11.7) the grain growth is independent of the applied external pressure [45, 104]. Nevertheless, it is responsible for increasing the densification rate, allowing reducing the sintering temperature and/or HT and consequently suppressing grain growth [105]. The grain size measurement also demonstrate that the grain overgrowth observed for lower doping concentrations by CS (see Fig. 5.10) can be suppressed using HP sintering technique at temperatures in the range 1000 – 1100 °C. The same trend was also observed by Mazaheri *et al.* [105] during the sintering of nanocrystalline ZnO compacts. The authors found a parabolic grain

growth during the final stage of sintering for both CS and HP methods, being such effect more moderate in HP compared to CS.

Three different hot-pressed targets were tested in the deposition of films: two 2" targets with respectively 0.5 and 2.0 wt. % Al_2O_3 and one 3" target with 0.5 wt. % Al_2O_3 (Fig. 5.37). The sintering cycle selected for each composition was chosen taking into account the best compromise between ρ_r, G_S and sintering time (Table 5.6): 2" targets with 0.5 and 2.0 wt. % Al_2O_3 were sintered at 1025 °C and 1150 °C for 1 h, respectively; the sintering cycle of the 3" target (0.5 wt. % Al_2O_3) was similar to the one of the 2" target with the same Al-doping level, presenting comparable characteristics in terms of ρ_r (99.4 %) and G_S (1.06 µm).

Fig. 5.37. *Picture of the 3" and 2" hot-pressed targets with an Al-doping concentration of 0.5 wt. % Al_2O_3 (targets sintered at 1025 °C for 1h).*

TEM and SEM images of the 3" AZO target (Fig. 5.38 a) and b), respectively) show small and regular grains size in the range of 0.5 and 1.0 µm with a roughly hexagonal habit, typical of the wurtzite phase. Contrary to the observed for AZO targets prepared by CS in air and/or Ar, $ZnAl_2O_4$ minor phase is hardly identified in both TEM and SEM images of HP targets independently of the composition or sintering temperature. Nevertheless, EDS mapping revealed some Al rich zones corresponding to the black spots observed in Fig. 5.38 b). In addition, XRD performed on the 3" sintered target (Fig. 5.39) revealed that besides the main wurtzite phase, a minor secondary $ZnAl_2O_4$ phase (gahnite) is still present. The same was observed for the 2" AZO targets independently on de Al-doping level.

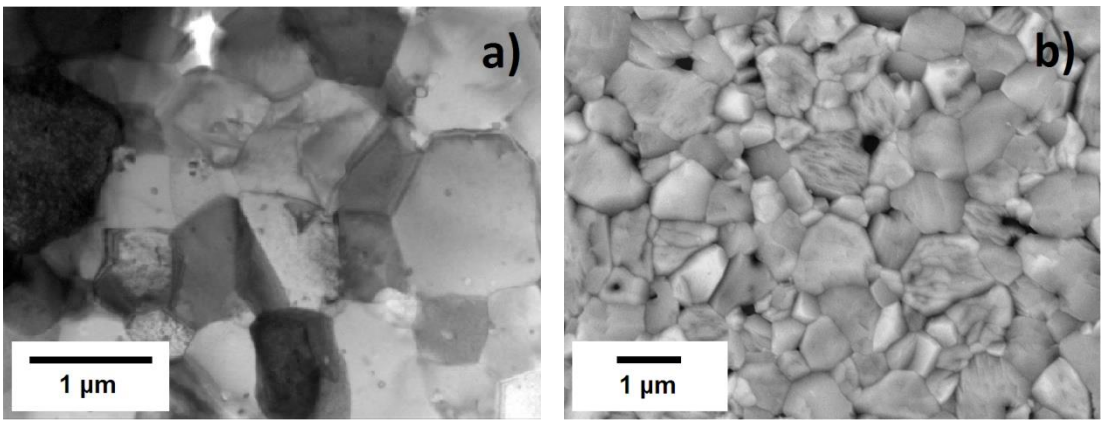

Fig. 5.38. *TEM sample thinned to 75 nm by FIB milling using a dual beam FEI Nova 600 Nanolab SEM a) and SEM b) images of the AZO target material sintered by HP at 1025 °C for 1 h at a constant heating/cooling rate of 10 °C.min^{-1} and an external pressure of 50 MPa.*

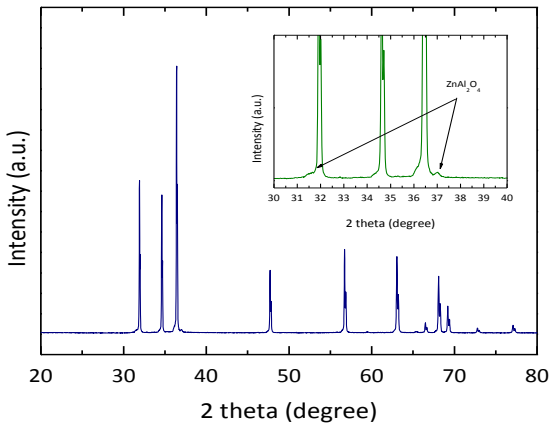

Fig. 5.39. *X-ray diffraction pattern of the 3" AZO target with 0.5 wt. % Al_2O_3 (1025 °C and 1 h of HT) sintered by HP.*

To confirm the presence of $ZnAl_2O_4$ phase, the samples were analyzed after polishing without thermal etching to reveal the grains. Fig. 5.40 shows the general morphology of 2" AZO target with 2.0 wt. % Al_2O_3. Two different phases can be identified in SEM image of the polished surface of the target. The dark grey spots correspond to the minor spinel phase gahnite, which is well distributed throughout the main wurtzite phase. Small isolate pores can also be identified and are mainly located near the spinel phase particles.

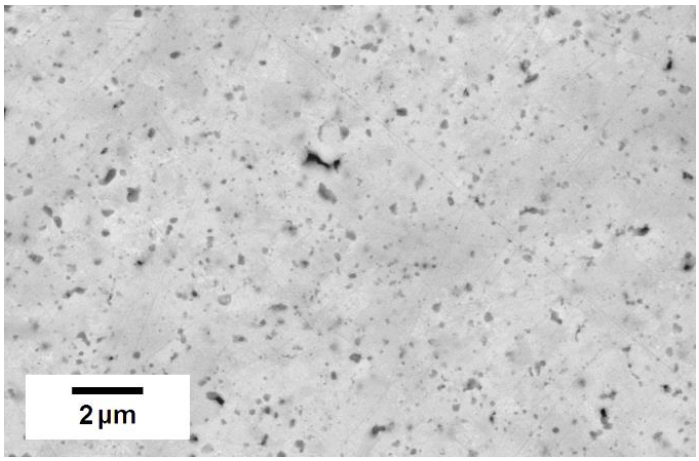

Fig. 5.40. *SEM image of the polished surface of 2" AZO target (2.0 wt. % Al_2O_3) without thermal etching.*

The electrical properties of the hot-pressed AZO targets used during sputtering deposition are shown in Table 5.7. Electrical resistivity values of ~4 x 10^{-4} Ωcm were obtained independently on the composition or target dimension. Comparing with targets prepared by CS in Ar, no considerable improvement was observed in terms of μ_e (~40 $cm^2V^{-1}s^{-1}$). However, N_e increases approximately six and four times compared with the targets prepared by CS in air (see Table 5.4) and argon (see Table 5.5), respectively. This increase in N_e and consequent reduction of ρ_e can be attributed to native defects formed during sintering.

As mentioned above, HP was carried-out in graphite dies under reduced atmosphere. Even with the hexagonal boron nitrate protection layer, at high temperatures, besides the substitution of Al atoms in ZnO lattice (eq. 5.6) the oxygen from the AZO target react with carbon from the graphite

die assembly, generating carbon monoxide (CO) gas. The CO gas will in turn react with Al-doped ZnO, thereby forming non-stoichiometric ZnO (ZnO_{1-x}) and carbon dioxide (CO_2), resulting in oxygen deficient ZnO as illustrated in eq. 5.7 and eq. 5.8 [103]:

$$Al_{Zn}^{x} \longrightarrow Al_{Zn}^{\bullet} + e^{-} \quad \text{(eq. 5.6)}$$

$$ZnO + CO \leftrightarrow ZnO_{1-x} + xCO_2 \quad \text{(eq. 5.7)}$$

$$O_O^x \rightarrow V_O^{\bullet\bullet} + 2e^{-} \quad \text{(eq. 5.8)}$$

Even removing their external layer, the target will have a strong oxygen deficiency (see chemical quantitative analysis in section 5.5) which increases the intrinsic defects of the AZO targets and consequently their N_e and conductivity. It should be noted that this oxygen deficiency is more pronounced during HP than throughout CS in Ar atmosphere, since during sintering, besides the absence of oxygen, the surrounding atmosphere is also propitious to obtain oxygen deficient AZO targets. As both native (V_O) and extrinsic (Al_{Zn}) defects were produced after sintering from chemical reduction and intentional Al doping respectively, large amount of free electrons are provided and so N_e was improved, leading to enhanced conductivity. Therefore, under controlled conditions, the use of reducing atmospheres during sintering can be a solution to prepare highly conductive AZO targets as already suggested by other authors [39, 40].

Table 5.7. *Electrical properties of hot-pressed AZO targets used in films deposition.*

Al-doping level (wt. % Al_2O_3)	Sintering cycle (°C/h)	Electrical properties		
		ρ_e $\times 10^{-3}$ (Ωcm)	μ_e ($cm^2V^{-1}s^{-1}$)	N_e $\times 10^{20}$ (cm^{-3})
2.0 (2"target)	1150/1h	0.37	43.7	3.86
0.5 (2" target)	1025/1h	0.43	42.1	3.45
0.5 (3" target)	1025/1h	0.41	38.7	4.03

5.2.1.2. Sputtering of hot-pressed AZO targets and their film properties

The thin films were deposited at RT under the same RF power and deposition pressure (P_{RF} = 250 W and P_{dep} = 0.2 Pa) as those used in the sputtering of the targets prepared by CS in air and Ar atmospheres.

A deeper investigation concerning the validation of the scale-up made on the target size and the optimization of lower Al-doping level sputtering target was performed. This work was developed in a partnership with CREST – Loughborough University using a 3" target with 0.5 wt. % Al_2O_3 (Fig. 5.41). The 3" target was deposited using an AJA International Orion 8HV sputter coater with an AJA 600 series RF power supply with no oxygen input and 5 SCCM (8.33 x 10^{-8} m^3s^{-1}) of argon. P_{RF} and P_{dep} were kept at 180 W and 0.13 Pa, respectively, whilst the temperature and deposition time were varied. Films were deposited over one, two and three hours, and the substrate temperatures used were RT, 100, 150, 200, 300 and 450 °C. Each deposition temperature was

used for each of the three deposition times. A second set of films was deposited from a commercially available target for comparison. These films were deposited at 150 °C. This temperature was chosen as it was found to give the best overall performance.

Fig. 5.41. *Picture of the 3" hot-pressed AZO target with an Al-doping concentration of 0.5 wt. % Al_2O_3 bonded to a cooper support.*

5.2.1.2.1. Properties of AZO films sputtered from hot-pressed 2" AZO targets

Fig. 5.42 a) and b) shows respectively the transmittance spectra in the wavelength range of 350 – 2000 nm and the XRD spectrum of the thin films deposited using the 2" targets with 0.5 and 2.0 wt. % Al_2O_3. The average transmittance (AVT) of produced films is ~80 % and the estimated E_{opt} is ~3.6 and ~3.7 eV, respectively for low and high Al-doping levels. The crystallite size of the films decreases from 49 nm to 35 nm as Al-doping increases from 0.5 to 2.0 wt. % Al_2O_3 showing the same trend of thin films deposited with targets produced by CS in air (section 5.1.7.4).

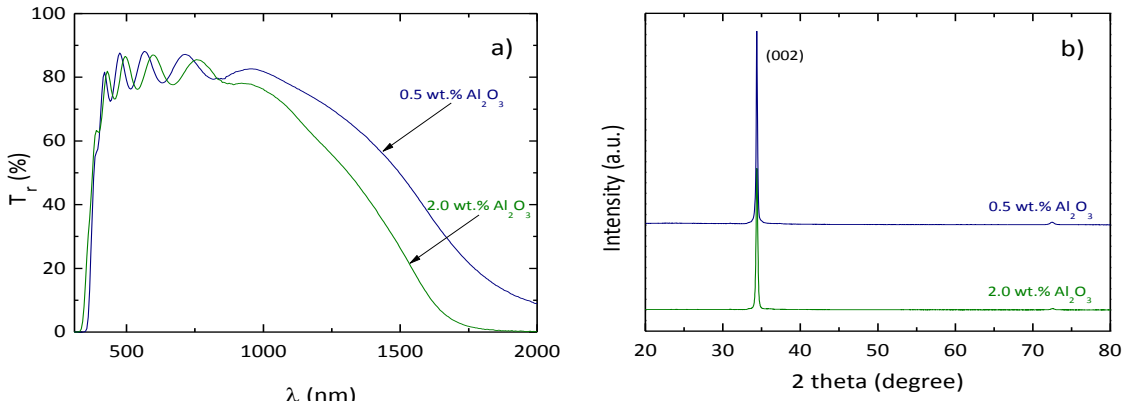

Fig. 5.42. *a) Transmittance spectra and b) XRD pattern of AZO thin films deposited at RT from the 98:2 wt.% and 99.5:0.5 wt.% AZO targets prepared by HP (P_{RF}= 250 W; P_{dep}= 0.2 Pa).*

The electrical properties of the thin films sputtered from 2" hot-pressed AZO targets at RT are summarized in Table 5.8. The films have a resistivity of about 6 – 7 × 10^{-4} Ωcm (reduction of ~35 % relatively to AZO layers deposited with CS targets prepared in air under the same conditions). In contrast to what was observed for the sputtering targets, the μ_e of the AZO layers decreased from 32.2. to 12.5 $cm^2V^{-1}s^{-1}$ with the Al-doping level while N_e increased from 2.88 × 10^{20} to 8.10 × 10^{20} cm^{-3}. A larger number of active carriers in the films compared to the targets may explain this behavior. As discussed before, the solubility limit in the thin films is much higher than the observed for the ceramic targets (sections 5.1.5.3 and 5.1.7.4.1). Consequently, some Al atoms

unavailable for conduction in the targets will be available in the sputtered films increasing N_e and decreasing μ_e. This increase of N_e is also responsible for a drop in the NIR region transmittance (Fig. 5.42 a)), mainly for the 2.0 wt. % Al_2O_3 composition.

Table 5.8 *Electro-optical properties of the TCO films deposited at RT from 2" hot-pressed AZO targets.*

Composition (wt. % Al_2O_3)	Thickness (nm)	DR (nm.min^{-1})	Electrical properties		
			ρ_e (Ωcm)	μ_e (cm^{2}V^{-1}s^{-1})	N_e (cm^{-3})
0.5	566	9.4	6.73× 10^{-4}	32.2	2.88× 10^{20}
2.0	523	8.7	6.16× 10^{-4}	12.5	8.10× 10^{20}

The growth rates of the films are ~9 nm.min^{-1}, which is substantially higher than that obtained with targets prepared by CS in air (6.0 nm.min^{-1}) and Ar (7.2 nm.min^{-1}) under the same deposition conditions. This correlation of higher DR and lower resistivity of ceramic sputtering targets was already stated by Minami *et al.* for thin films deposited by DC-magnetron sputtering [37, 38].

5.2.1.2.2. Properties of AZO films sputtered from hot-pressed 3" AZO target – effect of substrate temperature during deposition

Independently of the substrate temperature, the deposition rate was found to be approximately 5.5 nm.min^{-1}, with film thicknesses of ~330 nm after 1 h, ~660 nm after 2 h and ~1 µm after 3 h. Considering the applied P_{RF} (180 W) and P_{dep} (0.13 Pa) and extrapolating the DR based on the results from Fig. 5.20, the result is in good agreement with the 2" targets DR presented in the previous section (~9 nm.min^{-1}).

The sheet resistance as a function of the deposition temperature and time is shown in Fig. 5.43. The sheet resistance varies from 35 Ωsq^{-1} to around 3.1 Ωsq^{-1}, with specific values depending on both deposition temperature and film thickness. Although less apparent for thinner films, there is a trend for the sheet resistance to decrease slightly towards temperatures of 100 °C to 200 °C before rising slightly to 300 °C and then more rapidly beyond that.

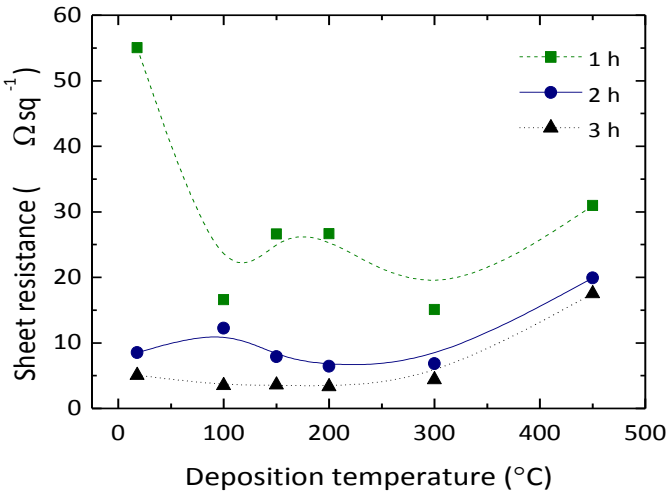

Fig. 5.43. *Sheet resistance dependence on deposition temperature and deposition time.*

Overall, N_e increases with increasing temperature up to 300 °C, which begins to plateau above 200 °C. The N_e drops significantly with a further increase in temperature from 300 to 450 °C. The μ_e doesn't change dramatically with increasing temperature, with films typically showing μ_e between 20 and 40 $cm^2V^{-1}s^{-1}$ (Fig. 5.44 a) and b)). The only thickness which demonstrates a clear trend is 1 µm (3 h of deposition), where μ_e increases up to a deposition temperature of 150 °C, before dropping off at higher deposition temperatures. The ρ_e of the thinner films decrease from 2.1×10^{-3} Ωcm at RT to values in the range of $4.1 - 9.1 \times 10^{-4}$ Ωcm between 100 °C and 300 °C, increasing for 1.0×10^{-3} Ωcm at 450 °C (Fig. 5.44 c)). Thicker films sputtered for 2 h (~660 nm) and 3 h (~1 µm) show ρ_e values of $3 - 5 \times 10^{-4}$ Ωcm at temperatures ≤ 300 °C which increases at 450 °C (> 1.0×10^{-3} Ωcm).

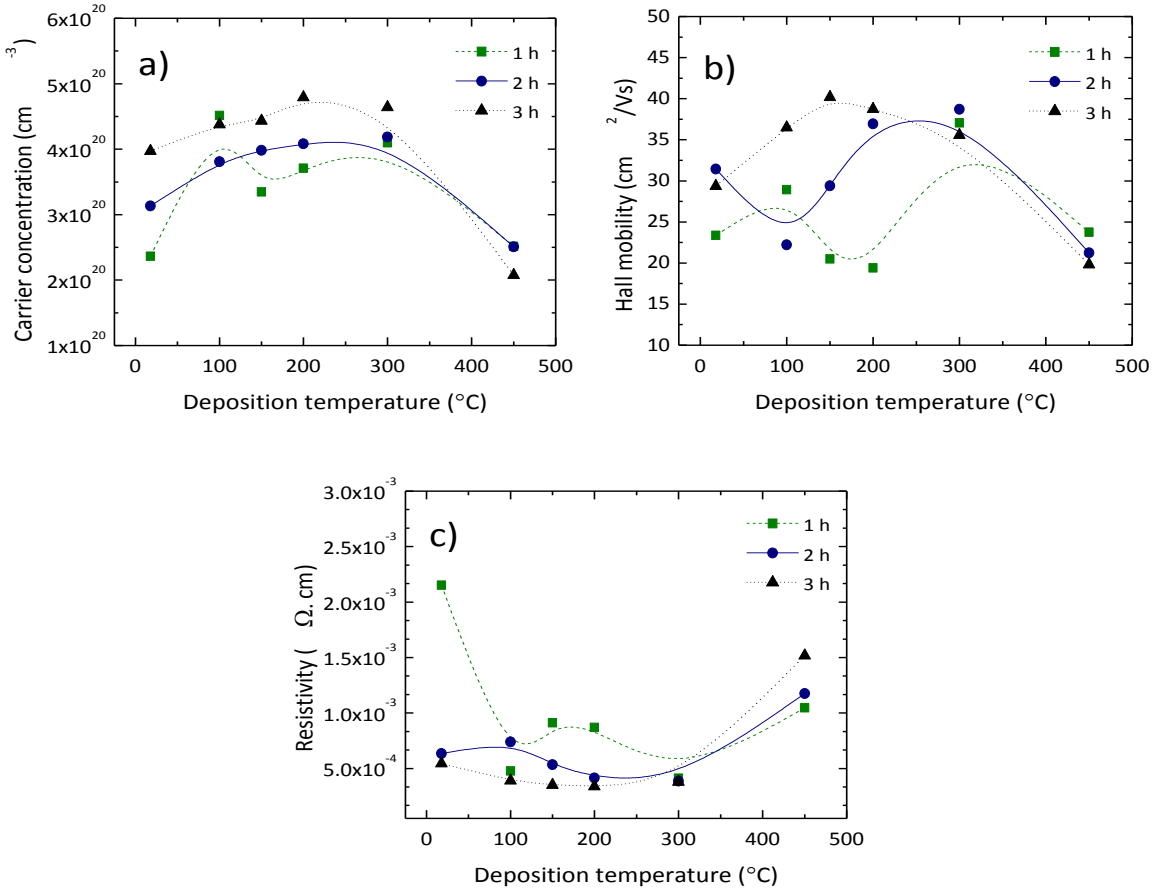

Fig. 5.44. *a) Carrier concentration, b) Hall mobility, and c) electrical resistivity dependence on deposition temperature and time of AZO thin films sputtered from 3" hot-pressed target (99.5:0.5 wt. % ZnO:Al_2O_3).The films thicknesses are ~330 nm, ~660 nm and 1 µm, respectively for deposition times of 1 h, 2 h and 3 h.*

The transmission in the visible range (400 – 800 nm) for these films is near or above 80 % independent of deposition temperatures and thicknesses (Fig. 5.45 a), c) and e)). The obtained spectra show that as the film thickness increases, transmission across both the visible and NIR wavelength ranges drops with the highest losses being in the NIR region. This was expected since thicker films tend to possess multiple internal reflections that occur inside the films reducing the overall transmittance [59]. The T_r decrease in the NIR appears greatest between the 330 nm and 660 nm thick films (Fig. 5.44 a) and c)) which is correlated to the increase in N_e of films [106]. The substrate temperature also influences T_r in the NIR, with the highest T_r values being attained for

films deposited at 450 °C, correlated with the drop in N_e observed for these films (see Fig. 5.44 a)). E_{opt} increases with deposition temperature up to a maximum value of 3.75 – 3.77 eV at 200 °C (Fig. 5.45 b), d) and f)). Above that temperature E_{opt} start to decrease with a significant drop observed at 450 °C, in agreement with the electrical properties presented above.

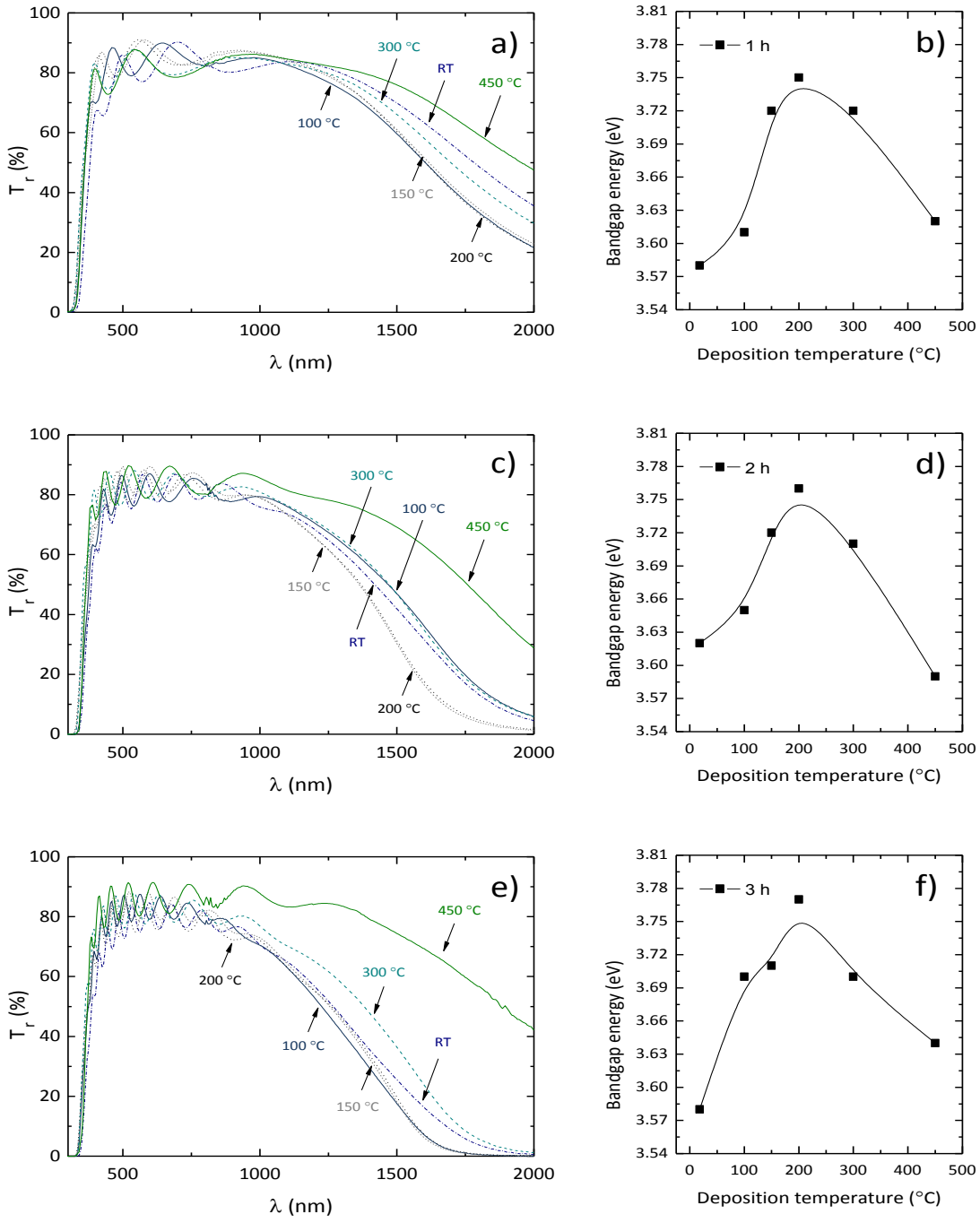

Fig. 5.45. *Optical transmittance (a), c) and e)) and bandgap energy (b), d) and f)) for AZO films of a), b) ~330 nm, c), d) ~660 nm and e), f) ~1 µm thickness versus substrate temperature.*

The top view of samples shown in the SEM images of (Fig. 5.46), reveal films with a surface morphology highly dependent of temperature. The films are largely crystalline with grain size increasing significantly with increasing temperature up to 150 °C. Further increasing the temperature reduces crystallinity dramatically, with films deposited at 300 °C and above

exhibiting again very small and well dispersed grains and an apparent increase in film surface defects (Fig. 5.46).

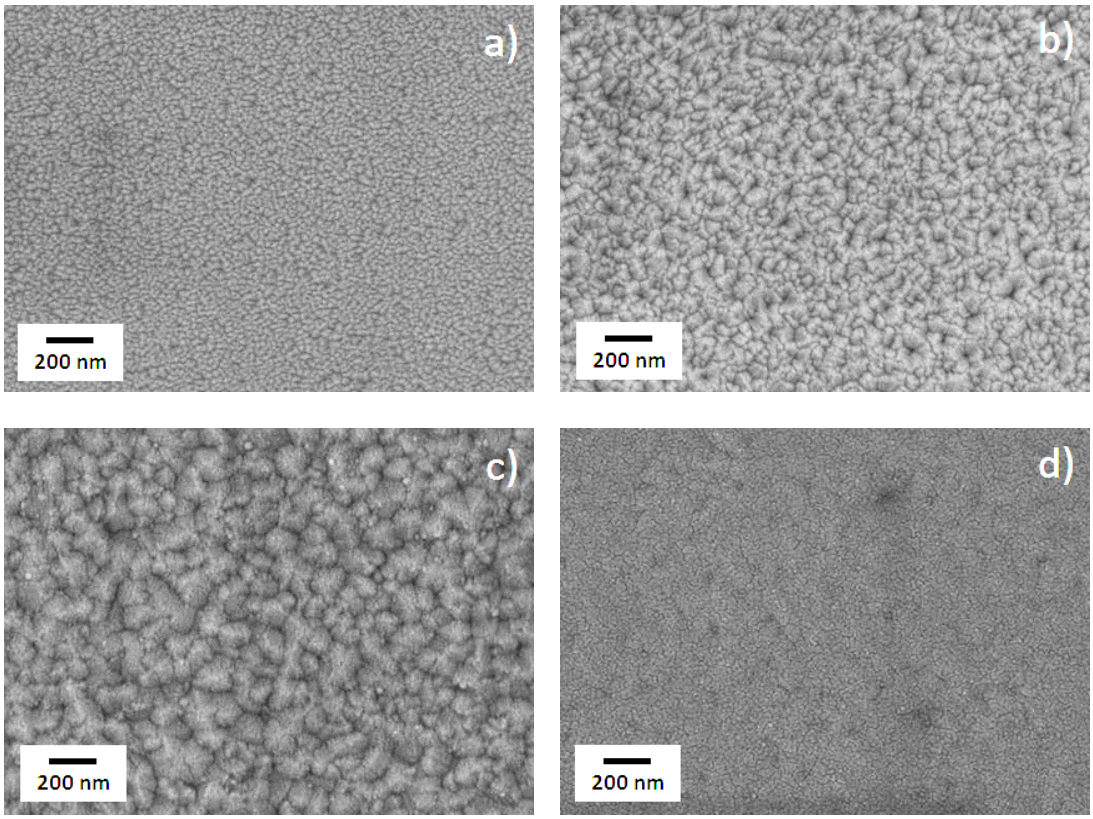

Fig. 5.46. *SEM images of samples deposited for 2 h (~660 nm thickness) at a) RT, b) 100 °C, c) 150 °C, and d) 300 °C.*

XRD analysis of Fig. 5.47 shows films with a single prominent peak from the (002) plane, with a very minor secondary (004) signal. This is something that other groups have noticed [37] and indicates that sputtered ZnO grows in the wurtzite (zincite) phase and preferentially along the c-axis. These XRD patterns have no evidence of $ZnAl_2O_4$ formation, despite trace amounts observed in XRD analysis of the target material (Fig. 5.39).

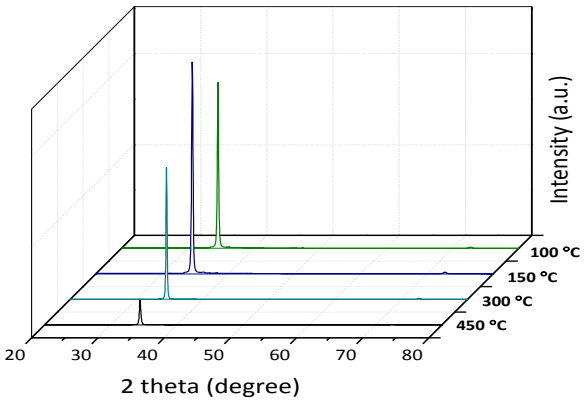

Fig. 5.47. *XRD patterns for films deposited for 3 h at 100 °C, 150 °C, 300 °C and 450 °C.*

Cross sectional TEM images of the samples (Fig. 5.48) confirm a preferential columnar grow, perpendicular to the substrate surface. However comparing Fig. 5.48 a) and b) we observe that

although retaining a certain degree of crystallinity, films deposited at 450 °C have smaller individual crystals and show a high level of defects when compared to films deposited at lower temperatures.

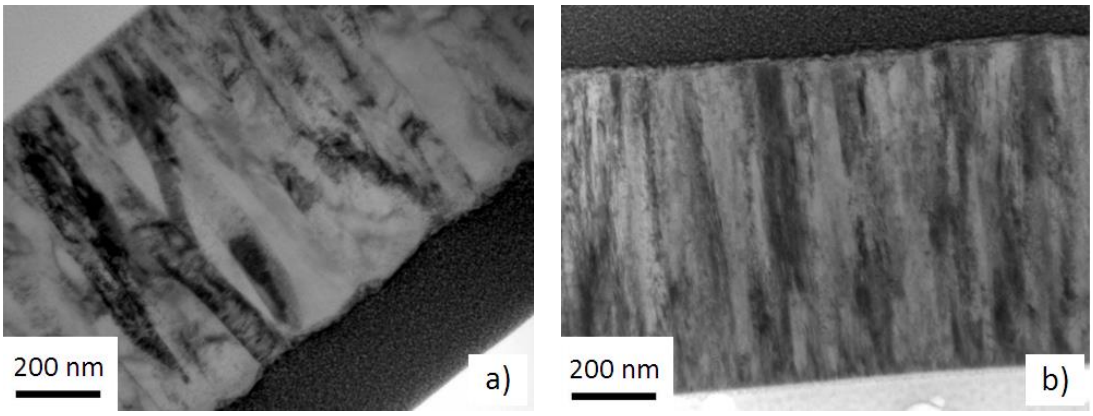

Fig. 5.48. *Cross sectional TEM images of films deposited for 3 h at a) 150 °C and b) 450 °C.*

Surface analysis performed by AFM confirmed that all the films are very smooth, with RMS surface roughness of between 1 and 3 nm. Overall, roughness was found to change in line with the observed changes in surface morphology shown in SEM images. Films grown at RT were the smoothest, with roughness increasing as the deposition temperature increases up to 200 °C. At higher temperatures, the roughness was found to decrease as grain size is reduced. The refractive index is 1.9 ± 0.04 at 550 nm for films deposited at temperatures up to 200 °C. This is in good agreement with literature values [107, 108]. The films deposited under a substrate temperature of 300 °C and 450 °C, have significantly lower refractive index, 1.6 ± 0.04.

The deterioration of the electrical and structural properties observed in AZO films prepared at temperatures above 300 °C was also reported by other groups in ZnO films doped with Si [109], Ga [110] and Al [76, 110-113], although the optimum substrate temperature varies upon the materials system and deposition method. The deterioration of electrical properties at high temperatures is due to a decrease in N_e and μ_e. In AZO films, changes of N_e during deposition has been related to the creation or annihilation of donor oxygen vacancies [70, 114, 115], as well as to the variations of crystallinity and crystal quality that alter the effective doping of Al onto Zn lattice sites [114, 116]. Several authors [50, 76, 109, 112, 113] studied the effect of substrate temperature in the final properties of AZO films. The degradation of electrical and structural properties for higher substrate temperatures to the Zn deficiency has been attributed to desorption (re-evaporation) of Zn (high vapour pressure of Zn) from the growing surface of the film and/or to the possible migration of Al to the grain boundaries where it forms Al_2O_3 rather than continuing to act as dopant, due to large up-take of oxygen (higher O/Zn ratio) for higher deposition temperatures. According to Kim *et al.* [76], both cases result in reduction of grain size.

Either effect would explain the drop in N_e and hence the increased ρ_e and NIR T_r. The highest temperature films appeared to be the least crystalline (Fig. 5.47) and contained the highest levels of defects (Fig. 5.48) suggesting that higher temperatures and hence increased system energy are the cause of the reduced conductivity. However, as the films deposited at 300 °C still demonstrated a good $\rho_e$value despite showing reduced crystal quality it is possible that the two are not directly related. Films deposited at lower temperatures were all found to be fully

crystalline, with crystal size increasing dramatically with increased temperature and deposition time. The lack of variation in resistivity and refractive index for lower temperature films indicates that whilst crystal size may have an impact on the optical and electrical properties, it is not the limiting factor. The most plausible explanations are either that crystal quality is of greater importance, or that the change in crystal quality is coincidental, and some concurrent change in either the doping level or film stoichiometry is the key.

Comparing with same Al-doping level commercially available AZO targets improved characteristics were achieved with this 3" AZO target. Transmission in the visible range is identical, although films deposited at lower temperature show lower T_r values in the IR region than films obtained with commercial targets. This is a result of N_e values roundly three times higher than that of the equivalent films deposited from commercial targets. The higher N_e of the films probably comes from the increased number of extrinsic and intrinsic defects of the targets inherent to manufacturing process. In fact, comparing with the films deposited from targets prepared by CS in air (section 5.1.7.4), the increase in N_e is evident from 1.4×10^{20} cm^{-3} to 2.9×10^{20} cm^{-3} (Table 5.8). Carrier mobility (μ_e) is similar for both, around 40 – 45 $cm^2V^{-1}s^{-1}$, and ρ_e is approximately a third of that shown by the films produced with 99.5:0.5 wt. % $ZnO:Al_2O_3$ commercial targets.

The overall properties of AZO films deposited with 0.5 wt. % Al_2O_3 3" target prepared by HP are suitable for many optoelectronic applications. Even considering the drop in the NIR transmittance observed for thicker films, the balance between optical and electrical properties shows that they can be applied on TFSCs production where high T_r from the visible to the NIR region is required. In fact, the NIR absorption can be a problem for some specific applications such as tandem and multi-junction solar cells devices where infrared light adds significantly to the photocurrent of the bottom absorber layers [117]. However for the vast majority of photovoltaic applications it is unlikely to be a problem as the transmission is consistently above 70 % as far as 1200 nm, which is into the infrared and equates to a bandgap of ~1 eV. An example is the silicon-based TFSCs, tandem solar cells with a bottom cell made of hydrogenated microcrystalline silicon (µc-Si:H). Microcrystalline Si has a similar absorption behavior to crystalline Si and thus can absorb light up to 1100 nm, implying that the front contact have a high optical transmission at this wavelength [118]. Thus, the 0.5 wt. % Al_2O_3 sputtered films (specially the films deposited between 150 and 300 ºC) meet the desired high quality TCOs requirements: 1) wide E_{opt} comparable to that of 2.0 wt. % Al_2O_3 films; 2) low absorption in the NIR region due to the lower N_e; 3) a slightly sharper transition from high visible and NIR transparency towards lower transparency for higher wavelengths caused by the higher μ_e; and 4) a low ρ_e of $3 – 4 \times 10^{-4}$ Ωcm, which is almost as low as for the routinely used 2.0 wt. % Al_2O_3 films.

In summary, the AZO samples described in this study deposited at temperatures of up to 300 °C show equivalent or lower sheet resistance of those found in literature for ITO [67]. This demonstrates that AZO is an ideal alternative to ITO, especially considering the scarcity and cost issues of In. In particular, films deposited at RT show excellent transmission and sheet resistance, making it ideal for applications that are temperature-sensitive such as organic electronics.

5.2.2. AZO sputtering targets by spark-plasma-sintering (SPS)

Spark-plasma-sintering (SPS) also known as field-assisted sintering technique (FAST) is a relatively new processing technique to reach high densities in a very short time (ultra-fast heating rates (100 – 500 °C.min^{-1}) and HT of only a few minutes) at temperatures below the ones traditionally required for CS and HP [119, 120], with the advantage of being applied a pulsed dc current passing through the pressure die and the sample. This process itself is similar to conventional HP, since the powders are located in a die made of conductor material (graphite), and subjected to a UP during sintering. However, instead of heating with an external source, a pulsed dc current is applied, passing through the pressure die and sample, so that the entire sample is heated. In addition to the heat and pressure, SPS utilizes the self-heating action caused by spark discharges between the particles, promoting material transport and densification enhancement [119]. The proposed methods for the rapid consolidation of particle systems are primarily focused on current effects within the powder system, such as localized joule heating, dielectric breakdown of oxides, and electro-migration [120].

Thus, considering the nanoscale of INNOVNANO AZO powders, SPS process might be advantageous in suppressing grain growth and improving morphological homogeneity. Furthermore, due to their reducing atmosphere, SPS promotes also the achievement of highly conductive targets.

5.2.2.1. Processing conditions and targets characterization

In this section, several 2" AZO targets with 98:2 wt.% ZnO:Al_2O_3 composition were prepared. The consolidation of the AZO compacts to dense sintered bodies was carried out in Spark Plasma Sinter equipment (FCT-HP D 25/1 of the company FCT Systeme GmbH) enabling 8000 A peak current at 8 V. The trials were performed under Ar atmosphere and the graphite die was coated with hBN. The heating/cooling rate and pressure were kept constant at 100°C.min^{-1} and 50 MPa, in that order. The applied pressure was ramped until 50 MPa at 20 MPa.min^{-1} and then released at the same rate after HT. Analogous to the targets prepared by HP, all the samples were machined and polished after sintering to remove the unwanted surface layer. The overview of experiments is shown in Table 5.9.

Table 5.9. *Relative density, weight loss and grain size variation with sintering cycle of several 2" AZO targets (98:2 wt.% ZnO:Al_2O_3) produced by spark-plasma-sintering.*

Sintering temperature (°C)	Holding time (min)	Relative density (%)	Grain size (μm)
900	15	97.2	0.38
900	30	98.4	0.46
925	15	99.2	0.57
1000	15	99.7	0.92
1100	15	99.7	1.94
1150	15	99.8	2.58

As shown, lower sintering temperatures are required to reach the same densification degree of samples sintered by CS and HP. Nearly full dense targets with small grain size (~400 nm) were achieved at 900 ºC for HT of 15 min. SEM images of Fig 5.49 reveal a regular microstructure composed by small and homogenous grains. However, the homogeneity of the grain sizes seems to be particularly affected by HT with a tendency to form bimodal distribution of the grain size (Fig. 5.49 b)). The homogeneity of the secondary phase distribution and size is clearly observed in Fig 5.49 d.

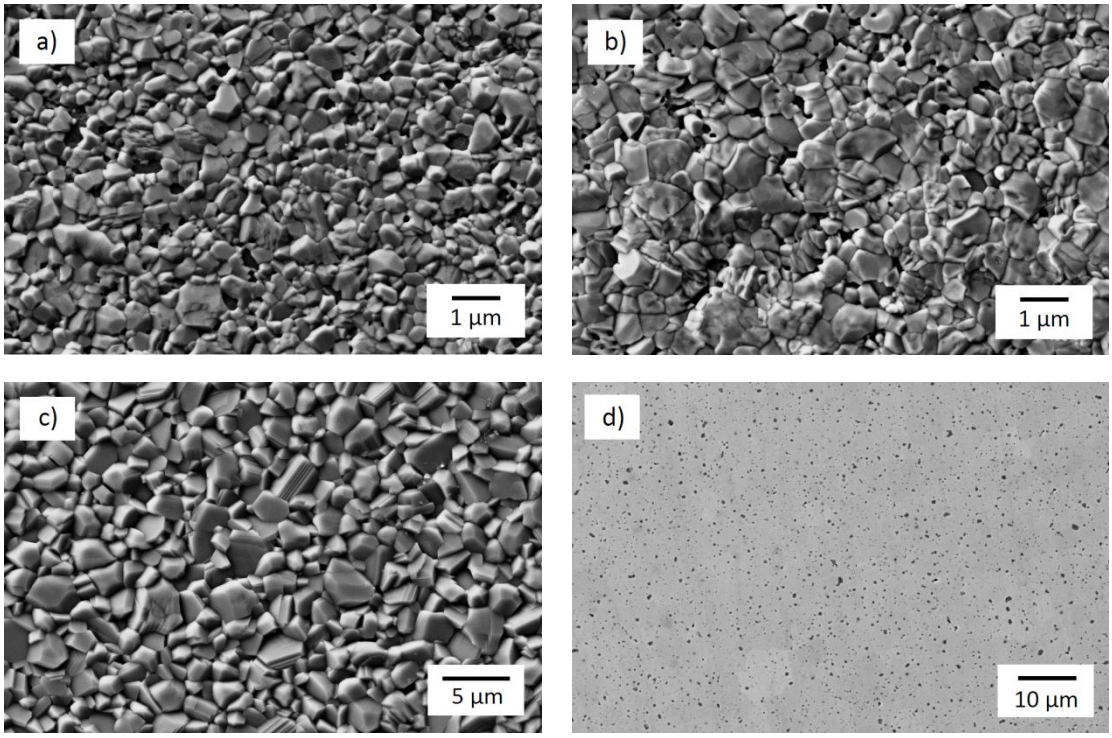

Fig. 5.49. *Microstructural analysis showing the morphology of INNOVNANO AZO targets sintered by SPS at: a) 900 °C/15 min, b) 900 °C/30 min; c) 1100°C/15 min. d) Shows the general overview of $ZnAl_2O_4$ phase distribution throughout the ZnO matrix (1150 °C/15 min).*

The structural characterization of several targets prepared by SPS is shown in Fig. 5.50. Despite the main phase wurtzite, phase quantification analysis reveals an amount of gahnite phase around ~3.5 wt. % which is independent on the sintering temperature and HT between 900 °C and 1150 °C.

Chemical composition of the targets was determined by Auger electron spectroscopy technique (described in section 3.2.2.2.1). The Al content of samples sintered between 900 °C and 1100 °C for 15 min is ~3.3 at. % indicating that the Zn/Al ratio does not vary during SPS (details in section 5.5).

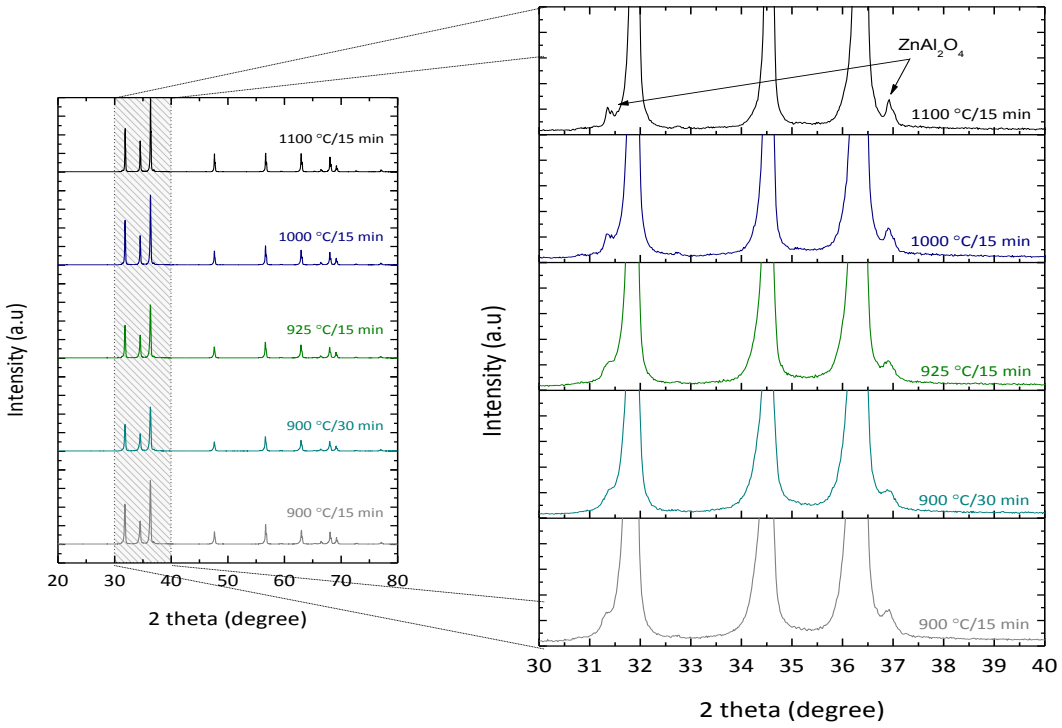

Fig. 5.50. *X-ray diffraction patterns of AZO 98:2 wt. % ceramic targets after SPS showing wurtzite as the main phase; Detail illustrating the presence of $ZnAl_2O_4$ spinel phase.*

5.2.2.2. Thin films – deposition and characterization

The deposition of the films was carried out using the 2" target sintered at 1000 °C for 15 min (less resistive target). The target has a ρ_e, μ_e and N_e of 4.60 x 10^{-4} Ωcm, 36.2 $cm^2V^{-1}s^{-1}$ and 3.75 x 10^{20} cm^{-3}, respectively. During depositions, P_{dep} was kept constant at 0.2 Pa and the P_{RF} varied between 150 and 250 W. The sputtering time was fixed at 1 h.

For the best condition tested (P_{RF} = 250 W) the electrical resistivity (ρ_e), μ_e and N_e of the films are respectively 6.8×10^{-4} Ωcm, 12.2 $cm^2V^{-1}s^{-1}$ and 7.44×10^{20} cm^{-3}. The sputtered film has a thickness of 487 nm corresponding to a DR ≈ 8.1 $nm.min^{-1}$, between the DR obtained for 98:2 ZnO:Al_2O_3 target sintered at 1300 °C/2h by CS in Ar (≈ 7.2 $nm.min^{-1}$) and that of hot-pressed target sintered at 1150 °C/1 h (≈ 8.7 $nm.min^{-1}$).

The optical properties of these films are also similar to those obtained from hot-pressed target (section 5.2.1.2.1) with an average transmittance of ~80 % (including glass substrate), optical bandgap (E_{opt}) of ~3.7 eV and a remarkable decrease in transmission at the wavelength between 1000 and 2500 nm (NIR). The crystallite size calculated from the XRD spectrum of the film (Fig. 5.51 a)) was 34 nm, in line with the SEM image depicted in Fig. 5.51 b).

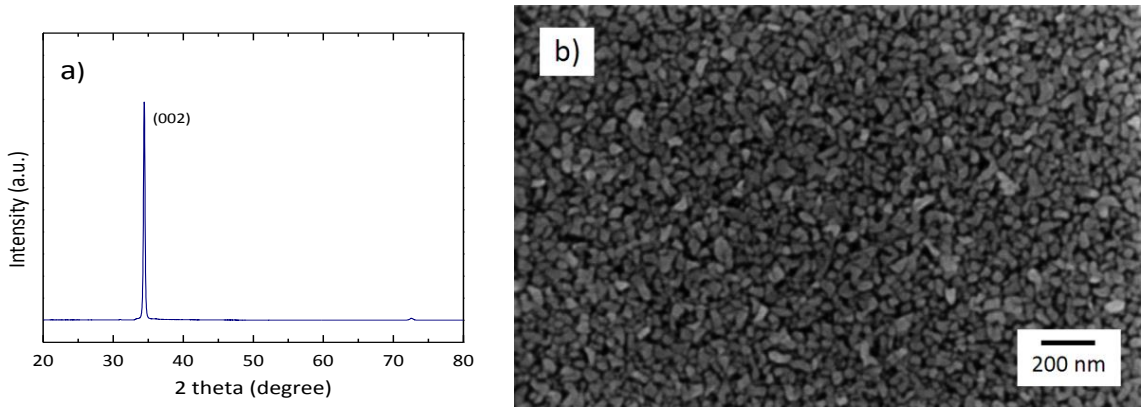

Fig. 5.51. *a) XRD spectrum and b) SEM image of AZO thin film sputtered at RT with a 98:2 wt. % target produced by SPS (P_{RF} = 250 W; P_{dep} = 0.2 Pa).*

SPS enabled the production of full dense 2" AZO sputtering targets with low ρ_e and small/homogeneous grain size, which were successfully applied in the production of high quality TCO thin films by sputtering. The time consumption during the sintering stage (considering standard sintering cycles used throughout this thesis) was reduced by a factor of 14 and 8 when compared with CS and HP, respectively. However, the extremely high costs associated to SPS equipment (especially for targets with large dimensions) and the heterogeneous structure widely observed owing to the different thermal cycles experienced by the target surface and its interior, have delayed its industrial application. Even though, it is expected that this technique will be widely used, especially for the production of nanoceramics.

5.2.3. Non-sintered AZO sputtering targets – thin films deposition and characterization

Considering the characteristics of the INNOVNANO synthesized AZO powders presented in section 4.2, a new and disruptive approach to the production of the AZO sputtering targets were performed. Low cost non-sintered targets based on INNOVNANO nanostructured powders were prepared and used in the production of Al-doped ZnO (98:2 wt. % ZnO:Al_2O_3) thin films by RF-magnetron sputtering at RT. The thin films were produced varying P_{dep} and the deposition time for a constant P_{RF} of 200 W, and then characterized with respect to their structural, optical, morphological, compositional and electrical properties. These thin films were subsequently applied as an interlayer in back electrode to a double a-Si:H pin solar cell and as source/drain contacts to GaInZnO thin film transistors (TFTs).

The obtained results show that non-sintered lab scale AZO targets obtained by EDSM are a viable alternative to the conventionally sintered and pressured assisted sintering techniques with a cost reduction that can be higher than 50 %. Furthermore, due to the high chemical homogeneity of the powders and the absence of a sintering stage, this approach can be extended to the production of a wide range of multi-component metal-oxide sputtering targets that up to now could not be produced using standard manufacturing methods, due to limitations in terms of undesired phases formation during sintering, volatilization of elements at low sintering temperatures, or due to the poor degree of homogeneity of certain compounds before and after sintering.

The non-sintered AZO sputtering targets were prepared using INNOVNANO powders after thermal treatment at 600 °C for 2 h and sieving at 150 µm. Note that the deagglomeration/disaggregation stage presented in section 4.2.2.5 was abolished since there are no sintering issues in this specific case. The powder was firstly uniaxially cold pressed using a steel die in a hydraulic press without binders or additives followed by CIP at 300 MPa for 30 min in order to enhance GD up to 62 % of TD (5.61 g cm^{-3}). The prepared target had the standard lab target dimensions of two inches diameter (~5 cm) and 3 mm thickness (see Fig. 5.52). The powder SSA and crystallite size are ~6 m^2g^{-1} and ~80 nm, respectively (see Fig. 4.20). The PSD of the powder is the same as presented in Fig. 4.22 for the powder before deagglomeration/disaggregation (AZO_BD) with a tri-modal distribution with nanometric, submicrometric and some micrometric (agglomerates and aggregates inherent to the synthesis process) particles.

Fig. 5.52. *Photograph of the powder after thermal treatment at 600 ℃ and a non-sintered ceramic target with two inches diameter.*

The main drawbacks of non-sintered AZO targets are their lower mechanical resistance and reduced deposition rate than that of the sintered ones, which constrains their use in sputtering systems. Even though, after fixing a maximum P_{RF} value that ensured a stable deposition process without consecutive breakdown of the target and an acceptable deposition rate (considering the low density of the target) (P_{RF} = 200 W), it was possible to obtain films with great properties using non-sintered AZO targets.

5.2.3.1. Effect of deposition pressure on AZO thin films properties

Fig. 5.53 a) shows the X-rays diffraction patterns of AZO thin films sputtered from non-sintered AZO target as a function of P_{dep}. The XRD patterns show a typical wurtzite structure of AZO films that are highly orientated along the c-axis. The crystallinity of the films decreases for higher P_{dep} values being the larger crystallite size reached at P_{dep} = 0.13 Pa as shown in the inset from Fig. 5.53.

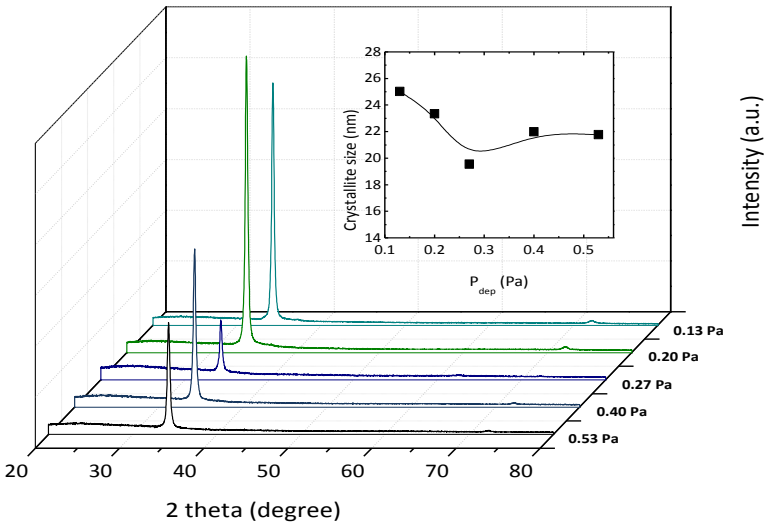

Fig. 5.53. *a) XRD patterns of the AZO thin films as a function of working pressure for a RF-magnetron power of 200 W; Inset shows the dependence of the crystallite size with* $\boldsymbol{P_{dep}}$ *(the diffractograms are normalized to the thickness of each film).*

Fig. 5.54 shows the electrical properties of AZO films as a function of P_{dep} prepared with the 2 wt. % Al_2O_3 non-sintered target at RT and P_{RF} = 200 W. All films present n-type conductivity as it is confirmed by the negative sign obtained for the Hall coefficient. ρ_e increases with P_{dep} due to a gradual decrease in both μ_e and N_e as already observed for the films deposited with sintered targets (in Fig 5.26). The lowest ρ_e was achieved at P_{dep} = 0.13 Pa ($\rho_e = 1.3 \times 10^{-3}$ Ωcm) which corresponds to N_e and μ_e values of 3.27 x 10^{20} and 15.1 $cm^2V^{-1}s^{-1}$, respectively. For higher working pressures the resistivity increases about 3 times, followed by the decrease of N_e and μ_e. Since all the films present N_e > 10^{20} cm^{-3}, the potential barriers associated to grain boundaries are narrow enough so that the electrons are able to tunnel through the barriers. This means that the grain barriers no longer limit the carrier scattering, being μ_e determined by the ionized impurity scattering mechanism (μ_{ii}), as it will be explained in section 5.4.

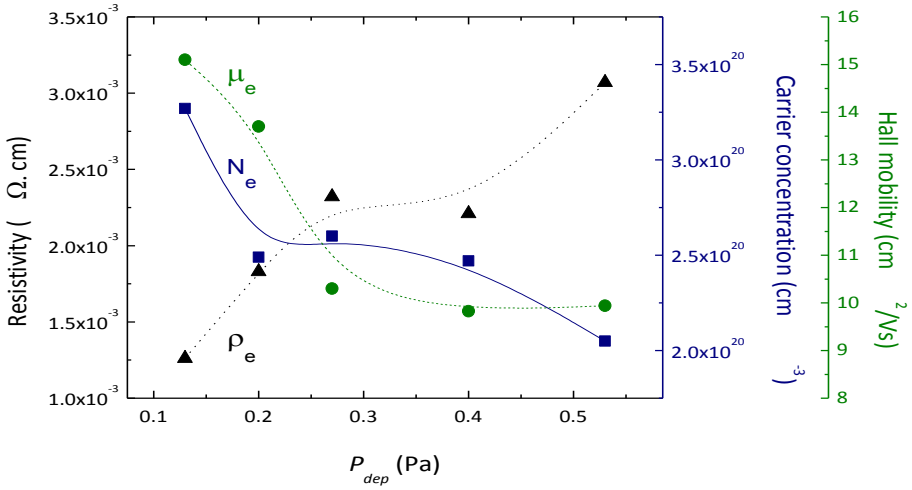

Fig. 5.54. *Electrical resistivity, carrier concentration and Hall mobility of AZO thin films sputtered from non-sintered targets as a function of* P_{dep} *deposited at an RF power of 200 W.*

The transmission spectra in the wavelength of 300 and 2500 nm for AZO films deposited at 200 W are illustrated in Fig. 5.55. The average transmittance of all the samples (including AZO film and glass substrate), in the visible range, is above 85 %. The E_{opt} shows a minor influence of the P_{dep} (between 3.61 eV and 3.52 eV - see inset in Fig. 5.55) and it is similar to E_{opt} values of AZO films obtained with AZO_D sintered targets prepared by CS in air (3.52 – 3.65 eV). The NIR transmittance tends to increase with P_{dep}, in line with the electrical behavior presented in Fig. 5.54. The films morphology do not reveal any remarkable correlation with P_{dep}, only a small decrease associate to the surface roughness from 2.9 nm to 1.7 nm when P_{dep} increases from 0.13 Pa to 0.53 Pa. These results are in line with the obtained structural and electrical properties.

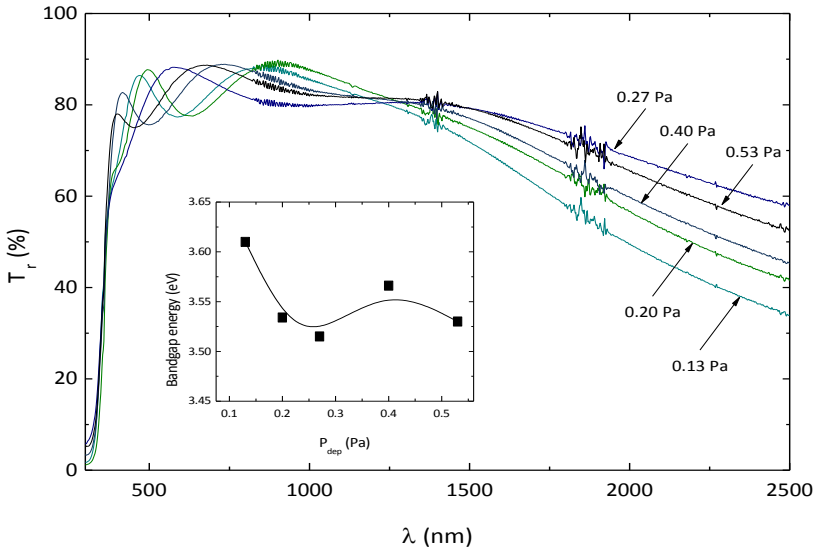

Fig. 5.55. *Transmittance spectra as a function of wavelength for AZO thin films sputtered from non-sintered AZO target at different working pressures (P_{RF}= 200 W). The inset shows the variation in E_{opt} with P_{dep}.*

5.2.3.2. Effect of film thickness on AZO thin films properties

The influence of thickness on the properties of AZO films was studied by keeping P_{RF} and P_{dep}constant at 200 W and 0.27 Pa, respectively. The XRD patterns of Fig. 5.56 show that the thickness of AZO films has no influence on their structure. All the films are highly-oriented perpendicular to the substrate with a single peak along (002) plane, being observed an improvement in the crystallinity as the film thickness increase, corresponding also to an increase of crystallite size: 14 nm to 39 nm as film thickness increase from 81 nm and 891 nm. With the increase of thickness the (002) peak position shifted to a higher angle (inset of Fig 5.56), which means that the interplanar spacing (d002) of the deposited films approaches to the bulk material one (ceramic target). This can be explained by the fact that the films are deposited on amorphous glass, which can induce large strain in very thin AZO films, leading to the increase of d002. Since the later grown layer can form high quality texture easier on former AZO polycrystalline layer, the stress in crystal grain is reduced and the interplanar spacing d002 of AZO films will decrease with the increase of film thickness.

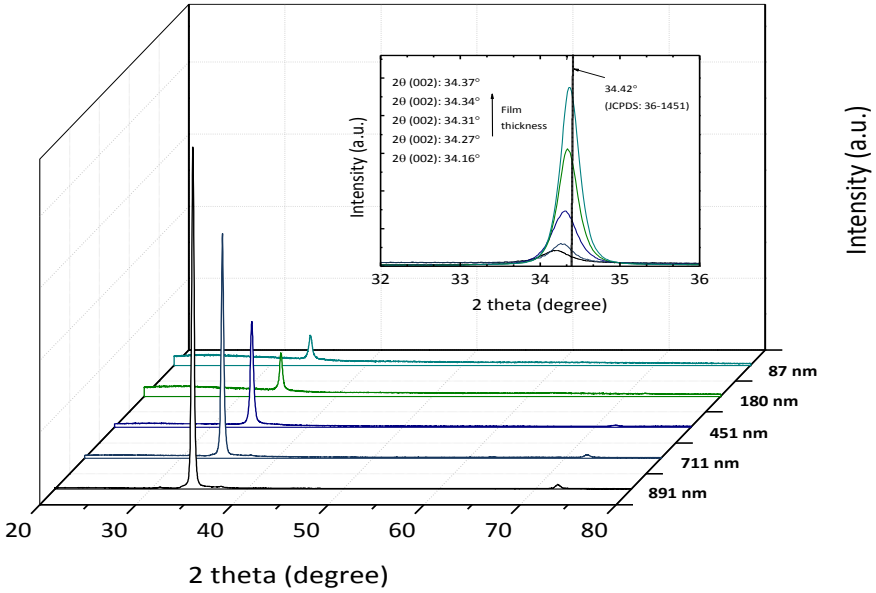

Fig. 5.56. *XRD patterns of the AZO thin films sputtered from non-sintered targets as a function of thickness. The inset shows the shift of (002) peak with the increase of the film thickness (the diffractograms are normalized to the thickness of each film).*

The cross-section SEM image of an AZO thin film with a thickness of ~900 nm (similar to the value obtained by profilometry measurements) shown in Fig. 5.57 reveals a very compact structure with the typical dense and columnar growth of this type of films, without visible defects or voids.

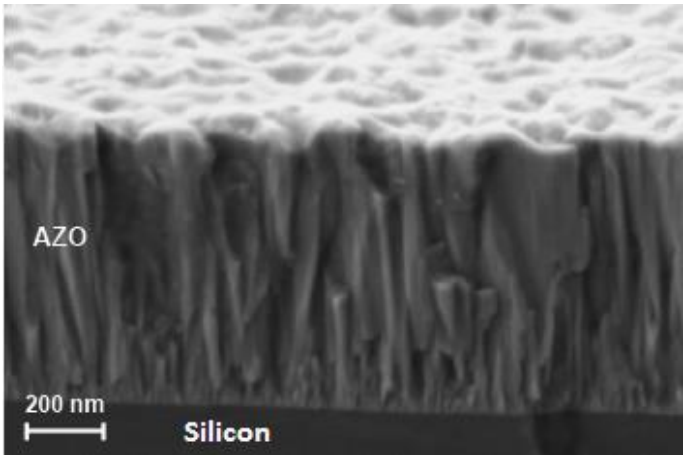

Fig. 5.57. *SEM cross-section of an AZO film with 891 nm of thickness (deposition time = 240 min; P_{RF} = 200 W; P_{dep} = 0.27 Pa).*

The dependence of the electrical properties of the AZO films as a function of thickness is presented in Fig. 5.58. As the film thickness increase up to 891 nm, ρ_e decreases reaching a minimum of 6.5 × 10^{-4} Ωcm. Concerning μ_e and N_e, both increase with thickness to maximum values of 16.8 $cm^2V^{-1}s^{-1}$ and 5.72 × 10^{20} cm^{-3}, respectively. This behaviour can be attributed to the increase of crystallinity with thickness as already demonstrated with a consequent reduction in the ionized impurity scattering (μ_{ii}). However, it should be noticed that the influence of thickness on μ_e and ρ_e is more prominent for smaller thicknesses (~100 – 400 nm).

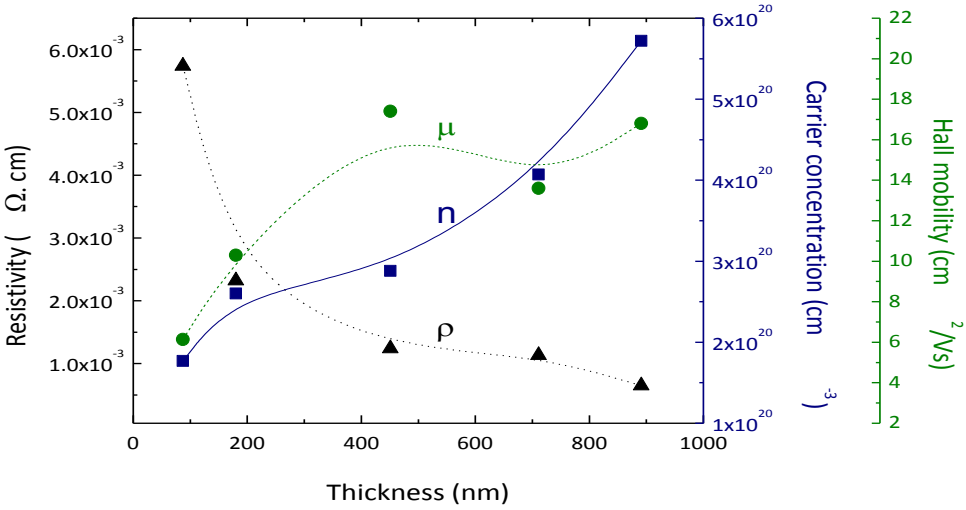

Fig. 5.58. *Electrical resistivity, carrier concentration and Hall mobility of AZO thin films sputtered from non-sintered targets as a function of film thickness for AZO films sputtered art RT (P_{dep} = 0.27 Pa and P_{RF} = 200 W).*

Fig. 5.59 shows the transmittance spectra as a function of wavelength in the visible and NIR region, for the AZO films with different thicknesses, being the average transmittance in the visible range (AVT) (AZO film plus glass substrate) above 80 % independent on the thickness. Oppositely, the NIR T_r is highly dependent on the films thickness. The decrease of T_r with film thickness arises from an increase of reflectance due to the plasma resonance of electron gas in the conduction band [121]. The E_{opt} (see inset from Fig. 5.59) increases from 3.44 eV to 3.63 eV as the thickness increases from 87 to 891 nm. This variation can be explained by the already described Burstein–Moss effect. Since N_e of the thinnest film, 87 nm, is the smallest one, the occupied states in valence band are less and lead to a decrease associated to the E_{opt}.

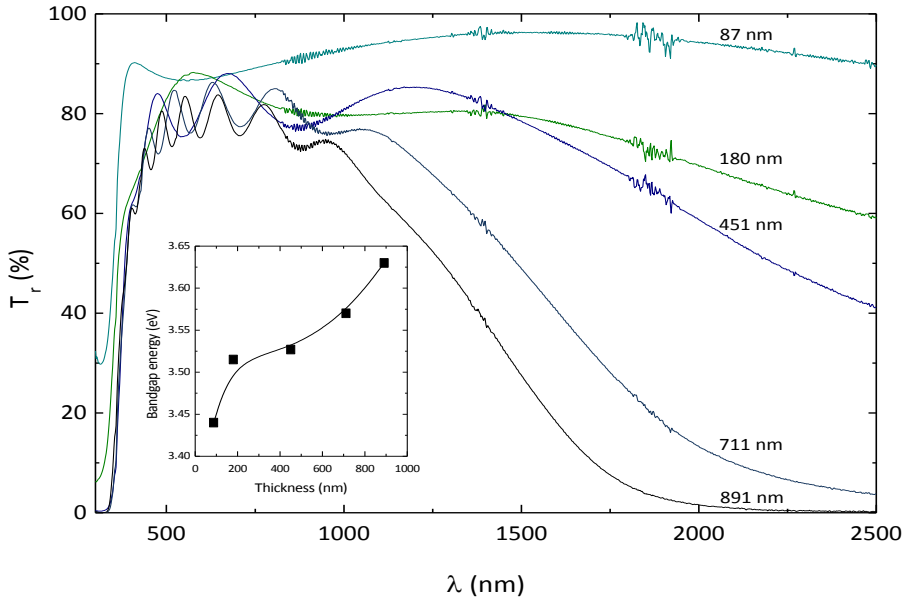

Fig. 5.59. *Transmittance spectra as a function of wavelength for AZO thin films with different thicknesses (87 – 891 nm) sputtered from non-sintered AZO target. The inset shows the variation in E_{opt} with thickness.*

The influence of films thickness on the surface morphology can be observed in SEM and AFM images of Fig. 5.60. SEM images confirm the enhancement of crystallite size with film thickness discussed during the XRD analysis of Fig. 5.56. Besides the crystallite size, a significant change in the surface morphology is observed, from hillocks-like (thinner films (87 and 180 nm)) to cratered-like growth (thicker films (451, 711 and 891 nm)). In the thick films some voids are identified, suggesting that the diffusion and transfer ability of surface atoms are improved, accelerating the crystallization of the films and promoting the surface roughness.

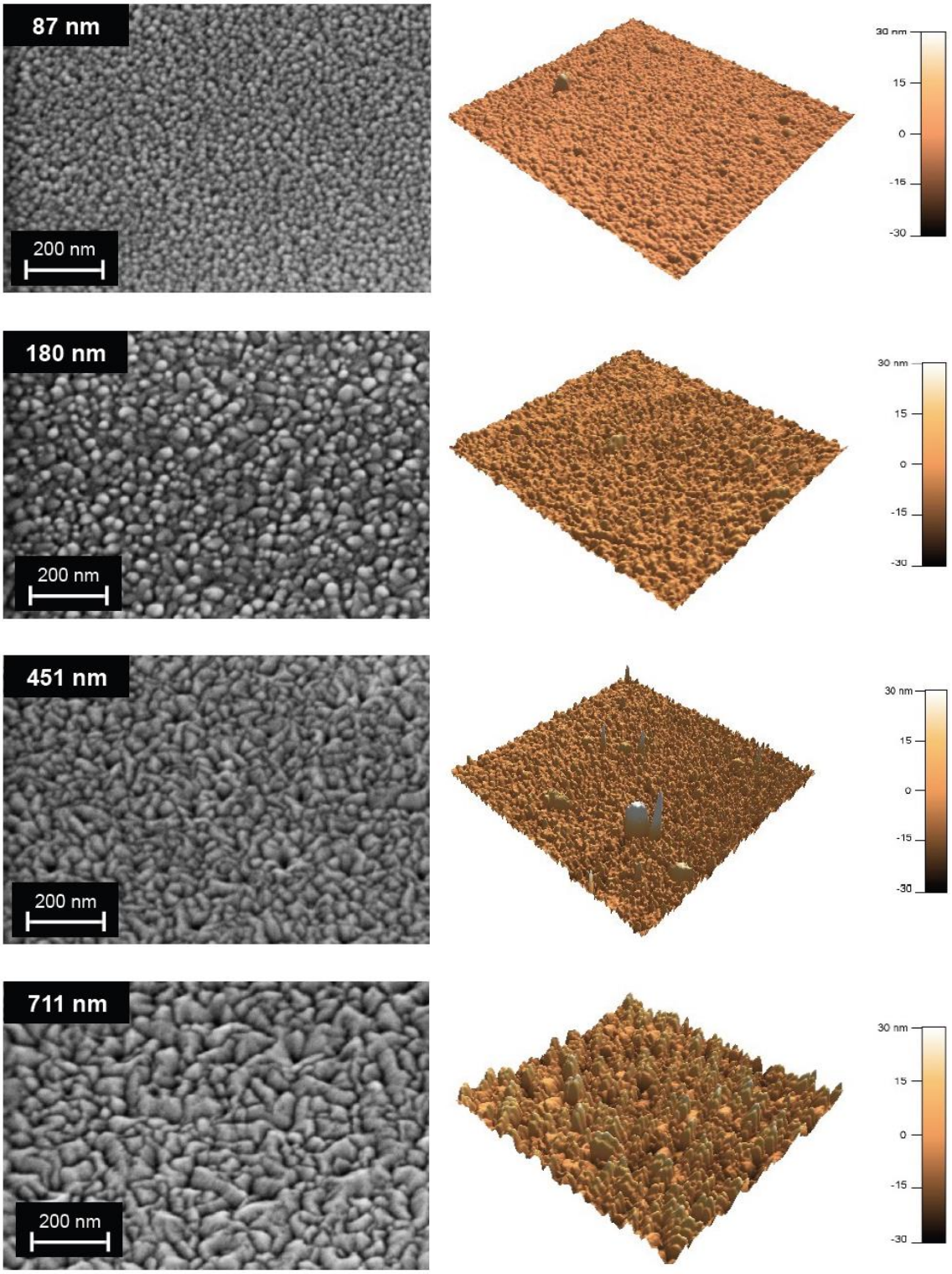

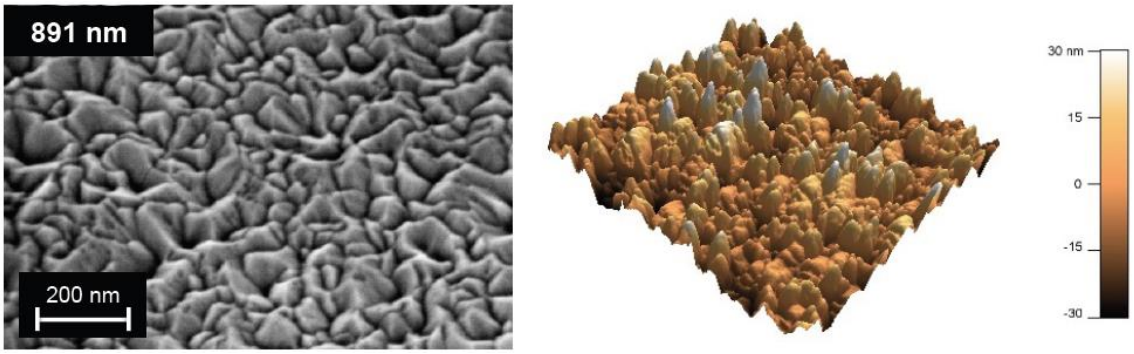

Fig. 5.60. *SEM and AFM images of AZO thin films with different thicknesses sputtered from non-sintered AZO target (98:2 wt. % ZnO:Al_2O_3).*

Fig. 5.61 shows the root-mean-square (RMS) of sputtered films obtained from AFM measurement. The RMS roughness increases from 1.8 nm to 11.9 nm as the film thickness increases. The change in crystallite size is the main responsible for the increase of roughness.

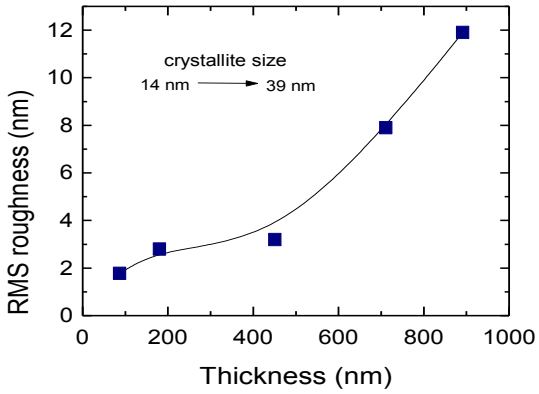

Fig. 5.61. *RMS roughness of the AZO thin films as a function of thickness.*

5.2.3.3. Deposition rate of Al-doped ZnO thin films

The deposition rate (DR) of the AZO thin films as a function of P_{dep} and film thickness is shown in Fig. 5.62 a) and b), respectively. The film thicknesses were systematically measured at the center of the substrates that also corresponds to the center of the sputtering targets. DR slows for higher P_{dep} values (Fig. 5.62 a)), while the opposite is observed for DR dependence on film thickness (Fig. 5.62 b)). Compared to thin films sputtered from conventionally sintered targets using the same P_{RF} (200 W) and P_{dep} (0.20 Pa), DR slightly decreases from 4.63 nm.min^{-1} to 3.87 nm.min^{-1}. Indeed, under the same sputtering conditions, DR is mainly influenced by two interrelated factors: target conductivity and target density [122]. In fact, even considering the perfect distribution of Al in ZnO matrix reached during the synthesis of the INNOVNANO powders, this decrease was expected since the non-sintered sputtering target has lower final density (62 % of TD) and higher electrical resistivity comparing with sintered targets.

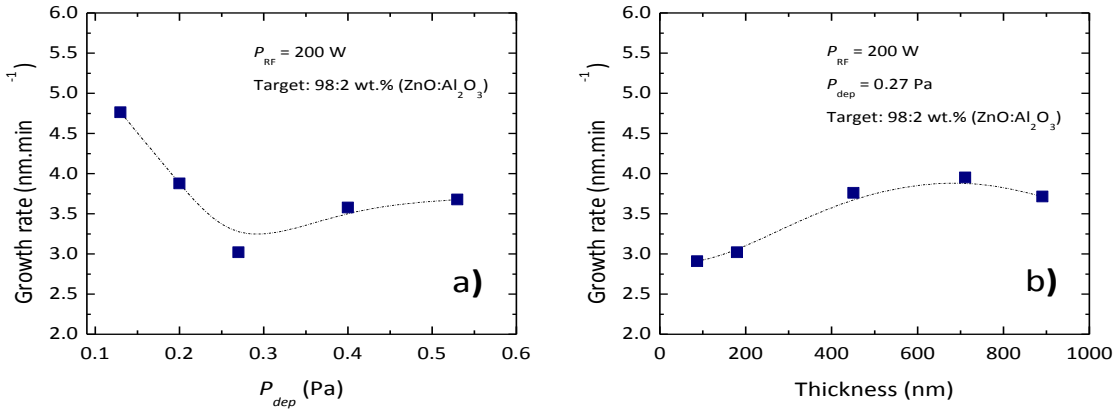

Fig. 5.62. *Deposition rate as a function of a) P_{dep} and b) film thickness using non-sintered AZO target.*

5.2.3.4. Application of AZO thin films to a-Si:H tandem solar cells and GIZO thin film transistors

Thin film solar cells (TFSCs) based on amorphous or microcrystalline silicon are receiving growing attention due to the significant cost reduction on PV systems [123, 124]. They have a typical efficiency of 5 to 7 % and are predominantly based on amorphous silicon as the absorber material [125]. Recently, great efforts have been undertaken worldwide to develop tandem solar cells with amorphous and microcrystalline Si absorber layers. For this type of solar cells, module efficiencies > 10 % appear to be feasible. Besides the silicon absorber layers, transparent conductive oxide (TCO) films are also important layers of thin film Si solar cells [126]. In these solar cells, the TCO is usually used as a front electrode and/or as part of the back contact, as an interlayer between the n-doped layer and metal contact.

When used as a front contact, the TCO layers have the function of: 1) being an effective coupling of light into the solar cell by refractive index matching; and 2) having an efficient trapping of light scattered into the solar cell at the rough TCO/silicon interface. In addition, since the lateral conductance of doped p/n silicon layers is not enough to avoid resistive losses over typical distances in the range of 1 cm, the TCO front layer is also used to avoid high series resistance [127]. When applied at the back contact of the solar cell, besides the current extraction enhancement, TCO layers are also responsible by the improvement of optical properties of the metal back contact. Direct contact of the metal (usually silver or aluminium) with silicon is known to cause optical absorption losses [128]. Furthermore, the long-term stability of the ZnO/metal back contact is superior to the metal layer in direct contact with silicon [129].

The TCOs used in the front contact of commercial thin film silicon solar cells are mainly based on indium-tin oxide (ITO) [130, 131], due to its high stability and low resistivity, or the newly commissioned amorphous TCOs such as indium molybdenum oxide and indium zinc oxide, produced at low temperatures [51, 132-135]. Nevertheless, as stated in section 2.5.3, the high demand for indium is leading to a decrease on its supply, and in the near future the increase of prices will limit its use, thus opening a window for the use of alternative oxides such as fluorine-doped tin oxide (FTO) [91, 136, 137] and aluminium-doped zinc oxide (AZO) [112, 138-140]. Presently, FTO is commonly applied as front contact in amorphous silicon solar cells due to its thermal resistance, chemical stability and texturized surface, guaranteeing a long lifetime and optimized efficiency of

solar cells [136, 137]. However, TCOs based on ZnO have received recently considerable attention due to their low cost, resource availability, non-toxicity and high thermal and chemical stability, which are very important properties for application in solar cells [141, 142]. Indeed, it was demonstrated that ZnO films doped with Al, Ga or B can have low resistivity, high transmittance and stability for a broad range of processing temperatures [112, 138-140, 143-145]. Moreover, compared to ITO and FTO their properties are more stable against hydrogen plasma and high deposition temperatures [142].

In the thin film silicon solar cells studied here the TCOs were used at three different positions: as a front contact; at the bottom (between the n-doped layer and the metal contact) [91, 141, 146] of the single junction; [147] and as an intermediate reflector of the tandem solar cells [148]. These TCOs must be highly transparent in the range of the solar spectrum, highly conductive, non-toxic, have high carrier mobility and high stability against atomic hydrogen, an appropriate refractive index for coupling of light into the silicon absorber material and high scattering ability. These parameters should be optimized as a function of the type of structure (substrate (nip) or superstrate (pin) configurations) and type of absorber silicon layer (a-Si:H or µc-Si:H) of the solar cell.

To evaluate the suitability of non-sintered AZO sputtering targets (AZO NST) as a source of high performance TCO layers for TFSCs the sputtered material was used as an intermediate layer composing the back contact structure of tandem pin/pin amorphous silicon solar cell, before an external metal contact of about the same geometrical size (SnO_2:F/pin–pin/TCO/Metal) (Fig. 5.63 a)). In order to assess the influence of the sputtering target manufacturing method on the final properties of the TFSCs, a conventionally sintered AZO target (AZO ST) was also deposited under the same conditions for comparison.

Another emerging area of research is oxide based thin film transistors (TFTs). Transparent conductors and semiconductors oxide materials are a good alternative to the conventional a-Si:H TFTs currently used in flat panel displays, due to their low processing temperature, transparency and good electrical performance. As thoroughly explained in section 5.2.4.4.2, in this study we substitute the metallic Ti/Au source and drain electrodes by AZO (sputtered from non-sintered targets) on GaInZnO (GIZO) based thin film transistors [149]. The schematic structure of the produced TFT is illustrated in Fig. 5.63 b).

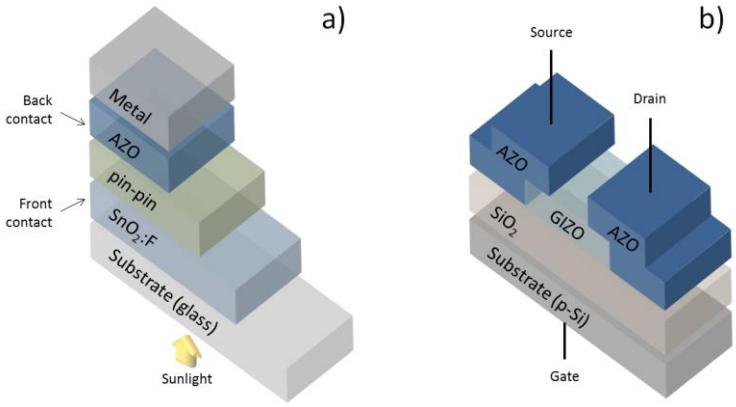

Fig. 5.63. *Schematic presentation of the structure of a) a-Si:H tandem thin film solar cell (TFSC) and b) bottom gate thin film transistor (TFT).*

As previously shown, no significant changes were observed regarding the structural, morphological, optical and electrical properties of the TCO layers sputtered from non-sintered and conventionally sintered AZO targets. Nonetheless, when applied in the manufacturing of optoelectronic devices such as TFSCs or TFTs, the sputtered TCO layers are known to have a large impact on the devices performance.

5.2.3.4.1. Devices – fabrication and characterization

As shown in previous sections, both non-sintered and conventionally sintered AZO 98:2 wt % $ZnO:Al_2O_3$ targets have similar optical and electrical properties. T_r values in the visible range (400 – 700 nm) above 80 %, with ρ_e around 1 x 10^{-3} Ωcm, N_e of the order of 10^{20} cm^{-3}, μ_e values above 12 $cm^2V^{-1}s^{-1}$, and roughness of ∼2.5 nm were obtained for film thicknesses around 350 – 450 nm. Besides optoelectronic properties, also the refractive index (n_{RI}) and the work function (ϕ) were determined for AZO films obtained with conventionally sintered and non-sintered AZO targets. A phase modulated-type spectroscopic Ellipsometer (HORIBA-Jobin Yvon UVISEL) was used to determine the n_{RI} in a spectral range of 0.6 – 6.5 eV, being the measurements analyzed with DELTAPSI2 Windows™ software. To obtain ϕ of the films, a Kelvin probe system (KP Technology Ambient KP5000) was used with a gold sample (with ϕ = 5.1 eV) as reference.

In the deposition as back contact in a-Si:H tandem solar cells and as a source and drain in GIZO TFTs, AZO layers were sputtered under the same conditions (P_{dep}= 0.27 Pa; P_{RF} = 200 W) independently on the target. Under these conditions, AZO films with ≈ 400 nm thickness deposited directly on soda-lime glass substrate have E_{opt}∼ 3.6 eV, n_{RI} close 2.0 in the visible range (λ = 400 – 700 nm) and ϕ of 4.8 – 5.0 eV. It may be noteworthy that TCO thin films, such as ITO, have ϕ in the range of 4.3 – 5.1 eV, depending on the stoichiometry, organic contamination and oxidation type.

a-Si:H tandem solar cells

The tandem solar cells were fabricated on SnO_2:F-coated glass substrates with the following structure: SnO_2:F/pin–pin/TCO/metal or SnO_2:F/pin–pin/Al. Individual doped and intrinsic silicon thin films were deposited by RF plasma-enhanced chemical vapour deposition (RF-PECVD) using a mixture of SiH_4 and H_2 for the intrinsic layer, while the addition of $B(CH_3)_3$ and PH_3 was used to obtain p- and n-type layers, respectively. The i_1 layer is 85 – 90 nm thick with 1.81 eV bandgap, while i_2 layer is about 410 nm with a 1.74 eV bandgap. The importance of using absorber layers with different optical gaps, leads to a broader absorption spectrum, and decreased photo-degradation thus obtaining solar cells with higher efficiencies. After the back contact deposition (∼200 nm thickness), the solar cells were annealed at 150 °C for 1.5 h, which is the standard procedure for improving the semiconductor/metal interface when Al contacts are used. Two samples of the same solar cell were used to study the influence of the AZO intermediate layer. Thus, was guaranteed that no possible changes in the performance of the solar cell are influencing the results. The I–V curves were measured in a calibrated Spire Sun Simulator 240 A at AM1.5 (100mWcm^{-2}) light conditions. Spectral response measurements were performed in the wavelength range from 400 to 800 nm using a tungsten halogen lamp and a Cornerstone 260 Newport monochromator. Bias light was provided by two high-power OSRAM Opto Semiconductors light emitting diodes at wavelengths of 470 and 625 nm.

For the electrical characterization of the fabricated cells, an external Al metal contact is placed in contact with the TCO. This external Al contact comes from the measurement setup and has the same area as the cell (A = 0.039 cm^2).

The cross-sectional view of the a-Si:H tandem solar cell without the back metal contact is shown in Fig. 5.64 a). As can be seen, the structure is highly compact and the thin films are following the highly textured SnO_2:F front contact.

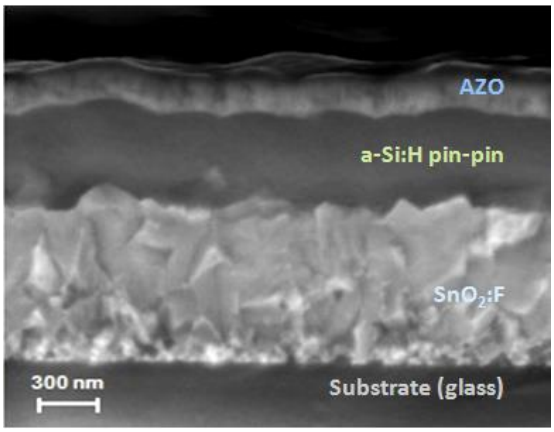

Fig. 5.64. *Cross sectional SEM micrograph of the solar cell without metal contact deposited on glass.*

Fig. 5.65 shows the I–V characteristics of the solar cells with both TCO thin films and external Al as back contact. These experiments were performed in more than ten samples where the films were always grown under the same process conditions. The photovoltaic parameters obtained from Fig. 4.65 are listed in Table 5.10. The solar cell characteristics obtained from the I–V measurements under AM1.5 illumination (Fig. 5.65) of the solar cells with AZO ST as the intermediate of the back contact structure before the external metal contact are lower than the one of the solar cell using only Al as back contact. This is mainly due to an FF deterioration by about 16 % that can be attributed to losses associated mainly to contact series resistance, once the TCO resistivity is more than two orders of magnitude larger than that of Al.

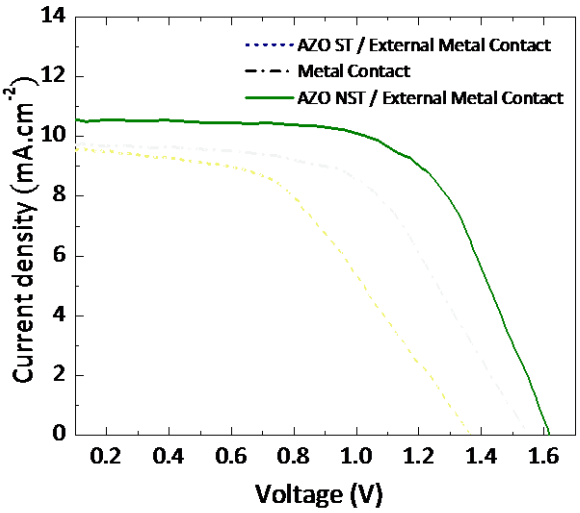

Fig. 5.65. *Current density–voltage characteristics of tandem solar cell with SnO_2:F/pin–pin/Al; SnO_2:F/pin–pin/AZO ST/back metal contact; SnO_2:F/pin–pin/AZO NST/back metal contact structure, respectively, under 100 $mWcm^{-2}$ (AM 1.5) solar simulator irradiation.*

Table. 5.10. *Comparison of solar cell external parameters as a function of the back contact. R_s is the series resistance, V_{OC} is the open circuit voltage, J_{SC} is the short-circuit current, FF is the filling factor and η_s is the efficiency.*

Back contact	Parameters				
	R_s (Ω)	V_{OC} (V)	J_{SC} (mA cm^{-2})	FF (%)	η_s (%)
AZO ST/Al	69.6	1.37	9.6	48	6.3
AZO NST/Al	40.2	1.62	10.8	63	11.0
Al	56.8	1.55	9.8	57	8.7

On the other hand, the solar cells with AZO NST as the intermediate layer of the back contact structure have higher efficiency than the cells with Al and AZO ST/Al back contacts, mainly owing to an improvement in the series resistance, V_{OC}, FF and J_{SC}. The V_{OC} enhancement (from 1.55 to 1.62 V) can be associated with the increase of built-in electric field [150-152] probably due to better interfaces between layers. Compared to the standard solar cells, all these contributions lead to an overall enhancement of ~20 % in the solar cell efficiency [153, 154].

In order to confirm the better collection efficiency of the photo-carriers in the presence of the AZO NST back contact, spectral response measurements were carried out. Fig. 5.66 presents the external quantum efficiency (EQE) of the tandem a-Si:H solar cells, deposited with metal and AZO NST/back metal contact. Compared to the standard cell with Al back contact, the solar cell prepared with AZO NST exhibits enhanced EQE in the entire wavelength range, indicating an enhancement in the carriers generated. Indeed, an increase of the short-circuit current (J_{SC}) is observed from 9.8 to 10.8 mAcm^{-2} (10 % enhancement).

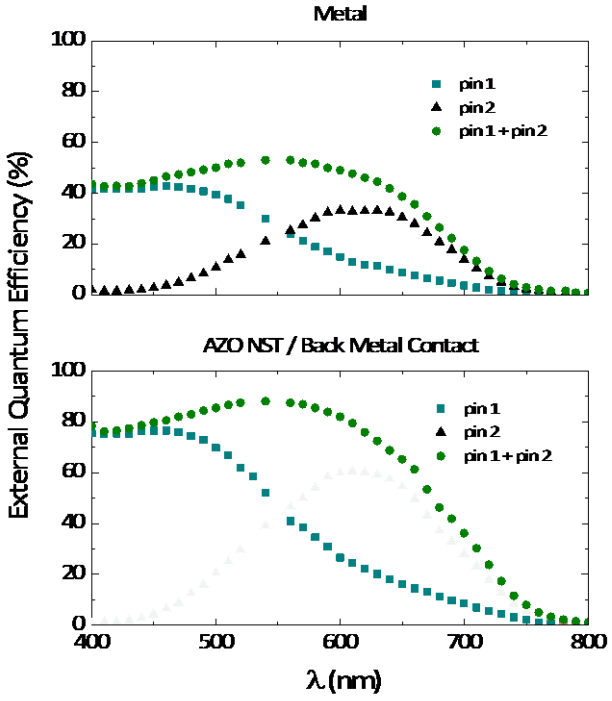

Fig. 5.66. *EQE of the set of solar cells showed in Fig. 5.68 where an enhancement of the quantum efficiency for the solar cell with AZO NST/back metal contact is noticed.*

GIZO thin film transistors

The TFTs were produced with the optimized procedure developed by CENIMAT/CEMOP: p-type silicon substrates ($N_A \approx 10^{17}$ cm^{-3}) were coated with 100 nm thick thermally grown SiO_2, which acted as the gate dielectric. Si was used simultaneously as the substrate and the common gate of the devices. A 50 nm thick a-GIZO layer (the semiconductor) was deposited by RF magnetron in a homemade sputtering system using a 3" diameter Ga_2O_3:In_2O_3:ZnO (1:2:2) ceramic target. The target to substrate distance was fixed at 15 cm, with a base pressure of 3 × 10^{-4} Pa, an oxygen partial pressure (P_{O_2}) of 1.5 × 10^{-3} Pa, a processing pressure (Ar+O_2) of 7 × 10^{-1} Pa and a P_{RF} of 50 W. For the electrodes, a layer of Ti/Au (5/70 nm) was e-beam evaporated at RT for the reference TFT while an AZO thin film with 100 nm has been deposited for comparison purposes. These electrodes and the channel layer were patterned by lift-off technique, with the final devices having a width to length ratio (W/L) of 50/40 µm. The TFTs were electrically characterized in air at RT, in the dark using a Cascade Microtech M150 microprobe station connected to a semiconductor parameter analyser (Agilent 4155C) controlled by the software Metrics ICS.

Fig. 5.67 a) and b) shows the transfer characteristics in saturation mode (V_{DS} = 20 V) for GIZO TFTs produced with different source and drain electrodes, Ti/Au and AZO respectively.

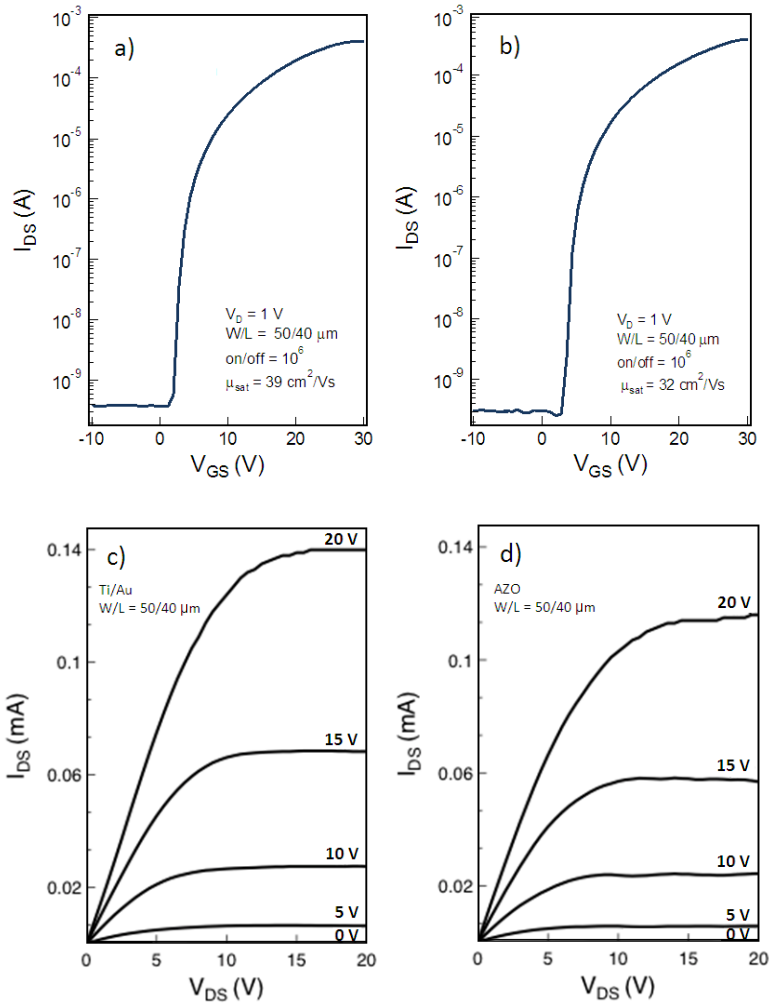

Fig. 5.67. *Transfer characteristics of GIZO based TFTs with a) Ti/Au and b) AZO thin film source and drain; Output characteristics of GIZO based TFTs with c) Ti/Au and d) AZO thin film source and drain.*

The on/off ratio of both devices is 10^6, the saturation mobility (μ_{sat}), calculated by the transconductance in the saturation regime is higher for the TFT with Ti/Au contacts, 39.2 $cm^2V^{-1}s^{-1}$, while for the TFT with AZO contacts is 32.0 $cm^2V^{-1}s^{-1}$. Since the semiconductor is the same for both devices, this can be explained by the higher resistance associated to the contacts/semiconductor interface (R_c). Fig. 5.67 c) and d) show the output characteristics of the GIZO TFTs produced, where it is observed a slight decrease of I_{DS} current when AZO is applied to source/drains contacts. This difference can also be related to the increase in R_c between the source/drain contacts and the channel layer.

5.3. Application of AZO thin films as a thermoelectric material

Efficient thermoelectric (TE) devices require materials with high Seebeck coefficient ($S = \Delta V/\Delta T$ (eq. 5.9)), low thermal conductivity (k), and low resistivity (ρ_e) to attain a large figure of merit ($ZT = S^2T/k\rho_e$ (eq. 5.10)). State of art ZT for bulk materials at low temperature (< 200 °C) is around 1 or less and belong to n-type PbTe (ZT∼0.8) and p-type $Si_{0.8}Ge_{0.2}$ or $Yb_{14}MnSb_{11}$ (ZT∼1) materials [155]. By using nanostructured materials the ZT value has improved to over 1 at RT, taking as example p-type Bi_2Te_2/Sb_2Te_2 SL (ZT = 2.5) and n-type PbSeTe (ZT = 1.5) materials [156]. Although Te based materials have already captured the market, their application in large volume production processes is unsustainable. Te is the ninth less abundant element on Earth [157, 158] and since Te standard modules require roundly 1 kg to produce 1 kW, costs versus benefits becomes a problem. On the other side, environmental issues concerning the use of Pb and its recyclability leaves no space to explore the commercialization of Pb alloys [158]. Therefore, more abundant and eco-friendly materials should be studied for TE applications.

ZnO fulfill these requirements and for TE applications it has mainly been explored with bulk dimension and with different dopants: $Zn_{1-x}M_xO$, AZO if M=Al and GZO if M=Ga [159], $Zn_{1-(x+y)}Ga_xIn_yO$ (x+y=0.007) [160] or ZnAlO/In-ZnAlO quantum wells multilayers [161]. More recently the interest in TE thin films (TE-TF) has increased substantially. While bulk TE materials are foremost applied in high power and high temperature regimes, TE-TF have its main field of application in low temperature and low power consumption electronic devices. Along with a reduction in material usage, TE-TF have also other advantages when compared to bulk: higher degree of freedom as the in-plane geometry can be adapted to the application requirements; and thin films can be deposited on flexible substrates as reported in the literature, for example, on polyamide substrates [162, 163]. Furthermore, as shown before, AZO thin films have high T_r in the visible range, so with the improvement of TE properties they would become suitable in transparent electronics devices, among others.

Although the TE properties of AZO thin films are scarce in the literature, some recent results have been reported [164, 165], showing maximum power factor ($PF = \sigma S^2$ (eq. 5.11)) of 1.5×10^{-4} $W.m^{-1}.K^{-2}$ with ZT below 0.1 at RT. Concerning bulk AZO, the reported PFs are superior (10^{-3} $W.m^{-1}.K^{-2}$) but as their thermal conductivity (k) is also higher [166] the ZT is even lower than 0.1 at RT, rising to 0.44 above 1000 °C [167, 168].

In this section, are presented the TE properties of AZO thin films deposited by RF and pulsed DC magnetron sputtering, using non-sintered (NST) and conventionally sintered (in air) (ST) AZO targets. The optimized AZO films show a maximum PF of 3.9×10^{-4} $W.m^{-1}.K^{-2}$ and low k (<1.19 $W.m^{-1}.K^{-1}$) leading to ZT values above 0.1 at RT.

5.3.1. AZO TE-TF – fabrication and characterization techniques

The TE properties were determined in AZO thin films deposited by two different methods: RF and pulsed DC magnetron sputtering using ST and NST AZO targets. The influence of Al doping concentration on the TE-TF properties was evaluated using thin films deposited by RF magnetron sputtering (RF-MS) from targets prepared by CS in air with different compositions (0.5 – 2.0 wt. % Al_2O_3) (see Table 5.4 form section 5.1.7). The films were deposited at P_{RF} = 250 W and P_{dep} = 0.2 Pa. The influence of film thickness was also studied based on the thin films deposited by RF-MS (P_{RF} = 200 W and P_{dep} = 0.27 Pa) from the NST AZO target with 2 wt. % Al_2O_3 already presented in section 5.2.3 DC magnetron sputtering is often used in industrial applications to obtain AZO films and for that reason it was used here, being studied the influence of P_{dep} on the TE-TF properties. Both ST and NST AZO targets were deposited by pulsed DC sputtering. The electrical properties were optimized for an applied power of 75 W using the NST target and 100 W for the sintered one, in both cases with a pulse break of 8 μs and a frequency of 10 kHz. When using the ST target it was necessary to heat the substrate up to 473 K and perform a post-deposition thermal treatment at 573 K during 1 h in vacuum. The films deposited using the NST target did not require any substrate heating nor post-deposition thermal treatment.

To determine the Seebeck coefficient and the power factor, a thermal gradient, ΔT was created by placing the sample between two Peltier modules, TEC1-12707, each connected to an independent power source. ΔT was monitored through a thermal image taken with a FLIRA310 thermal camera. The corresponding thermo-voltage, ΔV, was measured using a nano voltmeter Agilent 34420A while keeping the average temperature constant at 293 K. The composition of AZO films and the corresponding homogeneity along film thickness was evaluated by AES technique – Auger depth profiles (see section 3.2.2.2.1). The thermal conductivity was determined as described in paper of reference [169].

5.3.2. Properties of AZO TE-TF – Effect of composition, thickness, sputtering target and deposition method

The influence of target composition on the films properties confirmed the 98:2 wt. % ZnO:Al_2O_3 as the one that leads to optimized properties: $|S|$ value, 114 μV.K^{-1}; electrical conductivity of 4.0 x 10^4 (Ω.m)$^{-1}$); and PF of 3.9 x 10^{-4} W.m^{-1}.K^{-2}. It should be noted that, when compared to the electrical measurements presented before, a slight decrease in terms of the electrical conductivity of the films is observed for all compositions. This is due to non-uniformity through the entire substrate, very common in AZO thin films produced by sputtering (that also depends on the characteristics of the system), mainly the ones deposited from less conductive targets [37, 38, 40]. However, this fact has no influence on the observations/conclusions disclosed herein.

As previously shown in section 5.1.7.4, the μ_e of the films drops and N_e raises, when the Al_2O_3 content in the target increases from 0.5 to 2.0 wt. %. Therefore, we may correlate the improvement of electrical conductivity with the increase of N_e, while the drop of S can be attributed to the higher Al content. As shown in SEM images from Fig. 5.31, the increase of Al concentrations results in films with smaller grain sizes, which can be considered as scattering centers for electrons and phonons, helping to lower the thermal conductivity. However, if the interfaces of these smaller grains are incoherent it may reduce μ_e since the scattering of electrons increases and consequently the electrical conductivity drops [170]. As in this case the electrical

conductivity is enhanced when Al doping in AZO targets increases (Fig. 5.29), thus it is possible to infer that either the grain boundaries interface is coherent (for example with nano grains surrounded by an amorphous matrix) [170] or, as stated before, it may be influenced by the reduction of zinc interstitials concentration for charge compensation due to the high number of trivalent Al cations which interfere with the crystallite size and thin film crystallinity. The type of the majority carriers was established from Seebeck coefficient measurements. Since S is negative in all deposited films they exhibit typical n-type semiconductor behavior, in agreement with Hall effect data.

The influence of films thickness (d_{film}) on the TE properties (S and PF) of samples deposited by the RF process was studied using NST ZnO:Al_2O_3 (98:2 wt. %) target. The increase of thickness from 180 nm to 711 nm lead to a decrease in S from 90.2 µV.K^{-1} to 61.5 µV.K^{-1}, and since the electrical conductivity is uphold between 3.8 x 10^4 and 4.7 x 10^4 (Ωm)$^{-1}$ the PF follows the trend of S decreasing from 3.1 x 10^{-4} Wm^{-1}K^{-1} (d ≈ 180 nm) to 1.8 x 10^{-4} Wm^{-1}K^{-1} (d ≈ 711 nm). This behavior can be correlated to the substantial increase of the crystallite sizes with film thickness (see Fig. 5.60). Since films with smaller crystallite/grain sizes have more interfaces, this may explain the higher values of S and PF for the thinnest film (d ≈ 180 nm). Because, PF is more sensitive to S than to the electrical conductivity (eq. 5.11), even with the increase of conductivity with thickness (Fig. 5.58), the lower S values reached for thicker films lead to lower PF values. In fact, even considering the large number of interfaces (small grains) observed for thin layers, the scattering of electrons does not increase substantially when compared with thicker layers. In fact, besides grain size, the increase of thickness also promotes the raise of N_e counteracting with the growth of μ_e with grain size/thickness. A similar trend has been observed by other authors in Al doping TiO_2 [171].

In the above discussion possible dispersion effect along the film thickness of Al dopant have not been considered since the Auger depth profile reveals that Al is uniformly distributed along the cross section of both NST and ST AZO films, as shown in Fig. 5.68. In both profiles the Al concentration is practically the same and evaluated to be around 3.2 at % which is in agreement with the initial composition of the analyzed targets. The non-stoichiometry of ZnO and SiO_2 is due to phenomena such as reduction under electron beam deposition and/or preferential sputtering for the binary compound.

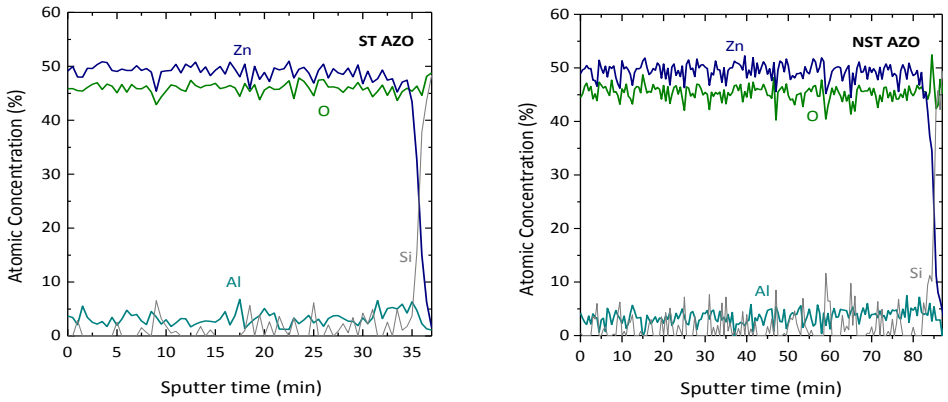

Fig. 5.68. *AES atomic concentration spectra of two AZO thin films. Left: Film deposited by RF with the ST target (363 nm thick); Right: Film deposited by RF with the NST-AZO target (711 nm thick). The sputtering rate was between 8 and 10 nm.min^{-1}.*

Since pulsed DC magnetron sputtering technique is the most used in industry, it was also tested in this study. Preliminary tests have also been performed to deposit AZO thin films through this technique, using ST targets and/or NST targets. In the first deposition trials, the influence of power (P_{DC}), P_{dep}, and type of target upon the TE properties of the AZO thin films have been evaluated and the best results achieved are shown in Table 5.11.

Table 5.11. *Properties of optimized AZO films produced by RF and pulsed DC sputtering methods with ST and NST AZO targets with ZnO:Al_2O_3 content of 98:2 wt. %.*

Deposition Method – Target	P_{dep} (Pa)	P_{RF} (W)	d (nm)	D_c (nm)	σ $(\Omega m)^{-1}$	S (μV/K)	PF (W/mK^2)
RF – ST	0.20	250	363	29	4.0×10^{4}	-98	3.9×10^{-4}
RF – NST	0.27	200	181	21	3.8×10^{4}	-90	3.1×10^{-4}
DC – ST	0.29	100	357	9.1	6.1×10^{3}	-134	1.1×10^{-4}
DC – NST	0.42	75	200	9.6	2.4×10^{3}	-132	4.2×10^{-5}

The AZO films deposited by pulsed DC using a sintered target show a typical hexagonal wurtzite structure of ZnO with a (002) main diffraction peak at 2θ ≈ 34.4º, as observed in the samples produced by the RF method. However, other diffraction peaks at 2θ ≈ 35.2º (011), 2θ ≈ 46.7º (012) and 2θ ≈ 61.8º (013) appear after the post-deposition annealing step and/or substrate heating during the deposition. The films produced from a NST target, also show the typical ZnO wurtzite structure but with two peaks (002), at 2θ ≈ 34.4º and 2θ ≈ 72.5º (004). The crystallite sizes related to main peak (002) are shown in Table 5.11 and were calculated from Scherrer's formula (eq. 3.9). Comparing the DC and RF method, and for the deposition conditions used, it was obtained better PF for AZO films produced by RF method. However the films produced by pulsed DC method, have smaller grain sizes, independently of the target used, which suggest better TE properties. Indeed, in these samples, S is slightly enhanced, but the electrical conductivity is one order of magnitude lower and so PF is also lower. It is important to emphasize that these are preliminary results and that further efforts should be made to improve the TE results and to understand better the physics in the involved mechanisms. The TE results achieved here in films deposited with NST targets using pulsed DC technique are already close to those reported in the literature (as shown in Table 5.12), demonstrating that it is possible to fabricate AZO thin films with advanced thermoelectric properties from NST targets produced with INNOVNANO AZO powders both by DC or RF sputtering techniques. Most importantly, by eliminating the sintering step, fabrication time and energy costs will be both reduced making the production process of targets more economic.

Table 5.12. *Comparison of the TE data of AZO films produced in this work with those of films and bulk material published in the literature. For the ZT* values denoted with * there was no information on the thermal conductivity, therefore, ZT was calculated using the same k as measured in the thin films presented in this work, namely 1.19 W.m^{-1}.K^{-1}, for comparison purposes. For the ZT** values denoted with ** there was no information concerning the k values and ZT was calculated using k from literature for bulk AZO, namely 30 W.m^{-1}.K^{-1}.*

ZnO:Al_2O_3 wt. %	Preparation Method	d_{film} (nm)	T_{work} (°C)	σ $(\Omega.m)^{-1}$	k (W/mK)	|S| (μV/K)	PF (W/mK)	ZT	Ref.
98:2	**RF (ST AZO target)**	**363**	**RT**	**4×10^{4}**	**< 1.19**	**98**	**3.9×10^{-4}**	**>0.1**	**in this work**
98.5:1.5	DC	120	RT	10^{4}	-	62	1.3×10^{-4}	~0.03*	[165]
98.5:1.5	DC	103	RT	10^{4}-10^{5}	-	68	1.5×10^{-4}	~0.04*	[172]
97.3:2.7	DC	716	RT	10^{4}	-	99	1.5×10^{-4}	~0.04*	[164]
98:2	PLD	500	RT	10^{4}	-	65	1.3×10^{-4}	~0.03*	[173]
98:2	Solid-state reaction (pressure)	bulk	RT	10^{4}-10^{5}	40.2	100-150	8×10^{-3}	6×10^{-3}	[174]
98:2	Solid-state reaction (pressure)	bulk	RT	10^{5}	-	62.5	3.8×10^{-4}	10^{-3}**	[175]
99:1	RF plasma and HP	bulk	RT	10^{4}	28	37	1.3×10^{-4}	2×10^{-3}	[176]
97:3	Chemical co-deposition and pressed	bulk	100	10^{4}	14	200	5×10^{-4}	~0.02	[177]
96:4	SPS	bulk	400	10^{4}	2	88	3.2×10^{-4}	0.085	[168]
98:2	SPS	bulk	900	10^{4}	5.15	120	8×10^{-4}	0.17	[178]

From the above results, it was demonstrated that both Al-doping level and films thickness control the TE, optical and structural properties of these films. Seebeck coefficient up to 98 μV.K^{-1} and electrical conductivity up to 4 x 10^{4} $(\Omega.m)^{-1}$ lead to power factor up to 3.9 x 10^{-4} W.m^{-1}K^{-2} and ZT > 0.1 at RT, which is above the state of art for similar materials, almost by a factor of three. These results were achieved in films with small crystallite sizes (< 30 nm). The importance of crystallite/grain sizes for TE properties has been demonstrated, being dependent on the deposition conditions and especially on the Al-doping concentration. Moreover, it has been demonstrated that similar results are obtained in films made with ST and NST targets both using RF and pulsed DC sputtering. The relevance of this conclusion is the elimination of the sintering

step, and therefore the reduction in fabrication costs, with direct consequence in lowering thermoelectric thin film modules cost, making them more appealing for large area TE applications.

5.4. Correlation between electrical resistivity, carrier concentration and mobility of the carriers – physical limits and active scattering mechanisms in sputtered AZO thin films

Undoped and Al-doped ZnO thin films have been prepared since more than thirty years with different deposition methods and large technological efforts has been put into this research attempting to improve the optoelectronic behavior of this material [72]. However, the reported values in terms of electrical properties have not changed significantly, despite the fact that a large number of groups have been working in this field. In addition to the influence of various processing and post-processing parameters in the electrical properties of the films, there is an interdependence between μ_e and N_e. Thus, its analysis proves to be important in understanding the transport mechanisms and limitations of AZO thin films.

The understanding of the mechanisms behind the TCOs carrier mobility has been widely investigated [72, 179-181]. TCO thin films such as CdO, SnO_2, In_2O_3 and other multicomponent TCOs like CdO–SnO_2–In_2O_3 or $ZnSnO_4$, are known to have octahedral coordination while ZnO has tetrahedral coordination of the cations [179-181]. Ingram *et al.* [180] observed that the decrease in both conductivity and mobility was also correlated to a decrease in the octahedral cation density in the structure in the order: CdO (rock salt) > In_2O_3 (bixbyite) > SnO_2 (rutile). Since high mobility with degenerate doping has only been reported for CdO and In_2O_3 based compounds with octahedrally coordinated cations, the associated cubic structure has been related with the achievement of TCOs with high mobilities [90]. However, up to now, this correlation is not fully proven and despite the tetrahedral coordination of the cations in undoped and doped ZnO, several efforts have been done in the optimization of the optoelectronic performance of this material as a TCO.

As presented in section 2.5.2.1. (eq. 2.5), μ_e is directly dependent on the life time between collisions (τ), which in turn are negatively correlated with N_e. From all the existing scattering mechanisms that can influence μ_e (eq. 2.6), ionized impurity scattering mechanism (μ_{ii}) is known to be the dominant dispersion mechanism in several highly degenerated TCOs, including AZO.

Bellingham *et al.* [182] examined the physical limits of the electrical resistivity of several TCO thin films (ITO, tin oxide and ZnO based materials) and compared it with a theoretical lower limit of the resistivity calculated under the assumption of a limitation of the mobility by μ_{ii}. They came to the conclusion that ionized impurities govern the transport for carrier densities above 10^{19} cm^{-3} and estimated a limiting μ_e of 90 $cm^2V^{-1}s^{-1}$ for the three mentioned TCO materials. To complement this study and get a more comprehensive picture of the carrier transport in ZnO, Ellmer [72] also depicted an overview of μ_e and ρ_e values of undoped and doped ZnO TCO thin films as a function of N_e. The author observed a clearer trend for ρ_e and μ_e values with N_e. In general, ρ_e decreases continuously to about N_e of 5×10^{20} cm^{-3} where it seems to saturate, while μ_e showed a significant scattering mainly at N_e above 10^{20} cm^{-3}, where the data belong exclusively to thin polycrystalline films [72]. The author found an N_e upper limit of about 1.5×10^{21} cm^{-3} (which corresponds to a dopant solubility limit of about 3.6 at. %) and a power law

dependence of $\mu_e \sim N_e^{-1/5.6}$ in the region $10^{19} < N_e < 10^{20}$ cm^{-3}. He also presented an upper limit of the μ_e in the region $N_e > 5 \times 10^{20}$ cm^{-3} of about 40 cm^{2}V^{-1}s^{-1}, concluding that ρ_e below 1.0 × 10^{-4} Ωcm for doped ZnO thin films are hardly achieved, due to a general limitation by μ_{ii} [72]. The same opinion was also shared by Minami [39] in a recent review of the possible limits of electrical transport parameters in polycrystalline ZnO. The author stated that for N_e = 1 – 10 x 10^{20} cm^{-3} the maximum mobility is limited by μ_{ii}. Finally, in a detailed study Young *et al.* [183] determined the scattering parameter for different scattering mechanisms in the range N_e = 1 x 10^{19} – 5 x 10^{20} cm^{-3} and also found μ_{ii} to be the dominant scattering mechanism in AZO system.

From the above discussions, it is indisputable that for higher N_e total mobility (μ_e) is limited by the scattering of the electrons at ionized impurities (intrinsic lattice defects or extrinsic dopants) (μ_{ii}), while grain boundary scattering mechanism (μ_{gb}) is the limiting factor for lower N_e and/or very small crystallite sizes [72, 118, 184]. All these researchers have focused mainly on the optimization of the deposition conditions (preparation of films with better crystallographic properties (larger grains, lower mechanical stress)) or/and the post-deposition annealing procedures (oxygen partial pressure, temperature, time, etc.). In this work, the path followed regarding the optimization of optoelectronic properties of AZO TCOs, consisted not only in studying the influence of deposition and post-deposition variables but also on the effect of the sputtering targets properties produced under different conditions.

Fig. 5.69 a) and b) shows how ρ_e is related to N_e and μ_e. The ρ_e is more closely related to μ_e than to N_e. In our experiments, the minimum value of ρ of 3.37 x 10^{-4} Ωcm is obtained from the AZO films prepared with hot-pressed 0.5 wt. % Al_2O_3 target sputtered at 200 °C for 3 h without O_2 flow, P_{RF} = 180 W and P_{dep}= 0.13 Pa. In this case μ_e are closely to the maximum value achieved in this work, while N_e reached its maximum (4.79 x 10^{20} cm^{-3}), considering the same doping level of 0.5 wt. % Al_2O_3. The lower ρ_e values were achieved for films with higher thicknesses and/or deposited from targets prepared by CS in Argon, HP and SPS, demonstration the relation between the target and thin films electrical conductivity. From Fig. 5.69 a) and b), it is possible to infer two distinct trends. For highly doped thin films, the conductivity seems to be mainly controlled by the number of free carriers, whereas in the case of 0.5 wt. % Al_2O_3, the high μ_e appears to be the dominant factor for the conductivity of the films.

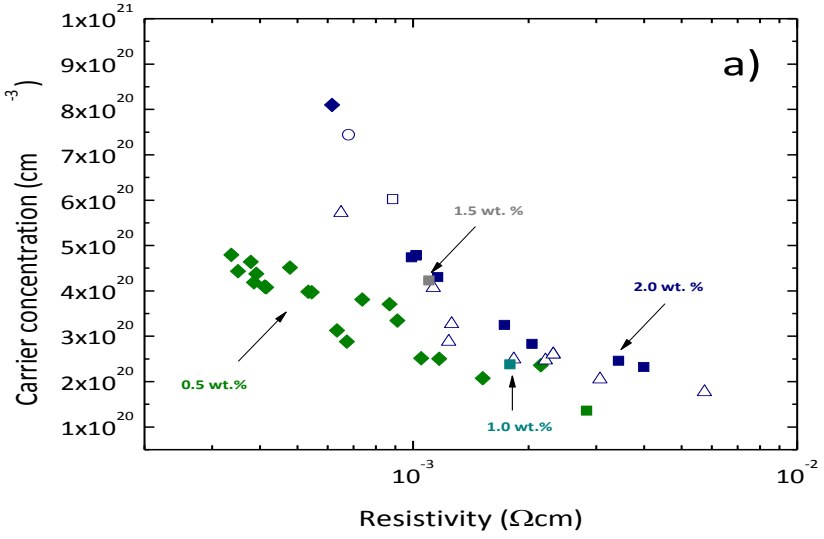

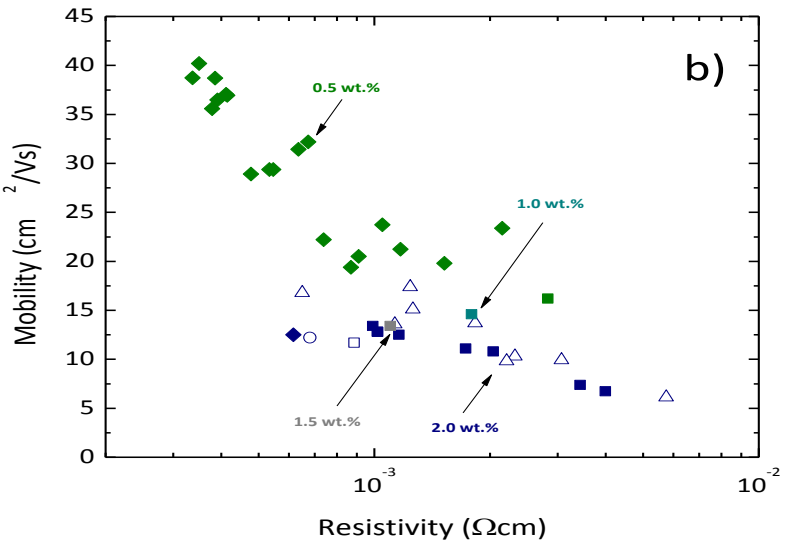

Fig. 5.69. *a) N_e and b) μ_e dependence on ρ_e of the Al-doped ZnO thin films sputtered under diverse conditions. Each point represents an AZO film sputtered with a different set of deposition parameters.*

It can be stated that under certain conditions the theoretical limit is nearly reached in the deposited AZO films. However, as demonstrated in Fig. 5.25, 5.28 and 5.32, if N_e is increased to reduce ρ_e, the TCO film transmission especially in the NIR region reduces as a result of absorption by free carriers or by metal-like reflection. Therefore, the only possibility to reduce ρ_e without decrease the NIR transmittance should pass by obtaining high N_e without sacrificing μ_e [90, 185]. In this respect, scattering at ionized defects cannot be avoided since high values of N_e will be always needed.

As previously demonstrated, for sputtering targets prepared in the same way and sputtered under optimized conditions, the lowest ρ_e values were achieved by using heavily extrinsically doped AZO ceramic targets (AZO_D) (Fig. 5.29), which leads to high N_e and thus also to high optical absorption in the NIR region (Fig. 5.32). This can be controlled by reducing the Al-doping level in the sputtered AZO thin films. Thus, it was possible to increase substantially μ_e without affect excessively N_e as it is demonstrated in Fig. 5.29 and Table 5.8, enabling to obtain highly conductive films with improved optical transmission.

For the further discussion we compiled the $\mu_e - N_e$ data for all thin films deposited in this study (Fig. 5.70). This included the variation in film thickness, T_{subs} , P_{RF}, P_{dep} for the films deposited with different Al doping concentrations and from targets manufactured in different ways. For degenerately doped semiconductors with N_e > 10^{19} cm^{-3}, it has been stated that μ_{ii} is the main scattering mechanism and a theoretical curve has been obtained representing the μ_e limit as a function of the N_e [72, 182]. This theoretical curve is also depicted in Fig. 5.70 (dashed line) together with the experimental data of this work.

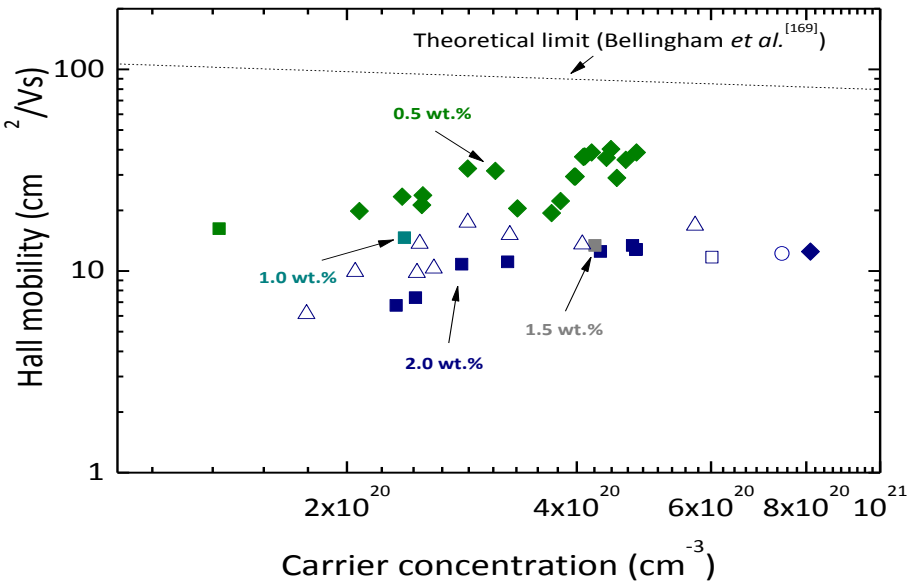

Fig. 5.70. *$\mu_e - N_e$ dependence of AZO films deposited under different conditions. Each point represents an AZO film sputtered with a different set of deposition parameters and/or sputtering target characteristic.*

The range of N_e varied from 1.36 x 10^{20} to 8.10 x 10^{20} cm^{-3} and was determined by several factors. The mainly influence comes from the Al doping level but the stoichiometric ratio O/Zn of the films, the substrate temperature (T_{subs}) during deposition, and the film thickness also have a direct influence on N_e of the AZO films. Carrier mobility (μ_e) also showed a wide variation between the lowest and higher value reached (6.7 and 40.2 $cm^2V^{-1}s^{-1}$), depending on the P_{RF}, P_{dep}, substrate temperature, oxygen content of the target, and primarily on the film thickness and Al doping level of the film. Other authors [66, 67] observed that the parameter with biggest influence on μ_e is the film thickness, increasing when the layer thickness and the mean crystallite size increase. However it should be noted that none of them has considered the effect of Al-doping level.

The overall maximum mobility of 40.19 $cm^2V^{-1}s^{-1}$ was achieved for an N_e = 4.43 x 10^{20} cm^{-3} using the lightest doping level (0.5 wt. % Al_2O_3) sputtered at 300 °C from a hot-pressed target. The observed $\mu_e - N_e$ dependence found in this work clearly indicates that whatever the deposition conditions or sputtering target used, a "practical" limit of μ_e exists for a given range of N_e, consistent with the literature [39, 72, 182, 183]. The maximum μ_e achieved for N_e > 5 x 10^{20} cm^{-3} are in close vicinity to this limit of μ_e presented by Ellmer (40 $cm^2V^{-1}s^{-1}$) [72].

As stated [184], the influence of μ_{gb} becomes very important when the width of the depletion layers becomes commensurate with the grain size of the crystallites. This fact is due to the creation of a potential barrier across the depletion region, impeding the carrier motion from one crystallite to another [184]. To determine if μ_{gb} has some influence in the type of electrical transport observed in the sputtered AZO films, the mean free path (MFP) values of the carriers have been estimated through the following [186]:

$$MFP = \left(\frac{h}{2e}\right)\left(\frac{3N_e}{\pi}\right)^{1/3}\mu_e \qquad \text{(eq. 5.12)}$$

where h is the Planck's constant, e is the unit charge of the electron and N_e and μ_e have their usual meaning. Since the obtained values of MFP for all sputtered films (~0.7 – 6.2 nm) are much smaller than the crystallite size values (~14 – 52 nm), μ_{gb} effect is extremely small in these films and can be ruled out. In fact, μ_{gb} is dominant to limit the μ_e only for those samples whose grain sizes are comparable with MFP or if lower N_e are used. It is important to notice that samples with such small grain sizes and very low μ_e and N_e are not applicable in practice to produce transparent and highly conducting films [184].

As previously mentioned, besides μ_{ii} and μ_{gb}, other mechanisms can act as scattering centers in AZO TCOs. For Al-doping concentrations much higher than the solubility limit of Al in ZnO lattice (not covered in this work), neutral impurities scattering (μ_{ni}) derived from the excess dopant that remains inactive after deposition must be also considered [187]. On the other side, lattice vibration scattering mechanism effect (μ_{ph}) also cannot be discarded, but only at high temperatures, where μ_{ph} is inversely proportional to the temperature [184]. According to these results and considering the range of N_e of the sputtered films, the experimental limit for the maximum μ_e found in our study is mainly determined by μ_{ii}.

5.5. Compositional analysis of AZO targets and sputtered films

The chemical composition of the manufactured AZO targets and corresponding thin films is of utmost importance for the understanding of the structural, optical or electrical properties. Throughout this research work, several AZO targets with different Al-doping levels were manufactured using different sintering techniques/atmospheres. In this section are compared the chemical compositions of various targets prepared by different ways and related to those of corresponding thin films. Hence, both AZO sputtering targets and films were analyzed by AES (Auger electron spectroscopy) using accurate standards. The use of these technique allowed the assessment of the chemical composition in both, the surface of the samples and the interior (Auger depth profiles). All the analyzed thin films were sputtered under the same RF power and deposition pressure (P_{RF} = 250 W and P_{dep} = 0.2 Pa) to avoid the possible effect of the deposition conditions in the final chemical composition. The O and Al content was performed considering respectively O/(O + Zn + Al) and Al/(Al + Zn) atomic ratios.

Auger depth profile analysis performed on several sputtering targets and thin films (not shown here) reveals that Al is uniformly distributed throughout both the targets and films cross sections, independent of the sintering atmosphere or composition, in line with the observed for thin films sputtered from AZO 98:2 wt. % ZnO:Al_2O_3 non-sintered and sintered target in air (Fig. 5.68).

The chemical composition of several targets and corresponding thin films used throughout this research work is presented in Table 5.13, together with the respective electrical resistivity of the analyzed targets and films. The presented Al and O content values are the average value considering the Al and O contents measured at various locations in the sintered targets and thin films.

Table 5.13. *Electrical resistivity and chemical composition of several manufactured AZO targets and sputtered thin films.*

Target	Sintering method/cycle	Sputtering target			Thin film		
		ρ_e $\times 10^{-3}$ (Ωcm)	Al content (at.%)	O content (at.%)	ρ_e $\times 10^{-3}$ (Ωcm)	Al content (at.%)	O content (at.%)
AZO_A	CS (air) 1100 °C/2h	5.83	0.84	50.2	2.83	0.78	47.1
AZO_B	CS (air) 1150 °C/2h	4.46	1.71	50.8	1.79	1.65	46.3
AZO_C	CS (air) 1300 °C/2h	4.01	2.53	51.9	1.10	2.39	46.5
AZO_D	CS (air) 1300 °C/2h	3.72	3.22	51.4	1.02	3.10	45.9
AZO_D	CS (air) 1400 °C/2h	5.47	3.42	54.3	---	---	---
AZO_D	CS (Ar) 1300 °C/2h	1.04	3.31	47.7	0.89	3.26	44.4
AZO_D	SPS 1000°C/15min	0.46	3.28	46.4	0.68	3.28	43.8
AZO_D	HP 1150°C/1h	0.37	3.27	46.8	0.62	3.24	43.4

As can be observed, the Al-doping concentration of both targets and films are near the expected doping levels (AZO_A: 0.80 at. %; AZO_B: 1.59 at. %; AZO_C: 2.37 at. %; AZO_D: 3.16 at. %). Generally, the Al doping concentration of the targets is slightly higher than that of the films, which can be related with the preferential pulverization of Zn in relation to Al [50]. However, this difference tends to be reduced when highly conductive targets are used.

The influence of sintering temperature on the chemical composition of the targets was also evaluated. When sintered by CS in air at high temperatures (≥ 1400 °C) the Al content quantified increases to 3.42 at.% (2.17 wt.% Al_2O_3). This result agrees with the weight loss observed at T ≥ 1400 °C (Fig. 5.3) and the predicted Zn volatilization at high temperatures.

All the targets prepared by CS in air presents an O excess independently of the composition. When sintered under controlled atmosphere, the O content of the targets decrease substantially giving rise to targets with O deficiency. The relationship between the O content in deposited thin films and that in the targets used for deposition is presented in Fig. 5.71.

The length of the bars associated with the data points indicates the amount of scattering achieved in the values of O content measured at different locations in both targets and films. The amount of oxygen quantified in sputtered films is smaller than the one of the targets. This fact is related

with the loss of O_2 (volatile element) during the material transport process between the target and the substrate [188].

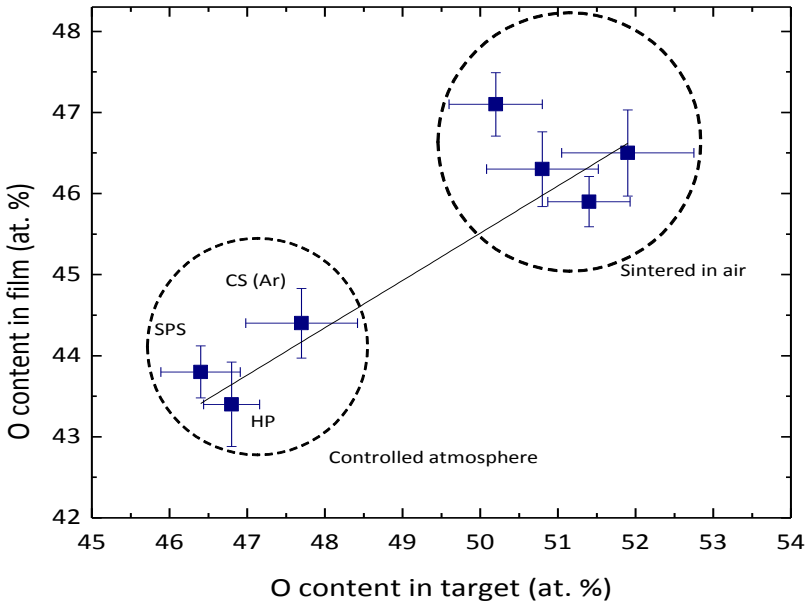

Fig. 5.71. *Oxygen content of the films versus oxygen content in targets.*

As shown, under the same deposition conditions, the oxygen content reaching the substrate is related to that in the target. This trend was also observed by Minami *et al.* [37]. The results agree with the electrical conductivity improvement observed for both, targets prepared under controlled atmosphere (Fig. 5.72 a)) and films sputtered from those targets (Fig. 5.72 b)). This relationship showing the increasing in the resistivity of targets with the O content was also confirmed by EDS and XPS.

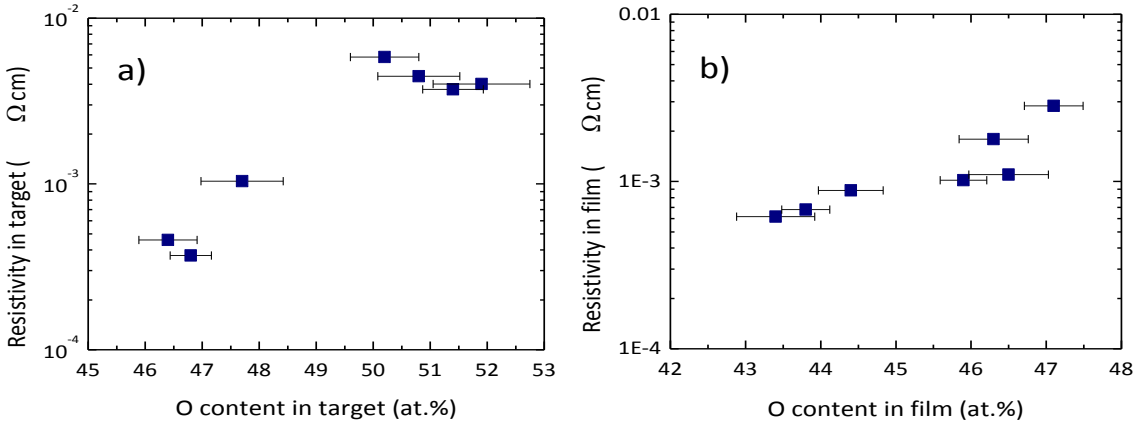

Fig. 5.72. *Electrical resistivity as a function of oxygen content for both a) targets and b) thin films.*

It should be noted that the evaluation methods used may still not be sufficiently accurate in quantifying the O content in both films and targets despite the small associated error of < 3 % AES measurements, because the measured O content could include chemically and physically adsorbed O on the grain boundaries surface as well as the oxygen atoms in the grains of the

ceramic targets that may be dependent on the evaluation methods used [37]. However, taking into account the chemical homogeneity observed throughout the cross sections of both films and targets (depth profiles), and the results from Fig. 5.71 and Fig. 5.72 a) and b), we can assure a clearly trend demonstrating that the deposition of TCO thin films of Al-doped ZnO with improved electrical conductivity requires the preparation of significantly reduced AZO targets with low oxygen content up to a minimum value, since purely Zn targets need the introduction of oxygen during the deposition.

Besides the minimum resistivity value, its spatial uniformity is also important for practical uses (e.g. photovoltaic device application). However, as presented in section 3.3.1.1, magnetron sputtering uses a magnetic field that confines the plasma in a torus-like region causing a non-uniform erosion of the target (ring-like erosion). During the sputter deposition, the longer the target was used, the deeper and wider the ring-like erosion crater was. This inhomogeneous erosion of the target material causes in a dependence of the film properties on the position on the substrate, with significant variations in terms of deposited film properties from the center to the edge of the substrate.

The use of highly conductive AZO ceramic targets, reduces the spatial variation of resistivity on the substrate [37, 38, 40, 53]**.** Minami *et al.* [38, 53] associated the lateral distribution phenomena to the non-uniform distribution and amount of oxygen reaching the film substrate interface, suggesting the use of a combined RF + DC sputtering, a less oxidizing atmosphere, or the use of AZO targets with lower oxygen content to reach more uniform films. Huang *et al.* [40] also found that using highly conductive AZO target with less oxygen, improved the uniformity of resistivity distribution of AZO thin films.

In this research work the effect of using more conductive targets in the spatial distribution of resistivity was not investigated in depth. However, analyzes performed in AZO thin films deposited with the 2" target prepared by HP (target composition: 98:2 wt.%) have enabled much higher homogeneity of resistivity values in the center and the edges of the substrate than the observed for several thin films deposited from targets prepared by CS in air, considering the same substrate area. A more detailed study concerning not only the effect of the sputtering target used in the spatial resistivity distribution, but also on film thickness variation throughout the substrate must be taken into account in future work.

5.6. Thermal and mechanical properties of AZO sputtering targets

Targets lifetime is strongly influenced by their thermal and mechanical properties. Thermal tensile stresses induced by a lower thermal diffusivity and thermal conductivity should be avoided in order to reduce the probability of thermal stresses (gradients) and cracks in the targets resulting from non-uniform heating during the sputtering process [49]. Furthermore, targets with improved thermal shock resistance characteristics allows to use higher P_{RF}, enhancing sputtering rates and consequently reducing processing and operation times, with direct effect on production costs. It is therefore preferred to increase the thermal conductivity within certain limits in order to assure enhanced thermal shock resistance characteristics of the targets increasing reliability and target life time [189, 190].

Additionally, the control of mechanical properties should also be considered. High final densities and controlled grain size improve the fracture toughness and flexural strength of the targets. On the other side, final machining to fix dimensions and correct possible defects of sintering is usually performed after sintering (before polishing). Thus becomes essential to know the hardness of the material to choose the right tools during the machining process. In this section, special attention is given to the thermal and mechanical characteristics of AZO ceramic targets and their relation with several parameters.

5.6.1. Thermal properties

Fig. 5.73 a), b) and c) shows respectively the thermal conductivity (k), specific heat (C_p), and thermal diffusivity (D) of AZO ceramic targets prepared by CS in air with different compositions analyzed between RT and 300 °C. For each composition two different targets were analyzed varying the final density.

As shown in Fig 5.74 a) and c), the values of k and D of all samples drops with temperature and Al-doping level. Thermal conductivity of high density targets (> 99.5 % of TD) (filled symbols) decrease from 45 to 40 $W.m^{-1}.K^{-1}$ at RT with increasing Al-doping concentration, while at 300 °C, k values decrease ~50 % to ~21 $W.m^{-1}.K^{-1}$, becoming almost independent of the Al content, in line with the observed by Cai *et al.* [191] and Tsubota *et al.* [192] for Al-doped ZnO samples with 0 – 5 mol% Al_2O_3. The thermal conductivity (k) of a solid is dependent on phonon (k_{PH}) and electric (k_{EL}) thermal conductivities ($k = k_{EL} + k_{PH}$ (eq. 5.13)) and can be varied greatly by extrinsic factor such as microstructure and/or impurities.

The disorder of the ZnO crystal lattice and the amount of interfaces between the ZnO and the $ZnAl_2O_4$ grains both increased with the Al content added, which increased the phonon scattering, explaining the observed decrease of k with the Al-doping level [168, 191]. Additionally, targets with lower final density (92.9 to 96.2 % of TD) (open symbols) also shows inferior k than full densified targets, with values of 31 – 36 $W.m^{-1}.K^{-1}$ and 15 – 18 $W.m^{-1}.K^{-1}$, respectively at RT and 300 °C. The influence of target final density on the thermal properties is similar to its influence on electrical conductivity. The higher the densification, greater the k and D values [193].

Independently on the final density and Al-doping level, both k and D has a non-linear behavior with T, showing a tendency to stabilize and be very close at higher temperatures (> 500°C (not shown here)). At lower temperatures, thermal conductivity of AZO is mainly dominated by (k_{PH}) [168, 191]. According to Cai *et al.* [191], as the temperature increases the contribution from electrons (k_{EL}) increases, therefore, k for all the samples at high temperatures is very close. It should be noted that all the k values presented here are substantially higher than the ones of ITO ceramic targets (7 – 13 $W.m^{-1}.K^{-1}$ depending on target composition) in the same range of temperatures [20, 49].

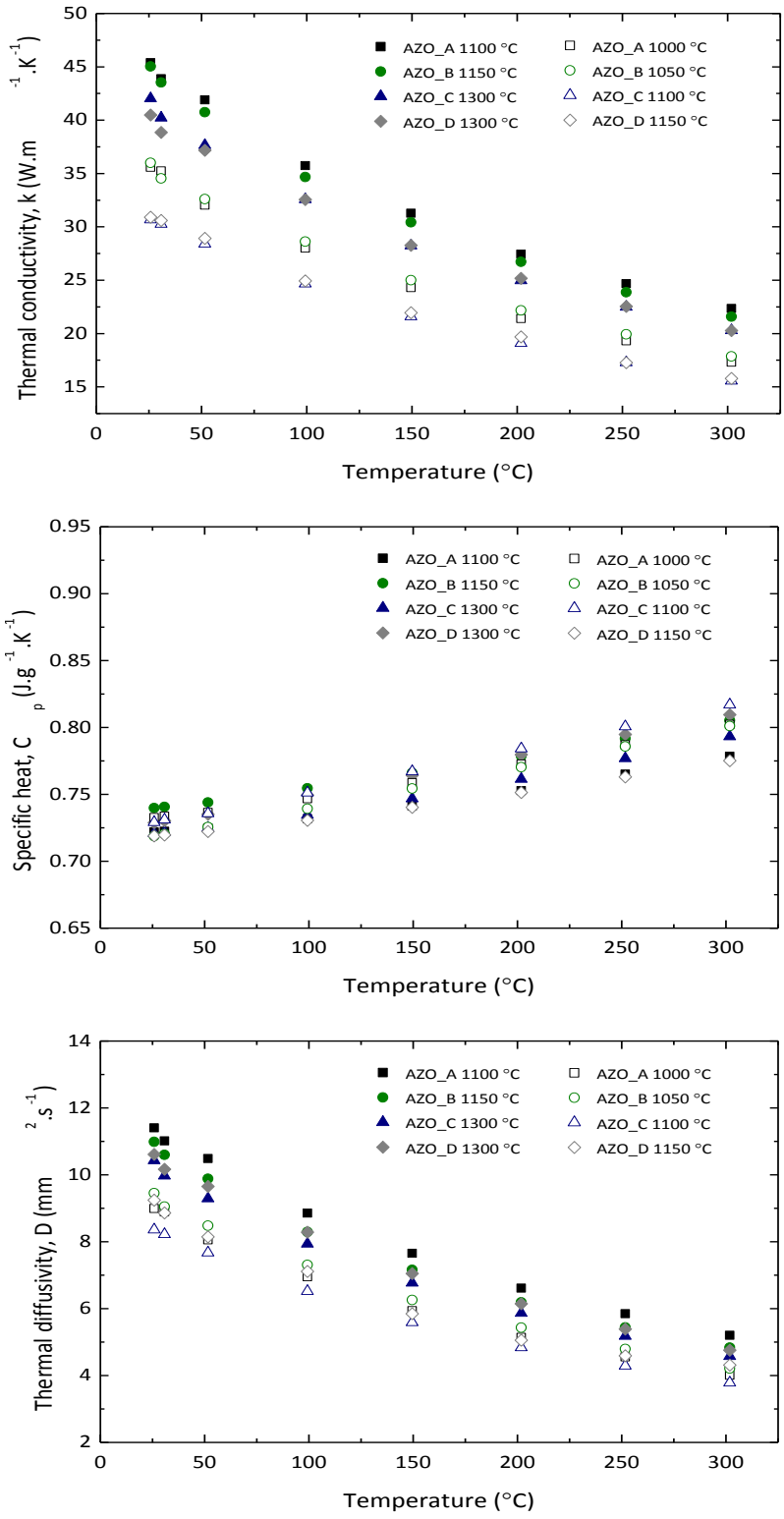

Fig. 5.73. *a) Thermal conductivity, b) specific heat, and c) thermal diffusivity of AZO ceramic targets prepared by CS in air (HT = 2 h) as a function of Al-doping concentration and sintering temperature.*

The thermal properties of two hot-pressed AZO targets with 0.5 and 2.0 wt. % Al_2O_3 sintered respectively at 1025 and 1150 °C for 1 h were also evaluated. Both samples show a similar trend with temperature than the targets prepared by CS in air. The k, D and C_p values at RT and 300 °C are presented in Table 5.14.

Table 5.14. *Effect of Al-doping concentration on thermal conductivity (k), thermal diffusivity (D) and specific heat (C_p) of AZO targets prepared by HP.*

Composition (wt. % Al_2O_3)	Thermal conductivity, k ($W.m^{-1}.K^{-1}$)		Thermal diffusivity, D ($mm^2.s^{-1}$)		Specific Heat, C_p ($J.g^{-1}.K^{-1}$)	
	RT	300 °C	RT	300 °C	RT	300 °C
0.5	47.3	22.8	12.3	5.4	0.74	0.81
2.0	43.5	20.9	11.0	4.9	0.72	0.78

Considering the same Al-doping concentration, hot-pressed samples presents higher k and D values than high density AZO_A and AZO_D samples prepared by CS in air. As shown before, hot-pressed samples have a smaller grain size than conventionally sintered samples, and consequently more grain boundaries affecting the thermal flow. Thus, one would expect a decrease of the k and D values [20], which was not observed. Furthermore, all the considered samples have a final density near the TD, discarding the effect of final density. So, the high k and D values observed for the hot-pressed samples are possibly related with the oxygen deficiency of the targets [189, 190].

Coefficient of thermal expansion (CTE) was also determined in the temperature range of 20 – 500 °C by dilatometry according to ISO 10545-8. The heating rate used was 5 °C.min^{-1}. The values of CTE of several AZO targets varied between 6.5 x 10^{-6} °K^{-1} and 7.2 x 10^{-6} °K^{-1} in the range 20 – 500 °C (lower than ITO ceramics (7.0 – 8.5 x 10^{-6} °K^{-1}) [20]), independently on the target composition and sintering conditions, which allows using similar compositions for metallization and bonding processes of AZO targets.

5.6.2. Mechanical properties

One important characteristic of a ceramic target is its mechanical properties. Several high density AZO targets were analyzed in terms of flexural strength, fracture toughness and hardness varying the Al-doping level and sintering method. The mechanical tests were carried out accordingly to the procedures presented in section 3.2.2.5. The obtained mechanical properties of the analyzed targets are presented in Table 5.15, showing quite reasonable values when compared to ITO ceramic targets [20] and that AZO ceramic are not intended for structural applications.

No significant effect of Al-doping concentration was observed in terms of flexural strength of the targets. However, the fracture toughness tends to be lower and the hardness has the propensity to increase with the Al-doping level.

Considering the same composition, hot-pressed samples presents higher flexural strength values than the samples prepared by CS in air, while the fracture toughness and hardness seems to be independent on the sintering technique used. As known, final density and grain size have a strong influence on mechanical properties of ceramics. Generally high density ceramics with reduced grain size leads to improved mechanical properties. Here, all the analyzed samples are fully densified. The grain size of the targets prepared by CS in air does not vary significantly with values in the range 2.12 µm – 3.14 µm. On the other side, hot-pressed samples have grain sizes of 0.84 and 1.24 µm for targets with respectively 0.5 and 2.0 wt. % Al_2O_3, which can justify the observed

improvement of flexural strength, despite the negative effect that high degrees of oxygen deficiency can induce on the final mechanical properties due to the formation of metal rich phases on the final microstructure [190].

Table 5.15. *Mechanical properties of several studied AZO ceramic targets.*

Target	Sintering method/cycle	Flexural strength (MPa)	Fracture toughness (MPa.m$^{1/2}$)	Hardness HV1 (MPa)
AZO_A	CS (air) 1100 °C/2h	216 ± 13	2.0 ± 0.08	208 ± 15
AZO_B	CS (air) 1150 °C/2h	234 ± 21	1.8 ± 0.04	234 ± 9
AZO_C	CS (air) 1300 °C/2h	221 ± 16	1.8 ± 0.06	250 ± 21
AZO_D	CS (air) 1300 °C/2h	247 ± 18	1.6 ± 0.08	266 ± 19
AZO_A	HP 1025 °C/1h	261 ± 14	1.9 ± 0.06	220 ± 14
AZO_D	HP 1150 °C/1h	288 ± 11	1.6 ± 0.07	268 ± 23

Considering the above results, we can conclude that the best compromise between thermal and mechanical properties is obtained for targets prepared by HP.

5.7. Industrial scale-up – manufacturing of large size AZO sputtering targets and its application as a TCO in thin film solar cells

The scale-up from lab targets to industrial size targets was performed by UP followed by CS in air, considering the deagglomerated powder with a composition 98:2 wt. % ZnO:Al_2O_3. As known, UP have several problems/limitations that hinder the attainment of green compacts free of defects, being this issue more evident for larger green compacts [4]. In order to minimize this issue, the optimization of powder characteristics is crucial. To this end, the industrial targets were produced with atomized powders. The homogeneous feed of the die, the reduction of the friction between the raw material and the die, the final GD and its homogeneity were some of the aspects taken into account during the preparation of the granulated powder, reducing the possibility of defects in the green compact and subsequent sintered AZO targets. The following sections describe the procedure followed during this research work to produce large size AZO ceramic tiles. It is also demonstrated the feasibility to use those tiles as sputtering targets in the deposition of a TCO layer for the production of commercial a-Si:H TFSCs.

5.7.1. Atomization

Powder flowability is a precondition for automated pressing operations, and for achieving reproducible filling densities during the filling stage. Ideally, agglomerates of a spherical shape with a homogenous packing of the primary particles and a defined porosity (not hollow) and agglomerate size distribution should result from the atomization process. Suitable granule diameters range between 20 µm and 200 µm [5]. A large number of process variable parameters are available and should be controlled in order to warranty the desired powder characteristics after atomization. Properties such as bulk density, tapped density or angle of repose can be determined and give an idea about the quality of the atomized powder [31, 194].

In this work, the fabrication of spray-dried granules with solid morphology and high flowability was performed after a previous optimization of the aqueous slurry characteristics (amount of solids, viscosity, binders', plasticizers and dispersant contents) and atomizer parameters (inlet and outlet temperatures, atomization pressure, suction fan, nozzle type). Pressing aids such as binders and plasticizers are commonly used to improve the powders performance during the subsequent pressing and sintering stages as well as reduce the tooling wear during pressing. The ideal amounts of binder (Optapix PA 4-88), pressing agents/lubricants (Zuzoplast 126/3 and Zuzoplast 9002) and dispersant (Dolapix CA) were evaluated. The total wt. % of additives (considering the powder weight) was 4.5 %. The solids content of the suspension was 40 wt. % and the viscosity was kept constant at ~2500 cP (Brookfield viscometer DV-II+Pro) during the atomization (after binders addition/homogenization). Lower solids contents and viscosities were tested; however, higher solids content suspensions with a high (but processable) viscosity showed the best results in terms of both granulated powder properties and productive capacity (kg/h of atomized powder). After atomization the powder was dried at 70°C for 8 h, mechanically sieved at 150 µm and ultrasonically sieved at 32 µm to improve the granules size distribution and flowability of the powder. Table 5.16 shows the main characteristics of the spray-dried AZO powder.

Table 5.16. *Some physical characteristics of INNOVNANO AZO powder (98:2 wt. % ZnO:Al_2O_3) after spray-drying.*

Property*		Granulated AZO powder
Moisture content (100 °C) (%)		0.5
Loss on ignition (L.O.I.) (1000 °C) (%)		5.1
Angle of repose (°)		33
Bulk density (g.cm^{-3})		1.5
Granules size distribution (µm)	D10	36
	D50	60
	D90	105

**All these properties were measured taking into account internal technical procedures of INNOVNANO based on the respective standards.*

The high loss on ignition value (5.1 %) is related with the amount of binders added to the suspension before atomization. The bulk density is defined as the mass of particles that occupies a unit of volume of a container, being important when determining the volume of transport vehicles, storage vessels and dies cavities [194]. It mostly depends on particle size, moisture, and chemical composition, but also on handling and processing operations. The presented bulk density (1.5 $g.cm^{-3}$) of granulate AZO powder is ideal for industrial processing, considering the small particle size and high SSA of the powder that usually affect negatively the bulk density. The granules size distribution (GSD) is also important, since the amount of powder in a container is dependent on the adjustment capability of the granules to occupy the free spaces inside the container. The final GSD of INNOVNANO AZO powder after atomization is unimodal (Fig. 5.74 a) and b)) and has been optimized to improve the bulk density and the angle of repose.

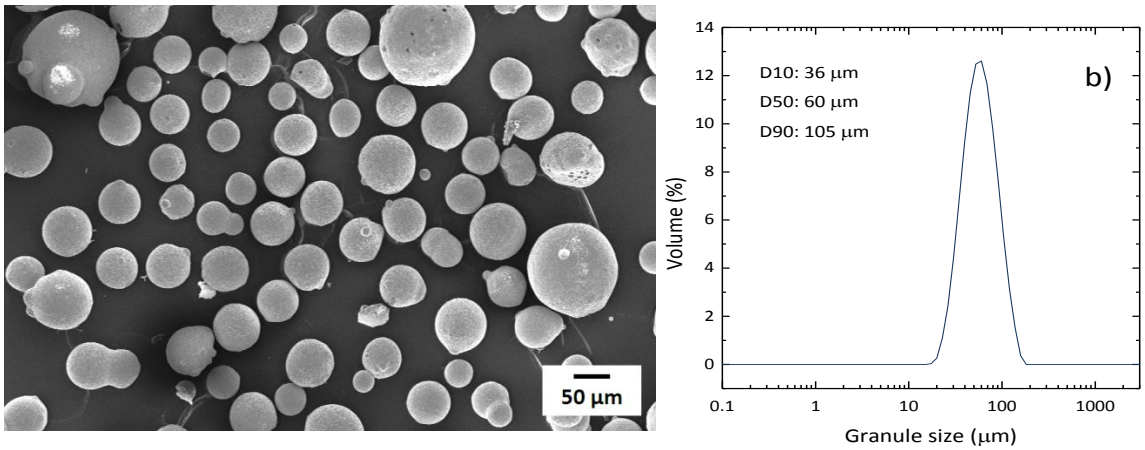

Fig. 5.74. *a) SEM image showing the typical morphology of INNOVNANO AZO powder after granulation, and b) Granules size distribution of INNOVNANO AZO 98:2 wt. % (ZnO:Al_2O_3) atomized powder.*

Defined as the angle between the horizontal and the slope of a heap of granular material dropped from some designated elevation, the angle of repose corresponds qualitatively to the flow properties of a material, and is a direct indication of potential flowability. Typically higher angles (i.e. 50 – 60°) indicate material with difficult flow, while a lower angle, such as 30 – 40°, represents material with easy flow [195]. The obtained value (33°) demonstrates the high flowability of the powder and consequently its viability to work as a feeding material.

5.7.2. Uniaxial pressing of the green compacts

The green compacts were uniaxially pressed using an industrial hydraulic press existing in Alphaceramics GmbH (Auchen, Germany). With high knowledge in the production of modular hydraulic presses, Alphaceramics developed their own automatic uniaxial pressing machines designed to improve the quality of the final green compacts by reducing significantly the defects and density gradients of the powder compacts. The pressing conditions were optimized considering the final GD (as higher as possible) and the absence of defects in the pressed compacts. Table 5.17 shows the main pressing parameters/compacts properties of the compacted tiles used for industrial targets production. Several compacts with 19.2 cm x 14.4 cm x 1.3 cm (length x width x thickness) were produced (Fig. 5.75).

Table 5.17. *Pressing parameters and green compacts properties of Al-doped ZnO granulated powder.*

Pressing parameter / green compacts properties	
Pressing force (MPa)	150
Filling height (cm)	4
Compression factor	~3.1
Load reduction upper die at ejection (bar)	65
Vacuum (mbar)	75
Powder weight (kg)	~1.25
Green density (g.cm^{-3} / % of TD)	3.5 / 62

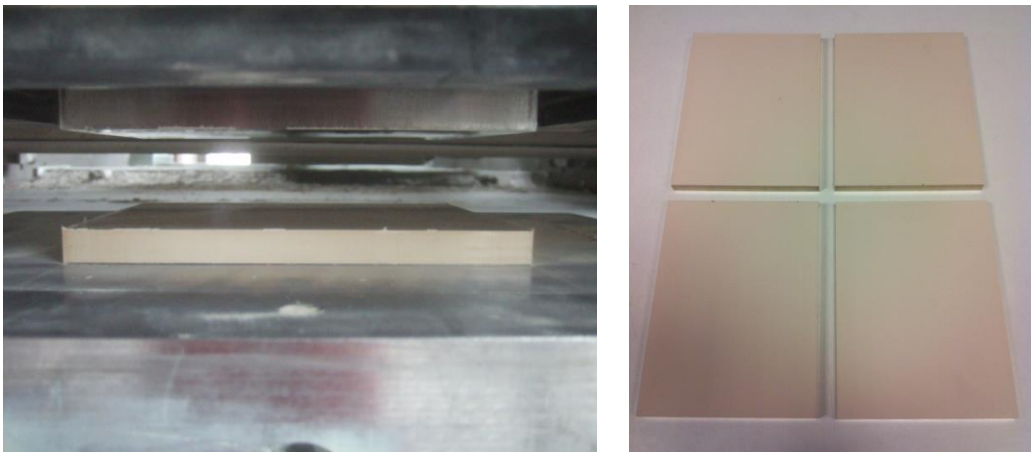

Fig. 5.75. *Uniaxial pressing trial of an AZO green compact (left) and several pressed tiles before sintering (right).*

5.7.3. Sintering, machining and bonding of the targets

The manufacturing of fully dense products is quite challenging for commercial ceramic processing. The quality of a DC magnetron sputtered thin film is generally improved when the ceramic targets have higher density [20]. The final density values strongly depend on the size of the compacts and firing conditions. Typically, the increase of tiles dimensions gives rise to lower final densities under the same sintering conditions. Due to the already described characteristics of INNOVNANO AZO powder, it was possible to produce full densified large tiles with some adjustments on the sintering cycle. In order to avoid possible defects inherent to the debinding stage, the green tiles were firstly heated with a CHR of 1.5 °C.min^{-1} until 550 °C and kept at this temperature for 4 h for complete removal of organics. After that, the tiles were heated at a CHR of 5 °C.min^{-1} until 1350 °C sintering at this temperature for 4 h. The sintered tiles had a final density > 98.5 % of TD with a final grain size of ~4.2 μm (Fig. 5.76). Values of 5.8 x 10^{-3} Ωcm, 13.6 cm^{2}V^{-1}s^{-1}, and 7.91 x 10^{19} cm^{-3} were obtained respectively for the electrical resistivity, μ_e, and N_e of the ceramic targets. After sintering, each tile was cut, ground and bonded to a metallic backing plate. The final block is

composed of several tiles with 13.7 cm x 10.7 cm x 0.9 cm (length x width x thickness) as illustrated in Fig. 5.77.

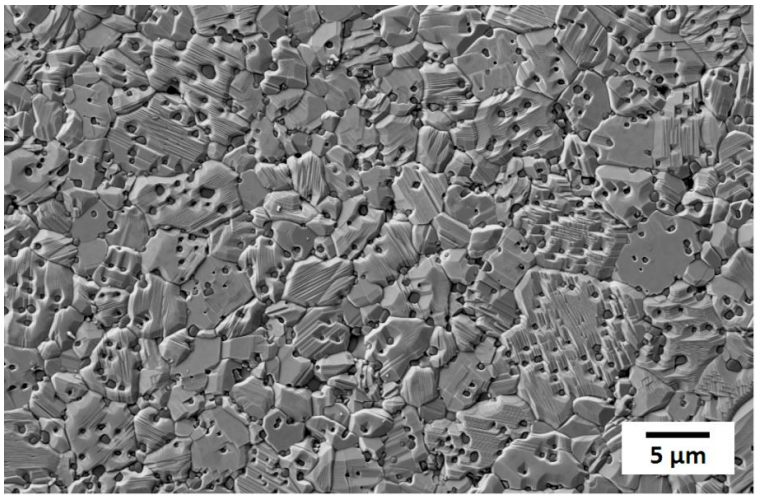

Fig. 5.76. *SEM image showing the typical morphology of INNOVNANO AZO large size tiles with an Al-doping concentration of 2.0 wt. %, conventionally sintered at 1350 °C for 4 h in air.*

Fig. 5.77. *Final block composed of several AZO tiles produced with INNOVNANO AZO 98:2 wt. % ZnO:Al_2O_3 powder.*

5.7.4. Application as a TCO material in commercial a-Si TFSCs

The performance evaluation of the manufactured large scale targets was done in a partnership with a Portuguese company, *Solar Plus*, dedicated to the production of a:Si:H TFSC photovoltaic panels. AZO has been widely used in the preparation of this type of cells, mainly due to the high stability in hydrogen containing atmospheres, e.g., in a silane (SiH_4) plasma discharge, which is used for the preparation of a-Si:H TFSCs [72]. In the case of thin film silicon tandem solar cells, the AZO material could be used at different positions such as front TCO and back reflector, which are crucial layers to increase light trapping in the solar cell [91]. In this work AZO layer was used as back contact layer considering two different approaches: Firstly, AZO layer was used as a reflective layer in *Solar Plus* standard non-transparent TFSCs panels (Fig. 5.78 a)); Finally, AZO layer was also applied as a reflective and conductive layer in *Solar Plus* semi-transparent TFSCs panels (Fig. 5.78 b)). For each type of TFSC, 48 panels with an area of 0.79 m^2 were produced under the same conditions, 24 using INNOVNANO targets and 24 with the AZO targets of the usual supplier of *Solar Plus* (denominated commercial targets throughout this section). The panels were processed

in *Solar Plus* facilities following their usual production process procedures (T_{subs}= 200°C; P_{dep}= 0.29 Pa; P_{DC} = 1.6 W.cm^{-2}).

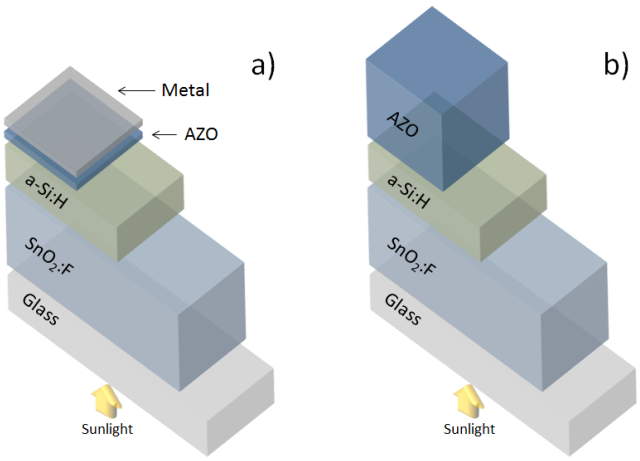

Fig. 5.78. *Schematic presentation of a) standard and b) semi-transparent TFSCs produced in Solarplus.*

Fig. 5.79 illustrates the in-situ AZO TCO layer deposition using the industrial DC magnetron sputtering system available in *Solar Plus*. The use of this type of equipment in the deposition of films is almost mandatory at industrial level. DC magnetron sputtering has been regarded as one of the most attractive and effective fabrication techniques in the mass production of AZO films, satisfying the demands of good film quality, high-rate and large-area deposition, and low cost of equipment for commercialization of TCO films [40].

During our trials, the production of the panels was carried out in continuous mode. It was observed a good stability of the plasma with a quasi-absence of arcing during the deposition process of the AZO layers throughout all the tests. In Fig. 5.80 are shown several panels produced using INNOVNANO large size sputtering targets.

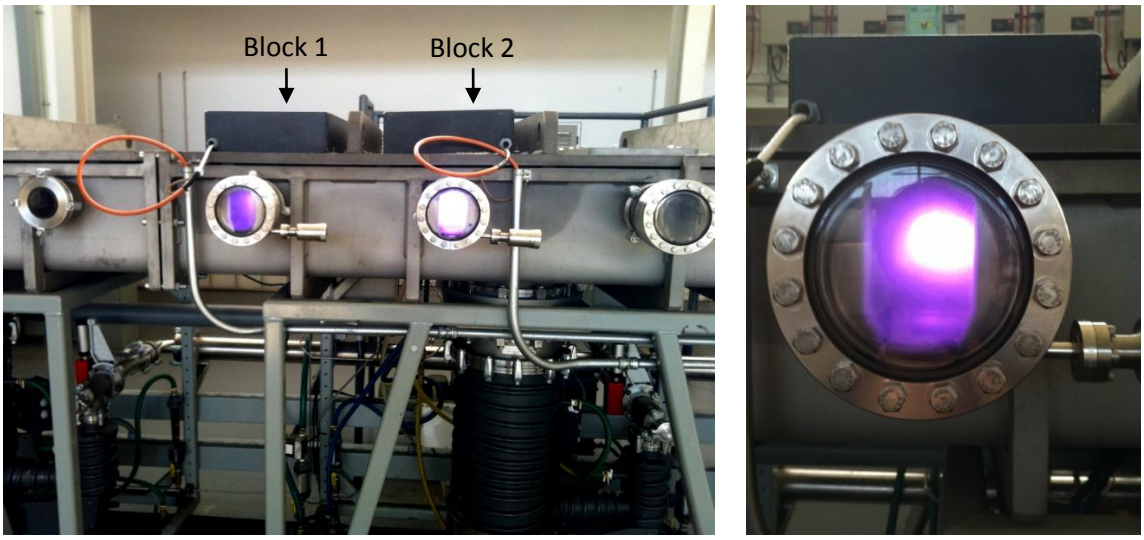

Fig. 5.79. *Images showing the manufactured large size sputtering targets working during the deposition of AZO TCO layer in commercial a-Si:H TFSCs produced by Solarplus.*

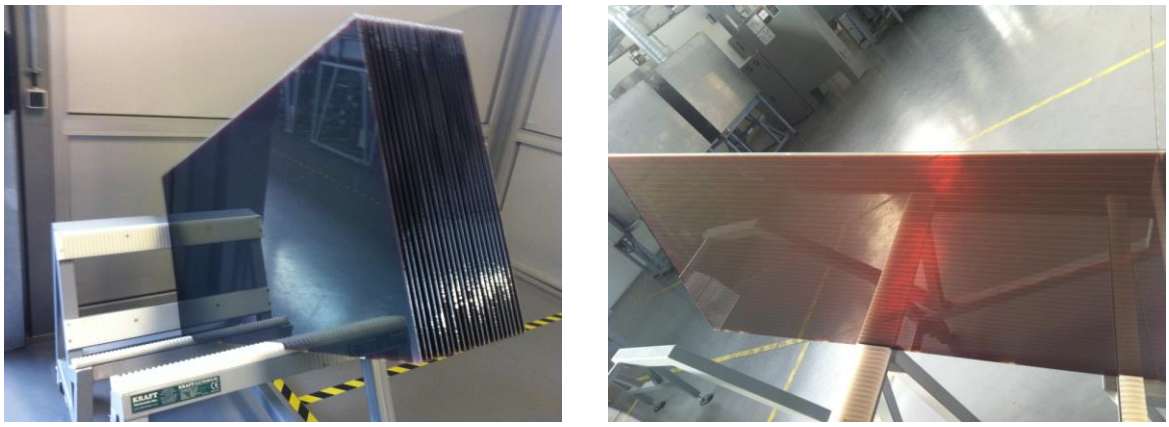

Fig. 5.80. *a-Si:H TFSC panels produced using INNOVNANO large size sputtering targets; Application of AZO as a reflective layer in Solarplus standard non-tranparent panels (left) and as a reflective and conductive layer in semi-transparent panels (right).*

SEM images presented in Fig. 5.81. shows, respectively, the cross section of a) standard and b) semi-transparent TFSC produced with INNOVNANO sputtering targets. As shown, AZO layer is much thicker (~ 1 µm) in the case of semi-transparent TFSC than for standard TFSCs (~ 100 nm). Because of the presence of Al as a metal over-layer in *Solar Plus* standard cells, the sheet resistance of the AZO is not so critical and a thin layer can serve the purpose in this type of cells. On the other hand, a high conducting thick ZnO has to be used in semi-transparent cells to reduce the sheet resistance in the absence of a metal back contact. According to the studies of Rath *et al.* [91], thick TCO layers, must have lower doping concentration when is required a high transmittance from the visible to the NIR region [90, 91, 196], and the bandgap narrowing due to the low Al-doping is not a concern, as short wavelength light does not reach the back surface [91]. For a thin back reflector layer a higher doping concentration seems to be most suitable acting as an optical reflector. Thus, it becomes necessary to make a balance between the optical and electrical properties of the sputtered TCO thin films with different doping concentrations, and the desired properties for each layer position in the solar cell structure. It should be noted that throughout this research work only the 98:2 wt. % ($ZnO:Al_2O_3$) composition was tested in the production of TFSCs.

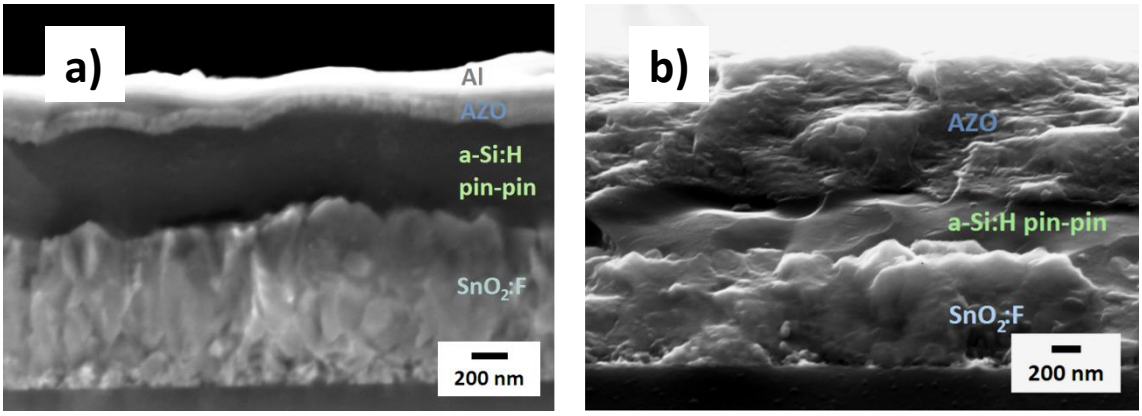

Fig. 5.81. *Cross sectional SEM micrographs of a) standard non-transparent a-Si:H TFSC and b) semi-transparent a-Si:H TFSC.*

After the deposition of all the layers that compose the respective TFSC, each panel was analyzed independently. The evaluation only took into account the I-V test results. In Table 5.18 are shown the comparison between several parameters of the standard panels produced with INNOVNANO targets and commercial ones. The presented results are an average of the values obtained in all the panels produced with each target. The results allow concluding that no significant difference was observed between the final properties of the cells using both commercial and INNOVNANO large size sputtering targets. Standard solar cells produced with commercial targets shows an open circuit voltage (V_{OC}) and a fill factor (FF), respectively 0.77 % and 2.24 % above the values reached using INNOVNANO targets. The short circuit current (J_{SC}) is approximately the same (0.1 % difference) using both targets which means that optically the films presents a similar behavior. The main difference (~3.5 %) is related with the sheet resistance (R_{sheet}), leading us to assume that the electrical component is the main responsible for the decrease in ~3 % of the average power of the cells produced with INNOVNANO targets. It should be noted that the higher R_{sheet} values using INNOVNANO targets were essentially observed in the first produced panels, which can be correlated with the removal of the superficial layer of the target. The average efficiency (η) of the panels were ~5.5 – 6.5 % (total area of 0.79 m^2) with a slightly tendency to be higher for panels produced with commercial AZO targets.

On the other side, semi-transparent TFSCs produced using INNOVNANO targets presents higher V_{OC} (1.23 %) and FF (2.23 %) than commercial targets. Additionally, the R_{sheet} values are close (slightly below) the values reached with commercial targets, resulting in an average power ~3 % above the values obtained with commercial targets. The average efficiency (η_s) of the panels were ~4.5 – 5.5 % (total area of 0.79 m^2) with the best results being in general achieved using INNOVNANO AZO targets.

It should noted that also in terms of reproducibility, the average deviations between each group of 24 panels produced with each target and for each type of cell, are in compliance with the minimum values required for acceptance by *Solar Plus*.

Table 5.18. *Comparison of standard and semi-transparent TFSCs external parameters as a function of the sputtering target used (A = commercial target and B = INNOVNANO target). V_{OC} is the open circuit voltage, J_{SC} is the short-circuit current, FF is the filling factor, R_{sheet} is the sheet resistance and Power is the maximum power from the solar cell.*

Type of TFSC		V_{OC}	J_{SC}	FF	R_{sheet}	Power
Standard	**A/B**	0.77 %	0.10 %	2.24 %	3.55 %	3.14 %
Semi-transparent		-1.23 %	0.68 %	-2.23 %	-0.44 %	-2.78 %

After the deposition of the panels, no signs of nodules formation were found in the targets. A general overview of the targets appearance is depicted in Fig. 5.82. Even considering the very low number of panels produced (each block of targets should be able to produce ~1500 standard and ~300 semi-transparent TFSCs) it can be a good indicator about the quality of the manufactured targets.

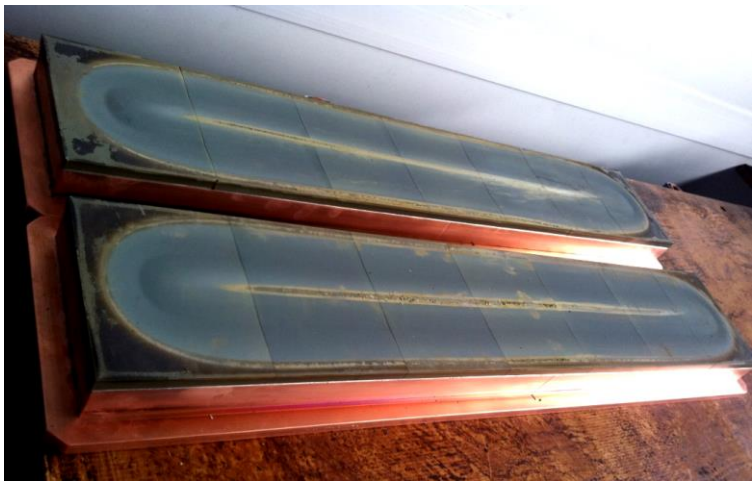

Fig. 5.82. *INNOVNANO large size sputtering targets after AZO layer depositon in series production of 48 panels.*

5.7.5. Arcing and nodules formation during sputtering

Has been mentioned throughout this dissertation, AZO targets (mainly the industrial ones produced by DC sputtering) are prone to nodule formation and excessive arcing, which degrades targets utilization and sputtered film quality [11]. The nodules which are made of compound oxides are electrically insulating and allow for a charge build-up that creates an arc. An arc rate of hundreds or even thousands of arcs per second is not uncommon and leads to reduced deposition rates and particle generation originating coating defects, which results in TCOs with inferior electro-optical properties. Typical coating defects include pinholes, micro-structural defects and texture imperfections [31]. Effective arc management and nodule growth containment have become increasingly popular topics of interest among process engineers performing AZO deposition [11]. The solution for all of them passes through the use of high quality DC power supplies with effective arc-management capabilities (involves the detection of either high current or low voltage anomalies that in turn invoke a temporary interruption of applied power in order to extinguish the event) and high-quality target materials. Here we are focused on the efforts related with sputtering targets optimization and the main findings in this field.

Contrarily to the uniform glow of a stable plasma, arcs are distinguished by an intensively focused and localized discharge supported by collective electron emission from a breakdown occurrence [46]. Energy concentrated at the site is often enough to form molten material at the location of the arc giving rises to the occurrence of explosive ejection of target macro-particles. Moreover, when severe, arcing disrupts the uniform and continuous delivery of power to the sputtering target. Since sputtering involves high ion fluxes to the target surface, any impurity, void or inhomogeneity on the target is a potential arc generation site [46].

Nauman [11] examined the effect of target properties on arcing and nodules formation using two different industrial targets produced with coarse- and fine-grain powder sizes and found that fine-grain-manufactured AZO targets materials have a much lower arc rate throughout the target life time. Although less substantial, the author also observed a little reduction in nodules formation. Margadant *et al.* [31] in their patent about the production of AZO sputtering targets, gives special relevance to the microstructural homogeneity of the targets and its influence on arcing and

consequent instability during DC magnetron sputtering. The authors consider that porosity, too large $ZnAl_2O_4$ second phase precipitates (> 2 μm) and even free Al_2O_3 residues (widely observed in several commercial sputtering targets) result in variations in conductivity of the target surface, or, in the case of free Al_2O_3, in dielectric centers that cause arcing during deposition and target lifetime reduction. According to the authors, target materials with a homogeneous microstructure increase process stability and efficiency during sputtering by avoiding arcing issues during sputtering. Fukushima [30] in his invention also makes reference to the influence of local resistivity gradients existing in the targets due to precipitates (second phase formation) or voids (porosity), correlating it with abnormal discharges (variations of the impedance of the discharge system during the sputtering) that can occur during the sputtering of AZO targets. The author concludes that to attain high quality sputtering targets, improvements concerning the reduction of porosity and large precipitates should be considered. Sittinger *et al.* [47] investigated several ceramic AZO targets from different manufactures. The authors found a direct correlation between the microstructure of the targets and arcing during sputtering. According to them, the arc rate reduces substantially when uniform fine grained targets are used instead of coarse grained structures.

Besides arcing, one of the major problems faced by AZO targets during sputtering deposition is process instabilities induced by nodules formation. Such nodules are mainly formed by re-deposition on target surfaces with weak or no erosion (for industrial planar targets this might be more than 50 % of the target surface area due to the formation of a racetrack) (see Fig. 5.83) [48]. Nodules give rise to micro-arcing and hence coating inhomogeneity during sputtering process. When the arc becomes too high, it is necessary to disrupt the process and venting the system so that the nodules are cleaned away mechanically [48]. Such cleaning is a source of coater dust causing surface defects during subsequent sputter deposition. Moreover, abrasive cleaning further reduces system uptime and causes lost of target material. The absence of nodules therefore increases both system uptime and product yield. Nodules formation/growth on sputtering targets is a complex phenomenon that occurs on the target surfaces during sputtering deposition. Nodules formed on AZO targets are typically black in appearance and exhibit high resistivity. Target density and its final microstructure are associated with the nodule formation/growth phenomenon. Lippens [48] found that high density targets with well dispersed second phase in the final microstructure (homogenous conduction electron density) improve the stability of the deposition without nodules formation and consequent need for cleaning. Inhomogeneous chemical composition and electrical properties also lead to charge accumulate (charging points) in certain targets surface area and arcing. Nodules can crack under thermal stress or be destroyed by an arc during deposition. Nodule breakups are followed by a large number of particles, which nucleate a new generation of nodules, explaining the often referenced exponential nodules growth [49]. The formation of nodules may come from different sources. Schlott *et al.* [189, 190] observed for ITO sputtering targets that one major source of nodule nucleation is dust and flaking originating from the sputtering system. Another source of nodules formation comes from the re-deposited material. Here the nodules nucleation by a re-deposition in the racetrack area and/or vicinity of the racetrack followed by sputtering of the re-deposits and also the flaking of the re-deposited material should be considered. Additional sources of nodule formation comprise the joints between different tiles in segmented targets (industrial sputtering

targets) where the dust/particles are easily collected, voids, insulating points on the surface and microcracks.

Following the same path of arcing, the reduction of the number of nodules during deposition can be attained using homogeneous fine raw materials that provide thinner and more uniform microstructures of the sintered targets [197].

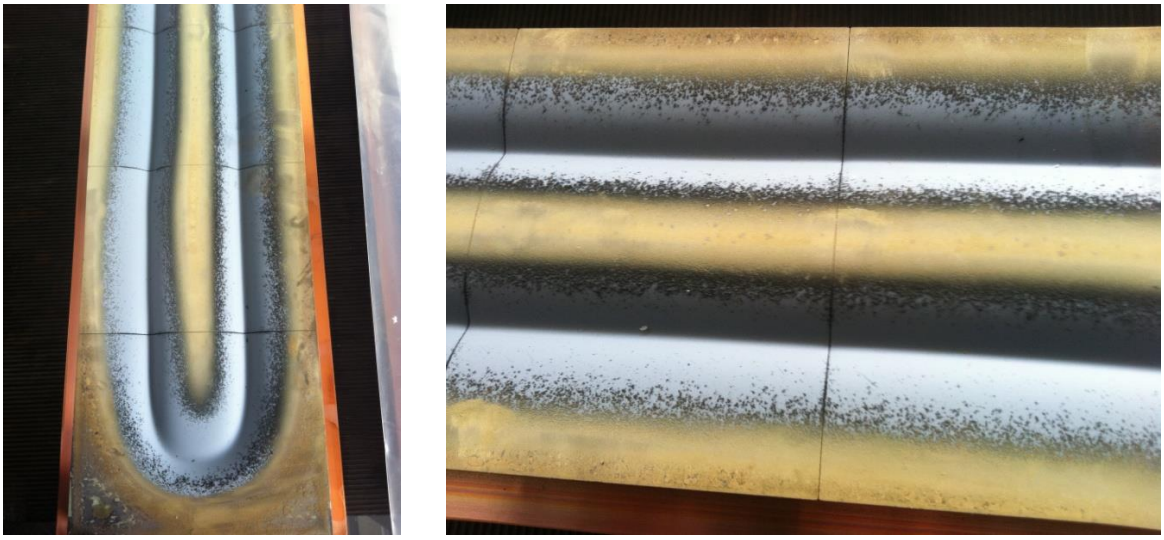

Fig. 5.83. *Commercial AZO target after several sputtering depositions showing the black nodules formation within the limits of the racetrack.*

INNOVNANO AZO targets agree well with the requirements enumerated in all the above studies. The small and homogeneous grain size, the improved $ZnAl_2O_4$ phase distribution, the absence of porosity, and good electrical conductivity (even considering the large tiles sintered by CS in air presented above) are favorable to the enhancement of the sputtering process, making the deposition more stable and consequently reducing the arcing and nodules formation during the deposition, improving target lifetime.

5.8. AZO targets available – market position of INNOVNANO

This section is devoted to the market position of the AZO targets developed during this research. With this aim, several 98:2 wt. % $ZnO:Al_2O_3$ market available AZO targets (named as target A – F) produced by some of the most influential world suppliers of lab and industrial targets were analyzed and compared with the ones produced in this work. SEM analyses of several commercially available targets are presented in Fig. 5.84. As shown in Fig 5.84 a) – d), there are suppliers that sell AZO targets with low density (< 85 % of TD) and non-homogeneous structure and dopant distribution. As can be seen in Fig. 5.84 a) and b) (target A) and Fig. 5.84 c) and d) (target B), the targets presents a lot of porosity and Al_2O_3 rich zones. Besides the reduced lifetime, the lower deposition rate, the inferior thermal and mechanical properties, and the worst plasma stability, these targets are limited to RF sputtering systems, since they cannot be used adequately in DC systems due to their low conductivity. Fig. 5.84 e) and f) of the polished surface of target C illustrate well one of the biggest issues related with the production of high density AZO targets. The high temperatures reached during sintering and the poor homogeneity of the doping element in the starting powder, promotes the appearance of large zones rich in Al, giving rise to the

formation of large $ZnAl_2O_4$ grains and extremely large pores nearby these zones during sintering hindering obtaining full dense targets. Target D (Fig. 5.84 g) and h)), target E (Fig. 5.84 i) and j)) and target F (Fig. 5.84 k) and l)) SEM micrographs shows high density targets (>98 % of TD) without significant porosity. Despite this, targets E and F also present a poor distribution of $ZnAl_2O_4$ through the ZnO main phase, with some big pores near large areas of $ZnAl_2O_4$. Again, the use of non-homogeneous raw materials and the large particle size of the initial powders are primarily responsible. These powders requires high sintering temperatures to reach high density targets even by using pressure-assisted systems, being responsible for the excessive grain growth of both ZnO and $ZnAl_2O_4$ phases and their poor homogeneity. From all the analyzed commercial targets, target D appears as the one with better density (>99.5 %) and spinel phase distribution. Only some bigger $ZnAl_2O_4$ grains with ~ 2 µm were observed sporadically.

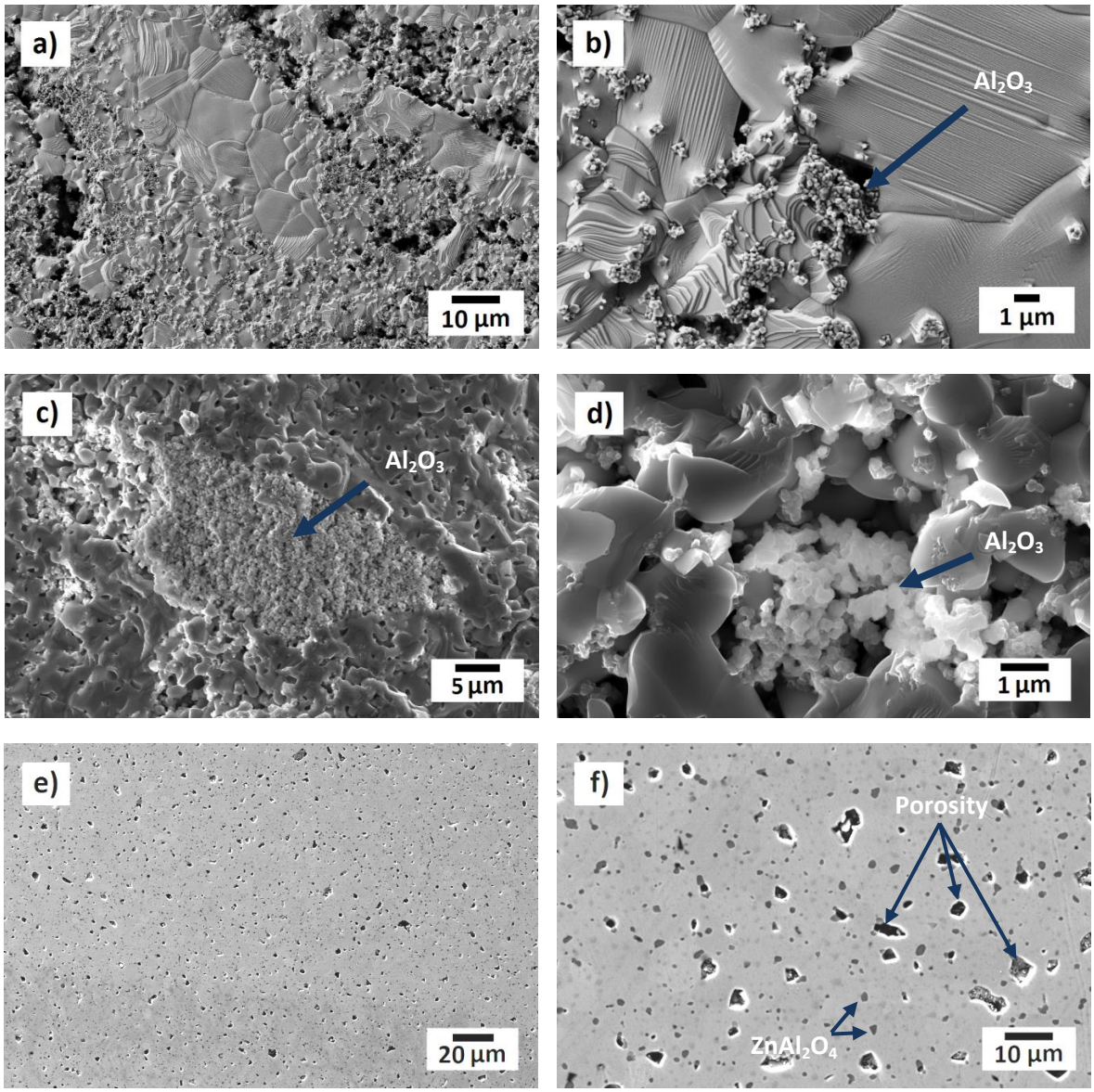

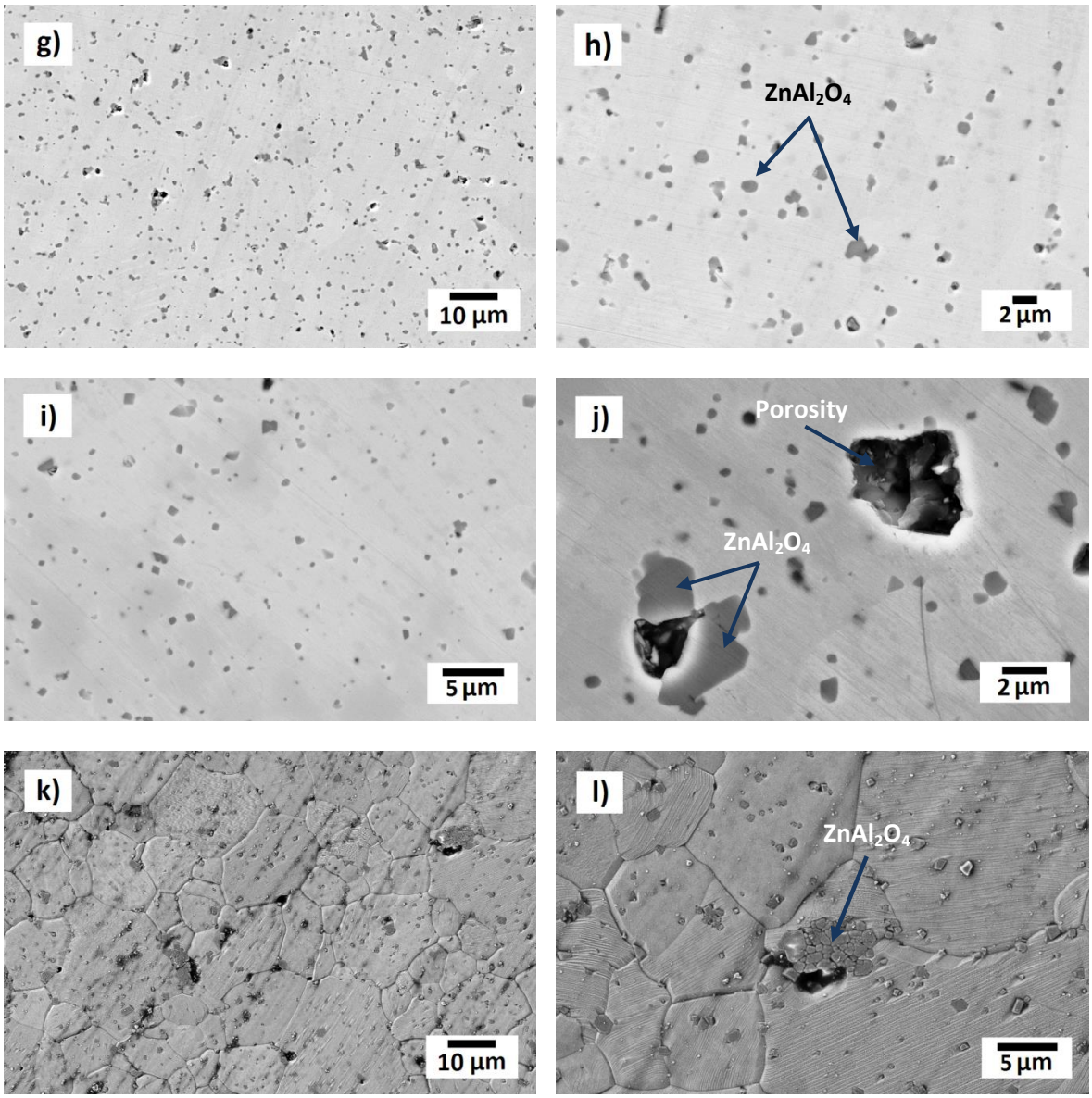

Fig. 5.84. *SEM micrographs of several commercial available lab and industrial AZO targets from different suppliers: a) – b) target A; c) – d) target B; e) – f) target C; g) – h) target D; i) – j) target E; k) – l) target F.*

With the exception of targets A and B ($\rho_e > 10^1$ Ωcm), all the analyzed commercial targets present acceptable values of electrical resistivity in the range 10^{-3} – 10^{-4} Ωcm. The lower electrical resistivities were reached respectively for target E (4.1×10^{-4} Ωcm) and target D (6.2×10^{-4} Ωcm). In terms of chemical composition, all the suppliers ensure purity levels between 3N and 4N.

In Table 5.19 is shown an overview of the main characteristics of INNOVNANO targets and their advantages over the ones available on the market. For this table it was only considered the results concerning the sintered targets. It should be noted that some of the features presented here where not quantified, being merely indicative as possible advantages taking into account the results achieved throughout this dissertation, the analysis of several commercial targets and the state-of-the-art.

Table 5.19. *Overview of the main characteristics of INNOVNANO AZO targets – Comparison with available AZO targets on the market.*

Raw materials		
Property	**INNOVNANO vs Competitors**	**Features**
Initial particle size	nanometric range vs submicro/micrometric range	Lower sintering temperatures; Production costs reduction; smaller grain size.
Specific surface area	Higher than conventional powders used	Higher reactivity / sinterability of the powders (reduction of sintering temperatures).
Dopant homogeneity	Improved distribution of Al in ZnO	Controlled and homogenous sintering process.
		Secondary phase perfectly distributed in final target microstructure.
		Absence of critical electrically resistive zones in the sintered target.
AZO targets characteristics		
Property	**INNOVNANO vs Competitors**	**Features**
Sintering temperature	Lower sintering temperatures than standard commercial PVD materials	Smaller grain sizes; Easily to reach high density targets with fine and homogeneous microstructure.
Final density	High final densities	High deposition rates; High deposition stability; Improved thermal properties; Lower arcing; Improved target lifetime.
Grain size	Smaller and homogeneous grain size	High stability during deposition; Improved mechanical properties; Lower arcing; Reduction of nodules formation; improved films homogeneity.
Secondary phase distribution	Good distribution vs preferential zones for secondary phase in final microstructure	Better uniformity of the final microstructure; Higher stability during deposition; Reduction of arcing and nodules formation; Homogeneous thin film properties (electrical, structural and optical);
Mechanical properties	Improved mechanical properties	Handling of the targets; Improved lifetime of the target; Reducing the amount of waste material.
Thermal properties	Good thermal conductivity and thermal diffusivity	High thermal stability of the target during deposition; Improved lifetime of the target;
Electrical properties	Highly conductive targets (mainly the ones sintered under controlled atmosphere)	Improved deposition rate; Improved stability during deposition in both DC and RF systems; Reduction of arcing and nodules formation; deposition of highly conductive thin films.

Taking into consideration the results presented throughout this dissertation and qualitatively presented in Table 5.19, we can conclude that INNOVNANO AZO targets are in a good position to

be part of the world market of AZO ceramic targets, mainly the ones produced under controlled atmosphere.

5.9. Conclusions

Throughout this chapter it was analyzed the influence of several processing parameters on the production of Al-doped ZnO ceramic targets as well as on AZO TCO thin films deposited using those targets. The correlation between the already described INNOVNANO AZO powders properties (chapter 4), the manufactured sputtering targets and corresponding sputtered thin films was also covered in this chapter, as well as the application of AZO as a TCO layer in different opto/electronic devices.

Three different approaches were followed regarding the manufacturing of the ceramic targets: Primarily the study was focused on the understanding and optimization of the manufacturing parameters of AZO targets prepared by conventional sintering (CS) in air; the second one considered the effect of sintering atmosphere on the final properties of the targets, where besides the conventional sintering in Ar, also two pressure-assisted sintering techniques were investigated: hot-pressing and spark-plasma-sintering. Finally, the third one was a more disruptive technique based on the manufacturing of non-sintered targets. Several targets prepared under these different conformation/sintering techniques were used in the deposition of AZO thin films by magnetron sputtering. In some cases, these sputtered layers were also applied as a TCO in different devices.

It was shown that compacts with higher green densities reach superior final densities, being this effect more noticeable at lower sintering temperatures. A systematic study has been conducted to investigate the effects of Al-doping level (0.5 – 2.0 wt. % Al_2O_3) on the densification and grain growth of AZO ceramic targets prepared by CS in air. High density targets (> 98 % of the TD) with controlled grain size and well dispersed spinel phase ($ZnAl_2O_4$) throughout ZnO microstructure can be sintered at substantially lower temperatures (1050 – 1250 °C, depending on the Al-doping level).

The final grain size increases with the sintering temperature being also highly dependent on the Al-doping level. The addition of Al inhibits the grain growth of ZnO due to the dragging effect of the $ZnAl_2O_4$ spinel phase on the movement of the grain boundaries. This dragging is more pronounced as the Al content increases. Under the same sintering conditions, the increase of the Al content gives rise to smaller grains on the final microstructure. The amount of spinel phase increases with the Al-doping concentration being stable at high temperatures.

It was observed that high density targets with controlled grain size and well dispersed $ZnAl_2O_4$ phase distribution promotes the enhancement of the targets electrical conductivity. For all the compositions, the targets with lower electrical resistivities were attained for densities > 99 % of TD and grain sizes between 2 and 4 μm depending on the Al content. The minimum value of electrical resistivity was identified for each composition being attained at different temperatures between 1100 – 1300 °C.

For targets sintered at lower temperatures the final density is the main factor affecting the electrical properties. On the other side, the volatilization of Zn, the abnormal grain growth, and

the microstructural inhomogeneity with large and poorly dispersed $ZnAl_2O_4$ grains (which acts as electron scattering centers lowering μ_e) are the main responsible for the deterioration of the electrical properties of the targets sintered at higher temperatures. The minimum electrical resistivity achieved for each composition varied between 3.86×10^{-3} Ωcm and 5.56×10^{-3} Ωcm, respectively for 2.0 and 0.5 wt. % Al_2O_3 doping levels and corresponds to the highest μ_e achieved for each composition. The proximity of these values and the non-significant variation of N_e values with Al content and sintering temperature ($4.81 - 6.77 \times 10^{19}$ cm^{-3}) shows that the maximum solubility limit was attained for all the compositions, in line with the much lower value of maximum solid solubility of Al in ZnO lattice achieved for samples with 0.5 wt. % Al_2O_3 (~0.09 at. %).

Due to the high sinterability of the powders, no scale-up effect was observed between the small targets and the manufactured two inches targets. One sputtering target of each composition was conventionally sintered in air under optimized conditions and used in thin films deposition. The effect of several deposition parameters were investigated based on 98:2 wt. % ($ZnO:Al_2O_3$) composition. Sputtered films deposited at RT with different Al-doping levels were also characterized and compared in terms of structural, optical and electrical properties.

The deposition rate of the films was found to increase with P_{RF} and decrease with P_{dep}. Under a constant P_{dep} = 0.2 Pa, the increase of P_{RF} between 100 and 250 W contributes to obtain highly conductive films being this fact directly related with the increase of μ_e, N_e and to the large crystallite size (higher crystallinity) of the films deposited at higher P_{RF} values. Sputtered AZO thin films have a hexagonal structure (wurtzite) highly oriented with the c-axis perpendicular to the substrate along the (002) plane. Optically, the bandgap (E_{opt}) energy increases from 3.44 to 3.66 eV with P_{RF} while the NIR transmittance decreases due to the increase of film thickness and N_e due to the so called Burstein-Moss effect.

Fixing the P_{RF} value in 250 W and varying the P_{dep} between 0.13 and 0.40 Pa it was observed an increase in electrical resistivity and a decrease in both N_e and μ_e with P_{dep}. The crystallite size also decreases with P_{dep} resulting in lower μ_e, while in terms of optical properties, the NIR transmittance and E_{opt} tends to decrease with the increase of P_{dep}.

The effect of Al-doping level on the electrical properties of the sputtered films was performed fixing the P_{RF} and P_{dep} values in 250 W and 0.2 Pa, respectively. It was observed an increment of N_e and a reduction of $\mu_e$with Al-doping level. The electrical resistivity tends to be lower for higher doping levels which is related to the high solubility limit of Al in ZnO thin films. For higher doping levels (1.5 and 2.0 wt. % Al_2O_3), the electrical resistivity is mainly due to high N_e values while for lower doping concentrations (0.5 and 1.0 wt. % Al_2O_3), the high μ_e values causes the lowering of electrical resistivity values of the sputtered films.

Similarly to the observed for the sputtering targets, the crystallite size of the films decreases with Al-doping level from 52 to 29 nm, being the segregation of Al (single or combined) in the grain boundaries and/or the formation of stress induced by the substitution of Zn ions by Al smaller ions appointed as the main responsible for this reduction. All the films are highly transparent (> 80 %) in the visible and also in the NIR regions. The E_{opt} increases almost linearly with the Al-doping level from 3.45 to 3.65 eV.

The effect of sintering atmosphere on the final properties of AZO targets prepared by CS was evaluated using an Ar atmosphere during sintering. No substantial differences were observed in terms of final density and grain size of samples sintered in air and Ar atmosphere for all the studied compositions. The main differences were observed in terms of electrical properties with the attainment of less resistive targets when sintered in Ar (between 1.11×10^{-3} Ωcm and 1.58×10^{-3} Ωcm) due to the increase in both μ_e and N_e. Comparing the electrical properties of the targets prepared by CS in air and in Ar, it is observed a substantially lower dependence in the last ones with sintering temperature, holding time (HT) and Al content.

The sputtering of a high density target with 2.0 wt. % Al_2O_3 prepared by CS in Ar (P_{RF} and P_{dep} values fixed in 250 W and 0.2 Pa, respectively) led to less resistive films (8.86×10^{-4} Ωcm) than that produced with the same composition sputtered from a target manufactured in air using similar temperature and HT (1.02×10^{-3} Ωcm). Despite its higher N_e value (5.64×10^{20} cm^{-3} compared to 4.78×10^{20} cm^{-3}), μ_e reduces slightly from 12.8 to 11.7 $cm^2V^{-1}s^{-1}$, indicating that the decrease in electrical resistivity was mainly influenced by the increase of N_e in the sputtered films. In this case, the electrical properties were improved due to both, extrinsic defects induced by the Al substitution into the lattice sites of Zn (Al_{Zn}), and intrinsic defects derived from the formation of non-stoichimetric ZnO_{1-x} with oxygen deficiency, being this applied to both sputtering targets and sputtered films.

In order to improve the targets and films properties, two different techniques were used: hot-pressing (HP) and spark-plasma sintering (SPS). Using these techniques it was possible to reduce considerably the sintering temperature and the final grain size of the targets. Furthermore, due to the reduced sintering atmosphere, full dense targets were reached with electrical resistivities of $\sim 3 - 5 \times 10^{-4}$ Ωcm and grain sizes between 0.9 – 1.2 µm (results from AZO targets with 2.0 wt. % Al_2O_3 sintered by HP and SPS). Using these targets, thin films with electrical resistivities between $6 - 7 \times 10^{-4}$ Ωcm were obtained using targets prepared by HP and SPS. A direct correlation was observed among the deposition rate and the target electrical conductivity. Under the same sputtering conditions, the deposition rate of the sputtered films increased with target electrical conductivity from 6.0 and 7.2 $nm.min^{-1}$ using targets prepared by CS in air and Ar, respectively, to 8.1 and 9 $nm.min^{-1}$ using targets manufactured by SPS and HP in that order.

The effect of substrate temperature during sputtering was evaluated using a 3” hot-pressed target with 0.5 wt. % Al_2O_3. SEM, TEM and XRD analysis of the films all show that crystallinity increases with increasing temperature up to 300 °C. Above this, crystal size and quality are reduced significantly. Crystallite size and quality is reflected in N_e, μ_e and sheet resistance data, with sheet resistances decreasing slightly with increasing temperatures and crystal size. Above 300 °C, sheet resistance increases dramatically. Consistent high quality RT films with good transmission values and low sheet resistances demonstrate that this material is ideally suited for use in temperature-sensitive applications. Compared with published ITO data, AZO films were found to display equivalent sheet resistances for a given average transmission value, demonstrating that AZO synthesized using the conditions described is an ideal alternative to ITO.

Low-cost non-sintered AZO target (98:2 wt. %) with a final density of ~ 62 % of TD have been used to prepare TCO films by rf-magnetron sputtering at RT. Polycrystalline films with a hexagonal structure having a preferential crystallographic c-axis orientation were obtained. The lowest

resistivity obtained was 6.5×10^{-4} Ωcm for a film thickness of 890 nm (sheet resistance 7.3 Ωsq^{-1}), with μ_e of 16.8 $cm^2V^{-1}s^{-1}$ and N_e of 5.7×10^{-20} cm^{-3}. The films have an average transmittance of 85% within the visible spectra. These films have been successfully applied as a back contact layer on standard glass/SnO2:F/pin–pin/TCO/metal amorphous silicon solar cell and as source/drain contacts to GaInZnO (GIZO) thin film transistors (TFTs).

The solar cells with AZO NST as back contact have enhanced electrical performances under AM 1.5 conditions, namely current density (J_{SC} = 11mAcm^{-2}), short-circuit voltage (V_{OC} = 1.6 V), fill factor (FF = 63 %) and initial efficiency of 11 % (far above the efficiency of 6.3 % obtained with an AZO layer sputtered form a target prepared by CS in air). Compared to the standard solar cell this improvement leads to a 10 % increase in J_{SC} and 20 % in efficiency of the solar cell and also in the EQE. When applied as source/drain contacts in TFTs, it was observed a slightly decrease related to the saturation mobility (from 39 $cm^2V^{-1}s^{-1}$ to 32 $cm^2V^{-1}s^{-1}$) as well as the saturation current, mainly due to an increase in the electrical resistance associated to the source/drain electrodes (R_C), reducing the current and the saturation mobility.

It has been demonstrated that similar TE results are obtained in AZO thin films sputtered from sintered and non-sintered targets both using RF and pulsed DC sputtering. The importance of crystallite/grain sizes has been demonstrated, being dependent on the deposition conditions and mainly on the Al doping level. Both Al doping concentration and film thickness control the thermoelectric, optical and structural properties of these films. Seebeck coefficients up to -134 μVK^{-1} and electrical conductivities up to 4×10^4 $(\Omega m)^{-1}$ leaded to power factors up to 3.9 x 10^{-4} $Wm^{-1}K^{-2}$. Moreover, the low thermal conductivity (<1.19 $Wm^{-1}K^{-1}$) yields a ZT value above 0.1, which is above the state of art for similar materials, almost by a factor of three. Despite its poor mechanical strength and reduced electrical and thermal conductivity, low-cost non-sintered targets were applied in DC systems successfully, being appointed as an appellative alternative to reduce the production costs of thermoelectric thin film modules.

The analysis of multiple targets prepared under different conditions throughout this research work, as well as the films sputtered with these targets, allowed the assessment on the strong correlation between targets and films characteristics. In this context, the oxygen content in the targets and that in the deposited films are related and indicated as key factor in the enhancement of the electrical properties in both targets and thin films, being concluded that the deposition of highly conductive TCO thin films of AZO requires the preparation of AZO targets with oxygen deficiency.

The assessment of the targets quality has also been validated in terms of thermal and mechanical properties. Between RT and 300 °C, thermal conductivity (k) and thermal diffusivity (D) decreases with the increase of Al-doping concentration and the reduction of final density. Thermal conductivities between 30 and 45 $W.m^{-1}.K^{-1}$ at RT were reached depending on the target properties reducing ~ 50 % at 300 °C. The obtained k values are substantially higher than the ones of ITO ceramic targets (7 – 13 $W.m^{-1}.K^{-1}$ depending on target composition) in the same range of temperatures. No significant effect of Al-doping concentration was observed in terms of flexural strength of the targets. However, the fracture toughness tends to be lower and the hardness has the propensity to increase with the Al-doping level. Considering the same composition, hot-pressed samples presents higher flexural strength values than the samples

prepared by CS in air, while the fracture toughness and hardness seems to be independent on the sintering technique used. Flexural strengths between 200 – 300 MPa were reached depending on the target. It was found that the best compromise between thermal and mechanical properties is obtained for targets prepared by HP.

Large-size AZO targets with a composition 98:2 wt. % $ZnO:Al_2O_3$ were successfully manufactured by uniaxial-pressing followed by CS in air. The powder characteristics, pressing conditions and sintering were optimized. The feasibility of these large scale targets was done in a partnership with a Portuguese company, *Solar Plus*, dedicated to the production of a:Si:H TFSC photovoltaic panels. The AZO material was successfully used as a reflective layer in standard non-transparent TFSCs panels and as a reflective and conductive layer in semi-transparent TFSCs panels.

This chapter finishes with the evaluation of the market position of the developed targets. Taking into consideration the results presented throughout this dissertation and the analysis performed on several lab and industrial AZO targets available in the market, it was demonstrated that several commonly referenced issues related with the production of AZO targets have been overcome, opening a new market opportunity for INNOVNANO.

5.10. References

[1] Mayo, M. J., Processing of nanocrystalline ceramics from ultrafine particles. *Int. Mater. Rev.*, 1996, **41**(3) 85-115.

[2] Krell, A. and Klimke, J., Effects of the homogeneity of particle coordination on solid-state sintering of transparent alumina. *J. Am. Ceram. Soc.*, 2006, **89**(6) 1985-92.

[3] Woolfrey, J. L., Effect of green density on the initial-stage sintering kinetics of UO_2. *J. Am. Ceram. Soc.*, 1972, **55**(8) 383-9.

[4] Richerson, D. W., Modern ceramic engineering – properties, processing and use in design. Third Edition, ISBN: 978-1574446937, Chapter 13, p. 403-472, Published 2006 by CRC Press – Taylor & Francis group.

[5] Riedel, R. and Chen, I.-W., Ceramics science and technology: Volume 3: Synthesis and processing. First edition, ISBN: 978-3527631964, p. 1-37, Published 2012 by Wiley-VCH.

[6] Zhang, J., Zhang, W., Zhao, E. and Jacques, H. J., Study of high density AZO ceramic target. *Mater. Sci. Semicond. Process.*, 2011, **14**(3-4) 186-92.

[7] Han, J., Mantas, P. Q. and Senos, A. M. R., Densification and grain growth of Al-doped ZnO. *J. Mater. Res.*, 2001, **16**(2) 459-68.

[8] Marx, D. and Murphy, R., Sputtering targets: Challenges for the 1990s. *Solid State technol.*, 1990, **33**(3) S11.

[9] Friz, M. and Waibel, F., Coating Materials. in *Optical Interference Coatings,* p. 105-130, Published 2003 by Springer. 105-130

[10] Zhang, Y., Wang, W., Tan, R., Yang, Y., Zhang, X., Cui, P. and Song, W. The solubility and temperature dependence of resistivity for aluminum-doped zinc oxide ceramic. *Int. J. Appl. Ceram. Technol.*, 2011, **9**(2) 374-81.

[11] Nauman, K., The effects of process power on arc rate and nodule formation during sputtering of aluminum doped zinc oxide. Society of vacuum coaters, 2011, 505/856-7188 – 54th annual technical conference proceedings, Chicago, ISSN 0737-5921.

[12] Lange, F., Powder Processing Science and Technology for Increased Reliability. *J. Am. Ceram.Soc.*, 1989, **72**(1) 3-15.

[13] Hong, W. and De Jonghe, L. C., Reaction sintering of ZnO-Al_2O_3. *J. Am. Ceram. Soc.*, 1995, **78**(12) 3217-24.

[14] Hansson, R., Hayes, P. C. and Jak, E. Experimental study of phase equilibria in the Al-Fe-Zn-O system in air. Metall. Mater. Trans. B, 2004, **35**(4) 633-42.

[15] Zhang, Y., Wang, W., Tan, R., Yang, Y., Zhang, X., Cui, P. and Song, W. The solubility and temperature dependence of resistivity for aluminum-doped zinc oxide ceramic. *Int. J. Appl. Ceram. Technol.*, 2011, **9**(2) 374-81.

[16] Qin, X. J., Shao, G. J., Liu, R. P., Wang, W. K., Sintering Characteristics of Nanocrystalline ZnO. *J. Mater.Sci., 2005,* **40**(18) 4943-6.

[17] Shirouzu, K., Ohkusa, T., Hotta, M., Enomoto, N. and Hojo, J., Distribution and solubility limit of Al in Al_2O_3-doped ZnO sintered body. *J. Ceram. Soc. Jpn.*, 2007, **115**(4) 254-8.

[18] Herring, C., Effect of change of scale on sintering phenomena. *J. Appl. Phys.*, 1950, **21** 301-3.

[19] Tanami, J., Nakano, H., Wakihara, T., and Komeya, K., Development of advanced ceramics by powder composite process, *Kona Powder and Part. J.*, 2010, **28** 227-40.

[20] Medvedovski, E., Alvarez, N., Yankov, O. and Olsson, M.K., Advanced indium-tin oxide ceramics for sputtering targets. *Ceram Int.*, 2008, **34**(5) 1173-82.

[21] Liu, C., Wang, X., Jiang, Y., Wang, Y. and Hao, S., Progress on grain growth dynamics in sintering of nano-powders. *Rare Met.,* 2006, **25**(6) 471-5.

[22] Mazaheri, M., Zahedi, A. M., Haghighatzadeh, M. and Sadrnezhaad, S. K., Sintering of titania nanoceramic: Densification and grain growth. *Ceram. Int.*, 2009, **35**(2) 685–91.

[23] Han, J., Sntering and electrical properties of Mn-doped and Al-doped ZnO ceramics. Ph. D. thesis, University of Aveiro, Aveiro, Portugal, 2001.

[24] Chou, Y.-H., Chau, J., Wang, W., Chen, C., Wang, S. and Yang, C., Preparation and characterization of solid-state sintered aluminum-doped zinc oxide with different alumina contents, *Bull. Mater. Sci.*, 2011, **34**(3) 477-82.

[25] Senos, A. M. R., Sintering kinetics in open porosity stages of zinc oxide. Ph.D. thesis, University of Aveiro, Aveiro, Portugal, 1993 (in potuguese).

[26] Rahaman, M. N., Ceramic processing and sintering. pp. 441-79, Published 1995 by Marcel Dekker, Inc.

[27] Brook, R. J., Controlled grain growth. In *treatise on materials science and technology*. Vol. 9, ed. F. F. Y. Wang, pp. 331-64, Published 1976 by Academic Press.

[28] Zener, C., as communicated by C. S. Smith, Grains, phases, and interfaces: an interpretation of microstructure. *Trans. Am. Inst. Metall, Soc.*, 1948, **175**, 15-51.

[29] Sbrockey, N. M. and Johnson, D. L., Influence of second phase particles to retard surface smoothing and sintering. *Mater. Sci. Res.*, 1980, **13** 177-86.

[30] Fukushima, H., Zinc oxide ceramics and a manufacturing method for the same, a sputtering target. Patent application publication US 2009/0197757 A1 (2009).

[31] Margadant *et al.*, Aluminum doped zinc oxide sputtering targets. Patent application publication US 2011/0284364 A1 (2011).

[32] Rietveld, H. M., A profile refinement method for nuclear and magnetic structures. *J. Appl. Cryst.*, 1969, **2** 65-71.

[33] Shirouzu, K., Kawamoto, T., Enomoto, N. and Hojo, J., Dissolution behavior of Al and formation process of $ZnAl_2O_4$ phases in Al_2O_3-doped ZnO sintered bodies. *Jpn. J. Appl. Phys.*, 2010, **49**(1) 010201-010201-3.

[34] Underwood, E. E., Quantitative Stereology. Addison-Wesley publishing company, Reading, Massachussets, USA, 1971, p. 119.

[35] Wiff, J. P., Kinemuchi, Y., Kaga, H., Ito, C. and Watari, K. Correlations between thermoelectric properties and effective mass caused by lattice distortion in Al-doped ZnO ceramics. *J. Eur. Ceram. Soc.*, 2009, **29**(8) 1413-8.

[36] Sedky, A., Al- Sawalha, A. and Yassin, A. M. Enhancement of electrical conductivity by Al-doped ceramic varistors. *Physica B*, 2009, **404**(20) 3519-24.

[37] Minami, T., Oda, J.-ichi, Nomoto, J.-ichi and Miyata, T., Effect of target properties on transparent conducting impurity-doped ZnO thin films deposited by DC magnetron sputtering. *Thin Solid Films,* 2010, **519**(1) 385-90.

[38] Oda, J.-ichi, Nomoto, J.-ichi, Miyata, T. and Minami, T., Improvements of spatial resistivity distribution in transparent conducting Al-doped ZnO thin films deposited b DC magnetron sputtering. *Thin Solid Films,* 2010, **518**(11) 2984-7.

[39] Minami, T., Transparent conducting oxide semiconductors for transparent electrodes. *Semicond. Sci. Technol.*, 2005, **20**(4) S35-S44

[40] Huang, H. S., Tung, H. C., Chiu, C. H., Hong, I. T., Chen, R. Z., Chang, J. T., *et al.*, Highly conductive alumina-added ZnO ceramic target prepared by reduction sintering and its effects on the properties of deposited thin films by direct current magnetron sputtering. *Thin Solid Films*, 2010, **518**(21) 6071-5.

[41] Wu, M.-W., Liu, D.-S. and Su, Y.-H., The densification, microstructure, and electrical properties of aluminum-doped zinc oxide sputtering target for transparent conductive oxide film. *J. Eur. Ceram.Soc.*, 2012, **32**(12) 3265-75.

[42] Liu, C. P. and Jeng, G. R., Properties of aluminum doped zinc oxide materials and sputtering thin films. *J Alloys Compd*, 2009, **468**(1–2) 343–9.

[43] Han, J., Mantas, P. Q. and Senos, A. M. R., Effect of Al and Mn doping on the electrical conductivity of ZnO. *J. Eur. Ceram. Soc.*, 2001, **21**(10-11) 1883-6.

[44] Jang, M., Ryu, M., Yoon, M., Lee, S., Kim, H., Onodera, A. and Kojima, S., A study on the Raman spectra of Al-doped and Ga-doped ZnO ceramics. *Curr. Appl. Phys.,* 2010, **9**(3) 651-7.

[45] X-ming, W., Xue, B., H-ying, D., Z-xia, S., Jing, S., S-gang, L. and S-tao, H., Preparation of Al-doped ZnO sputter target by hot pressing. *Trans. Nonferrous Met. Soc. China,* 2011, **21**(7) 1550-6.

[46] Carter, D. C., Arc prevention in magnetron sputtering process. Society of vacuum coaters, 2008, 505/856-7188 – 51st annual technical conference proceedings, Chicago, ISSN 0737-5921.

[47] Sittinger, V., Dewald, W., Werner, W. and Szyszka, B., Comparision of different ceramic Al-doped ZnO target materials. *Photovoltaics International*, 2009, **6** 101-8.

[48] Lippens, P., Ceramic TCO rotary targets for large area coating. Materials – The Umicore thin film production customer magazine, 2009, p6-7.

[49] Falk, G., Sintering of transparent conductive oxides: From oxide ceramic powders to advanced optoelectronic materials; pp 587-609 in *Sintering of ceramics – New emerging techniques*, Chapter 26, Germany, 587-610, 2012.

[50] Ellmer, K., Magnetron sputtering of transparent conductive zinc oxide: relation between the sputtering parameters and the electronic properties. *J. Phys. D: Appl. Phys.*, **33**(4) R17-R32 (2000).

[51] Fortunato, E., Pimentel, A., Gonçalves, A., Marques, A. and Martins, R., High mobility amorphous/nanocrystalline indium zinc oxide deposited at room temperature. *Thin Solid Films*, 2006, **502**(1-2) 104-7.

[52] Moutinho, A., Silva, M. and Cunha, M., Tecnologia de vácuo: Universidade Nova de Lisboa – Faculdade de Ciências e Tecnologia, 1980.

[53] Minami, T., Miyata, T., Yamamoto, T. and Toda, H., Origin of electrical property distribution on the surface of ZnO:Al films prepared by magnetron sputtering. *J. Vac. Sci. Technol. A*, 2000, **18**(4) 1584.

[54] Drift, A. Van der, Evolutionary selection, a principle governing growth orientation in vapor-deposited layers. *Philips Res. Rep.*, 1967, **22** 267-88.

[55] Xu, Z. Q., Deng, H:, Li, Y., Guo, Q. H: and Li, Y. R. Characteristics of Al-doped c-axis orientation ZnO thin films prepared by the sol-gel method. *Mater. Res. Bull.*, 2006, **41**(2) 354-8.

[56] Deng, H., Russell, J. J., Lamb, R. N., Jiang, B., Li, Y. and Zhou, X. Y., Microstructure control of ZnO thin films prepared by single source chemical vapor deposition. *Thin Solid films*, 2004, **458**(1-2) 43-6.

[57] Kim, K. H., Park, K. C. and Ma, D. Y., Structural, electrical and optical properties of aluminum doped zinc oxide films prepared by radio frequency magnetron sputtering. *J. Appl. Phys.*, 1997, **81**(12) 7764-72.

[58] Gardeniers, J. G. E., Rittersma, Z. M. and Burger, G. J., Preferred orientation and piezoelectricity in sputtered ZnO films. *J. Appl. Phys.*, 1998, **83** 7844.

[59] Kim, K. H., Wibowo, R. A. and Munir, B., Properties of Al-doped ZnO thin film sputtered from powder compacted target. *Mater. Lett.*, 2006, **60**(15) 1931-5.

[60] Jayaraj, M. K., Antony, A. and Ramachandran, M., Transparent conducting zinc oxide thin film prepared by off-axis rf magnetron sputtering. *Bull. Mater. Sci.*, 2002, **25**(3) 227-30.

[61] Fujimura, N., Nishihara, T., Goto, S., Xu, J. and Ito, T., Control of preferred orientation for ZnO**x** films: control of self-texture. *J. Cryst. Growth.*, 1993, **130**(1-2) 269-79.

[62] Patterson, A. L., The Scherrer formula for X-ray particle size determination. *Phys. Rev.*, 1939, **56**(10) 978-82.

[63] Chang, H. P., Wang, F. H., Wu, J. Y., Kung, C. Y. and Liu, H. W., Enhanced conductivity of aluminum doped ZnO films by hydrogen plasma treatment. *Thin Solid Films*, 2010, **518**(24) 7445-9.

[64] Fortunato, E., Gonçalves, A., Pimentel, A., Barquinha, P., Gonçalves, G., Pereira, P., *et al.*, Zinc oxide, a multifunctional material: from material to device applications. *Appl. Phys A*, 2009, **96**(1) 197-205.

[65] Filipchenko, A. S., Nasledov, D.N., Radaikin, L.N. and Ratner, I. I., The Moss-Burstein effect in n type crystals doped with Selenium and Tellurium. *Phys. Status solidi a*, 1972, **14**(1) 71-5.

[66] Lin, S. S. and Huang, J.L. Effect of thickness on the structural and optical properties of ZnO films by rf magnetron sputtering. *Surf. Coat. Technol.*, 2004, **185**(2-3) 222–7.

[67] Banerjee, A. N., Ghosh, C. K., Chattopadhyay, K. K., Minoura, H., Sarkar, A.K., Akiba, A., *et al.,* Low-temperature deposition of ZnO thin films on PET and glass substrates by DC-sputtering technique. *Thin Solid Films*, 2006, **496**(1) 112–6.

[68] He, H. P., Zhuge, F., Ye, Z. Z., Zhu, L. P., Wang, F.Z., Zhao, B.H. and Huang, J. Y., Strain and its effect on optical properties of Al–N codoped ZnO films. *J Appl Phys,* 2006, **99**(2) 023503.

[69] Suchea, M., Christoulakis, S., Katsarakis, N., Kitsopoulos, T. and Kiriakidis, G., Comparative study of zinc oxide and aluminum doped zinc oxide transparent thin films grown by direct current magnetron sputtering. *Thin Solid Films*, 2007, **515**(16) 6562-6.

[70] Bouderbala, M., Hamzaoui, S., Adnane, M., Sahraoui, T. and Zerdali, M., Annealing effect on properties of transparent and conducting ZnO thin films. *Thin Solid Films*, 2009, **517**(5) 1572–6.

[71] Guillén, C. and Herrero, J., Optical, electrical and structural characteristics of Al:ZnO thin films with various thicknesses deposited by DC sputtering at room temperature and annealed in air or vacuum. *Vacuum*, 2010, **84**(7) 924-9.

[72] Ellmer, K., Resistivity of polycrystalline zinc oxide films: current status and physical limit. *J. Phys. D: Appl. Phys.*, 2001, **34**(21) 3097.

[73] Moss, T. S., The interpretation of the properties of indium antimonide, Proc. Phys. Soc., 1954, **B67** 775.

[74] Burstein, E., Anomalous optical absorption limit in InSb, 1954, *Phys. Rev.*, **93** 632.

[75] Assunção, V., Fortunato, E., Marques, A., Gonçalves, A., Ferreira, I., Águas, H. and Martins, R., New challenges on gallium-doped zinc oxide films prepared by r.f. magnetron sputtering. *Thin Solid Films*, 2003, **442**(1-2) 102-6.

[76] Kim, Y. H., Lee, K. S., Lee, T. S., Cheong, B.-k., Seong, T.-Y. and Kim, W. M., Electrical, structural and etching characteristics of ZnO:Al films prepared by rf magnetron. *Curr. Appl. Phys.*, 2010, **20**(10) S278-81.

[77] Ayadi, Z.B., Mir, L. El, Djessas, K. and Alaya, S. The properties of aluminum-doped zinc oxide thin films prepared by rf-magnetron sputtering from nanopowder targets. *Mater. Sci. Eng., C*, 2008, **28**(5-6) 613-7.

[78] Deng, Z., Huang, C., Huang, J., Wang, M., He, H., Wang, H. and Cao, Y. Effects of Al content on the properties of ZnO:Al films prepared by Al_2O_3 and ZnO co-sputtering. *J. Mater. Sci.- Mater. Electron.*, 2010, **21**(10) 1030-5.

[79] Agashe, C., Kluth, O., Hüpkes, J., Zastrow, U. and Rech, B., Efforts to improve carrier mobility in radio frequency sputtered aluminum doped zinc oxide films. *J. Appl. Phys.*, 2004, **95**(4) 1911-7.

[80] Lee, J. H., Lee, J.-W., Hwang, S., Kim, S. Y., Cho, H. K., Lee, J. Y. and Park, J.- S. Effects of Al concentration on microstructural characteristics and electrical properties of Al-doped ZnO thin films on Si substrates by atomic layer deposition. *J. Nanosci. Nanotechnol.*, 2012, **12**(7) 5598-603.

[81] Musat, V., Teixeira, B., Fortunato, E., Monteiro, R. C. C. and Vilarinho, P., Al-doped ZnO thin films by sol-gel method. *Surf. Coat. Tchnol.*, 2004, **180-181** 659-62.

[82] Singh, A. V., Mehra, R. M., Yoshida, A. and Wakahara, A. Doping mechanism in aluminum doped zinc oxide films. *J. Appl. Phys.*, 2004, **95**(7) 3640-3.

[83] Nunes, P., Fortunato, E., Tonello, P., Fernandes, F. B., Vilarinho, P. and Martins. R. Effect of different dopant elements on the properties of ZnO thin films. *Vacuum*, 2002, **64**(3-4) 281-5.

[84] Zhou, H-M., Yi, D.-q., Yu, Z.-m., Xiao, L.-r. and Li. J., Preparation of aluminum doped zinc oxide films and the study of their microstructure, electrical and optical properties. *Thin Solid Films*, 2007, **515**(17) 6909-14.

[85] Chakravarty, R. and Periasamy, C. Effect of aluminium doping on structural and optoelectronic properties of sol-gel derived nanocrystalline ZnO thin film. *Sci. Adv. Mater.*, 2011, **3**(2) 276-83.

[86] Nunes, P, Malik, A, Fernandes, B, Fortunato, E, Vilarinho, P, Martins, R., Influence of the doping and annealing atmosphere on zinc oxide thin films deposited by spray pyrolysis. *Vacuum*, 1999, **52**(1-2) 45-9.

[87] Fujihara, S., Suziki, A. and Kimura, T., Ga-doping effects on electrical and luminescent properties of ZnO:(La,Eu)OF red phosphor thin films. *J. Appl. Phys.*, 2003, **94**(4) 2411.

[88] Minami, T., Nanto, H. and Takata, S. Properties of Aluminum Doped Zinc Oxide Thin Films Prepared by RF Magnetron Sputtering. *Jpn. J. Appl. Phys.*, 1985, **24**(2) L605-7.

[89] Muiva, C., Sathiaraj, T. and Maabong, K., Effect of doping concentration on the properties of aluminum doped zinc oxide thin films prepared by spray pyrolysis for transparent electrode applications, *Ceram. Int.*, 2011, **37**(2) 555-60.

[90] Calnan, S. and Tiwari, A., High mobility transparent conducting oxides for thin film solar cells. *Thin Solid Films*, 2010, **518**(7) 1839-49.

[91] Rath, J., Liu, Y., Jong, M., Wild, J., Schuttauf, J., Brinza, M. and Schropp, R., Transparent conducting oxide layers for thin film silicon solar cells. *Thin Solid Films*, 2010, **518**(24) e129-e135.

[92] Smith, R. A. Semiconductors (Cambridge University Press, Cambridge) 1987, p.294.

[93] Bazzani, M., Neroni, A., Calzolari, A. and Catellani, A., Optoelectronic properties of Al:ZnO: Critical dosage for an optimal transparent conductive oxide. *Appl. Phys. Lett.*, 2011, **98**(12) 121907.

[94] El Mir, L., Ayadi, Z. B., Saadoun, M., Djessas, K., von Bardeleben, H. J. and Alaya, S., Preparation and characterization of n-type conductive (Al, Co) co-doped ZnO thin films deposited by sputtering from Aerogel nanopowders. *Appl. Surf. Sci.*, 2007, **254**(2) 570-3.

[95] Sato, H., Minami, T., Takata, S., Miyata, T. and Ishii, M., Low temperature preparation of transparente conducting ZnO:Al thin films by chemical beam deposition. *Thin Solid Films*, 1993, **236**(1-2) 14-9.

[96] Erhart, P., Albe, K. and Klein, A., First-principles study of intrinsic point defects in ZnO: Role of band structure, volume relaxation, and finite-size effects. *Phys. Rev. B*, 2006, **73** 205203.

[97] Look, D.C., Hemsky, J. W. and Sizelove, J. R., Residual Native Shallow Donor in ZnO. *Phys. Rev Lett.*, 1999, **82** 2552.

[98] Tomlins, G. W., Routbort, J. L. and Mason, T. O., Zinc self-diffusion, electrical properties, and defect structure of undoped, single crystal zinc oxide. *J. Appl. Phys.*, 2000, **87** 117.

[99] Lany, S. and Zunger, A., Dopability, intrinsic conductivity, and nonstoichiometry of transparent conducting oxides. *Phys. Rev. Lett.*, 2007, **98** 45501.

[100] Chopra, K. L., Major, S. and Pandaya, D. K., Transparent conductors – A status review. *Thin Solid Films*, 1983, **102**(1) 1-46.

[101] Wendt, R. and Ellmer, K., Desorption of Zn from a growing ZnO:Al-film deposited by magnetron sputtering. *Surf. Coatings Technol.*, 1997, **93**(1) 27-31.

[102] Tsurumi, T., Nishizawa, S., Ohashi, N. and Ohgaki, T., Electric Properties of Zinc Oxide Epitaxial Films Grown by Ion-Beam Sputtering with Oxygen-Radical Irradiation. *Japan. J. Appl. Phys.*, 1999, **38**(1) 3682-8.

[103] Lo, C.-F. and Turn, J., Apparatus and method for making metal oxide sputtering targets. Pattent application publication US 6582641 B1 (2003).

[104] Kang, S.-J. L., Sintering – Densification, grain growth & microstructure. First edition, ISBN: 07506 63855 Published 2005 by Elsevier.

[105] Mazaheri, M., Hassanzadeh-Tabrizi, S. A. and Sadrnezhaad, S. K., Hot pressing of nanocrystalline zinc oxide compacts: Densification and grain growth during sintering. *Ceram. Int.*, 2009, **35**(3) 991-5.

[106] Ginley, D., S., Handbook of transparent conductors, First Edition, ISBN: 978-1441916372, Published 2010 by Springer.

[107] Yang, W., Liu, Z., Peng, D.-L., Zhang, F., Huang, H., Xie, Y. and Wu, Z., Room temperature deposition of transparent conducting Al-doped ZnO films by RF magnetron sputtering method. *Appl. Surf. Sci.*, 2009, **255**(11) 5669–73.

[108] Leem, J. W. and Yu, J. S., Structural, optical, and electrical properties of AZO films by tilted angle sputtering method. *Thin Solid Films*, 2010, **518**(22) 6285-8.

[109] Minami, T., Sato, H., Sonoda, T., Nanto, H. and Takata, S., Influence of substrate and target temperatures on properties of transparent and conductive doped ZnO thin films prepared by r.f. magnetron sputtering. *Thin Solid Films*, 1989, **171**(2) 307-11.

[110] Yamada, T., Miyake, A., Kishimoto, S., Makino, H., Yamamoto, N. and Yamamoto, T., Effects of substrate temperature on crystallinity and electrical properties of Ga-doped ZnO films prepared on glass substrate by ion-plating method using DC arc discharge. *Surf. Coat. Technol.*, 2007, **202**(4-7) 973-6.

[111] Szyszka, B., Transparent and conductive aluminum doped zinc oxide films prepared by mid-frequency reactive magnetron sputtering. *Thin Solid Films*, 1999, **351**(1-2) 164-9.

[112] Park, J. H., Shin, J. M., Cha, S.-Y., Park, J. W., Jeong, S.-Y., Pak, H. K. and Cho, C.-R., Deposition-temperature effects on AZO thin films prepared by RF magnetron sputtering and their physical properties. *J. Korean Phys. Soc.*, 2006, **49**(2) 584-8.

[113] Chang, J. F. and Hon, M. H., The effect of deposition temperature on the properties of Al-doped zinc oxide thin films. *Thin Solid Films*, 2001, **386**(1) 79-86.

[114] Lin, S. S., Huang, J. L. and Sajgalik, P., The properties of heavily Al-doped ZnO films before and after annealing in the different atmosphere. *Surf. Coat. Technol.*, 2004, **185**(2-3) 254-63.

[115] Hamad, O., Braunstein, G., Patil, H. and Dhere, N., Effect of thermal treatment in oxygen, nitrogen, and air atmospheres on the electrical transport properties of zinc oxide thin films. *Thin Solid Films*, 2005, **489**(1-2) 303-9.

[116] Dagamseh, A. M. K., Vet, B., Tichelaar, F. D., Sutta, P. and Zeman, M., ZnO: Al films prepared by rf magnetron sputtering applied as back reflectors in thin-film silicon solar cells. *Thin Solid Films*, 2008, **516**(21) 7844-50.

[117] Wenger, S., Seyrling, S., Tiwari, A. and Gratzel, M., Fabrication and performance of a monolithic dye-sensitized TiO_2/Cu(In,Ga)Se_2 thin film tandem solar cell. *Appl. Phys. Lett.*, 2009, **94**(17) 173508-1 - 173508-3.

[118] Ruske, F., Roczen, M., Lee, K., Wimmer, M., Gall, S., Hupkes, J., *et al.*, Improved electrical transport in Al-doped zinc oxide by thermal treatment. *J. Appl. Phys.*, 2010, **107** 013708 – 013708-8.

[119] Gao, L., Li, Q., Luan, W., Kawaoka, H., Sekino, T. and Niihara, K., Preparation and electric properties of dense nanocrystalline zinc oxide ceramics. *J. Am. Ceram. Soc.*, 2002, **85**(4) 1016-8.

[120] Walker, L. S., Pinc, W. R. and Corral, E. L., Powder processing effects on the rapid low-temperature densification of ZrB_2-SiC ultra-high temperature ceramic composites using spark plasma sintering. *J. Am. Ceram. Soc.*, 2012, **95**(1) 194-203.

[121] Jin, Z.-C., Hamberg, I. and Granqvist, C. G., Optical properties of sputter-deposited ZnO:Al thin films. *J. Appl. Phys.*, 1988, **64**(10), 5117.

[122] Wu, M.-W., Two-step sintering of aluminum-doped zinc oxide sputtering target by using a submicrometer zinc oxide powder. *Ceram. Int.*, 2012, **38**(8) 6229-34.

[123] Haug, F.-J., Soderstrom, T., Python, M., Terrazzoni-Daudrix, V., Niquille, X. and Ballif, C., Development of micromorph tandem solar cells on flexible low-cost plastic substrates. *Sol. Energy Mater. Sol. Cells*, 2009, **93**(6-7), 884-7.

[124] Águas, H., Ram, S. K., Araujo, A., Gaspar, D., Vicente, A., Filonovich, S. A., Fortunato, E., Martins, R. and Ferreira, I., Silicon thin film solar cells on commercial tiles. *Energy & Environmental Science*, 2011, **4**(11) 4620-32.

[125] Beyer, W., Hupkes, J. and Stiebig, H., Transparent conducting oxides for thin film silicon photovoltaics. *Thin Solid Films*, 2007, **516**(2-4) 147-54.

[126] Muller, J., Rech, B., Springer, J. and Vanecek, M., TCO and light trapping in silicon thin film solar cells. Sol. Energy, 2004, **77**(6) 917-30.

[127] Carlson, D. E. and Wronski, C. R. in: M. H. Brodsky (Ed.), Amorphous Silicon, topics in applied physics, vol. 36, published by Springer in 1979.

[128] Stiebig, H., Kreisel, A., Winz, W., Schultz, N., Beneking, C., Eickhoff, T., Wagner, H. and Meer, M., Proceedings of the IEEE 1st world conference on photovoltaic energy conversion, vol. 1, p. 603, 1994.

[129] Stiebig, H., Siebke, F., Beyer, W., Bencking, C., Rech, B. and Wagner, H., Interfaces in a-Si: H solar cell structures. *Sol. Energy Mater. Sol. Cells*, 1997, **48**(1-4) 351-63.

[130] Canhola, P., Martins, N., Raniero, L., Pereira, S., Fortunato, E., Ferreira, I. and Martins, R., Role of annealing environment on the performances of large area ITO films produced by rf magnetron sputtering. *Thin Solid Films*, 2005, **487**(1-2) 271-6.

[131] Baia, I., Quintela, M., Mendes, L., Nunes, P. and Martins, R., Performances exhibited by large area ITO layers produced by r.f. magnetron sputtering. *Thin Solid Films*, 2005, **337**(1-2) 171-5.

[132] Anna Selvan, J. A., Delahoy, A. E., Guo, S. and Li, Y. M., A new light trapping TCO for nc-Si:H solar cells. *Sol. Energy Mater. Sol. Cells*, 2006, **90**(18-19) 3371-6.

[133] Elangovan, E., Goncalves, G., Martins, R. and Fortunato, E., RF sputtered wide work function indium molybdenum oxide thin films for solar cell applications. *Sol. Energy Mater. Sol. Cells*, 2009, **83**(5) 726-31.

[134] Elangovan, E., Parthiban, S., Goncalves, G., Franco, N., Alves, E., Martins, R., and Fortunato, E., The electronic transport mechanism in indium molybdenum oxide thin films RF sputtered at room temperature. *Eur. Phys. Lett.*, 2012, **97**(3) 36002.

[135] Martins, R., Almeida, P., Barquinha, P., Pereira, L., Pimentel, A., Ferreira, I. and Fortunato, E., Electron transport and optical characteristics in amorphous indium zinc oxide films. *J. Non-Cryst. Solids*, 2006, **352**(9-20) 1471-4.

[136] Sanon, G., Rup, R. and Mansingh, A., Growth and characterization of tin oxide films prepared by chemical vapour deposition. *Thin Solid Films*, 1990, **190**(2) 287-301.

[137] Kambe, M., Matsui, T., Sai, H., Taneda, N., Masumo, K., Takahashi, A., Ikeda, T., Oyama, T., Kondo, M. and Sato, K., 34th IEEE Proc. Photovoltaic Specialists Conf. (PVSC), 2009, p. 001663.

[138] Mass, J., Bhattacharya, P. and Katyar, R. S., Effect of high substrate temperature on Al-doped ZnO thin films grown by pulsed laser deposition. *Mater. Sci. Eng. B*, 2003, **103**(1) 9-15.

[139] Fortunato, E., Nunes, P., Marques, A., Costa, D., Águas, H., Ferreira, I., Costa, M. E. V. *et al.* Transparent, conductive ZnO:Al thin film deposited on polymer substrates by RF magnetron sputtering. *Surf. Coat. Technol.*, 2002, **151–152** 247–51.

[140] Minami, T., Nanto, H. and Takata, S., Highly Conductive and Transparent Aluminum Doped Zinc Oxide Thin Films Prepared by RF Magnetron Sputtering. *Japan. J. Appl. Phys.*, 1984, **23**(2) L280.

[141] Fortunato, E., Ginley, D., Hosono, H. and Paine, D.C., Transparent conducting oxides for photovoltaics. *MRS Bulletin* , 2007, **32** 242-7.

[142] Raniero, L., Ferreira, I., Pimentel, A., Goncalves, A., Canhola, P., Fortunato, E. and Martins, R., Role of hydrogen plasma on electrical and optical properties of ZGO, ITO and IZO transparent and conductive coatings. *Thin Solid Films*, 2006, **511-512** 295-8.

[143] Fortunato, E., Assunção, V., Goncalves, A., Marques, A., Águas, H., Pereira, L., Ferreira, I., Vilarinho, P. and Martins, R., High quality conductive gallium-doped zinc oxide films deposited at room Temperature. *Thin Solid Films*, 2004, **451-452** 443-7.

[144] Lai, K. C., Liu, C. C., Lu, C. H., Yeh, C. H. and Houng, M. P., Characterization of ZnO:Ga transparent contact electrodes for microcrystalline silicon thin film solar cells. *Sol. Energy Mater. Sol. Cells*, 2010, **94**(3) 397-401.

[145] Lai, K. C., Wang, J. H., Lu, C. H., Tsai, F. J., Yeh, C. H. and Houng, M. P., Plasma-induced TCO texture of ZnO:Ga back contacts on silicon thin film solar cells. *Sol. Energy Mater. Sol. Cells*, 2011, **95**(2) 415-8.

[146] Veneri, P. D., Mercaldo, L. V. and Privato, C., Deposition pressure effects on material structure and performance of micromorph tandem solar cells. *Renew. Energy*, 2008, **33**(1) 42-7.

[147] Martins, R., Raniero, L., Pereira, L., Costa, D., Águas, H., Pereira, S., Silva, L., Goncalves, A., Ferreira, I. and Fortunato, E., Nanostructured silicon and its application to solar cells, position sensors and thin film transistors. *Phil. Mag.*, 2009, **89**(28-30) 2699-721.

[148] Fischer, D. *et al.*, Proc. 25th IEEE PVSC (Washington), 1996, p. 1053.

[149] Barquinha, P., Pereira, L., Gonçalves, G., Martins, R. and Fortunato, E., Toward High-Performance Amorphous GIZO TFTs. *J. Electrochem. Soc.*, **156**(3) H161-8.

[150] Caputo, D., Cesare, G. and Tucci, M., Built-in Enhancement in a-Si:H Solar Cell by Chromium Silicide Layer. *IEEE Electron. Device Lett.*, 2010, **31**(7) 689-91.

[151] Rached, D. and Mostefaoui, R., Influence of the front contact barrier height on the Indium Tin Oxide/ hydrogenated p-doped amorphous silicon heterojunction solar cells. *Thin Solid Films*, 2008, **516**(15) 5087-92.

[152] Dutta, U. and Chatterjee, P., The open circuit voltage in amorphous silicon *p-i-n* solar cells and its relationship to material, device and dark diode parameters. *J. Appl. Phys.*, 2004, **96** 2261.

[153] Haug, F.-J., Soderstrom, T., Cubero, O., Terrazzoni-Daudrix, V. and Ballif, C., Influence of the ZnO buffer on the guided mode structure in Si/ZnO/Ag multilayers. *J. Appl. Phys.*, 2009, **106** 044502.

[154] Yue, G. Z., Sivec, L., Owens, J. M., Yan, B., Yang, J. and Guha, S., Optimization of back reflector for high efficiency hydrogenated nanocrystalline silicon solar cells. *Appl. Phys. Lett.*, 2009, **95** 263501.

[155] Snyder, G. J. and Toberer, E.S., Complex thermoelectric materials. *Nature Mater.*, 2008, **7** 105-14.

[156] Vineis, C. J., *et al.*, Nanostructured Thermoelectrics: Big efficiency gains from small features. *Adv. Mater.*, 2010, **22**(36) 3970-80.

[157] Vaqueiro, P. and Powell, A. V., Recent developments in nanostructured materials for high-performance thermoelectrics. *J. Mater. Chem.*, 2010, **20**(43) 9577-84.

[158] Meyer, B. K. and Klar, P. J., Sustainability and renewable energies - a critical look at photovoltaics. *Phys. Status Solidi (RRL) - Rapid Research Letters*, 2011, **5**(9) 318-23.

[159] Jung, K. -H., *et al.*, Phase analysis and thermoelectric properties of $Zn_{1-x}M_xO$ (M = Al, Ga) samples. *Surf. Interface Anal.*, 2012, **44**(11-12) 1507-10.

[160] Takemoto, H., *et al.*, Thermoelectric Properties of $Zn_{1-(x+y)}Ga_xIn_yO$ (x + y = 0.007) system. *Procedia Eng.*, 2012, **36** 434-8.

[161] Teehan, S., Efstathiadis, H. and Haldar, P., Thermoelectric power factor enhancement of AZO/In-AZO quantum well multilayer structures as compared to bulk films. *J. Alloy. Compd.*, 2012. **539**: p. 129-136.

[162] Takeda, M., *et al.*, Improvement of thermoelectric properties of alkaline-earth hexaborides. J. Solid State Chem., 2006. **179**(9) 2823-6.

[163] Izaki, R., *et al.*, Roll-type thermoelectric devices with InN thin films. *Appl. Phys. Lett.*, 2005, **87**(24) 243508.

[164] Fan, P., *et al.*, Thermoelectric properties optimization of Al-doped ZnO thin films prepared by reactive sputtering Zn–Al alloy target. *Appl. Surf. Sci.*, 2013, **284** 145-9.

[165] Li, L., *et al.*, Influence of oxygen argon ratio on the structural, electrical, optical and thermoelectrical properties of Al-doped ZnO thin films. *Physica E Low Dimens. Syst. Nanostruct.*, 2008, **41**(1) 169-74.

[166] Tritt, T. M., Thermal Conductivity: Theory, properties and applications (Physics of Solids and Liquids). ISBN-13: 978-0306483271, Published 2004 by Springer.

[167] Jood, P., *et al.*, Al-doped zinc oxide nanocomposites with enhanced thermoelectric properties. *Nano Lett.*, 2011, **11**(10) 4337-42.

[168] Ma, N., *et al.*, Microstructure and thermoelectric properties of $Zn_{1-x}Al_xO$ ceramics fabricated by spark plasma sintering. *J. Phys. Chem. Solids*, 2010, **71**(9) 1344-9.

[169] Cahill, D. G., Thermal conductivity measurement from 30 to 750 K: the 3ω method. *Rev. Sci. Instrum.*, 1990, **61**(2) 802-8.

[170] Kamiya, T., Nomura, K. and Hosono, H., Present status of amorphous In–Ga–Zn–O thin-film transistors. *Sci. Technol. Adv. Mater.*, 2010, **11**(4) 044305.

[171] Xu, L., Garrett, M.P. and Hu, B., Doping effects on internally coupled Seebeck coefficient, electrical, and thermal conductivities in Aluminum-doped TiO_2. J. Phys. Chem. C, 2012, **116**(24) 13020-5.

[172] Li, L., *et al.*, X-ray photoelectron spectroscopy study and thermoelectric properties of Al-doped ZnO thin films. *J. Electron. Spectrosc.*, 2009 **173**(1) 7-11.

[173] Mele, P., *et al.*, Effect of substrate on thermoelectric properties of Al-doped ZnO thin films. *Appl. Phys. Lett.*, 2013, **102**(25) 253903.

[174] Ohtaki, M., *et al.*, High-temperature thermoelectric properties of $(Zn_{1-x}Al_x)O$. *J. Appl. Phys.*, 1996, **79**(3) 1816.

[175] Bérardan, D., Byl, C. and Dragoe, N., Influence of the preparation conditions on the thermoelectric properties of Al-doped ZnO. *J. Am. Ceram. Soc.*, 2010, **93**(8) 2352-8.

[176] Cheng, H., *et al.*, Characterization of Al-doped ZnO thermoelectric materials prepared by RF plasma powder processing and hot press sintering. *Ceram. Int.*, 2009, **35**(8) 3067-72.

[177] Qu, X., *et al.*, Thermoelectric properties and electronic structure of Al-doped ZnO. *Solid State Commun.*, 2011, **151**(4) 332-6.

[178] Han, L., *et al.*, The influence of α- and γ-Al_2O_3 phases on the thermoelectric properties of Al-doped ZnO. *J. Alloy. Compds.*, 2013, **555** 291-6.

[179] Shannon, R. D., Gillson, J. L. and Bouchard, R. J., Single crystal synthesis and electrical properties of $CdSnO_3$, Cd_2SnO_4, In_2TeO_6 and $CdIn_2O_4$. *J. Phys. Chem. Solids*, 1977, **38**(8) 877-81.

[180] Ingram, B. J., Gonzalez, G. B., Kammler, D. R., Bertoni, M. I. and Mason. T. O., Chemical and structural factors governing transparent conductivity in oxides. *J. Electroceram.*, 2004, **13**(1-3) 167-75.

[181] Young, D. L., Williamson, D. L. and Coutts, T. J., Structural characterization of zinc stannate thin films. *J. Appl. Phys.*, 2002, **91**(3) 1464-71.

[182] Bellingham, J., R., Phillips, W., A. and Adkins, C., J., Intrinsic performance limits in transparent conducting oxides. *J. Mater. Sci. Lett.*, 1992, **11**(5) 263-5.

[183] Young, D.L., Coutts, T. J., Kaydanov, V. I., Gilmore, A. S. and Mulligan, W. P., Direct measurement of density-of-states effective mass and scattering parameter in transparent conducting oxides using second-order transport phenomena. *J. Vac. Sci. Technol. A*, 2000, **18**(6) 2978-85.

[184] Zhang, D. H. And Ma, H.L., Scattering mechanisms of charge carriers in transparent conducting oxide films. *Appl. Phys. A*, 1996, **62**(5) 487-92.

[185] Tahar, R. B. H. and Tahar, N. B. H., Mechanism of carrier transport in aluminum-doped zinc oxide. *J. Appl. Phys.*, 2002, **92**(8) 4498-501.

[186] Pei, Z. L., Zhang, X. B., Zhang, G. P., Gong, J., Sun, C., Huang, R F. and Wen, L. S., transparent conductive ZnO:Al thin films deposited on flexible substrates prepared by direct current magnetron sputtering. *Thin Solid Films*, 2006, **497**(1-2) 20-3.

[187] Erginsoy, C., Neutral impurity scattering in semiconductors. *Phys. Rev.*, 1950, **79**(6) 1013-14.

[188] Ellmer, K. and Wendt, R., D.c. and r.f. (reactive) magnetron sputtering of ZnO:Al films from metallic and ceramic targets: a comparative study. *Surf. Coat. Technol.*, 1997, **93**(1) 21-6.

[189] Schlott, M., et. al, Method of preparing indium oxide / tin oxide target for cathodic sputtering, Patent US 6187253, Leybold Materials GmbH (2001).

[190] Schlott, M., *et. al*, Annealing powder mixture consisting of coprecipitated indium oxide and tin oxide to form solid solution of specified grain size, partially reducing, compacting by hot isostatic pressing, Patent US 6187253/B1, Leybold Materials GmbH (2001).

[191] Cai, K. F., Muller, E., Drasar, C. and Mrotzek, A., Preparation and thermoelectric properties of Al-doped ZnO ceramics. *Mater. Sci. Eng. B*, 2003, **104**(1-2) 45-8.

[192] Tsubota, T., Ohtaki, M., Eguchi, K. and Arai, H., Thermoelectric properties of Al-doped ZnO as a promising oxide material for high-temperature thermoelectric conversion. *J. Mater. Chem.*, 1997, **7**(1) 85-90.

[193] Kim, B. C., *et al.*, M., Effect of phase transformation on the densification of coprecipitated nanocrystalline indium tin oxide powders. *J. Am. Ceram. Soc.*, 2002, **85**(8) 2083-8.

[194] Ganesan, V., Rosentrater, K. A. and Muthukumarappan, K., Flowability and handling characteristics of bulk solids and powders – a review with implications for DDGS. *Biosystems engineering*, 2008, **101**(4) 425-35.

[195] Carr Jr., R. L., Evaluation flow properties of solids. *Chem. Eng.*, 1965, **72**(3) 163-8.

[196] Chang, P.-K., Tsai, F.-J., Lu, C.-H., Yeh, C.-H., Wang, N.-F. and Houng, M.-P., Improvement of AZO/p-a-SiC:H contact by the p-μc-Si-H insertion layer and its application to a-Si:H solar cells. *Solid-state Electron.*, 2012, **72** 48-51.

[197] Nakashima, K. and Kumuhara, Y., Effect of tin oxide dispersion on nodule formation in ITO sputtering. *Vaccum*, 2002, **66**(3-4) 221-6.

Chapter 6. Final conclusions and further work

The research work presented in this dissertation was divided into three main areas: The synthesis and characterization of the undoped and Al-doped ZnO powders, the production and characterization of the ceramic sputtering targets, and the deposition and characterization of thin films and devices. In this chapter are presented general conclusions about these topics, as well as some further work and perspectives concerning the future developments based on the achieved results.

6.1. Final conclusions

As a start-up company, INNOVNANO is interested in taking advantage of its novel synthesis method to produce high value added materials for specific markets. This dissertation has been developed always taking into account the commercial interests of the company, having as its main purpose the development of Al-doped ZnO ceramic sputtering targets with advantages over the main competitors in the market. Such approach was only possible by the research and development of all the chain between the raw-materials and final application.

Emulsion detonation synthesis method (EDSM) was successfully used in the production of undoped and Al-doped ZnO nanostructured powders. Due to the singular synthesis conditions of EDSM, it was possible to reach AZO powders with Al distributed through the ZnO matrix. Depending on the precursors and synthesis conditions, AZO particles with different morphologies are achieved demonstrating the versatility of EDSM. During this research, metallic precursors were chosen to synthesize the powders used in the production of the ceramic sputtering targets. The selection of such precursors was based on the balance between synthesized powders characteristics and the economic viability associated with the use of each type of precursor.

Chemical, structural and morphological characterizations reveal that for Al-doping levels in the studied range (0.5 – 2.0 wt. % Al_2O_3), the Al content does not influence the detonation process. Besides ZnO, also $ZnAl_2O_4$ phase was identified in the synthesized AZO powders suggesting that Al^{3+} ions occupy the position of Zn^{2+} ions in the ZnO lattice as a substitutional atom reaching the solubility limit during synthesis, reacting the remaining Al with ZnO to form $ZnAl_2O_4$. After synthesis, the subsequent stages of thermal treatment, disaggregation and drying of the powders were optimized to allow high sinterability at lower temperatures. Dilatometric studies performed in samples prepared with the disaggregated nanostructured powders show high sinterability and consequently are the most adequate for fabrication of high density AZO ceramic targets of different compositions.

Concerning the production of AZO targets with enhanced properties, this work was envisaged to meet the requirements of the sputtering industry of highly conductive and full densified targets with a fine and homogeneous microstructure. The effect of different processing parameters in structural, morphological, compositional, electrical, thermal and mechanical properties of the AZO ceramic sputtering targets was investigated and simultaneously correlated with the sputtered TCOs thin films properties. The performance of targets and thin films were confirmed by the deposition of AZO layers in the production of TFSCs, TFTs and as a thermoelectric thin film material.

In a first approach, this research was focused on the production of targets by uniaxial pressing followed by conventional sintering in air. The obtained main conclusions are as follows:

- From the study related to the influence of pressing and sintering conditions of undoped and Al-doped ZnO powders prepared by conventional sintering in air, it was concluded that the compaction stage has a strong impact in the final properties of the targets. Under the same sintering conditions, the compacts of higher green densities allowed obtaining superior final densities and consequently a reduction in sintering temperature required to reach dense targets (> 98 % of the TD). High density targets with controlled grain size and uniformly dispersed spinel phase ($ZnAl_2O_4$) in ZnO matrix can be manufactured by CS at considerably lower temperatures (1050 – 1250 °C, depending on the Al-doping level). The Al addition inhibits the grain growth of ZnO due to the dragging effect of the $ZnAl_2O_4$ spinel phase on the movement of the grain boundaries, being this effect more evident for higher Al-doping levels where the amount of spinel phase is also higher.

- Al-doped ZnO ceramic targets with high density (>99 % of theoretical density), controlled grain size (between 2 and 4 μm depending on the Al content) and well dispersed $ZnAl_2O_4$ phase distribution have optimized electrical conductivity. The lowest electrical resistivities of the targets prepared by CS in air were attained at different temperatures between 1100 – 1300 °C with 2 h of holding time, varying between 3.9×10^{-3} Ωcm and 5.6×10^{-3} Ωcm, respectively for 2.0 and 0.5 wt. % Al_2O_3 doping levels and corresponds to the highest μ_e achieved for each composition. The final density is the main factor affecting the electrical conductivity for targets sintered at low temperatures. At high sintering temperatures, the volatilization of Zn, the abnormal grain growth, and the microstructural inhomogeneity with large and poorly dispersed $ZnAl_2O_4$ grains acting as electron scattering centers, are the main responsible for the deterioration of the electrical properties of the targets.

Due to the high sinterability of the disaggregated powders, no significant differences in terms of structural, morphological and electrical characteristics were observed between the investigated small targets and the scaled-up two inches targets. To assess the behavior of the targets during RF sputtering deposition, four different targets with two inches diameter and Al doping of 0.5, 1.0, 1.5 and 2.0 wt. % Al_2O_3 were conventionally sintered in air under optimized conditions and used in the deposition of AZO thin films at RT. Sputtering parameters were adjusted and sputtered films were characterized and compared in terms of chemical, structural, morphological, optical and electrical properties. The main findings are presented below:

- From the analysis of the sputtered films produced using 98:2 wt. % ($ZnO:Al_2O_3$) composition target, it was found that the deposition rate increases with RF power (P_{RF}) and decrease with deposition pressure (P_{dep}). The electrical resistivity decreases for higher P_{RF} and lower P_{dep} values. Fixing the P_{dep} value at 0.2 Pa, and increasing P_{RF} from 100 W to 250 W, are obtained thicker films with large crystallite sizes, in which both μ_e and N_e were increased while the electrical resistivity is reduced. Sputtered AZO films grow preferentially through the c-axis, perpendicular to the substrate along the (002) plane, showing the typical hexagonal structure of wurtzite. The films are highly transparent in the visible range with a transmittance > 80 %. The optical bandgap energy (E_{opt}) increases

from 3.44 to 3.66 eV with P_{RF} while the near-infra-red (NIR) transmittance decreases when the film thickness and also N_e increase, due to the so called Burstein-Moss effect. Under a constant P_{RF} = 250 W the increase of P_{dep} promotes an enhancement of electrical resistivity resulting in a decrease in both N_e and μ_e. The crystallite size also decreases with P_{dep} resulting in lower μ_e. Therefore the NIR transmittance tends to increase while E_{opt} diminish as P_{dep} increases.

- The influence of Al-doping level on the electrical properties was studied in films deposited at fixed P_{RF} (250 W) and P_{dep} (0.2 Pa). It was observed an increment in N_e and a reduction of μ_e with Al-doping level. Electrical resistivity of the films reduces from 2.8×10^{-3} Ωcm to 1.0×10^{-3} Ωcm as Al-doping concentration increases. The high N_e values ($4 - 5 \times 10^{20}$ cm^{-3}) for AZO films obtained with target of 1.5 and 2.0 wt. % Al_2O_3) explains the obtained low electrical resistivity values, while for thin films sputtered from targets with 0.5 and 1.0 wt. % Al_2O_3, the high μ_e ($14 - 17$ $cm^2V^{-1}s^{-1}$) might be the reason for the lower electrical resistivity values achieved. The crystallite size of the films decreases with Al-doping level, being the segregation of Al (single or combined) in the grain boundaries and/or the formation of stress induced by the substitution of Zn ions for Al smaller ions appointed as the main responsible for this reduction. The Al-doping level has no influence on the transmittances in the visible region which is above 80 %. At higher wavelengths the increase of the Al-content enhances absorption in the NIR region. Optical bandgap energy increases almost linearly from 3.45 to 3.65 eV with the Al-doping level.

In order to improve the characteristics of targets and of corresponding sputtered thin films other sintering processes were investigated. The influence of sintering atmosphere on targets prepared by CS, the use of different pressure-assisted sintering techniques, and a new approach based on AZO films deposition from non-sintered targets were considered. In the following are presented the main conclusions:

- The influence of the sintering atmosphere on the final properties of AZO targets prepared by CS was evaluated using Ar as carrier gas. Both the final density and grain size are independent on the sintering atmosphere, however the electrical properties are different of the ones obtained at air atmosphere: μ_e and N_e increased when sintered in Ar, resulting in the reduction of the electrical resistivity to values between 1.1×10^{-3} Ωcm and 1.6×10^{-3} Ωcm depending on the Al-doping level. This improvement of electrical properties may be caused by both, extrinsic defects induced by the Al substitution into the lattice sites of Zn (Al_{Zn}), and intrinsic defects derived from the formation of non-stoichimetric ZnO_{1-x} with oxygen deficiency. Under similar conditions, thin films sputtered from 2.0 wt. % Al_2O_3 target sintered by CS in Ar are less resistive (8.9×10^{-4} Ωcm) than the corresponding one deposited by CS in air. This improvement is related to the lower oxygen content presented in the films, resulting in the increase of N_e.

- The use of pressure-assisted sintering techniques (hot-pressing (HP) and spark-plasma-sintering (SPS)) reduced considerably the sintering temperature and consequently the final grain size of the targets. Full density targets with electrical resistivity of $\sim 3 - 5 \times 10^{-4}$ Ωcm and grain sizes between 0.9 – 1.2 μm (obtained with AZO targets of 2.0 wt. % Al_2O_3 sintered by HP and SPS) were manufactured. Independently on the composition the films

produced with targets prepared by HP and SPS show electrical resistivity between 6 – 7 × 10^{-4} Ωcm. A complementary study concerning the influence of substrate temperature during deposition was performed using a 3" hot-pressed target with 0.5 wt. % Al_2O_3. The obtained data shows that sheet resistance decreases slightly with increasing temperature up to 300 °C due to the enhancement of crystallite size. Above 300 °C the sheet resistance increases dramatically. Overall study showed that high quality films were sputtered at RT demonstrating that this material is ideally suited for temperature-sensitive applications.

- Non-sintered AZO target with a final density of ~ 62 % of TD and 2.0 wt. % Al_2O_3 was successfully used in the deposition of TCO thin films by RF-magnetron sputtering at RT. The lowest resistivity obtained was 6.5×10^{-4} Ωcm for a film thickness of 890 nm (sheet resistance 7.3 Ωsq^{-1}), with μ_e of 16.8 $cm^2V^{-1}s^{-1}$ and N_e of 5.7 × 10^{-20} cm^{-3}. The sputtered films have an average transmittance > 80 % within the visible region and a preferential c-axis orientation, typical of wurtzite structure. These films have been successively applied as a back contact layer of standard glass/SnO2:F/pin–pin/TCO/metal amorphous silicon solar cells and as source/drain contacts of GaInZnO (GIZO) thin film transistors (TFTs). Efficiencies of 11 % (far above the efficiency of 6.3 % obtained with an AZO layer sputtered form a target prepared by CS in air). Compared to the standard solar cell this improvement leads to a 10 % increase in JSC and 20 % in efficiency of the solar cell and also in the EQE. When applied as source/drain contacts in TFTs, it was observed a slightly decrease related to the saturation mobility (from 39 $cm^2V^{-1}s^{-1}$ to 32 $cm^2V^{-1}s^{-1}$) as well as the saturation current, mainly due to a slightly increase of electrical resistance associated to the source/drain electrodes (R_C), reducing the current and the saturation mobility.

- AZO thin films with enhanced thermoelectric (TE) properties were deposited by radio frequency (RF) and pulsed Direct Current (DC) magnetron sputtering at RT, being obtained similar results in AZO films sputtered from conventionally sintered and non-sintered targets both using RF and pulsed DC sputtering. It was demonstrated that crystallite size, film thickness and Al-doping level control the optical, structural and thermoelectric properties of these films. Electrical conductivities up to 4 × 10^4 $(\Omega m)^{-1}$ and Seebeck coefficients up to -134 μVK^{-1} leaded to power factors up to 3.9 x 10^{-4} $Wm^{-1}K^{-2}$. In addition, the low thermal conductivity (<1.19 $Wm^{-1}K^{-1}$) yields a ZT value above 0.1, which is above the state of art for similar materials, almost by a factor of three.

The quality of the manufactured targets was also evaluated in terms of thermal and mechanical properties. Depending on targets characteristics, thermal conductivity (k) values between 30 and 45 $W.m^{-1}.K^{-1}$ were reached at RT, decreasing ~ 50 % at 300 °C. These values are higher than the ones of ITO targets (7 – 13 $W.m^{-1}.K^{-1}$ depending on target composition) which is an advantage when using high powers, mainly during DC sputtering deposition. The mechanical properties of the targets show that flexural strength is not affected by the Al-doping between 0.5 and 2.0 wt. % Al_2O_3, with values between 200 and 300 MPa, while the fracture toughness tends to be lower and the hardness has the propensity to increase with the Al-doping level. Hot-pressed samples showed higher flexural strength values than the samples prepared by CS in air, while the fracture toughness and hardness seems to be independent on the sintering technique used. The best compromise between thermal and mechanical properties was obtained for targets prepared by HP.

The scale-up for large-size AZO targets (13.7 cm x 10.7 cm x 0.9 cm) was successfully demonstrated by producing several tiles with a doping level of 2.0 wt. % Al_2O_3 by uniaxial-pressing followed by CS in air. The targets were tested in a Portuguese company, *Solar Plus*, dedicated to the production of a:Si:H TFSC photovoltaic panels. The AZO material was successfully applied as a reflective layer in standard non-transparent TFSCs panels and as a reflective and conductive layer in semi-transparent TFSCs panels.

6.2. Further work

The results obtained during this research work cover the entire chain from the raw materials synthesis until the final application of the sputtered films. It was demonstrated that the properties of the films are strongly correlated with the targets characteristics which in turn depends on the initial powder properties. The development of high quality lab targets passed through the achievement of high density and highly conductive targets with a fine and homogeneous microstructure overcoming several well-known issues related with AZO ceramic targets manufacturing. In summary the main goal of this investigation was reached with the development of a superior product, placing INNOVNANO in a good position to enter in the market of AZO sputtering targets production.

However, as in any research work, several questions and paths still remain unanswered and unexplored. Based on the results presented herein and potential market opportunities for INNOVNANO, some recommendations for further work are suggested below:

- During this research, AZO was used in the manufacturing of several devices. At a lab scale, was applied in TFSCs, TFTs and as a thermoelectric layer, while industrially was used in the production of TFSCs. However, only non-sintered and conventionally sintered (in air) targets were used. Further work regarding the utilization of targets prepared by SPS and mainly by HP should be considered, both in lab and industrial scale devices fabrication. Here, the development of large tiles produced under controlled atmosphere must be taken into account.

- This investigation was focused on the production of lab and industrial planar targets. The well-known issues related with the reduced lifetime of industrial targets due to the large amount of wasted material (preferential sputtered zones), led to the development of a new type of targets known as rotatable (tubular) sputtering targets. These targets have been used mainly in the deposition of large area thin films (industrial production), being expected the entire replacement of the planar targets market very short. Thus, for a possible entry in the industrial targets market, is essential for INNOVNANO to develop high quality rotatable AZO targets. Here, air plasma spray (APS) appears as the main technique used in the production of rotatable AZO targets. Once the best quality targets produced in this work were sintered under reduced atmosphere, controlled atmosphere plasma spraying (CAPS) may be a good alternative to achieve rotatable AZO targets with improved quality.

- During the production of TFSCs AZO layer was always applied as a back contact TCO. Due to their outstanding electrical and optical properties (mainly the ones sputtered from

targets produced by HP and SPS), the deposited AZO TCOs are also a good alternative over SnO_2:F and ITO as a front contact in TFSCs. In this field, besides the already tested a-Si:H, also CIGS TFSCs should be considered, since AZO is already the widely used front TCO material in this kind of cells. Finally, architectural and window glasses industries are great consumers of this kind of TCOs films, which are essentially deposited by sputtering. All these applications are good market opportunities for INNOVNANO and should be considered for both planar and rotatable (after development) industrial sputtering targets.

- Going against all theories concerning the characteristics that a high quality AZO ceramic target should have, low-cost non-sintered AZO lab targets were manufactured and successfully used in the deposition of TCO thin films using both RF and DC magnetron sputtering. Even considering the main drawbacks of this kind of targets (low deposition rate, poor mechanical, thermal, and electrical properties), which preclude their use in industrial DC sputtering systems, it´s important for INNOVNANO to have a deeper knowledge about the mechanism behind the huge enhancement of a-Si:H TFSCs performance. Confirmed the good results and their causes, the next approach should pass by the improvement of the mechanical and thermal properties of the targets without affect their singular characteristic, having in mind a possible entry in the lab targets market with a low-cost non-sintered AZO target.

- During this investigation only AZO thin films were characterized as a thermoelectric material. However, AZO ceramics have also been widely investigated as a high-temperature thermoelectric material for power harvesting from heat. The knowledge about the structural, morphological, compositional, electrical and thermal characteristics of AZO ceramic targets acquired during this work can be applied in the development of AZO ceramics with enhanced thermoelectric properties broadening the range of applications and possible markets of this product.

- Sputtering was used to efficiently produce TCOs without intentional substrate heating. However, this does not invalidate that other techniques are explored for the production of these materials. In this field, several low-cost solution deposition techniques, such as spin-coating, spray pyrolysis or ink-jet assumes themselves as alternatives for the production of thin films. Here AZO nanopowders synthesized by EDSM using nitrates as precursors appear as the best approach.

- Finally, the production of sputtering targets should not be restricted to AZO. INNOVNANO needs to be focused on the market requirements concerning the metal oxide ceramic targets, without neglecting the limitations and advantages of its synthesis process. Even considering that targets specifications vary from one material to another, the know-how acquired in terms of ceramic targets manufacturing is transversal and transposable to the development and production of different metal oxide sputtering targets.

As a final note, it is relevant to point out that the work developed in the course of this dissertation makes a bridge between research and industry, worlds often considered opposites, but perfectly combined and complemented throughout this thesis.